Universidade de Brasília
Instituto de Geociências
Programa de Pós-graduação em Geologia

Late Cenozoic co-evolution of tectonics, weathering, and climate in the Amazon Basin: Insights from neodymium and hafnium isotopes

GABRIEL RIBEIRO MOIZINHO

Orientador: Prof. Dr. Roberto Ventura Santos

Co-orientadores: Prof. Dr Martin Roddaz (UT) e Dr. Germain Bayon (IFREMER)

TESE DE DOUTORADO N° 224

Brasília, 12 de Dezembro de 2025

Universidade de Brasília
Instituto de Geociências
Programa de Pós-graduação em Geologia

Co-evolução entre tectônica, intemperismo e clima no Cenozoico Superior da Bacia Amazônica: evidências a partir dos isótopos de neodímio e háfnio

Late Cenozoic co-evolution of tectonics, weathering, and climate in the Amazon Basin: Insights from neodymium and hafnium isotopes

GABRIEL RIBEIRO MOIZINHO

Tese em cotutela, apresentada ao Programa de Pós-Graduação em Geologia – Universidade de Brasília (UnB) e à Universidade de Toulouse (UT), como requisito parcial obrigatório para a obtenção do título de Doutor em Geologia.

Área de concentração: Geologia Regional

Orientador: Prof. Dr. Roberto Ventura Santos

Co-orientadores: Prof. Dr. Martin Roddaz e Dr. Germain Bayon

Comissão Examinadora:

Prof. Dr. Cristiano Mazur Chiessi (Universidade de São Paulo)

Prof.ª Dr.ª Emmanuelle Pucéat (Université de Bourgogne Franche-Comté)

Prof.ª Dr.ª Lucieth Cruz Vieira (Universidade de Brasília)

Dr.ª Nathalie Vigier (CNRS Cote d'Azur)

Dr.ª Marina Rabineau (CNRS Bretagne et Pays de la Loire)

RÉPUBLIQUE FRANÇAISE
Liberté
Égalité
Fraternité

Ifremer

Université de Toulouse

Doctorat de l'Université de Toulouse

délivré en cotutelle avec Université de Brasília, Brésil

préparé à l'IFREMER, Brest

Intérêt des isotopes du néodyme et de l'hafnium pour déterminer la coévolution de l'altération, du climat et de la tectonique au Cénozoïque supérieur dans le bassin Amazonie

---

Thèse présentée et soutenue, le 12 décembre 2025 par

Gabriel RIBEIRO MOIZINHO

École doctorale

SDU2E - Sciences de l'Univers, de l'Environnement et de l'Espace

PPGG-IG-UnB - Programa de Pós-graduação em Geologia, Instituto de Geociências, Universidade de Brasília

Spécialité

Sciences de la Terre et des Planètes Solides

Unité de recherche

UMR 5563 – GET / UMR 6538 - GEO-OCEAN / PPGG-IG-UnB

Thèse dirigée par

Martin RODDAZ et Roberto VENTURA SANTOS

Composition du jury

M. Cristiano MAZUR CHIESSI, Rapporteur, Universidade de São Paulo

Mme Emmanuelle PUCÉAT, Rapporteure, Université de Bourgogne Franche-Comté

Mme Nathalie VIGIER, Examinatrice, CNRS Cote d'Azur

Mme Lucieth CRUZ VIEIRA, Examinatrice, Universidade de Brasília

Mme Marina RABINEAU, Examinatrice, CNRS Bretagne et Pays de la Loire

M. Martin RODDAZ, Directeur de thèse, Université de Toulouse

M. Roberto V. SANTOS, Directeur de thèse, Universidade de Brasília

M. Germain BAYON, Encandrant de thèse, IFREMER Plouzané

Ficha catalográfica elaborada automaticamente,
com os dados fornecidos pelo(a) autor(a)

RM715l

Ribeiro Moizinho, Gabriel
Late Cenozoic co-evolution of tectonics, weathering and climate in the Amazon Basin: Insights from neodymium and hafnium isotopes / Gabriel Ribeiro Moizinho; orientador Roberto Ventura Santos; co-orientador Martin Roddaz. Brasília, 2025.
385 p.

Tese(Doutorado em Geologia) Universidade de Brasília, 2025.

1. Andes-Amazônia. 2. Hafnio-Neodímio. 3. Intemperismo Químico. 4. Ciclo do carbono. 5. Elementos Terras Rara. I. Ventura Santos, Roberto, orient. II. Roddaz, Martin, co-orient. III. Título.

Agradecimentos

Em primeiro lugar, agradeço aos meus pais, Delma e Valdir, por me incentivarem durante a minha trajetória acadêmica, em especial à minha mãe, que não mediu esforços e sacrifícios para que eu alcançasse meus objetivos. Agradeço também à minha companheira, Ellen, que deixou sua família nos Estados Unidos para estar ao meu lado desde o mestrado em Brasília e posteriormente durante o doutorado na França. Sua paciência, amor e companheirismo fizeram essa jornada muito mais leve e significativa. Não posso deixar de agradecer à Bia, minha melhor amiga e companheira de todas as horas. Eu dedico essa tese à nossa família e aos amigos que deixamos no Brasil e nos Estados Unidos.

O projeto desta tese foi, sem dúvida, um projeto dos sonhos. Trabalhar no sistema Andes-Amazonia e contribuir para um melhor entendimento da relação entre a formação dos Andes e a evolução do maior sistema fluvial do planeta e de como esse processo pode ter influenciado o clima global foi um privilégio. Por isso, agradeço demais aos meus orientadores Roberto Ventura Santos, Martin Roddaz e Germain Bayon por confiarem em mim e me proporcionarem a oportunidade de participar em um projeto dedicado ao estudo de um dos maiores patrimônios naturais do planeta Terra: a Bacia Amazônica.

Para que essa oportunidade fosse possível, contei também com o apoio fundamental dos professores Elton Dantas, Lucieth Cruz Vieira e Afonso Nogueira, que me acolheram durante o início da minha trajetória acadêmica em projetos de iniciação científica e mestrado. Agradeço igualmente os professores Guilherme Gonçalves, Eliza Inez Peixoto, Carlos Emanoel de Souza Cruz, Marco Iannuruberto e Natalia Hauser pelos ensinamentos e discussões ao longo dos meus anos de formação na Universidade de Brasília

Na França tive a oportunidade de expandir meus horizontes e trabalhar ao lado de pessoas brilhantes, incluindo Marina Rabineau, Agnes Baltzer, Daniel Aslanian, Natalia Vazques, Andre Droxler, Thiago Santos, além de muitos outros. Estar no IFREMER me permitiu embarcar em duas expedições, experiências únicas que impactaram profundamente a minha formação científica e pessoal. A todas as tripulações e colegas dessas expedições, deixo o meu sincero agradecimento. Agradeço também à equipe de secretariado do IFREMER, Anne-Marie,

Alexandre e Nathalie, que, com paciência e dedicação, me auxiliaram a navegar pelas águas tortuosas da burocracia francesa.

Por fim, deixo o meu sincero agradecimento aos colegas e amigos que fizemos ao longo dessa caminhada. Felizmente, a lista é extensa, e mencioná-la por completo correria o risco de cometer a injustiça de esquecer alguém. Ainda assim, não posso deixar de agradecer de forma especial a Will e Johanna.

O presente trabalho foi realizado com apoio da Coordenação de Aperfeiçoamento de Pessoal de Nível Superior – Brasil (CAPES) – Código de Financiamento 001 e do projeto ECLIP-SED da *Agence Nationale de la Recherche* (ANR-20-01-CE).

Resumo

A Bacia Amazônica, o maior sistema fluvial da Terra, desempenha um papel fundamental na regulação dos fluxos globais de sedimentos, nos ciclos biogeoquímicos e no clima a longo prazo. No entanto, o exato momento e os mecanismos por trás de sua integração transcontinental, bem como as interações entre tectonismo, clima e intemperismo, permanecem incompletamente compreendidos. Esta tese aplica um conjunto de traçadores geoquímicos, incluindo padrões de elementos terras raras (ETR) e isótopos de neodímio (Nd) em frações pareadas de argilas e Fe-(oxi-hidróxidos) (FeOOH), juntamente com isótopos de háfnio (Hf) em argilas detríticas, tanto em sedimentos fluviais modernos quanto em um registro de 4.800 m do delta submarino do Amazonas (poço BP-3). O objetivo principal é reconstruir a evolução do transporte sedimentar, do intemperismo e do ciclo do carbono ao longo do Cenozoico superior na maior bacia tropical do planeta. Primeiro, o trabalho de calibração com sedimentos modernos coletados durante a expedição AMANAUS 2023 demonstra que as frações de argila e FeOOH registram aspectos complementares do intemperismo continental. As diferenças isotópicas de Nd entre essas fases (ΔεNd) constituem um traçador sensível capaz de distinguir o intemperismo de silicatos daquele de rochas sedimentares, enquanto os padrões de distribuição dos ETR permitem identificar os diferentes processos de formação das fases de FeOOH transportadas pelos rios, seja como precipitados secundários formados durante o intemperismo de silicatos, produtos oxidativos do intemperismo de pirita ou FeOOH marinho antigo retrabalhado pela erosão. Esses resultados validam o uso combinado de proxies das frações argilosas e FeOOH para distinguir o intemperismo de silicatos, que sequestra CO_2 atmosférico, do intemperismo de rochas sedimentares, que pode ser uma fonte de CO_2 para a atmosfera. Um novo modelo de idade ajustado astronomicamente estende o registro do Leque Amazônico até ~24 Ma, fornecendo a resolução temporal necessária para vincular processos continentais a mudanças globais de clima e nível do mar. As taxas de sedimentação permaneceram baixas durante o Mioceno Tardio, apesar do aumento do soerguimento andino e da precipitação, sugerindo um armazenamento significativo de sedimentos em bacias continentais. Em contraste, o Plioceno Inicial testemunhou um aumento de uma ordem de magnitude nas taxas de acumulação, sincrônico ao aumento do nível do mar e à intensificação das chuvas. Os isótopos de Nd das argilas revelam uma evolução em etapas da integração da drenagem: exportação andina inicial em ~12 Ma, captura progressiva das cabeceiras andinas centrais entre 7–4 Ma e estabilização em um sistema duplo Solimões–Madeira após 4 Ma. Nossos proxies também registram uma contribuição persistente de FeOOH derivado do intemperismo oxidativo de folhelhos negros até ~4,5 Ma, após o que as assinaturas de FeOOH e os isótopos de Hf indicam uma transição para um intemperismo predominantemente de silicatos sob condições quentes e úmidas do Plioceno, intensificando a remoção de CO_2 atmosférico. Em conjunto, esses resultados refinam a cronologia da integração do rio Amazonas, revelam o duplo papel da bacia no ciclo do CO_2 e estabelecem o

Leque Amazônico como um arquivo singular para investigar a evolução acoplada entre tectonismo, intemperismo e clima. Mais amplamente, esta tese destaca a importância dos processos de intemperismo sob as condições tropicais do sistema fonte-depósito Andes–Amazônia no ciclo do carbono em longo prazo e oferece novas abordagens metodológicas para aplicações globais

Résume

Le bassin amazonien, le plus grand système fluvial de la planète, joue un rôle essentiel dans la régulation des flux sédimentaires mondiaux, des cycles biogéochimiques et du climat à long terme. Toutefois, le calendrier et les mécanismes de son intégration transcontinentale, ainsi que les interactions entre tectonique, climat et altération, demeurent encore imparfaitement compris. Cette thèse mobilise un ensemble de traceurs géochimiques, incluant les spectres des éléments terres rares (ETR) et les isotopes du néodyme (Nd) dans des fractions appariées d'argiles et d'oxydes-hydroxydes de fer (FeOOH), ainsi que les isotopes de l'hafnium (Hf) dans les argiles détritiques, appliqués à des sédiments fluviaux modernes et à une carotte de 4 800 m issue du cône amazonien (puits BP-3). L'objectif principal est de reconstituer l'évolution cénozoïque tardive du transfert sédimentaire, de l'altération continentale et du cycle du carbone au sein de la plus vaste région tropicale du globe. Les travaux de calibration réalisés sur des sédiments modernes prélevés lors de la campagne AMANAUS 2023 montrent que les fractions argileuses et FeOOH enregistrent des aspects complémentaires de l'altération continentale. Les différences isotopiques de Nd entre ces phases ($\Delta\varepsilon$Nd) constituent un traceur sensible permettant de distinguer l'altération des silicates de celle des roches sédimentaires, tandis que les distributions des ETR identifient les différentes voies de formation des phases FeOOH transportées par les rivières, qu'il s'agisse de précipités secondaires issus de l'altération des silicates, de produits oxydants de la pyrite ou de FeOOH marins anciens remobilisés par l'érosion. Ces résultats valident l'utilisation combinée des proxys argile–FeOOH pour distinguer l'altération des silicates, un puits net de CO_2 atmosphérique, de l'altération des roches sédimentaires, susceptible d'en libérer vers l'atmosphère. Un nouveau modèle d'âge calé astronomiquement prolonge le registre du cône amazonien jusqu'à environ 24 Ma, offrant la résolution temporelle nécessaire pour relier les processus continentaux aux variations globales du climat et du niveau marin. Les taux de sédimentation demeurent faibles durant le Miocène supérieur, malgré un soulèvement andin et des précipitations accrus, ce qui suggère un stockage sédimentaire important dans les bassins continentaux. À l'inverse, le début du Pliocène se caractérise par une augmentation d'un ordre de grandeur des taux d'accumulation, synchronisée avec la hausse du niveau marin et l'intensification des précipitations. Les isotopes de Nd des argiles révèlent une évolution progressive de l'intégration du réseau hydrographique : export andin initial vers ~12 Ma, capture partielle des têtes de bassin andines centrales entre 7 et 4 Ma, puis stabilisation d'un système double Solimões–Madeira après 4 Ma. Nos proxys indiquent également une contribution persistante de FeOOH issu de l'altération oxydante de schistes noirs jusqu'à ~4,5 Ma, suivie d'une transition vers un FeOOH majoritairement dérivé de l'altération des silicates sous les conditions chaudes et humides du Pliocène, renforçant la séquestration du CO_2 atmosphérique. Ensemble, ces résultats affinent la chronologie de l'intégration du fleuve Amazone, révèlent le double rôle du bassin dans le cycle global du carbone et établissent le

cône amazonien comme une archive unique pour explorer l'évolution couplée de la tectonique, de l'altération et du climat. Plus largement, cette thèse met en évidence l'importance des processus d'altération sous les conditions tropicales du système source-à-puits Andes–Amazone dans la régulation à long terme du cycle du carbone terrestre et propose de nouveaux cadres méthodologiques applicables à l'échelle mondiale.

Abstract

The Amazon Basin, the largest fluvial system on Earth, plays a fundamental role in regulating global sediment fluxes, biogeochemical cycles, and long-term climate. Yet, the timing and mechanisms behind its transcontinental integration, and the interplay between tectonics, climate, and weathering, remain incompletely resolved. This thesis applies a suite of geochemical tracers, including rare earth element (REE) patterns and neodymium (Nd) isotopes in paired clay and Fe-(oxyhydr)oxide (FeOOH) fractions, together with hafnium (Hf) isotopes in detrital clays, to both modern river sediments and a 4,800-m-long record from the Amazon Fan (BP-3 well). The overarching goal is to reconstruct the late Cenozoic evolution of sediment routing, weathering, and carbon cycling across the world's largest tropical basin. Calibration work on modern sediments collected during the 2023 AMANAUS cruise demonstrates that clays and FeOOH fractions record complementary aspects of continental weathering. Nd isotopic offsets between these phases (ΔεNd) serve as a sensitive tracer for distinguishing silicate from sedimentary rock weathering, while REE distribution patterns effectively identify the formation pathways of FeOOH phases transported by rivers, whether as secondary precipitates produced during silicate weathering, as oxidative products of pyrite weathering, or as ancient marine FeOOH reworked during erosion. These results validate the combined use of clay and FeOOH proxies to disentangle silicate weathering, a net sink of atmospheric CO_2, from sedimentary rock weathering, which can release CO_2 to the atmosphere. A new astronomically tuned age model extends the Amazon Fan record back to ~24 Ma, providing the temporal resolution needed to link continental processes to global climate and sea-level changes. Sedimentation rates remained low during the Late Miocene despite intensified Andean uplift and precipitation, suggesting substantial sediment storage within continental basins. In contrast, the Early Pliocene witnessed an order-of-magnitude increase in accumulation rates, synchronous with global sea-level rise and enhanced precipitation. Clay Nd isotopes reveal a stepwise evolution of drainage integration: initial Andean export at ~12 Ma, progressive capture of central Andean headwaters between 7–4 Ma, and stabilization into a dual Solimões–Madeira system after 4 Ma. Our proxies further record a persistent FeOOH contribution derived from oxidative weathering of black shales until ~4.5 Ma, after which FeOOH signatures and Hf isotopes indicate a shift toward more silicate-derived weathering under warm and humid Pliocene conditions, intensifying CO_2 drawdown. Together, these findings refine the timing of Amazon River integration, reveal the dual CO_2 role of the basin, and establish the Amazon Fan as a unique archive for exploring the coupled evolution of tectonics, weathering, and climate. More broadly, this thesis highlights the importance of weathering processes under the tropical conditions of the Andes-Amazon source-to-sink system on the long-term carbon cycle and offers new methodological frameworks for global application.

Contents

Resumo 7

Résume 9

Abstract 11

I Introduction 18

Declaration/ Declaração/ Déclaration 19

1.1. Tectonics, weathering, and the long-term CO_2 cycle 21

1.2. Earth's Cenozoic climate evolution 26

1.3. The Andes-Amazon source-to-sink system 28

1.2.1. The Late Cenozoic evolution of Northern South America 36

1.2.2. Neogene climate evolution in South America 39

1.2.3. Weathering events in the Amazon Basin 45

1.4. Geochemical tracers of continental weathering processes 47

1.4.1. Rare Earth Elements 47

1.4.2. Neodymium and Hafnium Isotopes 48

1.4.3. Paired clay and Fe Oxide fraction: a novel proxy 53

1.5. Thesis outline and objectives 59

II Materials and Methods 62

Declaration/ Declaração/ Déclaration 63

2.1. Study sites and sampling 64

2.1.1. Amazon Basin River sediments 65

2.1.2 Neogene sediments of the Upper Madeira Basin 66

2.1.3 The Foz do Amazonas Neogene Deposits 67

2.2. Bulk-rock geochemistry 68

2.3. Sequential extraction of labile Fe oxide phases 69

2.4. Grain-size separation via low-speed centrifugation 71

2.5. Clay Mineralogy 72

2.6. Sample Digestion 72
2.7. Major and trace elements 72
2.8. Hf-Nd Isotopes 78
2.9. Use of generative AI 79
III Tracing black shale weathering using REE and Nd isotopes in riverine Fe oxides: insights from the Amazon Basin 80
3. Declaration/ Declaração/ Déclaration 81
Abstract 82
3.1 Introduction 83
3.2 Materials and Methods 85
3.2.1 Study area and sampling 85
3.2.2 Labile Fe (oxy)hydroxides extraction and detrital clay separation 88
3.2.3 Major and trace elements analysis 89
3.2.4 Nd Isotopes 89
3.3 Results 90
3.3.1 Major and trace elements 90
3.3.2 Nd Isotopes 94
3.4 Discussion 96
3.4.1 Cratonic Domain: Silicate weathering and the input of exogenous radiogenic Nd 96
3.4.2 Solimões Domain: the imprint of ancient marine sedimentary rock weathering 98
3.4.3 Madeira Domain: Sulfide oxidation and MREE enrichment in Fe-Oxides 101
3.4.4 Implications on the utility of REE and Nd isotopes for tracing silicate vs. sedimentary rock weathering on continents 104
3.5 Conclusions 105
IV Orbital and sea-level controls on long-term sediment deposition in the Amazon Fan 106
Declaration/ Declaração/ Déclaration 107
Abstract 108

4.1. Introduction 109
4.2. Regional setting 112
4.3. Methodology 114
4.3.1. 1-BP-3-APS well-log data 114
4.3.2. Prior biochronology of BP-3 Well and a novel astronomical time scale 116
4.3.3. A Bayesian age model approach for the Plio-Pleistocene interval 119
4.4. Results 120
4.5. Discussion 125
4.5.1. Orbital Pacing and Global Mean Sea Level in the Amazon Fan 125
4.5.2. The imprint of orbital forcing on sedimentation rates at the Amazon Fan 129
4.5.3. The Quaternary Ice Ages and the mid-Pleistocene Transition 132
4.6. Conclusions 136
Acknowledgments 137
V The geochemistry of the upper Amazon Fan detrital record from the BP-3 Well 139
Declaration/ Declaração/ Déclaration 140
5.1. Samples 141
5.2. Results 142
5.2.1. Bulk Rock Geochemistry 142
5.2.2. Clay fractions 144
5.3. Zircon Effect 154
5.4. Mineralogical and chemical integrity of the BP-3 Well cuttings 155
5.4.1. Foreword: Drilling muds and their footprint 155
5.4.2. Barium enrichment and possible sources 157
5.4.3. Impacts of exogenous barite on the chemical composition and isotopic systems of the detrital fraction of exploration drill cuttings 160
5.5. Conclusions 164
VI Characterization of leached Fe-Mn fractions in the BP-3 Well and its integrity for tracing continental weathering processes 166

Declaration/ Declaração/ Déclaration 167
6.1. Introduction 168
6.2. Results and Discussion 170
6.2.1. Major and Trace Elements 170
6.2.2. Rare Earth Elements 172
6.2.3. Nd Isotopes 175
6.3. Identification of leached mineral phases 177
6.4. Contributions of different mineral phases to the HH leach REE pool and their impacts on distribution patterns and Nd isotopes 182
6.4.1. REE Budget 182
6.4.2. REE distribution patterns 185
6.4.3. La anomalies and their impact on the concativity index 186
6.4.4. Nd Isotopes 189
6.5 Preservation of easily reducible FeOOH phases under anoxic conditions 191
6.6. Conclusions 192
VII Reconciling Neogene continental and marine records in the Amazon Basin 194
Declaration/ Declaração/ Déclaration 195
Abstract 196
7.1. Introduction 197
7.2. Results and Discussion 200
1.4.1. Onset of Andean sediment supply in the Amazon Fan 200
1.4.2. Stages of a transcontinental Amazon Fan 205
1.4.3. Reconciling continental and marine records of basin evolution 210
7.8. Conclusions 218
VIII Late Cenozoic co-evolution of tectonics, climate, and weathering in the Amazon Basin 220
Declaration/ Declaração/ Déclaration 221
Abstract 222
8.1. Introduction 223

8.2. Materials and methods 226
8.2.1. Study site, age model, and sedimentation rates..... 226
8.2.2. Sample preparation and grain size separation 226
8.2.3. Disentangling silicate vs. sedimentary rock weathering in the geological record 227
8.2.4. Tracing silicate weathering intensity 228
8.3. Results 229
8.4. Discussion 231
8.4.1. Late Cenozoic co-evolution of tectonics, weathering, and climate in the Amazon Basin 231
8.4.2. Implications for the CO_2 cycle 237
9. Conclusions 241
IX Conclusions and perspectives 242

I

Introduction

Declaration/ Declaração/ Déclaration

This thesis forms part of the ANR project *ECLIP-SED* (*Erosion–climate interactions: isotopic constraints from the sedimentary record*), coordinated by Dr. Germain Bayon (IFREMER – *Institut Français de Recherche pour l'Exploitation de la Mer*). The research was carried out under a co-tutelle agreement between the Universidade de Brasília (UnB) and the Université Paul Sabatier – Toulouse III (UPS), with supervision from Prof. Dr. Roberto Ventura Santos (UnB), Prof. Dr. Martin Roddaz (UPS), and Dr. Germain Bayon (IFREMER). The following chapter provides the background and motivation for the work presented in this thesis. It begins with an overview of the links between tectonics, chemical weathering, and the long-term carbon cycle. I then summarize the main features of Cenozoic climate evolution, before turning to the Andes–Amazon source-to-sink system, a key region for investigating these processes. The state of the art on the geological and climatic evolution of the Amazon Basin during the Late Cenozoic is then reviewed. Finally, I introduce the geochemical tracers applied in this study to distinguish between silicate and sedimentary sources and to assess patterns of chemical weathering during mountain-building events and their implications on CO_2 feedbacks.

[PT] Esta tese integra o projeto ANR *ECLIP-SED* (*Erosion–climate interactions: isotopic constraints from the sedimentary record*), coordenado pelo Dr. Germain Bayon (IFREMER – *Institut Français de Recherche pour l'Exploitation de la Mer*). A pesquisa foi desenvolvida em regime de co-tutela entre a Universidade de Brasília (UnB) e a Université Paul Sabatier – Toulouse III (UPS), sob a supervisão do Prof. Dr. Roberto Ventura Santos (UnB), do Prof. Dr. Martin Roddaz (UPS) e do Dr. Germain Bayon (IFREMER). O capítulo a seguir apresenta o contexto e a motivação do trabalho desenvolvido nesta tese. Ele começa com uma visão geral das relações entre tectônica, intemperismo químico e o ciclo do carbono em escala de tempo geológica. Em seguida, são resumidas as principais características da evolução climática do Cenozóico, antes de abordar o sistema fonte-depósito Andes–Amazônia, uma região chave para a investigação desses processos. Na sequência, é revisado o estado da arte sobre a evolução geológica e climática da Bacia Amazônica durante o Cenozóico tardio. Por fim, são apresentados os traçadores geoquímicos empregados neste estudo para distinguir entre fontes

silicáticas e sedimentares e para avaliar os padrões de intemperismo químico durante eventos orogênicos e suas implicações nos feedbacks de CO_2.

[FR] Cette thèse s'inscrit dans le cadre du projet ANR *ECLIP-SED* (*Erosion–climate interactions: isotopic constraints from the sedimentary record*), coordonné par le Dr. Germain Bayon (IFREMER – *Institut Français de Recherche pour l'Exploitation de la Mer*). La recherche a été réalisée dans le cadre d'une co-tutelle entre l'Université de Brasília (UnB) et l'Université Paul Sabatier – Toulouse III (UPS), sous la direction du Prof. Dr. Roberto Ventura Santos (UnB), du Prof. Dr. Martin Roddaz (UPS) et du Dr. Germain Bayon (IFREMER). Le chapitre suivant présente le contexte et la motivation du travail développé dans cette thèse. Il débute par un aperçu des liens entre tectonique, altération chimique et cycle du carbone à long terme. Les principales caractéristiques de l'évolution climatique du Cénozoïque sont ensuite résumées, avant de se tourner vers le système source-puits Andes–Amazone, une région clé pour l'étude de ces processus. L'état de l'art sur l'évolution géologique et climatique du bassin amazonien au Cénozoïque tardif est ensuite passé en revue. Enfin, les traceurs géochimiques utilisés dans cette étude sont introduits, permettant de distinguer les apports silicatiques des apports sédimentaires et d'évaluer les dynamiques d'altération chimique au cours des événements orogéniques ainsi que leurs implications sur les rétroactions du CO_2.

1.1. Tectonics, weathering, and the long-term CO_2 cycle

A central question in Earth sciences is how tectonics, erosion, and climate interact to regulate atmospheric CO_2 over geological timescales. The late Cenozoic has long been used as a benchmark for this discussion, with global cooling often attributed to enhanced chemical weathering triggered by tectonic uplift (Caves Rugenstein et al., 2019; Goddéris and François, 1996; Misra and Froelich, 2012; Raymo and Ruddiman, 1992; Willenbring and von Blanckenburg, 2010). Since CO_2 is a key greenhouse gas, its long-term concentrations must have been maintained within relatively stable bounds: never low enough to trigger complete ocean glaciation, nor high enough to sterilize the planet. These stability points point to feedback mechanisms in the carbon cycle that operate as a thermostat for the Earth (**Fig. 1.1**).

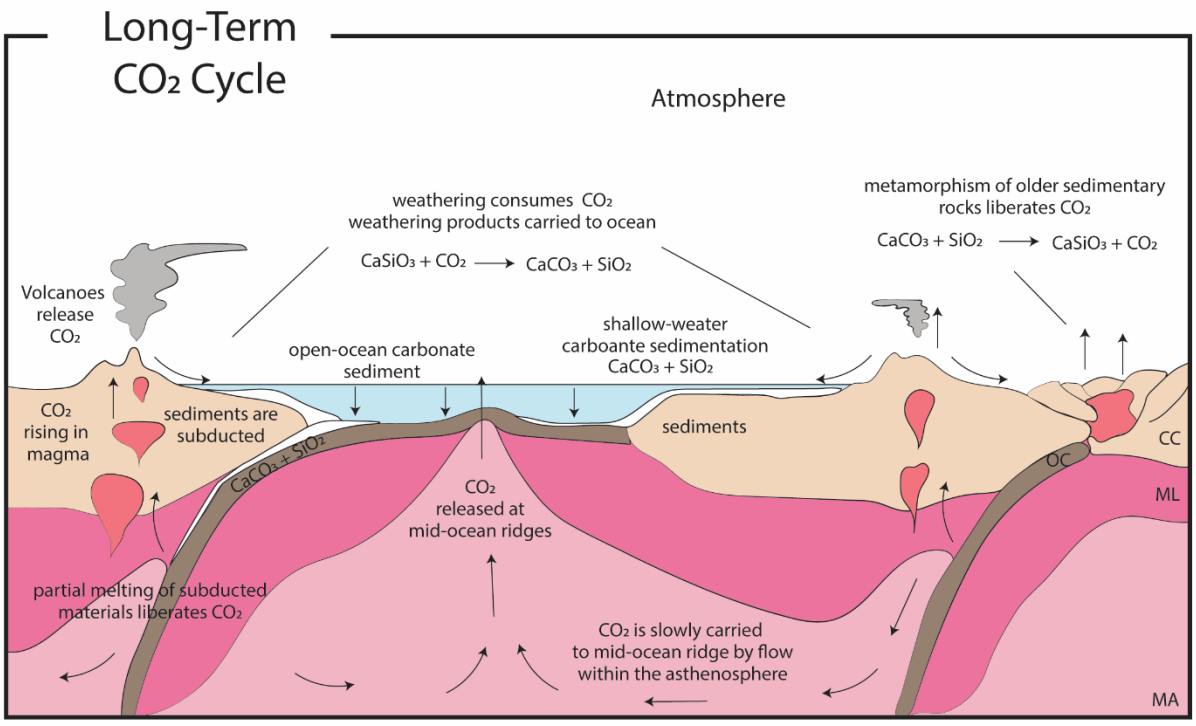

Figure 1.1. Schematic representation of the long-term carbon cycle showing the flows (arrows) of carbon that are important on time scales larger than 100 kyr. Carbon is added to the atmosphere through metamorphic degassing and volcanic activity on land and at mid-ocean ridges. Atmospheric carbon is used in the weathering of silicate minerals in a temperature-sensitive dissolution process; the products of this weathering are carried by rivers to the oceans. Carbonate sedimentation extracts carbon from the oceans and ties it up in the form of limestone. CC = continental crust, OC = oceanic crust, ML = mantle lithosphere; MA = mantle asthenosphere. Adapted from Berner et al. (1983).

On million-year timescales, geological processes dominate the balance of CO_2 sources and sinks (Berner, 1999; Trapp-Müller et al., 2025). Inputs include volcanism at mid-ocean ridges and arcs, metamorphic decarbonation, thermal breakdown of organic matter during burial, and oxidative weathering of organic-rich shales (Hilton and West, 2020). On the other hand, removal occurs primarily via the hydrolysis of Ca- and Mg-silicate minerals, or simply silicate weathering, which releases Ca^{2+}, Mg^{2+}, and HCO_3^- to rivers (**Table 1.1**). These solutes are ultimately buried as marine carbonates, locking away CO_2 (Berner et al., 1983).

Table 1.1. Summary of major chemical weathering pathways, their representative minerals, simplified reactions, and net effect on atmospheric CO_2

Rock / Mineral Type	Example Mineral	Simplified Weathering Reaction	Net CO_2 Effect
Silicate minerals	$CaSiO_3$ (wollastonite, proxy for feldspar/pyroxene)	$CaSiO_3 + 2\ CO_2 + 3\ H_2O \rightarrow Ca^{2+} + 2\ HCO_3^- + H_4SiO_4$	Consumes 1 mol CO_2 per mol Ca^{2+} exported (long-term sink after $CaCO_3$ burial)
Fe(II)-silicate weathering	Fe_2SiO_4 (olivine)	$Fe_2SiO_4 + 4\ CO_2 + 4\ H_2O \rightarrow 2\ Fe^{2+} + 4\ HCO_3^- + H_4SiO_4$	Consumes CO_2 if Fe^{2+} → Fe-carbonate burial; neutral if Fe^{2+} oxidizes to Fe^{3+} (acid generation)
Phosphate mineral weathering (carbonic acid)	$Ca_5(PO_4)_3F$ (apatite)	$Ca_5(PO_4)_3F + 4\ CO_2 + 6\ H_2O \rightarrow 5\ Ca^{2+} + 3\ H_2PO_4^- + 4\ HCO_3^- + F^-$	Consumes CO_2 (minor sink, similar to silicates)
Carbonates (carbonic acid weathering)	$CaCO_3$ (calcite)	$CaCO_3 + CO_2 + H_2O \rightarrow Ca^{2+} + 2\ HCO_3^-$	No net CO_2 change (temporary sink in rivers)
Carbonates (sulfuric acid weathering)	$CaCO_3 + H_2SO_4$	$CaCO_3 + H_2SO_4 \rightarrow Ca^{2+} + SO_4^{2-} + CO_2 + H_2O$	Releases 1 mol CO_2 (source)
Sulfide oxidation	FeS_2 (pyrite)	$FeS_2 + 15/4\ O_2 + 7/2\ H_2O \rightarrow Fe(OH)_3 + 2\ SO_4^{2-} + 4\ H^+$	Produces acidity, no direct CO_2 effect — but dissolves carbonates → indirect CO_2 release
Organic matter oxidation	CH_2O (generic organic C)	$CH_2O + O_2 \rightarrow CO_2 + H_2O$	Releases CO_2 (source)

Building on this framework, Raymo and Ruddiman (1992) proposed the uplift–weathering hypothesis: tectonic uplift enhances global silicate weathering by exposing fresh minerals through faulting and denudation, pulverizing rocks via glacial/periglacial grinding, and sustaining high runoff from orographic or monsoonal rainfall. Weathered debris is then transported downstream, where continued reactions in floodplains and lowlands amplify CO_2 drawdown. This idea directly links mountain building with late Cenozoic climate cooling. However, subsequent work has revealed a more complex picture. Chemical weathering rates are not controlled by uplift alone, but also by climate, hydrology, erosion intensity, biological activity,

and lithology. Warm and wet conditions accelerate hydrolysis reactions, whereas arid settings tend to retain solutes in soils (Brady, 1991; Gaillardet et al., 1999; Hilley and Porder, 2008; White and Blum, 1995). The relationship between physical and chemical erosion is non-linear: at moderate denudation rates, chemical weathering scales with erosion in a "supply-limited" regime, but at very high rates, sediments are removed too quickly for extensive alteration, yielding a "kinetically limited" regime (West et al., 2005). Biological activity, from root respiration to microbial release of organic acids, further enhances mineral dissolution, though the role of humic compounds remains debated. Among all controls, lithology exerts the strongest influence: basalts weather more rapidly, granitoids more slowly, while ancient deeply weathered cratons supply little fresh material (Gaillardet et al., 1999).

These complexities underpin the Cenozoic isotope–weathering paradox (Li et al., 2021; Willenbring and von Blanckenburg, 2010). While mountainous regions with high erosion generally exhibit elevated silicate weathering fluxes (West et al., 2005), proxy records (e.g., Sr, Os, Li, Nd isotopes) often suggest more muted global CO_2 variations during major tectonic pulses. A key explanation lies in lithological heterogeneity: active orogens commonly expose not only crystalline basement but also sedimentary cover sequences rich in carbonates, pyrite, and organic matter. Alteration of these rocks can act as a net CO_2 source, offsetting the sink effect of silicate weathering (Torres et al., 2014, 2017; Hilton & West, 2020; Horan et al., 2017; Zondervan et al., 2023). In particular, sulfide oxidation coupled with carbonate dissolution represents a major CO_2 source during orogeny, while oxidation of OC_{petro} releases ~68 MtC yr^{-1} globally, a flux comparable to silicate weathering uptake (Zondervan et al., 2023). Thus, depending on the lithology, mountain belts may act as net CO_2 sources rather than sinks (**Table 1.1**).

For decades, the uplift of the Himalayan–Tibetan system (**Fig. 1.5**) was viewed as the primary driver of late Cenozoic CO_2 decline (France-Lanord and Derry, 1997; Raymo and Ruddiman, 1992). However, despite sustained uplift, Neogene global silicate weathering fluxes appear to have remained relatively invariant (Clift et al., 2024b; Zhang et al., 2025). Instead, the emergence of mafic and ultramafic terrains in tropical arc–continent collision zones has been highlighted as disproportionately effective CO_2 sinks. Arc exposures in Papua New Guinea and Southeast Asia, when subjected to warm and humid climates of the tropics, weather rapidly and have been linked to transitions between nonglacial and glacial climate states (Bayon et al.,

2023; Clift et al., 2024a; Macdonald et al., 2019). Indeed, modern global carbon fluxes confirm that the highest CO_2 consumption occurs in tropical–subtropical regions, which account for ~88% of the global total (**Fig. 1.2**; Zhang et al., 2021).

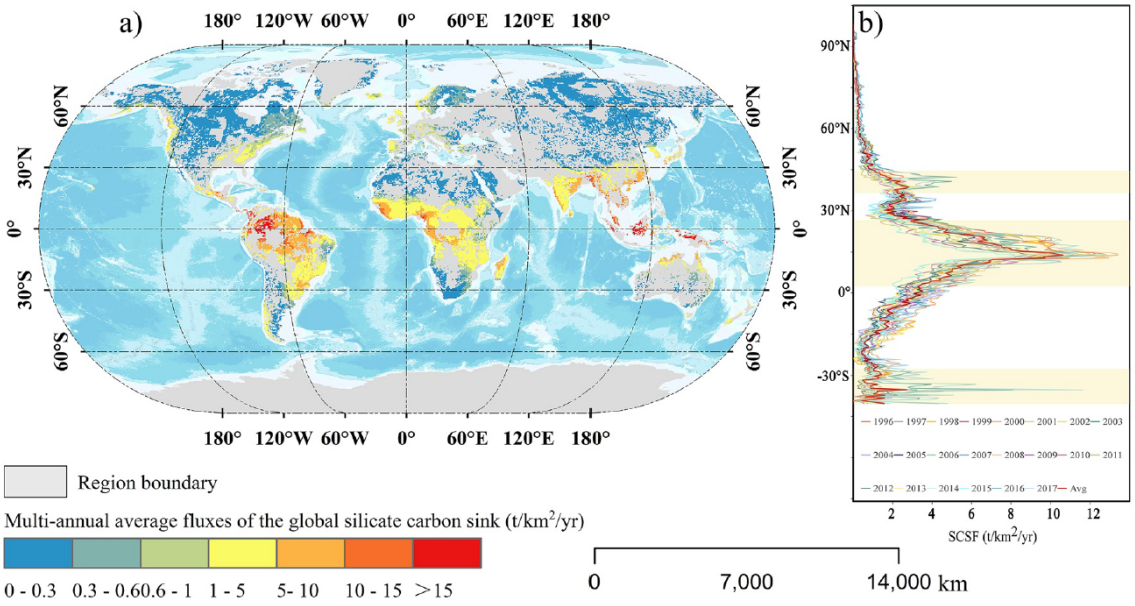

Figure 1.2. Spatial distribution (a) and latitudinal variation (b) of average annual silicate rock weathering carbon sink flux (SCSF) during 1996-2017. Source: **(Zhang et al., 2021)**

In parallel, the spatial domain of chemical weathering has gained renewed attention. While orogens supply vast quantities of reactive minerals, foreland floodplains/lowlands act as dynamic reactors where substantial CO_2 fluxes are generated (**Fig. 1.3**). Quaternary records demonstrate climate-driven alternations between highland- and floodplain-dominated weathering (Yu et al., 2020). In the Amazon Basin, more than half of OC_{petro} oxidation occurs downstream in foreland floodplains, effectively doubling CO_2 release compared with the Andes alone (Dellinger et al., 2023). This highlights the need to account for both highland inputs and lowland transformations in global weathering budgets (Trapp-Müller et al., 2025).

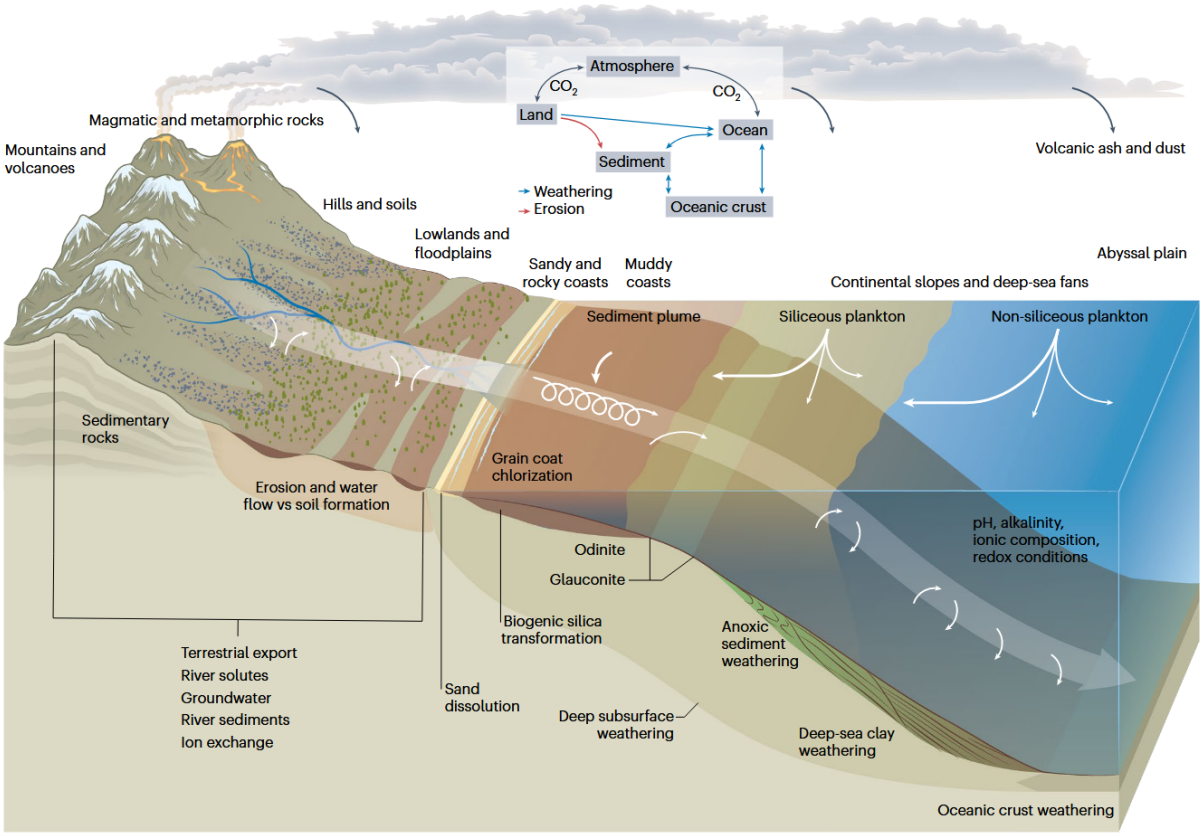

Figure 1.3. Schematic overview of the global weathering–sediment cycle and its link to the carbon cycle. Continental weathering of magmatic, metamorphic, and sedimentary rocks supplies solutes and sediments to rivers, which transport material through lowlands and floodplains until the coastal zones and the open ocean. In marine settings, biogenic inputs, diagenetic reactions, and deep-sea clay and crustal weathering further transform sediments, controlled by pH, alkalinity, ionic composition, and redox conditions. Together, these processes regulate elemental fluxes and the long-term balance of atmospheric CO_2. Source: Trapp-Müller et al., 2025

In summary, uplift and weathering are tightly coupled processes that regulate the long-term carbon cycle. Yet the balance between silicate weathering (a CO_2 sink) and sedimentary weathering (a CO_2 source) and the interplay between highland erosion and lowland reactivity remains uncertain. This forms the core of the Cenozoic isotope–weathering paradox. Addressing this challenge requires tracers capable of disentangling lithological contributions and quantifying their impact on the long-term carbon cycle, which is the central focus of this thesis.

1.2. Earth's Cenozoic climate evolution

Earth's climate over the Cenozoic was shaped by a combination of external and internal drivers operating across multiple timescales. External forcings such as variations in Earth's orbital parameters paced glacial–interglacial cycles (Berger and Loutre, 1994), while shorter-term influences included solar variability and cosmic ray fluxes. Internal Earth system processes provided the background state against which orbital forcing operated. These include long-term changes in atmospheric CO_2 linked to silicate weathering, volcanism, and organic carbon burial (Kump et al., 2000), tectonic uplift and mountain building that reshaped circulation and erosion (Raymo & Ruddiman, 1992), and the opening or closure of oceanic gateways that reorganized global circulation (O'Dea et al., 2016).

At the million-year scale, the Cenozoic climate system was punctuated by several major reorganizations. The onset of Antarctic glaciation at the Eocene–Oligocene boundary (~34 Ma) marked the first large-scale expansion of a continental ice sheet in the Southern Hemisphere (**Fig. 1.4**). This long-term cooling trend was briefly interrupted by the Mid-Miocene Climatic Optimum (MMCO, 17–15 Ma), when global warmth and atmospheric CO_2 (~400–500 ppm) reached levels comparable to near-future projections (Holbourn et al., 2018; Rae et al., 2021). Cooling resumed thereafter, culminating in the expansion of Northern Hemisphere ice sheets during the late Pliocene (~3 Ma) and, later, the Mid-Pleistocene Transition (~1 Ma), which lengthened and intensified glacial cycles (Eldrett et al., 2007; Holbourn et al., 2018; Lisiecki and Raymo, 2005a; Maslin et al., 1998). These global shifts reflected the interplay between CO_2 decline, cryosphere expansion, and feedbacks involving ocean circulation.

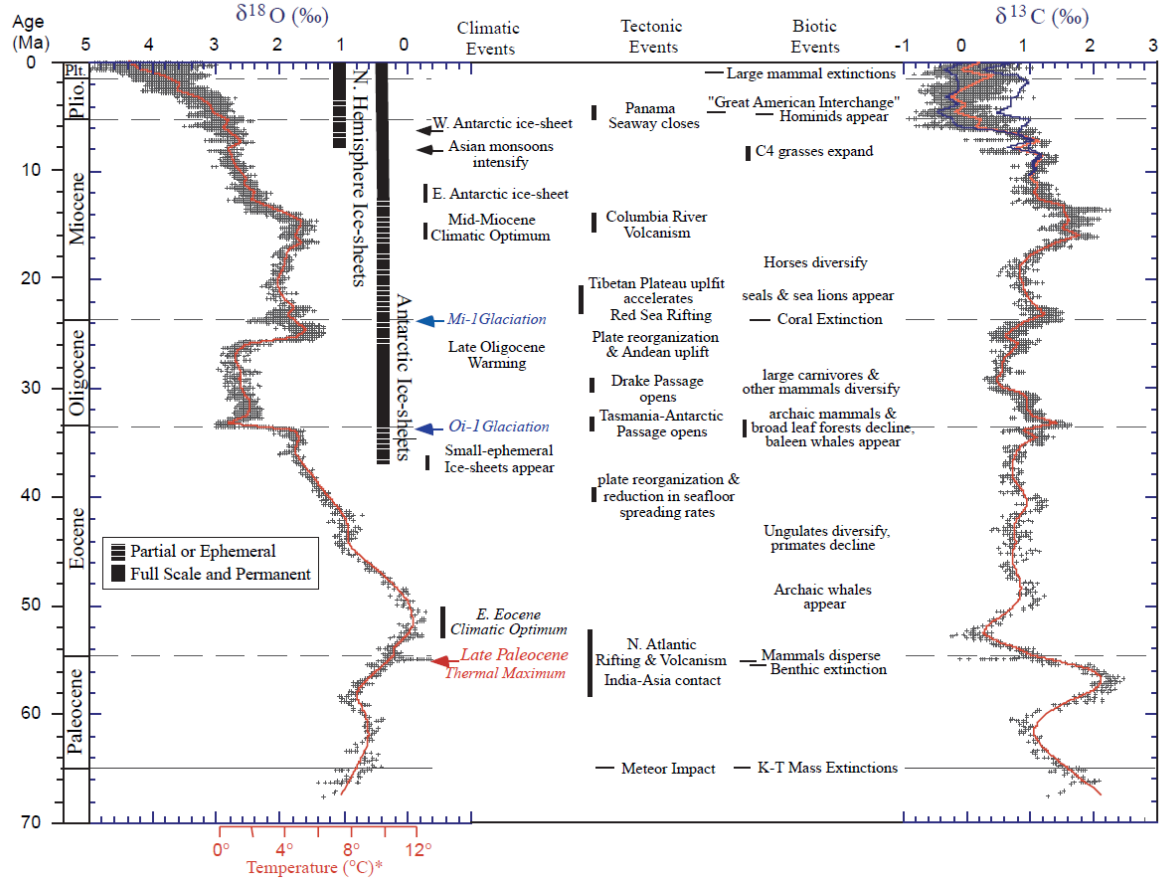

Figure 1.4. Global benthic $\delta^{18}O$ and $\delta^{13}C$ records compiled from >40 DSDP/ODP sites. Data are based on pelagic carbonate-rich sediments and long-lived benthic foraminifera (Cibicidoides, Nuttallides), smoothed with a running mean. The $\delta^{18}O$ curve reflects changes in deep-ocean temperature and ice volume, while the $\delta^{13}C$ record highlights evolving basin-to-basin gradients. Vertical bars provide a qualitative estimate of ice volume relative to the Last Glacial Maximum and major tectonic and biotic events. Source: **(Zachos, 2001)**

Superimposed on this long-term cooling trend was the dynamic behavior of the Intertropical Convergence Zone (ITCZ), the planet's primary tropical rain belt. The ITCZ migrates toward the warmer hemisphere or receives more net energy, thus transmitting high-latitude and ocean circulation anomalies into the tropics (McGee et al., 2018). In particular, variations in the Atlantic Meridional Overturning Circulation (AMOC) strongly modulate cross-equatorial heat transport, shifting the annual-mean ITCZ position northward during strong AMOC states and southward during weak ones (Liu et al., 2024). Northern and central South America lay at the crossroads of these processes. Positioned in the deep tropics, the continent was directly affected by ITCZ migrations, while the progressive uplift of the Andes acted as a powerful amplifier, redistributing rainfall via orographic ascent and creating rain shadows that reshaped regional hydroclimate (Barnes et al., 2012; Ehlers and Poulsen, 2009; Poulsen et al., 2010). The

Amazon Basin, in turn, integrated these climatic and tectonic drivers, transmitting their signal downstream into the sedimentary record of the Atlantic margin (e.g., Amazon Fan and Ceara Rise). Combined with the immense scale of the basin, its contrasting lithologies, and strong gradients in relief and climate, these features make the Andes-Amazon system an unparalleled natural laboratory for investigating tectonic, climatic, and geochemical interactions in a source-to-sink framework.

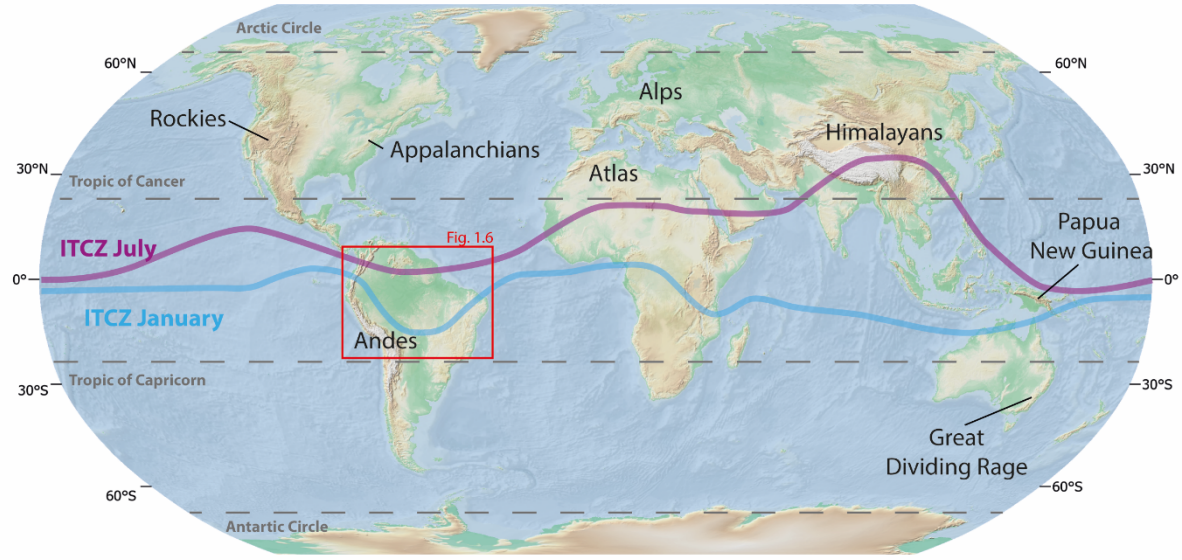

Figure 1.5. Global distribution of major mountain ranges (labeled) and seasonal positions of the Intertropical Convergence Zone (ITCZ), shown for July (purple) and January (blue). The red box highlights the Andes and Amazon Basin region.

1.3. The Andes-Amazon source-to-sink system

The Amazon River Basin is the largest drainage system on Earth, spanning ~6 million km^2 across seven countries and discharging ~200,000 m^3/s of water to the Atlantic Ocean, nearly three times the flow of the Congo, the world's second-largest river (**Fig. 1.6**; Dai and Trenberth, 2002; Richey et al., 1989). It delivers ~1.2 × 10^9 tons of sediment annually, ~90% sourced from the Andes (Meade, 1994; Meade et al., 1985), making it both a major driver of global denudation and a critical component of Earth's hydrological and biogeochemical cycles. Defining the basin's western margin, the Andes rise to over 6,000 m and stretch more than 7,000 km along the Pacific coast of South America. In addition to supplying most of the sediment, the Andes

exert a strong orographic influence on climate: acting as an extensive longitudinal barrier, they force the uplift and condensation of Atlantic-sourced moisture on their eastern slopes, driving high rainfall over the foreland and creating a steep east–west precipitation gradient across tropical South America (e.g., Barnes et al., 2012). Uplift of the orogen also feeds back on atmospheric circulation, intensifying monsoonal systems that enhance erosion and weathering in the upper basin (Ehlers and Poulsen, 2009; Fisher et al., 2023; Poulsen et al., 2010). The Andes are therefore both agents and products of climate change, tightly linking orogen dynamics, weathering processes, and the carbon cycle.

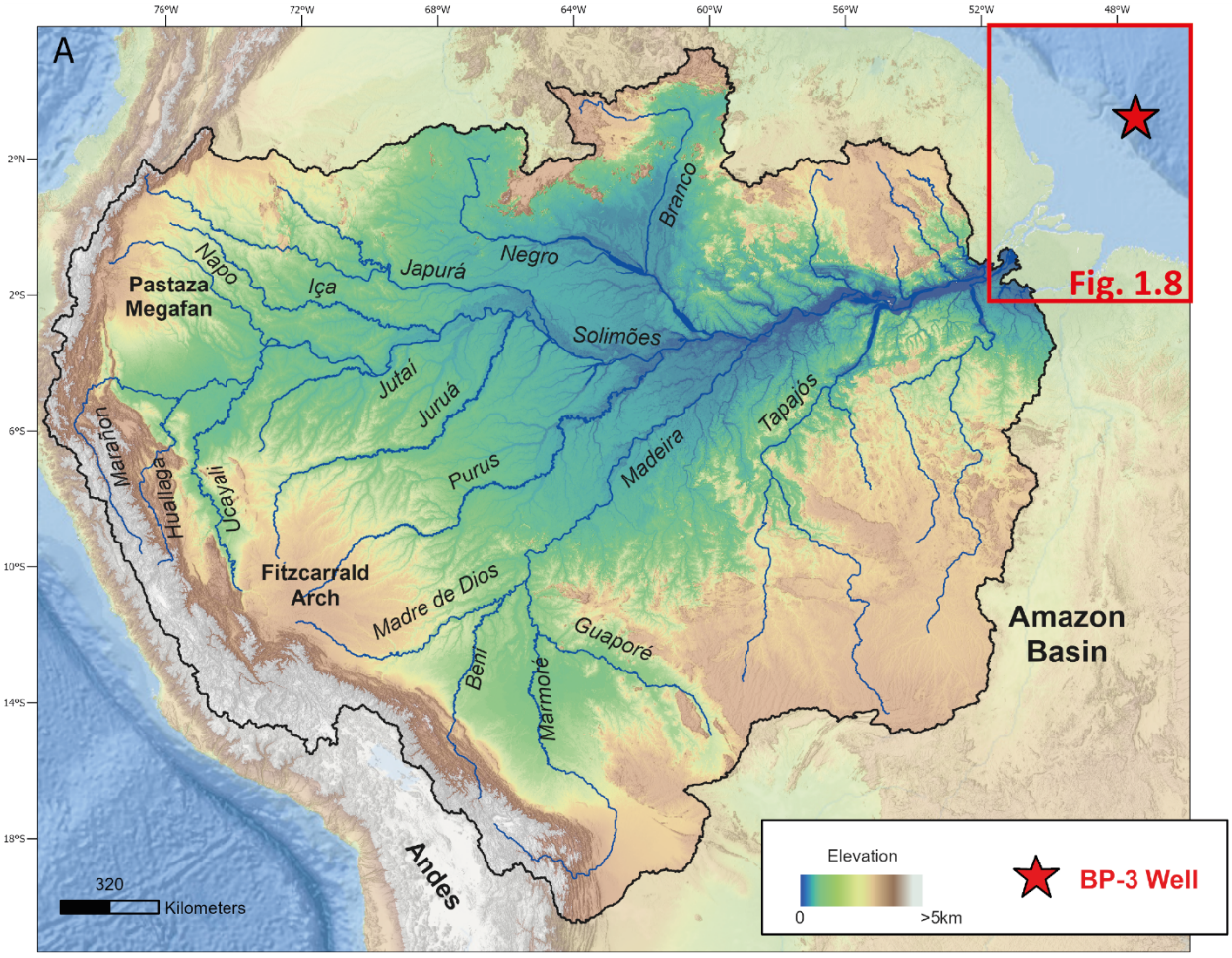

Figure 1.6. Elevation map of Northern South America with focus on the Amazon Basin watershed. The main tributaries of the lower Amazon River are shown along with expressive geomorphic features such as the Pastaza Megafan and the Fitzcarrald Arch.

From a geomorphic and geochemical perspective, the basin can be divided into four main domains: the Andes, the forelands and lowlands, the cratonic shields (Brazilian and Guiana), and the extensive floodplains (**Fig. 1.7A**; (Dellinger et al., 2015; Stallard and Edmond, 1983). Each domain exhibits distinct topographic, lithologic, and hydrological characteristics that together control the basin's sediment production, transport, and weathering regimes.

Andes

The Andean domain, forming the primary sediment source of the basin, encompasses elevations ranging from ~500 m to over 6,700 m (**Figs. 1.6; 1.7A**). It is characterized by steep relief, intense rainfall (150–3,400 mm yr^{-1}; Moquet et al., 2011), and some of the highest erosion rates on Earth. In the north (Peru and Ecuador), the drainage network includes the Napo, Tigre, Morona, Pastaza, Marañón, Huallaga, and Ucayali rivers, tributaries of the Solimões. In the south (Bolivia), the Madre de Dios, Beni, and Mamoré rivers drain toward the Madeira system (**Fig. 1.6**). Lithologically, the Solimões basin includes both sedimentary and intermediate igneous rocks, such as andesites from the active volcanic arc of Ecuador (Stallard & Edmond, 1983; Dosseto et al., 2006b), whereas the Madeira basin is dominated by uplifted Paleozoic silicate sedimentary rocks and minor Tertiary–Quaternary deposits (Moquet et al., 2011). Rivers draining these regions, commonly referred to as *"white waters"* (Gibbs, 1967), carry extremely high suspended particulate matter (SPM; 500–5,000 mg L^{-1}; Guyot et al., 1996; Wittmann et al., 2011) and display silicate weathering rates between 7 and 75 t km^{-2} yr^{-1} (mean ≈ 22; Moquet et al., 2011). The prevailing regime is *kinetically limited*, where erosion outpaces chemical dissolution and primary minerals are exported before reaching equilibrium with surface conditions (West et al., 2005).

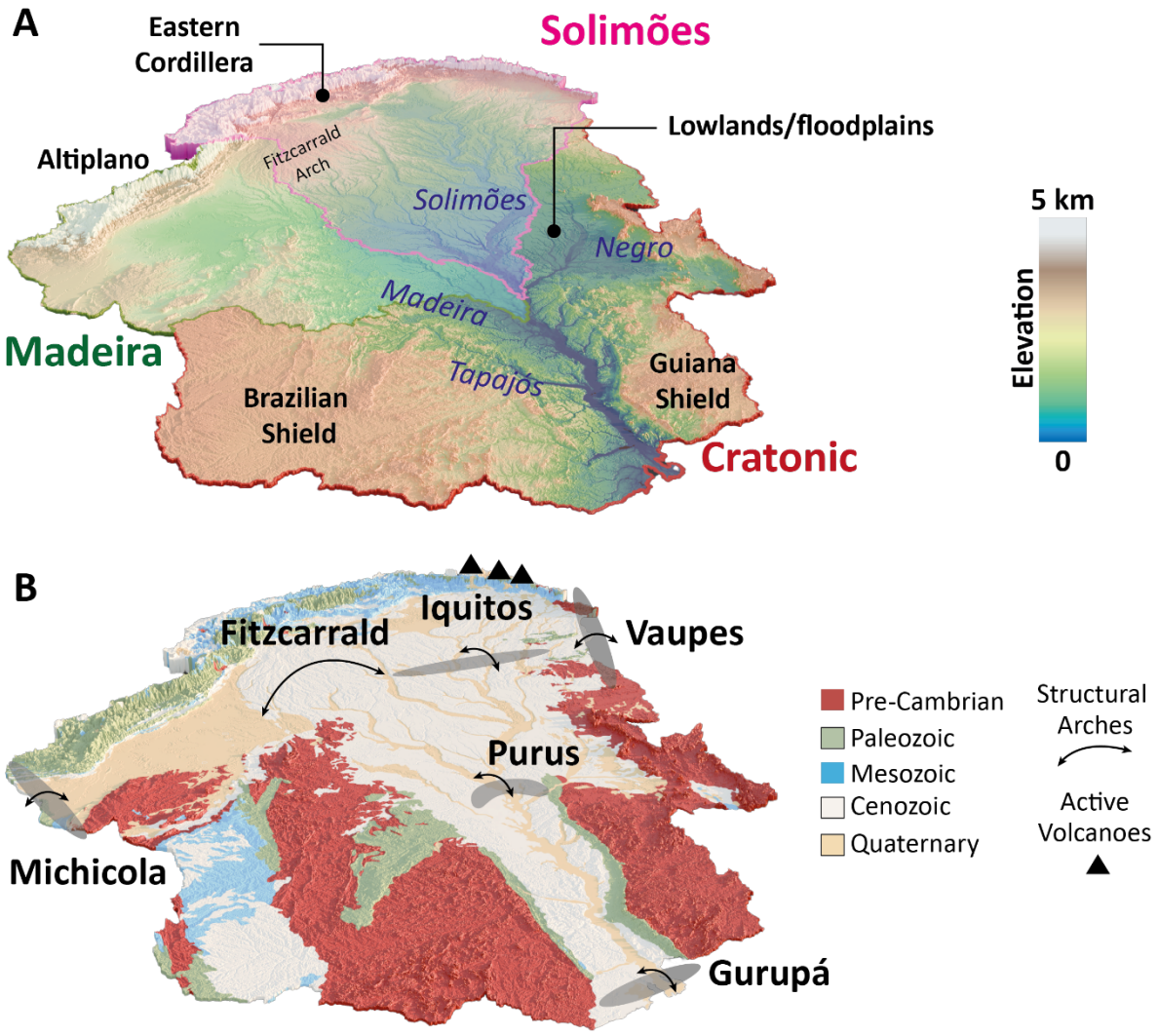

Figure 1.7. 3D Elevation models of A) main geomorphological features and geochemical endmembers, and B) simplified geological map of the Amazon Basin (SGB, 2025)

Foreland and Lowlands

Downstream of the Andes, the lowlands and forelands (< 500 m; **Fig. 1.7A**) form broad depositional plains composed mainly of reworked Tertiary–Quaternary sediments derived from Andean erosion (**Fig. 1.7B**). These regions act as large sediment sinks that promote further chemical alteration under warm and humid conditions (Bouchez et al., 2011; Lupker et al., 2012). The average composition of these sediments approximates the Post-Archean Australian Shale (PAAS), though parts of the Solimões basin retain a more andesitic geochemical signature (Roddaz et al., 2005). Rivers draining only the lowlands transport relatively dilute "clear waters," with SPM concentrations generally < 100 mg L^{-1} and silicate weathering rates below

12 t km^{-2} yr^{-1} (Moquet et al., 2011). Despite their lower particulate fluxes, these areas play a key role in secondary weathering processes and nutrient recycling across the basin (Dellinger et al., 2023).

Guiana and Brazilian Shields

The Guiana and Brazilian shields define the crystalline margins of the basin, reaching elevations between 500 and 3,000 m (**Fig. 1.7A**). They are underlain by Precambrian igneous and metamorphic rocks (**Fig.1.7B**), mostly intermediate to acidic in composition, covered by deeply weathered lateritic profiles (Stallard & Edmond, 1983; Gaillardet et al., 1997). Erosion and denudation rates are extremely low, and SPM rarely exceeds 20–30 mg L^{-1} (Moreira-Turcq et al., 2003; Wittmann et al., 2011). Two main hydrochemical types characterize shield rivers (Stallard & Edmond, 1983): *clear waters*, draining kaolinite-rich lateritic soils with low dissolved organic carbon (DOC), and *black waters*, which flow through forested podzolic soils composed mainly of quartz and containing very high DOC concentrations. Silicate weathering rates are correspondingly low, typically 1–10 t km^{-2} yr^{-1} (Gaillardet et al., 1997; Bouchez et al., 2014).

Floodplains

The floodplains represent dynamic interfaces between Andean sediment inputs and the main Amazon trunk stream (**Fig. 1.7A**). These low-lying areas continuously receive, store, and rework Andean detritus while exchanging dissolved and particulate matter with the active channel (Dunne et al., 1998; Bouchez et al., 2012). Sediment residence times here are much longer than in soils, allowing intense secondary weathering reactions and oxidation of petrogenic organic carbon (West et al., 2002; Lupker et al., 2012; Frings et al., 2014; Dellinger et al., 2023). Consequently, floodplains act as critical biogeochemical reactors that modulate the basin's CO_2 balance by enhancing mineral transformation and organic-carbon turnover.

An alternative but complementary division distinguishes three major sources of sediments and dissolved ions to the Amazon Basin (**Fig. 1.7A** (Moquet et al., 2016, 2011). The Solimões Domain (~2.2 million km^2) drains the northern Andes (Peru, Ecuador), contributing the

largest water and sediment flux, derived from diverse lithologies including volcanics, metapelites, carbonates, evaporites, and foreland sediments (Roddaz et al., 2005; Stallard and Edmond, 1983). The Madeira Domain (~1.4 million km^2) sources the central Andes of Bolivia, where uplifted Paleozoic rocks, with extensive black shale outcrops, and recycled foreland deposits, yield high sediment loads and enhanced oxidative weathering (Dellinger et al., 2023; Santos et al., 2015; Torres et al., 2016). Finally, the Cratonic Domain (~2.4 million km^2) comprises shield-draining rivers with low erosion but substantial dissolved and organic carbon export (Ansart et al., 2025). Together, these domains feed the trunk of the Amazon River, which integrates their contrasting signals before exporting them to the Atlantic.

Sedimentary Basins and Structural Arches

The term *Amazon Basin* commonly refers to the modern Amazon River watershed, yet within this vast area lies a complex mosaic of sedimentary basins of distinct ages and tectono-sedimentary histories, separated by long-lived structural arches. Although a detailed review of their evolution is beyond the scope of this thesis, these features are frequently cited as geographic and geological reference points.

The sedimentary basins within the modern Amazon watershed can be grouped into foreland and intracratonic basins, delineated by basement uplifts and arches that record successive tectonic events from the Proterozoic to the Cenozoic. The Andean foreland basins are divided into northern and southern sectors by the Fitzcarrald Arch, a broad positive morphostructure formed by lithospheric flexure and dynamic uplift during the late Miocene, linked to Nazca Ridge subduction beneath South America (Roddaz et al., 2005; Espurt et al., 2007; Regard et al., 2009). The Northern Andean Foreland Basins (NAFB) include the Marañón, Napo, Putumayo, Santiago, Huallaga, and Ucayali basins, while the Southern Andean Foreland Basins (SAFB) comprise the Madre de Dios and Beni basins.

Further east, the intracratonic basins occupy the interior of the Amazonian Craton and include the Acre, Solimões, Amazonas, Tapajós, and Parecis basins. In the Brazilian sector, early petroleum exploration (CNP, 1939; Petrobras, 1953) identified three major basement arches, the Iquitos, Purus, and Gurupá, that subdivide the Upper, Middle, and Lower Amazon sub-basins (Morales, 1957, 1959; Schobbenhaus et al., 2004). The Gurupá Arch corresponds

to the shoulder of the Marajó rift, formed during the Early Cretaceous opening of the Central Atlantic (Caputo, 2012). The Purus Arch originated as a Middle Proterozoic graben later inverted in the Late Proterozoic, remaining a structural high through the Paleozoic (Wanderley Filho, 1991). The Iquitos Arch developed as a Neogene peripheral forebulge due to lithospheric flexure under Andean loading (Caputo, 1991, 2012; Roddaz et al., 2005). In western Brazil, the Envira Arch, associated with the Late Jurassic Juruá Orogeny, marks the boundary between the Acre and Solimões basins (Caputo, 2014).

.

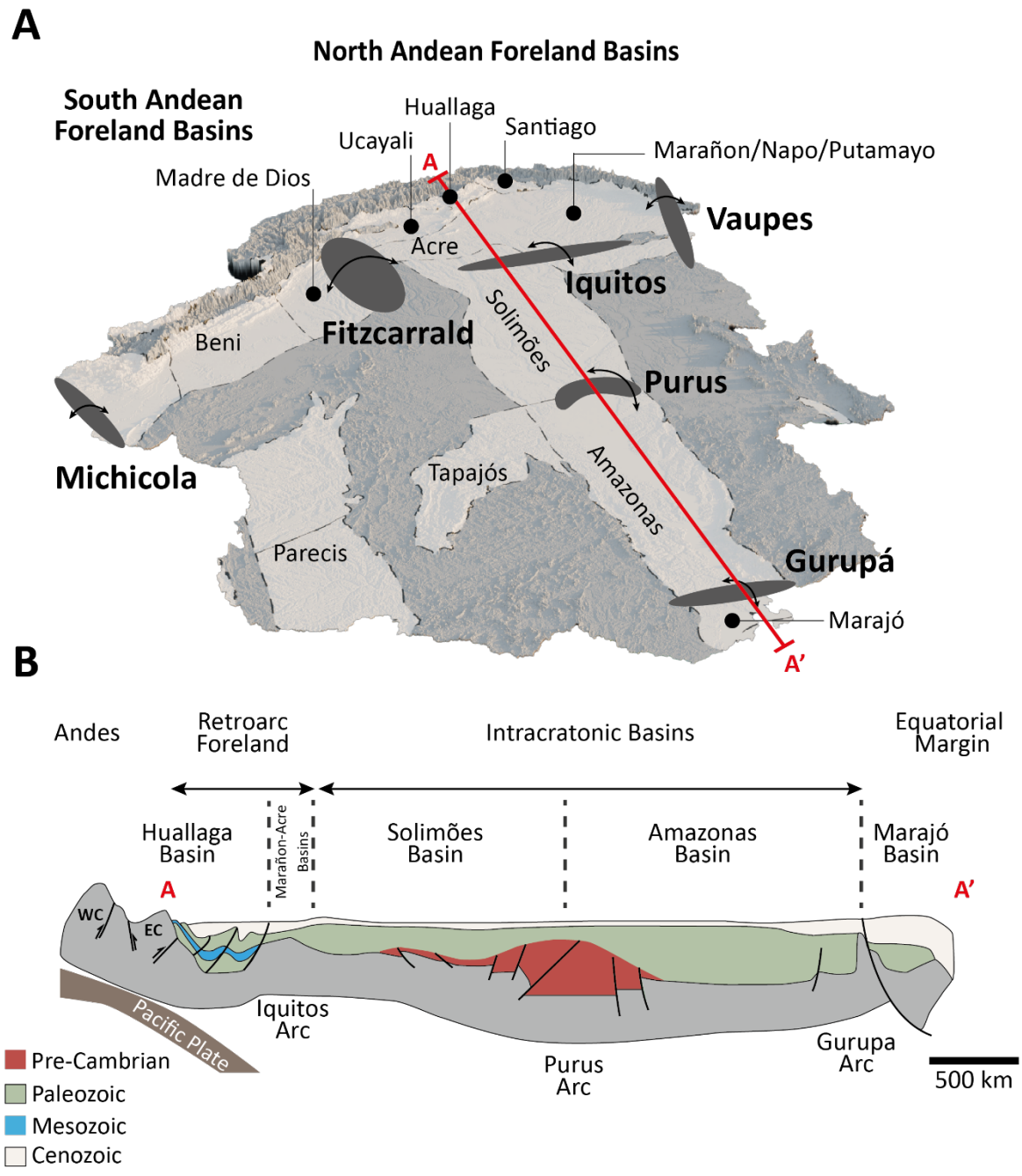

Figure. 1.8. (A) Simplified map of the main sedimentary basins and structural arches within the modern Amazon Basin watershed. The basins are subdivided into foreland (Acre, Beni) and intracratonic (Solimões, Amazonas, Tapajós, Parecis) domains, which are segmented by long-lived basement uplifts, including the Fitzcarrald, Iquitos, Purus, and Gurupá arches. **(B)** Simplified crustal-scale cross-section (A–A') illustrating the Andean orogenic wedge and flexural foreland system transitioning eastward into the intracratonic Amazon basins. The Fitzcarrald Arch forms a major positive relief associated with Nazca Ridge subduction and dynamic uplift of the central Andean retroarc region. WC = Western Cordillera; EC = Eastern Cordillera (Modified after Custódio 2024).

The Amazon Fan

The Amazon Fan, the largest deep-sea fan on Earth, represents the terminal sink of the Andes–Amazon source-to-sink system (**Fig. 1.9**). Situated along the Brazilian Equatorial Margin, it preserves a ~24 Myr sedimentary archive that captures the coupled history of Andean uplift, Amazon Basin drainage evolution, and long-term climate–weathering interactions (Albert et al., 2018; Harris and Mix, 2002; Hoorn et al., 2017). The initiation of fan sedimentation has long been associated with the suppression of carbonate accumulation on the shelf and the onset of large-scale siliciclastic delivery to the deep sea (Cruz et al., 2019; Figueiredo et al., 2009). However, the timing of fan formation, and by extension the establishment of a transcontinental Amazon River, remains debated. Early estimates, based on extrapolated Quaternary sedimentation rates, suggested an onset between 16.5 and 8.0 Ma (Damuth, 1977). Later correlations of well data, seismic profiles, and isotopic records revised this interval to 11.8–10.0 Ma (Figueiredo et al., 2009). More recently, biostratigraphic constraints from nannofossil zonation calibrated to GTS 2012 indicate the first arrival of Andean-derived sediments at the fan between ~9.4 and 9.0 Ma (Hoorn et al., 2017).

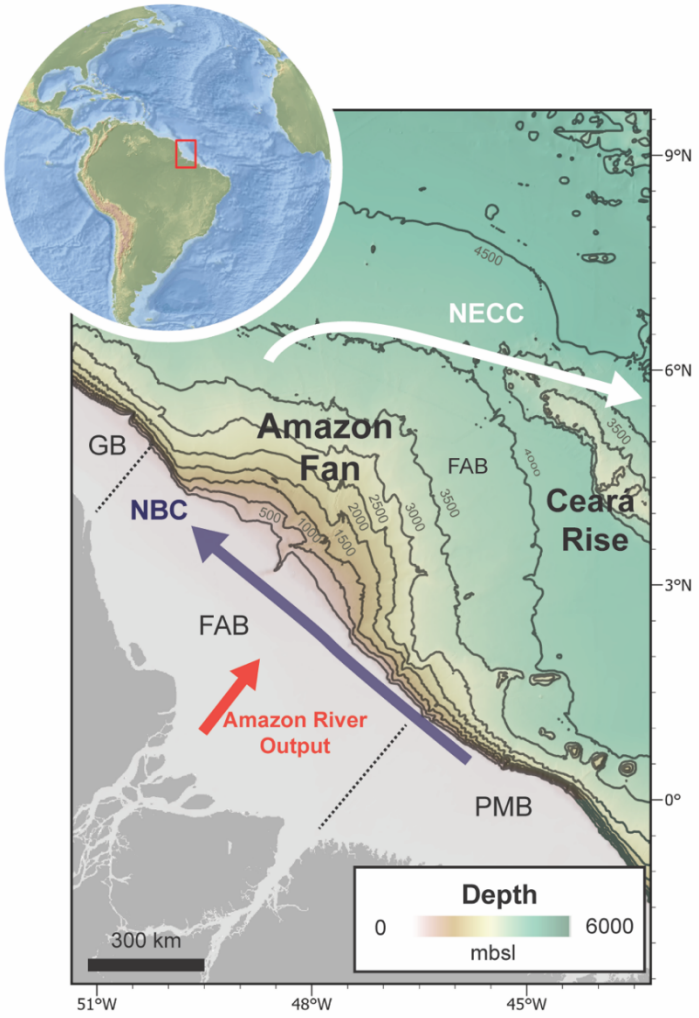

Figure 1.9. Bathymetric map of the NW Equatorial Brazilian Margin, a thick blue arrow shows the North Brazilian Current (NBC).

1.2.1. The Late Cenozoic evolution of Northern South America

The late Cenozoic witnessed the combined effects of orogeny, surface processes, and climate culminating in the establishment of the Amazon, the world's largest drainage basin (**Fig. 1.10**; (Bicudo et al., 2019; Figueiredo et al., 2009; Hoorn and Wesselingh, 2010; Roddaz et al., 2005; Sacek et al., 2023). Central to this evolution was the uplift of the central and northern Andes, which has remained the dominant driver of Amazonian landscape development. Although the Andean uplift began during the Late Cretaceous, the present configuration of the range took shape in the Cenozoic through the eastward propagation of an orogenic wedge involving pre-orogenic sedimentary and metamorphic rocks and syn-orogenic deposits (Roddaz et al., 2006a, b). By 10–15 Ma, the southern Peruvian Andes had already attained elevations of ~4 km (**Fig. 1.10C**; (Boschman, 2021; Sundell et al., 2019). During the late Miocene, the range

widened, extending ~450 km inland in southern Peru and northern Bolivia and reaching altitudes of 4–5 km (Garzione et al., 2017). Growth was most pronounced in the central–southern Andes, whereas relief in northern Peru, Ecuador, and Colombia remained subdued. A continuous high cordillera in the northwestern Amazon margin only emerged around 4–5 Ma, when the northern Andes reached elevations of ~3 km (Mora et al., 2008). Once the Andes north of the Altiplano rose above ~2.5 km, they began to obstruct atmospheric circulation, enhancing rainfall along the eastern foothills and driving major climatic reorganizations across tropical South America (Ehlers & Poulsen, 2009).

Andean uplift also drove crustal deformation and flexural subsidence in western Amazonia, generating accommodation space for long-lived wetlands. Between ~23 and 10 Ma, much of the region was occupied by the extensive Pebas megawetland (Hoorn et al., 2010). This system was episodically influenced by shallow marine incursions(Alvim et al., 2021; Hoorn et al., 2010; Leandro et al., 2022; Sacek, 2014), , while Andean-derived sediments accumulated in large alluvial fans, retroarc foreland basins, and hinterland depocenters (Horton, 2018).

By ~10 Ma, the Pebas system began to wane and was replaced by fluvial megafans and the Acre fluvial system (Hoorn et al., 2010), reflecting a fundamental reorganization of drainage patterns. This transition likely resulted from accelerated Andean uplift and late Miocene climate changes that intensified erosion and sediment fluxes (Baby et al., 2025). Its impacts propagated downstream, influencing depositional systems as far as the Atlantic margin. A marked shift from cratonic to Andean sediment sources between 11.8 and 8.7 Ma is documented both in Sub-Andean basins (Parra et al., 2009; Roddaz et al., 2005) and in the marine record of the Brazilian Equatorial Margin (Figueiredo et al., 2009; Hoorn et al., 2017; van Soelen et al., 2017). These signals underpin the widely cited late Miocene age for the onset of the transcontinental Amazon River.

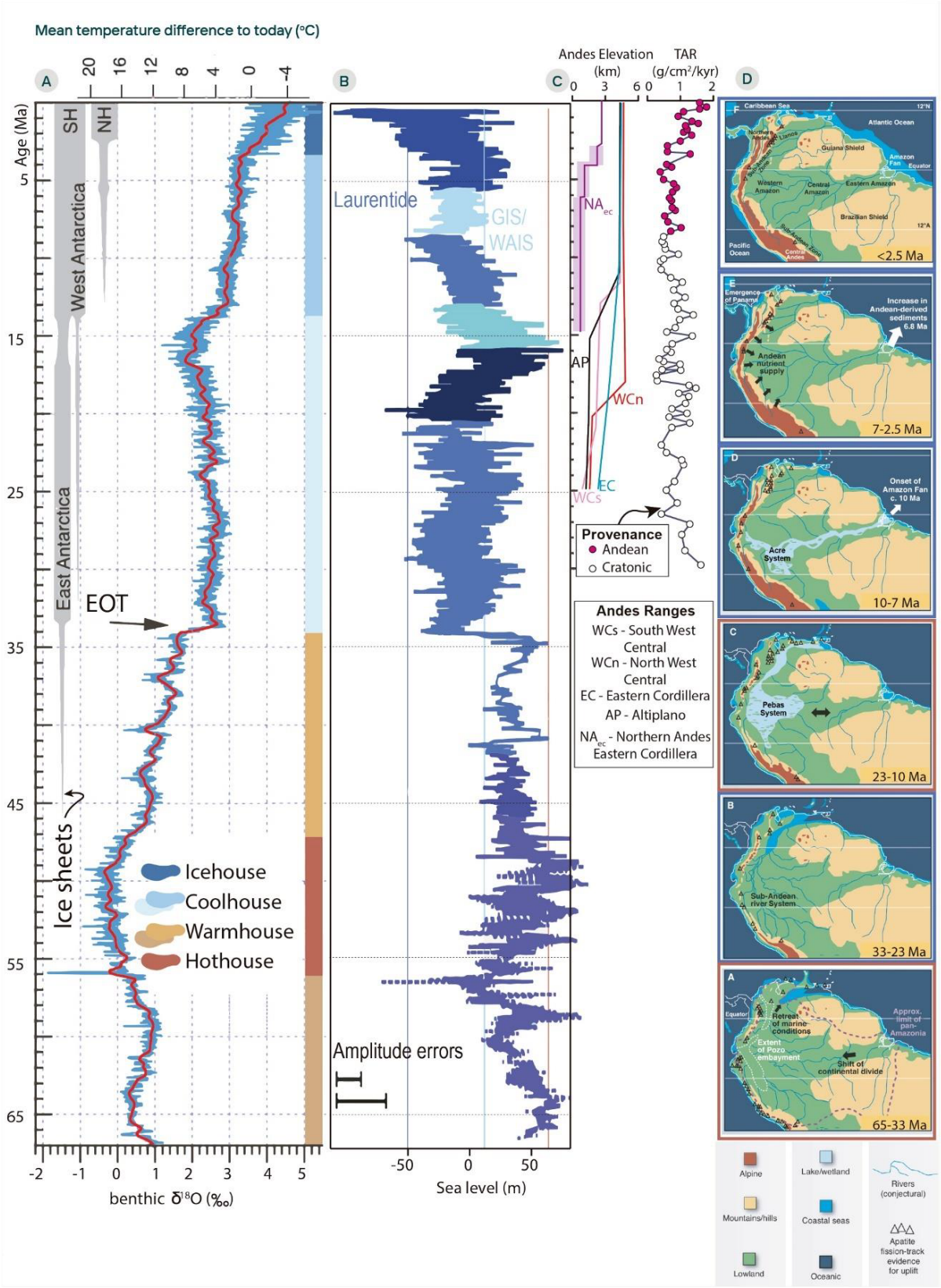
Mean temperature difference to today (°C)
A
B
C
D
Age (Ma)
SH
NH
West Antarctica
East Antarctica
Ice sheets
EOT
Icehouse
Coolhouse
Warmhouse
Hothouse
benthic δ18O (‰)
Laurentide
GIS/
WAIS
Amplitude errors
Sea level (m)
Andes Elevation (km)
TAR (g/cm²/kyr)
NAec
AP
WCn
EC
WCs
Provenance
Andean
Cratonic
Andes Ranges
WCs - South West Central
WCn - North West Central
EC - Eastern Cordillera
AP - Altiplano
NAec - Northern Andes Eastern Cordillera
<2.5 Ma
7-2.5 Ma
10-7 Ma
23-10 Ma
33-23 Ma
65-33 Ma
Alpine
Mountains/hills
Lowland
Lake/wetland
Coastal seas
Oceanic
Rivers (conjectural)
Apatite fission-track evidence for uplift

Figure 1.10 A) Global Cenozoic temperature curve (from Westerhold *et al.* 2020); **B)** Global Cenozoic sea level curve (from Miller *et al.* 2020); **C)** Past elevation estimates for the Central Andes (after Sundell et al., 2019), and temporal variations in εNd in the Amazon submarine fan (red, after Figueiredo et al. 2009; Hoorn et al, 2017), Ceará Rise (black, after van Soelen et al, 2017) and Terrigenous Accumulation Rates (TAR) at the Amazon outlet near the Ceará Rise; **D)** Paleogeographic maps illustrating the transition from Amazon Craton to Andes-dominated landscapes: (a) The Amazon once extended over most of northern South America. The breakup of the Pacific plates changed the geography, and the Andes started uplifting. (b) The Andes continued to rise with the main drainage toward the northwest. (c) Mountain building in the Central and Northern Andes (~30 Ma, especially from 12 Ma) and wetland progradation into the western Amazon. The Middle Miocene Climate Optimum and high sea level caused marine ingressions and estuarine conditions in the heart of the Amazon. (d) Uplift of the Northern Andes restricted "pan-Amazonia" and facilitated allopatric speciation and extirpation [e.g., (21)]. (e) The mega-wetland disappeared and *terra firme* rainforests expanded, closing the Panama Isthmus and the start of the Great American Biotic Interchange (GABI). (f) Quaternary. Note that South America migrated northward during the course of the Paleogene. Source: Val et al. 2022

The precise timing of this transition, however, remains contested. Some continental records suggest an earlier Miocene origin (Campbell et al., 2006; Cremon et al., 2016; Horbe et al., 2019, 2013; Jaramillo et al., 2017; Nogueira et al., 2013; Rossetti et al., 2023, 2015), whereas marine archives often support a late Miocene establishment (Dobson et al., 2001; Figueiredo et al., 2009; Gorini et al., 2014; Heinrich and Zonneveld, 2013; Hoorn et al., 2017; Lammertsma et al., 2018; van Soelen et al., 2017). Other interpretations place the emergence of the TAR in the Pliocene (~4.5 Ma; (Latrubesse et al., 2010; Ribas et al., 2012) or even as late as the Pleistocene (<2.6 Ma; Rossetti et al., 2015). These discrepancies reflect differences in the definition of the "Amazon River," in dating approaches, and in the persistence of geomorphic features. Despite this debate, it is clear that large-scale drainage reorganization during the late Neogene laid the foundations for the modern transcontinental Amazon system.

1.2.2. Neogene climate evolution in South America

Oligocene-Miocene Boundary (23-20 Ma)

At the transition from the Oligocene to the Miocene, hemispheric cooling events demonstrated how high-latitude climate could influence tropical rainfall via ITCZ shifts. Marine dust and clay provenance records indicate a southward ITCZ displacement during Northern Hemisphere cooling at this boundary (Hyeong et al., 2014). Climate simulations confirm that AMOC strength exerts a powerful control: enhanced AMOC pushes the ITCZ northward by

transporting more heat across the equator, whereas a weakened AMOC drives southward ITCZ migration (Liu et al., 2024). This establishes the physical lever that recurs throughout the Neogene: AMOC ↔ ITCZ ↔ tropical rainfall. Although direct reconstructions from South America remain limited for this interval, the mechanism implies that Northern Hemisphere cooling episodes or AMOC slowdowns would have displaced the ITCZ southward, favoring wetter conditions in the southern Amazon and subtropics and drying in the north. At the same time, incipient Andean uplift began to impose orographic controls on moisture pathways, strengthening convection on the eastern slopes and foreshadowing the stronger rain-shadow effects that would emerge later (Ehlers & Poulsen, 2009).

Early-Middle Miocene (20-11 Ma): MMCO warmth and Andean uplift

Globally, the Early Miocene climate was relatively warm, culminating in the Mid-Miocene Climatic Optimum (MMCO, 17–15 Ma), when atmospheric CO_2 reached ~400–500 ppm and global mean temperatures rose to levels comparable to near-future projections (Holbourn et al., 2018). Reduced equator–pole temperature gradients during this interval altered Hadley circulation and weakened high-latitude cryospheric constraints, producing a climate state with more vigorous tropical hydrological cycling.

In tropical South America, these global boundary conditions translated into markedly different rainfall regimes. Isotopic evidence from the Guajira Peninsula (Colombia) shows that precipitation seasonality during the MMCO was much stronger than today, with $\delta^{18}O$ variations in Turritella shells more than double those in modern analogues (Scholz et al., 2020). Such values imply a northward-displaced mean ITCZ and enhanced seasonal rainfall over northern South America, a region that is semi-arid at present. Complementary freshwater bivalve records from Peru also point to intensified tropical hydrological cycling under MMCO warmth (Kaandorp et al., 2005).

At the same time, the Andean uplift was beginning to exert a growing influence on regional hydroclimate. Climate–isotope modeling indicates that once elevations exceeded ~2 km, convective rainfall intensified on the eastern flanks, producing more depleted $\delta^{18}O$ values in precipitation through the amount effect (Ehlers & Poulsen, 2009; Poulsen et al., 2010). Thus, during the Early to Middle Miocene, South American hydroclimate reflected both global forcing,

high CO_2, weak gradients, northward ITCZ, and regional tectonic feedbacks, with uplift amplifying rainfall contrasts and setting the stage for later drainage reorganizations that shaped the Amazon Basin.

Late Miocene (11-5 Ma): Global cooling and orographic amplification

Following the MMCO, Earth entered a phase of progressive late Miocene cooling, driven by declining atmospheric CO_2 and the expansion of Antarctic ice sheets. This global shift steepened equator–pole temperature gradients, strengthened Hadley circulation, and increased the sensitivity of the ITCZ to orbital forcing. Marine records from Africa reveal orbitally paced ITCZ migrations of ~2–3° latitude tied to precession (Colin et al., 2014). In tropical South America, these global trends intersected with ongoing Andean uplift to reshape rainfall patterns. Sedimentary and isotopic records from foreland basins show that between ~9 and 7 Ma, topographic growth deflected the South American low-level jet, reorganizing precipitation across the flanks and foreland plains (**Fig. 1.11C**; Mulch et al., 2010; Rohrmann et al., 2016). The Andes thus amplified modest ITCZ shifts into sharp east–west rainfall gradients, transforming regional hydroclimate. The late Miocene, therefore, marked the emergence of a hybrid climate system in South America: the rhythm of tropical rainfall was paced by orbital-scale ITCZ shifts, while the amplitude and spatial expression of precipitation were increasingly controlled by Andean orography.

Pliocene (5-2.6 Ma): Warm climates and a northward ITCZ

Globally, the early Pliocene was a period of relative warmth, culminating in the Mid-Pliocene Warm Period (MPWP, 3.3–3.0 Ma), when global mean temperature was ~2–3 °C above preindustrial values and atmospheric CO_2 approached ~400 ppm. Proxy reconstructions and PlioMIP2 simulations indicate reduced meridional temperature gradients and weakened cryospheric constraints, with climate states broadly comparable to future warming scenarios (Haywood et al., 2020; Zhang et al., 2021). These conditions displaced the mean ITCZ northward by ~1–3°, producing wetter conditions in northern Amazonia and relative drying in the southern tropics (Pontes et al., 2022, 2020). Leaf-wax isotope records and marine sediments from the tropical Atlantic confirm this dipole. At the same time, ENSO amplitude was reduced,

muting interannual variability and producing a more stable, but spatially uneven, rainfall regime (Oldeman et al., 2021). Within South America, continued Andean uplift reinforced these zonal contrasts by focusing easterly moisture into foreland basins and sustaining high precipitation along the eastern flanks. Thus, Pliocene hydroclimate in Amazonia combined the influence of a northward-shifted ITCZ under global warmth with orographic feedbacks that accentuated spatial rainfall gradients.

Plio-Pleistocene transition (3-2Ma)

The transition into the Pleistocene was marked by the rapid expansion of Northern Hemisphere ice sheets, global cooling, lower sea levels, and steeper thermal gradients (Fedorov et al., 2013; Miller et al., 2020; Westerhold et al., 2020). These changes reinforced Walker and Hadley circulation and made the ITCZ more sensitive to interhemispheric energy imbalances (Etourneau et al., 2010). In South America, this period saw the strengthening of the South American Summer Monsoon (SASM) as ITCZ seasonality intensified. Rainfall partitioning across the Amazon became increasingly tied to Atlantic SST gradients, leading to stronger hydroclimatic dipoles between the northern and southern basins. Proxy evidence points to enhanced spatial contrasts in precipitation as these processes interacted with orbital forcing. Ongoing Andean uplift amplified these reorganizations, sustaining high orographic rainfall on the eastern slopes while intensifying rain shadows in intermontane basins. The onset of Northern Hemisphere Glaciation thus established the template for the strongly partitioned hydroclimate regimes that would characterize the Quaternary.

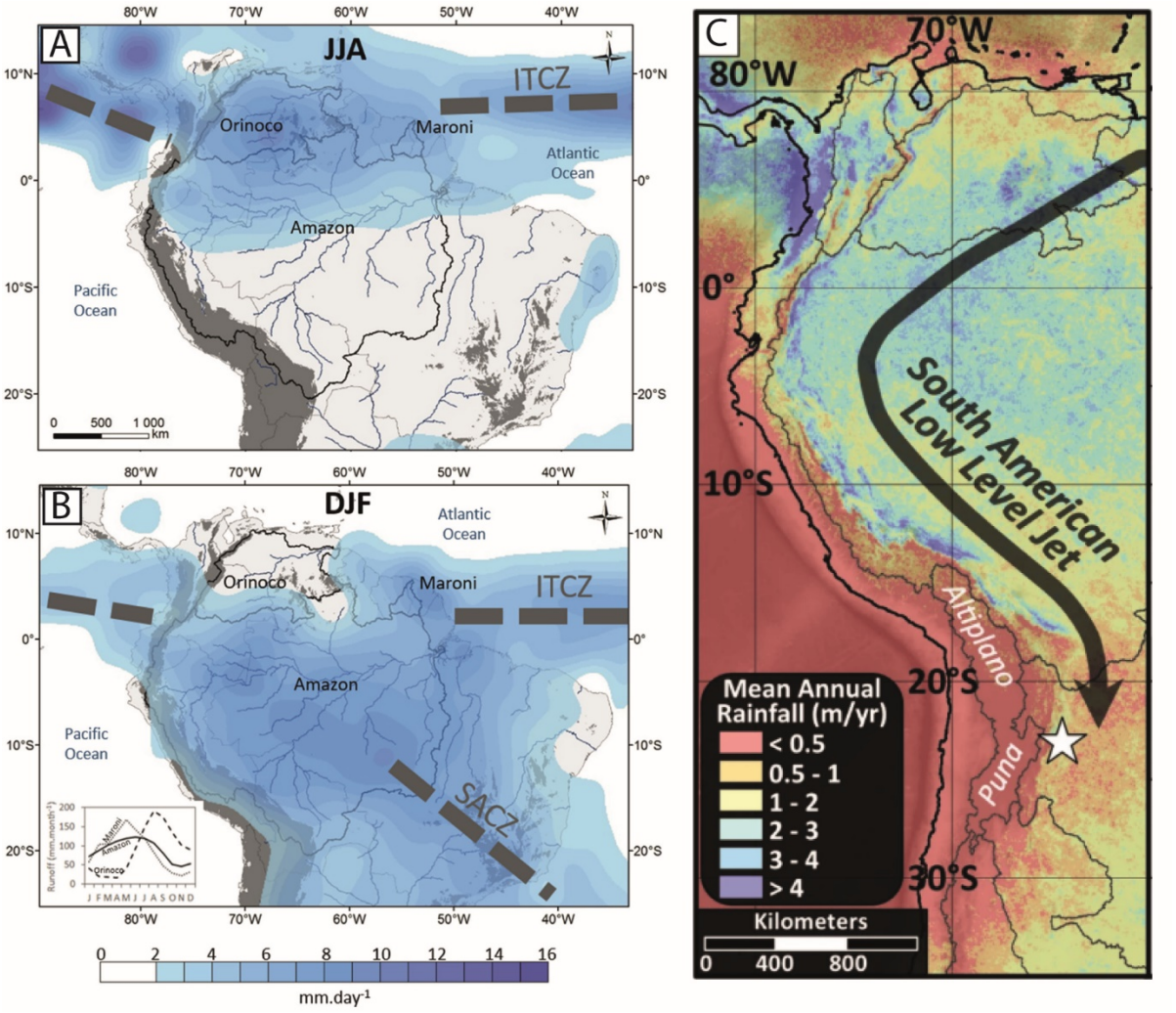

Figure 1.11. Seasonal rainfall distribution and atmospheric circulation over tropical South America. (A) Modern mean rainfall during boreal summer (June–July–August, JJA) shows the northward position of the Intertropical Convergence Zone (ITCZ). **(B)** Mean rainfall during austral summer (December–January–February, DJF) with the southward displacement of the ITCZ and development of the South Atlantic Convergence Zone (SACZ). Inset shows seasonal rainfall variability for representative basins (Source: Rousseau et al., 2019). **(C)** Mean annual rainfall and the trajectory of the South American Low-Level Jet (SALLJ), which transports Amazonian moisture toward the subtropics, interacting with Andean topography (Altiplano and Puna; Source: Fischer et al., 2022).

Pleistocene and Holocene

Global climate variability during the Pleistocene was paced by orbital cycles, with obliquity-dominated 40-kyr glacial–interglacial rhythms in the early Pleistocene giving way to eccentricity-modulated 100-kyr cycles after the Mid-Pleistocene Transition (~1 Ma). These longer, colder, and dustier glacials reflected the growth of large ice sheets and intensified ocean–atmosphere feedbacks (Chalk et al., 2017; Lisiecki and Raymo, 2005a). In the tropics, ITCZ migrations transmitted these high-latitude changes into South America. At the Last Glacial Maximum (~21 ka), the ITCZ shifted ~3° southward, creating drier conditions in northern Amazonia while allowing overall forest resilience to persist (Häggi et al., 2017; McGee et al., 2018). During Heinrich Stadial 1 (~17–15 ka), an AMOC collapse drove a stronger southward ITCZ displacement, creating north–south rainfall dipoles and vegetation reorganizations (Akabane et al., 2024; Grigolato et al., 2025). Similar events during earlier stadials confirm that ITCZ sensitivity was state-dependent: glacial climates amplified migrations, while interglacials dampened them (Kraft et al., 2025).

Finally, in the Holocene, ITCZ seasonality stabilized within its modern migration range (~10°S–15°N; Garreaud, 2009). Interannual variability was increasingly modulated by ENSO and the Atlantic Multidecadal Oscillation (Rousseau et al., 2019; Moquet et al., 2019). Modern river isotope records demonstrate how these modes redistribute rainfall and sediment provenance across the Amazon, offering analogues for interpreting past hydroclimatic variability.

Taken together, the Cenozoic climate history of South America reflects the interplay of global boundary conditions, tropical rain-belt dynamics, and regional tectonic feedbacks. Orbital forcing and high-latitude cryosphere evolution set the pace of ITCZ migrations, while Andean uplift amplified spatial rainfall gradients and reshaped hydroclimate patterns. The Amazon Basin, at the heart of these interactions, integrates signals from global climate drivers and regional tectonics, transmitting them to the Atlantic margin where they are preserved in long-term sedimentary archives.

1.2.3. Weathering events in the Amazon Basin

Weathering in the Amazon Basin is now understood as a polyphase process shaped by long-term climate variability, tectonic uplift, and drainage evolution. Lateritic profiles across central Amazonia record multiple discrete episodes of intense chemical alteration rather than continuous background weathering (Ansart et al., 2025; Dos Santos Albuquerque et al., 2025, 2020; Gautheron et al., 2022). Geochronological studies of kaolinite and Fe-oxides reveal Paleogene phases of kaolinite formation under stable humid conditions, later rejuvenated during the Miocene and Pliocene with the development of ferruginous duricrusts and poorly ordered kaolinites (**Fig. 1.12**). These episodes coincide with major paleoenvironmental changes, including the Pebas megawetland system (23–10 Ma), Andean uplift, and the establishment of a transcontinental Amazon River. Mineralogical shifts, such as the replacement of goethite by hematite or the overprinting of earlier kaolinites, highlight the alternation between persistently humid regimes and intervals of greater seasonality or drier conditions.

Lateritic duricrusts and bauxites across central and northern Amazonia further illustrate the sensitivity of weathering to climatic oscillations and landscape change. Goethite-rich assemblages, indicative of humid conditions, dominate during phases of strong rainfall and efficient drainage, while hematite-rich crusts formed during drier intervals with oscillating water tables (Dos Santos Albuquerque et al., 2025, 2020). The preservation of these profiles atop plateaus contrasts with truncated weathering sequences along valley slopes, reflecting the role of neotectonic incision and fluvial rejuvenation in shaping the Amazonian landscape (Gautheron et al., 2022). These archives demonstrate that lateritization was neither spatially uniform nor temporally continuous, but rather a polycyclic process of mineral dissolution and reprecipitation superimposed on evolving geomorphic surfaces.

Offshore records from the Ceara Rise provide a basin-scale counterpart to these continental archives. Terrigenous mass accumulation rates (TMAR) and clay mineral ratios over the last 13 Ma document changes in erosion and weathering regimes across tropical South America (Harris & Mix, 2002). While long-term variations correlate most closely with lowland hydroclimate—particularly aridity and precipitation-driven shifts in soil mineralogy—stepwise increases in sediment flux near ~8 and ~4.5 Ma align with tectonic events that expanded

drainage into more erodible Andean and foreland regions. Together, the continental laterite chronologies and Ceara Rise sedimentary record underscore the dual control of climate (e.g., ITCZ migration, monsoon intensity) and tectonics (e.g., Andean uplift, Purus Arch disruption) on Amazonian weathering. This integrated perspective highlights the Amazon Basin as both a sensitive recorder of tropical weathering dynamics and a critical modulator of sediment fluxes, landscape evolution, and the global carbon cycle.

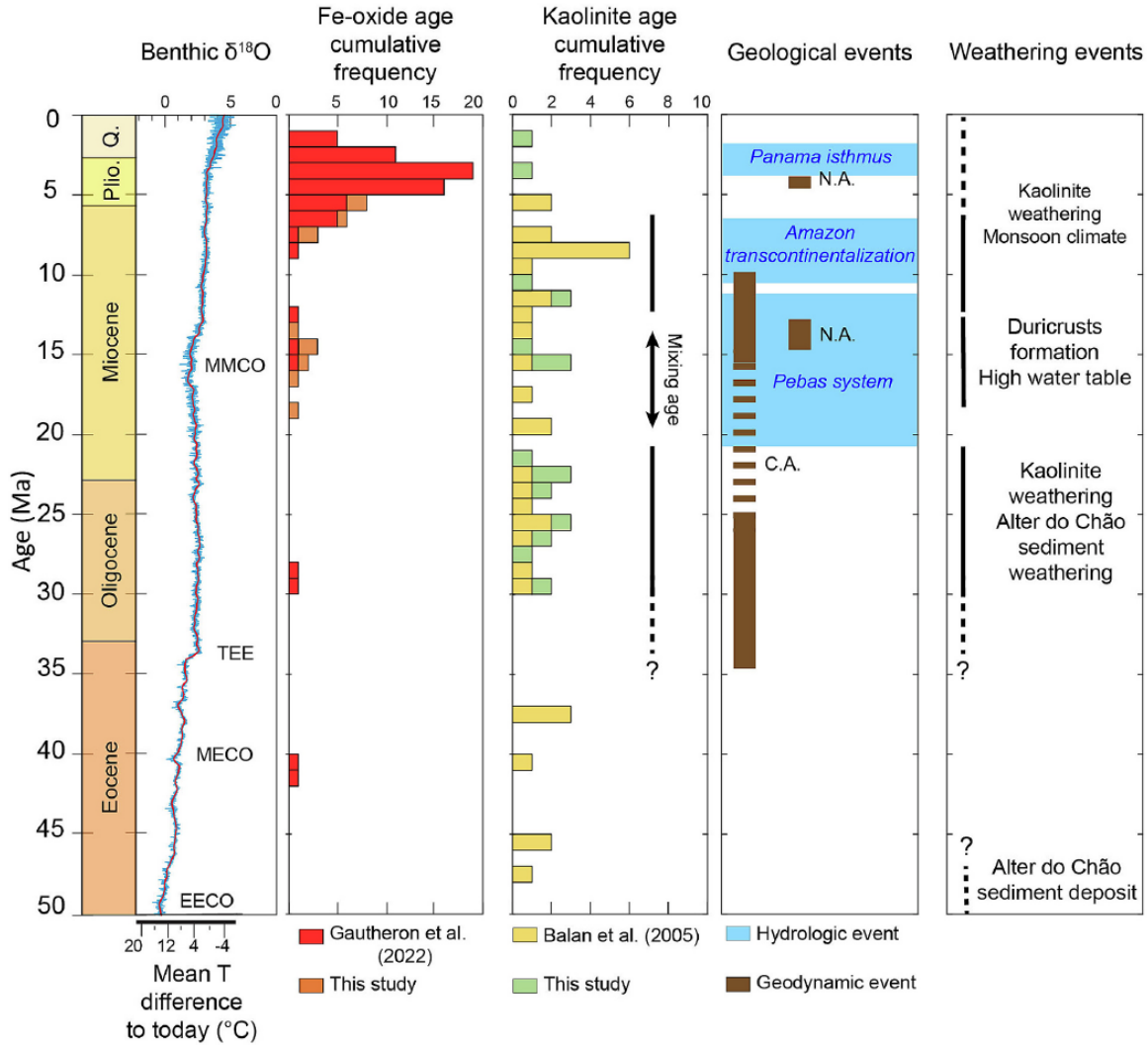

Figure 1.12. Compilation of climate data, hydrologic and geologic events in South America, and available geochronological data on secondary minerals. EECO: Early Miocene Climate Optimum; MECO: Middle Eocene Climate Optimum; TEE: Terminal Eocene Event; MMCO: Middle Miocene Climate Optimum. Geodynamic events refer to periods of intensified uplift in Central Andes (C.A.) or in Northern Andes (N.A.). Source: Ansart et al., 2025

1.4. Geochemical tracers of continental weathering processes

Geochemical tracers offer powerful tools for investigating both past and present dynamics of the carbon cycle and climate. Preserved in natural archives such as marine sediments and ice cores, they serve as proxies for reconstructing past climate variability. In addition, geochemical tracers are widely applied to track physical and chemical weathering at Earth's surface, providing critical insights into the links between tectonics, weathering, the carbon cycle, and climate.

1.4.1. Rare Earth Elements

The rare earth elements (REEs) comprise the fourteen naturally abundant lanthanides (La–Lu, Z = 57–71). They share similar chemical and physical properties due to the filling of the 4f electron shell, which results in a predominance of the +3 oxidation state (Henderson, 1984). Two notable exceptions occur under specific conditions: europium can occur as Eu^{2+}, and cerium as Ce^{4+}. Across the series, the progressive decrease in ionic radius from La^{3+} (1.032 Å) to Lu^{3+} (0.861 Å), the so-called *lanthanide contraction*, exerts a strong control on their geochemical behavior. REEs tend to form covalent bonds with oxygen and, like Fe^{3+}, they hydrolyze easily, leading to generally low solubility and mobility in natural waters (Henderson, 1984). Their high charge and large ionic size make them moderately incompatible elements during partial melting, generating systematic fractionations in igneous and sedimentary environments (Taylor and McLennan, 1985).

In natural samples, the combined effects of nuclear stability, odd–even atomic mass differences, and lanthanide contraction produce a characteristic "sawtooth" abundance distribution. To facilitate interpretation, REE concentrations are routinely normalized to a reference shale composition (e.g, PAAS; Taylor and McLennan, 1985) or an average of modern river sediments (WRAS, Bayon et al., 2015). Normalization yields relatively flat patterns for average continental crust, allowing deviations caused by geochemical processes to be highlighted. REE spectra are typically divided into three groups: light REEs (LREEs; La–Nd), middle REEs (MREEs; Sm–Tb), and heavy REEs (HREEs; Dy–Lu). The relative enrichment or depletion of these groups provides valuable insights into source lithology and weathering

processes. For instance, felsic rocks often exhibit negative Eu anomalies (Eu/Eu* < 0.8), whereas mafic rocks show smaller or absent anomalies. Similarly, negative Ce anomalies (Ce/Ce* < 1) can signal an oxidative marine influence, since Ce is uniquely prone among the REEs to oxidation to the insoluble Ce^{4+} state (Barrat et al., 2023; Piper, 1974).

1.4.2. Neodymium and Hafnium Isotopes

Neodymium

Samarium (Sm) and neodymium (Nd) are light rare earth elements whose isotopic system provides a powerful tracer of mantle–crust differentiation and sediment provenance (Bayon et al., 2015; DePaolo, 1988; McCulloch and WasseXrburg, 1978). The radioactive isotope ^{147}Sm decays to ^{143}Nd with a half-life of ~10^6 Ga, while ^{144}Nd serves as a stable reference isotope. Because mantle-derived rocks are enriched in Sm relative to Nd, they evolve toward higher $^{143}Nd/^{144}Nd$ ratios over time, yielding characteristically radiogenic signatures (**Fig. 1.13**). In contrast, continental crust is relatively depleted in Sm, leading to lower initial $^{143}Nd/^{144}Nd$ ratios. Therefore, the isotopic evolution of crustal rocks depends on their age and Sm/Nd ratio, such that older continental lithologies typically display more unradiogenic values than younger mantle-derived materials.

Because the bulk Earth is assumed to have formed with a chondritic Sm/Nd ratio, its long-term isotopic evolution can be referenced to the Chondritic Uniform Reservoir (CHUR; (Jacobsen and Wasserburg, 1980). Variations are expressed in epsilon notation as parts per 10,000 deviations from CHUR (DePaolo and Wasserburg, 1976):

$$\varepsilon_{Nd(t)} = \left[\frac{\left(\frac{^{143}Nd}{^{144}Nd}_{Sample(t)}\right) - \left(\frac{^{143}Nd}{^{144}Nd}_{CHUR(t)}\right)}{\left(\frac{^{143}Nd}{^{144}Nd}_{CHUR(t)}\right)} \right] x10^4$$

where $(^{143}Nd/^{144}Nd)_{CHUR} = 0.512630$ (Bouvier et al., 2008).

Mantle-derived rocks, enriched in Sm relative to Nd, evolve toward radiogenic $^{143}Nd/^{144}Nd$ and thus positive εNd values. In contrast, continental crust, which is relatively depleted in Sm, yields lower $^{143}Nd/^{144}Nd$ ratios and negative εNd values. Because Sm and Nd

both exist almost exclusively in the +3 oxidation state, their isotopic fractionation during surface processes is minimal, and their long half-lives prevent measurable alteration on human or glacial–interglacial timescales. As such, εNd is considered one of the most robust tracers of provenance in sediments, waters, and detrital minerals (DePaolo and Wasserburg, 1976; Bayon et al., 2016).

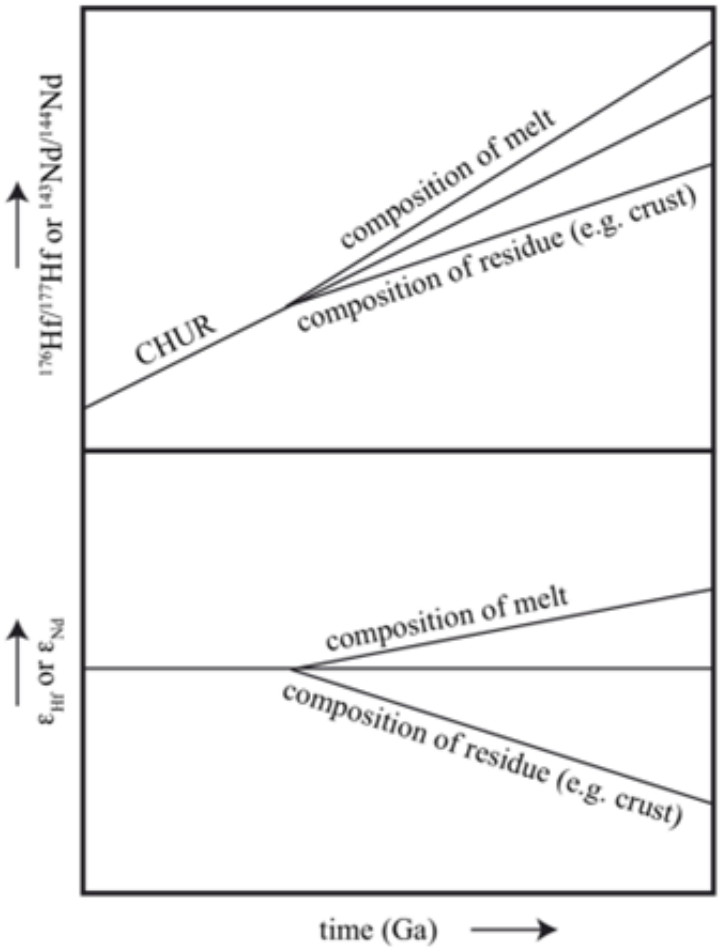

Figure 1.13. The Hf and Nd isotope evolution over time. During igneous processes, the elemental fractionation of SM/Nd and Lu/Hf leads to different isotopic evolution of the residue (e.g., crust) and the melt over time.

Finally, Nd isotopes are also only weakly incorporated into biogenic carbonates, sulfides, or quartz, but are concentrated in silicate minerals (feldspars, biotite) and scavenged efficiently by secondary phases such as Fe–Mn oxides and phosphates (apatite, monazite, zircon). This makes εNd a particularly sensitive tracer of lithological contributions to sedimentary loads and, by extension, a critical parameter for deconvolving the silicate versus non-silicate weathering balance that governs long-term CO_2 fluxes.

Hafnium

The lutetium–hafnium (Lu–Hf) system provides a complementary tracer to Sm–Nd. ^{176}Lu (half-life 37 Ga) decays to ^{176}Hf, while ^{177}Hf serves as a reference isotope. Because Lu is a heavy REE that behaves differently from Hf (a high field strength element), mantle–crust differentiation imparts contrasting Lu/Hf ratios and thus divergent isotopic evolutions in mantle-derived and crustal rocks (**Fig. 1.13**). As with Nd, isotopic compositions are reported in epsilon notation relative to CHUR

$$\varepsilon_{Hf(t)} = \left[\frac{\left(\frac{^{176}Hf}{^{177}Hf}_{Sample(t)}\right) - \left(\frac{^{176}Hf}{^{177}Hf}_{CHUR(t)}\right)}{\left(\frac{^{176}Hf}{^{177}Hf}_{CHUR(t)}\right)}\right] x10^4$$

where $(^{176}Hf/^{177}Hf)_{CHUR}$ = 0,282785 (Bouvier et al., 2008).

Because both the Sm–Nd and Lu–Hf systems “behave” (fractionate) similarly during magmatic processes, terrestrial rocks define a broad “Terrestrial Array” of correlated εNd–εHf values (Vervoort et al., 1999; **Fig. 1.14**). Mantle-derived rocks lie at the radiogenic end (high εNd, high εHf), whereas ancient crust lies at the unradiogenic end (low εNd, low εHf). However, during surface weathering, the two systems can become decoupled. Sm and Nd remain largely immobile, so εNd in weathering products closely reflects the source rock (Rickli et al., 2013). In contrast, weathering and sediment transport processes generate weathering products with a hafnium isotopic composition that differs from the source rock. The correlation between εNd and εHf observed in weathering products, specifically in the clay fraction, is referred to as the "Clay array" (Bayon et al., 2016). This array differs from the "Seawater array, characterized by the radiogenic composition in εHf of iron and manganese oxides (Albarède et al., 1997), and the "Terrestrial array" consisting of oceanic basalts, continental crustal rocks, and sediments (Vervoort et al., 1999).

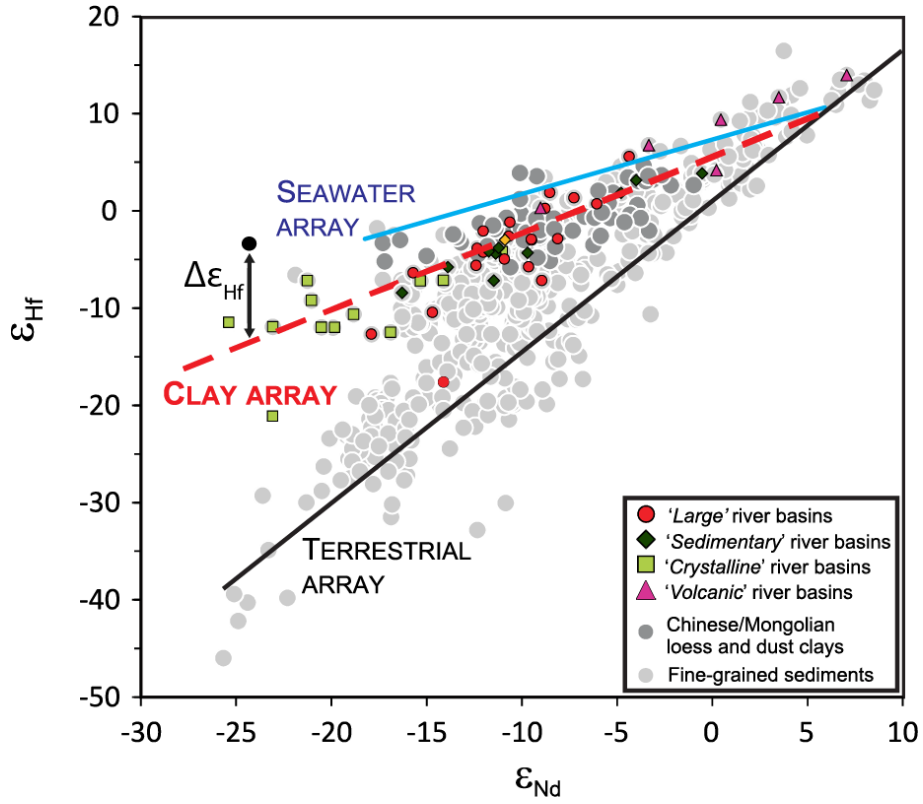

Figure 1.14. Compilation of published Hf and Nd isotopic compositions for fine-grained sediments and other sedimentary rocks. The sediment data (grey circles) include present-day εHf and εNd values for: marine sediments river particulates and bedloads loess deposits and aeolian dust (apud Bayon et al. 2016). The Seawater Array (Albarède et al., 1998) and the present-day Terrestrial Array (Vervoort et al., 2011) are shown for comparison, together with 3 other correlations identified in previous studies for fine-grained sediments (the 'zircon-free sediment array', Bayon et al., 2009), coarse-grained sediments (the 'zircon-bearing sediment array'; Bayon et al., 2009), and Mongolian and Chinese dust clays (the 'clay-sized array'; Zhao et al., 2014).

The difference in Hf composition can be attributed to the variation in εHf from the least weathering-resistant mineral to the most resistant mineral (**Fig. 1.15**; Bayon et al., 2006; Rickli, 2013). This process is often referred to as *incongruent dissolution*. For instance, a substantial fraction of the Hf budget in rocks and sediments is hosted in zircon grains, a mineral characterized by very unradiogenic isotopic compositions (i.e. low $^{176}Hf/^{177}Hf$ ratios or εHf values). Zircon grains are highly resistant to weathering and preferentially sorted into coarse-grained fractions during sediment transport and thus deposited in the sandy fraction, close to the shelf, whereas clay minerals (characterized by high Lu/Hf) are transported further (Patchett et al., 1984). Silicate weathering also leads to the preferential dissolution of Lu-rich mineral phases such as apatite and sphene, which releases radiogenic Hf (i.e. high $^{176}Hf/^{177}Hf$ ratios or εHf values) to river waters and presumably to seawater (Bayon et al., 2006).

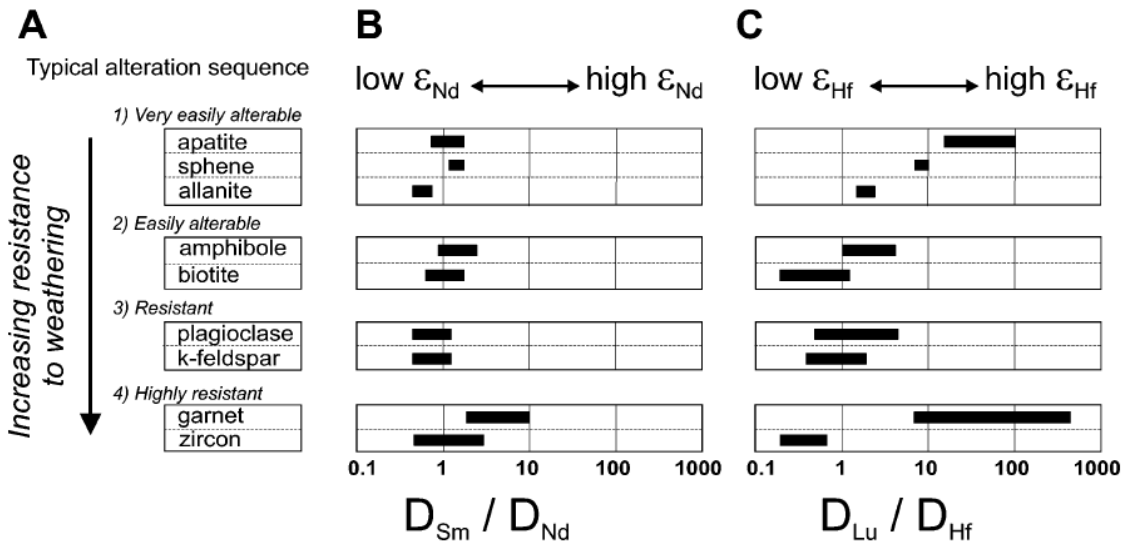

Figure 1.15. Representation of the link between Hf isotopes and the intensity of silicate weathering (modified from Bayon et al., 2006). A) Alteration sequence of a granitic rock, **B)** Ratios of mineral-liquid partition coefficients Sm-Nd, **C)** Ratios of mineral-liquid partition coefficients Lu-Hf. Source: **(Bayon et al., 2006)**

In addition to the "zircon effect," the relative contribution of radiogenic clays in the <2 µm fine-grained fraction of sediments, compared to fine-grained primary minerals with a less radiogenic Hf isotopic composition, can impact the εHf of the clay fraction in sediments. Increased weathering intensifies the deviation of εHf from the clay line. This deviation, referred to as $\Delta\varepsilon Hf_{clay}$ (**Fig. 1.14**), represents the vertical difference from the "Clay array" and reflects the relative contribution of unaltered primary detrital minerals with low εHf and secondary clay minerals with a pronounced εHf. Therefore, within the zircon-depleted clay fraction of river sediments, $\Delta\varepsilon Hf_{clay}$ has been shown to provide valuable information about the intensity of chemical weathering of silicates in the source regions, with higher ΔεHf values indicating more intense chemical weathering (Bayon et al., 2016).

1.4.3. Paired clay and Fe Oxide fraction: a novel proxy

Rivers transport dissolved and particulate rare earth elements REEs, representing a major pathway by which these elements are supplied to the oceans. The distribution and isotopic composition of REEs in river waters and sediments reflect the lithology of the rocks undergoing weathering within a watershed and span a wide range of signatures (Goldstein and Jacobsen, 1987, 1988a; Goldstein et al., 1984). Although REEs are not expected to strongly fractionate during low-temperature processes, measurable variations do occur in riverine sediments. For example, both REEs and associated major and trace elements can fractionate as a function of grain size (Bouchez et al., 2011; Bayon et al., 2015). This fractionation results from the preferential alteration of feldspars and accessory minerals, producing progressive enrichment of light REEs (LREEs) and Eu in clay-sized particles relative to coarser silts. For this reason, the detrital fraction considered in this thesis focuses on clays (<2 µm), which provide the most sensitive archive of weathering signals and avoid the contamination of REE-rich phases that are resistant to chemical weathering (e.g., zircon, monazite).

Because of their systematic fractionation behaviour, REEs are widely employed as tracers of sediment provenance and chemical weathering (Taylor and McLennan, 1985). River clays draining different lithologies display distinctive REE patterns: relatively flat spectra for average crustal and sedimentary rocks, and heavy REE (HREE)-enriched spectra for volcanic terrains (Bayon et al., 2015). Such features are particularly useful for distinguishing contributions from cratonic, volcanic, and sedimentary sources to large river systems (**Fig. 1.16**). Importantly, REE signatures preserved in both detrital silicates and authigenic phases such as Fe oxides capture not only the imprint of primary mineral sources, but also secondary processes associated with weathering, transport, and deposition.

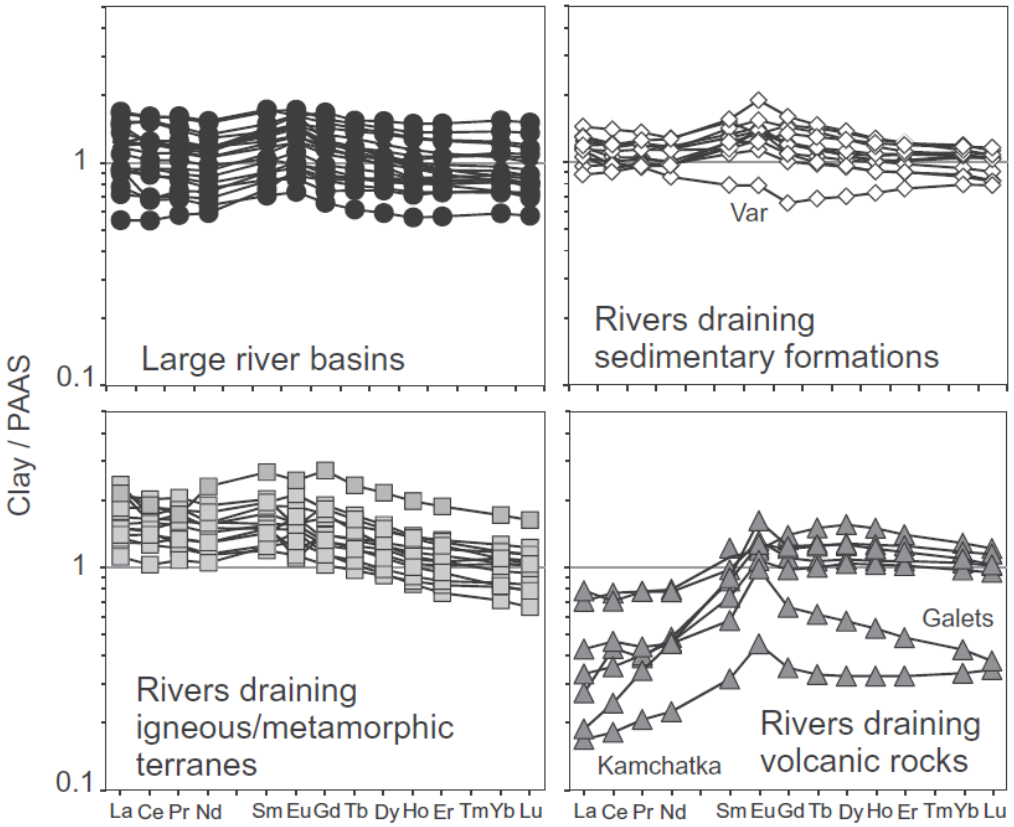

Figure 1.16. Shale-normalized (PAAS; Taylor and McLennan, 1985) REE patterns for World River clay fractions. Source: Bayon et al. 2015

Eroded continental rocks and river sediments host a variety of authigenic mineral phases, including Fe oxides, which play a crucial role in geochemical cycling in Earth's surface environments (**Fig. 1.17**). Labile iron oxide and oxyhydroxide phases (e.g, ferrihydrite, lepidocrocite) transported by rivers are either formed as secondary weathering products in soils or originate from the erosion of ancient sedimentary rock formations in source regions, making them integral carriers of continental weathering signals (Bayon et al., 2020b). Recent studies have shown that REEs and the Nd isotopic compositions in paired detrital fraction and labile (oxy)hydroxides phases leached from river sediments can be a powerful tool for distinguishing the bedrock lithology and weathering processes within watersheds (Bayon et al., 2020b; Hindshaw et al., 2018; Jang et al., 2024, 2020; Larkin et al., 2021; Süfke et al., 2019; Von Blanckenburg et al., 2015). Two particularly informative tracers applied to Fe oxides are: (i) the degree of mid-REEs (MREEs) enrichment in shale-normalized patterns and (ii) the Nd isotopic decoupling between sedimentary Fe oxides and corresponding detrital fractions, expressed as $\Delta\varepsilon Nd_{Feox\text{-}Det}$ (Bayon et al., 2020).

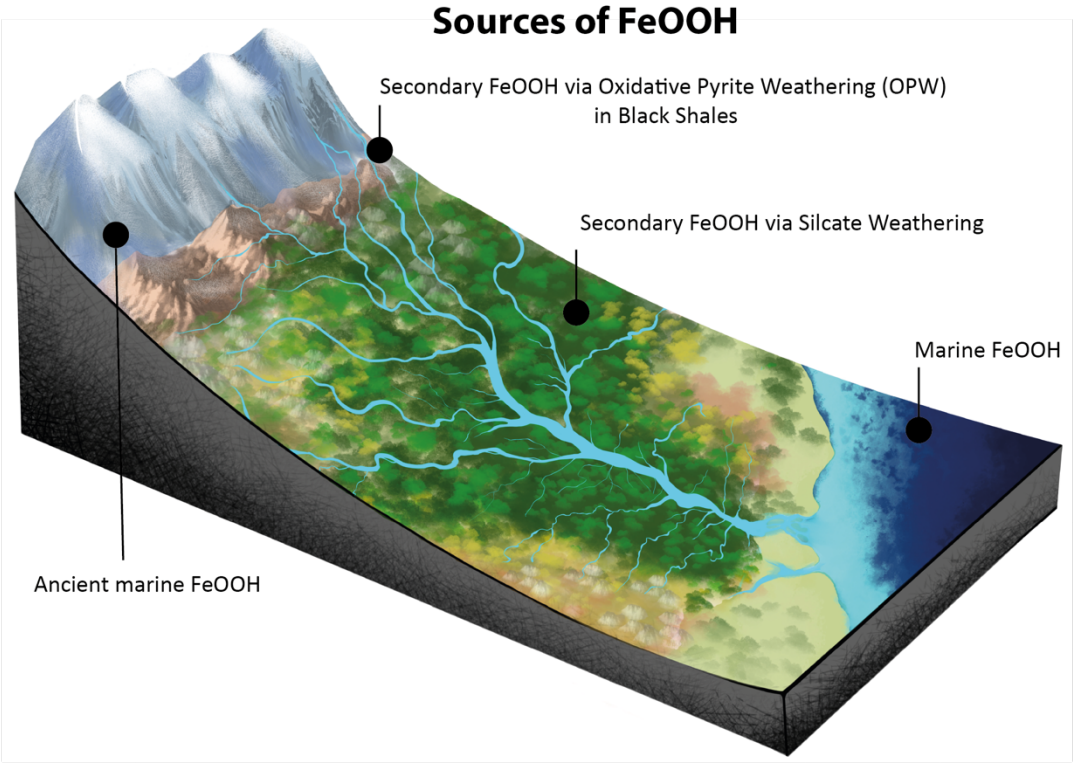

Figure 1.17. Sources of labile FeOOH phases to riverine fluxes. Illustration by Vinicius Reis.

The degree of MREE enrichment can be quantified using the *concativity index* (CI), defined as:

$$CI = Gd_n/(La_N^6 \times Yb_N^7)^{1/13}$$

This formulation allows REE distribution to be parametrized in a two-dimensional space, where theoretical values of CI can be visualized on an $(Gd/Yb)_N$ vs $(La/Gd)_N$ diagram (**Fig. 1.18**):

$$(La/Gd)_N = [(Gd/Yb_N) \times 1/x]^{7/6}/x$$

In catchments draining crystalline igneous and metamorphic rocks, Fe oxides mostly correspond to secondary Fe oxides formed during the chemical weathering of the underlying bedrock and exhibit minimal MREEs enrichment (CI = 1.2–2). In contrast, river basins dominated by sedimentary rocks typically carry riverine Fe oxide phases with intermediate CI values (~2–2.5), interpreted as reflecting the presence of ancient marine and/or diagenetic Fe oxyhydroxide precipitates eroded from upstream source regions. In sedimentary catchments, exceptionally high CI values (>2.5) have been reported in glacial environments and catchments hosting substantial black shale deposits, such as Svalbard and the Mackenzie Basin, which

were attributed to sulfide weathering processes (Jang et al., 2024; Larkin et al., 2021; Bayon et al., 2020a). While the exact mechanism remained elusive, these authors proposed that intense pyrite oxidation in such catchments results in sulfuric acid-mediated dissolution of sedimentary phosphate minerals (apatite) characterized by pronounced MREE enrichments, thereby leading to subsequent precipitation of secondary Fe oxyhydroxide phases in soils with inherited high CI values (Jang et al., 2024).

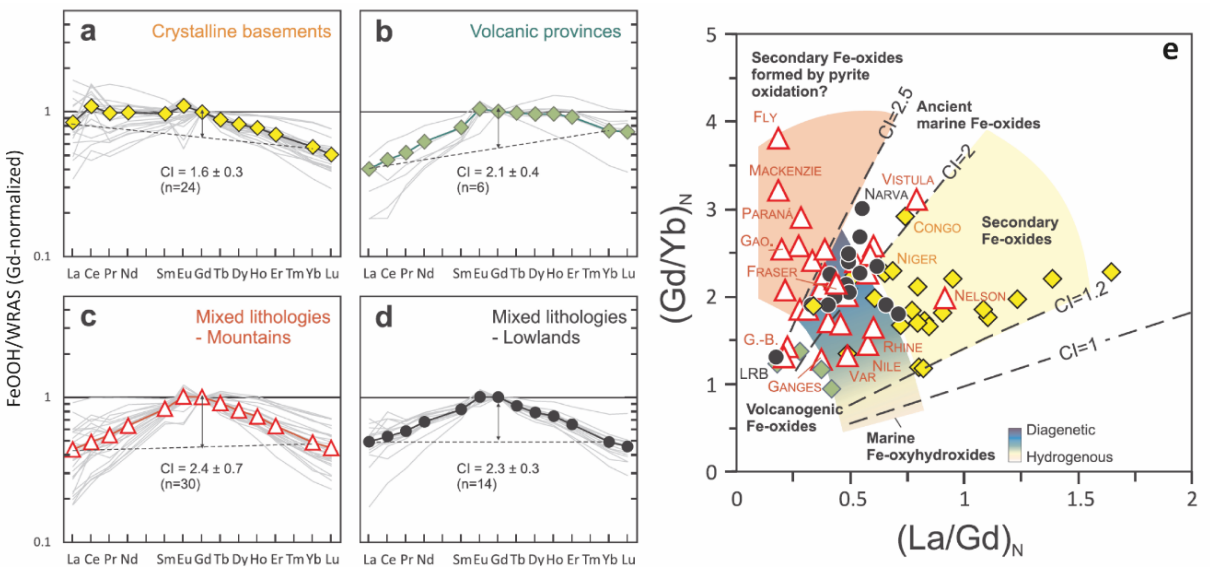

Figure 1.18. Shale-normalized (WRAS; Bayon et al., 2015) REE patterns for riverine Fe oxides. (A) igneous and metamorphic crystalline basements; **(B)** volcanic provinces; **(C)** low-elevation regions (< 1000 m) draining sedimentary and multi-lithological catchments regions; and **(D)** mountainous regions (> 1000 m) draining sedimentary and multi-lithological catchments. For clarity, note that the REE data for leached sediment fractions (reported relative to the initial mass of bulk sediment) were also normalized to Gd WRAS. The thin grey lines correspond to individual samples, while the thicker line with symbols represents the average shale normalized pattern for each sample category. **(E)** WRAS-normalized Gd/Yb and La/Gd ratios and calculated theoretical concativity index lines. Fields indicate the sources of FeOOH phases. Source: Bayon et al., 2020

The application of Nd isotopes on paired detrital and Fe oxide fractions of river sediments offers additional insight into the nature of weathered source rocks on continents (Bayon et al., 2020a). In crystalline-rock catchments (granitic, metamorphic, basaltic), Fe-oxides typically exhibit εNd values like coexisting silicate residues, indicating a common origin through silicate weathering (**Fig. 1.19**). Conversely, in sedimentary or mixed-lithology watersheds, the Nd isotopic composition of riverine Fe oxides commonly departs from ε_{Nd} values of the coexisting detrital fractions (Bayon et al., 2020a; Jang et al., 2020; Hindshaw et al., 2018). This isotopic decoupling is best explained as reflecting the influence of REE contributions

sourced from non-silicate rocks in riverine Fe oxyhydroxides, such as ancient marine Fe oxides eroded from sedimentary strata (Bayon et al., 2020a; Jang et al., 2020).

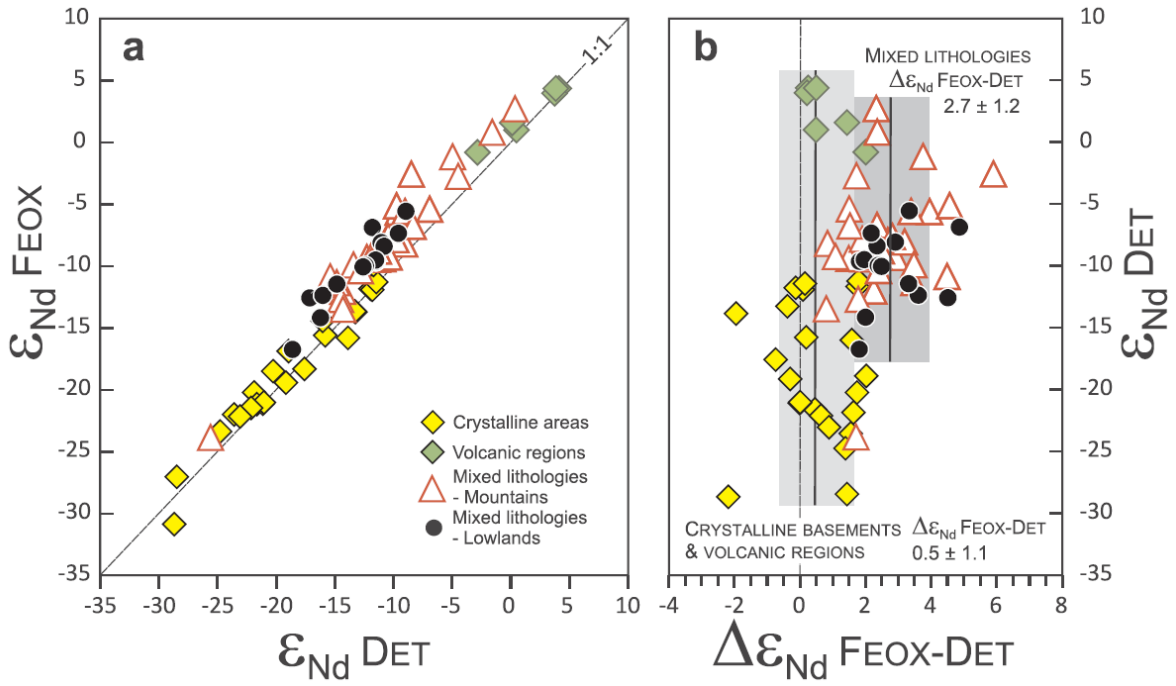

Figure 1.19. Distribution of Nd isotopes in paired Fe-oxide and silicate detrital fractions of world river sediments. (A) Dotted line corresponds to a 1:1 relationship between Nd isotopes (expressed using the epsilon notation εNd in Fe oxide and detrital fractions. **(B)** ΔεNdFeox-Det represents the Nd isotopic difference measured between paired Fe-oxide and detrital silicate fractions. Source: Bayon et al., 2020.

When considered together, $\Delta\varepsilon Nd_{FeOx-Det}$ and CI values reveal coherent trends: catchments dominated by silicate weathering generally show ΔεNd < 1.6 and CI < 2, while systems influenced by sedimentary rock alteration display ΔεNd > 1.6 and CI > 2 (**Fig. 1.20**). Interestingly, extreme MREE enrichments (CI > 2.5) in black-shale catchments are not necessarily accompanied by higher ΔεNd, implying that REE patterns and Nd isotopes provide complementary, rather than redundant, information on Fe-oxide sources.

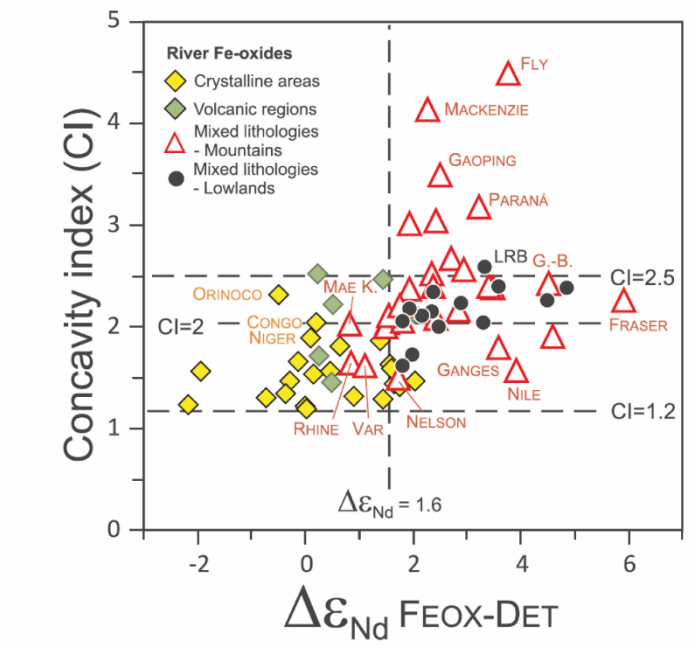

Figure 1.20. REE concativity index (CI versus $\Delta\varepsilon Nd_{Feox\text{-}det}$ in leached Fe oxide fraction.

Beyond lithological control, these proxies also capture climatic and geomorphic influences. In lowland regions, $\Delta\varepsilon Nd_{FeOx-Det}$ correlates with temperature in an Arrhenius-like fashion, reflecting enhanced silicate alteration and secondary Fe oxide formation under warmer conditions (Bayon et al. 2020). In high-elevation basins, ΔεNd instead scales with maximum basin elevation, consistent with thicker soils and warmer environments at lower altitudes, which favor intensified weathering. Together, these relationships suggest that sedimentary rock alteration dominates in high-relief environments, whereas silicate weathering processes prevail in floodplains (Jang et al., 2024).

Overall, the paired clay–Fe oxide approach offers a powerful new means of disentangling silicate from non-silicate weathering contributions in modern rivers. By jointly analyzing detrital clays and labile Fe oxides, this framework overcomes a key limitation of earlier isotope records, which often conflated lithological variability with changes in silicate flux. When combined with established silicate weathering indicators, such as Hf isotopes of the clay fraction, the dual-fraction method provides an integrated toolset for deconvolving provenance and weathering signals in continental source-to-sink systems. Yet its application to ancient sediments remains untested. A crucial prerequisite is to verify that leached Fe-oxide phases in sedimentary archives faithfully reflect river-borne oxides, and to assess how early diagenesis or other post-depositional processes may alter their original REE and Nd isotope compositions.

1.5. Thesis outline and objectives

This thesis addresses a series of interrelated scientific questions by applying a consistent set of geochemical tools to a diverse range of sedimentary archives. The main objectives are:

1. **Calibrate new geochemical proxies**, REE and Nd isotopic compositions of paired Fe-(oxyhydr)oxides (FeOOH) and clay fractions, against modern climatic, topographic, and lithologic parameters in the Amazon Basin.
2. **Establish a high-resolution astronomical age model** for the Neogene Amazon Fan record, enabling robust correlation with global climate and sea-level signals.
3. **Evaluate the integrity of easily reducible FeOOH phases** in deep-marine sedimentary archives, particularly the Amazon Fan, to assess their reliability for constraining continental weathering processes.
4. **Characterize the provenance of Amazon Fan sediments** using clay Nd isotopes and mixing models, in order to resolve the timing and pathways of transcontinental drainage integration.
5. **Disentangle silicate versus sedimentary rock weathering** during Andean uplift and assess its implications for the long-term carbon cycle and climate regulation.

This introductory chapter has outlined the state of the art regarding the long-term carbon cycle, climate change, the geological evolution of the Amazon Basin, and the geochemical proxies applied in this thesis. The remainder of the manuscript addresses the objectives above, structured into the following chapters:

- **Chapter II** describes the study areas, sampling strategy, laboratory procedures, and analytical methods used to obtain geochemical measurements.
- **Chapter III** presents the calibration of REE and Nd isotope proxies in riverine sediments collected during the AMANAUS cruise in 2023 (currently under review in *Chemical Geology*).

- **Chapter IV** develops an astronomically tuned age model for the BP-3 Well, which underpins the chronological framework of this thesis. This work was published in Global and Planetary Change in September 2025.
- **Chapter V** examines the detrital record of the BP-3 core, including potential contamination by drilling muds, and evaluates sample integrity.
- **Chapter VI** characterizes the leached Fe–Mn fraction in BP-3 sediments and assesses its suitability as a tracer of continental weathering processes.
- **Chapter VII** provides a comprehensive provenance reconstruction of the Amazon Fan over the last 23 Ma, incorporating both new results and compiled literature data across northern South America.
- **Chapter VIII** integrates the late Cenozoic co-evolution of tectonics, climate, and weathering in the Amazon Basin, drawing on the multiproxy datasets developed in this work.
- **Chapter IX** synthesizes the main findings and presents the conclusions of the thesis.

Appendix 1 contains a paper published in the *Journal of South American Earth Sciences*, where I am the first author, entitled *"New constraints on the Late Miocene–Pliocene deformational and depositional evolution of the Eastern Cordillera and Sub-Andean Zone in southern Peru."* This study addresses the uplift history, sedimentology, and provenance of the southern sector of the Madre de Dios Basin in Peru.

Appendix 2 includes a manuscript submitted to a special issue of *Geological Magazine*, where I am a co-author, entitled *"Neogene paleo-drainage divide in western Amazonia (Madre de Dios Basin, Peru): provenance evidence and implications."* This work explores contrasts between the northern and southern sectors of the basin and evaluates their implications for the interpretation of regional-scale provenance signals.

II

Materials and Methods

Declaration/ Declaração/ Déclaration

Study sites, sampling, laboratory preparation, and analysis are summarized in this chapter. All sample handling, such as sieving, drying, and weighing of sediments, was carried out under normal laboratory conditions. Sediment leaching, sample digestion, dilutions, and column chemistry were carried out in a class 1000 clean laboratory at IFREMER. HCl and HNO_3 used in dissolution and column chemistry were distilled at IFREMER in Teflon sub-boiling units. Following IFREMER's guidelines, for insurance reasons, all chemistry involving HF must be conducted by a permanent contract employee. Therefore, Germain Bayon carried out sample digestion and HF isotope chemistry. Reagents were diluted with ultra-pure de-ionized water with a resistivity of 18.2 MΩ (MQ). Teflon beakers and plasticware (e.g., centrifuge tubes, Nalgene bottles) used to collect, dry down, react, or dissolve samples were pre-cleaned with 6M HCl or 2% HNO_3. Unless otherwise specified, all analysis was carried out on analytical instruments of the Pôle Spectrométrie Océan (Brest, France).

[PT] *Os locais de estudo, a amostragem, a preparação laboratorial e as análises são resumidos neste capítulo. Todo o manuseio de amostras, como peneiramento, secagem e pesagem de sedimentos, foi realizado em condições laboratoriais normais. A extração sequencial dos sedimentos, a digestão das amostras, as diluições e a química de colunas foram realizadas em um laboratório limpo classe 1000 no IFREMER. O HCl e o HNO_3 utilizados nas etapas de dissolução e na química de colunas foram destilados no IFREMER em unidades de sub-ebulição de Teflon. De acordo com as diretrizes do IFREMER, por razões de seguro, toda a química envolvendo HF deve ser conduzida por um funcionário com contrato permanente. Assim, Germain Bayon realizou a digestão das amostras e a química isotópica envolvendo HF. Os reagentes foram preparados com água deionizada ultrapura, com resistividade de 18,2 MΩ (MQ). Béqueres de Teflon e materiais plásticos (por exemplo, tubos de centrífuga, frascos Nalgene) usados para coletar, evaporar a seco, reagir ou dissolver as amostras foram previamente limpos com HCl 6 M ou HNO_3 a 2%. Salvo indicação em contrário, todas as análises foram realizadas nos instrumentos analíticos do Pôle Spectrométrie Océan (Brest, França)*.

[FR] Les sites d'étude, l'échantillonnage, la préparation en laboratoire et les analyses sont résumés dans ce chapitre. Toutes les manipulations d'échantillons — tamisage, séchage et pesée des sédiments — ont été réalisées dans des conditions de laboratoire standard. L'extraction séquentielle des sédiments**,** la digestion des échantillons, les dilutions et la chimie de colonne ont été effectuées dans un laboratoire propre de classe 1000 à l'IFREMER. Le HCl et le HNO_3 utilisés pour les dissolutions et la chimie de colonne ont été distillés à l'IFREMER dans des unités de sub-ébullition en Téflon. Conformément aux directives de l'IFREMER, pour des raisons d'assurance, toute chimie impliquant le HF doit être réalisée par un employé en contrat permanent. En conséquence, Germain Bayon a effectué la digestion des échantillons et la chimie isotopique impliquant le HF. Les réactifs ont été dilués avec de l'eau désionisée ultrapure d'une résistivité de 18,2 MΩ (MQ). Les béchers en Téflon et les consommables plastiques (p. ex., tubes de centrifugation, flacons Nalgene) utilisés pour collecter, évaporer à sec, réagir ou dissoudre les échantillons ont été préalablement nettoyés avec du HCl 6 M ou du HNO_3 à 2 %. Sauf indication contraire, toutes les analyses ont été réalisées sur les instruments analytiques du Pôle Spectrométrie Océan (Brest, France).

2.1. Study sites and sampling

In this thesis, we investigated three key regions that comprise the Andes–Amazon Fan source-to-sink system: (I) the upper Madeira Basin, (II) the lower Amazon River and its major tributary confluences, and (III) the Amazon Fan (**Figure 2.1**). Detailed sampling location, methodology, and geology specific to each region are discussed in their dedicated chapters.

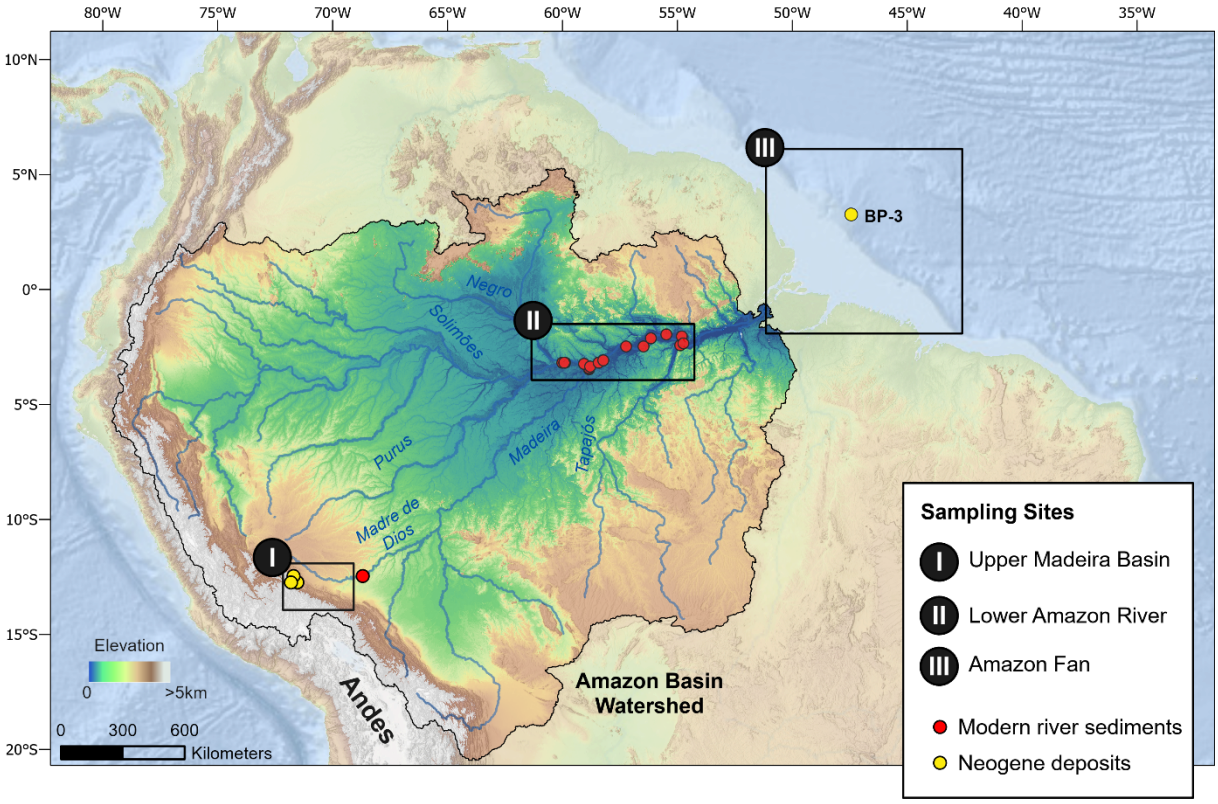

Figure 2.1. The Andes–Amazon Fan source-to-sink system. The study areas are: (I) the upper Madeira Basin, (II) the main stem of the Amazon River, and (III) the Amazon Fan. Sampling locations are indicated by yellow circles (Neogene deposits) and red circles (modern sediments).

A total of 202 samples were collected and analyzed (**Table 2.1**), comprising 18 modern riverine samples and 163 Miocene–Pleistocene sediment samples recovered from an exploration well drilled in the Foz do Amazonas Basin (FAB). In addition, nine Neogene samples from the upper Madeira River (Madre de Dios Basin), originally collected during the PhD thesis of M. Lauterbach (2014), were also included.

Table 2.1. Summary of the samples analyzed in this study.

Study Site	Sediment Fraction	Sample Count	Analysis	Elements/Isotopes	Instrument
Amazon Basin	> 63µm	13		Major & trace elements Nd Isotopes	
	63-10µm	19		Major & trace elements Nd Isotopes	
	10-2µm	19	SF-ICP-MS MC-ICP-MS	Major & trace elements Nd Isotopes	Element XR Neptune
	< 2µm	19		Major & trace elements Hf-Nd Isotopes	
	Fe Oxides	19		Major & trace elements Nd Isotopes	
Amazon Fan	Bulk	38	WD-XRF	Major elements	Bruker S8
	< 2µm	44	XRD	Clay mineralogy	Bruker D8
		141	SF-ICP-MS MC-ICP-MS	Major & trace elements Hf-Nd Isotopes	Element XR Neptune
	Fe Oxides	141	SF-ICP-MS MC-ICP-MS	Major & trace elements Nd Isotopes	Element XR Neptune
Upper Madeira Basin	Fe Oxides	9	SF-ICP-MS	Major & trace elements	Element XR

2.1.1. Amazon Basin River sediments

The collection of river sediments for chemical and isotopic analyses typically involves sampling either suspended particulate matter (SPM), riverbank, and/or bedload sediments. SPM is most commonly isolated from river water through membrane filtration using vacuum or pressure-driven systems. However, there is no universally standardized filtration method or membrane pore size, leading to variability in the operational definition of the particulate phase across studies (Tipper et al., 2025 and references therein). As an alternative, large volumes of river water may be collected and allowed to settle, enabling sediment to accumulate over time.

In this study, river sediments were collected during the AMANAUS cruise (PIs: M. Rabineau and D. Aslanian) in July 2023 at 18 sites along the lower Amazon River and four major tributaries, the Solimões, Negro, Madeira, and Tapajós, between the cities of Manaus and Santarém (**Fig. 2.1**; Chapter III). This sampling occurred during the high-water season (February to August), a period characterized by peak discharge and low SPM concentrations in Amazonian rivers (Rousseau et al., 2019; Martinez et al., 2015; Filizola and Guyot, 2009; Viers et al., 2008). At each site, approximately 15 liters of surface water were collected from the mid-channel at a

depth of ~30 cm using pre-cleaned plastic containers. Samples were left to settle undisturbed for 14 days, after which the sediment was carefully transferred to 50 mL centrifuge tubes.

This method yielded at least 2 grams of sediment per sample in the lower Amazon and its Andean-fed tributaries (e.g., Solimões and Madeira), which was sufficient for subsequent chemical and isotopic analyses. However, due to inherently low SPM concentrations in the Negro and Tapajós rivers, this approach did not provide enough material. To supplement the dataset, recently deposited riverbank sediments were collected at these sites, as well as at several others, to obtain material representative of modern or near-modern sedimentation within the past few centuries.

Previous studies have documented significant vertical heterogeneity in sediment concentration, grain size, mineralogy, and geochemistry within the Amazon River water column (Bouchez et al., 2011). Given that our dataset includes both SPM and riverbank samples, we focused specifically on the <2 µm clay-sized fraction to represent the detrital component (see Section 2.3). Targeting this fine fraction helps minimize the effects of grain-size sorting and improves comparability across different sample types and river systems.

2.1.2 Neogene sediments of the Upper Madeira Basin

The nine Neogene samples from western Amazonia were collected from river outcrops within the upper Madeira Basin, specifically the Madre de Dios sub-basin (**Fig. 2.1**; Appendix 1). Six samples were recovered from the Inambari River in the southern part of the basin, and three from the upper reaches of the Madre de Dios River. One modern riverbank sample was collected downstream of the Madre de Dios River. This region was selected due to its significance as a hotspot for sulfide and organic carbon oxidation, key processes associated with the chemical weathering of black shales (Dellinger et al., 2023; Torres et al., 2015, 2016; Moquet et al., 2011, 2014). An in-depth discussion of the geodynamic evolution of this region can be found in Moizinho et al., (2024) and Roddaz et al. (under review), both of which are attached as appendices to this thesis.

2.1.3 The Foz do Amazonas Neogene Deposits

Since the Late Miocene the Amazon submarine fan has been the primary depocenter for siliciclastic sediments along the Brazilian Equatorial Margin, trapping the immense terrigenous load of the Amazon River and preserving a high-fidelity archive of Neogene geodynamic and climatic change of Northern South America (Figueiredo et al., 2009; Gorini et al., 2014; Hoorn et al., 2017).

In this thesis, we analyzed ditch-cutting samples recovered from exploration well BP-3-APS (hereafter referred to as BP-3), drilled by British Petroleum in 2005 on the upper Amazon Fan (3° 2' 58.660" N, 47° 44' 45.801" W, water depth 754 m; total depth 5655 mbsl; **Fig. 2.1**). It's important to note that, ditch cuttings are the only geological material available on the region and that this specific well have been the main Neogene record of the Amazon Fan evolution and extensively investigated in the literature. This BP-3 has appeared under various designations, including Well 2 (Figueiredo et al., 2009; Hoorn et al., 2017; Lammerstma et al., 2018), Well 4 (Gorini et al., 2014), and Well P1 (Reis et al., 2016). An age model for BP-3 was initially established using calcareous nannofossil biostratigraphy (Figueiredo et al., 2009) and later updated to the GTS2012 timescale (Hoorn et al., 2017). This study focuses on the interval between 1450 and 4800 mbsl, spanning the Late Oligocene (NP25) to the Pleistocene (NN19).

Petrobras and the Brazilian National Agency of Petroleum, Natural Gas, and Biofuels (ANP) made the well report available to this study under the process (SAA 48610.204116/2022-88). It was accompanied by lithological descriptions and basic downhole data, including sonic, gamma ray, and caliper density logs. Five casings were installed throughout the sampled section during drilling to prevent borehole collapse (Hoorn et al., 2017). The lithostratigraphy of this interval consists of alternating limestone and mudstone between 4800 and 4080 mbsl, followed by a transition to siltstone and fine sandstone down to 3620 mbsl, and interbedded mudstone and siltstone from that depth up to 1450 mbsl.

2.2. Bulk-rock geochemistry

The major element composition of the bulk rock fraction from a subset of 38 samples collected from the Amazon Fan was determined using wavelength-dispersive X-ray fluorescence (WD-XRF) analysis on fused glass beads, performed with a Bruker S8 Tiger spectrometer. The analytical procedure began with calcination of the dried samples at 1050 °C to remove volatile components such as carbon, which are not detected by WD-XRF. Following calcination, 0.1 g of the resulting powder was mixed with 6 g of flux (90% $Li_2B_4O_7$ – 10% LiF; SCP Sciences) and 500 µL of a non-wetting agent (a 250 $g{\cdot}L^{-1}$ solution of LiBr; Merck). The mixture was then fused at 1100 °C in an automatic fusion furnace to produce glass beads for analysis.

A calibration curve was established using certified geochemical reference materials prepared using the same fusion protocol. These standards included materials from the Canadian Certified Reference Materials Project (CCRMP) and the United States Geological Survey (USGS). Measurement quality was evaluated through the analysis of two certified reference materials, REE-2 and SYMP-1. Overall, the accuracy for most major oxides was better than 4%, with the exception of MnO and Na_2O in SYMP-1 (**Fig. 2.2**)

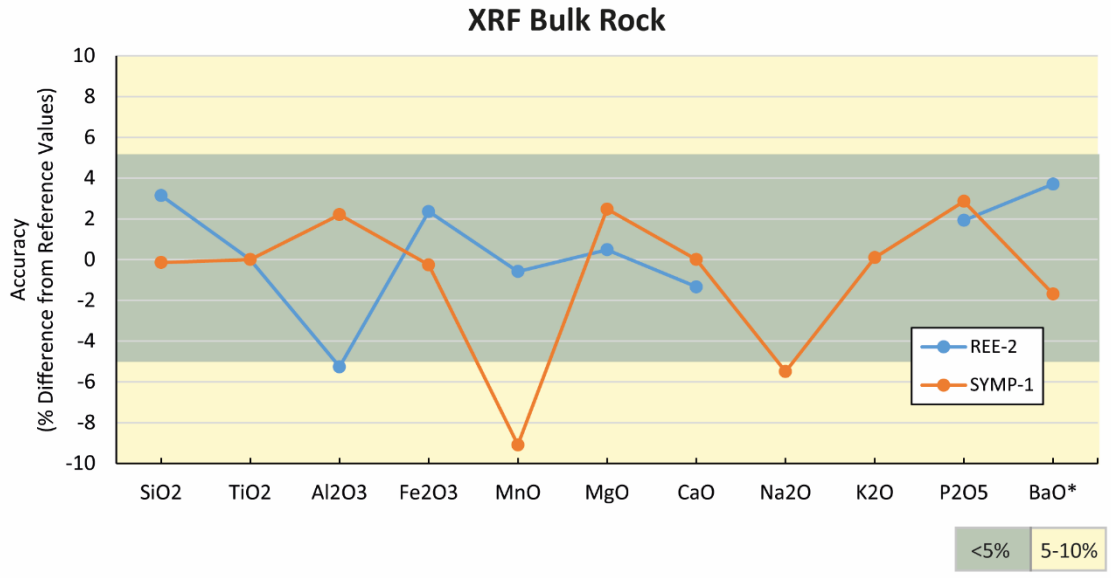

Figure 2.2. Accuracy of measurements on certified reference materials during XRF analytical session. **R**EE-2 (CRM for Carbonatite with Rare Earth Elements; CCRMP, 2016) and SYMP-1 (Mountain Pass Syenite; Webb et al., 2016).

2.3. Sequential extraction of labile Fe oxide phases

With the exception of the samples that went for bulk XRF analyses, all samples in this thesis underwent a sequential leaching procedure to selectively separate different reactive phases within the sediment. The method is outlined in **Table 2.2** and **Figure 2.3** and explained in detail below.

Approximately 1 g of sieved (<63µm) powdered bulk samples was transferred into 50 ml polyethylene centrifuge tubes. Carbonates were dissolved using 20 ml of 5% (v/v) acetic acid (CH_3COOH) on a mechanical shaker for 2–3 hours, followed by centrifugation at 2000 rpm for 2 minutes to separate the supernatant. To extract more resistant carbonate phases and easily reducible Fe-Mn (oxy)hydroxides (e.g., ferrihydrite, lepidocrocite; Poulton and Canfield, 2005), 20 ml of a 15% (v/v) acetic acid and 0.5 M hydroxylamine hydrochloride (HH) solution were added to the residue. The tubes were shaken for 48 hours and then centrifuged at 3000 rpm for 2 minutes. The leachate was filtered through a 0.20 µm cellulose acetate membrane, evaporated to dryness on a hot plate, redissolved in concentrated HNO_3 to remove HH, and finally taken up in 4 M HCl for subsequent analysis. This final solution is referred to as ***Fe oxides mother solutions***.

Table 2.2. Sequential extraction procedure

Stage	Reagent	Volume of Reagent	Target Phase	Procedure
1	5% (v/v) Acetic Acid (CH_3COOH)	20 mL	Carbonates	Mechanical shaker for 2-3hours, centrifuge 2 mins @ 2000 rpm
2	15% (v/v) Acetic Acid and 0.5 M hydroxylamine hydrochloride	20 mL	Fe-Mn (oxy)hydroxides	Mechanical shaker for 48hours, centrifuge 2 mins @ 3000 rpm
3	35% (v/v) Hydrogen Peroxide (H_2O_2)	20 mL	Organic Matter	Mechanical shaker for 72 hours, centrifuge 2 mins @ 2500 rpm
4	0.1 M disodium ethylenediaminetetraacetate dihydrate (Na_2-EDTA)	10 mL	Desorb surface-bound trace elements	Mechanical shaker for XX hours, centrifuge 2 mins @2500 rpm

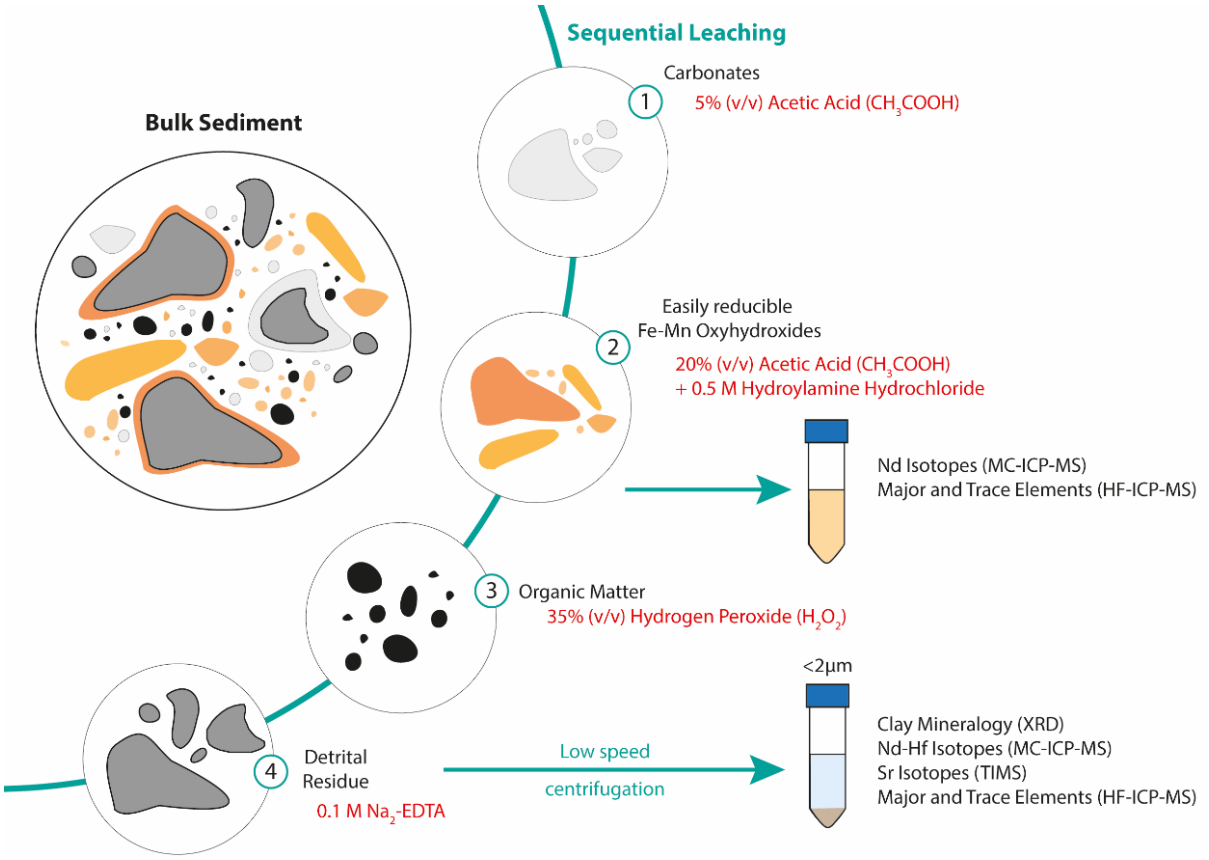

Figure 2.3. A diagram illustrating the sequential leaching procedure for bulk sediments. Numbers 1 to 4 indicate the order in which the chemical leaches are sequentially separated (Table 2.2). After step 4, the <2 µm fraction was separated via low-speed centrifugation (see text for details). Illustration generated with the help of Adobe Illustrator proprietary generation AI.

The residual detrital fraction was rinsed with 10 mL of ultrapure water and centrifuged again at 2000 rpm for 2 minutes. Organic matter was removed by adding 20 ml of 35% (v/v) hydrogen peroxide (H_2O_2), with samples left on a mechanical shaker for 72 hours. After centrifugation at 2500 rpm for 2 minutes, the residues were rinsed with ultrapure water and centrifuged at 3000 rpm for 2 minutes. Finally, to desorb surface-bound trace elements (e.g., Hf, Nd) released during earlier leaching steps, 10 ml of 0.1 M disodium ethylenediaminetetraacetate dihydrate (Na_2-EDTA) was added to the samples, mixed for 3 hours in the mechanical shaker, centrifuged, and then rinsed with MQ water.

2.4. Grain-size separation via low-speed centrifugation

Following final rinsing steps with ultrapure water after the final sequential leaching step, the clay-sized fraction (<2 μm) was isolated from the coarser detrital material by low-speed centrifugation, using parameters calculated with *Sedicalc* freeware (Krumm, 2006), following the protocol of Bayon et al. (2015). This separation step effectively excludes zircon grains >1.5 μm ($\rho \approx 4.85$ g/cm^3) and is also likely to remove dense (>4.5 g/cm^3), coarse-grained diagenetic LREE-bearing phosphates such as monazite and xenotime, which may precipitate in coarse-grained, shallow-water, marine sediments durig early diagenesis (e.g., Rasmussen et al., 1996, 2001; Wing et al., 2003). This method is shown in **Table 2.3**.

Table 2.3. Procedure for separation of the < 2 μm fraction from the detrital residue.

Stage	Solution	Procedure
1	20 mL of MQ H_2O	Centrifuge 2 mins @1000 rpm
	Transfer clays	
2	20 mL of MQ H_2O in the residue	Centrifuge 2:30 mins @800 rpm
	Transfer clays	
3	1 mL of conc. Acetic Acid into the clay tube	Centrifuge 3 mins @3500 rpm
	Throw away supernatants	

Exclusively for the modern Amazon River sediments, the residual silt fraction was further separated into coarse/medium silt (10-63μm) and fine silt (2-10μm) by centrifuging the residue at 200 rpm for 2 minutes.

2.5. Clay Mineralogy

A selected number (45) of clay fractions from the Amazon Fan were selected for clay mineralogy analysis. Clays were oriented on glass slides and subjected to X-ray diffraction analysis (XRD). These analyses were conducted at 2.36 2θ using a Bruker D8 Advance at the Geoscience Environment Toulouse (GET). Three tests were performed on the oriented mounts: (1) untreated sample, (2) glycolated sample (saturated for 12 hours in ethylene glycol), and (3) sample heated at 490°C for 2 hours (Holtzapffel, 1985). Identification was carried out using the Diffrac Eva processing software supplied by Bruker. Each clay mineral was identified by its layer plus interlayer interval. Semi-quantitative estimation of clay mineral abundances (±10%) followed the method detailed by Holtzapffel (1985) and was performed using the MacDiff software developed by R. Petschick. Diffractograms are attached to the appendix.

2.6. Sample Digestion

After the addition of a Tm spike, detrital sediment fractions (between 40-80mg) were digested in PTFE vials using a mixture of concentrated ultrapure HF, HNO_3, and HCl. Samples were left on a hot plate at 140 °C for 5 days to ensure thorough breakdown of silicate minerals. After evaporation to dryness, 6 M HCl was added, and the samples were refluxed for an additional 2 days at 140 °C to eliminate fluoride complexes and achieve complete dissolution. This digestion procedure consistently yielded clear solutions, except for occasional black carbon particles observed in some organic-rich samples. The products of our sample digestion procedure are referred to as ***detrital mother solutions***.

2.7. Major and trace elements

Abundances for selected major and trace element were determined using a Thermo Scientific Element XR sector field inductively coupled plasma mass spectrometer (SF-ICP-MS). Analyses were performed on 2% HNO_3 solutions prepared from aliquots of the ***mother solutions.***) Prior to major and trace analysis Fe-Mn oxyhydroxides leachate mother solutions were spiked with 10 μm of Tm solution during sample dilution. Major elements (^{23}Na, ^{24}Mg, ^{27}Al,

^{31}P, ^{44}Ca, ^{47}Ti, ^{55}Mn, ^{56}Fe) were measured at medium mass resolution, while rare earth elements (REEs) and selected trace elements (^{88}Sr, ^{89}Y, ^{90}Zr, ^{138}Ba, ^{178}Hf, ^{232}Th, ^{238}U) were acquired in low-resolution mode. A solution prepared with BHVO-2 was run after every three samples and used for both calibration and instrumental drift corrections, following the procedure of Barrat et al., (2012, 1996)

Raw intensities were first corrected for instrumental drift, procedural blanks, and known spectral interferences. Preliminary elemental concentrations were calculated from these corrected data; however, they do not yet represent absolute abundances. At this stage, measured Er and Yb concentrations were used to interpolate the Tm content in each sample. Final elemental abundances were calculated based on the known amount of Tm added during sample preparation and the interpolated Tm concentration. This Tm addition method minimizes the impact of potential signal drift on the results, yielding more robust and reproducible data. Final concentrations are reported relative to the working values established for BHVO-2 (Barrat et al., 2012).

A total of 404 mother solution samples were analyzed over four sessions conducted between 2023 and 2024. Data quality was assessed using a suite of certified reference materials (CRMs), including BCR-1, AGV-1, DNC-1, W-2, SBC-1, NOD-A1, NOD-P1, GSPN-2, GSPN-3, and GSMC-3, digested using the HF–HNO_3–HCl protocol described in Section 2.3. **Figures 2.4–2.7** illustrate analytical precision (as relative standard deviation, RSD) and accuracy (as deviation from certified values) for both major and trace elements.

In the **Amazon Fan Clays** analytical session, replicate analyses of BCR-2, W-2, and SBC-1 were used to assess data quality (**Fig. 2.4**). Most elements showed good reproducibility, with RSDs generally <10% for BCR-2 and W-2 and <5% for SBC-1. Precision was particularly high for REEs, Fe_2O_3, and abundant oxides such as Al_2O_3 and CaO. Accuracy was typically within ±10% for all elements across these CRMs. Exceptions included Na_2O and low-abundance elements such as Lu and U, which showed higher variability, likely due to greater uncertainty near detection limits.

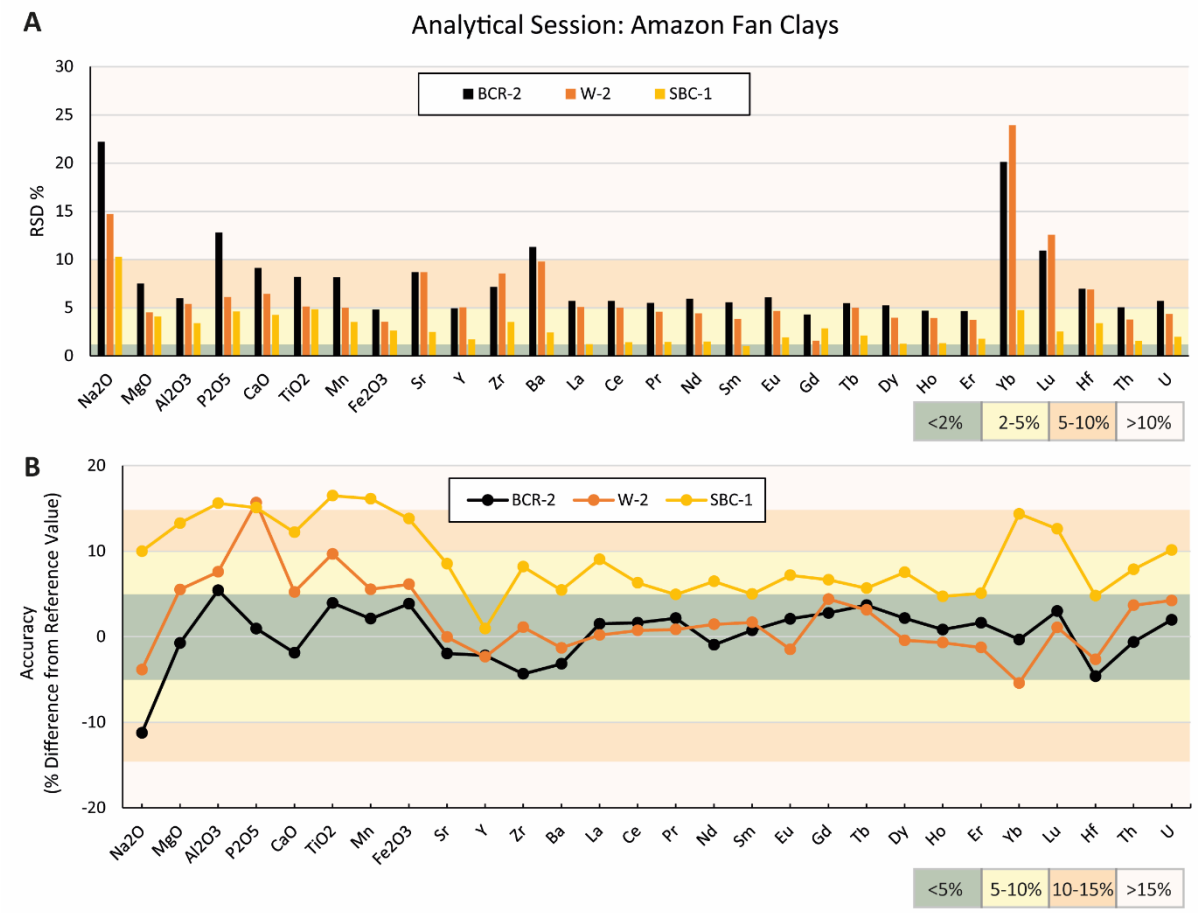

Figure 2.4. Precision and accuracy of certified reference materials during the "Amazon Fan Clays" analytical session. BCR-2 (Basalt; Jochum et al., 2016), W-2 (Diabase; Jochum et al., 2016), and SBC-1 (Shale; Webb et al., 2011)

In the **Amazon Fan HH leach/Fe oxyhydroxide** session, seven CRMs (BCR-1, AGV-1, DNC-1, NOD-A1, NOD-P1, GSPN-2, and GSPN-3) were analyzed (**Fig. 2.5**). Good agreement with certified values was achieved for most REEs and trace elements, with accuracy typically within ±10% and RSDs <10%. Volcanic rocks (BCR-1, AGV-1) and the dolerite standard (DNC-1) showed strong performance. Major elements exhibited greater deviations, with discrepancies exceeding 30% in some cases. These discrepancies highlight the limitations of single-point calibration for major elements and emphasize the importance of matrix-matched standards.

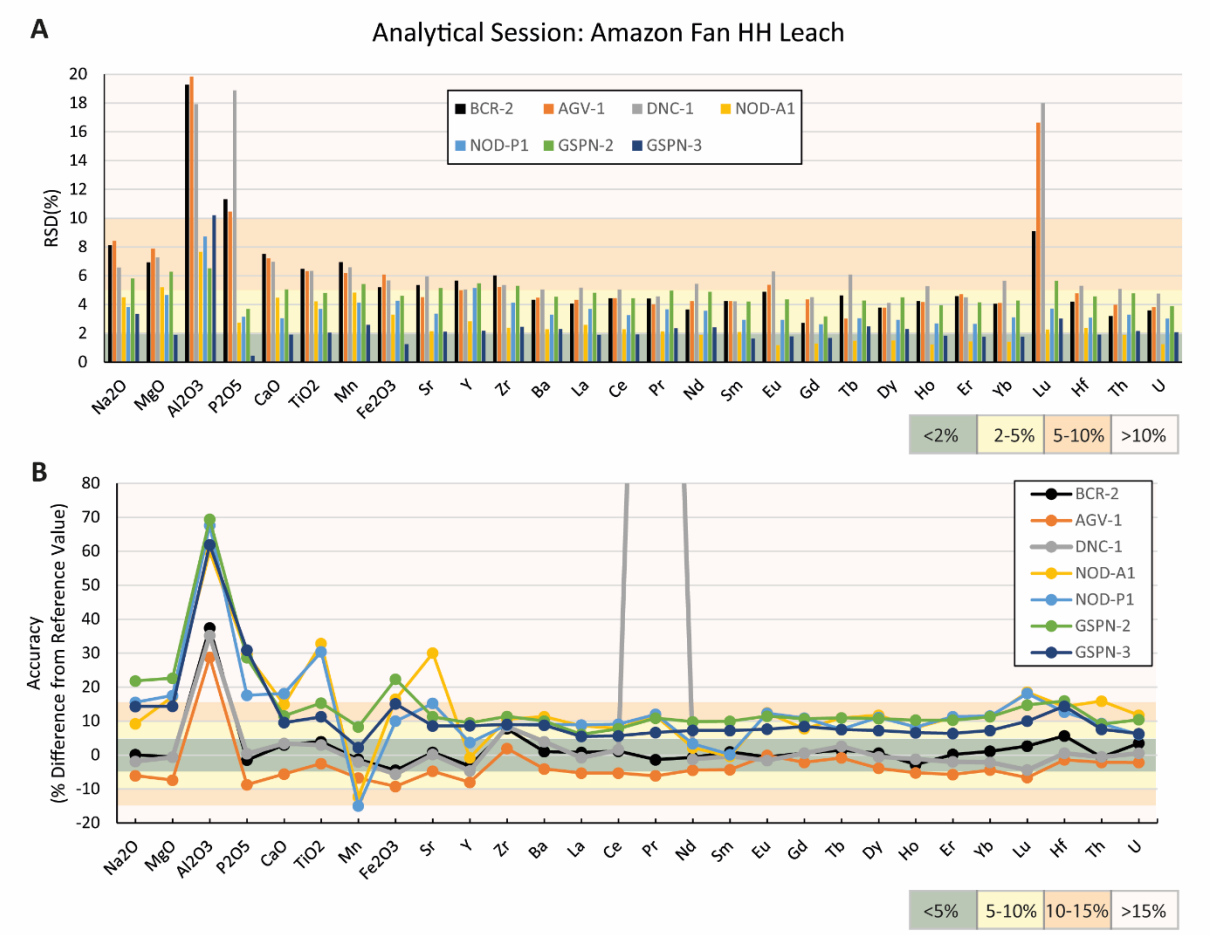

Figure 2.5. Precision and accuracy of certified reference materials during the "Amazon Fan HH leach/Fe oxides" analytical session. BCR-2 (Basalt; Jochum et al., 2016), AGV-1 (Andesite; Jochum et al., 2016), DNC-1 (Dolerite; Flanagan, 1984), NOD-A1 (Mn-Nodule; Charles et al., 2021), NOD-P1 (Mn-Nodule; Charles et al., 2021), GSPN-2 (Polymetallic Nodule; Charles et al., 2021), GSPN-3 (Polymetallic Nodule; Charles et al., 2021).

For the **Amazon River sediments** session, quality control included analyses of BCR-2, W-2, DNC-1, and SBC-1. REE concentrations were highly consistent, with deviations within ±5% and RSDs typically <3%, indicating excellent precision **(Fig. 2.6)**. Major elements, however, showed greater variability, especially in SBC-1 and W-2, likely due to incomplete digestion or matrix mismatches. Notably, Th was substantially underestimated in DNC-1 (–29%), while Al_2O_3, Fe_2O_3, and TiO_2 were consistently low in SBC-1 (–16% to –19%). Despite these discrepancies, trace element and REE measurements remained robust across all matrices.

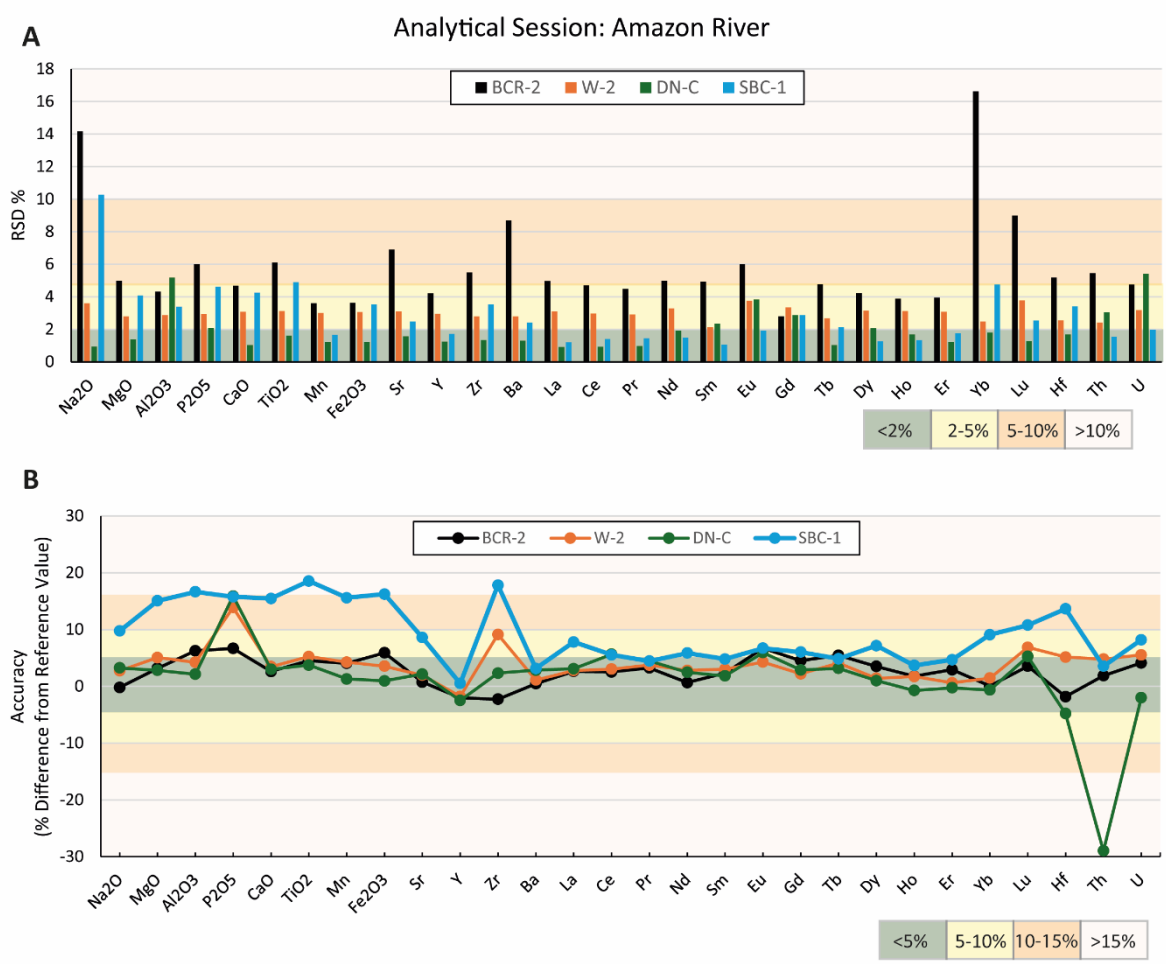

Figure 2.6. Precision and accuracy of certified reference materials during the "Amazon River sediments" analytical session. BCR-2 (Basalt; Jochum et al., 2016), W-2 (Diabase; Jochum et al., 2016), DNC-1 (Dolerite; Flanagan, 1984), and SBC-1 (Shale; Webb et al., 2011).

In the final **Upper Madeira** session, data quality was evaluated using five CRMs (BCR-2, DNC-1, GSPN-2, GSPN-3, GSMC-3). REE concentrations were within ±7% of reference values, with RSDs generally <2%, confirming excellent analytical precision (**Fig. 2.7**). Slight underestimations (–3% to –6%) were observed for some heavy REEs (e.g., Er, Yb, Lu) in GSPN-2 and GSPN-3. Th and U were also underestimated by up to 12% in several standards, possibly reflecting matrix effects or partial recovery. Major elements showed variable agreement: Na_2O, Al_2O_3, and Fe_2O_3 were generally accurate (<5% deviation), whereas CaO and TiO_2 in mafic-rich CRMs (e.g., GSPN-3) were underestimated by up to 16.5%. These results reinforce the method's high reproducibility and reliability for REE and trace element analysis across diverse matrices, while also underscoring the challenges of accurate major element quantification in complex geological materials.

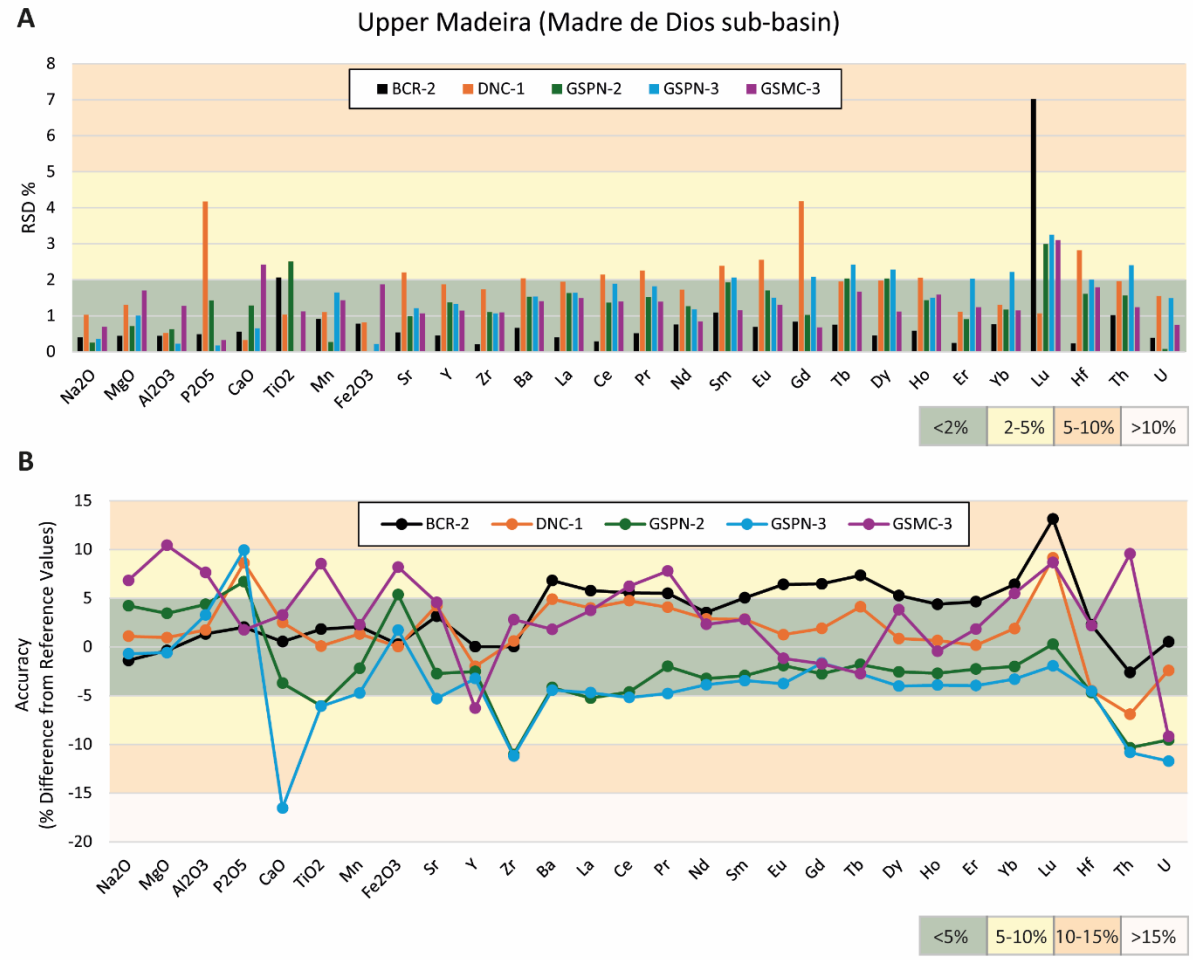

Figure 2.7. Precision and accuracy of certified reference materials during the "Upper Madeira" analytical session. BCR-2 (Basalt; Jochum et al., 2016), DNC-1 (Dolerite; Flanagan, 1984), GSPN-2 (Polymetallic Nodule; Charles et al., 2021), GSPN-3 (Polymetallic Nodule; Charles et al., 2021), and GSMC-3 (Cobalt-rich seamount crust; Wang et al. 2003).

In summary, the analytical protocol employed using SF-ICP-MS provided high-precision and reproducible measurements for rare earth and trace elements across a wide range of geological matrices. REE consistently matched certified values within ±10%, with relative standard deviations typically below 5%. While major elements exhibited larger variability, particularly in Al-rich and mafic samples, these discrepancies were largely attributable to matrix effects or challenges in complete digestion. The use of multiple certified reference materials throughout all analytical sessions ensured rigorous quality control and confirmed the reliability of the data, particularly for REEs and trace elements.

2.8. Hf-Nd Isotopes

Neodymium and hafnium were separated by conventional ion chromatography (Bayon et al., 2012; Chu et al., 2002), and isotopic measurements were performed with a Thermo Scientific Neptune multi-collector ICP-MS. Both Nd and Hf isotopic compositions were determined using sample-standard bracketing methods, during which standard solutions of Nd-SPEX and AMES-Grenoble were analyzed every two samples, respectively. Mass-bias corrections were made using the exponential law, using $^{146}Nd/^{144}Nd = 0.7219$ and $^{179}Hf/^{177}Hf = 0.7325$. Measured $^{143}Nd/^{144}Nd$ and $^{176}Hf/^{177}Hf$ ratios were corrected for isobaric interferences from ^{144}Sm, ^{176}Lu, and ^{176}Yb by monitoring interference-free ^{147}Sm, ^{175}Lu, and ^{173}Yb masses, respectively. During the course of this study, repeated analyses of JNdi-1 and JMC-475 standard solutions gave $^{143}Nd/^{144}Nd$ of 0.512114 ± 0.000005 (2σ, n=58) and $^{176}Hf/^{177}Hf$ of 0.282164 ± 0.000008 (2σ, n=17), in full agreement with recommended values of 0.512115 (Tanaka et al., 2000) and 0.282163 (Blichert-Toft et al., 1997). Associated uncertainties on JNdi-1 and JMC-475 analyses correspond to external reproducibility of ± 0.09 ε and ± 0.29 ε (2σ), respectively. Epsilon values were calculated using present-day chondritic (CHUR) values for $^{143}Nd/^{144}Nd$ (0.512630) and $^{176}Hf/^{177}Hf$ (0.282785) from Bouvier et al. (2008).

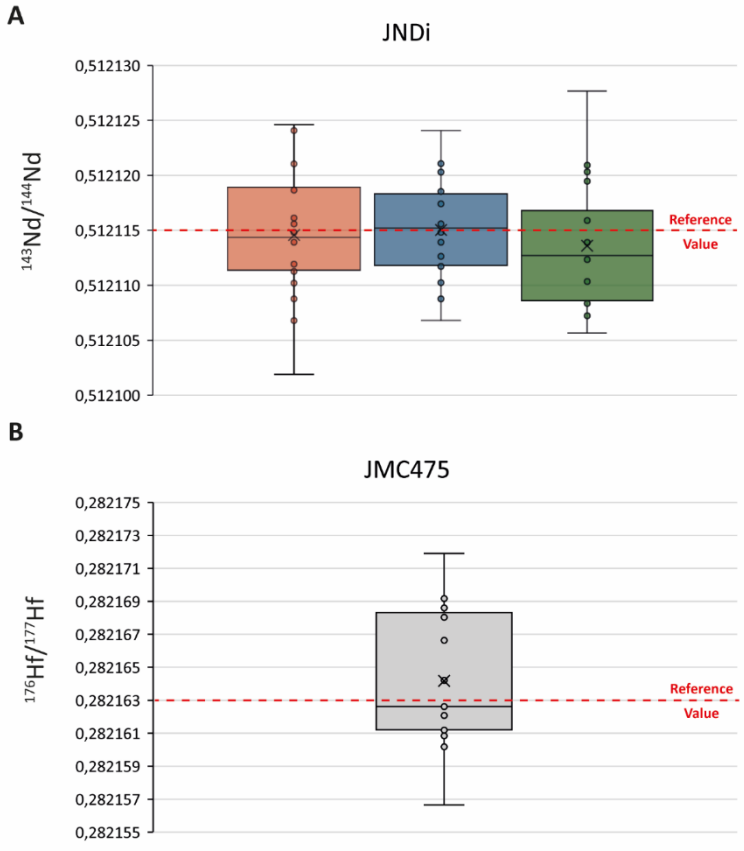

Figure 2.8. Accuracy of measurements on certified reference materials. A) $^{143}Nd/^{144}Nd$ ratios of JNDi (Tanaka et al., 2000) and B) JMC475 (Blitchert-Toft et al., 1997).

2.9. Use of generative AI

Throughout this thesis, I used a limited set of AI-assisted tools to streamline my workflow. Selected vector illustrations were generated with Adobe Illustrator's built-in generative features; where applicable, these are cited in the figure captions. A small number of plots that exceeded Excel's capabilities were produced with assistance from R or Python codes generated by ChatGPT. During writing, I used the Grammarly add-in for Microsoft Word for spelling and grammar checks. Finally, translations to French were double-checked with DeepL. All analyses, interpretations, and final editorial decisions are my own.

III

Tracing black shale weathering using REE and Nd isotopes in riverine Fe oxides: insights from the Amazon Basin

3. Declaration/ Declaração/ Déclaration

This chapter examines the use of rare earth elements (REEs) and neodymium (Nd) isotopes in paired clay and Fe oxide fractions from Amazon River Basin sediments to assess sediment provenance and disentangle lithology-specific weathering signals. Particular attention is given to the ability of these geochemical proxies to trace the oxidative weathering of black shales, a key process influencing CO_2 fluxes during chemical weathering. While the primary focus is on the <2 μm clay and Fe oxide fractions, major and trace element compositions and Nd isotopes were also analyzed in fine and medium–coarse silt fractions; these additional results are provided in Appendix 3. The study was first presented at the Working Group of Sediment Generations (WGSG) meeting at University College London (UCL) in July 2024, is currently under review in Chemical Geology, and forms the basis for ongoing collaborations with colleagues at the University of Milano and UCL on sediment mineralogy and geochronology.

[PT] Este capítulo examina o uso de elementos terras raras (ETRs) e isótopos de neodímio (Nd) em frações emparelhadas de argilas e óxidos de ferro de sedimentos da Bacia Amazônica para avaliar a proveniência sedimentar e distinguir sinais de intemperismo específicos de litologias. Atenção especial é dada à capacidade desses proxies geoquímicos de rastrear o intemperismo oxidativo de folhelhos negros, um processo-chave que influencia os fluxos de CO_2 durante o intemperismo químico. Embora o foco principal esteja nas frações de argila <2 μm e de óxidos de ferro, também foram analisadas as composições de elementos maiores e traços e os isótopos de Nd nas frações de silte fino e médio-grosso; estes resultados adicionais estão incluídos no Apêndice X. O estudo foi apresentado inicialmente no encontro do *Working Group of Sediment Generations* (WGSG) na University College London (UCL) em julho de 2024, encontra-se atualmente sob revisão na revista *Chemical Geology* e serve de base para colaborações em andamento com colegas da Universidade de Milão e da UCL sobre mineralogia e geocronologia de sedimentos.

[FR] Ce chapitre examine l'utilisation des éléments terres rares (ETR) et des isotopes du néodyme (Nd) dans les fractions couplées d'argiles et d'oxydes de fer provenant de sédiments du bassin de l'Amazone afin d'évaluer la provenance des sédiments et de distinguer les signaux d'altération spécifiques aux lithologies. Une attention particulière est portée à la capacité de ces traceurs géochimiques à suivre l'altération oxydative des schistes noirs, un processus clé influençant les flux de CO_2 lors de l'altération chimique. Bien que l'accent principal soit mis sur les fractions <2 μm d'argiles et d'oxydes de fer, les compositions en éléments majeurs et traces ainsi que les isotopes de Nd ont également été analysés dans les fractions de limon fin et de limon moyen-grossier; ces résultats complémentaires sont présentés à l'Annexe X. L'étude a été présentée pour la première fois lors de la réunion du Working Group of Sediment Generations (WGSG) à l'University College London (UCL) en juillet 2024, est actuellement en cours de révision dans Chemical Geology et constitue la base de collaborations en cours avec des collègues de l'Université de Milan et de l'UCL sur la minéralogie et la géochronologie des sédiments.

Abstract

Continental chemical weathering fundamentally controls global biogeochemical cycles and atmospheric CO_2 over geological timescales, which strongly depends upon the nature of eroded source rocks. Yet disentangling the contributions of specific lithologies to weathering fluxes in large river catchments remains challenging. Here, we use rare earth elements (REEs) and neodymium (Nd) isotopic compositions in paired clay and Fe-oxide fractions separated from riverine sediments to investigate sediment provenance and chemical weathering patterns across the Amazon River system. Our results reveal distinct geochemical signatures among the three primary sources of sediments in the lower Amazon River, the Solimões, Madeira, and Cratonic domains. The cratonic Tapajos and Negro rivers exhibit shale-normalized REE patterns characterized by low mid-REE enrichment relative to both light and heavy-REE, as expressed by low concavity index values (CI ~ 1.4) and minimal Nd isotopic decoupling ($\Delta\varepsilon Nd_{FeOx\text{-}Clays}$ <1), typifying a silicate weathering regime. The Solimões Domain and Lower Amazon River are characterized by high $\Delta\varepsilon Nd_{FeOx\text{-}Clays}$ values (4.5–5.5) with intermediate CI values of Fe oxides (~2) interpreted as largely reflecting erosion and/or chemical weathering of ancient marine sediment deposits. Finally, the Madeira River exhibits intermediate $\Delta\varepsilon Nd_{FeOx\text{-}Clays}$ values (~3) and significantly higher CI values of Fe oxides (>2.5) compared to other domains across the Amazon watershed. We show that such mid-REE enrichment in riverine Fe phases relates to oxidative weathering of black shales in upstream source regions of the Madeira catchment. Our findings further demonstrate the utility of combining detrital clay and associated Fe oxide geochemistry for reconstructing sediment routing and lithology-specific chemical weathering signals in river systems. Future application of this approach to sedimentary archives at continental margins could provide unique constraints on past linkages between tectonics, chemical weathering, and the long-term carbon cycle over million-year timescales.

3.1 Introduction

Chemical weathering is a fundamental process that shapes Earth's surface and regulates global biogeochemical cycles. It governs the mobilization and transport of dissolved elements from continents to oceans while also playing a key role in both the sequestration and release of atmospheric CO_2 in the Critical Zone (Brantley et al., 2014; Soulet et al., 2021; Torres et al., 2016). Whether chemical weathering acts as a net source or sink for atmospheric CO_2 depends on the balance between alkalinity generation, through carbonate and silicate dissolution, and acid production via sulfide oxidation (Torres et al., 2014). Chemical weathering of silicate rocks via carbonic acid coupled with subsequent carbonate precipitation in the ocean typically acts as an atmospheric CO_2 sink over geological timescales (Berner et al., 1983). However, terrestrial oxidative weathering of petrogenic carbon and sulfide minerals can lead to CO_2 release in the atmosphere, notably via sulfuric acid-mediated weathering of carbonaceous rocks (Calmels et al., 2007; Torres et al., 2016). This process is critical in rapidly eroding regions, such as high-altitude areas (Ma et al., 2011), tectonically active mountain belts (Blattmann et al., 2019; Torres et al., 2016, 2015), and floodplains (Dellinger et al., 2023), and is likely to offset the silicate weathering sink at the global scale (Zondervan et al., 2023). Consequently, there is still significant uncertainty surrounding the Earth's climate sensitivity to continental weathering over geological timescales; one of the major challenges is distinguishing the individual contributions of silicate and sedimentary rocks to overall weathering rates during mountain erosion.

Eroded continental rocks and river sediments host a variety of authigenic mineral phases, including Fe oxides, which play a crucial role in geochemical cycling in Earth's surface environments. Iron oxide and oxyhydroxide phases transported by rivers are either formed as secondary weathering products in soils or originate from the erosion of ancient sedimentary rock formations in source regions, making them integral carriers of continental weathering signals (Bayon et al., 2020b). Recent studies have shown that rare earth elements (REEs) and neodymium (Nd) isotopic compositions in paired detrital fraction and labile (oxy)hydroxides phases leached from river sediments can be a powerful tool for distinguishing the bedrock lithology and weathering processes within watersheds (Bayon et al., 2020b; Hindshaw et al., 2018; Jang et al., 2024, 2020; Larkin et al., 2021; Süfke et al., 2019; Von Blanckenburg et al., 2015). Two particularly informative tracers applied to Fe oxides are: (i) the degree of mid-REEs

(MREEs) enrichment in shale-normalized patterns, which can be measured by the concavity index ($CI = Gd_N / (La^6_N \times Yb^7_N)^{(1/13)}$(Barrat and Bayon, 2024; Bayon et al., 2020b; Lawrence et al., 2006), and (ii) the Nd isotopic decoupling between sedimentary Fe oxides and corresponding detrital fractions, expressed as $\Delta\varepsilon Nd_{Feox\text{-}Det}$ (Bayon et al., 2020a). In catchments draining crystalline igneous and metamorphic rocks, Fe oxides mostly correspond to secondary Fe oxides formed during the chemical weathering of the underlying bedrock and exhibit minimal MREEs enrichment (CI = 1.2–2). In contrast, river basins dominated by sedimentary rocks typically carry riverine Fe oxide phases with intermediate CI values (~2–2.5), interpreted as reflecting the presence of ancient marine and/or diagenetic Fe oxyhydroxide precipitates eroded from upstream source regions. In sedimentary catchments, exceptionally high CI values (>2.5) have been reported in glacial environments and catchments hosting substantial black shale deposits, such as Svalbard and the Mackenzie Basin, which were attributed to sulfide weathering processes (Jang et al., 2024; Larkin et al., 2021; Bayon et al., 2020a;). While the exact mechanism remains elusive, it has been proposed that intense pyrite oxidation in such catchments results in sulfuric acid-mediated dissolution of sedimentary phosphate minerals (apatite) characterized by pronounced MREE enrichments, thereby leading to subsequent precipitation of secondary Fe oxyhydroxide phases in soils with inherited high CI values (Jang et al., 2024). The application of Nd isotopes on paired detrital and Fe oxide fractions of river sediments offers additional insight into the nature of weathered source rocks on continents (Bayon et al., 2020a). In crystalline-rock catchments (granitic, metamorphic, basaltic), Fe-oxides typically exhibit εNd values like coexisting silicate residues, indicating a common origin through silicate weathering. Conversely, in sedimentary or mixed-lithology watersheds, the Nd isotopic composition of riverine Fe oxides commonly departs from ε_{Nd} values of the coexisting detrital fractions (Bayon et al., 2020a; Jang et al., 2020; Hindshaw et al., 2018). This isotopic decoupling is best explained as reflecting the influence of REE contributions sourced from non-silicate rocks in riverine Fe oxyhydroxides, such as ancient marine Fe oxides eroded from sedimentary strata (Bayon et al., 2020a; Jang et al., 2020).

This study examines the application of the aforementioned geochemical proxies in the Amazon Basin (**Fig. 3.1A**). Beyond being the world's most extensive tropical river system, the Amazon spans a remarkable range of geomorphological terrains, from the high-elevation Andean headwaters, rising to 6.5 km above sea level, where sediments are rapidly generated

and transported, to the extensive lowland floodplains, which function almost as a vast chemical weathering reactor. The basin drains a wide variety of lithologies, including crystalline basement rocks, carbonates, evaporites, and black shale deposits, and in which sulfide weathering is believed to represent a major biogeochemical process (**Fig. 3.1B**; Moquet et al., 2016, 2011; Torres et al., 2016, 2015; Callede et al., 2006; Stallard and Edmond, 1987). This combination of lithological diversity, extreme elevation gradients, and different weathering regimes makes the Amazon Basin an exceptional natural laboratory for investigating continental weathering processes and their geochemical imprint on riverine Fe oxides.

Here, we investigate rare earth element (REE) patterns and neodymium (Nd) isotopic compositions in the labile Fe-oxide fraction of Amazon River suspended material to: (i) evaluate the extent to which Fe oxides may record black shale weathering, (ii) assess the role of sulfide oxidation in influencing REE fractionation patterns, and (iii) explore the implications of these processes for large-scale biogeochemical cycling and sediment transport.

3.2 Materials and Methods

3.2.1 Study area and sampling

The Amazon River Basin, the world's largest drainage system, spans approximately 6.1 million km^2, extending from the Andes Mountains to the Atlantic Ocean. The Amazon Basin plays a crucial role in global hydrological and biogeochemical cycles, carrying immense volumes of water and sediment from across diverse geological landscapes. The basin is fed by numerous tributaries, which vary significantly in geology, sediment load, water chemistry, and discharge patterns (Barroux et al., 2006; Moquet et al., 2016, 2011; Viers et al., 2008). Based on these characteristics, the Amazon Basin can be divided into three major geomorphological and geochemical provinces: the Solimões, Madeira, and Cratonic Domains (**Fig. 3.1C**).

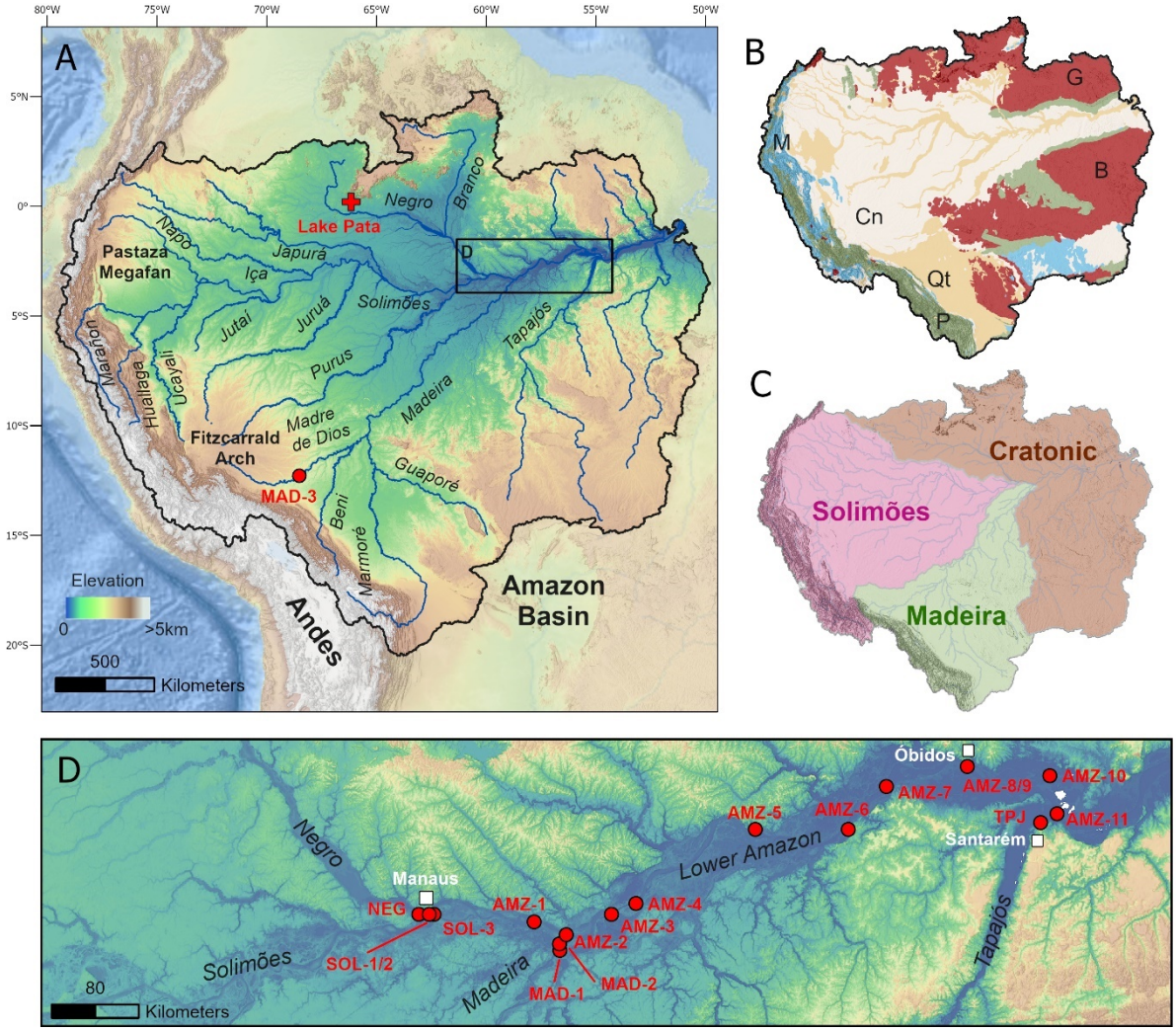

Figure 3.1. A) Topographic map of the Amazon Basin showing major geomorphological features and a simplified drainage network, including the principal tributaries of the lower Amazon River, the upstream Madre de Dios River sample, and the location of Lake Pata (see text for details). **B)** Simplified geological map of the Amazon Basin, modified from GMSA (2019). Key lithological units are indicated: G – Guiana Shield, B – Brazil Shield (cratonic basement rocks); P – Paleozoic; M – Mesozoic; Cn – Cenozoic; Qt – Quaternary deposits. **C)** Map of the three primary geochemical endmembers in the basin: the Solimões, Madeira, and Cratonic domains. **D)** Inset of the sampling area between Manaus and Santarém (White squares) cities. The red dots symbolize the location of the sampling sites (also in **Fig. 3.1A**).

The Solimões Domain (covering approximately 2.2 million km^2) is a high-elevation watershed where sediment undergoes rapid transport (Armijos et al., 2013; Dosseto et al., 2006) and a reduced degree of chemical weathering (Barroux et al., 2006; Viers and Wasserburg, 2004; Stallard and Edmon, 1987). This region contributes the most significant water discharge, dissolved load, and suspended particulate matter (SPM) to the lower Amazon River (Moquet et al., 2016). It encompasses the upper Amazon Basin, where the Solimões River,

as the Amazon is called in Brazil before merging with the Negro River, receives inputs from Andean tributaries such as the Napo, Marañón, and Ucayali Rivers (**Fig. 3.1A**). These rivers drain diverse lithologies, including Precambrian metamorphic rocks, Paleozoic evaporite-rich metapelites, intermediate volcanic rocks, and Cenozoic fluvio-lacustrine deposits (Roddaz et al., 2005; Stallard and Edmond, 1983). The Madeira Domain (1.4 million km^2) is sourced from Andean highlands that experience the highest denudation rates in the Amazon Basin (Pepin et al., 2013). The Madeira River is fed by major Andean rivers such as the Beni, Madre de Dios, Guaporé, and Mamoré (**Fig. 3.1A**), which supply large volumes of sediment from Precambrian crystalline rocks, uplifted Paleozoic sedimentary rocks with extensive black shale outcrops, and foreland basin deposits recycled from the Brazilian Shield (Moizinho et al., 2024; Roddaz et al., 2005). Finally, the Cratonic Domain (2.4 million km^2) encompasses rivers draining exclusively the Guiana and Brazilian Shields (**Fig. 3.1B,C**). This domain is characterized by Precambrian basement rocks and highly weathered terrains dominated by lateritic or bauxitic soils (Ansart et al., 2025; Moquet et al., 2011; Santos et al., 2000).

The lower Amazon River and four tributaries, the Solimões, Negro, Madeira, and Tapajós rivers, were sampled in 18 sites between the cities of Manaus and Santarém in July 2023 during the AMANAUS cruise (**Table 3.1**; **Fig. 3.1D**). Additionally, given that the upper Madre de Dios Basin (Madeira Domain) is known to undergo sulfide and organic carbon weathering processes (Dellinger et al., 2023; Torres et al., 2016, 2015), we also analyzed one sample from the Madre de Dios River (**Fig. 3.1A**). All sediment samples consist of suspended particulate material or were collected from recently deposited riverbanks, representing modern or relatively recent sediments likely deposited within the past few centuries.

Table 3.1. Geographical locations and description of the studie river sediments

#	River	Sample	Sampling Site	Type	Lat	Long
	Negro					
1		NEG-1	Manaus	Riverbank	-3,1737	-60,0129
	Solimões					
2		SOL-1	Careiro	SPM	-3,1752	-59,8869
3		SOL-2	Careiro	Riverbank	-3,1752	-59,8869
4		SOL-3	Catalão	SPM	-3,1522	-59,1519
	Madeira					
5		MAD-1	Urucutiba	SPM	-3,4697	-58,8499
6		MAD-2	Urucutiba	Riverbank	-3,1670	-58,8506
		MAD-3	Madre de Dios	Riverbank	-12,577	-69,2082
	Tapajós					
7		TAP	Alter do Chão	Bedload	-2,4187	-56,4664
	Amazon					
8		AMZ-1	*Camaleão* Island	SPM	-3,2358	-59,0617
9		AMZ-2	Pre-Madeira	SPM	-3,3428	-58,7971
10		AMZ-3	Post-Madeira	SPM	-3,1728	-58,4224
11		AMZ-4	Paranã do Serpa	SPM	-3,0843	-58,2214
12		AMZ-5	Mocambo	Riverbank	-2,4748	-57,2333
13		AMZ-6	Parintins	SPM	-2,4718	-56,4664
14		AMZ-7	Juruti	Riverbank	-2,1182	-56,1534
15		AMZ-8	Óbidos	SPM	-1,9531	-55,4833
16		AMZ-9	Óbidos	Riverbank	-1,9531	-55,4833
17		AMZ-10	AMA-08	Riverbank	-2,0288	-54,8018
18		AMZ-11	Post-Tapajós	SPM	-2,3440	-54,7438

3.2.2 Labile Fe (oxy)hydroxides extraction and detrital clay separation

Bulk sediment samples were sieved to <63 µm and treated with a sequential leaching procedure based on Bayon et al. (2002). First, carbonates were removed using 5% (v/v) acetic acid (AA) for three hours. Next, easily reducible Fe oxyhydroxides, such as ferrihydrite and lepidocrocite, were leached overnight using a mixed solution of 15% (v/v) AA and 0.5 M hydroxylamine hydrochloride (HH). The resulting solution was filtered (0.20 µm), dried on a hot plate, redissolved in HNO_3 to eliminate HH, and finally taken in 4M HCl. The residual detrital fraction was treated (48 h) with 5% hydrogen peroxide (H_2O_2) to remove organic compounds and then rinsed with ultrapure water. Coarser silt-size particles were separated from the finest clay-size (<2µm) particles through low-speed centrifugation (Bayon et al., 2015). After powdering, each detrital clay fraction (between 60 and 80 mg) was digested in PTFE vials with

concentrated HF-HNO_3-HCl and left for a minimum of 5 days at 140°C on a hot plate. Following evaporation, the final residue was taken in 6M HCl and allowed to react on a hot plate at 140°C to ensure total sample dissolution.

3.2.3 Major and trace elements analysis

Major and trace element abundances were determined at the Pôle Spectrométrie Océan (Brest, France) using a Thermo Scientific Element XR sector field (SF) ICP-MS. Elemental concentrations were calculated using the Tm addition method, following procedures outlined by (Barrat et al., 1996, 2012). A series of certified reference materials (BCR-2, W-2, and DN-C) was analyzed to assess the precision and accuracy of our data. The precision for major and trace elements was better than 4%, and the accuracy of measured concentrations was typically <5 % (**Supplementary Tables 3.1 and 3.2**). The REE abundances were normalized to values for the World River Average Silt (WRAS: Bayon et al., 2015), denoted by the subscript "N".

3.2.4 Nd Isotopes

Neodymium isotopes were separated using conventional ion chromatography (Bayon et al., 2012). Their isotopic measurements were carried out with a Thermo Scientific Neptune multi-collector ICP-MS at the Pôle Spectrométrie Océan (Brest, France). The Nd isotopic ratios were determined using a sample-standard bracketing method, where a standard solution of Nd-SPEX was analyzed after every two samples. Mass-bias corrections were performed using the exponential law and $^{146}Nd/^{144}Nd = 0.7219$. The $^{143}Nd/^{144}Nd$ ratio was corrected for isobaric interference from ^{144}Sm by monitoring ^{147}Sm. Repeated analyses of JNdi-1 standard solutions yielded a $^{143}Nd/^{144}Nd$ ratio of 0.512113 ± 0.000011 (2σ, n=16), consistent with the recommended value of 0.512115 (Tanaka et al., 2000). The uncertainties associated with JNdi-1 analyses correspond to an external reproducibility of ± 0.22Ɛ. ƐNd values were calculated using the present-day chondritic (CHUR) values for $^{143}Nd/^{144}Nd$ (0.512630) from (Bouvier et al., 2008) using the following equation:

$$\varepsilon Nd = [(^{143}Nd/^{144}Nd)_{sample}/(^{143}Nd/^{144}Nd)_{Chur} - 1] \times 10^4$$

3.3 Results

3.3.1 Major and trace elements

The REE concentrations for clays and Fe-oxides fractions are reported in **Table 3.2**. Other trace and major element concentrations are displayed in Supplementary Table 2. Note that the REE data for leached Fe-oxide fractions are reported relative to the initial mass of bulk sediment. REE concentrations in the clay fraction vary notably among the Amazonian rivers studied. For instance, the Madeira River exhibits the highest Nd concentration in clays with 62.5 µg/g, followed by the lower Amazon River (38.4–48.8 µg/g), the Tapajós River (37.6 µg/g), and the Solimões River (35.3–41.4 µg/g). In comparison, the Negro River shows clays with the lowest Nd concentration (27.5 µg/g). These measured values are in good agreement with previously reported SPM Nd concentrations, which span 28.7–59.7 µg/g for the Solimões, 22.2–76.3 µg/g for the Madeira, 6–27 µg/g for the Negro, and 36–51 µg/g for the Tapajós (Bouchez et al., 2011; Gaillardet et al., 1997; Gerard et al., 2003). In the Fe-oxide fraction, the highest Nd concentration is observed in the Tapajós River at 11.2 µg/g, followed by 6.71–8.94 µg/g in the Solimões, 4.26–8.44 µg/g in the lower Amazon, 2.59–6.22 µg/g in the Madeira River, and only 1.91 µg/g in the Negro River.

The WRAS-normalized REE distribution patterns for detrital clays and Fe oxides are shown in **Figures 3.2** and **3.3**, respectively. Clays from all three domains exhibit LREE enrichment relative to MREE and HREE, like previously observed trends for river clays worldwide (Bayon et al., 2015). In Fe-oxide leachates (**Fig. 3.3**), the Cratonic Domain exhibits LREE and MREE enrichment over HREE, characterized by a low concavity index (CI = 1.4 ± 0.5, n = 2). In contrast, domains influenced by Andean tributaries show pronounced MREE enrichment. The Solimões Domain (CI = 2.1 ± 0.1, n = 3) and lower Amazon River (CI = 2.3 ± 0.3, n = 11) exhibit similar intermediate concavity indices, whereas the Madeira Domain displays the highest MREE enrichment, with a CI of 3.2 ± 0.1 (n = 3).

1 **Table 3.2.REE concentrations in leached phases of Amazon River Basin sediments. 1- World River Average Silt (Bayon et al., 2015).**

Sample	Fraction	La	Ce	Pr	Nd	Sm	Eu	Gd	Tb	Dy	Ho	Er	Yb	Lu	$(Gd/Yb)_N$	$(La/Gd)_N$	CI
River		(µg/g)	(µg/g)	(µg/g)	(µg/g)	(µg/g)	(µg/g)	(µg/g)	(µg/g)	(µg/g)	(µg/g)	(µg/g)	(µg/g)	(µg/g)			
Negro																	
NEG-1	Clay	46	72	8.3	27.5	4.31	0.78	3.19	0.48	2.86	0.60	1.75	1.94	0.29			
	Fe-Ox	2.8	6.4	0.54	1.9	0.31	0.06	0.29	0.04	0.23	0.05	0.12	0.10	0.01	1.3	1.8	1.2
Tapajós																	
TAP-1	Clay	72.2	122	12.11	37.6	5.97	1.06	4.35	0.67	3.87	0.82	2.34	2.67	0.38			
	Fe-Ox	10.3	25.2	2.98	11.2	2.02	0.36	1.64	0.23	1.24	0.23	0.58	0.47	0.06	0.87	2.0	1.6
Solimões																	
SOL-1	Clay	50.6	94.6	10.9	38.1	6.33	1.11	4.19	0.64	3.96	0.81	2.35	2.65	0.39			
	Fe-Ox	6.7	18.3	2.10	8.94	2.01	0.44	2.07	0.29	1.57	0.30	0.76	0.57	0.07	0.45	2.1	2.2
SOL-2	Clay	54.7	104	11.8	41.5	6.84	1.18	4.82	0.68	4.04	0.87	2.56	2.85	0.41			
	Fe-Ox	6.35	17.5	1.98	8.51	1.92	0.42	1.94	0.28	1.50	0.28	0.72	0.55	0.07	0.45	2.06	2.1
SOL-3	Clay	44.5	86.1	9.87	35.3	6.15	1.15	4.61	0.65	3.67	0.75	2.16	2.36	0.34			
	Fe-Ox	5.1	13.3	1.57	6.71	1.54	0.33	1.58	0.24	1.27	0.24	0.60	0.45	0.05	0.44	2.05	2.1
Madeira																	
MAD-1	Clay	77.3	139	17.3	62.4	11.4	2.05	7.76	1.04	5.71	1.11	3.13	3.27	0.47			
	Fe-Ox	3.64	11.2	1.34	6.22	1.66	0.40	1.93	0.27	1.40	0.25	0.58	0.38	0.05	0.26	2.9	3.3
MAD-2	Clay	70.9	138	15.9	57.5	10	1.78	6.85	0.92	5.10	1.05	2.95	3.20	0.46			
	Fe-Ox	2.48	7.62	0.91	4.26	1.19	0.28	1.40	0.20	1.04	0.18	0.42	0.29	0.03	0.24	2.8	3.4
MAD-3	Clay	62.4	124	14.8	54.6	10.1	1.95	7.58	1.15	6.68	1.34	3.76	3.74	0.53			
	Fe-Ox	1.68	4.83	0.56	2.59	0.69	0.16	0.76	0.11	0.58	0.10	0.24	0.17	0.02	0.30	2.7	3.0
Lower Amazon																	
AMZ-1	Clay	54.2	101	11.6	40.6	6.69	1.22	4.65	0.68	4.03	0.85	2.51	2.78	0.40			
	Fe-Ox	6.28	17.1	1.83	7.53	1.61	0.34	1.59	0.23	1.22	0.23	0.57	0.44	0.06	0.54	2.11	2.0

AMZ-2	Clay	50.6	96.8	11.01	38.5	6.50	1.15	4.40	0.66	3.92	0.83	2.50	2.70	0.38			
	Fe-Ox	5.89	17	1.82	7.68	1.70	0.37	1.77	0.25	1.34	0.26	0.65	0.49	0.06	0.46	2.10	2.1
AMZ-3	Clay	59.7	114	13.	45.9	7.85	1.40	5.44	0.76	4.44	0.92	2.73	2.93	0.43			
	Fe-Ox	5.48	15.4	1,71	7,29	1,67	0,38	1.75	0.25	1.36	0.25	0.64	0.46	0.06	0.43	2.19	2.2
AMZ-4	Clay	52.6	102	11.60	41.6	7.32	1.32	5.14	0.74	4.27	0.88	2.52	2.81	0.40			
	Fe-Ox	3.80	10.4	1.21	5.25	1.26	0.28	1.32	0.20	1.03	0.19	0.48	0.35	0.04	0.39	2.20	2.3
AMZ-5	Clay	55.8	106	12.12	43.12	7.48	1.33	5.44	0.74	4.38	0.90	2.66	2,84	0.42			
	Fe-Ox	4.81	13.8	1.47	6.29	1.42	0.32	1.49	0.22	1.16	0.22	0.55	0.41	0.05	0.44	2.12	2.2
AMZ-6	Clay	61.6	118	13.5	48.8	8.27	1.39	5.47	0.79	4.65	0.98	2.80	3.15	0.43			
	Fe-Ox	3.60	9.37	1.16	5.04	1.19	0.24	1.24	0.18	0.93	0.17	0.42	0.31	0.04	0.40	2.31	2.4
AMZ-7	Clay	58.2	111	12.8	45.9	7.43	1.30	4.92	0.70	3.98	0.84	2.42	2.75	0.38			
	Fe-Ox	2.86	7.57	0.93	4.03	0.98	0.21	1.03	0.15	0.80	0.14	0.36	0.26	0.03	0.38	2.27	2.4
AMZ-8	Clay	57.6	11	12.6	43.9	7.39	1.28	5.04	0.73	4.20	0.89	2.64	2.77	0.40			
	Fe-Ox	5.56	16	1.74	7.47	1.71	0.39	1.77	0.26	1.38	0.26	0.64	0.48	0.06	0.43	2.13	2.2
AMZ-9	Clay	54.7	104	12	42.2	6.90	1.21	4.70	0.63	3.70	0.77	2.24	2.51	0.36			
	Fe-Ox	5.22	14.2	1.64	7.05	1.69	0.36	1.75	0.26	1.35	0.25	0.63	0.46	0.05	0.41	2.19	2.3
AMZ-10	Clay	51.4	100	11.5	41	7.04	1.24	4.76	0.65	3.65	0.76	2.23	2.44	0.36			
	Fe-Ox	2.96	8.15	0.97	4.26	1.05	0.23	1.10	0.16	0.87	0.16	0.40	0.29	0.03	0.37	2.20	2.4
AMZ-11	Clay	62.3	116	13.3	46.8	7.73	1.34	5.31	0.77	4.38	0.94	2.81	2.95	0.45			
	Fe-Ox	6.61	17,4	2.01	8.44	1.87	0.41	1.91	0.27	1.45	0.27	0.66	0.49	0.06	0.48	2.25	2.2
WRAS[1]		37.8	77.7	8.77	32.7	6.15	1.19	5.19	0.82	4.95	1.02	2.97	3.01	0.46	-	-	-

2

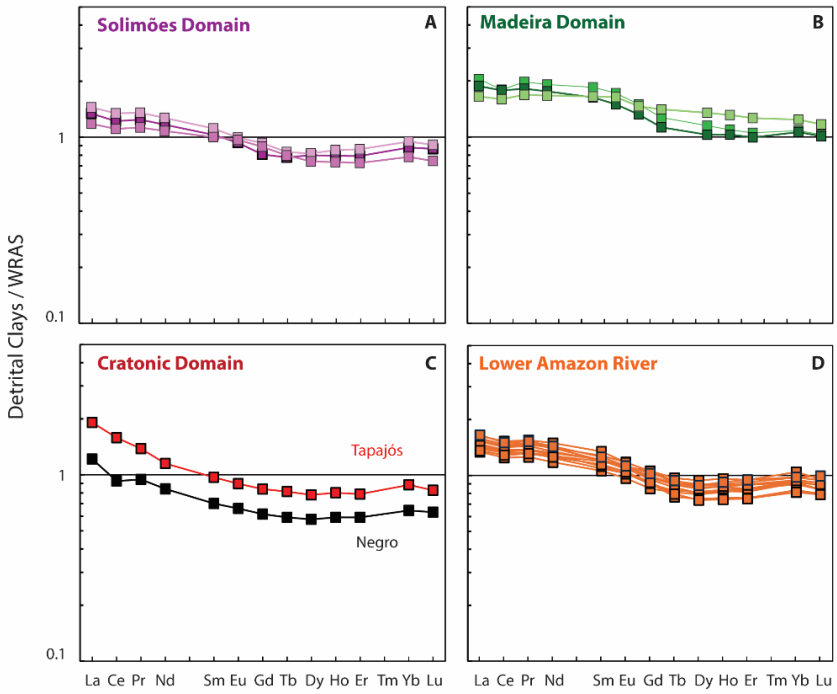

Figure 3.2. Shale-normalized (WRAS; Bayon et al., 2015) REE patterns for detrital clays from different domains in the Amazon Basin and lower Amazon River.

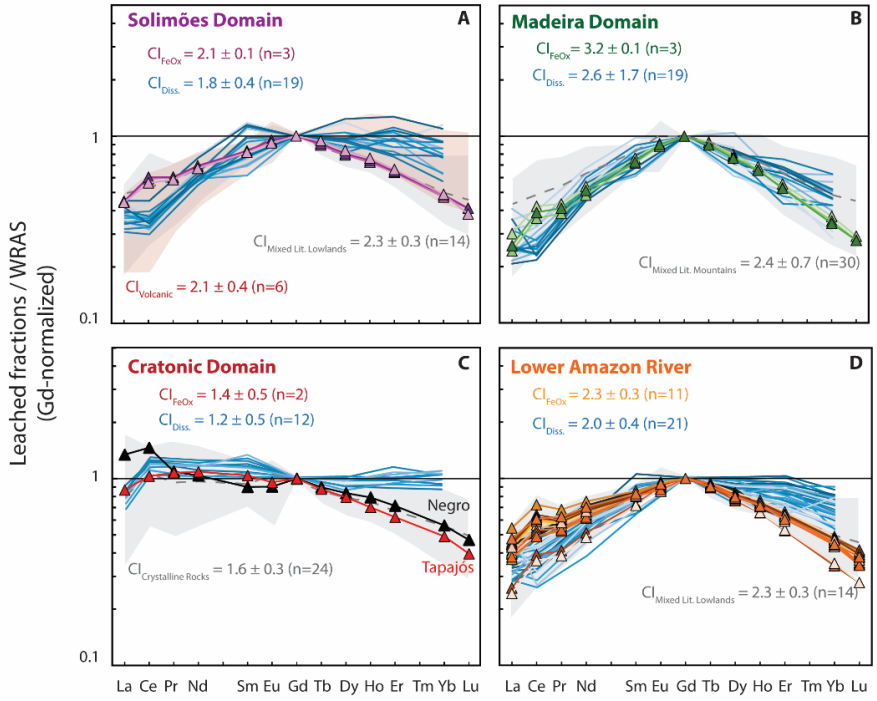

Figure 3.3. WRAS and Gd_{WRAS} normalized REE patterns for the leached Fe oxide phases from Amazon Basin samples. Blue thin lines correspond to dissolved REEs' patterns from river water (Goldstein and Jacobsen, 1998; Baroux et al., 2006; Merschel et al., 2017; Xu et al., 2023). Shaded gray areas correspond to the range of REE distributions of Fe oxides leached from sediments recovered in watersheds draining volcanic, crystalline basements, and mixed lithologies (Bayon et al. 2020). Also reported are the concavity indices (CI) for each category of rivers, calculated using the weighted geometric means of shale-normalized La and Yb (see text for details).

3.3.2 Nd Isotopes

Nd isotopic data for detrital clays and leached Fe oxide fractions are presented in **Table 3.3** and **Figure 3.4**. In the Cratonic Domain, the Negro sample shows nearly identical $^{143}Nd/^{144}Nd$ ratios for clays and Fe oxides, with εNd values of –15.0 and –15.2, respectively, resulting in a minimal $\Delta\varepsilon Nd_{FeOx\text{-}Clays}$ of 0.15. The Tapajós sample also exhibits low ratios and εNd values (–17.0 and –17.9), yielding a small $\Delta\varepsilon Nd_{FeOx\text{-}Clays}$ of 0.9. In the Solimões Domain, Fe oxides display more radiogenic $^{143}Nd/^{144}Nd$ composition (from –4.9 to –5.2) than clays (–9.4 to –10.5), leading to $\Delta\varepsilon Nd_{FeOx\text{-}Clays}$ values of 4.5 to 5.5. The Madeira samples display intermediate isotopic ratios and εNd values (–8.0 to –7.8 for Fe oxides, and –11.3 to –11.7 for clays), with $\Delta\varepsilon Nd_{FeOx\text{-}Clays}$ values around 3.3–3.9. For the Lower Amazon, εNd values for Fe oxides range between –5.5 and –7.3. Clay fractions consistently show lower ratios, with $^{143}Nd/^{144}Nd$ and εNd values from –10.1 to –11.4, resulting in $\Delta\varepsilon Nd_{FeOx\text{-}Clays}$ values varying from 3.5 to 5.9, except for AMZ-11, which has a lower $\Delta\varepsilon Nd_{FeOx\text{-}Clays}$ of 2.2. Apart from the Negro and Tapajos samples, which display more radiogenic Nd isotopic values, all the other results are consistent, within uncertainty, with previously reported Nd isotopic values for SPM and dissolved loads for corresponding tributaries (**Fig. 3.5**; (Rousseau et al., 2019; Höppner et al., 2018; Merschel et al., 2017; Horbe et al., 2014; Bouchez et al., 2011; Viers et al., 2008; Allègre et al., 1996).

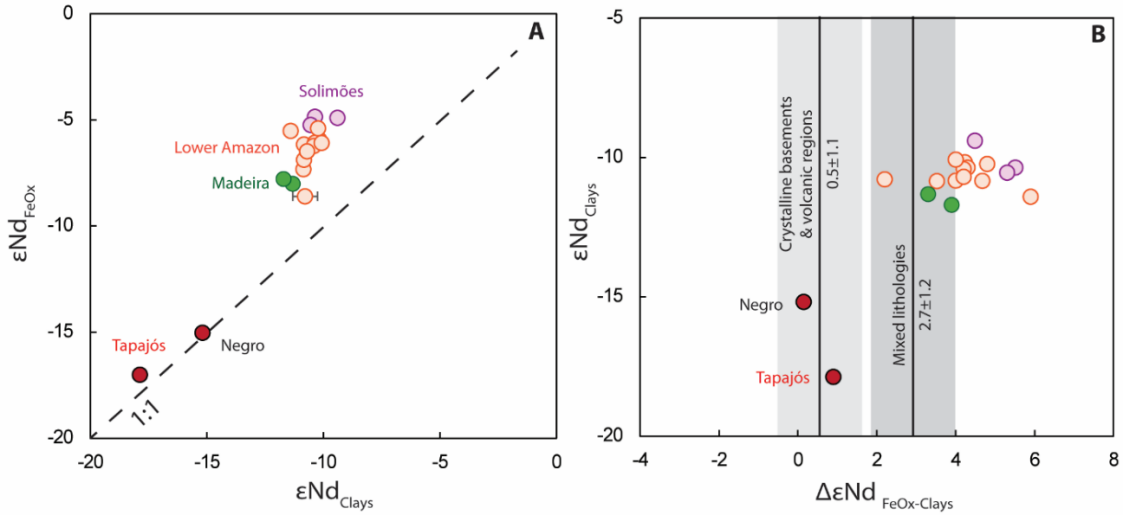

Figure 3.4. The distribution of Nd isotopes in paired Fe oxide and clay fraction of Amazon Basin sediments. In **(a)**, the dashed line corresponds to a 1:1 relationship between Nd isotopes (expressed using the epsilon notation εNd) in Fe-oxide and clay fractions. In **(b)**, $\Delta\varepsilon Nd_{Feox\text{-}Clays}$ represents the Nd isotopic difference measured between paired Fe-oxide and detrital clays fractions. The shaded grey areas correspond to the average of world rivers' Fe oxide fractions from Bayon et al. (2020) draining crystalline basements, volcanic regions, and mixed lithologies.

Table 3. Nd isotopic compositions of leached Fe oxide phases and detrital clay fractions of Amazon River Basin sediments.

River	$^{143}Nd/^{144}Nd_{clays}$	2se	$\varepsilon Nd(0)_{clays}$	2 σ	$^{143}Nd/^{144}Nd_{FeOx}$	2se	$\varepsilon Nd(0)_{FeOx}$	2 σ	$\Delta\varepsilon Nd_{FeOx\text{-}Clays}$
Sample									
Negro									
NEG-1	0,511852	0,000006	-15,2	0,1	0,511859	0,000005	-15,0	0,1	0,15
Tapajós									
TAP-1	0,511714	0,000007	-17,9	0,1	0,511758	0,000005	-17,0	0,1	0,9
Solimões									
SOL-1	0,512099	0,000009	-10,4	0,2	0,512381	0,000008	-4,9	0,2	5,5
SOL-2	0,512090	0,000009	-10,5	0,2	0,512362	0,000009	-5,2	0,2	5,3
SOL-3	0,512148	0,000005	-9,4	0,1	0,512378	0,000005	-4,9	0,1	4,5
Madeira									
MAD-1	0,512050	0,000006	-11,3	0,1	0,512219	0,000007	-8,0	0,1	3,3
MAD-2	0,512030	0,000007	-11,7	0,1	0,512231	0,000007	-7,8	0,1	3,9
MAD-3	0.512119	0,000009	-10,0	0,1	0.512363	0.000004	-5.2	0.1	4.8
Lower Amazon									
AMZ-1	0,512074	0,000007	-10,9	0,1	0,512254	0,000010	-7,3	0,2	3,5
AMZ-2	0,512109	0,000007	-10,2	0,1	0,512325	0,000007	-5,9	0,1	4,2
AMZ-3	0,512075	0,000004	-10,8	0,1	0,512314	0,000006	-6,2	0,1	4,7
AMZ-4	0,512099	0,000005	-10,4	0,1	0,512319	0,000007	-6,1	0,1	4,3
AMZ-5	0,512096	0,000004	-10,4	0,1	0,512310	0,000007	-6,2	0,1	4,2
AMZ-6	0,512045	0,000012	-11,4	0,2	0,512347	0,000006	-5,5	0,1	5,9
AMZ-7	0,512106	0,000009	-10,2	0,2	0,512353	0,000005	-5,4	0,1	4,8
AMZ-8	0,512075	0,000004	-10,8	0,1	0,512277	0,000007	-6,9	0,1	4
AMZ-9	0,512082	0,000010	-10,7	0,2	0,512298	0,000007	-6,5	0,1	4,2
AMZ-10	0,512113	0,000006	-10,1	0,1	0,512318	0,000006	-6,1	0,1	4
AMZ-11	0,512077	0,000027	-10,8	0,5	0,512189	0,000013	-8,6	0,3	2,2

3.4 Discussion

3.4.1 Cratonic Domain: Silicate weathering and the input of exogenous radiogenic Nd

The Cratonic Domain of the Amazon Basin exhibits enriched light rare earth element (LREE) patterns on the clay fraction, a low Fe oxide concavity index (1.1), and minimal Nd isotopic decoupling ($\Delta\varepsilon Nd_{FeOx\text{-}Clays}$). These characteristics align with global trends in rivers draining crystalline basement terrains (**Fig. 3.4B**; (Bayon et al., 2020b, 2015). Dissolved load data similarly show LREE enrichment and comparable concavity index values to riverine Fe oxides, but with a flatter heavy rare earth element (HREE) pattern (**Fig. 3.3C**), consistent with higher HREE stability in aqueous solution (Merschel et al., 2017; Elderfield et al., 1990). Interestingly, our data also reveal that both detrital clay and Fe oxide fractions in the Negro and Tapajós tributaries unexpectedly exhibit slightly more radiogenic values than corresponding SPM and dissolved load (**Fig. 3.5**).

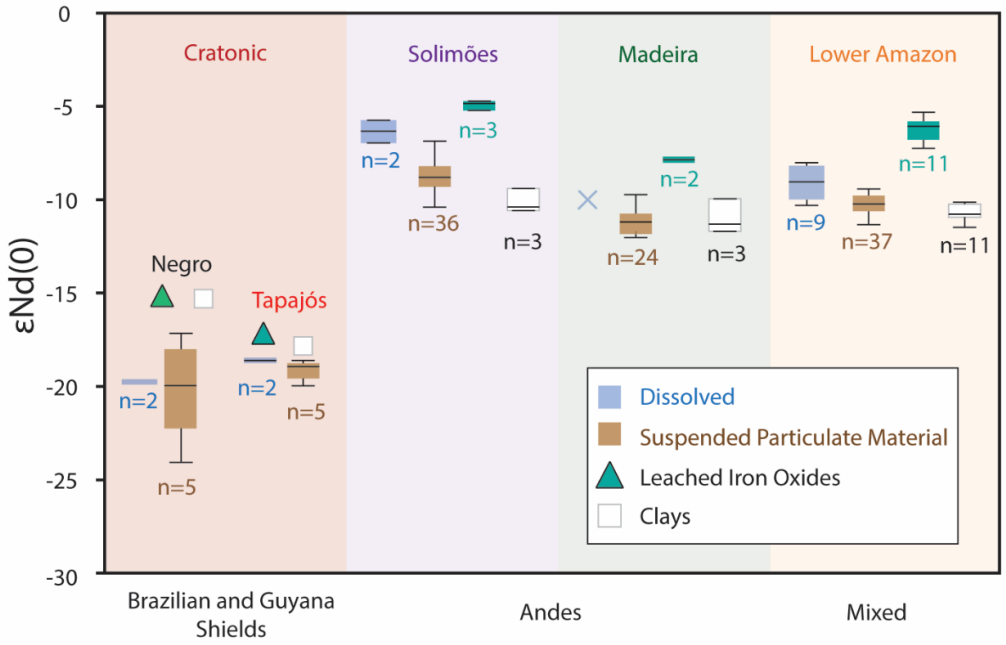

Figure 3.5. Compiled εNd values in the Amazon basin. Dissolved phases (Merschel et al., 2017), suspended particulate matter (Rousseau et al., 2019; Höppner et al., 2018; Horbe et al., 2014; Bouchez et al., 2011; Viers et al., 2008; Allégre et al., 1996), and detrital clay and leached Fe oxide fractions from this study, presented by domain and for the lower Amazon River.

In tropical lowland settings like the Cratonic Domain, most riverine clays and associated Fe oxides come from secondary weathering products formed in soil, especially in floodplains and other transport-limited areas where thick lateritic soils, low denudation rates, and intense silicate weathering prevail (e.g., West et al., 2005). In catchments dominated by crystalline igneous and metamorphic rocks, both detrital clays and Fe oxyhydroxide phases typically display similar Nd isotopic compositions, which reflect average inherited εNd signatures of parental rocks (Bayon et al., 2020a).

A recent study on lateritic profiles in the Cratonic Domain of Central Amazonia highlight a significant vertical Nd isotope variability, with some profiles showing values up to 8 ε-units higher than the underlying bedrock (-20.17 ± 2.1, n=11), along with elevated Zr, Th, Y, and REE concentrations (Horbe et al., 2022). While incongruent weathering of silicate rocks in soils overlying crystalline rocks can lead to the preferential dissolution of minerals with slightly different Nd isotopic compositions, the resulting εNd decoupling between soil horizons is typically limited to a few ε-units (Ohlander et al., 2014; Berger et al., 2014). Similarly, a global comparison of Nd isotopes in clay and silt fractions from rivers draining Precambrian crystalline terrains shows minimal size-dependent Nd fractionation ($\Delta\varepsilon Nd_{Clay\text{-}Silt}$ = 0.2 ± 1.4; n=11; Bayon et al., 2015).

Holocene sediments from a core recovered in the Lake Pata, located in the upper Negro River Basin, and aerosol samples collected at the Amazon Tall Tower Observatory (ATTO) near Manaus exhibit considerably radiogenic εNd values (-0.4 to 1.2 and -6.3 to -12.3, respectively; **Fig. 3.1A**; Nogueira et al., 2021) when compared to the local cratonic crystalline basement. These signatures have been interpreted as evidence of dust inputs, including contributions from African deserts, Andean soils, and Argentine loess (Nogueira et al., 2021). Building on these constraints, we argue that an additional sediment source, potentially linked to exogenous dust deposition in the Amazon rainforest (Bristow et al., 2010; Koren et al., 2006), could contribute to REE remobilization in Amazonian soils and fine-grained river sediments across the Cratonic Domain. This hypothesis is consistent with previous observations of significant Nd isotope decoupling in lateritic sequences influenced by Saharan dust deposition (Bayon et al., 2024; Viers and Wasserburg, 2004). Consequently, our data suggest that the radiogenic Nd signature observed in river clays and Fe-oxide fractions in the Cratonic Domain cannot be solely attributed to local weathering processes, supporting an additional exogenous contribution.

3.4.2 Solimões Domain: the imprint of ancient marine sedimentary rock weathering

The geochemical characteristics of the Solimões and lower Amazon rivers are strongly influenced by inputs of geologically recent volcanogenic material from the Equatorial Andes (Moquet et al., 2011, 2016; Santos et al., 2015; Bouchez et al., 2011; Viers et al., 2008; Barroux et al., 2006; Allégre et al., 1996). Indeed, previous works have reported Nd isotopic compositions for dissolved and SPM in the Solimões Rivers up to 3 ε units more radiogenic than in the Madeira River, where volcanic input is minimal (**Fig. 3.5**; Rousseau et al., 2019; Höppner et al., 2017; Merschel et al., 2017; Bouchez et al., 2011; Viers et al., 2008). Furthermore, the widespread presence of Neogene detrital zircon grains in bedload sediments of the lower Amazon River also provides evidence for the erosion of Andean volcano-sedimentary sequences (Jackson and Horton, 2025). On continents, preferential remobilization and alteration of volcanogenic sediments typically result in significant Nd isotope size-decoupling in river sediments, with fine-grained fractions and dissolved loads being up to 8 ε units higher relative to associated coarser material (Bayon et al., 2020a; Garçon and Chauvel, 2014). In this study, our data indicate that the Nd isotopic composition of detrital clays in the Solimões River (-10.1 ± 1.2, n = 3) overlaps within uncertainty with values for the Madeira River (-11 ± 1.8, n = 3). Together with evidence that measured shale-normalized REE concentrations of Solimões clays do not display the typical LREE-depleted pattern of volcanic material (**Fig. 3.2**; Bayon et al., 2015), these results hence highlight a mixed composition of fine-grained sediment transported by the Solimões and, to some extent, the lower Amazon River, typical of large river basins draining mixed lithologies (Bayon et al., 2015).

Previous works on the clay mineralogy of river sediments across the Amazon Basin further support this inference. As Amazonian rivers exit the Andes, clay mineral assemblages of suspended material show a marked decline in illite and chlorite contents, accompanied by a progressive increase in smectite and kaolinite along the floodplain (Guyot et al., 2007). This mineralogical transition underscores the critical role of bank erosion and sediment remobilization in shaping the detrital clay budget of the lower Amazon River. Kaolinite is predominantly sourced from the weathering of lowland soils, while smectite may come from the erosion of Mesozoic marine deposits in the Marañón watershed (**Fig. 3.1B**) and Neogene

deposits of the Pebas system within the Andean foreland and adjacent floodplains. The Pebas system, a complex network of swamps, lakes, and fluvial environments occasionally influenced by brackish shallow marine incursions (Hoorn et al., 2023; Leandro et al., 2022; Alvim et al., 2021), has since then been uplifted and eroded in the Pastaza Megafan and Fitzcarrald Arch regions (Espurt et al., 2007; Guyot et al., 2007). Thus, we interpret the observed Nd isotopic signatures and REE compositions of detrital clays in the lower Solimões River to reflect the combined influences of sedimentary contributions from these distinct geological sources.

Additional insights into sediment provenance and weathering processes in the Solimões Domain can be gained using REE in leached riverine Fe oxide fractions. In a La/Gd vs. Gd/Yb diagram, studied Fe oxides from the Solimões and lower Amazon rivers clearly plot within the compositional range of ancient marine deposits, characterized by intermediate CI values (2–2.5; **Fig. 3.6**; Bayon et al., 2020a). Marine or marine-influenced Mesozoic and Cenozoic deposits are widespread in upstream high-elevation source regions, where high physical erosion rates and minimal soil development are likely to inhibit the precipitation of secondary Fe oxides via silicate weathering. Thus, the erosion of ancient marine sedimentary rocks in the Andean headwaters appears to represent the dominant source of Fe oxides in the Solimões Domain.

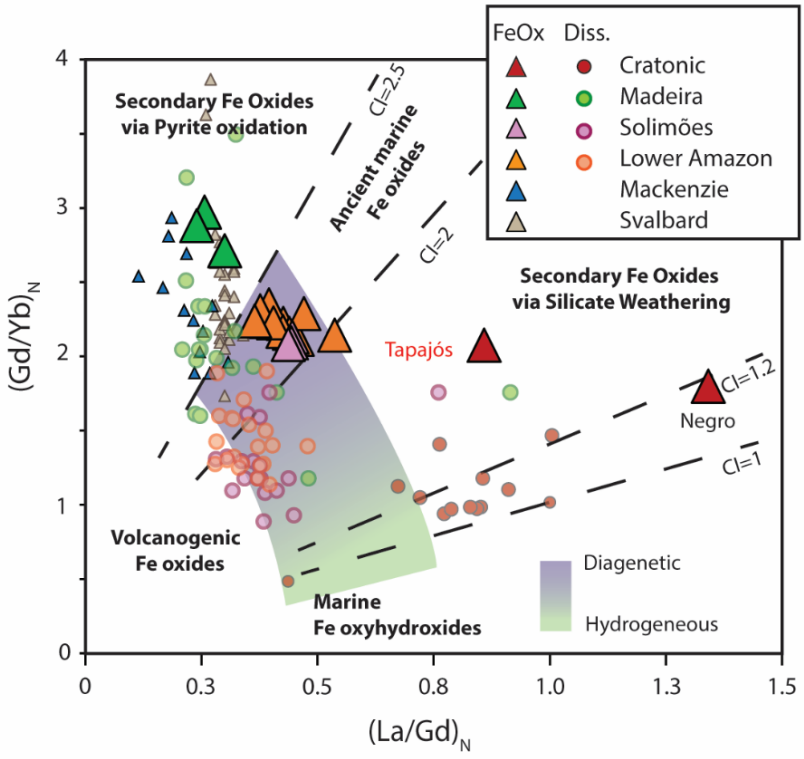

Figure 3.6. WRAS-normalized $(Gd/Yb)_N$ versus $(La/Gd)_N$ diagram of leached Fe oxide fractions from Amazonian sediments. Dashed lanes correspond to theoretical values of the concativity index (CI) of corresponding shale-normalized REE patterns, which distinguish the source of Fe oxides in sediments. The shaded field represents the compositional range of marine Fe oxyhydroxides inferred from pore water data. The color gradient from yellow to blue illustrates progressive changes in pore water REE signatures, reflecting a continuum from hydrogenous Fe-oxides formed under oxic conditions to diagenetic Fe oxides formed under suboxic conditions. For comparison, the reported REE measurements of leached Fe-oxides from riverine sediments in Svalbard (grey triangles; Jang et al., 2024) and Mackenzie (blue triangles; Larkin et al., 2021) rivers. We also added the composition of the dissolved load of Amazonian waters, as they also tend to follow the same trends as the Fe-oxides (circles; Goldstein and Jacobsen, 1998; Baroux et al., 2006; Merschel et al., 2017; Xu et al., 2023).

This hypothesis is further supported by the fact that both the Solimões Domain and the lower Amazon River exhibit particularly high $\Delta\varepsilon Nd_{FeOx\text{-}Clays}$ values (4.5–5.5). Such a degree of Nd isotopic decoupling between riverine Fe oxides and corresponding detrital fractions even exceeds the global average for river basins draining mixed lithology bedrock (2.7 ± 1.2; **Fig. 3.4B**; Bayon et al., 2020a). In the Solimões Domain, the highly radiogenic εNd signature preserved in riverine Fe oxides is best interpreted as reflecting their formation in a marine environment, in which diagenetic precipitation of Fe oxyhydroxide phases below the sediment-water interface would have captured the εNd signature of overlying bottom water masses at that time (Haley et al., 2017; Bayon et al., 2020a; Larkin et al., 2021). This hypothesis is supported by the evidence that the average εNd value of Fe oxides in the Solimões (–5 ± 0.5, n = 3) closely matches the average Nd isotopic composition of Central Pacific seawater over Meso-Cenozoic times (~–4.7; Frank et al., 2005, 1999; (Lacan et al., 2012). Accordingly, we thus infer that the riverine Fe oxides transported in the Solimões River relate to ancient diagenetic Fe oxide phases eroded and/or chemically weathered from uplifted sedimentary rocks in upstream Andean regions. This finding is consistent with previous inferences that river water geochemistry in the Marañón and Ucayali tributaries of the Solimões River is strongly influenced by chemical weathering of marine sedimentary rocks, with more than 70% of the total dissolved solids (TDS) load being released by weathering of Cretaceous evaporites and carbonate formations from the Andean and Foreland sub-basins (Moquet et al., 2011).

To summarize, both Nd isotopes and REE highlight the role of recycling ancient marine sediment deposits in controlling the composition of authigenic Fe oxide fractions within the Solimões Domain. It is important to emphasize that these results do not preclude a contribution from volcanic sources to Solimões River sediments.

3.4.3 Madeira Domain: Sulfide oxidation and MREE enrichment in Fe-Oxides

The high concativity index values determined for the Madeira Domain (CI = 3.2 ± 1, n = 3) depart from the observed MREE enrichment in riverine Fe-oxides from mixed-lithologies watersheds worldwide (CI = 2.4 ± 0.7, n = 30) and from those of the Solimões Domain and lower Amazon River in this study (**Table 3.2**, **Fig. 3.3**). This degree of MREE enrichment cannot be explained solely by erosion and/or chemical weathering of marine sedimentary rocks, as discussed above for the Solimões Domain.

In the Critical Zone, the mobility of MREE is strongly influenced by water pH, with acidic conditions enhancing preferential MREE mobilization (Ling et al., 2015; Ma et al., 2011). One of the main drivers of acidification in natural waters is the oxidative weathering of pyrite and other sulfide minerals commonly found in black shales (Horan et al., 2017; Torres et al., 2014; Konhauser et al., 2011). Sulfide oxidation produces sulfuric acid and secondary Fe-oxide phases, as summarized by the equation:

$$4FeS_2 + 15O_2 + 14H_2O \leftrightarrow 4Fe(OH)_3 + 8H_2SO_4$$

Tributaries of the Madeira River, such as the Madre de Dios, Beni, and Marmoré Rivers show pH values as low as 4.0, 5.1, and 3.8, respectively (Moquet et al., 2016), and sulfur isotope data from the Madre de Dios sub-basin indicate ongoing sulfide oxidation as the primary source of dissolved sulfate (Torres et al., 2016). Various positive relationships between pH, dissolved SO_4, and MREE contents have also been observed in mine soil leaching experiments (Larkin et al., 2021; Pérez-López et al., 2010) and in the Mackenzie Basin, in which chemical weathering of black shales associated with pyrite oxidation acts as a major biogeochemical process (Larkin et al., 2021; Pérez-López et al., 2010).

Yet, sulfide oxidation alone cannot explain the magnitude of MREE enrichment in riverine Fe-oxides, since common sulfide minerals (e.g., pyrite, sphalerite, galena) generally have low CI values (~1.1 ± 3.7, n = 16; Jang et al., 2024). Following pyrite oxidation, the release of sulfuric acid is likely to dissolve MREE-enriched phosphate minerals such as apatite, which are ubiquitous in black shales, with an average CI of 4.9 ± 3.7 (n=58; (Zhang and Shields, 2023; Zhao et al., 2022; Ohr et al., 1994). This MREE-enriched dissolved pool, released into solution, can

then be subsequently incorporated into secondary Fe oxyhydroxide phases, thereby leading to the observed high-CI signatures in sedimentary Fe oxides in catchments where extensive sulfide oxidation weathering occurs (Jang et al., 2024; Bayon et al., 2020a).

In the Amazon Basin, this assumption is further supported by the positive correlation between MREE enrichment in leached Fe-oxide fractions and phosphate contents in associated clays, as inferred from a CI and the $(P/Al)_{clay}$ ratio (**Fig. 3.7A**; R^2=0.66; **Supplementary Table 3.2**). Samples from the Madeira Domain exhibit the highest $(P/Al)_{clay}$ ratios and CI values (**Fig. 3.7A**), suggesting a link between sedimentary REE distribution and phosphate contents. Such high P contents in Madeira detrital clays could be related to the presence of residual apatite or more resistant secondary phosphate phases associated with clays (Bayon et al., 2023; Berger et al., 2014), or to the presence of crystalline Fe oxide phases, such as goethite and hematite, unleached during our AA+HH leaching step (N'nanga et al., 2025), thereby explaining the observed high $(P/Al)_{clay}$ ratios.

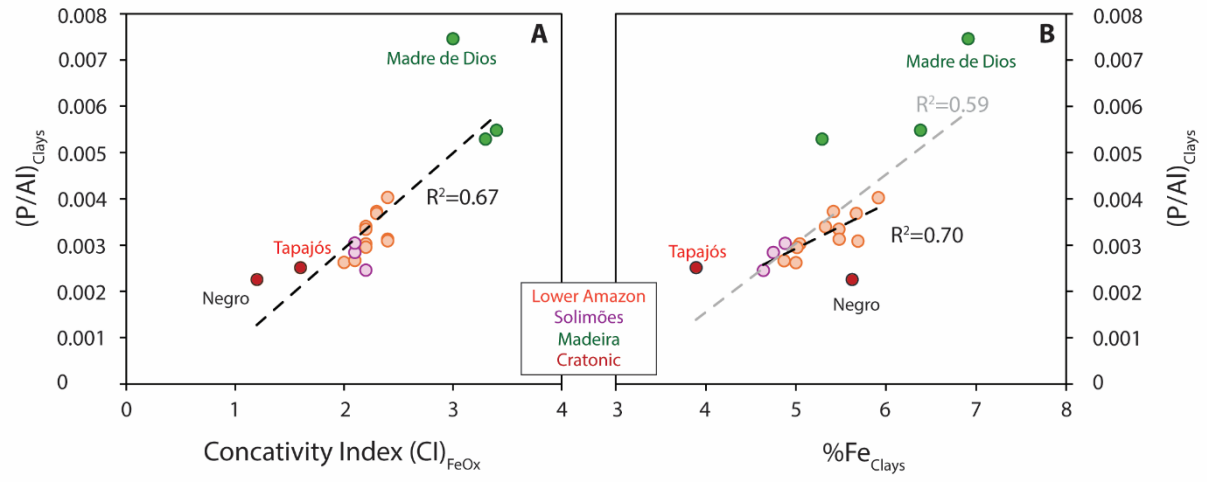

Figure 3.7. Relationship between phosphate mineral abundance, MREE enrichment in easily reducible leached Fe oxide phases, and residual Fe oxide content in the Amazon Basin. A) MREE concavity index of leached Fe oxide phases plotted against $(P/Al)_{clays}$, highlighting a positive correlation between MREE enrichment in easily reducible Fe oxides and phosphorus content. **B)** Percentage of residual Fe in clays ($\%Fe_{clays}$) versus $(P/Al)_{clays}$, illustrating the association between residual Fe-rich phases and phosphate mineral abundance. The black dashed line represents the regression for samples from the Solimões Domain and Amazon River, while grey dashed lines show the regression for the full dataset.

Similarly high CI values (>2.5) in sedimentary Fe oxides have been previously reported in glacial catchments, such as in Svalbard (with CI = 2.8 ± 0.6; Jang et al., 2024) and the Mackenzie Basin (3.2 ± 0.6; Larkin et al., 2021), or in black shale-bearing watersheds worldwide (**Fig. 3.8**; Bayon et al., 2020a). In glacial and alpine environments, sulfide oxidation is fueled by glacial abrasion, a process that exposes reactive minerals, including sulfides, from the bare bedrock (Torres et al., 2017; Wadham et al., 2019). In a similar fashion, high denudation rates in the Andean headwaters of the Madeira River (Pepin et al., 2013), as well as the presence of rainfall hotspots in the upper part of the Madre de Dios, Beni, and Mamoré rivers (Espizona et al., 2015), are likely to enhance fresh exposure of sulfide-bearing black shales prone to oxidation. While rapid sediment transport must limit in situ chemical reactions (Torres et al., 2016), we speculate that prolonged sediment residence in floodplains downstream (Dosseto et al., 2006; Baby et al., 1999) could be accompanied by sustained sulfide oxidation (Dellinger et al., 2023), hence enhancing sulfuric-acid-mediated phosphate dissolution and subsequent precipitation of MREE-enriched Fe-oxyhydroxide phases.

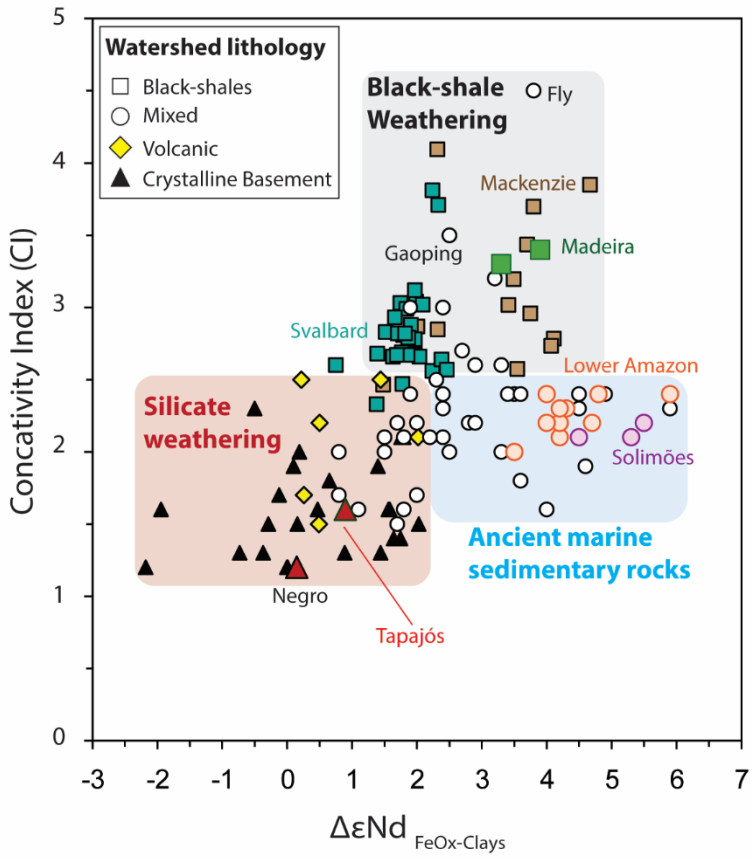

Figure 3.8. REE concativity index (CI) versus $\Delta\varepsilon Nd_{FeOx\text{-}Det}$ in leached Fe oxide fractions from the rivers in the Amazon Basin (this study), Mackenzie Basin (Larkin et al., 2021), Svalbard (Jang et al., 2021, 2024), and world compilation (Bayon et al., 2020).

3.4.4 Implications on the utility of REE and Nd isotopes for tracing silicate vs. sedimentary rock weathering on continents

The distinct geochemical signatures observed between the Solimões, Madeira, and Cratonic domains, and the lower Amazon River underscore the powerful use of REE patterns and Nd isotopes in paired detrital clays and Fe oxides as tracers of bedrock lithology and weathering processes in the Amazon Basin. These signatures reflect contrasting geological substrates, from Andean volcanic and sedimentary rocks to ancient cratonic shields, and their associated weathering regimes. In this context, riverine Fe oxides act as an integrative record of chemical weathering processes operating in upstream source regions, capturing both bedrock lithology geochemical signatures and the nature of weathering reactions along the sediment transport pathway.

Beyond the Amazon Basin, a particularly compelling application of the approach used in this study is to identify and quantify the weathering of black shales and other organic-rich sedimentary rocks. These lithologies play a disproportionate role in regulating atmospheric CO_2 because their oxidative weathering can release both carbon dioxide and sulfuric acid, thereby acting as a source of CO_2 to the atmosphere (Hemingway et al., 2018; Torres et al., 2014, 2016; Calmels et al., 2007). This process contrasts with the well-known CO_2 consumption mechanism associated with silicate rock weathering (Raymo and Rudiman, 1992), highlighting the importance of distinguishing among weathered rock types when assessing the impact of continental chemical weathering on climate. Tectonically active and rapidly eroding regions, such as the Andes, Himalayas, or other major orogens worldwide, are hotspots for such oxidative processes, where the exposure of black shales and other organic-rich sedimentary rocks is enhanced by physical denudation (Hilton and West, 2020). Our results show that in such settings, the use of REE and Nd isotopes bound to riverine Fe oxides can provide an integrative signal of upstream sediment inputs that can help identify the contribution of CO_2-releasing lithologies to riverine fluxes. Future REE and Nd isotope investigations of riverine Fe oxides preserved in sedimentary archives such as marine fans, floodplains, or deltaic deposits could thus serve for reconstructing past changes in continental weathering regimes, which could help testing hypotheses about the linkages between mountain building, monsoonal

systems, and carbon cycle evolution, all central components in understanding Earth's climate sensitivity over millions of years.

3.5 Conclusions

This study demonstrates the utility of REE patterns and Nd isotopic compositions in paired detrital clays and Fe oxides as robust tracers of sediment provenance and chemical weathering processes across the Amazon Basin. By leveraging the distinctive geochemical signatures of the main sub-catchments of the Amazon Basin, we show that the Fe oxide phases transported by the Madeira River display pronounced MREE enrichment, reflecting pyrite oxidation and oxidative weathering of black shales in upstream source regions.

These findings demonstrate that the combination of REE and Nd isotopes in river sediments can effectively disentangle the influences of lithology and chemical weathering signals, even in complex river systems such as the Amazon Basin. Importantly, our results highlight the value of riverine Fe-oxide phases in recording upstream lithological signals, offering a unique window into both present-day and past continental weathering regimes. The ability to trace the oxidative weathering of black shales via application of REE and Nd isotopes to sedimentary Fe oxides has far-reaching implications for understanding the balance of atmospheric CO_2 sources and sinks in orogenic systems over geological timescales.

Acknowledgements

M. Ianniruberto, C. Trindade, A. Baltzer, P. Guyavarch, and the crew of the AMANAUS cruise are thanked for their assistance with fieldwork. G.R.M. was funded by the Coordination for the Improvement of Higher Personnel – Brazil (CAPES) – Finance Code 001 and the Agence Nationale de Recherche ECLIP-SED project (ANR-20-CE01-0003) for his PhD thesis. Additional funds for fieldwork in the Amazon River were provided by the ISblue project, Interdisciplinary graduate school for the blue planet (ANR-17-EURE-0015), and co-funded by a grant from the French government under the program "Investissements d'Avenir" embedded in France 2030.

IV

Orbital and sea-level controls on long-term sediment deposition in the Amazon Fan

Declaration/ Declaração/ Déclaration

This chapter presents the development of an astronomically tuned age model for the BP-3 well, drilled in the upper Amazon Fan. The main objective was to refine the existing nannofossil-based chronology, allowing for a more precise alignment of proxy records with globally recognized sea-level and temperature variations. The work was conducted in collaboration with Prof. Thiago P. Santos (University of São Paulo) and Natalia Vázquez Riveiros (IFREMER), within the framework of the CAPES-COFECUB project *"Role of South Atlantic Ocean Circulation on the Climate of South America: Past, Present, and Future."* The results were first presented at the French–Brazilian Fall School in South Atlantic Paleoceanography and Paleoclimatology, held at the University of São Paulo in April 2025, and were subsequently published in *Global and Planetary Change* in September 2025.

[PT} Este capítulo apresenta o desenvolvimento de um modelo de idade ajustado astronomicamente para o poço BP-3, perfurado no setor superior do Leque Amazônico. O principal objetivo foi refinar a cronologia existente baseada em nanofósseis, permitindo um alinhamento mais preciso dos registros proxy com as variações globais de nível do mar e de temperatura. O trabalho foi realizado em colaboração com o Prof. Thiago P. Santos (Universidade de São Paulo) e Natalia Vázquez Riveiros (IFREMER), no âmbito do projeto CAPES-COFECUB "Papel da circulação do Oceano Atlântico Sul no clima da América do Sul: passado, presente e futuro." Os resultados foram apresentados inicialmente na French–Brazilian Fall School in South Atlantic Paleoceanography and Paleoclimatology, realizada na Universidade de São Paulo em abril de 2025, e posteriormente publicados na revista Global and Planetary Change em setembro de 2025.

[FR] Ce chapitre présente le développement d'un modèle d'âge calé astronomiquement pour le forage BP-3, réalisé dans la partie supérieure de l'éventail amazonien. L'objectif principal était de raffiner la chronologie existante basée sur les nannofossiles, afin de permettre un alignement plus précis des enregistrements proxy avec les variations globales du niveau marin et de la température. Le travail a été mené en collaboration avec le Prof. Thiago P. Santos (Université de São Paulo) et Natalia Vázquez Riveiros (IFREMER), dans le cadre du projet CAPES-COFECUB « Rôle de la circulation de l'océan Atlantique Sud sur le climat de l'Amérique du Sud : passé, présent et futur. » Les résultats ont été présentés pour la première fois lors de la French–Brazilian Fall School in South Atlantic Paleoceanography and Paleoclimatology, organisée à l'Université de São Paulo en avril 2025, puis publiés dans la revue Global and Planetary Change en septembre 2025.

Abstract

The Amazon Fan, one of the largest deep-sea fans on Earth, is a vital archive of the Amazon Basin's long-term climate and tectonic evolution. However, the factors driving sediment deposition patterns during the Neogene remain poorly understood. Here, we present an astronomical age model for a 4800 m-long sedimentary record (BP-3 well), spanning the past ~24 million years, a key interval encompassing the Amazon River's evolution into a transcontinental system. Gamma-ray (GR) data reveal strong Milankovitch cyclicity, highlighting the fan's sensitivity to orbital climate variability and enabling correlations with global mean sea level (GMSL). Our analysis shows persistently low sedimentation rates (~5–13 cm/kyr) during the late Miocene, despite Andean uplift and increased precipitation, likely due to sediment trapping by mega-wetlands in Western Amazonia. A marked increase in sedimentation (~50 cm/kyr) during the Early Pliocene (5.1–4.8 ± 1.78 Ma) reflects the collapse of these barriers, facilitating sediment transport to the Atlantic despite high GMSL. The GR record also captures the transition from obliquity- to eccentricity-dominated glacial-interglacial cycles during the mid-Pleistocene Transition (~1.3 Ma). These findings align with GMSL and benthic $\delta^{18}O$ data, supporting a minimal tuning approach and emphasizing the Amazon Fan's sensitivity to global climate changes. Our revised chronology provides a robust framework for understanding the Neogene evolution of the Amazon River and its links to Andean tectonics and climate variability.

4.1. Introduction

Continental margins host unique sediment records of past fluvial discharge to the oceans, sea-level fluctuations, oceanic circulation, and geodynamic and climate change (Clift et al. 2008). Submarine fans are particularly significant among these deposits, representing continental margins' largest deep-water sedimentary systems that can be used to reconstruct the interplay of terrestrial climate, regional tectonics, and sea-level variations over geological timescales (Flood and Piper, 1995). The Amazon Fan, situated at the mouth of the Amazon River, ranks among the world's largest deep-sea fan systems, spanning an area of approximately 375,000 km^2 (**Fig. 4.1**; Figueiredo et al., 2009). The Amazon Fan developed in the mid-to-late Miocene, driven by Andean orogeny and dynamic topography, which reorganized river systems across the Amazon Basin to flow eastward toward the Atlantic Ocean (Hoorn et al., 2017; Shephard et al., 2010). Since its inception, the Amazon Fan has served as the primary depocenter for sediments along the Brazilian Equatorial Margin (Figueiredo et al., 2009; Gorini et al., 2014; Hoorn et al., 2017), accumulating tremendous amounts of terrigenous material transported from the Amazon Basin. This scenario places the Amazon Fan as an exceptional repository for reconstructing northern South America's geodynamic and climatic evolution during the Neogene.

Previous efforts in this direction were conducted on sediment records drilled during the Ocean Drilling Program (ODP) Leg 155 Expedition (**Fig. 4.1B**), leading to various investigations exploring terrestrial organic carbon accumulation in the fan, the interplay between surface and deep ocean circulation, regional moisture availability and freshwater discharge, and the evolution of the Amazon rainforest (Burns and Maslin, 1999; Maslin et al., 2000). The ODP Leg 154, while located in a more distal setting on the Ceará Rise, has been instrumental in documenting the onset of the Amazon River as a transcontinental system and the far-reaching impact of riverine discharge on the western Atlantic over million-year timescales (Stewart et al., 2016; Van Soelen et al., 2017). Recent high-resolution reconstructions of the last glacial-interglacial cycle have further emphasized the interactions between the Amazonian climate and high-latitude regions, highlighting their potential impact on vegetation via changes in the Atlantic Meridional Overturning Circulation (Akabane et al., 2024, and references therein).

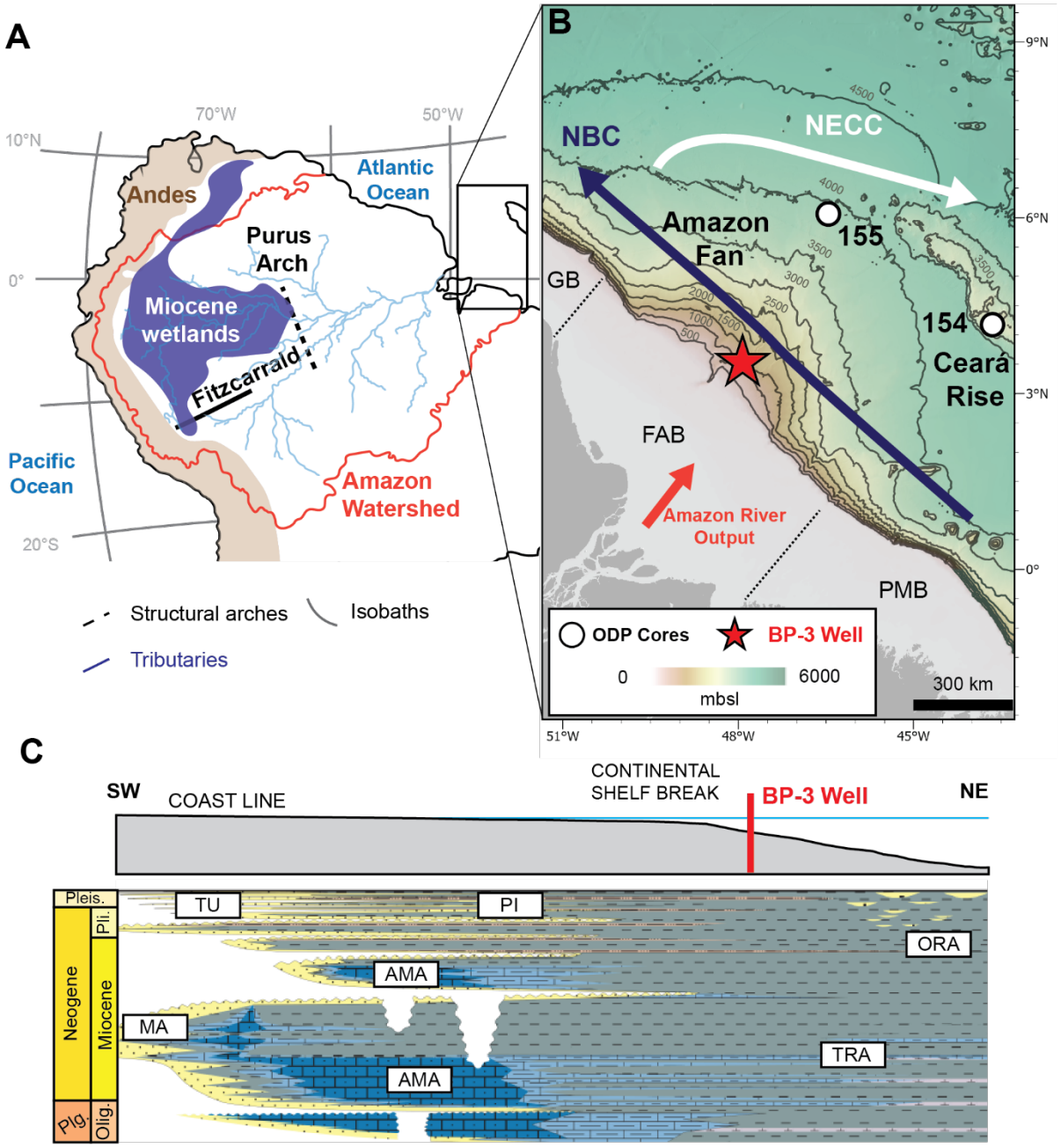

Figure 4.1. (a) Map of South America illustrating the modern drainage configuration of the Amazon Basin and the sediment transport pathways of the Amazon source-to-sink system. The purple area indicates the approximate extent of the Miocene mega-wetlands in Western Amazonia **(b)** The offshore sedimentary basins of the Brazilian Equatorial Margin are indicated as follows: GB: Guyana Basin, FAB: Foz do Amazonas Basin, PMB: Pará-Maranhão Basin. Arrows indicate the positions of the Northern Brazilian Current (NBC) and Northern Equatorial Counter Current (NECC) **(c)** Upper Paleogene-Neogene stratigraphic chart of the FAB central shelf, simplified from Cruz (2019). TU: Tucunaré, PI: Pirarucu, ORA: Orange, AMA: Amapá, MA: Marajó, and TA: Travosas Formations

Seismic analyses indicate that cyclic sedimentation in the Amazon Fan comprises successions of pelagic interglacial calcareous oozes, channel-levee systems, and regionally extensive mass-transport deposits (Manley and Flood, 1988; Maslin et al., 1998). During the past 11,000 years (and likely during older interglacials), the Amazon Fan was temporarily inactive as Amazon River sediments were mostly trapped on the inner continental shelf due to high sea level and surface water circulation (Maslin et al., 2005). In contrast, fan growth was most pronounced during periods of low sea level, when the Amazon River extended across the exposed continental shelf and discharged terrigenous sediments directly into the Amazon Fan complex through the canyon and distributary channels (Figueiredo et al., 2007).

The interpretation of sedimentary sequences in the Amazon Fan is complicated by the interplay between global mean sea level (GMSL) variability and autocyclic processes like channel avulsion or mass transport deposits. Simultaneously, GMSL carries a strong imprint of orbital signals driven by Milankovitch forcing (Miller et al., 2005). Under progressively colder climate conditions since the mid-Oligocene, the growth of massive ice sheets has been highly sensitive to the interaction of precession, obliquity, and eccentricity, directly influencing GMSL and the formation of third-order eustatic sequences worldwide (Boulila et al., 2011; Laskar et al., 2004; Pälike et al., 2006; Westerhold et al., 2020). Astronomical forcing also plays a significant role in controlling long-term tropical hydroclimate variability and the positioning of precipitation belts, as seasonal rainfall and temperature gradients are significantly modulated by insolation, which can largely be predicted by precession and obliquity (Clement et al., 2004; Laskar et al., 2004). The well-established periodicity of precession, obliquity, and eccentricity for the last 40 million years provides an opportunity to use their sedimentary imprints as geochronometers, enabling the refinement of geological timescales and the development of high-resolution astronomically tuned chronologies (Hinnov, 2013). Such efforts have advanced our understanding of the evolution of the Neogene and the broader Cenozoic climate (Westerhold et al., 2020).

Surprisingly, cyclostratigraphy and astronomical tuning have yet to be thoroughly applied to the Neogene Amazon Fan record. Although an astronomical age model was developed for the Cretaceous Limoeiro Formation, it pertains to a period predating the Amazon River's establishment (Boulila et al., 2020). Cyclic sediment deposition, likely influenced by obliquity, has been proposed as a driver of floodplain fill packages in the Miocene wetlands of

western Amazonia (Hoorn et al., 2022b). However, this hypothesis did not explicitly test the presence or absence of astronomical variability. This study recasts well-log data from the 1-BP-3-APS exploration well drilled in the upper Amazon Fan. Using the boundaries established by previous nannofossil biostratigraphic analyses (Figueiredo et al., 2009; Hoorn et al., 2017), we construct an astronomical timescale with uncertainties derived from gamma-ray (GR) well-log data. Our study uncovers previously unrecognized details of Amazon Fan deposition, offering the first explicit comparison with GMSL for the past ~24 million years. Despite the relatively consistent correlation between GMSL and long-term GR patterns, we propose that the exceptional sedimentation rate from the Plio-Pleistocene cannot be attributed solely to the decline in GMSL during this period.

4.2. Regional setting

The Foz do Amazonas Basin (FAB), the westernmost segment of the Brazilian Equatorial Margin, is bordered by the Guiana Basin to the west and the Pará-Maranhão Basin to the east (**Fig. 4.1B**). Covering an area of approximately 360,000 km^2, the FAB hosts sedimentary deposits up to 9,000 meters thick. Between the late Paleocene and late Miocene (ca. 61.7–8.0 Ma), carbonate platforms were the dominant depositional environment in the basin, resulting in the accumulation of around 4,000 meters of mixed carbonate-siliciclastic shelf sediments (Marajó and Amapá Formations) and deep-water calcilutites and mudstones (**Fig. 4.1C**; Figueiredo et al., 2007). During the Langhian stage of the mid-Miocene (~15.2 Ma), a globally warm climate led to high sea levels, marked in the FAB by a maximum flooding surface on the Amapá Platform. This transgressive event caused the Marajó Formation coastal systems to retreat and promoted carbonate platform development on the outer shelf (Figueiredo et al., 2007). However, subsequent sea-level decline during the Tortonian (~9.5–8.0 Ma), coupled with an increase in siliciclastic sediment supply, heightened water turbidity, and drove shoreline progradation. These processes led to the exposure and erosion of carbonate platforms, effectively terminating carbonate deposition in the FAB (Figueiredo et al., 2009; Gorini et al., 2014). Cruz et al. (2019) further revealed a south-to-north sedimentary filling pattern in the FAB, with siliciclastic deposition beginning in the southeast around ~8 Ma and reaching the northwest by ~3.7 Ma. This progressive sedimentation preserved carbonate deposition in the

northwest FAB for a more extended period, reflecting spatial variability in sediment delivery and deposition dynamics.

The Neogene sedimentary history of the Amazon Fan reflects the interplay of Andean orogeny, dynamic topography, climate variability, and sea-level changes (Shepard et al., 2010; Hoorn et al., 2017; Albert et al., 2018). During the mid-Miocene (~16–11.5 Ma), Andean surface uplift induced flexural subsidence, resulting in the formation of the Pebas system, a long-lived mega-wetland composed of swamps, lakes, and fluvial systems influenced by marine incursions (Jaramillo et al., 2017; Leandro et al., 2022). At that time, the Purus Arch, a prominent structural high in Central Amazonia, may have acted as a critical barrier preventing the western drainage from connecting to the eastern Amazon Basin until the late Miocene (Figueiredo et al., 2009). However, other authors have suggested that the Purus Arch only breached during the Pleistocene, following the deposition of the Iça Formation (Nogueira et al., 2013; Horbe et al., 2013; Rossetti et al., 2015). While the significance of the Purus Arch remains debated, alternative scenarios suggest that the Amazon fluvial system may have bypassed this barrier during the Neogene (Hoorn et al., 2017). Eventually, the interplay of tectonics and long-term climate change led to the demise of these mega-wetlands, the bypass of the Purus Arch, and the connection of eastern and western Amazonia, facilitating the development of the modern transcontinental Amazon River.

Finally, the formation of the Amazon Fan, commonly linked to the onset of the transcontinental Amazon River, remains a topic of ongoing debate. The Amazon Fan formed on the continental slope initially, becoming the primary depocenter for siliciclastic input from the late Miocene onward. Early estimates, based on extrapolated Quaternary sedimentation rates from core samples, placed the onset of the transcontinental Amazon River between 16.5 and 8.0 Ma (Damuth et al., 1977). Subsequent studies correlating well data, seismic profiles, and isotopic data suggested a later age of 11.8–10.0 Ma (Figueiredo et al., 2007, 2009). More recently, Hoorn et al. (2017), using nannofossil zonation calibrated to GTS 2012, proposed that Andean-derived sediments were first exported to the Amazon Fan between ~9.4 and 9.0 Ma.

4.3. Methodology

4.3.1. 1-BP-3-APS well-log data

The 1-BP-3-APS (hereafter BP-3) is an industry well drilled in the upper Amazon Fan (3° 2' 58.660" N, 47° 44' 45.801" W; 754 meters below sea level – mbsl – **Figs. 4.1B and 4.2A**) reaching a max depth of 5655 mbsl. This well has been referenced under various names in prior studies, including Well 2 (Figueiredo et al., 2009; Hoorn et al., 2017; Lammerstma et al., 2018), Well 4 (Gorini et al., 2014), and Well P1 (Reis et al., 2016). The GR well-log data was acquired by Schlumberger and provided by the Brazilian Petroleum and Gas Agency (ANP). GR data have a vertical resolution of 15 – 20 cm, and values are presented in API (American Petroleum Institute) units. This study focuses on the interval between 1450 and 4800 mbsl. The lithology of this interval includes alternating limestone and mudstone from 4800 to 4080 mbsl, transitioning to siltstone and fine sandstone until 3620 mbsl, and intercalated mudstone and siltstone down to 1450 mbsl. Due to drilling-related artifacts, the GR well-log is discontinuous; therefore, we divided it into three internally consistent intervals (**Fig. 4.2A**): section 3 (S3, 4425–4800 mbsl), section 2 (S2, 3680–4415 mbsl), and section 1 (S1, 1480–3670 mbsl). It should be noted that these 10 m non-measurement segments are not caused by stratigraphic discontinuities. The break between S1 and S2 coincides with a total mud loss at 3679 m during casing and cementing operations. This caused a baseline shift in the GR record by reducing the attenuation typically provided by drilling mud. Similarly, the break between S2 and S3 corresponds to a sequence of severe mud losses during casing operations. These events altered the absolute magnitude of the GR baseline but did not affect the relative variability of the signal, which remains consistent with lithological changes. For this reason, S1, S2, and S3 are treated as independent GR segments that can be interpreted stratigraphically within each interval but are not directly comparable in absolute values across boundaries.

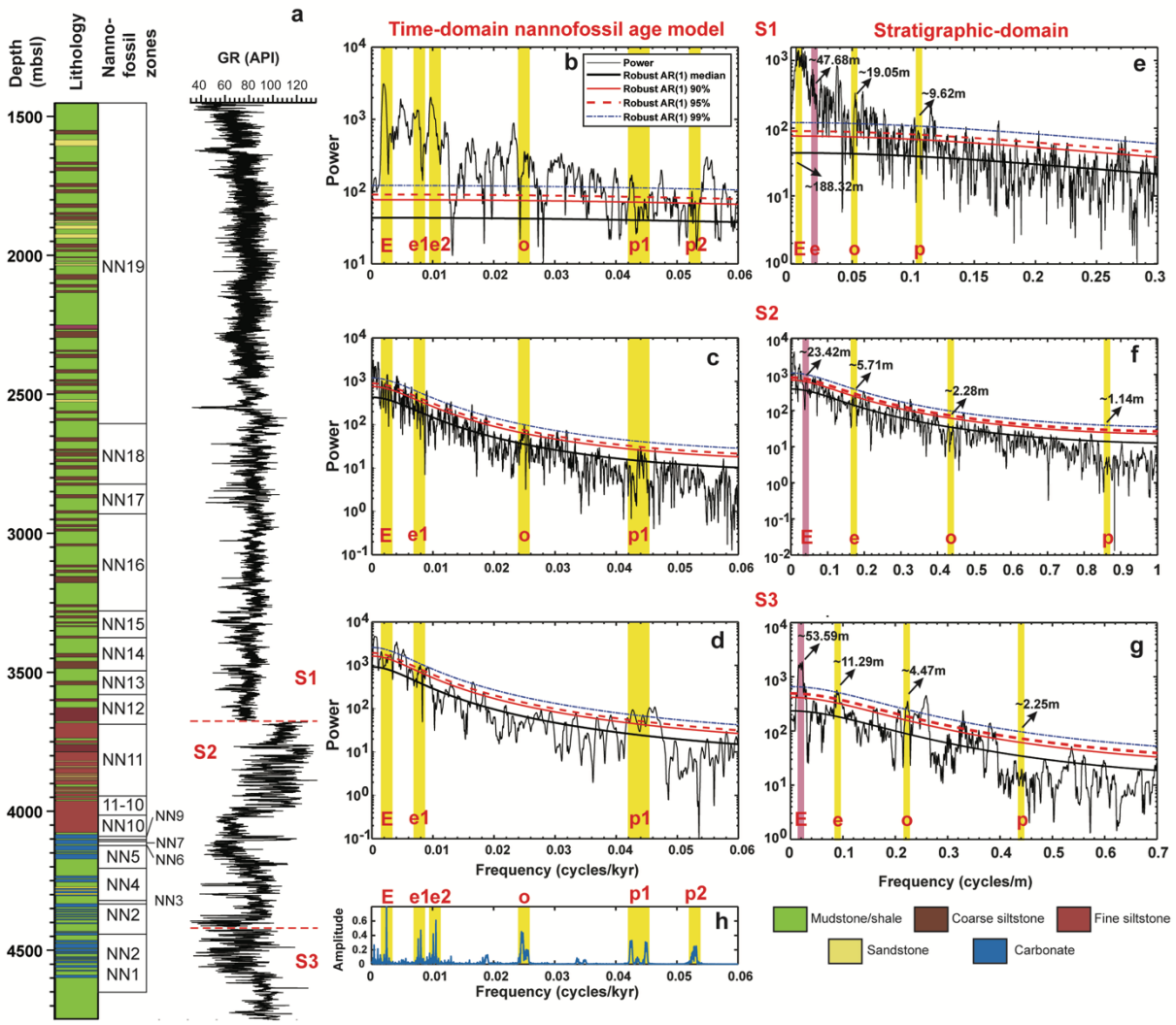

Figure 4.2. (a) GR data from the BP3 well plotted alongside lithological information and Nannofossil zonation from previous studies (Figueiredo et al., 2009; Hoorn et al., 2017). **(b)**, **(c)**, and **(d)** Multi-taper spectral analysis of GR data in the time domain, tuned to the biostratigraphic age model. Yellow bars highlight spectral bands corresponding to 405-kyr long eccentricity (E), ~100-kyr short eccentricity (e1 and e2), 41-kyr obliquity (o), and ~21-kyr precession (p1 and p2) cycles. **(e)**, **(f)**, and **(g)** multi-taper spectral analysis of GR data in the stratigraphic domain, with yellow bars indicating filtered wavelengths associated with orbital signals. **(h)** The spectral amplitude of the orbital solution (Laskar et al., 2004) for the past ~24 Myr.

4.3.2. Prior biochronology of BP-3 Well and a novel astronomical time scale

An age model for BP-3 was initially developed using calcareous nannofossil biostratigraphy on ditch-cutting samples (Varol, 2004; Figueiredo et al., 2009) and was subsequently updated to the GTS2012 timescale (Hoorn et al., 2017). According to this prior biostratigraphic evaluation, the 1450 to 4800 mbsl interval encompasses the Late Oligocene (NP25) to Pleistocene (NN19) period. Unlike the continental shelf or deeper fan regions, sedimentation on the upper fan has remained relatively uninterrupted during past sea-level fluctuations. However, stratigraphic breaks have been reported immediately above 4145, 3338, and 2654 mbsl. The first hiatus above 4145 m (section S2) corresponds at least to the complete absence of biozone NN8. The hiatuses at 3338 and 2654 mbsl are associated with the partial absence of the lower parts of biozones NN16 and NN19, estimated at ~1.0 and 0.73 Ma, respectively (Varol, 2004; Hoorn et al., 2017). It should be recognized that chronological inferences within a given biozone based on sparse biostratigraphic data remain problematic, as the limited temporal resolution imposes serious constraints on any refined internal interpretation. In addition, short-term intervals of poor preservation, whether caused by carbonate dissolution, dilution from the sudden influx of siliciclastic material, or other ecological factors, may further bias such analyses. Later in the manuscript (Section 3.3), based on the suite of statistical analyses conducted here, we challenge these earlier interpretations and, within the bounds of our uncertainty evaluation, argue instead for a largely complete chronostratigraphic succession in section S1.

The nannofossil biostratigraphy published by Figueiredo et al. (2009) was accompanied by a portion of the GR data employed in the current study. However, to date, the potential of these data for constructing a coherent astronomical time scale has not been explored. We investigated the eventual expression of orbital forcing using statistical cyclostratigraphic methods, applying these techniques to the GR data from the BP-3 well. GR data reflect the combined radiogenic emission of potassium, thorium, and uranium, typically present in minerals such as feldspar, mica, clays, and organic-rich particles. Consequently, higher GR values are likely associated with clay- or organic-rich sediments, while lower GR values generally correspond to coarser carbonate and sandstone components (Cantalejo and

Pickering, 2015). The balance between these sediment fractions within a basin is strongly influenced by the surrounding climate, which enhances the GR signal-to-noise ratio and enables more efficient detection of astronomical signals from stratigraphic noise (Li et al., 2019; Weedon, 2003). Limitations on this assumption rely on the non-climatic factors influencing the radiogenic signatures of the mentioned elements, possibly linked to high concentrations of heavy minerals, such as zircons (Šimíček et al., 2012).

Our approach begins with an independent verification of astronomical periodicities before orbital tuning. We leveraged nannofossil biostratigraphic published by Figueiredo et al. (2009) and subsequently updated by Hoorn et al. (2017) as a prior age-depth control. This biostratigraphic age model was applied across the three segments where the GR data were collected, placing the intervals S3, S2, and S1 between the late Oligocene and late Pleistocene. At present, biostratigraphy remains the only viable means of anchoring this well to an absolute timescale. The use of biostratigraphic constraints to guide subsequent cyclostratigraphic refinement is a well-established strategy in astrochronological studies (e.g., Groeneveld et al., 2021; Koutsodendris et al., 2021; Raffi and Backman, 2022).

After applying the nannofossil age-depth model to each GR section, we performed a linear interpolation based on their respective mean temporal resolution and detrended the data using a LOWESS regression with a 35% window. This process was designed to remove very long, non-astronomical frequencies mixed in the data. The significant frequencies preserved in each GR section were verified using power spectral analysis through the prolate multi-taper spectral estimator (MTM) (Thomson, 1982). The analysis was performed with 2π tapers and a robust red noise null hypothesis model supported by a theoretical first-order autoregressive process fitted to the data and reported regarding the 90%, 95%, and 99% spectral confidence levels (**Fig. 4.2**).

Subsequently, we searched for the respective orbital cycle found in the first step, but in the stratigraphic domain, choosing the one with exactly the same number of cycles. A Gaussian bandpass filter was used to isolate the most appropriate wavelength (in terms of number of cycles) in each section. We followed a minimum tuning approach, aligning each minimum in our filtered data with a corresponding minimum in the target astronomical signal for the chronological interval yielded by the biostratigraphic age model (Hinnov, 2013; Laskar et al., 2004). For intervals S3 and S2, the target astronomical frequency was the $g_2 - g_5$ 405-kyr cycle,

also known as the 'metronome'. The 405-kyr cycle is considered the most stable astronomical cycle (Laskar, 2020). For sections S3 and S2, we filtered frequencies corresponding to 1/0.01866 and 1/0.04269 cycle/m (wavelengths of ~53.59 m and ~23.42 m, respectively) (**Figures 4.2F and G**). For interval S1, the target astronomical frequency was the $g_4 - g_5$ ~ 95-kyr short eccentricity cycle. Among the various eccentricity cycles within this band, the ~ 95-kyr cycle exhibits the highest power spectrum during the Plio-Pleistocene interval (Laskar et al., 2004). For section S1, we filtered the frequency at 1/0.02097 cycles/m (wavelength of ~47.68 m). In **figures 4.2E-G**, we indicated additional frequencies with respect to the distribution related to the frequency ratio method (20:5:2:1) (Laskar et al., 2004); however, we reinforce that they were not used for tuning purposes since some of them do not overcome the spectral confidence levels.

Uncertainty evaluation remains a topic of ongoing debate in cyclostratigraphy, with no standardized methodology for quantifying it (Sinnesael et al., 2019). Age uncertainty can arise from various factors, including the non-linear response of the climate system, which can distort climate signals, the effects of sampling and statistical methods, resolution limitations, and the inherently incomplete nature of the stratigraphic record (Meyers, 2019). Insights from stochastic sedimentation modeling suggest that the average deviation in total duration when tuning to the 405-kyr and ~ 100-kyr cycles is approximately 14.5% and 21.5%, respectively (Wang et al., 2024). We directly incorporated the average deviation of 14.5% for interval S3. For intervals S2 and S1, in addition to the average deviation for the 405-kyr and ~ 100-kyr cycles, we accounted for an additional uncertainty of approximately 1.2 Ma and 0.19 Ma due to the potential absence of three 405-kyr and two ~ 95-kyr cycles, respectively (Figures 3 and 4). In fact, Figueiredo et al. (2009) report the absence of calcareous nannofossil zone NN8 for the interval S2, which, in terms of elapsed time, corroborates our evaluation of the three missing 405-kyr cycles. Ultimately, our age model did not diverge significantly from previous efforts based on biostratigraphic data (Figueiredo et al., 2009; Hoorn et al., 2017) (**Supplementary Figure 4.1**). Still, it substantially improves chronostratigraphic control while addressing more realistic uncertainties not previously assumed (**Supplementary Figure 4.1**). **Supplementary Tables 1–3** (**Appendix 4**) present the age models for intervals S1, S2, and S3, including their uncertainty estimates and the Gaussian band-pass filters used for astronomical tuning.

4.3.3. A Bayesian age model approach for the Plio-Pleistocene interval

An additional experiment was conducted in the upper part of section S1 (upper ~3000 mbsl). In this interval, we examined the capabilities of Integrated Prediction Error Filter Analysis (INPEFA), a feature within Cyclolog® software (Djin Nio et al., 2005). INPEFA calculates prediction error by creating new data points based on prior samples, with each point representing the numerical error between predicted and observed values at corresponding depths. A 10 m moving window was applied to the data. Assuming the record exhibits cyclic patterns due to climatic variations, INPEFA leverages these patterns to assess continuity and discontinuity in the dataset by quantifying spectral changes. The approach generates new sample points where each value represents either a positive or negative prediction error, indicating overestimation or underestimation of the GR values. Overestimation (negative error) suggests a "sandy" and more regressive segment, while underestimation (positive error) suggests a "muddy" and more transgressive trend. We interpret that significant changes in the depositional system occur at inflection points between predominantly negative and positive trends (Djin Nio et al., 2005). In this study, we worked exclusively on the mid-term INPEFA output.

Then, we attempt a probabilistic tuning between the results of the INPEFA analysis and the reference deep-ocean benthic oxygen isotope ($\delta^{18}O$) LR04 stack (Lisiecki and Raymo, 2005) to generate an alternative age model for the upper part of section S3. This experiment employed Bayesian Inference, Gaussian Process regression, and Multiproxy Alignment for Continuous Stacks (BIGMACS) (Lee et al., 2023). BIGMACS is a newly developed software package designed to probabilistically align ocean sediment core data and construct multiproxy age models. It formally incorporates multiple sources of age uncertainty to produce probabilistic alignments that are more informative and less subjective than traditional tie-point approaches (Lee et al., 2023). Median age models and their uncertainties are derived from the distribution of Markov chain Monte Carlo samples. Lastly, the correlation between mid-term INPEFA and global mean sea level (GMSL) was assessed using Pyleoclim, a Python 3.9 application (Khider et al., 2022). Both datasets were interpolated to their mean resolution and standardized using Pyleoclim tools. We applied time-series correlation with the default isospectral method,

supported by 5,000 Monte Carlo simulations. As mentioned in Section 3.2 and later on discussed in Section 5.3, the exceptional results obtained through the combined application of INPEFA and BIGMACS indicate a nearly complete stratigraphic succession for the upper ~3000 mbsl. This evidence leads us to question the existence of the hiatus associated with the partial absence of biozone NN19 at 2654 mbsl. A similar reasoning may be applied to the reported hiatus for biozone NN16 at 3338 mbsl, given its comparable nature.

4.4. Results

The GR values of the BP-3 well range from 40 to 130 API, with the maximum values occurring near the top of interval S2 (~ 4000 – 3600 mbsl; **Fig. 4.2A**). An abrupt change in mean values marks the transition between intervals S2 and S3 (~3600 mbsl), where GR decreases from approximately 120 to 80 API. In interval S1, a noticeable shift to higher frequency variability is observed around ~2450 mbsl, accompanied by a gradually decreasing trend toward the top of the well (**Fig. 4.2A**).

Aligned with the nannofossil biostratigraphic age model, intervals S3, S2, and S1 are constrained to 24.8–19.6 Ma, 19.2–5.09 Ma, and 5.03–0.43 Ma, respectively. The MTM power spectral analysis indicates that intervals S3 and S2 are predominantly characterized by lower frequency variability (>1/100 cycles/ka) (**Figs. 4.2C and 4.2D**). Within this frequency band, the 405-kyr cycle was identified, exceeding the 90% and 99% confidence levels for intervals S3 and S2, respectively. Lower frequency variability is also observed in interval S1, with well-defined 405-kyr-long eccentricity and ~100 and ~130-kyr short eccentricity cycles (99% confidence level) (**Fig. 4.2B**). Additionally, higher-frequency variability within obliquity and precession bands is thoroughly represented in section S1, while in sections S3 and S2, their representation is not constant (**Fig. 4.2C and D**). It is crucial to highlight that no orbital tuning was conducted at this stage, underscoring the significant influence of orbitally induced climate modulation on this dataset.

In the stratigraphic domain, the equivalent long eccentricity cycles for intervals S3 and S2, and the short eccentricity cycle for interval S1, were isolated using Gaussian bandpass filtering. For intervals S3 and S2, the long eccentricity cycle corresponds to wavelengths of

approximately 53.5 and 23.4 cycles/m, respectively. In interval S1, the short eccentricity cycle is associated with a frequency of about 47.68 cycles/m (**Figs. 4.2E-G**). The minimal tuning approach aligned each minimum in the filtered wavelengths with the corresponding orbital cycle within the periods indicated by the biostratigraphic data (**Figs. 4.3 – 4.5**). For intervals S3 and S2, the orbital solution suggests the presence of seven and 35 minima in the 405-kyr band, while seven and 31 sedimentary cycles are likely associated with the 405-kyr band, respectively (**Figs. 4.4 and 4.5**). We interpret that no missing beats occur in interval S3, while approximately 1.2 Ma may be absent in interval S2. For interval S1, the orbital solution indicates the existence of 49 minima in the ~ 95-kyr eccentricity band, while 46 sedimentary cycles are correlated. The caveats listed in section 3.2, plus the existence of hiatuses, as outlined in Figueiredo et al. (2009) and Hoorn et al. (2017), result in final astronomical age models with root mean square error constrained between 24.9 – 22.0 ± 0.003 Ma, 17.6 – 5.1 ± 2.0 Ma and 4.81 – 0.42 ± 0.65 Ma for sections S3, S2 and S1, respectively (**Figs. 4.3 –4. 5; Supplementary Figure 4.1**).

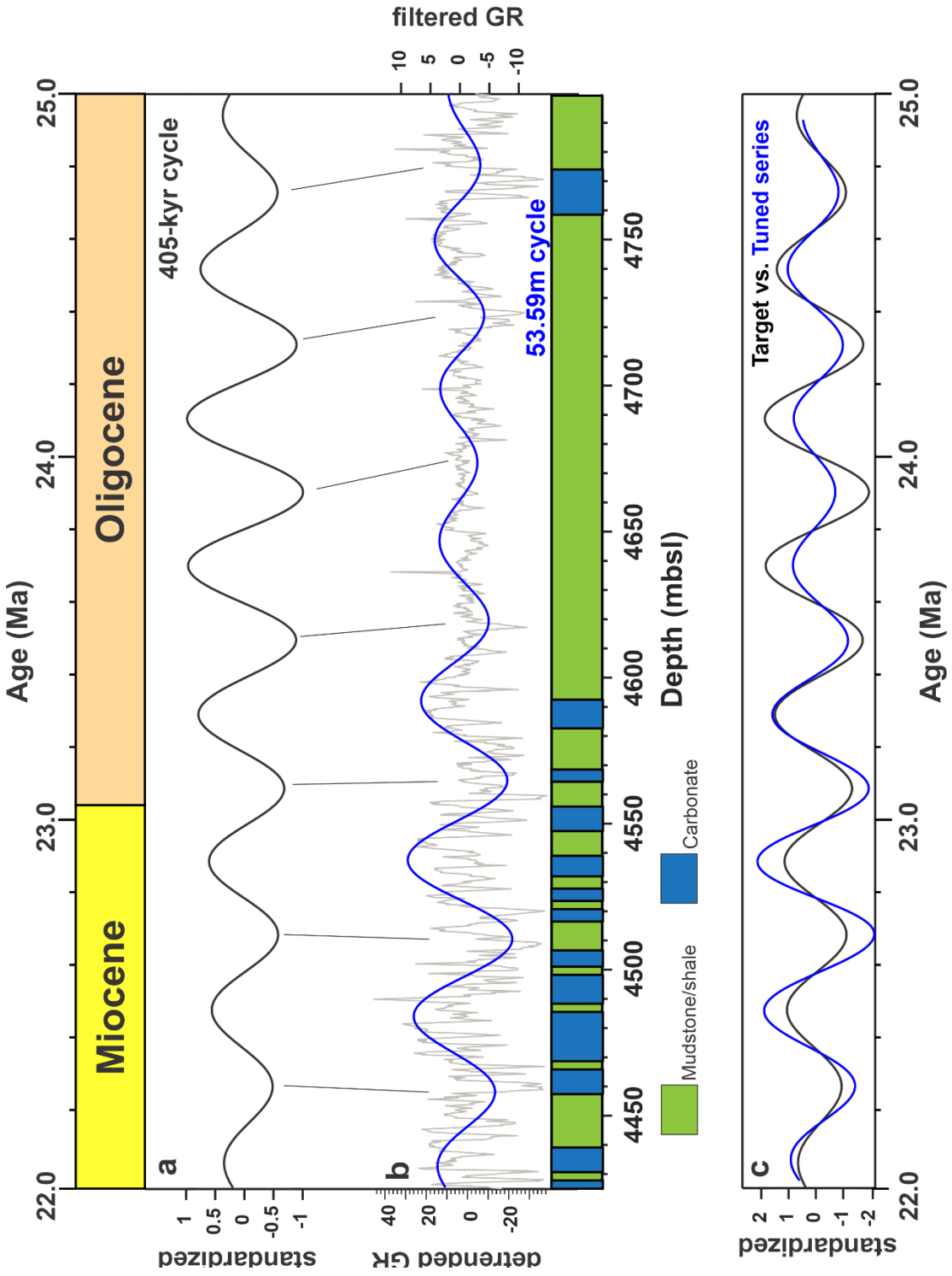

Figure 4.3. Astronomical tuning for interval S3 of BP3 well. (a) Representation of the 405-kyr long eccentricity cycle (Laskar et al., 2004). (b) LOWESS-detrended gamma ray (GR) data from BP3 well (light grey) together with the Gaussian bandpass filter applied to GR data (blue), with cutoff frequencies of 0.0149 – 0.0224 cycles/m, in the stratigraphic domain. Thin black lines indicate the alignment of each eccentricity minimum in filtered GR data. (c) Target 405-kyr cycle (black) compared with filtered GR data (black) in the time domain.

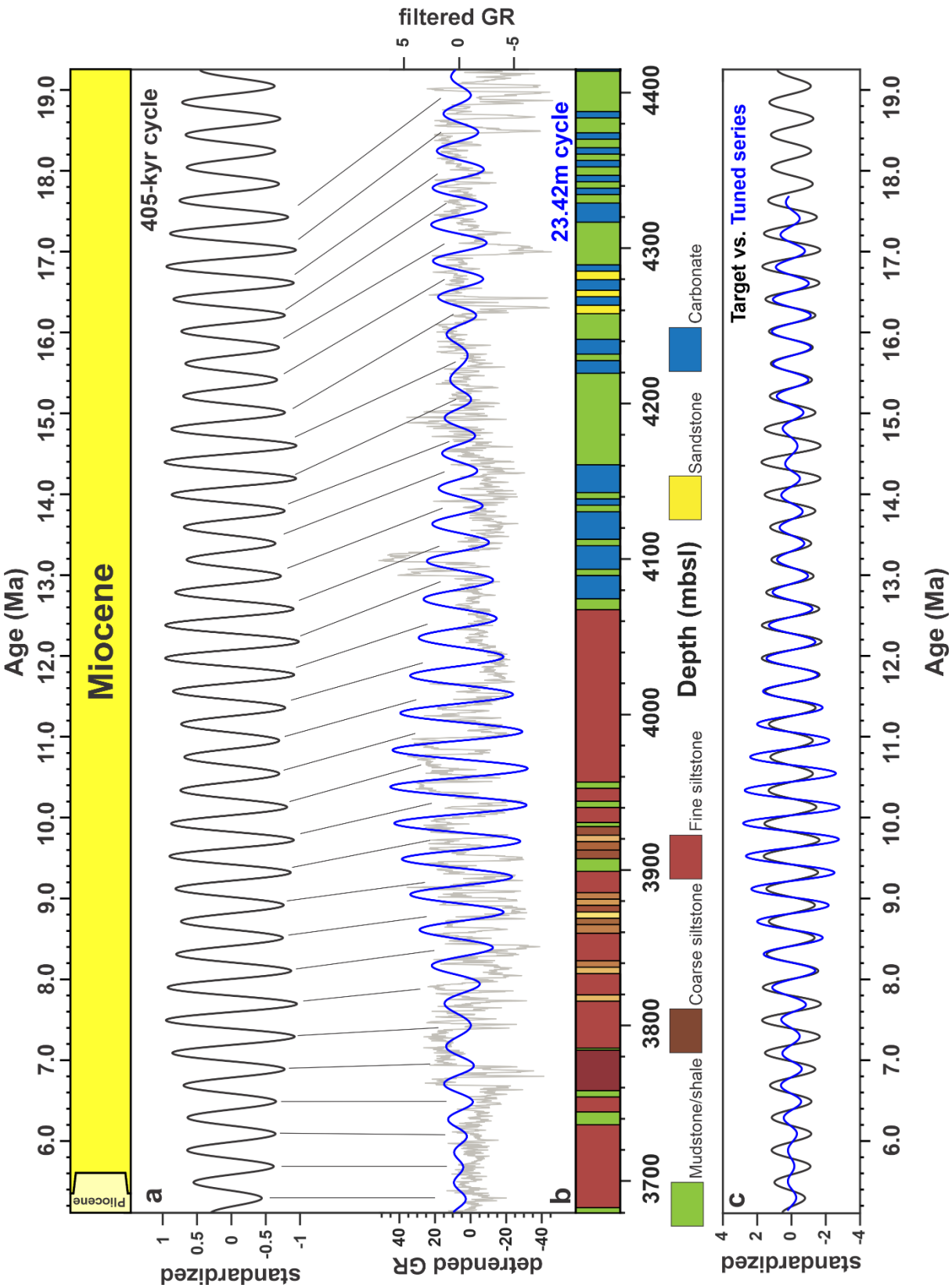

Figure 4.4. Astronomical tuning for interval S2 of BP3 well. (a) Representation of the 405-kyr long eccentricity cycle (Laskar et al., 2004). **(b)** LOWESS-detrended gamma ray (GR) data from BP3 well (light grey) together with the Gaussian bandpass filter applied to GR data (blue), with cutoff frequencies of 0.03869 – 0.04669 cycles/m, in the stratigraphic domain. Thin black lines indicate the alignment of each eccentricity minimum within the filtered GR data. **(c)** The target 405-kyr cycle (black) compared with the filtered GR data (black) in the time domain.

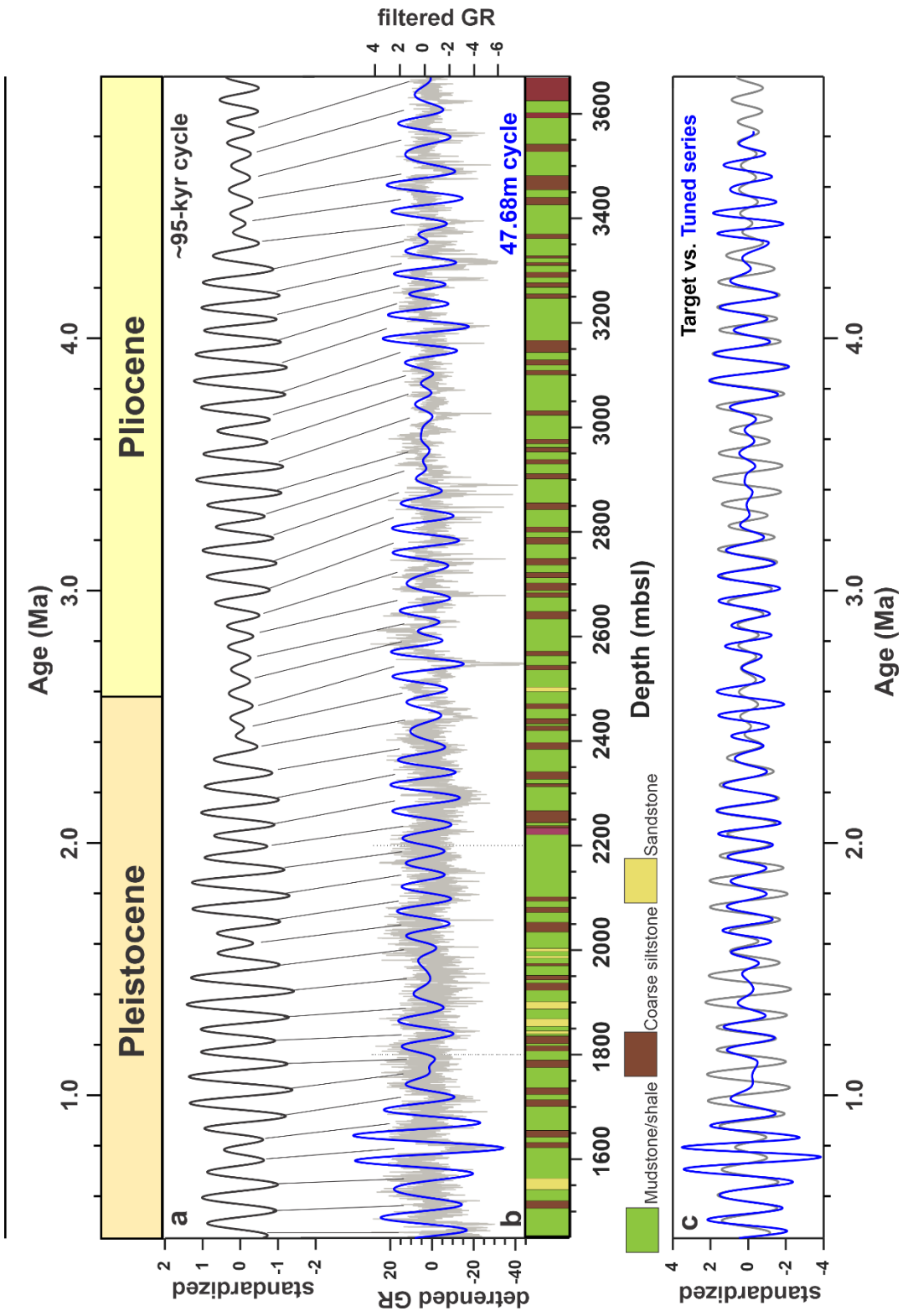

Figure 4.5. Astronomical tuning for interval S1 of the BP3 well. (a) Representation of the ~95-kyr short eccentricity cycle (Laskar et al., 2004). **(b)** LOWESS-detrended gamma ray (GR) data from the BP3 well (light grey) alongside the Gaussian bandpass filter applied to the GR data (blue), with cutoff frequencies of 0.01697 – 0.02497 cycles/m, in the stratigraphic domain. Thin black lines indicate the alignment of each eccentricity minimum within the filtered GR data. **(c)** The target ~95-kyr cycle (black) compared with the filtered GR data (black) in the time domain.

4.5. Discussion

4.5.1. Orbital Pacing and Global Mean Sea Level in the Amazon Fan

The Neogene history of sediment deposition in the Amazon Fan is highly complex, driven by the interaction between Andean orogeny, dynamic topography, climate variability, and sea-level fluctuations (Hoorn et al., 1995). The interplay of these processes is believed to have facilitated the formation of diverse environments, ranging from shallow marine conditions to extensive fluvio-lacustrine mega-lakes in the western Amazon during the early- to mid-Miocene (Boonstra et al., 2015; Jaramillo et al., 2017; Leandro et al., 2022). Over time, these geological and climatic factors contributed to the development of the transcontinental Amazon River and played a crucial role in shaping the remarkable biodiversity of the Amazon Basin (Sawakuchi et al., 2022).

A numerical model developed to investigate the formation of the Amazon River, incorporating tectonic activities, climate variations, and global mean sea level (GMSL) changes, indicates that sea level played a critical role in controlling intermittent marine incursions in the western Amazon (Sacek et al., 2023). Additionally, in coastal regions, periods of sea level drop were generally associated with increased sedimentation rates (Sacek et al., 2023). Furthermore, the application of detrital zircon geochronology indicates that sea-level fluctuations played a critical role in controlling sediment sources in the Amazon Fan in the Pleistocene (Mason et al., 2019). During warm interglacial periods, sea-level highstands promoted a greater influx of craton-derived sediments. In contrast, glacial intervals were marked by shelf incision, base-level lowering, and enhanced connectivity between terrestrial, shelf, and deep-sea environments. These conditions facilitated the downslope transport of Andean-sourced zircons (Mason et al., 2019). Gamma ray (GR) data from sedimentary records spanning the continental shelf to the upper slope further reflect the impact of sea-level oscillations (Li et al., 2018; Tortarolo, 2023). Transgressive phases and sea-level highstands typically coincide with increased deposition of fine-grained pelagic sediments, terrigenous clay minerals, and organic matter—resulting in elevated GR values (Wagreich and Koukal, 2020). In

contrast, regressive phases and sea-level lowstands are associated with the preferential accumulation of coarser siliciclastic and carbonate sediments, reflected by lower GR values.

Figure 4.6 compares the GR data for the BP-3 well, aligned with the developed astronomical timescale, to the GMSL of Miller et al. (2020). A general agreement is observed between the long-term trends in GR and GMSL, both during periods above and below present-day sea level. Notable correlations are evident in intervals S3 and S1 (**Figs. 4.6A and C**), while in interval S2, the relationship is stronger during the near ice-free conditions of the Miocene Climatic Optimum. In the mid-Miocene, the GMSL declines in two distinct steps, although this pattern is not precisely mirrored in the GR data. However, during the late Miocene, both proxies exhibit a similar upward trend toward the Pliocene (**Fig. 4.6B**). The Plio-Pleistocene is characterized by a gradual GR increase in the BP-3 well from ~4.7 to 2.6 Ma, aligning with periods of high sea level during the Pliocene Climatic Optimum. Subsequently, both proxies display a gradual decline throughout the Pleistocene. The mechanism unifying GR and GMSL is likely the dynamic interplay between the growth and decay of continental-scale glaciations, which began in Antarctica during the early Oligocene and was later intensified by Northern Hemisphere glaciation (Miller et al., 2020). Eustatic sea-level fluctuations driven by ice volume changes ultimately influence depositional dynamics and the nature of sediments in deltaic, upper slope, and deep-sea fan environments, all affecting the GR signal.

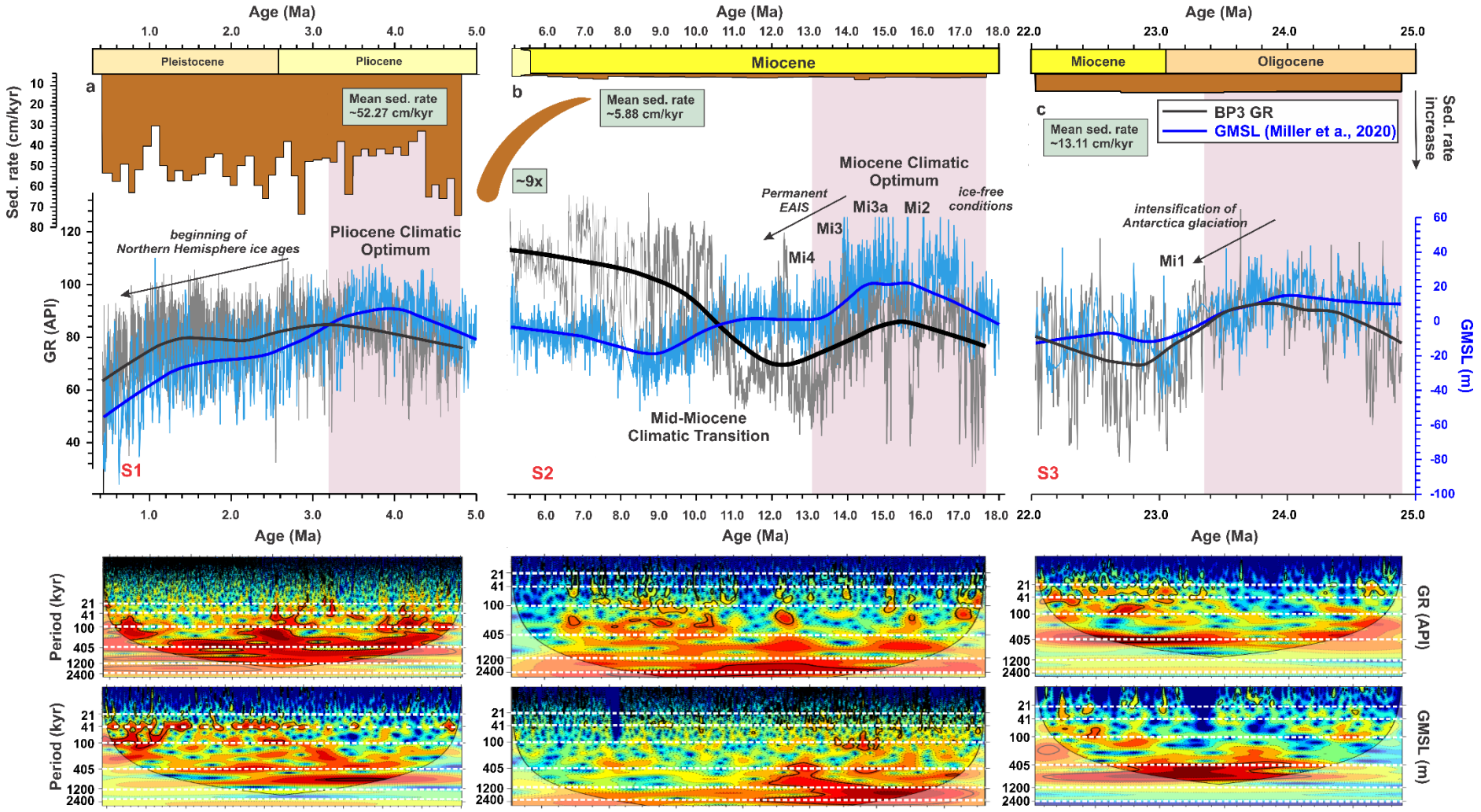
Age (Ma)
Pleistocene
Pliocene
Miocene
Oligocene
a
b
c
Mean sed. rate ~52.27 cm/kyr
Mean sed. rate ~5.88 cm/kyr
Mean sed. rate ~13.11 cm/kyr
~9x
Sed. rate (cm/kyr)
Sed. rate increase
BP3 GR
GMSL (Miller et a., 2020)
GR (API)
GMSL (m)
beginning of Northern Hemisphere ice ages
Pliocene Climatic Optimum
Miocene Climatic Optimum
Permanent EAIS
ice-free conditions
Mi4
Mi3
Mi3a
Mi2
Mi1
intensification of Antarctica glaciation
Mid-Miocene Climatic Transition
S1
S2
S3
Period (kyr)
21
41
100
405
1200
2400

Figure 4.6. Estimated sedimentation rates derived from the astronomical age model, and comparison of gamma-ray (GR) data with global mean sea level (GMSL) (Miller et al., 2020). Panels (a-c) from top to bottom: sedimentation rate (cm/kyr; shaded brown area); GR data (thin black line) with a 35% LOWESS regression (thick black line); GMSL (thin blue line) with a 35% LOWESS regression (thick blue line); and wavelet transform (Torrence and Compo, 1998) of standardized GR data. Dashed white lines denote the positions of obliquity (1.2-Myr) and eccentricity (2.4-Myr) amplitude modulations, long eccentricity (405-kyr), short eccentricity (~100-kyr), obliquity (41-kyr), and precession (21-kyr).

The waxing and waning of ice sheets since the late Oligocene exhibit strong orbital pacing, with GMSL responding to 21-kyr precession, 41-kyr obliquity, ~100-kyr, and 405-kyr eccentricity cycles, along with amplitude modulation of obliquity and eccentricity at ~1.2- and ~2.4-Myr rhythms, respectively (Boulila et al., 2011; Miller et al., 2020; Pälike et al., 2006). A wavelet transform analysis (Torrence and Compo, 1998) of the GR data reveals that deposition in the Amazon Fan also preserves a wide range of Milankovitch frequencies (**Fig. 4.6**). During the sea-level fall associated with the Mi1 event at the Oligo-Miocene transition (~23 Ma), spectral power in the 405-kyr band is prominent in both GR and GMSL records. Benthic $\delta^{18}O$ and $\delta^{13}C$ records from the western equatorial Atlantic (ODP Site 926 – Ceará Rise) indicate an increase in the 405-kyr cycle amplitude across the Mi1 event, suggesting a pivotal shift in the global climate system driven by positive feedback mechanisms on the global carbon cycle (Zachos, 2001). In the early Miocene, the GMSL lowstand is further marked by strong spectral power in the 21-kyr precession and 41-kyr obliquity bands in the BP-3 data (**Fig. 4.6C**). Additionally, a longer temporal variability at Myr-scale (~1.2/2.4-Myr cycle) is evident in interval S2 (early to mid-Miocene), agreeing with GMSL (**Fig. 4.6B**). Continental margin deposition may act as a low-pass filter, amplifying Myr-scale variability and aliasing higher-frequency signals, particularly under low sedimentation rates (<6 cm/kyr) (Miller et al., 2020). Like the early Miocene, higher frequencies in the 41-kyr and ~100-kyr bands are also observed in the GR data, corresponding with the series of GMSL falls (Mi2–Mi4) marking the end of the Miocene Climatic Optimum (**Fig. 4.6B**).

The GMSL record exhibits a weak expression of the 405-kyr cycle during the Plio-Pleistocene interval, and the underlying cause remains uncertain (Miller et al., 2020). Conversely, the 405-kyr cycle is clearly preserved in the GR data (**Fig. 4.6A**). Coupled simulations of global ice volume over the past 5 million years suggest that the 405-kyr modulation is present in Plio-Pleistocene ice volume variability but becomes obscured due to

the dominant influence of Northern Hemisphere ice sheets linked to the 41- and ~100-kyr cycles since 2.9 Ma (De Boer et al., 2014). Cosmogenic radionuclide data from the southern Andes provide direct evidence of a 405-kyr cyclic control over erosion rates (Fisher et al., 2023). This may reflect a direct influence of the long eccentricity cycle on moisture transport from the Atlantic or, more likely, an indirect effect through amplitude modulation of the 21-kyr precession. Such mechanisms could explain the consistent expression of the 405-kyr cycle in the GR data, as tropical hydroclimate is notably sensitive to seasonal insolation changes, particularly within the precession band (e.g., Cheng et al., 2013; Marzocchi et al., 2015). The nonlinear interaction of orbitally driven climatic factors, such as continental precipitation, with GMSL variability may account for the observed discrepancies between the GR data and GMSL at this point.

Furthermore, geochemical and environmental magnetic proxy records on the northwest Australian shelf show strong modulation of the monsoon dynamics by the 405-kyr cycle between 2.9 and 1.6 Ma, providing direct support for the preservation of this cycle in certain Quaternary sedimentary records (Zhao et al., 2024). Thus, the persistence of the 405-kyr cycle within the last ~ 4.8 Ma section of BP-3 is consistent with other records. The last ~1.3 Myr period also displays an enhanced expression of the ~100-kyr cycle, which will be examined in detail in the subsequent section (**Fig. 4.6B**). Detecting multiple astronomical signals in the BP-3 GR spectrograms ultimately validates our minimal tuning approach and suggests no inherent bias toward the selected target frequency for each interval (**Fig. 4.6**).

4.5.2. The imprint of orbital forcing on sedimentation rates at the Amazon Fan

The novel astronomical age model for the BP-3 well also enables a reassessment of Neogene sedimentation rates in the Amazon Fan. Figueiredo et al. (2009) proposed three stages of development that led to the exceptionally high sedimentation rates observed in the most recent period: 1) before approximately 6.8 Ma, when sedimentation rates were relatively low (<5 cm/kyr); 2) between ~6.8 and 2.4 Ma when sediment discharge increased sixfold despite a general rise in GMSL; and finally, 3) from 2.4 Ma to the present, a period characterized by a

notable increase in sedimentation rates with a mean value of 122 cm/kyr, but punctually peaking at 1116 cm/kyr (Figueiredo et al., 2009). Our revised estimate for the sedimentation rate during the Plio-Pleistocene interval is more moderate, as the regular placement of tie-points by cyclostratigraphy avoids abrupt time compressions. In our model, the substantial increase in sediment discharge occurred between 5.1 – 4.8 ± 1.78 Ma (**Fig. 4.6A and B and Supplementary figure 1**), slightly later than Figueiredo et al. (2009) suggested, but still consistent when considering the full uncertainty range. Paleogeographic reconstructions based on 2D and 3D seismic data (Rouby et al., 2023) show that the BP-3 site remained within the main depocenter of the Brazilian Equatorial Margin throughout the 23-0 Ma interval. Thus, the marked increase in sedimentation rates after ~5 Ma is best interpreted as reflecting an overall increase in sediment supply to the Amazon Fan system, consistent with the regional signal documented by Figueiredo et al. (2009), rather than a lateral migration of fan lobes. This increased sedimentation rate is also consistent with observations of a Messinian worldwide tectonic revolution, as summarized by Leroux et al. (2017).

Notably, despite the evident influence of GMSL on the GR signal, no comparable effect on sedimentation rates is observed. In the S3 section, the calculated sedimentation rate changes are minimal (<1 cm/kyr). The transition from S3 to S2 is marked by a two-fold decrease in sedimentation rates, and although S2 exhibits more significant fluctuations (~2 cm/kyr), these variations are unlikely to be attributed to the ~30 m GMSL drop from the late Oligocene to the late Miocene (**Figs. 4.6B and C**). The early Pliocene in section S1 is a critical period for this evaluation. When approaching the Pliocene Climatic Optimum, the sea level was approximately 20 m above the present, and, despite this, the Amazon Fan experienced significant sediment discharge of ~50 cm/kyr. This suggests that the sea-level highstand of the early Pliocene did not impede substantial sediment transport to the Atlantic Ocean.

This persistently low sedimentation rate in the Amazon Fan until approximately 5 Ma may be attributed to the presence of mega-wetland systems in the western Amazon Basin (Boonstra et al., 2015; Hoorn et al., 2022a). This system, known as the Pebas system, comprised a complex mosaic of swamps, lakes, and fluvial networks influenced by episodic marine incursions. Acting as a sediment trap, the Pebas system likely retained the majority of Andean and cratonic sediments within the Amazon Basin. While the Pebas System is considered to have existed no later than ~13 Ma (Hoorn et al., 2022a; Jaramillo et al., 2017),

other findings suggest that a connection between western Amazonia and the Caribbean region may have persisted longer (Aguilera et al., 2013; Espinosa et al., 2021). Minor marine influences have been identified in the early Pliocene (~4.7, 4.2–4.1, and 3.8 Ma) (Leandro et al., 2022), potentially contributing to the observed low sedimentation rates during this time. If such marine incursions impacted sediment discharge to the Amazon Fan, they might explain why sedimentation rates remained low until the early Pliocene. However, it should be noted that this scenario of prolonged marine incursions in western Amazonia is not supported in all models (Sacek et al., 2023). Applying our astronomical age model in conjunction with previously published neodymium (Nd) isotopic data from the same well (Hoorn et al., 2017), we observe the influx of Andean-derived sediment as early as 12.2 ± 1.3 Ma. This transition is marked by an abrupt shift in εNd values from highly negative (-18.8 ± 1.7, n = 9) to more radiogenic signatures (-10.7 ± 1.8, n = 15), reflecting the increased contribution of juvenile material sourced from Andean volcano-sedimentary Cenozoic deposits. This finding indicates that while sediment traps such as the Pebas System significantly delayed sediment export, they did not entirely hinder the onset of transcontinental drainage and sediment delivery to the deep sea during the Late Miocene.

If GMSL decline was not the primary driver of the massive sediment discharge starting in the early Pliocene, another mechanism must have been at play. Geochemical proxies indicate that the northern Altiplano experienced rapid uplift between 9.1 and 5.4 Ma, likely reaching its modern elevation during this period (Kar et al., 2016). This surface uplift facilitated the organization and intensification of the South American Low-Level Jet, leading to substantial (>400%) increases in precipitation across the central Altiplano. This increase was due to convective activity triggered by latent heat release as air masses converged on the plateau (Poulsen et al., 2010). Fossil flora evidence suggests that precipitation in the central Altiplano was nearly three times higher than current levels during the mid-Miocene, with these wet conditions persisting into the early Pliocene (Martínez et al., 2020). Additionally, pollen records from equatorial South America indicate continuously wet conditions during the early Pliocene, supporting the idea of a southward displacement of the Intertropical Convergence Zone, which would have transported moisture from the Atlantic across Amazonia (Grimmer et al., 2018). This increase in humidity from the mid-Miocene onward likely intensified the denudation rates of Andean rocks due to enhanced precipitation (Sacek et al., 2023). In addition, the Pliocene

uplift of the Fitzcarrald Arch (Espurt et al., 2007), a positive topographic area that covers 400,000 km^2 of the Peruvian-Brazilian retroarc basins (Regard et al., 2009), may have been an additional trigger in favoring erosion of the Amazonian retroarc foreland basin sediments and in reducing the accommodation space in the Amazon retroarc foreland basins. Therefore, we propose that the resulting sediments were initially retained within wetland systems in western Amazonia, acting as efficient sediment traps. With the disappearance of these barriers during the early Pliocene, sediments produced by these processes found an unrestricted pathway to the Atlantic Ocean. This sediment flush was so substantial that it exceeded the influence of high GMSL during the early Pliocene.

To summarize, the spectral analysis of BP-3 GR data reveals a comprehensive archive of orbital-induced climate variability influencing sedimentation at the Amazon Fan and, consequently, the stacking of sedimentary units from Amazon River-derived material. The developed astronomical timescale enables a detailed comparison between Amazon Fan dynamics and GMSL over the past ~24 million years, facilitating the identification of the factors that led to an exceptional sedimentation rate in this region.

4.5.3. The Quaternary Ice Ages and the mid-Pleistocene Transition

The middle portion of section S1, corresponding to the last ~3.5 Myr (upper ~3000 mbsl), is marked by a shift to a high-frequency variability in GR data. This shift is unrelated to the astronomical tuning, as observed in the stratigraphic domain (**Figs. 4.1 and 4.2**). Globally, the late Pliocene to early Pleistocene transition is characterized by a fundamental shift in Earth's climate, as inferred from benthic foraminifera δ18O marine records (Lisiecki and Raymo, 2005; Westerhold et al., 2020). During this period, the oxygen isotopic composition of the global oceans became progressively heavier, indicating an expansion in global ice volume with a concomitant sea-level decrease and a reduction in global temperature (Shackleton, 1987). The amplitude of benthic δ18O variability also gradually increased, leading to the series of ice ages that punctuated the Quaternary period. These changes significantly impacted GMSL, with amplitude variability reaching approximately 120 meters during more recent glacial intervals (Miller et al., 2020).

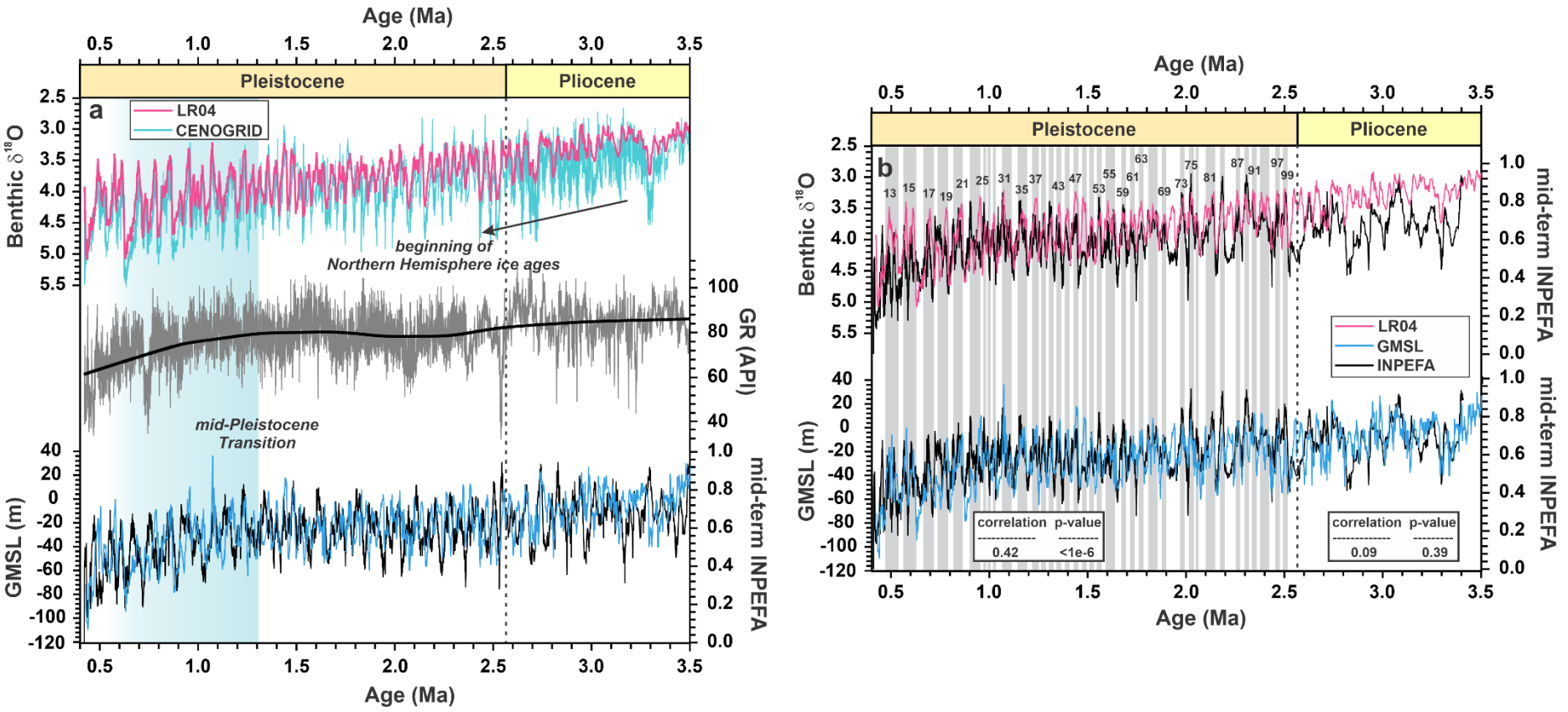

Figure 4.7. Comparison of gamma ray (GR) data and the mid-term Integrated Prediction Error Filter Analysis (INPEFA) results for the upper ~3600 mbsl of the BP3 well. **(a)** from top to bottom: reference benthic oxygen isotope ($\delta^{18}O$) records from CENOGRID (light blue line) (Westerhold et al., 2020) and LR04 (pink line) **(Lisiecki and Raymo, 2005b)**; GR data (thin black line) with a 35% LOWESS regression (thick black line); GMSL (blue line) (Miller et al., 2020) and mid-term INPEFA signal summed with the 35% LOWESS regression used for GR data. **(b)** same as **(a)**, but the mid-term INPEFA signal is plotted using the probabilistic age model developed with BIGMACS (Lee et al., 2023). Vertical grey bars highlight interglacial periods, and numbers indicate selected Marine Isotope Stages between ~ 0.5 – 2.58 Ma.

To further quantify the linkages between global climate change and Amazon Fan dynamics, we applied INPEFA over the upper ~ 3000 m. The inflection points of the INPEFA curves indicate significant shifts in depositional regimes, likely influenced by GMSL and climate change (Djin Nio et al., 2005). INPEFA outputs successfully identified the depositional changes associated with GMSL in the Espírito Santo basin (western South Atlantic) from the late Paleocene to the early Miocene (Santos et al., 2023). When aligned to the developed astronomical model for section S1 and compared with the GMSL, we found a striking visual association, mainly from the Pleistocene onset at 2.58 Ma (**Fig. 4.7A**). The sequence of peaks in the mid-term INPEFA nearly corresponds to elevated GMSL (and lower benthic foraminifera δ18O) constrained during the brief Pleistocene interglacials.

Interestingly, the distribution of spectral content in mid-term INPEFA exhibits strong power, mainly at the obliquity band during the early to mid-Pleistocene (**Fig. 4.8**). From ~1.3 – 1.2 Ma, there is a clear increment in the ~100-kyr frequency that prevailed until the uppermost part of the record. These features are consistent with the glacial-interglacial variability observed in benthic foraminiferal δ18O records, which shifts from obliquity- to eccentricity-dominated signal at ~1.3 – 1.2 Ma (**Fig. 4.8**). This transition is known as the mid-Pleistocene Transition and is characterized by an increased resilience of northern hemisphere ice caps, making ice ages spent longer (Berends et al., 2021; Clark and Pollard, 1998) (**Fig. 4.7A**). Why Earth's climate responded so strongly to a weak forcing in eccentricity at that time still remains fiercely debated in the literature (e.g., Barker et al., 2022). However, identifying these Pleistocene climate shifts in our GR series tuned to ~100-kyr eccentricity demonstrates that the same climate variability was recorded in the Amazon Fan sedimentary system.

To further explore the apparent coupling between mid-term INPEFA and both GMSL and benthic foraminiferal δ18O records, we applied a probabilistic tuning approach for the upper part of the S1 section, aligning our data directly with the benthic foraminifera LR04 reference (Lisiecki and Raymo, 2005) using the routine of BIGMACS software (Lee et al., 2023). In our case, BIGMACS facilitated a probabilistic stratigraphic alignment of benthic δ18O with mid-term INPEFA. The resulting age model was slightly compressed (~0.42 – 3.40 Ma) relative to that generated by minimal tuning with the ~100-kyr cycle (~0.42 – 3.50 Ma) but with an order of magnitude lower uncertainty, ranging ± 0.01 – 0.025 Ma (**Supplementary Figure 2**).

Interestingly, the association between mid-term INPEFA and GMSL was notably robust, with a clear imprint of Marine Isotope Stages (MIS) in the variability of the well-log data (**Fig. 4.7B**). This is not easily found, but when available, it supports building accurate high-resolution age models (e.g., Dearing Crampton-Flood et al., 2020; Zhang et al., 2019).

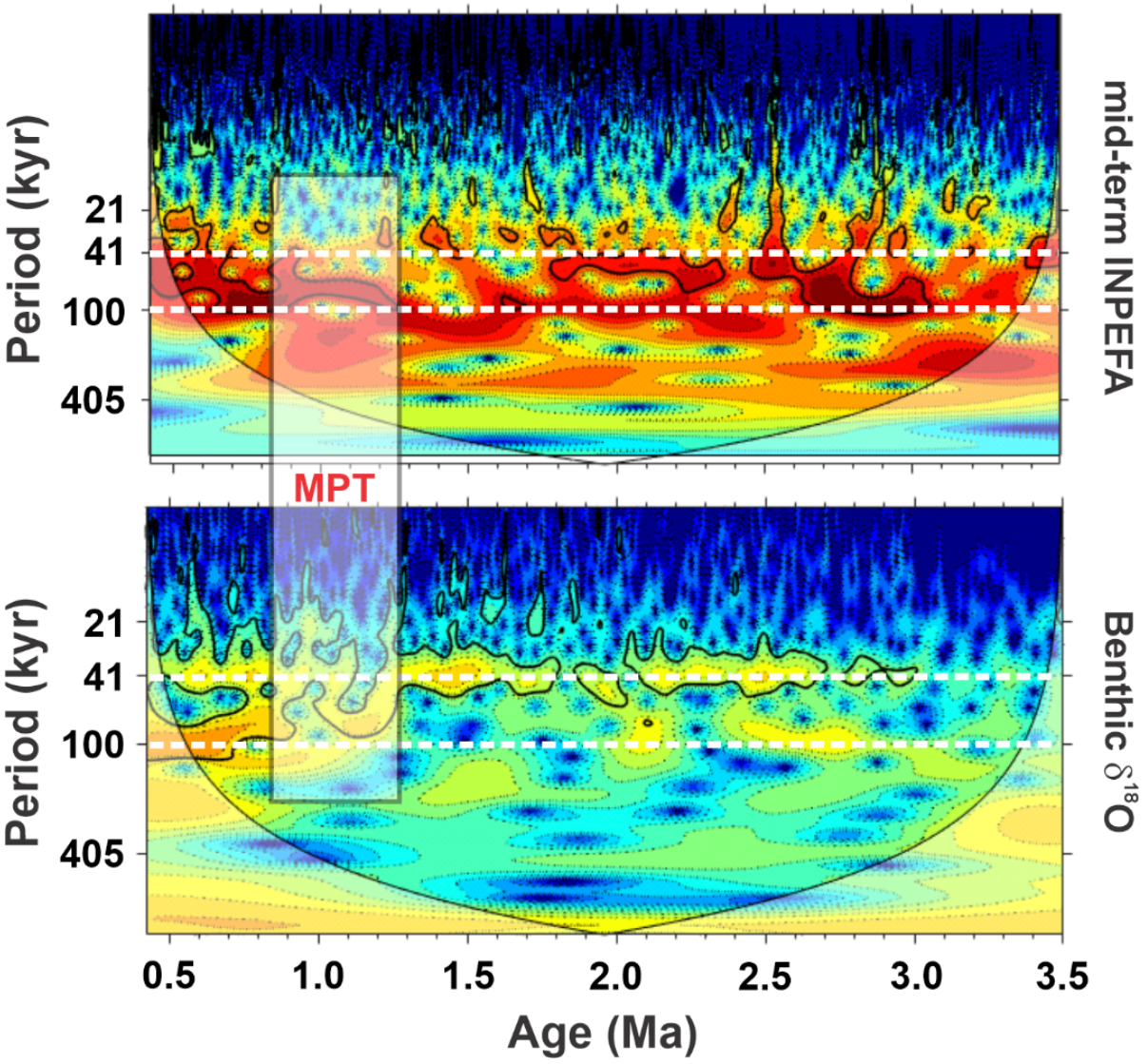

Figure 4.8. Wavelet transform of the standardized mid-term Integrated Prediction Error Filter (INPEFA) applied to BP3 gamma ray (GR) data in the time domain for the upper part of the S3 section (upper panel) and the benthic foraminifera oxygen isotope record ($\delta^{18}O$) from the LR04 reference stack (lower panel) (Lisiecki and Raymo, 2005b). The white rectangle highlights the interval associated with the mid-Pleistocene Transition (MPT). Dashed white lines indicate the spectral bands corresponding to 41-kyr and ~100-kyr orbital cycles.

In the late Pliocene (~ 2.6 – 3.5 Ma), visual alignment between INPEFA and GMSL remains consistent. However, the isospectral correlation test indicates a lack of statistical significance in this portion ($R = 0.09$, $p = 0.39$), likely due to the software's limited capacity to match finer-scale variability between GMSL and mid-term INPEFA. A marked shift occurs at 2.6 Ma, where INPEFA cyclicity aligns closely with individual MIS, with peaks (lows) in INPEFA matching interglacial (glacial) periods characterized by higher (lower) sea levels and lower (higher) benthic δ18O values (**Fig. 4.7B**). Exceptions to this alignment are solely observed during MIS 101, 85, and 71. We argue that the identification of nearly all MIS between ~2.5 and 0.5 Ma provides strong evidence that the upper ~3000 mbsl of BP-3 constitutes an essentially complete stratigraphic section, rendering the hiatus inferred from the partial absence of biozone NN19 more unlikely (Hoorn et al., 2017). A similar interpretation may be extended to the lower hiatus associated with the partial absence of biozone NN16. However, this inference should be approached carefully, as this lower interval was not examined with the same set of analytical tools. Ultimately, this fourth to fifth-order stratigraphic analysis reveals that the BP-3 site holds a continuous sediment record spanning the last ~3.0 Myr, making it a compelling target for scientific coring to investigate Plio-Pleistocene variability in the Amazon River system. The statistically significant correlation ($R = 0.42$, $p < 0.05$) between mid-term INPEFA and GMSL underscores the Amazon Fan's high sensitivity to the onset of early Pleistocene glaciations. This sensitivity initially structured sedimentary architecture in response to the 41-kyr glacial-interglacial cycles and later to the 100-kyr cycles (**Figs. 4.7 and 4.8**).

4.6. Conclusions

This study underscores the interplay between orbital forcing, sea-level changes, and regional geodynamic events in controlling sediment deposition in the Amazon Fan. Our reassessment of the GR data for the BP-3 well reveals a strong imprint of Milankovitch cycles over the last 24 million years, emphasizing the fan's sensitivity to orbital climate variability. Our new astronomically tuned age model refined prior chronologies, enabling robust correlations between sedimentary cycles and GMSL. We show that low sedimentation rates prevailed during the Miocene, at a time when the combination of active Andean tectonics, uplift of the Fitzcarrald Arch, and enhanced regional precipitation in the Amazon Basin was most likely

associated with high erosion rates. This discrepancy is best interpreted as reflecting efficient sediment trapping by mega-lake systems in western Amazonia. The subsequent drastic increase in sediment discharge to the Atlantic starting from the Early Pliocene indicates a major drainage reorganization across the Amazon Basin at that time, most likely caused by the breach of the Purus Arch, leading to enhanced sediment export to the Atlantic Ocean. Finally, in the Plio-Pleistocene, the GR record captures a major sensitivity of the fan to the GMSL changes imposed by the glacial-interglacial variability seen through the expression of isotopic stages. In this sense, the glaciation of the northern hemisphere has become a major force in fan sedimentary architecture. The shift from obliquity- to eccentricity-dominated glacial-interglacial cycles characterizing the mid-Pleistocene Transition (~1.3 Ma) further highlights the Amazon Fan's responsiveness to global climatic shifts. These findings provide a new framework for future high-resolution proxy investigations of the detailed evolution of the Amazon Basin during the Neogene and its link to global climate

Acknowledgments

This research had financial support from the Coordination for the Improvement of Higher Personnel – Brazil (CAPES) – Finance Code 001, the Agence Nationale de Recherche ECLIP-SED project (ANR-20-CE01-0003), and the CAPES-COFECUB program through their funding of actions 32/2022 and Te 1003/23 (project numbers 8881.712022/2022-1 and 49558SM). TPS also thanks the Programa de Apoio a Novos Docentes (process 22.1.09345.01.2) of the University of São Paulo. We acknowledge the Brazilian Oil and Gas Agency (ANP) for giving access to the BP-3 well data (SAA 48610.204116/2022-88).

V

The geochemistry of the upper Amazon Fan detrital record from the BP-3 Well

Declaration/ Declaração/ Déclaration

This chapter presents a comprehensive assessment of the geochemistry of the detrital record (bulk and clay fractions) from the Amazon Fan over the past 24 million years, highlighting its significance for reconstructing continental processes. The chapter begins with a detailed presentation of the geochemical dataset, followed by a critical evaluation of potential contamination from drilling muds and their impact on mineralogical and geochemical signatures, with particular attention to the implications for the reliability of these proxies.

[PT} Este capítulo apresenta uma avaliação abrangente da geoquímica do registro detrítico (frações totais e de argilas) do Leque Amazônico ao longo dos últimos 24 milhões de anos, ressaltando sua importância para a reconstrução dos processos continentais. O capítulo inicia com uma apresentação detalhada do conjunto de dados geoquímicos, seguida por uma avaliação crítica do potencial de contaminação por fluidos de perfuração e de seus impactos nas assinaturas mineralógicas e geoquímicas, com especial atenção às implicações para a confiabilidade desses proxies.

[FR] Ce chapitre présente une évaluation complète de la géochimie de l'archive détritique (fractions totale et argileuse) de l'éventail amazonien au cours des 24 derniers millions d'années, en soulignant son importance pour la reconstitution des processus continentaux. Le chapitre commence par une présentation détaillée de l'ensemble des données géochimiques, suivie d'une évaluation critique du risque de contamination par les boues de forage et de leur impact sur les signatures minéralogiques et géochimiques, en mettant particulièrement l'accent sur les implications pour la fiabilité de ces traceurs.

5.1. Samples

The BP-3 core spans a total of 3,300 meters, and we manage to have an average sampling resolution of approximately 23 meters. This resolution varies slightly depending on sample availability, as not all depths were released by the Brazilian Petroleum Agency. **Figure 5.1** presents the sampling distribution for bulk sediment analysis, clay mineralogy, and the geochemical and isotopic characterization of clays and Fe oxides. The astronomically tuned age model established in **Chapter V** is also plotted for reference.

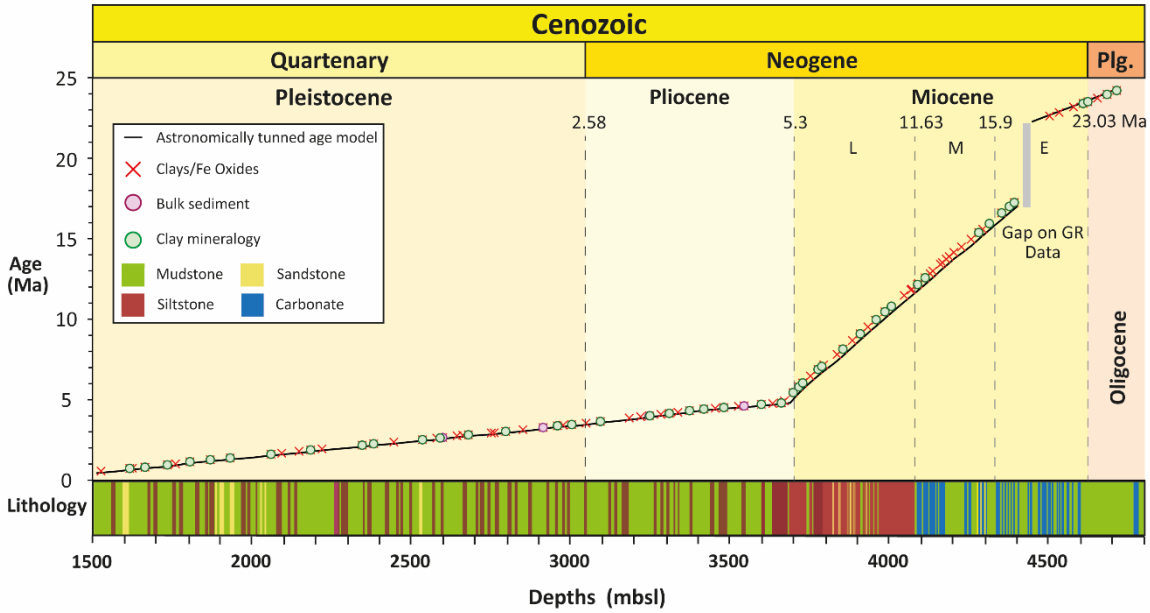

Figure 5.1. Lithostratigraphy, depth-age model, and sampling intervals for the BP-3 drill core. The lithologic column (down) shows alternating intervals of mudstone, siltstone, sandstone, and minor carbonate layers. The central panel displays the astronomically tuned age model (black line) spanning from the Pleistocene to the Oligocene, with corresponding depth (meters below sea-level, MBSL) and age (Ma) on the vertical and horizontal axes, respectively. Colored symbols denote sampling intervals for different analyses: red crosses for clays/Fe-oxide leachates, pink circles for bulk sediment, and green circles for clay mineralogy. Major chronostratigraphic boundaries are indicated, along with a data gap at ~4450 mbsl associated with missing gamma-ray records.

5.2. Results

5.2.1. Bulk Rock Geochemistry

Bulk sediments recovered from the BP-3 core span a depth interval from 1617 to 4711 meters below sea level (mbsl), corresponding to an age range of approximately 0.7 to 24.2 million years (**Fig. 5.1**). Full results are displayed in **Table S5.1** in **Appendix 5** and illustrated in **Figure 5.2**. Silica (SiO_2) ranges from 38.1 to 58.7 wt%, with the lowest values recorded in the deepest samples and a general increase upward. Alumina (Al_2O_3) fluctuates between 11.5 and 17.7 wt%, while iron oxide (Fe_2O_3) varies from 5.0 to 7.4 wt%. Manganese (MnO) concentrations remain low throughout the core, consistently close to or below 0.05 wt%. Calcium (CaO) exhibits a wide range, from 0.7 to 16.7 wt%, with peak values observed in shallow intervals, likely associated with increased carbonate content. Magnesium (MgO) concentrations span from 0.93 to 1.64 wt%, and potassium (K_2O) varies from 0.6 to 2.66 wt%, with values generally increasing upward. Sodium (Na_2O) ranges from 0.53 to 1.43 wt%, while titanium (TiO_2) remains relatively stable between 0.50 and 0.89 wt%. Phosphorus (P_2O_5) concentrations lie between 0.07 and 0.19 wt%. Finally, barium (Ba) shows extreme variability, ranging from ~8,500 to over 98,000 ppm. Compared to the Upper Continental Crust (UCC; Rudnick and Gao, 2003), Ba concentrations are exceptionally elevated, averaging over 69 times the UCC value. Al_2O_3, Fe_2O_3, and TiO_2 are close to UCC levels, and elements like MgO, K_2O, and Na_2O are moderately depleted.

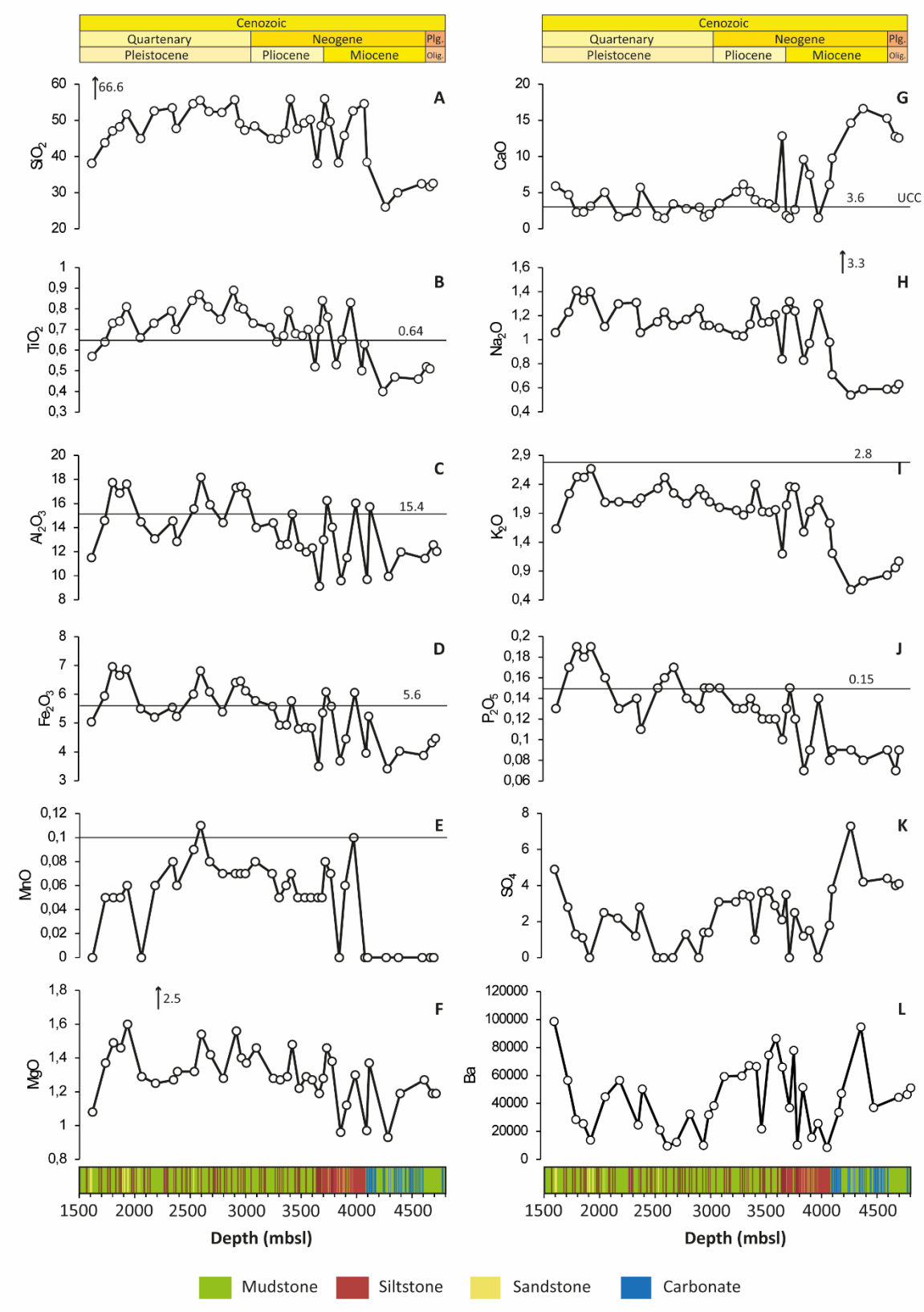

Figure 5.2. Downcore variations of XRF measurements of major element oxide concentrations (wt%) in the bulk sediment fraction of the BP-3 well. (A–L) Profiles include SiO_2 (A), TiO_2 (B), Al_2O_3 (C), Fe_2O_3 (D), MnO (E), MgO (F), CaO (G), Na_2O (H), K_2O (I), P_2O_5 (J), SO_3 (K), and Ba (L). Horizontal lines in selected panels indicate average Upper Continental Crust (UCC) values from Rudnick and Gao (2003) for reference.

5.2.2. Clay fractions

Mineralogy

The full set of diffractograms acquired from XRD analysis of the <2 μm fraction of Amazon Fan sediments is provided in **Appendix 5**. The most frequently identified clay minerals include kaolinite, illite, chlorite, clinochlore, smectite, and montmorillonite. Muscovite is also consistently detected throughout the record, and quartz is present in nearly all samples as a common detrital silicate (**Fig. 5.3A**). Sepiolite was also identified in the deepest samples (4681-4711 mbsl; **Fig. 5.3B**).

Figure 5.4 presents the relative abundances of smectite, kaolinite, chlorite, and illite. At depths between 4711 and 4621 mbsl, kaolinite and illite occur in moderate to high proportions (59–64% and 10–14%, respectively), with smectite reaching up to 22% and chlorite remaining below 10%. From 4606 to 4111 mbsl, kaolinite dominates, peaking at 89% at 4111 mbsl; smectite ranges from 0 to 27%, illite from 5 to 11%, and chlorite stays below 10%. Between 4087 and 3957 mbsl, kaolinite ranges from 26 to 43%, illite increases slightly (up to 47% at 3907 mbsl), smectite remains low (0–13%), and chlorite varies from 11 to 14%. From 3907 to 3775 mbsl, illite reaches its highest value (54% at 3907 mbsl), while kaolinite ranges from 25 to 36%, smectite from 0 to 10%, and chlorite from 11 to 15%. Between 3727 and 3597 mbsl, smectite increases (up to 26%), kaolinite varies between 25 and 43%, illite ranges from 29 to 42%, and chlorite from 12 to 22%. From 3480 to 2796 mbsl, kaolinite fluctuates between 33 and 52%, illite remains between 29 and 44%, smectite between 0 and 14%, and chlorite between 9 and 16%. In the upper section of the core (2679 to 1617 mbsl), kaolinite remains the dominant phase (30–49%), with illite between 34 and 42%, smectite from 0 to 17%, and chlorite from 9 to 19%.

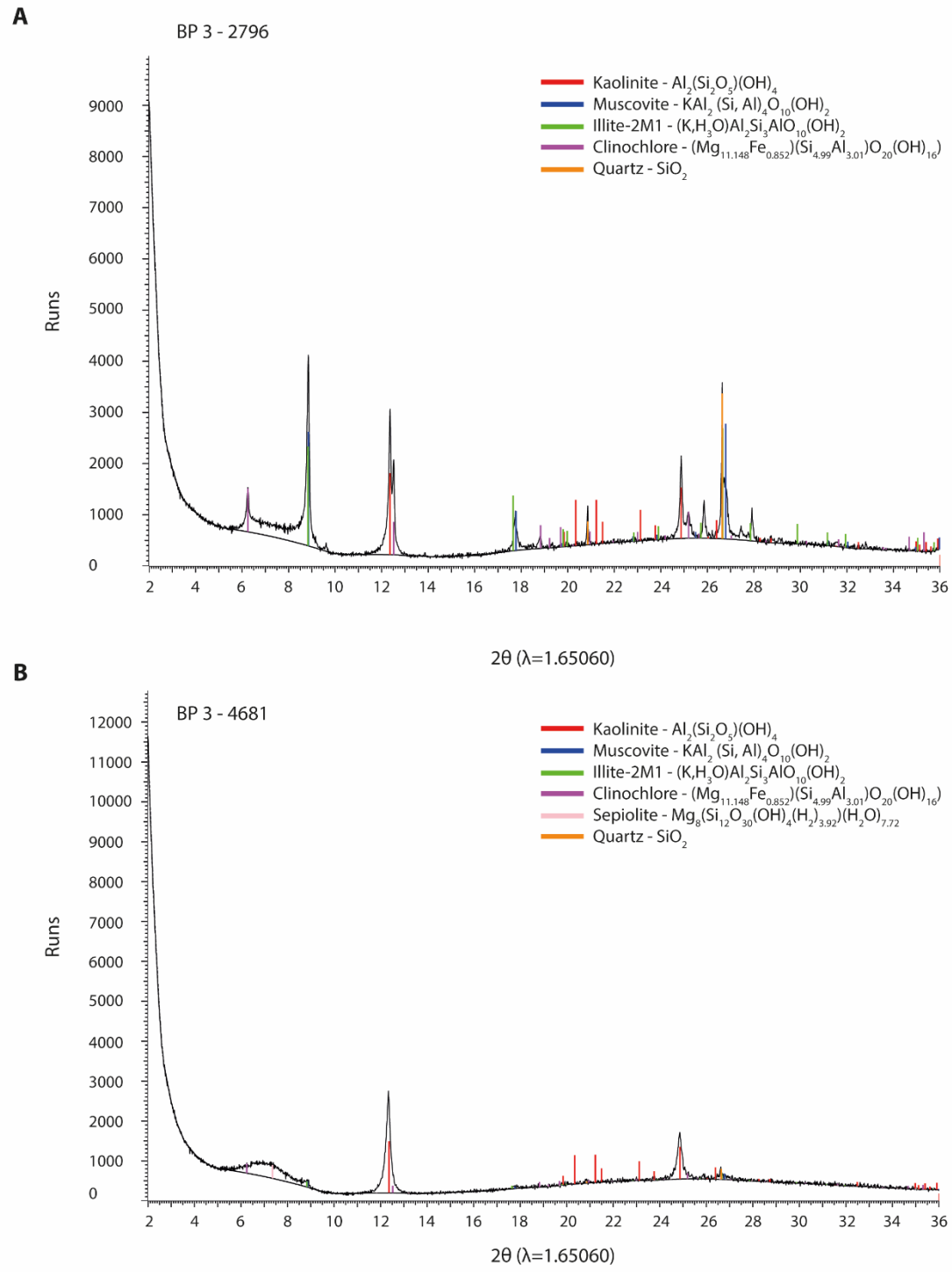

Figure 5.3. Diffractograms of the <2 µm clay fraction of representative samples from the BP-3 well. A) Most common composition of clays (B) occurrence of sepiolite

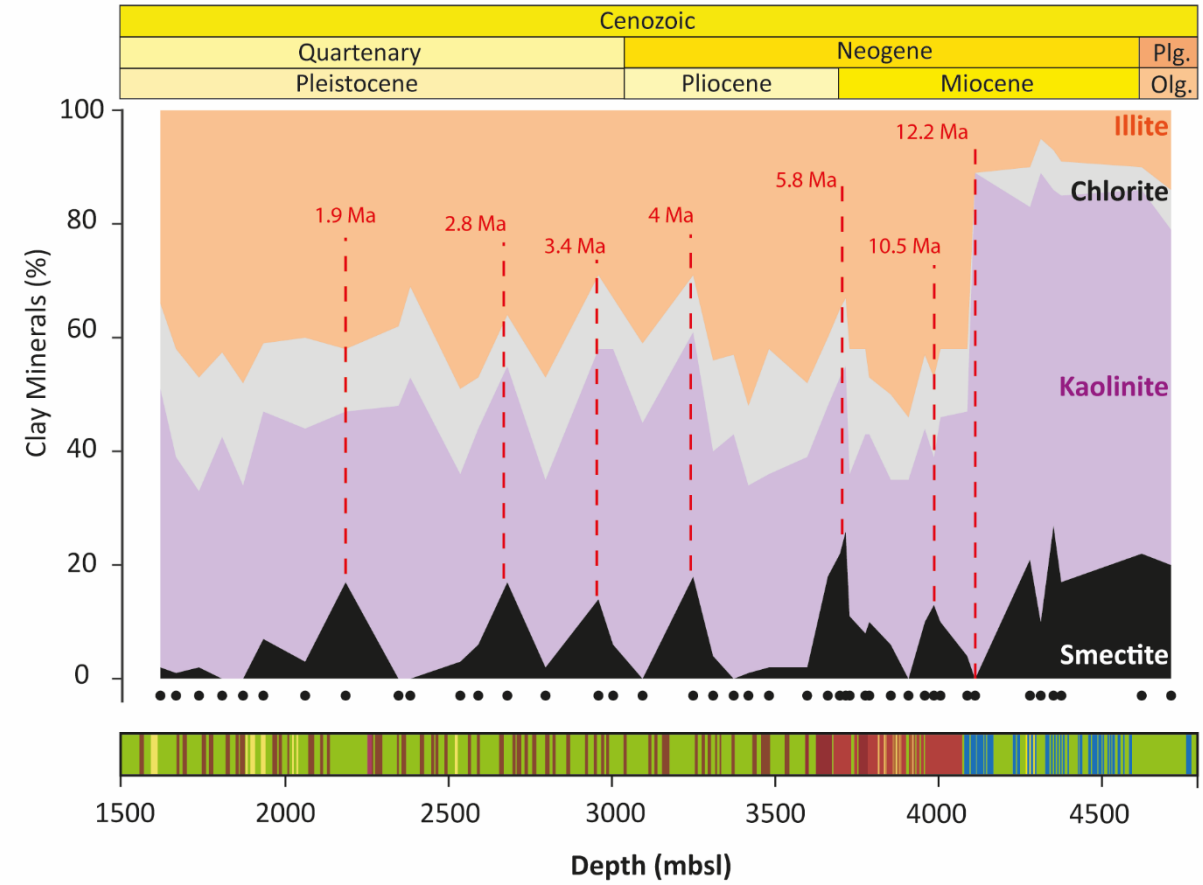

Figure 5.4. Downcore distribution of clay mineral assemblages (%) in the <2µm fraction of the BP-3 well. The stacked area plot shows the relative proportions of illite (orange), chlorite (gray), kaolinite (purple), and smectite (black) from 1500 to 4700 mbsl. Kaolinite and illite are dominant throughout the core, while smectite appears intermittently and in generally low proportions. A marked increase in kaolinite content and a corresponding decrease in illite is observed below ~4000 mbsl. Black dots indicate analyzed samples.

Major and Trace Elements

The abundance of all major and trace elements analyzed for the clay fraction is presented in **Table S5.3** in **Appendix 5**. The downcore concentrations of selected major elements and their deviations from the World River Average Clay (WRAC; Bayon et al., 2015) values are illustrated in **Figure 5.5**. Al_2O_3 concentrations range from 17.5% to 22.4%, generally aligning with the WRAC value of 21.84%. Fe_2O_3 values span between 7.9% and 11.1%, with several intervals showing values above the WRAC reference of 9.80%. TiO_2 concentrations remain relatively stable, fluctuating between 0.6% and 0.9%, and are mostly close to or slightly below the WRAC value of 0.87%. MgO contents vary from 1.6% to 2.7%, while K_2O ranges between 2.2% and 3.0%, both comparable to the WRAC values of 2.59% and 2.91%, respectively. CaO concentrations are low throughout the core, ranging from below detection to

a maximum of 0.2%, and fall below the WRAC benchmark of 0.53%. P_2O_5 concentrations remain low across all samples, ranging from 0.03% to 0.15%, and do not reach the WRAC reference of 0.34%.

The abundance of trace elements is illustrated in **Fig. 5.6**. When available, the concentration of the WRAC is also plotted for comparison. Lithium (Li) concentrations range from approximately 58 to 110 ppm, within WRAC values (80±34 ppm). Strontium (Sr) exhibits a broader range, from 90 to 375 ppm, with most values exceeding the WRAC benchmark of 110 ppm. The highest Sr concentrations occur between 1600 and 1700 mbsl, where values consistently exceed 300 ppm. Zirconium (Zr) shows more moderate variability, with concentrations spanning from 78 to 191 ppm. Compared to the WRAC value of 148 ppm, Zr concentrations alternate between slightly depleted and slightly enriched, with enrichments observed at 2796, 3309, 4069, and 4177 mbsl. Barium (Ba) presents the most pronounced variability and highest enrichment among these elements, with concentrations ranging from approximately 217 ppm to over 35000 ppm. All Ba values substantially exceed the WRAC reference of 380 ppm throughout the entire core. This enrichment is particularly prominent between 4069 and 4177 mbsl, where Ba concentrations peak close to 180000 ppm. Among the high-field-strength elements, Hafnium (Hf) concentrations range from ~2.6 to 5.0 ppm, closely surrounding the WRAC average of 3.81 ppm. Thorium (Th) values range from ~11 to 23 ppm (WRAC: 15.1 ppm), with most samples showing concentrations above the reference value. Uranium (U) concentrations are lower, ranging between ~1.4 and 3.1 ppm, similar to the WRAC value of 2.86 ppm.

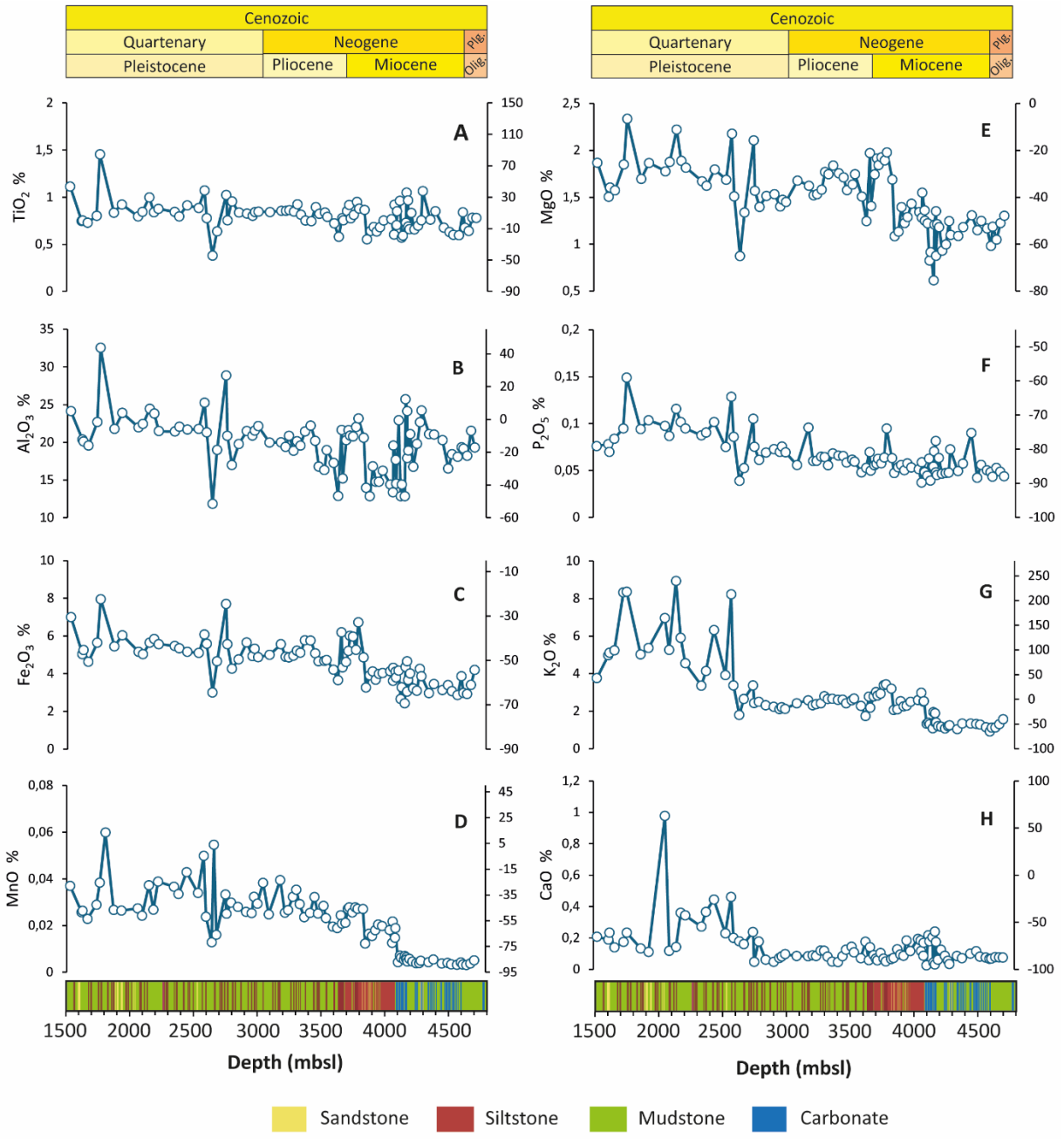

Figure 5.5. Downcore variation of major elements concentrations (%weight) and their standard variation (σ) from the WRAC values in the <2 µm clay fraction of BP-3 well sediments. (A–I) Profiles include TiO_2 (A), Al_2O_3 (B), Fe_2O_3 (C), MgO (D), MnO (E), Na_2O (F), P_2O_5 (G), K_2O (H), and CaO (I). The horizontal black line refers to the values of the World River Average Clays (WRAC; Bayon et al., 2015). Red labels highlight anomalously high values. Most elements show relatively stable profiles with scattered peaks, while MnO displays a gradual decline below ~3000 mbsl. CaO and Na_2O exhibit isolated enrichments, possibly linked to lithological changes.

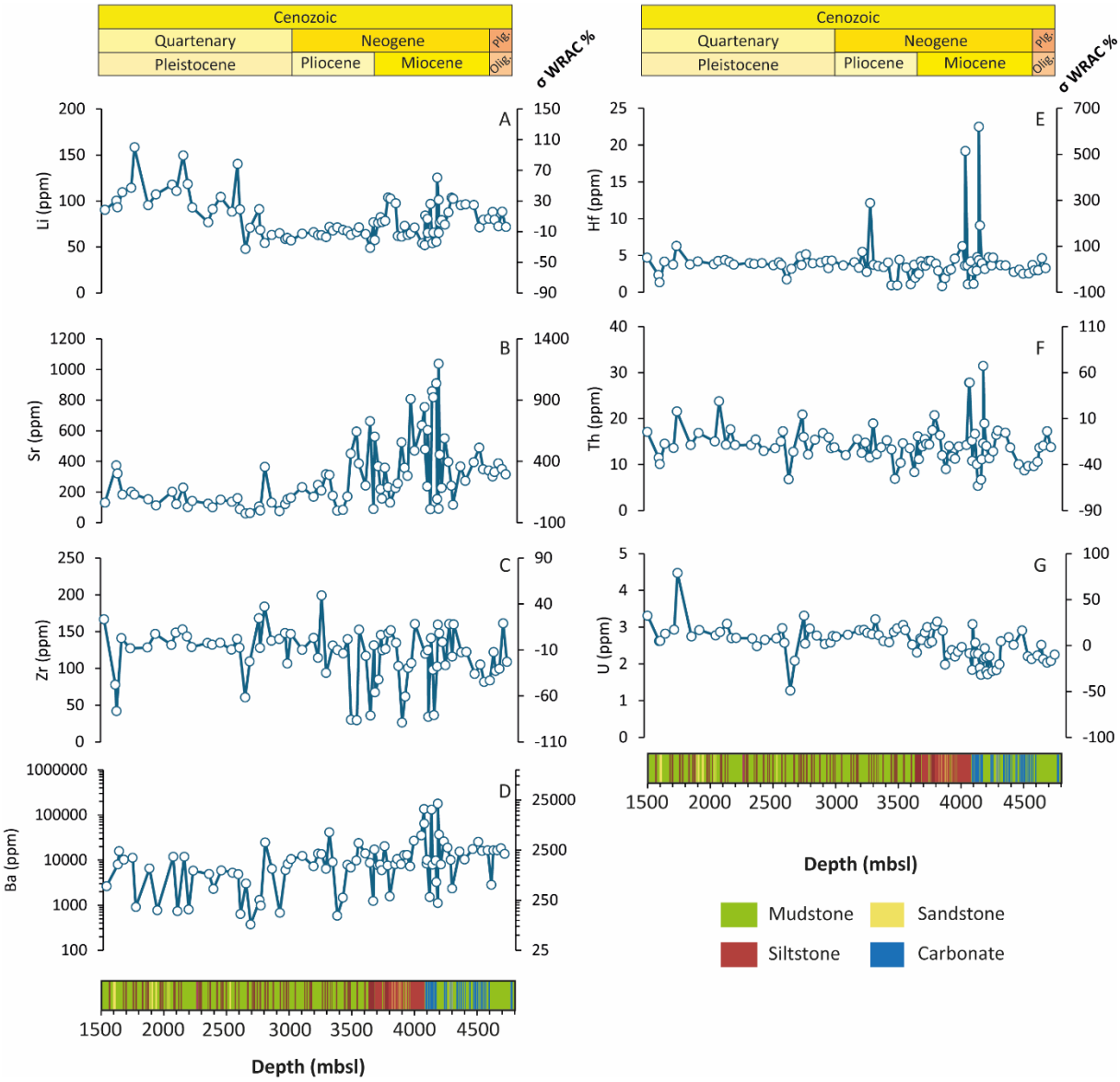

Figure 5.6. Downcore trace element concentrations (ppm) variations and their standard variation (σ) from the WRAC values in the <2 µm clay fraction of BP-3 well sediments. (A–G) Profiles include Li (A), Sr (B), Zr (C), Ba (D), Hf (E), Th (F), and U (G). The horizontal black line refers to the values of the World River Average Clays (WRAC; Bayon et al., 2015). Ba (D) exhibits extreme variability, with concentrations exceeding 400,000 ppm in several horizons between 3000 and 4200 mbsl. Zr and Hf (C, E) show elevated values in deeper intervals, while Sr (B) displays a gradual increase with depth. Other elements, including Th and U (F, G), show less pronounced variations.

Rare Earth Elements

REE concentrations show downcore variability across the light, middle, and heavy REE groups (**Table 5.3**). Neodymium (Nd) abundances, representative of the light REEs, range from ~26 to 44 ppm; gadolinium (Gd), a middle REE, varies between ~3.7 and 6.1 ppm; and ytterbium (Yb), among the heavy REEs, ranges from ~2.1 to 3.1 ppm. The WRAS-normalized REE patterns (**Fig. 5.7**) are coherent throughout until 4100 mbsl and consistently reflect LREE enrichment. Below this depth, HREE is significantly and anomalously depleted. Most samples show normalized values >1 for La and Ce, followed by a progressive decline across the MREEs (Sm–Dy) and a near-unity to sub-unity plateau for the HREEs (Ho–Lu). The La/La* anomaly varies from 0.5 to 1.4, with most values concentrated between 0.7 and 0.8. Notably, positive La anomalies (La/La* ≈ 1.4) are observed in 1806 and 4126 mbsl. The Ce/Ce* anomaly is generally stable across the depth profile, with values close to 0.9–1.0, although weak negative anomalies emerge in the deeper section of the core. Europium anomalies (Eu/Eu*) are mostly uniform (1.0–1.3) but increase markedly at certain depths. Positive Eu anomalies up to 1.8–2.3 are recorded at 3985, 4045, and below 4450 mbsl.

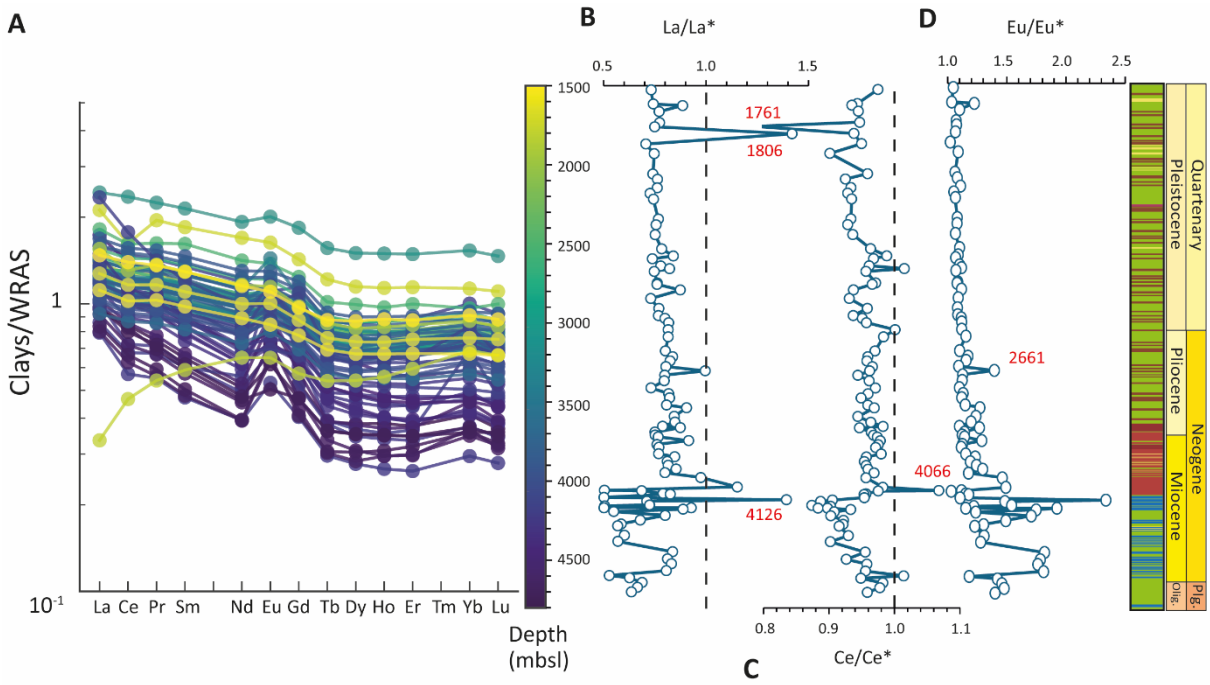

Figure 5.7. Rare earth element (REE) patterns and anomalies in the <2 µm clay fraction of BP-3 well sediments. (A) WRAS-normalized REE patterns (La–Lu) across the core, color-coded by sample depth (mbsl). Most samples show light REE (LREE) enrichment and middle-to-heavy REE (MREE–HREE) depletion relative to WRAS, with a clear downward shift in overall concentrations with depth. (B–D) Downcore profiles of selected REE anomalies: La/La* (B), Ce/Ce* (C), and Eu/Eu* (D). Dashed vertical lines indicate reference values of 1.0. Red labels denote selected depth points with notable excursions.

Hf-Nd Isotopes

Results for measured $^{143}Nd/^{144}Nd$ and $^{176}Hf/^{177}Hf$ ratios and calculated εNd(0), εHf(0), and $\Delta\varepsilon Hf_{CLAYS}$ values are provided in **Appendix 5**, **Table S5.4**, with downcore variations illustrated in **Figures 5.8** and **5.9**. At the base of the core, εNd(0) values are highly unradiogenic, ranging from –20.2 to –18.2. Above 4090 mbsl, values increase sharply, reaching –11 by 4045 mbsl. A brief return to more negative values is observed until ~3750 mbsl, with a minimum of –12.5. This is followed by a plateau between –11 and –10.5 extending to 3372 mbsl. From that depth upward, εNd(0) values gradually shift to more unradiogenic again, reaching –12.2 at 2382 mbsl, after which a renewed radiogenic trend develops, with values ranging between –11.7 and –11.4 in the uppermost part of the core. Hafnium isotopic compositions exhibit broadly similar trends to εNd(0), with coeval radiogenic and unradiogenic excursions throughout the record.

$\Delta\varepsilon Hf_{CLAYS}$ values at the base of the core are moderately negative, ranging from –2.4 to –1.2 between 4711 and 4651 mbsl. From there to ~4500 mbsl, values increase gradually toward zero, followed by minor fluctuations between –1 and +0.5 up to ~4280 mbsl. A sharp negative excursion occurs between 4255 and 4100 mbsl, with $\Delta\varepsilon Hf_{CLAYS}$ dropping below –5.0 and reaching a minimum of –9.8 at 4111 mbsl. Above this depth, values shift rapidly into the positive range, exceeding +1 by 3985 mbsl. Between 3950 and 3660 mbsl, $\Delta\varepsilon Hf_{CLAYS}$ remains positive and variable, peaking at +4.6. From 3660 to 3372 mbsl, values remain moderately positive, generally ranging from +0.4 to +1.5. A brief negative shift is observed between 3372 and 3003 mbsl, reaching –2.4, followed by a positive excursion from 3003 to 2760 mbsl, culminating at +3.3. A second local maximum of +2.6 is recorded at 2467 mbsl. In the uppermost section, from 2382 to 1527 mbsl, $\Delta\varepsilon Hf_{CLAYS}$ values fluctuate between –2.8 and +2.3, with no consistent trend.

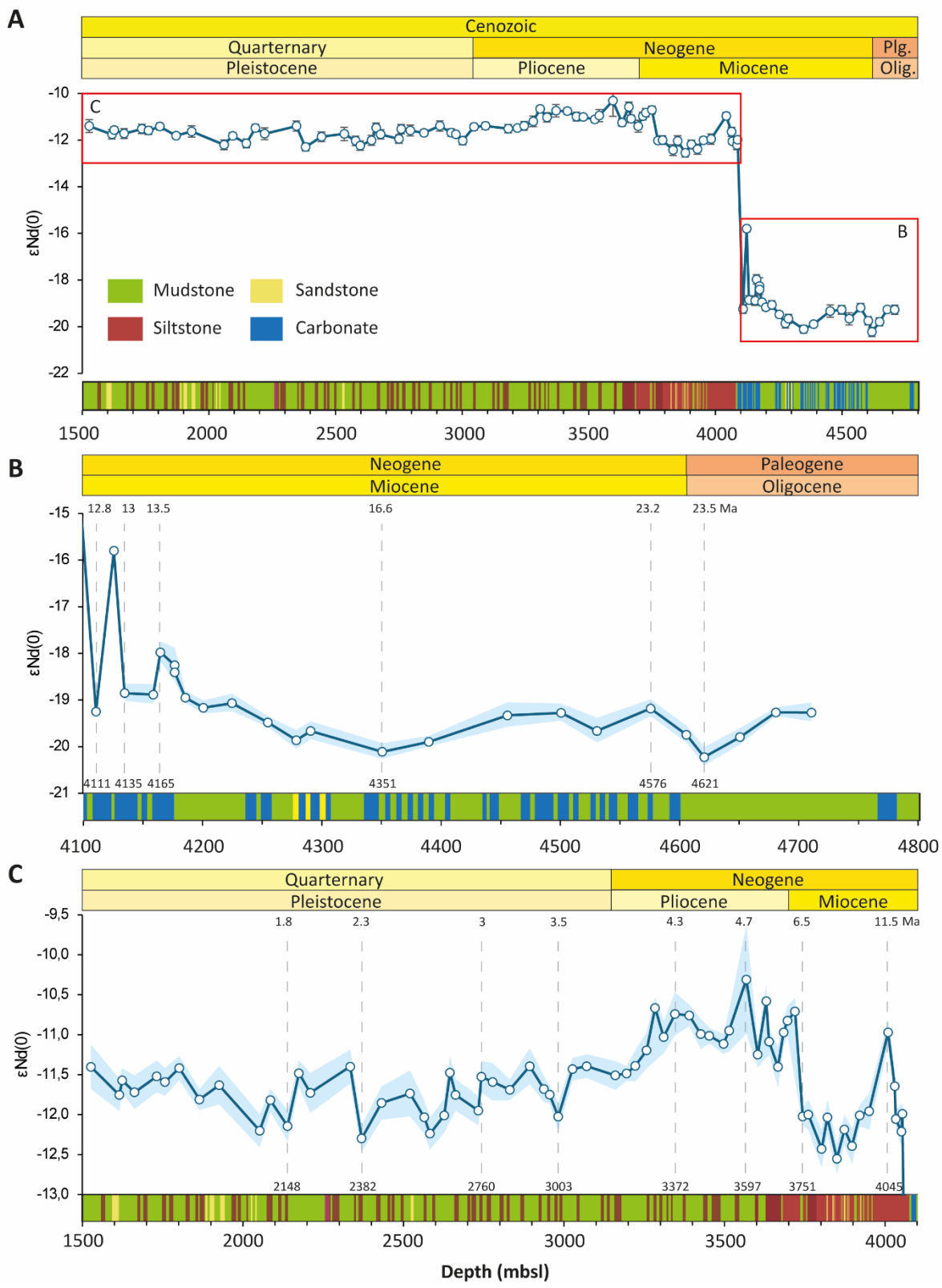

Figure 5.8. Downcore variations in εNd(0) values in the <2 µm clay fraction of BP-3 well sediments. (A) Overview of the entire εNd(0) dataset from 1500 to 4800 mbsl, showing a major shift near 4000 mbsl separating two distinct isotopic domains. **(B)** Detailed view of the deeper portion of the record (4100–4800 mbsl), corresponding to the late Oligocene and early Miocene. εNd(0) values in this interval are markedly unradiogenic, typically below –18, with a pronounced excursion reaching –20.2 at 4621 mbsl. **(C)** Expanded view of the upper 1500–4100 mbsl interval, spanning the middle Miocene to the Holocene. εNd(0) values in this section are

consistently more radiogenic, ranging between –10.5 and –12.8, with moderate fluctuations superimposed on a relatively stable background. Notable depth markers and age tie points are labeled throughout the profile.

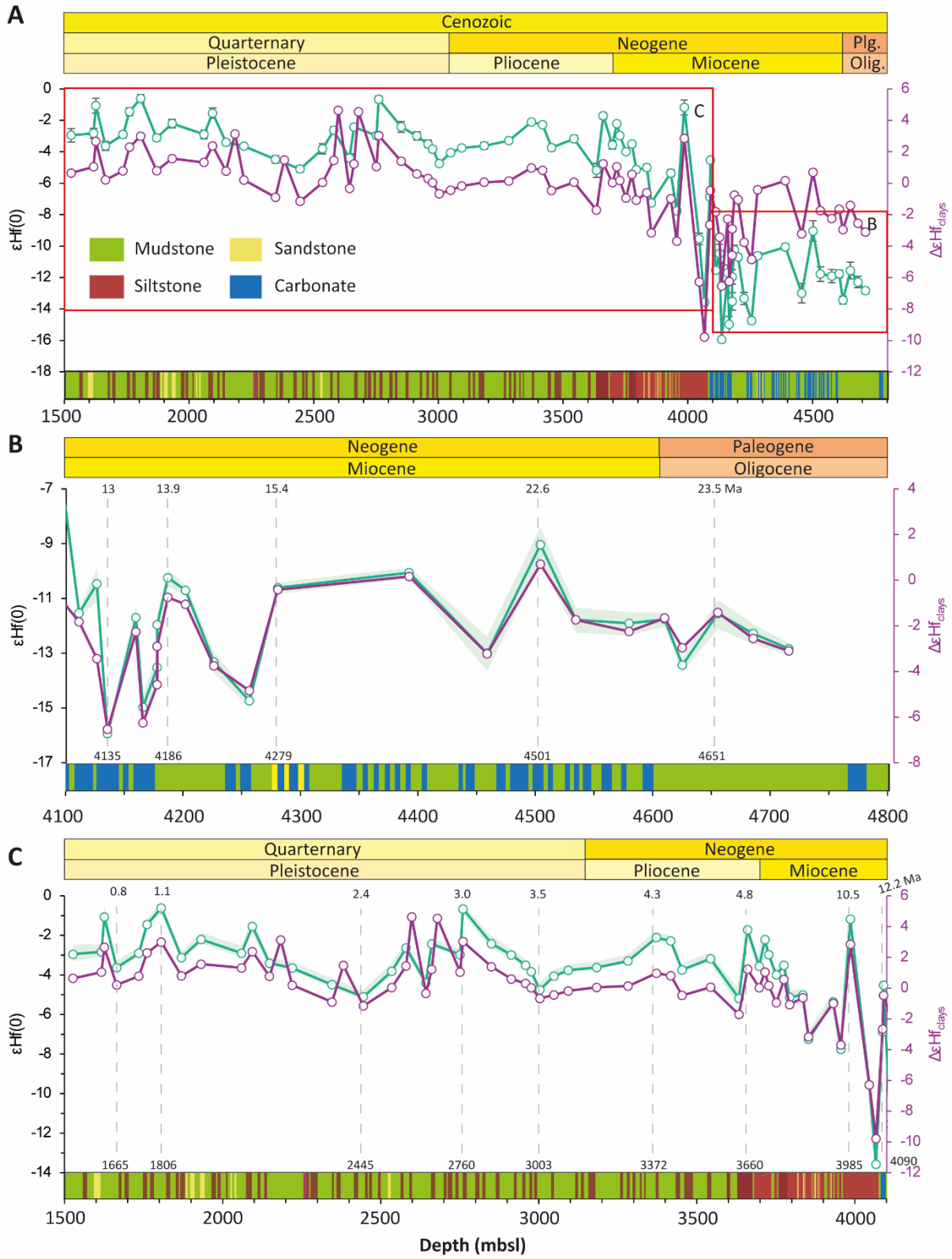

Figure 5.9. Downcore variation in εHf(0) and $\Delta\varepsilon Hf_{CLAYS}$ values in the <2 µm clay fraction of the BP-3 well. (A) Overview of the εHf(0) record from 1500 to 4800 mbsl, subdivided into two highlighted zones: **(B)** a deeper interval (~4100–4800 mbsl) showing strongly unradiogenic values and **(C)** a shallower interval (~1500–4100 mbsl) with generally more radiogenic compositions. **(B)** Expanded view of the deepest part of the core, where εHf(0) values are highly negative, reaching a minimum of -16.0 at 4135 mbsl. **(C)** Expanded view of the upper section of the record, characterized by more variable but generally higher εHf(0) values, peaking at –0.6 around 1806 mbsl.

5.3. Zircon Effect

Before Hf–Nd isotopic compositions in the clay fraction can be reliably used as silicate weathering proxies, it is essential to ensure that $\Delta\varepsilon Hf_{CLAYS}$ variability downcore is not controlled by the presence of zircon. This step is critical because residual zircon can also significantly impact measured REE patterns, due to its high HREE content relative to clay minerals, and shift Hf isotopic compositions toward more unradiogenic values (Bayon et al., 2016). Although our separation protocol is designed to quantitatively remove zircon grains larger than 1.5 µm, we performed a careful evaluation of elemental data from all clay-sized fractions to identify any samples that may still contain trace amounts of zircon.

In the Amazon River Basin, the average Zr concentration in clay sediments is 144 ± 35 µg/g (n = 11; Chapter III**, Table 3.1**), with a maximum of 208 µg/g observed in the Tapajós River. In comparison, the clay-sized fractions of BP-3 cuttings yield an average Zr content of 133 ± 129 µg/g (2SD, n = 89; excluding samples 4069 and 4177, which contain anomalously high Zr levels of 704 and 804 µg/g, respectively). These values are broadly consistent with the range observed in modern fluvial clays (**Fig. 5.10**; Bayon et al., 2015). However, a subset of samples (n = 9), specifically 1761, 1806, 2661, 3048, 4045, 4069, 4177, 4186, and 4442, exhibit Zr concentrations exceeding 210 µg/g, approaching the typical values observed in silt-sized fractions of global river sediments (Bayon et al., 2015). As a result, these samples were excluded from further interpretations.

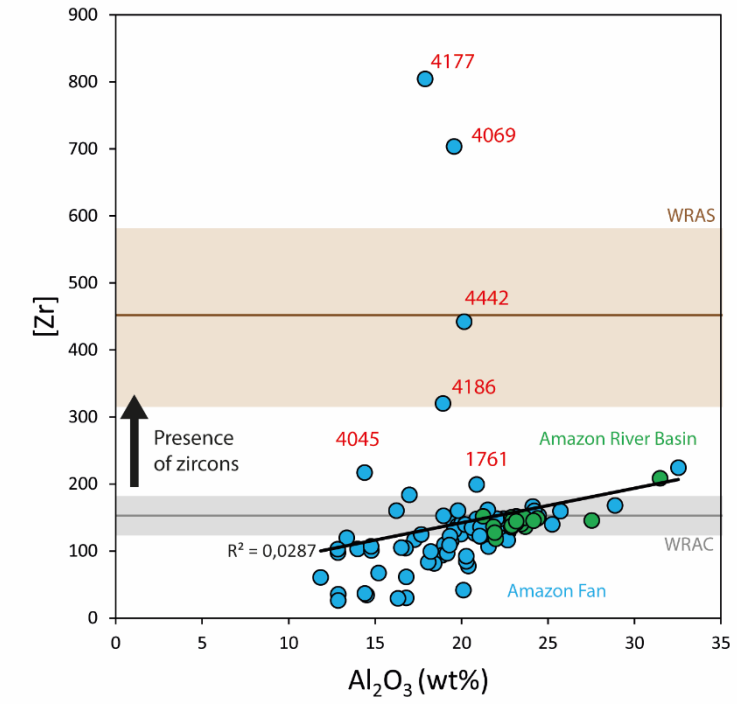

Figure 5.10. Zr concentrations (µg/g) plotted against Al_2O_3 content (wt%) for clay-sized fractions from BP-3 well cuttings. The shaded horizontal bands represent the average Zr concentration of clay-sized fractions in world river sediments (WRAC, gray) and silt-sized fractions (WRAS, beige), based on Bayon et al. (2015). The solid black line shows the linear regression for the dataset (R^2 = 0.0287). Samples with Zr concentrations exceeding the clay baseline are labeled in red.

5.4. Mineralogical and chemical integrity of the BP-3 Well cuttings

5.4.1. Foreword: Drilling muds and their footprint

Though essential for borehole stability and cuttings transport, drilling muds can significantly alter recovered sediments' mineralogical and geochemical characteristics. These fluids, especially those based on oil or water emulsions, commonly contain active clays like bentonite (smectite), which may interact with detrital or authigenic minerals via ion exchange, hydration, or flocculation. Such interactions can modify the original mineralogical identity of clays (Zhang et al., 2020). Mechanical effects during drilling can further bias the sample by fragmenting fine-grained minerals, leading to preferential loss or underrepresentation of phases like kaolinite or illite (Sanei et al., 2020). Additionally, alkaline pH conditions associated with drilling fluids can promote dissolution or recrystallization of sensitive minerals (Jurkovic et al., 2010; Hormozi et al., 2023).

Common mud additives, including barite ($BaSO_4$), attapulgite, and sepiolite, can further complicate interpretation. Barite, in particular, may contribute to elevated Ba concentrations that mimic signals of authigenic productivity or hydrothermal input (Fowler & Zierenberg, 2016;

Griffith & Paytan, 2012), thus distorting environmental proxies such as Ba/Al or Ba/REE ratios (Alzughoul et al., 2022). Moreover, elemental ratios like K/Al, Fe/Al, or Mg/Al, frequently used to infer source composition, can be skewed by mud-derived K-bearing polymers or Fe-based additives (Wenger et al., 2004). The Chemical Index of Alteration (CIA), which is sensitive to changes in alkalis and alumina, may also be compromised, yielding artificially high or low values unrelated to true weathering intensity (Nesbitt & Young, 1982). Finally, drilling muds may interfere with trace metal and REE measurements. REEs can be introduced directly via additives or adsorbed onto mud-derived clays, producing misleading anomalies in Ce/Ce* or Eu/Eu* that do not reflect true redox or diagenetic conditions (Hormozi et al., 2023; Carignan et al., 2001).

Operational documentation from the BP-3 exploration well adds further context. Although the type of drilling fluid used is not explicitly stated, several log entries indicate the use of oil-based mud (OBM), especially in deeper intervals. These include repeated gas anomalies and events such as circulation losses and influxes, particularly between 3868 and 4010 m, with notations like “Circ. B/U prior to POOH” and “influx,” which typically reflect conditions managed with OBM. Additionally, $\delta^{13}C$ data and strong gas anomalies at depths ≥4292 m support the interpretation of hydrocarbon-bearing formations being encountered, circumstances that commonly require OBM. One of the most common mud additives includes barite, attapulgite, and sepiolite (Neff, 2008). According to API (1993) and USEPA (1985) specifications, drilling mud barite is ≥92% pure, with the median grain size typically ranging from 10–20 μm to maintain suspension during circulation. Reported Ba concentrations in such material range from 507,000 to 538,000 ppm (Neff, 2008), showing that even small residual amounts could significantly elevate Ba levels in cuttings. Furthermore, sepiolite, a fibrous clay mineral rarely found in Amazon Fan sediments, was occasionally identified in the deeper intervals (**Fig. 5.3A**).

This section evaluates these challenges in the context of the BP-3 exploration well, critically assessing the mineralogical and geochemical fidelity of the recovered clay fractions and exploring the implications of potential drilling mud contamination.

5.4.2. Barium enrichment and possible sources

The bulk XRF analyses of unprocessed cuttings reveal a high variability in barium (Ba) concentrations, with the highest at 98600 ppm and the lowest at 8500 averaging 43107 (**Fig. 5.11**). In marine sediments, Ba can be associated with carbonates, organic matter, and biogenic silica (Robin et al., 2013), as well as with inorganic phases such as barite ($BaSO_4$), Fe–Mn oxyhydroxides, and aluminosilicates (Dymond et al., 1992). The sequential leaching and centrifugation procedures applied in this study should have removed most Ba-bearing phases, as carbonate and organic matter-bound Ba were dissolved in the early leaching steps, and dense minerals like barite (density >4.5 g/cm^3) were presumably excluded from the <2 µm clay fraction during low-speed centrifugation (Section 2.4). Nevertheless, ICP-MS analyses of the clay-sized fraction show persistently anomalous Ba concentrations, between 217 and 179710 ppm with an average of ~15,000 ppm (**Fig. 5.11**). Such high Ba values, both for the bulk and clay fraction, are much higher than concentrations reported in marine sediments elsewhere (**Table 5.1**).

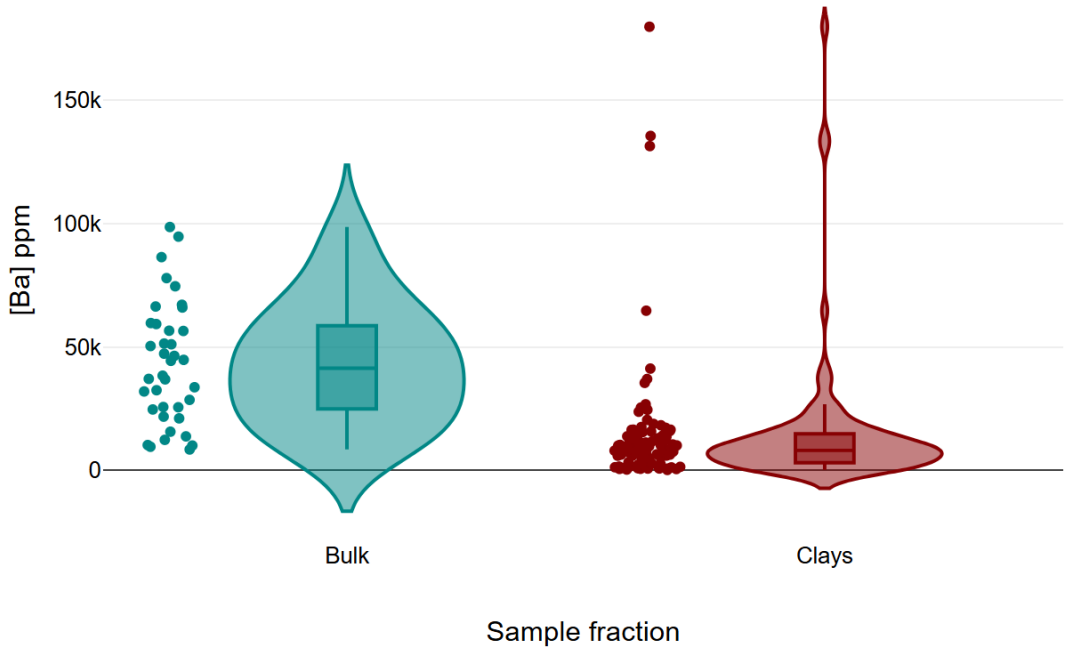

Figure 5.11. Violin and box and whisker plots of the Ba concentration in ppm in both bulk and clay fractions of BP-3 samples.

Table 5.1. Average concentrations of Ba and Al and Ba/Al ratios of bulk marine sediments worldwide.

Reference	Location	Ba	Al	Ba/Al
		ppm	ppm	
Gigele and Dahmke, (1994) ; Rutch et al. (1995)	South Atlantic (West Africa)	1100	-	-
McManus et al. (1999)	Southern California Margin	4988	-	-
Babu et al. (2002)	Arabian Sea	343	3	113
Reitz et al. (2004)	South Atlantic and Pacific	845	-	-
Hernandez-Sanchez et al. (2011)	Southern Ocean	1200	-	-
Saizhang et al. (2013)	Antarctica	700	-	-
Bridgestock et al. (2018)	South Atlantic	582	65756	0.0088

Interestingly, XRD analyses of the clay fraction do not identify barite in any sample (Section 5.4.1). Instead, the mineralogical assemblage is consistently dominated by aluminosilicate clays (kaolinite, illite, and chlorite, with minor smectite) as well as quartz. This mineral assemblage is in accordance with detrital clays transported by the modern Amazon River (Guyot et al., 2007). The apparent discrepancy between the absence of barite peaks in XRD and elevated Ba concentrations suggests that barite may be present in forms undetectable by XRD, such as amorphous or nanocrystalline phases.

Without getting into much detail, Ba concentration and $\delta^{138/134}$Ba isotope ratios in marine sediments are widely used as paleoproductivity proxies (Dymond et al., 1992; Reitz et al., 2004; Griffith et al., 2012; Brigdestock et al., 2017). Given the location of the BP-3 site, directly beneath the nutrient-rich outflow of the Amazon River, high Ba concentrations could reflect either enhanced marine productivity or elevated Ba delivery from the continent. The concept of Ba Excess (Ba_{xs}), or biogenic Ba, is commonly applied to disentangle these influences (Reitz et al., 2004; Babu et al., 2002; Nürnberg et al., 1987). This metric represents the fraction of Ba not supplied by terrigenous material and is calculated as:

$$Ba_{Biogenic} = Ba_{XS} = Ba_{Sample} - \left(\frac{Ba}{X}\right)_{Reference} \times X_{Sample}$$

where Ba_{sample} is the measured Ba concentration, X is a conservative element reflecting terrigenous input (typically Al or Ti), and $(Ba/X)_{Reference}$ is the ratio in a reference material such as UCC, PAAS, NASC, or regional river sediments.

Here, Ba_{xs} was calculated using the Amazon River clay baseline (Ba/Al = 0.033) and plotted against Ba/Al (**Fig. 5.12A**). Most samples plot well above the baseline (green horizontal line), indicating significant Ba input beyond what is expected from the Amazon basin detrital sources. The data exhibit a strong exponential trend (R^2 = 0.9677), with most samples exceeding both the Amazon River clay average (green vertical line) and the South Atlantic marine sediment range (dashed vertical black line; Bridgestock et al., 2018). The highest Ba_{xs} values surpass 180,000 ppm, suggesting localized enrichment likely linked to barite-rich particles or coatings that were not fully removed during sample processing. This consistent and marked Ba excess in the clay fraction strongly supports an external input, rather than natural sedimentary processes.

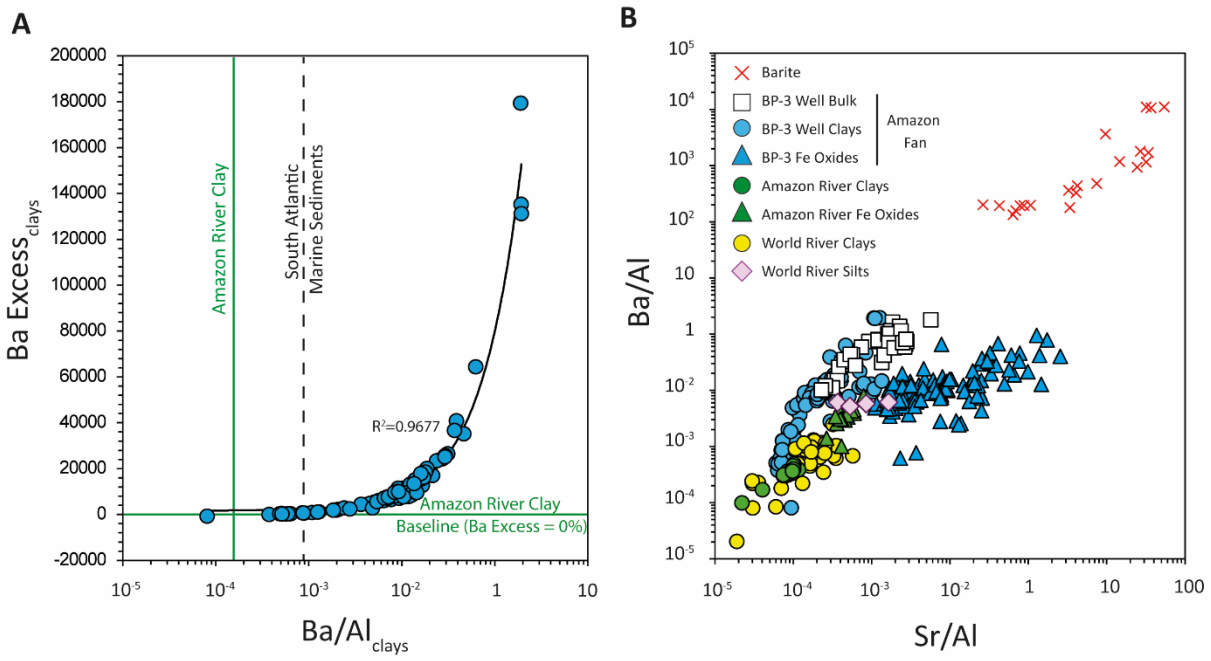

Figure 5.12. Geochemical indicators of barium enrichment and drilling mud contamination in BP-3 cuttings. **(A)** Ba_{XS} in the clay-sized fraction plotted against Ba/Al. The Amazon River clay baseline is shown in green, with the green vertical line indicating the average Ba/Al ratio of Amazon clays, and the black dashed line marking the average for South Atlantic marine sediments. The exponential fit (black line) indicates a strong correlation (R^2 = 0.9677), suggesting systematic Ba enrichment. **(B)** Ba/Al vs. Sr/Al crossplot showing that BP-3 clays (blue circles) and bulk sediments (grey squares) exhibit significantly higher Ba/Al ratios compared to Amazon River clays and global riverine sediments (Bayon et al., 2015). Most BP-3 samples follow a trend toward barite compositions (red Xs; REF), while Amazon River clays and Fe oxides remain confined to lower Ba/Al and Sr/Al ranges. Amazon River and Fan HH leaches and marine sediments (GSMS-1,2, and 3; IRMA, GeoReM).

Previous studies have shown that barite introduced via drilling muds can occur as fine-grained coatings on sediment particles, significantly elevating Ba and Sr concentrations without necessarily altering other geochemical signatures (Stuckman et al., 2019). A Ba/Al vs. Sr/Al crossplot (**Fig. 5.12B**) illustrates that clays and HH leachates extracted from the modern Amazon River (this study), global river sediments (Bayon et al., 2015), and South Atlantic hemipelagic deposits (Bridgestock et al., 2018) consistently exhibit low Ba/Al ratios and a relatively broad range of Sr/Al values. In contrast, both bulk and clay samples from the BP-3 well display markedly higher Ba/Al ratios, aligning closely along a trend that converges with the composition of pure barite (Hormozi et al., 2023; Hein et al., 2007). Meanwhile, although slightly enriched in Ba, the HH leachates from Amazon Fan sediments show disproportionately high Sr levels (**see Chapter VI for discussion**).

Overall, the geochemical evidence supports partial contamination of the BP-3 cuttings by drilling-derived materials, especially barite. While the broader clay mineralogy remains consistent with Amazon Fan detrital assemblages, the combination of elevated Ba concentrations, presence of sepiolite, and operational records indicating oil-based mud use highlights the need for careful screening of affected samples before geochemical or isotopic interpretations.

5.4.3. Impacts of exogenous barite on the chemical composition and isotopic systems of the detrital fraction of exploration drill cuttings

The exogenous contamination of barite from drilling fluids raises two primary concerns. First, barite is known to incorporate a variety of trace elements such as Sr^{2+}, Ca^{2+}, K^{+}, Rb^{2+}, Pb^{2+}, potentially altering the bulk geochemical composition of the analyzed sediment fractions (Griffith and Paytan, 2012). In addition, although barite hosts a small amount of REEs, drilling-grade barite may contain accessory phases such as siderite, pyrrhotite, gypsum, anhydrite, and pyrite, which could further complicate geochemical interpretations. Second, extremely high Ba-to-MREE ratios pose a significant analytical challenge for quantifying europium (Eu) by ICP-MS. This issue arises from the partial oxidation of Ba in the plasma, which leads to the formation of BaO^{+} species that generate isobaric interferences, particularly $^{135}Ba^{16}O^{+}$ on $^{151}Eu^{+}$ and $^{137}Ba^{16}O^{+}$ on $^{153}Eu^{+}$ (Shibata et al., 1993; Barrat et al., 1996).

Major and trace elements

As briefly noted in the previous section, Ba exhibits a moderate positive correlation with Sr and, in fact, shows the strongest correlation among all elements analyzed. The relationship between Ba/Al and Sr (R^2 = 0.41; **Fig. 5.13A**) reflects their common association in barite, indicating that barite contamination can significantly elevate Sr concentrations, independent of detrital or carbonate sources. This observation raises concerns regarding the reliability of Sr isotopes in sediment cuttings recovered from exploration wells. In contrast, Ba shows little to no correlation with Ca and K (**Fig. 5.13B and C**), suggesting that these elements are largely unaffected by barite and instead reflect natural mineralogical inputs. More notably, Ba displays moderate negative correlations with Ti, Fe, and P (R^2 = 0.22–0.34; **Fig. 5.13D–F**), implying that increasing barite content indiscriminately dilutes the relative abundance of these elements within the clay fraction.

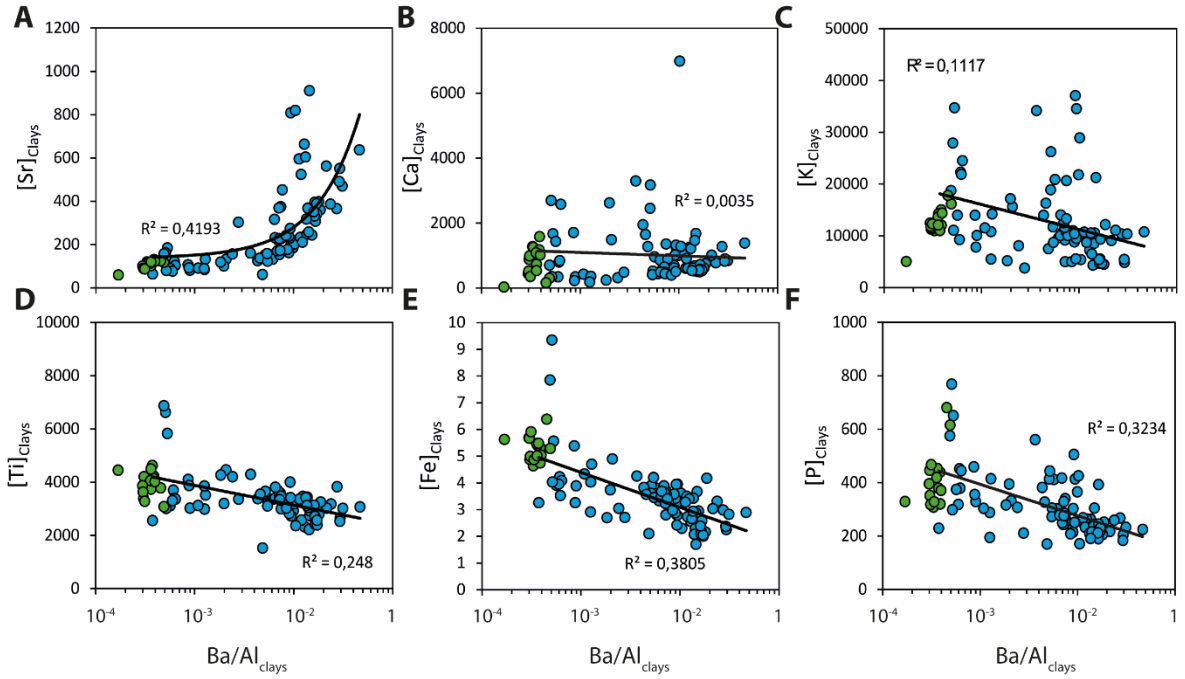

Figure 5.13. Crossplots of Ba/Al versus other major and trace elements: (A) Si, (B) Ca, (C) K, (D) Ti, (E) Fe, and (F) P. Except for Fe, which is in %w/w, element concentrations are in µg/g, and Ba/Al is plotted on a logarithmic scale. Samples from the Amazon River Basin are also plotted (green circles) for comparison.

Rare Earth Elements

Isobaric Ba oxide interference on ICP-MS measurements can be easily detected using Eu/Sm vs. Ba/Sm diagrams (Barrat and Bayon, 2024) and by analyzing elemental anomalies calculated using the geometric extrapolation, such as Eu/Eu* (Barrat et al., 2023). A clear non-linear increase in both Eu/Sm (**Fig. 5.14A**) and Eu/Eu* (**Fig. 5.14B**) is observed with increasing Ba or Ba/Sm values. Such a relationship indicates that Eu concentrations are affected by isobaric BaO interferences generated in the plasma and are mostly incorrect. Therefore, the concentrations or anomalies of Eu and other elements affected by Ba isobaric interference, such as La ($^{138}BaH^+$ on $^{139}La^+$; Barrat et al., 2024) should not be taken into consideration.

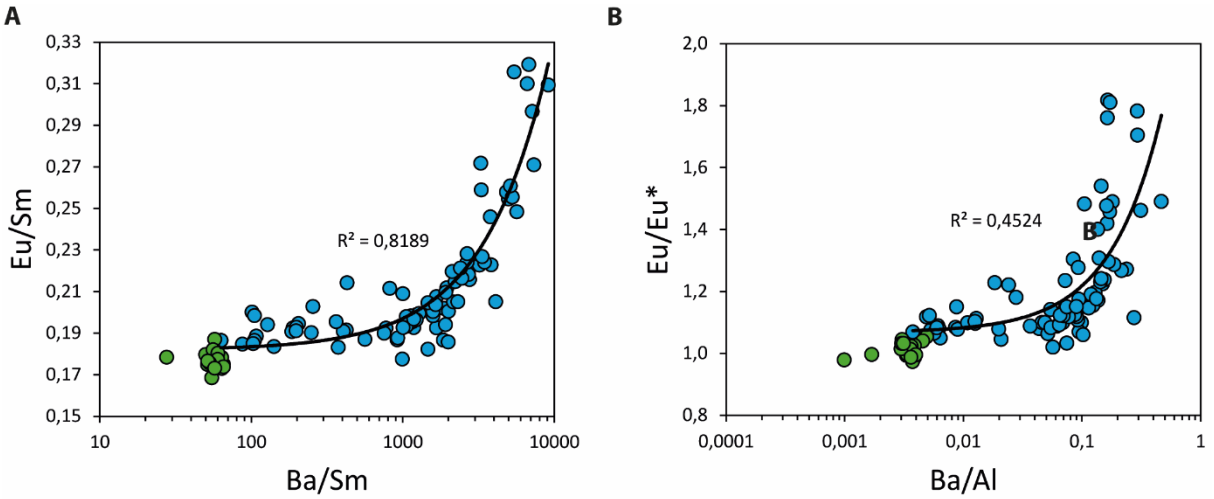

Figure 5.14. Relationships between barium concentrations and REE ratios or anomalies in the <2 µm clay fraction from the BP-3 drill core. (A) Eu/Sm ratio plotted against Ba/Sm, showing a strong positive trend (R^2 = 0.45), particularly at higher Ba/Sm values, indicating potential interference on Eu. **(B)** Eu/Eu* anomaly as a function of Ba_{clays},

Furthermore, Ba/Al ratios were compared against both concentration and normalized REE parameters to further evaluate potential barite-related effects on REE systematics in the clay fraction. **Figure 5.15A-B** shows that both Nd and Yb concentrations decrease with increasing Ba/Al ratios, displaying weak negative correlations (R^2 = 0.20, 0.10, respectively). The REE fractionation indices in Panels C and D—Yb_n/Nd_n and Sm_n/Yb_n—exhibit weaker relationships with Ba/Al. These observations indicate that while barite contamination affects the concentration of individual REEs, normalized REE distribution patterns used to assess provenance and weathering remain largely unaffected.

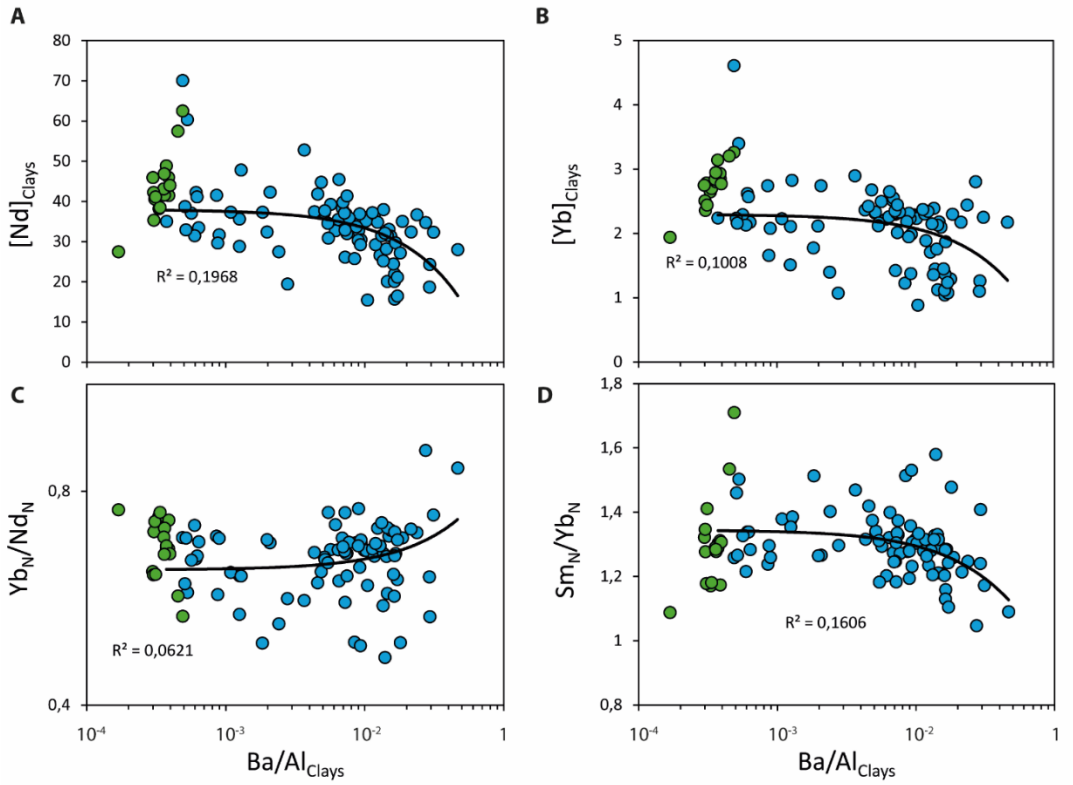

Figure 5.15. Crossplots showing the relationship between Ba/Al ratios and REE concentrations and fractionation indices in clay-sized fractions. (A) [Nd]clays vs. Ba/Al; **(B)** [Yb]clays vs. Ba/Al; **(C)** Yb_n/Nd_n vs. Ba/Al; and **(D)** Sm_n/Yb_n vs. Ba/Al. Blue circles represent Amazon Fan samples; green circles represent Amazon River reference clays.

Hf-Nd Isotopes

Finally, to ensure that exogenous barite contamination does not impact the integrity of measured Nd and Hf isotopic data, we examined the relationship between Ba/Al ratios and both elemental concentrations and isotopic compositions of Nd and Hf in the studied clay-sized fractions (**Fig. 5.16**). Although [Nd] and [Hf] show some dispersion and weak negative trends with increasing Ba/Al, their respective isotopic compositions remain remarkably stable. Panel A shows that while [Nd] tends to decrease with higher Ba/Al ratios, consistent with the dilution effect previously observed for trace elements, εNd(0) values are tightly grouped within the range defined by modern Amazon River sediments (green band), regardless of Ba content. Similarly, in Panel B, [Hf] concentrations are unaffected by Ba/Al variation, and εHf(0) values also remain well constrained within the modern fluvial domain.

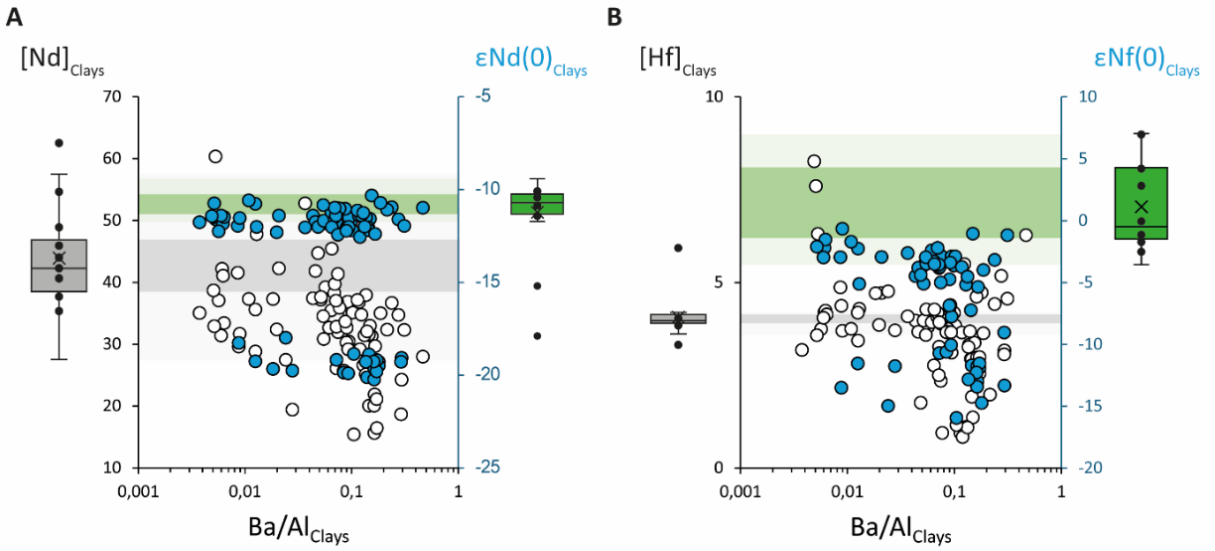

Figure 5.16. Ba/Al versus Nd and Hf contents in the clay fraction. (A) Nd concentrations (white) and εNd(0) (blue) values. **(B)** Hf concentrations (white) and εHf(0) (blue) values. Box and whisker plots represent values for Amazon River Basin clays, also highlighted by the shaded areas.

5.5. Conclusions

This chapter examined the efficiency of our protocol to separate the clay fraction from the zircon-rich silt fraction and the influence of exogenous barite from drilling fluids on the geochemical and isotopic composition of detrital fractions in exploration drill cuttings. While barite introduces noticeable Ba enrichment and associated increases in Sr, its effects on other major and trace elements are limited to dilution rather than alteration of natural geochemical signatures. Despite these compositional shifts, REE fractionation patterns remain stable across the entire dataset, confirming that normalized REE ratios are not compromised by barite contamination. Eu and La anomalies are the only REE parameters directly affected, due to isobaric interferences from Ba oxide species during ICP-MS analysis. The remaining REE dataset provides a reliable record of detrital provenance and weathering processes by identifying and excluding these artificially enhanced Eu signals. Crucially, Hf and Nd isotopic compositions are unaffected by barite contamination. Both elemental concentrations and εNd(0) and εHf(0) values fall within the range of modern Amazon River sediments, demonstrating that the radiogenic signatures of clays robustly preserve source information, independent of drilling-derived inputs. Although barite slightly modifies bulk geochemical concentrations, the core provenance indicators, REE fractionation patterns, and Hf-Nd isotopic ratios remain intact. This highlights the resilience of these geochemical systems, reinforcing

their utility for reconstructing weathering and sediment transport histories even when using drill cuttings as the primary sedimentary archive

VI

Characterization of leached Fe-Mn fractions in the BP-3 Well and its integrity for tracing continental weathering processes

Declaration/ Declaração/ Déclaration

This chapter presents an assessment of the hydroxylamine hydrochloride (HH) leaching protocol, a method widely applied in marine geochemistry to isolate reactive Fe and Mn (oxyhydr)oxides for trace metal and isotopic analysis. While the approach has been increasingly used for paleo-redox reconstructions and sediment provenance studies, its potential as a tool for reconstructing chemical weathering signals—particularly through rare earth element (REE) geochemistry—remains largely unexplored in sediment core records. Here, we evaluate for the first time the use of HH leachates as archives of continental chemical weathering. Specifically, we investigate the mineralogical composition, geochemical characteristics, and extraction behavior of HH-leachable phases in a 3.3 km–long core, with the aim of assessing their reliability as proxies for continental weathering processes.

[PT] Este capítulo apresenta uma avaliação do protocolo de lixiviação com cloridrato de hidroxilamina (HH), um método amplamente utilizado em geoquímica marinha para isolar fases reativas de Fe e Mn (oxi-hidróxidos) em análises de metais-traço e isótopos. Embora sua aplicação tenha se expandido para reconstruções paleo-redox e estudos de proveniência sedimentar, seu potencial como ferramenta para reconstruir sinais de intemperismo químico — em particular por meio da geoquímica de elementos terras raras (ETRs) — permanece pouco explorado em registros de testemunhos sedimentares. Aqui, avaliamos pela primeira vez o uso de lixiviados HH como arquivos do intemperismo químico continental. Especificamente, investigamos a composição mineralógica, as características geoquímicas e o comportamento de extração das fases lixiviáveis por HH em um testemunho de 3,3 km de comprimento, com o objetivo de avaliar sua confiabilidade como proxies de processos de intemperismo continental.

[FR] Ce chapitre présente une évaluation du protocole de lixiviation au chlorhydrate d'hydroxylamine (HH), une méthode largement utilisée en géochimie marine pour isoler les phases réactives de Fe et Mn (oxy-hydroxydes) dans les analyses des métaux traces et des isotopes. Bien que son application se soit élargie aux reconstitutions paléo-redox et aux études de provenance des sédiments, son potentiel en tant qu'outil de reconstitution des signaux d'altération chimique — en particulier à travers la géochimie des éléments terres rares (ETR) — reste largement inexploré dans les archives de carottes sédimentaires. Ici, nous évaluons pour la première fois l'utilisation des lixiviats HH comme archives de l'altération chimique continentale. Plus précisément, nous examinons la composition minéralogique, les caractéristiques géochimiques et le comportement d'extraction des phases lixiviables par HH dans une carotte de 3,3 km de long, afin d'évaluer leur fiabilité en tant que traceurs des processus d'altération continentale.

6.1. Introduction

Rare earth element concentrations and Nd isotopic compositions in sediments are powerful tools for tracing sediment provenance and chemical weathering (Taylor and McLennan, 1985). When applied to leached Fe-oxide fractions, these methods assume that the isotopic signal reveal the source of the reactive Fe-bearing phases. While this assumption generally holds for bulk silicate residues, interpreting trace element and isotopic values from leached Fe oxides is more complex due to the multiple origins and transformations these phases undergo from their formation on land to deposition on the seafloor (Bayon et al., 2020).

Iron oxides are ubiquitous products of continental weathering, forming through the oxidative alteration of primary silicate and sulfide minerals, as well as through the erosion of older marine or diagenetic Fe oxyhydroxide precipitates from upstream source regions. These Fe-bearing phases are typically transported to river systems as fine-grained detrital particles, often adsorbed onto or embedded within clay aggregates, and ultimately delivered to estuarine and marine environments (Bayon et al., 2004; Kraft et al., 2013). Upon entering estuarine systems, however, these particles undergo rapid physicochemical transformations. In low-salinity zones, REEs are efficiently scavenged from the dissolved phase via coprecipitation with freshly formed Fe oxyhydroxides and through the flocculation of organic colloids (Sholkovitz and Szymczak, 2000; Rousseau et al., 2015). As salinity increases downstream, partial dissolution of lithogenic particles can remobilize REEs into the dissolved pool, often imparting a more radiogenic εNd signature (Oeklers et al., 2011). These released REEs may subsequently be reincorporated into authigenic mineral phases that form in the estuarine and shelf sediments, further modifying the original continental signal.

One of the key complications in interpreting Fe leachate signals extracted from buried marine sediments arises from reverse weathering reactions. On the Amazon shelf, rapid formation of authigenic clay minerals such as nontronite and glauconite occurs via interactions between reactive Fe/Al oxides and biogenic silica (Michalopoulos and Aller, 1995, 2004). These authigenic phases commonly display REEs abundances that depart from typical shale-normalized patterns, hence indicating the influence of estuarine or early diagenetic conditions rather than continental provenance. Sequential extractions by Vosteen et al. (2022) confirmed that up to 22% of river-derived reactive Fe is transformed into Fe-bearing clay minerals in

Amazon shelf sediments, highlighting reverse weathering as both a sink for reactive Fe and a source of isotopically distinct phases that may bias provenance interpretations. Furthermore, a recent investigation of REE in glauconitic pellets formed at the Congo shelf suggested that marine clay authigenesis could possibly act as a source of dissolved REE to seawater (Bayon et al., 2023).

As introduced in Chapter I, the use of paired clays-Fe oxide fraction REE distribution and Nd isotopic composition has emerged as a potential proxy for disentangling continental chemical weathering processes, including the Amazon Basin (Chapter III). However, uncertainty remains about whether it can be applied to deeply buried marine sediment records. In addition to the estuarine processes described above, early diagenetic redox cycling adds further complexity. Reductive dissolution of Fe(III) and Mn(IV) oxides during organic matter degradation releases Fe^{2+} and Mn^{2+} to sediment porewaters, where they may diffuse upward and reprecipitate or be sequestered into secondary minerals such as siderite, vivianite, or authigenic clays (Aller et al., 1986). These transformations vary spatially with sedimentation rate, organic matter input, and bioturbation intensity. Additionally, benthic fluxes and submarine groundwater discharge introduce dissolved REEs with distinct isotopic signatures to bottom waters and porewaters (Johannesson and Burdige, 2007). For example, Xu et al. (2024) showed that Nd released from Amazonian mangrove porewaters (εNd ≈ –17.8) may contribute up to 64% of the dissolved Nd in margin seawater, far exceeding the riverine dissolved flux and highlighting the importance of diagenetic sources. Despite these processes, several studies have demonstrated that Fe-oxide leachates can still preserve terrestrial εNd signals in systems with high fluvial input. Investigations in the Congo, Ganges–Brahmaputra, and Amazon systems have shown that εNd values in Fe-oxide fractions often match those of riverine suspended matter, suggesting partial retention of the source signature despite diagenetic overprinting (Bayon et al., 2004, 2009, 2020; Kraft et al., 2013; Jang et al., 2020).

Building on these insights, this chapter begins by identifying the mineral phases mobilized during HH leaching using stoichiometric modeling of major elements to estimate the proportions of Fe-Mn (oxyhydr)oxides, carbonates, and phosphates in the leached fraction. We then assess the selectivity and efficiency of the HH step by comparing leachate and bulk sediment elemental concentrations, establishing the geochemical fidelity of the procedure. Together, these results provide the foundation for evaluating the REE pool associated with HH-

leachable phases, analyzing normalized fractionation patterns, Nd isotopic signatures, and exploring the broader utility of HH leachates as archives of past chemical weathering changes.

6.2. Results and Discussion

6.2.1. Major and Trace Elements

Elemental concentrations of the leached Fe oxide fraction are presented in **Appendix 6, Tables 6.1 and 6.2,** with downcore variations of selected elements summarized in **Figures 6.1 and 6.2**. Among the major elements, Fe concentrations increase markedly from ~1,000–4,300 ppm below 4600 mbsl to a peak of ~17,660 ppm at 3931 mbsl, then stabilize at ~11,000–13,000 ppm in the upper core. Mn mirrors this pattern, rising from ~20–50 ppm in deeper samples to ~590 ppm at 3931 mbsl, and remaining elevated (~350–390 ppm) above 3000 mbsl. P shows the strongest depth gradient, increasing from ~130–200 ppm at the base to ~730 ppm in the shallowest samples. Al increases from ~260 to 1,500 ppm, while Mg peaks modestly at ~2,400 ppm near 3900 mbsl and then decreases toward the top. Ca is highly variable, spiking at ~45,500 ppm at 4651 mbsl before declining to ~9,000–12,000 ppm in the upper core. Na remains consistently low (~130–360 ppm), and K increases steadily from ~50–90 to ~274 ppm toward the top.

Among the trace elements, Sr is elevated at depth (~106–159 ppm below 4600 mbsl), peaks at ~194 ppm at 3931 mbsl, and decreases progressively to ~32 ppm in the shallowest sample. Ba follows a similar trajectory, rising from ~176 ppm at 4651 mbsl to ~211 ppm at 3931 mbsl, and stabilizing between 130–150 ppm in the upper core.

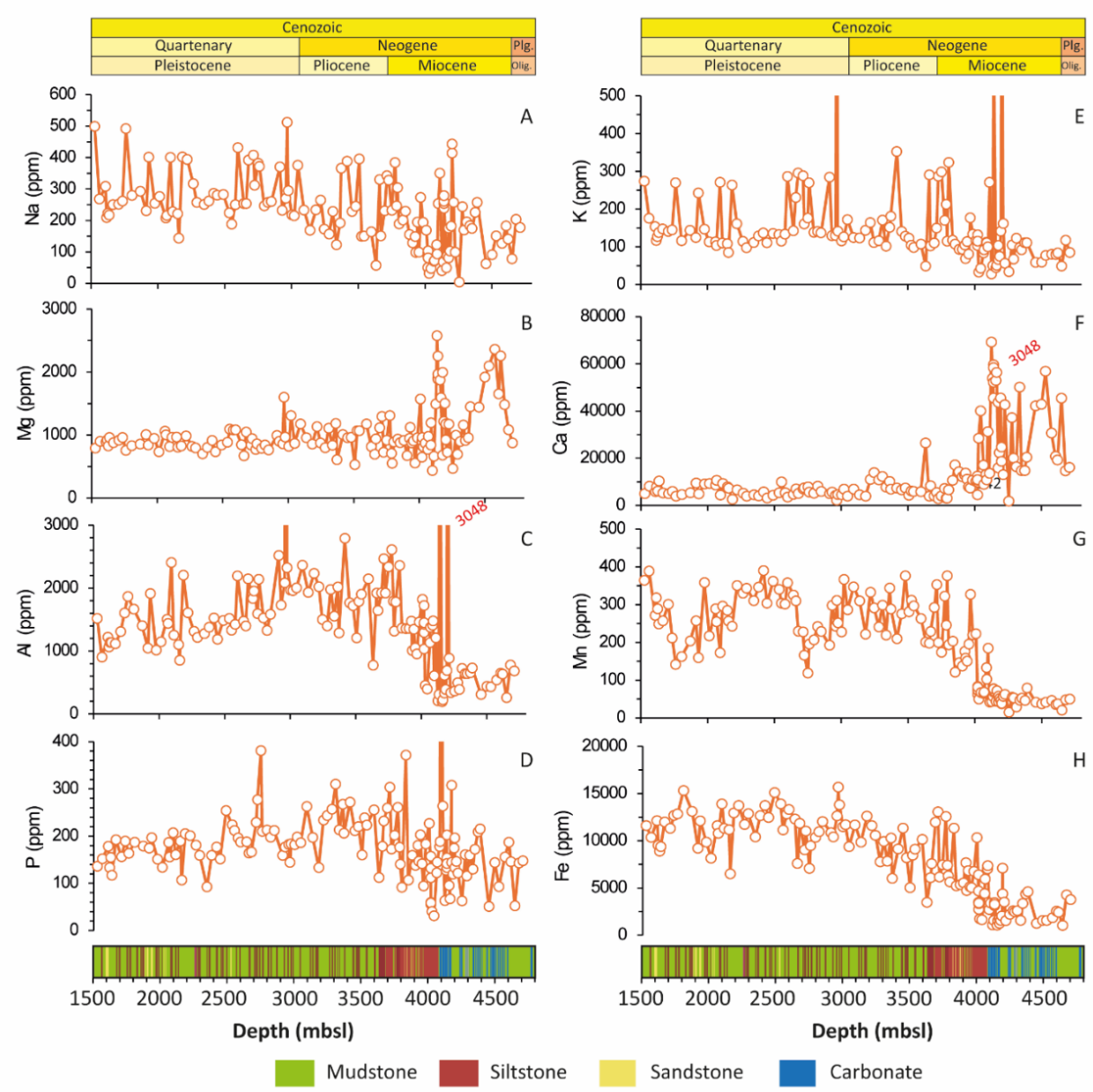

Figure 6.1. Downcore profiles of major element concentrations (in ppm) in the HH leach fraction of the BP-3 well. (A–D) Variations in Na, Mg, Al, and P concentrations. (E–H) Variations in K, Ca, Mn, and Fe concentrations.

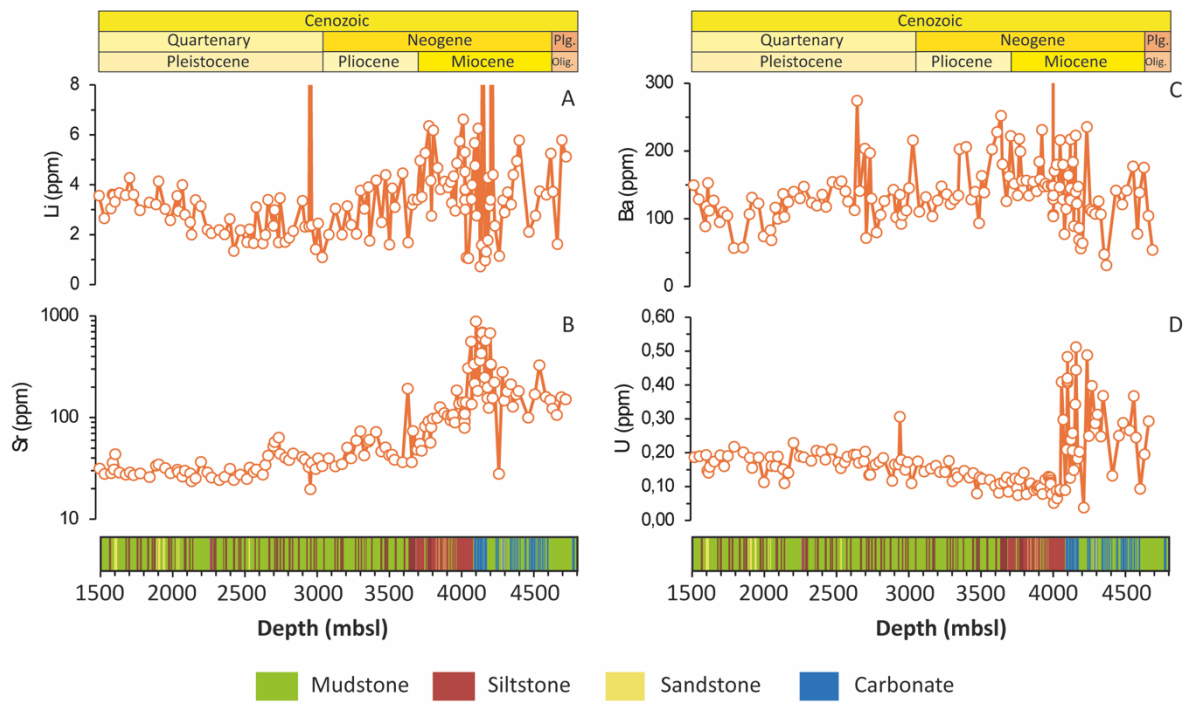

Figure 6.2. Downcore variations of selected trace element concentrations (in ppm) in the HH leach fraction of the BP-3 well. (A–D) Profiles of Li, Sr, Ba, and U, note the logarithmic scale used for Sr.

6.2.2. Rare Earth Elements

Concentrations of rare earth elements (REEs) in the HH leach fraction display consistent up-core enrichment, which aligns with Fe oxide accumulation (**Table 6.2, Appendix 6**). Among the light REEs, Nd increases from ~1.7 ppm at 4651 mbsl to ~4.1 ppm at 1527 mbsl. The middle REE Gd rises from ~0.45 to 0.95 ppm, with the most pronounced increase between 4200 and 3700 mbsl. Yb, representing the heavy REEs, increases from ~0.17 to 0.60 ppm, especially above 4000 mbsl. All REE groups show strong covariation with Fe, suggesting progressive enrichment of REEs in amorphous or poorly crystalline Fe oxides during sediment burial. This behavior highlights the potential of leached Fe oxide fractions as sensitive carriers of REE signals in continental margin sediments.

The WRAS-normalized REE patterns (**Fig. 6.3A**) reveal a bell-shaped distribution, with most profiles enriched in MREEs relative to both LREEs and HREEs. This shape becomes increasingly pronounced in the upper core (see below). The La/La* anomaly (**Fig. 6.3B**) ranges from 0.5 to 1.0, with most values below unity (see discussion in Section 6.4.3). The Ce/Ce* anomaly (**Fig. 6.3C**) is uniform across the profile (0.9–1.1), with weak negative excursions

restricted to deeper intervals. Europium anomalies (Eu/Eu*) range from 0.9 to 1.4, with consistently positive values throughout the core (**Fig. 6.3D**).

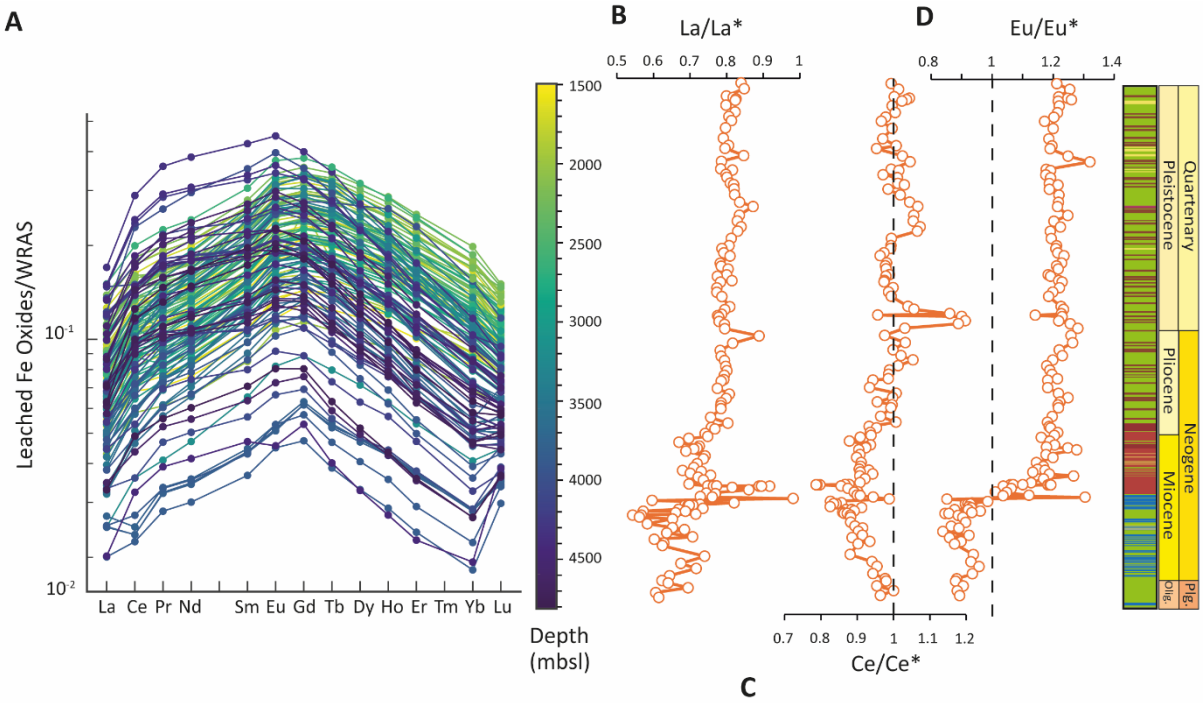

Figure 6.3. Rare earth element (REE) distributions and anomalies in the HH leach fraction of the BP-3 well. **(A)** WRAS-normalized REE patterns for leached Fe oxides show strong MREE enrichment and prominent tetrad effects, especially in deeper samples. (B–D) Vertical profiles of selected REE anomalies: **(B)** La/La*,**(C)** Ce/Ce*, and **(D)** Eu/Eu*. La/La* and Eu/Eu* generally remain above unity, indicating LREE enrichment and positive Eu anomalies. At the same time, Ce/Ce* shows variable values, including slight negative and positive anomalies across the core. Anomalies were calculated using geometric interpolation (Barrat et al., 2023).

To better visualize MREE enrichment across the core, REE concentrations in the HH leach fraction were normalized to Gd (**Fig. 6.4A**). The resulting patterns reveal a consistent bell-shaped distribution throughout most of the core, marked by enrichment in MREEs (Sm–Gd) relative to both LREEs and HREEs. The REE distributions in the deepest samples (>4100 mbsl) are notably flatter among the LREEs and more depleted toward the HREE end, suggesting lower HREE retention and a subdued MREE bulge. The patterns become more pronounced between ~3600 and 4100 mbsl, with clearer MREE enrichment and increasingly concave shapes. This is reflected in the concavity index (**Fig. 6.4B**), which rises above 2.5 in this interval, indicating significant MREE enrichment relative to LREE and HREE averages. In the mid-core section (~3000–3600 mbsl), concavity values stabilize between ~1.6 and 2.0. Approaching shallower

intervals, particularly above 2500 mbsl, the REE patterns shift again, displaying more substantial LREE depletion and flatter or slightly HREE-enriched profiles. The most pronounced MREE enrichment occurs at ~2000 mbsl, where the concavity index exceeds 3.0, marking the highest value recorded in the core. Above 2000 mbsl, the concavity index declines slightly towards approximately 1.7.

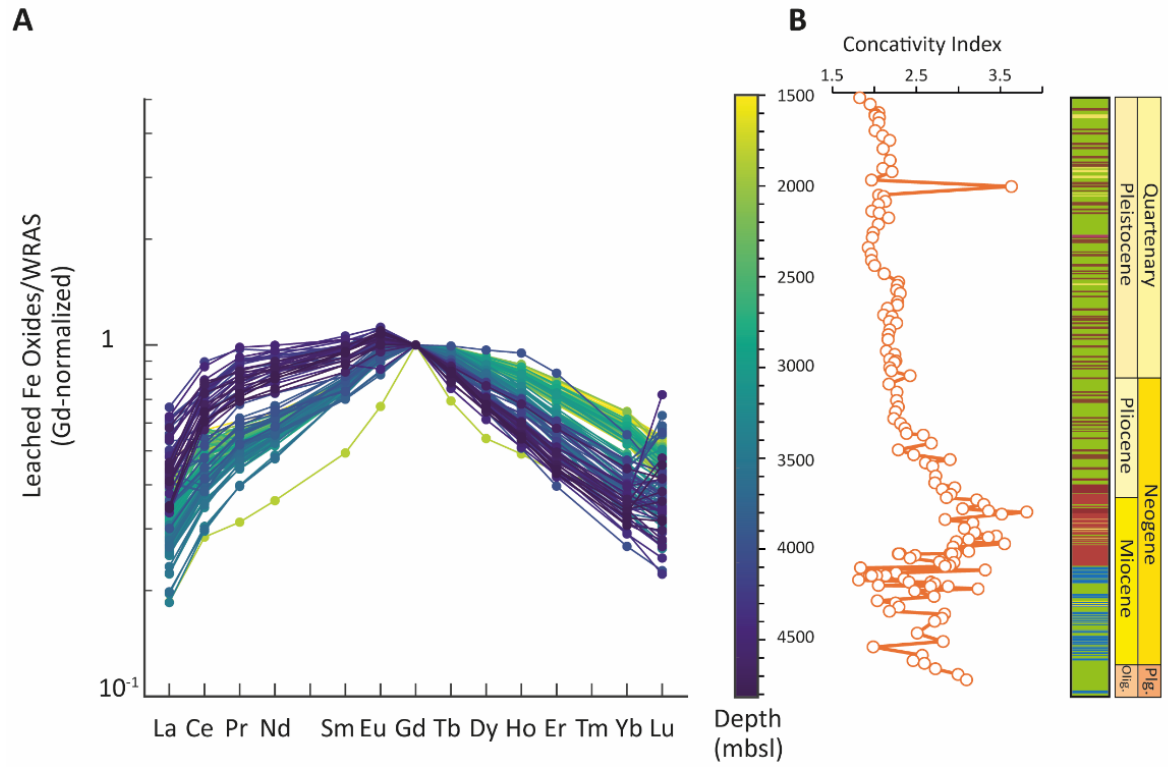

Figure 6.4. Middle rare earth element (MREE) enrichment and concavity index in the leached Fe-oxide fraction of the BP-3 well. (A) Gd-normalized REE patterns (WRAS-normalized) for the leached Fe oxide fraction, highlighting the prominent convex upward curvature centered on the MREEs. **(B)** The concavity index was calculated for each depth, reflecting the degree of MREE enrichment or depletion relative to neighboring LREE and HREE abundances.

The observed patterns are consistent with those documented for modern HH leachates from Amazon River sediments (**Chapter III**, **Fig. 3.3**). To place these results in a broader context, **Figure 6.5** compares Y/Ho molar ratios with WRAS-normalized Er/Nd across dissolved, detrital, clay, and HH-leached fractions from the Amazon system (this study; Filho et al., 2024; Xu et al., 2024, 2023; Baturin and Gordev, 2019; Merschel et al., 2017). Amazon Fan HH leachates fall within the crustal Y/Ho range (25–45) and display $(Er/Nd)_N$ ratios consistent with a dominantly lithogenic composition (Bau et al., 1996; Nozaki et al., 1997). These signatures

confirm that the BP-3 HH leachates primarily reflect continental phases rather than seawater-like or purely authigenic inputs.

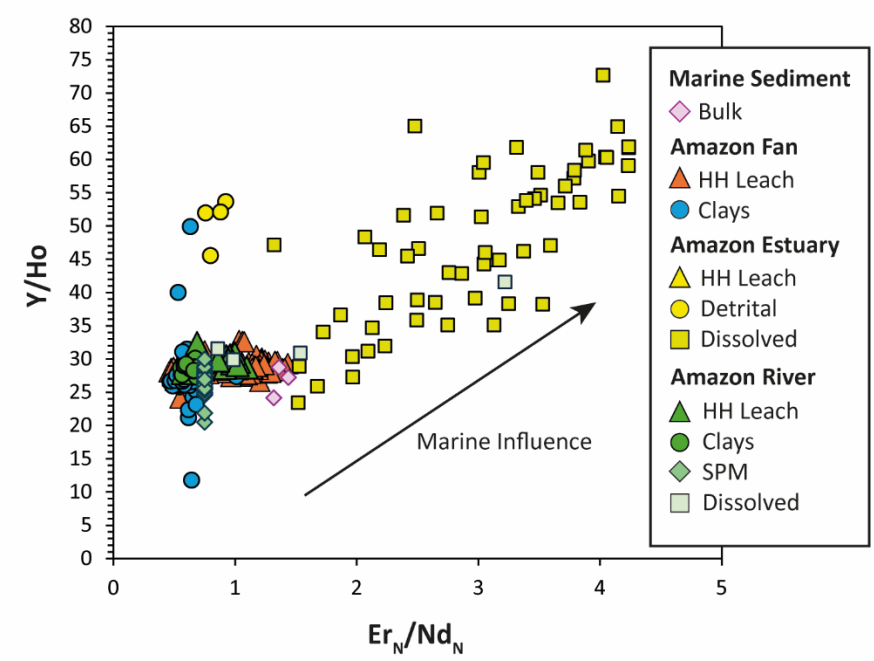

Figure 6.5. Y/Ho molar ratios plotted against WRAS-normalized Er/Nd across the Amazon system.

6.2.3. Nd Isotopes

Neodymium isotopic compositions (εNd(0)) of the HH leach fraction show distinct trends along the BP-3 core, with a pronounced isotopic discontinuity near 4066 mbsl separating two contrasting intervals (**Appendix 6 Table 7.2**; **Fig. 6.6A**). Below this boundary, from ~4650 to 4066 mbsl, εNd(t) values are markedly radiogenic, ranging from –21.7 to –16.0 (**Fig. 6.5B**). Within this lower interval, values are consistently less radiogenic than -18.0, with minor fluctuations around 4291 and 4456 mbsl corresponding to ~15.6 and ~22.1 Ma, respectively. Above 4066 mbsl, a sharp isotopic shift occurs, with εNd(t) values abruptly increasing to more radiogenic signatures between –11.7 and –7.0 (**Fig. 6.5C**). From the Late Miocene to the present, this upper section displays more variable but generally less negative values. εNd(t) ranges from –11.7 to –8.4 between ~4066 and 3400 mbsl (11.8 to ~4.3 Ma), followed by a shift toward more radiogenic compositions from –9.0 to –7.0 in the Pliocene and Pleistocene intervals (<4.3 Ma). These values are in total agreement with modern Amazon Basin FeOOH (**Chapter III**)

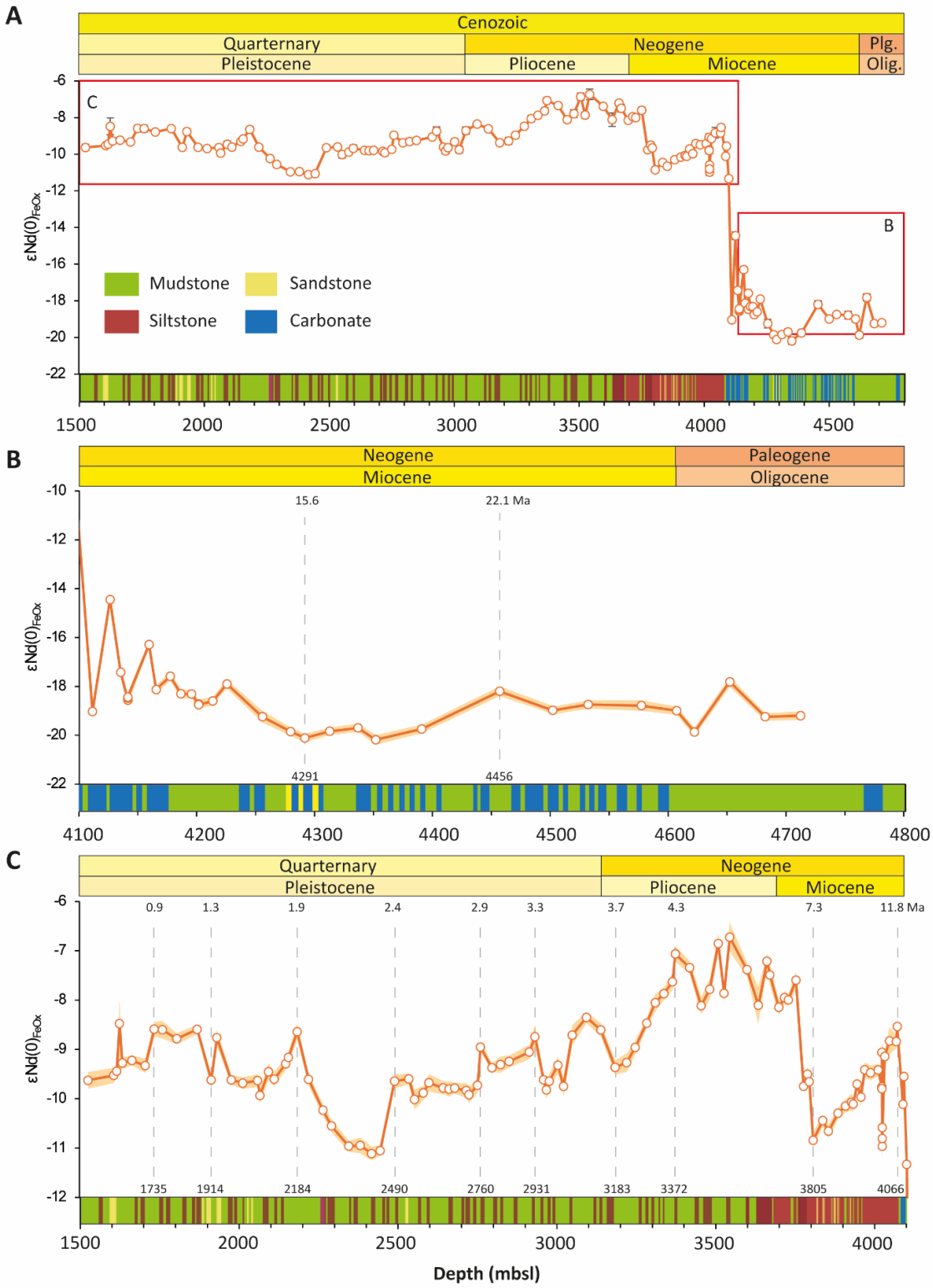

Figure 6.6. Downcore variations in εNd(0) values in the HH leach fraction of the BP-3 well. (A) Full depth profile from 1500 to 4800 mbsl, showing a distinct isotopic shift at ~4066 mbsl. **(B)** Close-up of the lower section (4100–4800 mbsl), spanning the Miocene to Oligocene. **(C)** Detail of the upper section (1500–4066 mbsl), spanning the Pleistocene to Late Miocene.

6.3. Identification of leached mineral phases

Sequential leaching procedures are inherently non-selective and may mobilize mineral phases beyond their intended targets (Zhang and Shields, 2023). As such, accurately characterizing the mineralogical composition of the leached fraction is essential for reliable interpretation of geochemical signals. In this study, the HH leach was employed to target amorphous and poorly crystalline Fe and Mn (oxyhydr)oxides and weakly adsorbed trace elements (Bayon et al., 2002). However, other studies have demonstrated that the HH step can also mobilize unintended phases. For instance, Hannigan and Sholkovitz (2001) showed phosphate minerals can be released under acid conditions. Similarly, the acidified HH solution can dissolve phosphorus associated not only with Fe–Mn oxides, but also with exchangeable, carbonate-bound, and detrital or authigenic phosphate pools (Poulton and Canfield, 2006). In addition, residual carbonates that were not entirely removed during the preceding acetic acid leach (see **Chapter II, Section 2.3**) may persist and partially dissolve during the HH step (Bayon et al., 2020; Zhang and Shields, 2023). These potential interferences underscore the importance of quantifying the actual mineral phases extracted during each leaching stage in order to isolate environmentally sensitive components confidently.

We begin our assessment by converting leachate concentrations of Fe, Mn, Ca, Mg, Sr, and P into equivalent mineral masses using representative stoichiometries to estimate the mineral phases mobilized by the HH leach. Fe was modeled primarily as ferrihydrite [$Fe(OH)_3$; 106.87 g/mol], consistent with its high reactivity under reducing conditions. Mn was assumed to occur as Mn(IV) forms (MnO_2; todokorite, birnessite; 86.94 g/mol), while P was modeled as apatite [$Ca_5(PO_4)_3OH$; 502.31 g/mol], requiring three mol of P per mole of mineral. Carbonate phases were estimated from Ca, Mg, and Sr, assuming their presence as calcite ($CaCO_3$), magnesite ($MgCO_3$), and strontianite ($SrCO_3$), respectively. To assess the degree of potential detrital contamination occurring during the HH leaching step, we consider K concentrations expressed as K_2O wt%. Assuming that the average Amazon sediment displays K_2O = 2% (**Table XX-Appendix XX**) we can estimate the degree of contamination of silicate minerals. The calculated mineral masses were then normalized to sample mass to derive first-order estimates of the leachable fraction's mineralogical composition (**Fig. 6.7; Table S6.X Appendix 6**).

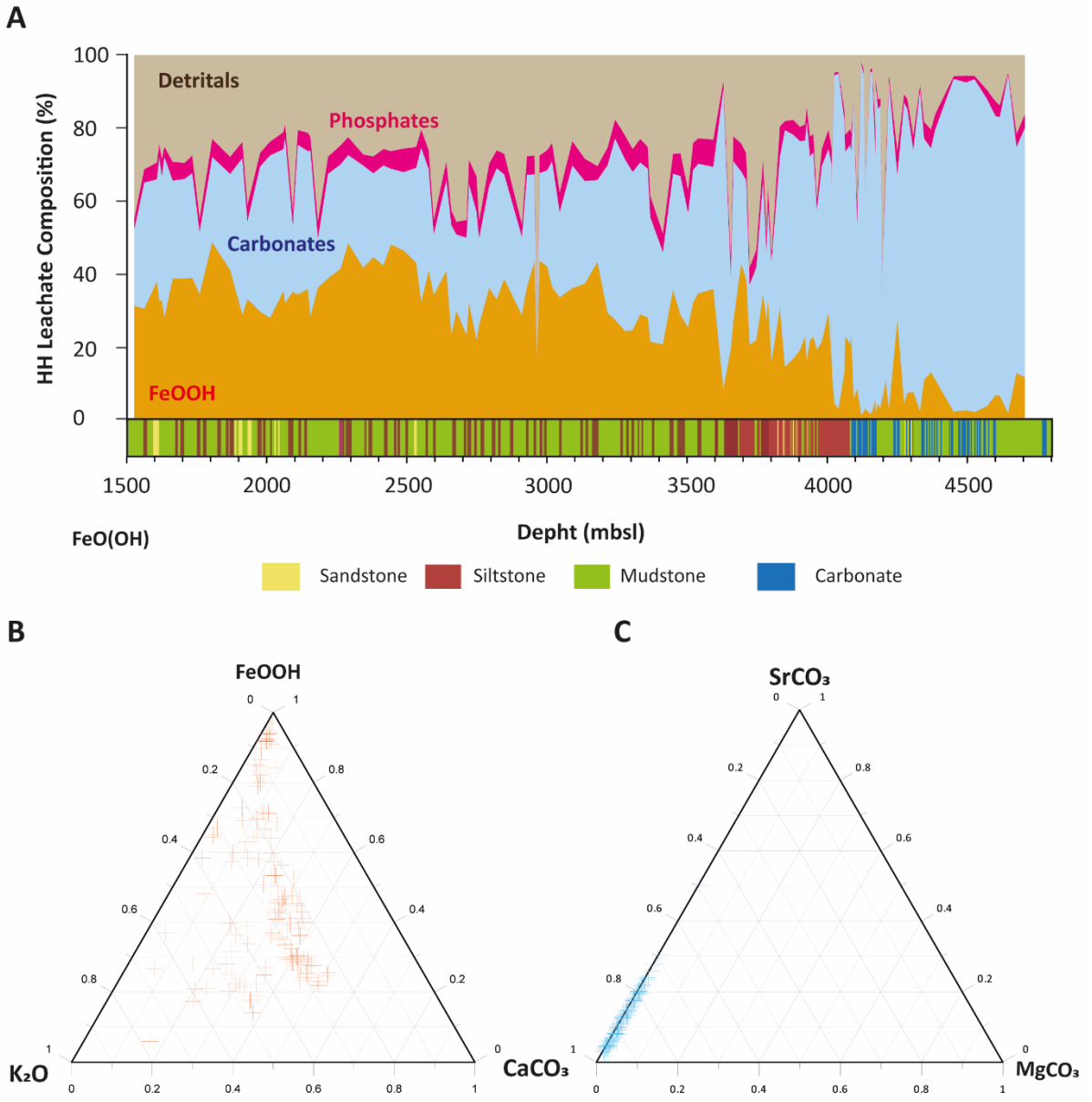

Figure 6.7. Composition of the HH-leachable mineral fraction across the BP-3 sediment core. **(A)** 100% stacked area plot showing the relative contributions of modeled mineral phases (Fe (oxyhydr)oxides, carbonates, phosphates, and detritals estimated from K_2O) to the HH leachate composition with depth. **(B)** Ternary plot of FeO(OH), carbonates, and detritals, illustrating that most samples fall along a binary mixing array between Fe oxides and carbonates, with variable but generally minor detrital influence and minimal phosphate contribution. **(C)** Ternary plot of the carbonate sub-fraction, demonstrating that $CaCO_3$ overwhelmingly dominates the carbonate pool, with only minor $MgCO_3$ and negligible $SrCO_3$ contributions, consistent with dissolution of calcite or low-Mg carbonate material.

Figure 6.7 illustrates the modeled distribution of leached phases across the BP-3 core. Above 4100 mbsl, Fe (oxyhydr)oxides dominate the HH leachates, accounting for ~30–50 wt% of the extracted fraction, with occasional peaks approaching 60% (**Fig. 6.7A**). In these intervals, detrital inputs estimated from K_2O are also significant (20–45%), while carbonate phases generally range between 20–40%. Below 4100 mbsl, however, carbonate phases become the main leachable fraction, reaching values as high as 90%, whereas Fe oxides and detritals both decline markedly. Phosphates remain consistently minor throughout the entire record (<5%), and given their close association with Fe oxides (Slomp et al., 1996), their contribution is likely overestimated. These trends highlight the strong influence of lithological variation, particularly the expansion of carbonate-rich intervals at depth, on the composition of the leachable pool. This relationship is further emphasized in **Figure 6.7B**, where samples plot along a continuum between Fe oxides, carbonates, and detritals, revealing a dominant binary control between Fe oxides and detrital material in the upper fan and a shift toward carbonate-rich compositions at depth. Finally, the carbonate end-member itself is almost entirely composed of $CaCO_3$, with only minor $MgCO_3$ and negligible $SrCO_3$ contributions (**Fig. 6.7C**), consistent with dissolution of calcite or low-Mg carbonates rather than mixed carbonate sources.

While these stoichiometric conversions provide a first-order approximation of the leached mineral phases, evaluating how efficiently each element was mobilized relative to its total abundance in the sediment is also instructive. This helps constrain the selectivity of the HH leach and assess potential interference from detrital or diagenetic sources. To determine this, we compared elemental concentrations in the HH leachates to their corresponding bulk sediment values where available (**Figure 6.8**). Mn was the most efficiently extracted element, with $Mn_{HH/MnT}$ ratios reaching 60–80% in the upper core but dropping sharply below ~3800 mbsl. P also showed moderate leachability (30–50%), reflecting its association with reactive Fe oxides or loosely bound phosphates. Fe was mobilized at moderate but consistent efficiency (20–30%), suggesting that while a significant fraction remains in detrital silicates (e.g., clays), carbonates (e.g., siderite), or crystalline Fe oxides (e.g., goethite, hematite), easily reducible Fe oxides are still present throughout the sediment. Ca and Sr were only partially mobilized (5–20%), except for a notable spike in Ca extraction (~50%) at ~3950 mbsl, likely due to incomplete carbonate removal during the acetic acid step. Mg and Al showed minimal extraction (<15% and <5%, respectively), indicating limited dissolution of detrital

aluminosilicates. Ba exhibited variable extractability (0.2–1.8%), possibly reflecting minor desorption from oxide surfaces or trace contamination from barite-rich drilling muds. Finally, K displayed low to moderate leachability (generally <5% but occasionally up to ~20%), indicating that only a small fraction of K-bearing phases, likely loosely bound interlayer K in clays or amorphous weathering products, was mobilized during the HH step. This reinforces that most K remains locked in detrital silicates, making K a robust tracer for assessing detrital contamination.

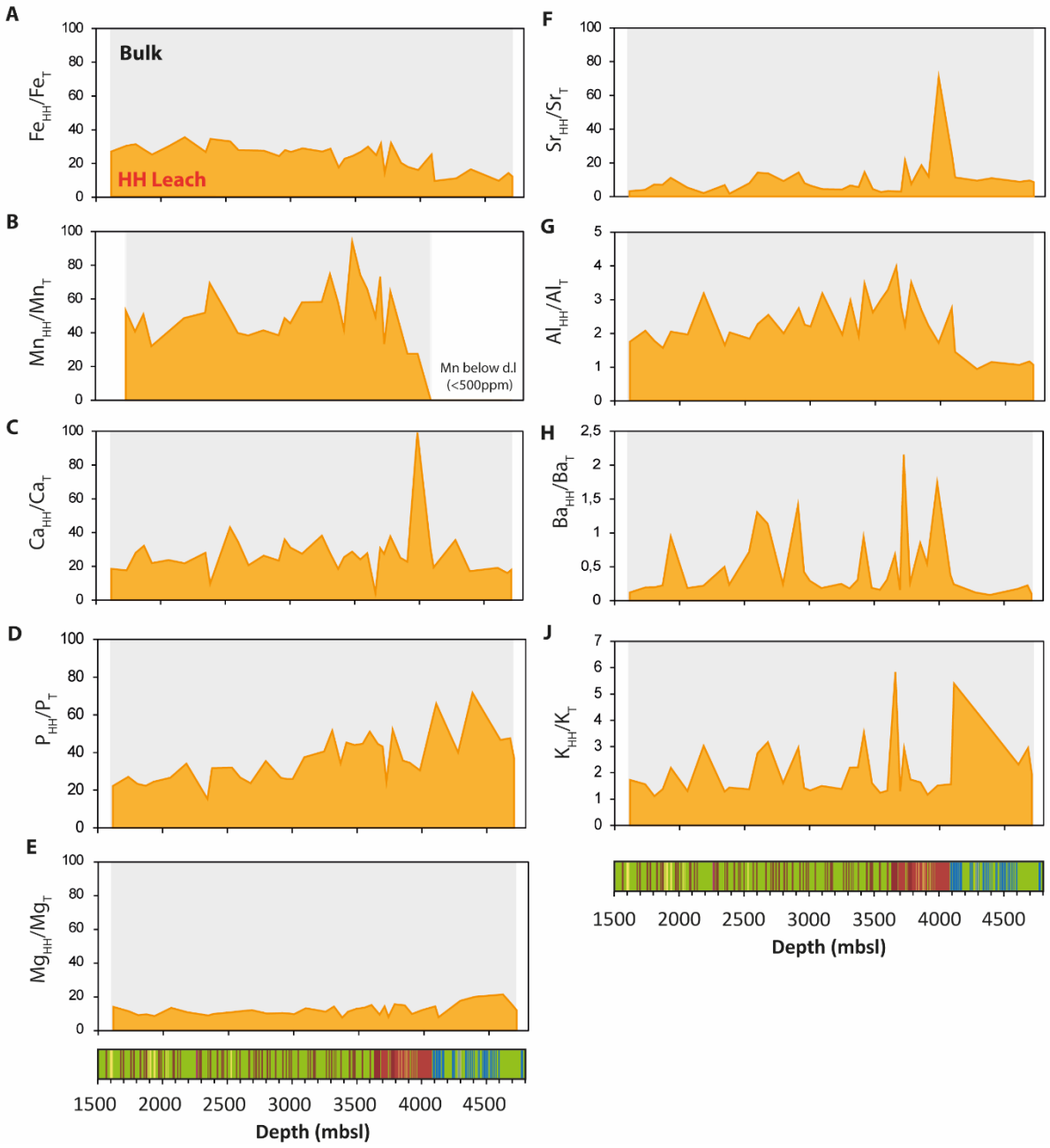

Figure 6.8. Downcore profiles of major element concentrations (in ppm) in the HH leach fraction of the BP-3 well. (A–E) Variations in Fe, Mn, Ca, P, and Mg relative to their bulk abundances. **(F–J)** Variations in Sr, Al, Ba, and K relative to bulk abundances. Mn shows the highest mobilization efficiency, with values reaching up to ~80% in the upper core but decreasing sharply below ~3800 mbsl. P and Fe display moderate extraction efficiencies (30–50% and 20–30%, respectively), while Ca and Sr remain low except for localized spikes linked to incomplete carbonate removal. Al and Mg are consistently low (<15%), reflecting minimal dissolution of detrital aluminosilicates. Ba extraction is minor and variable, whereas K shows low to moderate values (<5–20%), highlighting that most K remains hosted in detrital silicates.

The results demonstrate that the sequential leaching protocol applied here effectively isolates a reactive sediment fraction dominated by FeOOH, with subordinate but significant contributions from carbonates, phosphates, and a detrital component reflected in K. Importantly, we show that redox-sensitive Fe oxide phases, most likely ferrihydrite and lepidocrocite, can be preserved and mobilized even under the strongly reducing conditions characteristic of the Amazon Fan (e.g., Michalopoulos and Aller, 2004). By combining modeled mineral proportions with extraction efficiencies, we provide a robust framework for interpreting the HH leachates in terms of both source mineralogy and selective reactivity. This framework reveals that while Fe–Mn oxides remain the principal reactive sink, carbonates can locally dominate in deeper intervals, phosphates remain consistently minor, and most K is retained in detrital silicates. Establishing this mineralogical context is essential for evaluating how rare earth elements partition within the leachates and for assessing the extent to which their signatures reflect true weathering signals versus diagenetic or detrital overprints. In the following section, we therefore investigate REE distributions across the leached phases, quantify their contribution to the total sedimentary REE budget, and examine shale-normalized fractionation patterns to test the fidelity of HH leachates as archives of chemical weathering.

6.4. Contributions of different mineral phases to the HH leach REE pool and their impacts on distribution patterns and Nd isotopes

6.4.1. REE Budget

Although Fe-Mn oxides are the main extracted phase of the HH leach, the evidence for substantial leaching of carbonate phases and, to a lesser extent, of phosphate minerals calls for caution when interpreting REE and Nd isotopic data. Whether partial or complete, leaching of carbonate and phosphate can introduce important complexity into HH-derived data and requires careful mineralogical and geochemical consideration.

A first-order assessment of the relationships between ΣREE and the main potential REE hosts, represented by Fe, Mn, Ca, and P, provides an overview of these controls (**Fig. 6.9**). For comparison, we also added Amazon River samples. At first glance, the leached REE fraction of Amazon Fan sediments (expressed here as ΣREE) exhibits a poor relationship with Mn (R^2 = 0.0066) and Ca (R^2 = 0.0307), and a weak correlative trend with Fe (R^2 = 0.1178) and P (R^2 = 0.1977). In contrast, in Amazon River sediments, ΣREE correlates strongly with Fe (R^2 = 0.6374) and P (R^2 = 0.7148), reflecting the well-established scavenging of REE and P by Fe–Mn (oxyhydr)oxides (Slomp et al., 1996) and phosphate phases in controlling the fluvial REE pool. The ΣREE–Mn correlation is moderate (R^2 = 0.17), while the ΣREE–Ca relationship is weak (R^2 = 0.1802), suggesting that carbonates play only a minor role in controlling leached REE abundances in Amazon River sediments.

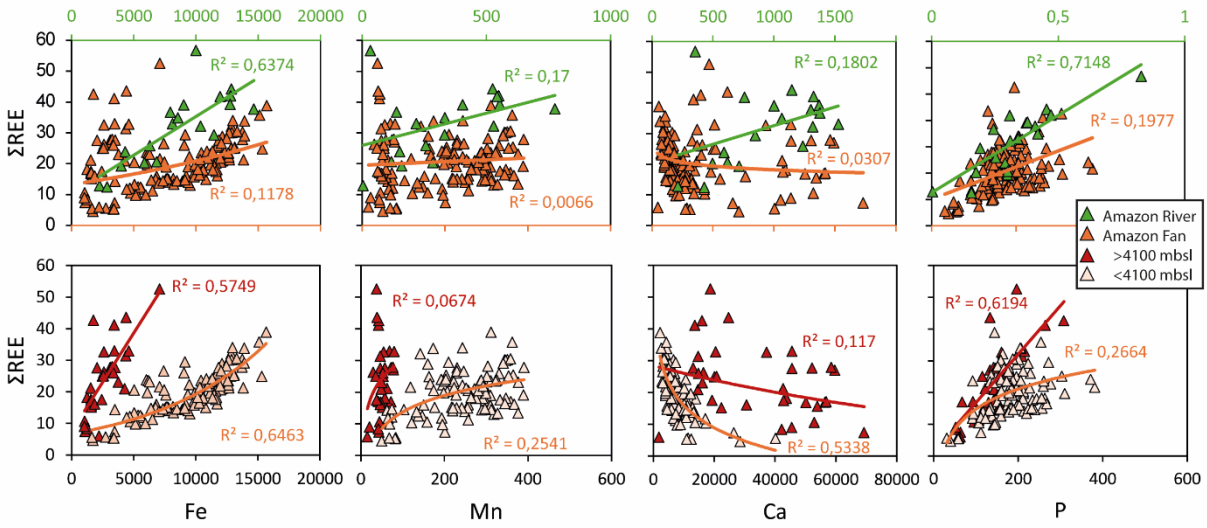

Figure 6.9. REE budget (ΣREE) as a function of Fe, Mn, Ca, and P in the HH leachates of the Amazon Fan. Upper panels show Amazon Fan and Amazon River HH leachates for comparison. Lower panels highlight the differences between Amazon Fan HH leachates recovered below and above 4100 mbsl.

However, clearer patterns emerge when the Amazon Fan dataset is split by depth. In sediments deposited above 4100 mbsl (light orange), ΣREE shows a strong positive correlation with Fe (R^2 = 0.6463) and a moderate relationship with Mn (R^2 = 0.2541), suggesting that Fe–Mn oxides dominate the REE pool in these intervals. In contrast, ΣREE exhibits a negative relationship with Ca, indicating that carbonate-rich intervals are not a source of REEs to the HH leachates. Instead, these phases dilute the overall REE budget. The ΣREE–P relationship is moderate (R^2 = 0.2664), suggesting only a limited contribution from phosphate phases. In deeper sediments deposited below 4100 mbsl (dark red), ΣREE continues to correlate strongly with Fe (R^2 = 0.5749) but shows almost no relationship with Mn (R^2 = 0.0674). The ΣREE–Ca relationship remains weak (R^2 = 0.117), reinforcing the minimal role of carbonates as REE sources. By contrast, the ΣREE–P relationship becomes the strongest in the dataset (R^2 = 0.6194), implying a more substantial proportional influence of phosphate phases on the REE pool at depth. Yet, the highest P concentrations do not always coincide with the highest ΣREE values, indicating that phosphate abundance alone cannot explain REE variability. The relationship between P and Fe (plot not shown) provides additional insight into the role of phosphate phases in the HH leachates. In both depth intervals, P and Fe show moderate positive correlations (R^2 = 0.3098 above 4100 mbsl; R^2 = 0.2917 below 4100 mbsl), suggesting that these two elements are not entirely independent within the leachable fraction. This co-variation may arise from the partial dissolution of phosphate minerals (Zhang and Shields et al., 2023), or from P adsorbed or co-precipitated onto oxide surfaces (Slomp et al., 1996). Such an association explains why phosphate phases can contribute to the REE budget without fully controlling it, and why high-P samples do not always correspond to the highest ΣREE values (**Fig. 6.9**). It also underscores that phosphate-related REE enrichment is frequently entangled with Fe–Mn–oxide contributions, making it difficult to isolate their respective roles based solely on elemental correlations.

The same constraints can be assessed for potassium (K), which may serve as a proxy for dissolution of K-bearing clay minerals (**Fig. 6.10**). In sediments above 4100 mbsl, ΣREE shows a moderate correlation with K (R^2 = 0.3906), while the relationship is stronger in deeper

sediments below 4100 mbsl (R^2 = 0.4486). This trend suggests that clays play a secondary but non-negligible role in the REE budget of Amazon Fan sediments. Importantly, the influence of K-bearing phases appears to increase with depth. Nevertheless, the weaker ΣREE–K correlations relative to those with Fe or P indicate that clays are unlikely to be the dominant REE host. Instead, they probably provide an additional retention pathway, either through adsorption onto exchange sites or through incorporation during secondary mineral transformations.

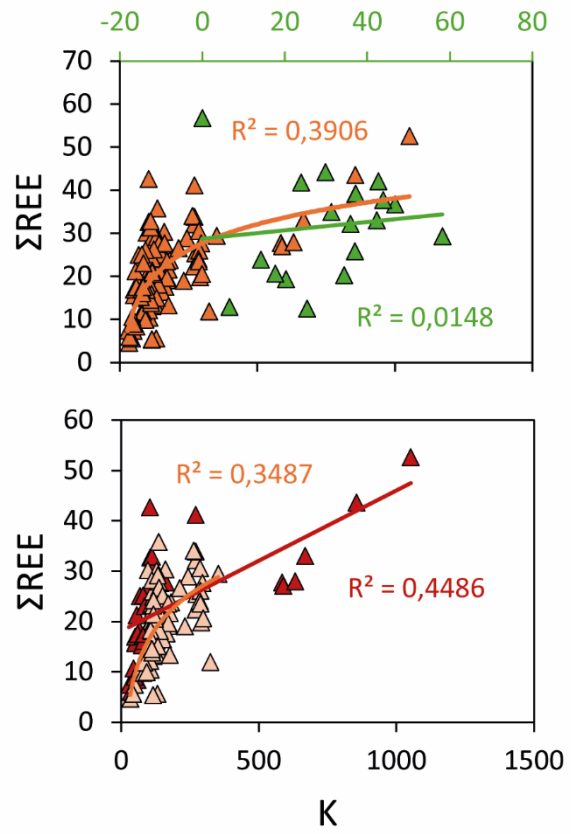

Figure 6.10. Relationships between ΣREE and potassium (K) in Amazon Fan sediments. (Top) Samples deposited above 4100 mbsl (light orange, green). (Bottom) Samples deposited below 4100 mbsl (dark red, dark orange). Linear regressions and corresponding coefficients of determination (R^2) are shown. ΣREE exhibits moderate correlations with K in shallower intervals and stronger correlations at depth, suggesting a secondary contribution of K-bearing clays to the leached REE pool.

Taken together, these results highlight the composite nature of the HH-leached REE pool. Above 4100 mbsl, the REE budget is largely governed by Fe–Mn oxides, with limited contributions from phosphates and clays. At greater depth, the REE pool reflects a more mixed control, with phosphate phases and K-bearing clays assuming greater importance alongside Fe oxides. This complexity underscores the need for caution when interpreting REE and Nd isotope signals from HH leachates, as multiple mineral hosts can contribute variably across depth and depositional contexts.

6.4.2. REE distribution patterns

Beyond elemental relationships, the shape of the REE pattern provides an additional lens to evaluate the influence of different mineral hosts. Samples deposited above 4100 mbsl consistently exhibit concave shale-normalized REE distributions, characterized by MREE enrichment (**Figs. 6.3A and 6.4A**). In contrast, samples deposited below 4100 mbsl show flatter LREE–MREE distributions and therefore a higher LREE/HREE fractionation. This difference is well illustrated by Nd_N/Yb_N ratios (**Fig. 6.11**).

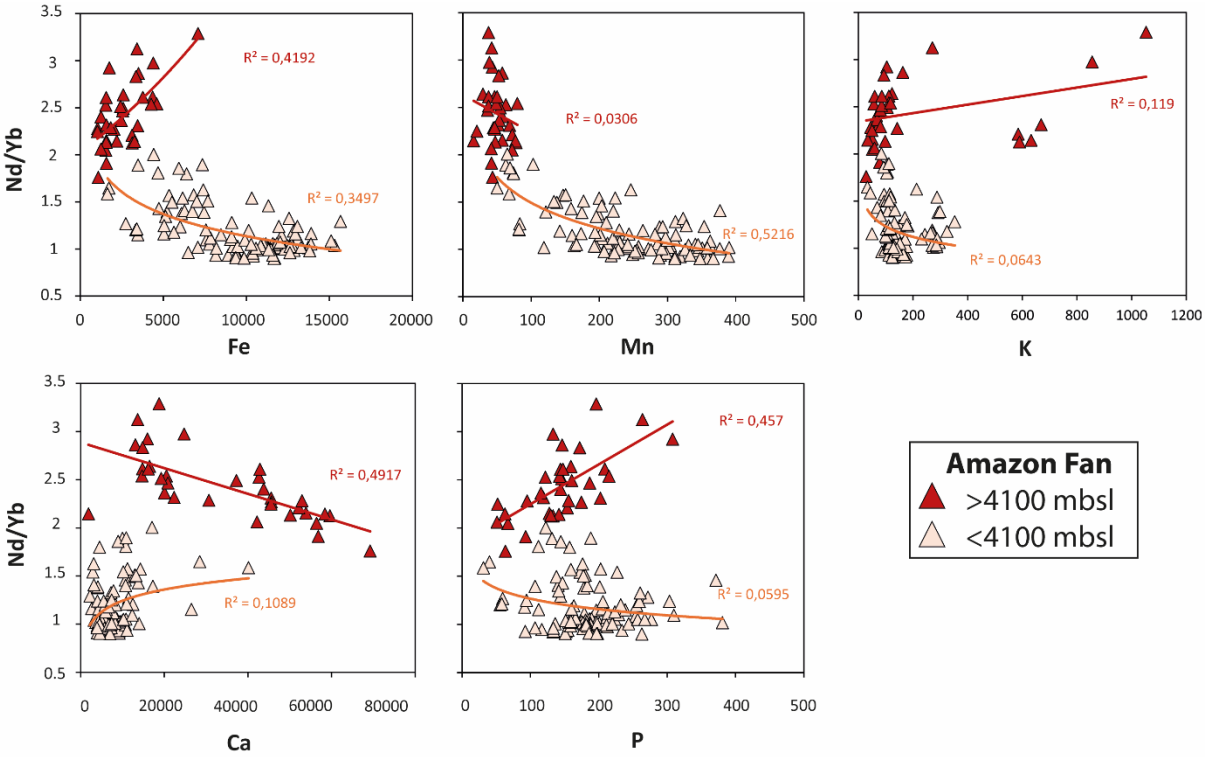

Figure 6.11. Nd/Yb fractionation as a function of Fe, Mn, Ca, P, and K in the HH leachates from the Amazon Fan. Linear regressions and corresponding coefficients of determination (R^2) are shown.

In deeper sediments, Nd_N/Yb_N correlates positively with Fe (R^2 = 0.4192) and P (R^2 = 0.457), suggesting that both Fe oxides and phosphate phases contribute to LREE enrichment relative to HREE. Conversely, Nd_N/Yb_N shows a negative relationship with Ca (R^2 = 0.4917), reinforcing that carbonate phases dilute rather than enhance the REE budget. In shallower sediments (<4100 mbsl), Nd_N/Yb_N is most strongly influenced by Mn (R^2 = 0.5216) and, to a lesser degree, Fe (R^2 = 0.3497). Here, higher Fe–Mn contents correspond to lower LREE/HREE fractionation, producing the characteristic MREE-enriched concave patterns. The relationship with K provides

additional nuance (**Fig. 6.11**). In shallow intervals, Nd_N/Yb_N shows almost no dependence on K (R^2 = 0.0643), consistent with the dominant role of Fe–Mn oxides in driving MREE uptake. By contrast, at depth, Nd_N/Yb_N exhibits a weak but positive correlation with K (R^2 = 0.119), suggesting that K-bearing clays may exert a secondary influence on LREE/HREE fractionation in older sediments. While the effect is less pronounced than that of Fe and P, the trend indicates that clays can subtly shape REE distributions, either through adsorption processes or through incorporation into secondary clay phases formed during diagenesis. Importantly, even within comparable P concentrations to deeper sediments, shallow HH leachates show limited LREE uptake, demonstrating that phosphate phases influence but do not fully control REE partitioning. In summary, with additional constraints from bulk geochemistry, clay mineralogy, and isotopic data (see next chapter), these results suggest that HH leachates capture major shifts in riverine provenance at 4100 mbsl. While Fe–Mn oxides remain the principal host of REEs throughout the record, phosphate contributions become proportionally more important at depth, and K-bearing clays provide a minor but detectable control, whereas carbonates consistently play no role in enriching the HH leachable pool.

6.4.3. La anomalies and their impact on the concativity index

Another striking feature of the HH leachates from sediments below 4100 mbsl is the development of pronounced Lanthanum (La) anomalies (La/La*; **Fig. 6.3B**). Given that the concavity index (CI), a sensitive parameter describing MREE enrichment relative to both LREE and HREE (Bayon et al., 2020), is calculated as:

$$Gd_N/(La_N^6 \times Yb_N^7)^{1/13}$$

Therefore, the presence of La anomalies has direct implications for interpreting MREE enrichment. First of all, La anomalies could partly reflect analytical artifacts, such as isobaric interferences from Ba (e.g., $^{138}BaH^+$ on $^{139}La^+$; Barrat et al., 2023). However, we don't observe any meaningful relationship between negative La anomalies and Ba concentration; therefore, plasma-induced isobaric interference can be discarded.

La anomalies are commonly observed in seawater and marine authigenic phases (e.g., Elderfield, 1988; Tostevin et al., 2016), although their origin remains debated. One possibility is

that they reflect the relatively higher stability of La in solution compared to other light REEs (De Baar et al., 1985; Byrne and Kim, 1990; Byrne et al., 1996). Another proposed mechanism involves the role of marine barite, which may participate in shaping La anomalies in seawater (Grenier et al., 2018). Indeed, positive La anomalies have been reported in barite (Hein et al., 2007). More recently, a series of studies has shown that biological processes may also fractionate LREEs. For instance, Pol et al. (2014), Picone and Op den Camp. (2019), Semrau et al. (2018), and Bayon et al. (2020a) documented (micro)biological influences on La behavior, while Wang et al. (2020) reported positive La anomalies in methanotrophic mussels from methane seep environments, which they attributed to enzymatic processes associated with aerobic methane oxidation. Collectively, these studies highlight that La anomalies may result from a combination of inorganic and biological processes, and under certain circumstances, can even serve as indicators of past microbial activity.

The Amazon Fan HH leachates display markedly different behaviors of La anomalies across depth intervals (**Fig. 6.12**). In the shallower sequence (<4100 mbsl, light orange), La/La* values cluster close to unity, with no strong correlations to Fe, Mn, Ca, P, or K ($R^2 < 0.1$ in all cases). In contrast, sediments deposited below 4100 mbsl (dark red) exhibit systematically negative La anomalies (La/La* < 0.7), which correlate strongly with major elements. The clearest trend occurs with Ca ($R^2 = 0.7226$), where La anomalies become progressively less negative as carbonate concentrations increase. This pattern reinforces that carbonates are not a direct REE source (as shown in ΣREE vs. Ca; **Fig. 6.8**) but may buffer La depletion by introducing seawater-derived signals or through diagenetic re-equilibration. Conversely, the relatively flat correlation with P/(Fe+Mn) indicates that La anomalies intensify with increasing oxide- and phosphate-bound REEs. A weak but consistent negative relationship with K ($R^2 = 0.0666$) suggests that K-bearing clays may also play a minor role, potentially by contributing to the diagenetic redistribution of REEs at depth.

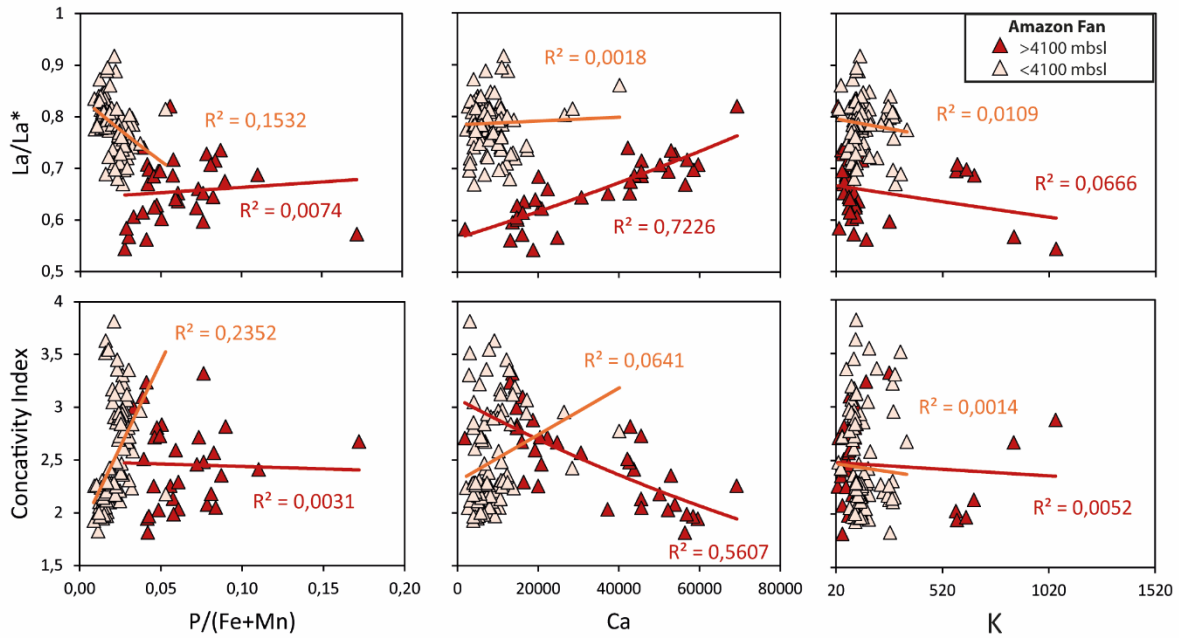

Figure 6.12. Lanthanum anomalies La/La* and the concativity index (CI) as a function of Fe, Mn, Ca, and P in the HH leachates from the Amazon Fan.

The occurrence of HH leachates exhibiting negative La anomalies below 4100 mbsl is unclear. The fact is that corresponding clay fractions also display anomalous shale-normalized REE patterns characterized by pronounced HREE depletion and also negative La anomalies (**Chapter V, Fig. 5.7**). These characteristics point towards possible clay authigenesis (Bayon et al., 2023), hence suggesting that intense diagenetic transformation may have disturbed pristine geochemical signals recorded in buried Fe-oxyhydroxides. Additionally, the observed relationships with Ca (and P) could indicate a contribution from shallower carbonate platform sediments. Although the direct cause of negative La/La* is not fully understood, these have direct implications for MREE quantification indices such as the concavity index (**Fig. 6.4B**). In the shallow interval, CI values remain relatively stable and show weak correlations with major elements, consistent with oxide-dominated REE pools. Below 4100 mbsl, however, CI exhibits a strong negative correlation with Ca (R^2 = 0.5607) and a moderate negative correlation with Fe (R^2 = 0.3097). This demonstrates that carbonate-rich intervals are associated with less negative La anomalies and, in turn, lower CI values, whereas higher oxide and phosphate contents amplify La depletion and artificially elevate CI. K also shows a weak inverse relationship with CI (R^2 = 0.0052), underscoring that clays exert only a very minor control on apparent MREE curvature.

In conclusion, while oxide phases dominate REE signatures in the upper Fan, the deeper interval reflects a complex interplay between oxide- and phosphate-bound REEs and carbonate buffering, with La anomalies exerting a disproportionate influence on REE curvature metrics. Careful screening of La anomalies is therefore essential before interpreting CI values, as apparent MREE enrichment may simply indicate La depletion rather than genuine mineralogical signals.

6.4.4. Nd Isotopes

Finally, to assess potential elemental controls on Nd isotopic compositions, we compared εNd(0) values in HH leachates against Fe, Mn, Ca, and P (**Fig. 6.13**). As with the fractionation patterns, the results reveal distinct depth-dependent behaviors. In the shallow interval (<4100 mbsl), εNd(0) values cluster around –10 and show only a weak positive relationship with P/(Fe+Mn) (R^2 = 0.1621) and virtually no correlation with Ca (R^2 = 0.0101). This suggests that phosphate phases exert only a minor isotopic influence in the upper Fan, while carbonates play no measurable role. In contrast, deeper sediments (>4100 mbsl) consistently record unradiogenic signatures around –20. Here, εNd(0) remains insensitive to P/(Fe+Mn) (R^2 = 0.0384) but exhibits a modest correlation with Ca (R^2 = 0.2337). These trends indicate that, at depth, Nd isotopes are overwhelmingly controlled by Fe-oxide–hosted Nd derived from old cratonic sources, while carbonate-rich intervals may slightly modulate the isotopic signal with a more seawater-like isotopic signature, without serving as a primary Nd reservoir.

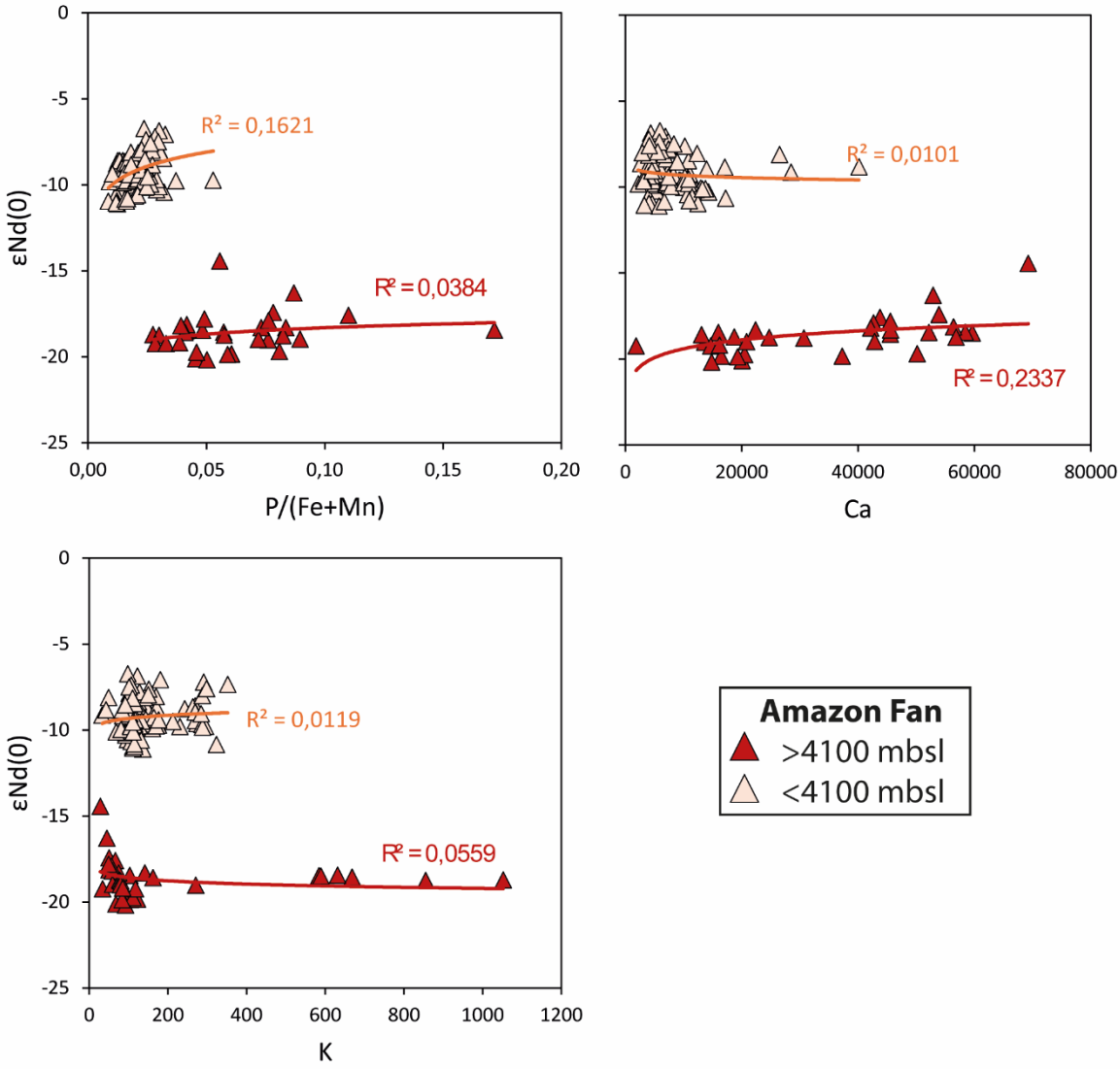

Figure 6.13. Neodymium isotopic compositions (εNd(0)) of Amazon Fan HH leachates plotted against P/(Fe+Mn) (left) and Ca concentrations (right). Open triangles represent samples from shallower intervals (<4100 mbsl), while filled triangles denote deeper intervals (>4100 mbsl).

6.5 Preservation of easily reducible FeOOH phases under anoxic conditions

The Amazon Fan has long been recognized as a highly reducing depositional environment, where labile Fe (oxyhydr)oxides should, in principle, be rapidly dissolved during early diagenesis (Michalopoulos & Aller, 2004). This expectation complicates the interpretation of Fe-leachate signals, as phases such as ferrihydrite or lepidocrocite are generally unstable under anoxic porewater conditions and are expected to either dissolve or transform into more stable mineral assemblages. Nevertheless, our results suggest that easily reducible FeOOH phases are not only preserved but remain relatively abundant throughout the record (**Fig. 6.7A**). One possible explanation lies in organo-mineral interactions. Lalonde et al. (2012) demonstrated that a significant fraction of sedimentary organic carbon is bound to reactive Fe phases, forming stable organo-ferric complexes that can inhibit microbial degradation and limit reductive dissolution. Likewise, Hemingway et al. (2019) showed that mineral protection is a globally coherent mechanism that extends the lifetime of both organic carbon and associated minerals. In the Amazon Fan, FeOOH% appears to covary with TOC in samples <4100 mbsl (**Fig. 6.14**), consistent with feedback in which organic ligands hinder FeOOH dissolution and recrystallization, while FeOOH provides binding surfaces that stabilize organic matter.

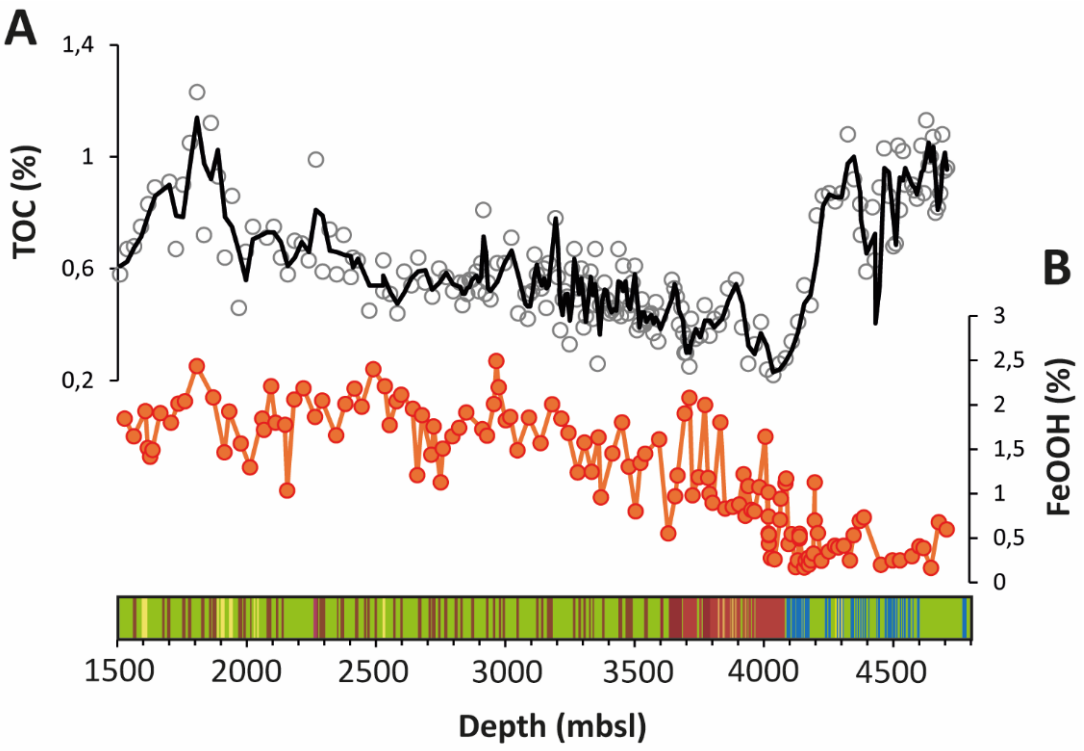

Figure 6.14. Downcore variations in **(A)** total organic carbon (TOC, %) and **(B)** FeOOH (%) in Amazon Fan sediments. Grey circles represent individual TOC measurements, with the black line showing a smoothed spline fit. TOC values are taken from the BP-3 well report, while FeOOH is expressed as weight percent of the bulk sediment.

Although this evidence points toward a dual protection mechanism, whereby organo-ferric associations promote the persistence of metastable FeOOH under strongly reducing conditions, this remains a working hypothesis. Further investigation is required to assess whether the observed covariation between FeOOH and TOC indeed indicate causal stabilization, or if other diagenetic or depositional factors contribute to their co-preservation. If confirmed, such associations would have important implications for the long-term preservation of reactive Fe phases and for the fidelity of Fe-leachates as provenance and weathering archives.

6.6. Conclusions

This chapter demonstrates that although the hydroxylamine hydrochloride (HH) leach is designed to target reactive Fe–Mn oxides, carbonate, detrital (loosely bound clay minerals), and minor phosphate phases can also contribute to the extracted pool. In the BP-3 Well, above 4100 mbsl, REE budgets in leached HH fractions are dominated by Fe–Mn oxides, producing concave, MREE-enriched patterns with minimal La anomalies, crustal-like Y/Ho ratios, and εNd values that closely resemble the modern Amazon River. Below 4100 mbsl, increased P concentration indicates that phosphate phases exert a stronger relative influence, La anomalies become systematically negative, and carbonate-rich intervals dilute REE concentrations while dampening concavity index artifacts. These depth-dependent differences are unclear but point towards diagenetic transformations, underscoring the need to evaluate mineralogical contributions when interpreting HH leachate signals.

Taken together, these observations highlight a clear depth dependency in REE systematics within Amazon Fan HH leachates. In the upper sequence (<4100 mbsl), REE distributions are tightly linked to Fe–Mn oxide scavenging, with only minor La-specific effects and stable concavity index values. By contrast, below 4100 mbsl, REE signatures become more complex: negative La anomalies, stronger correlations with Ca and P, and exaggerated CI values all point

to the increasing influence of carbonate and phosphate phases. Yet, the exact origin of these features remains uncertain. The fact that the corresponding clay fractions also show negative La anomalies and unusual HREE depletion suggests that diagenetic transformations, including possible clay authigenesis (e.g, Bayon et al., 2023), may have overprinted pristine oxide-bound signatures. Additional contributions from shallow carbonate platform material cannot be excluded. We therefore emphasize that interpretations of MREE enrichment and La anomalies in the deeper Fan should be treated with caution, as they may partly reflect diagenetic re-equilibration rather than primary continental inputs.

VII

Reconciling Neogene continental and marine records in the Amazon Basin

Declaration/ Declaração/ Déclaration

Determining the provenance evolution of Amazon Fan sediments is essential for tracing the silicate weathering signal back to its source regions. Previous studies at this site have provided important insights, but they were limited by low sampling resolution and a primary focus on constraining the timing of the onset of a transcontinental Amazon River. In this chapter, we revisit that event while placing greater emphasis on the subsequent evolution of the Amazon Basin after transcontinental drainage was established. To this end, we investigate the Nd isotopic evolution of the Amazon Fan and compare it with an extensive dataset of Nd isotopic signatures from across northern South America. The results and discussion presented here are being prepared for submission to *Earth-Science Reviews* in late October/November 2025.

[PT] Determinar a evolução da proveniência dos sedimentos do Leque do Amazonas é fundamental para rastrear o sinal do intemperismo de silicatos até suas regiões-fonte. Estudos anteriores neste local forneceram contribuições importantes, mas foram limitados por baixa resolução amostral e pelo foco principal em definir o momento do início do Rio Amazonas transcontinental. Neste capítulo, revisitamos esse evento, dando maior ênfase à evolução subsequente da Bacia Amazônica após o estabelecimento da drenagem transcontinental. Para isso, investigamos a evolução isotópica de Nd no Leque do Amazonas e a comparamos com um extenso conjunto de dados de assinaturas isotópicas de Nd em toda a região norte da América do Sul. Os resultados e discussões apresentados aqui estão sendo preparados para submissão à *Earth-Science Reviews* no final de outubro/novembro de 2025.

[FR} Déterminer l'évolution de la provenance des sédiments du cône sous-marin de l'Amazone est essentiel pour retracer le signal de l'altération des silicates jusqu'à ses régions sources. Les études précédentes menées sur ce site ont apporté des contributions importantes, mais elles étaient limitées par une faible résolution d'échantillonnage et se concentraient principalement sur la datation de la mise en place du fleuve Amazone transcontinental. Dans ce chapitre, nous revisitons cet événement tout en accordant une attention particulière à l'évolution ultérieure du bassin amazonien après l'établissement du drainage transcontinental. À cette fin, nous étudions l'évolution isotopique du Nd dans le cône de l'Amazone et la comparons à un vaste ensemble de données d'empreintes isotopiques du Nd provenant de l'ensemble du nord de l'Amérique du Sud. Les résultats et discussions

présentés ici sont en cours de préparation pour une soumission à *Earth-Science Reviews* à la fin octobre/novembre 2025.

Abstract

The emergence of the transcontinental Amazon River fundamentally reshaped South American landscapes, global sediment fluxes, and Neotropical biodiversity, yet its timing and mechanisms remain contested. Here we use rare earth element patterns and Nd isotopes of clays from the Amazon Fan (BP-3), anchored to a new astronomically tuned age model spanning the past 24 Myr. Our results identify the first sustained arrival of Andean-derived detritus at the Atlantic margin at 12.2 ± 1.3 Ma, substantially predating previous estimates. Mixing models resolve three isotopic stages of progressive drainage integration. Stage I (12.2–7 Ma) records embryonic Andean export dominated by Madeira-like sources, likely routed through southern bypasses around the Purus Arch. Stage II (6.9–4 Ma) marks a shift towards the radiogenic Nd signatures and enhanced Solimões input, reflecting partial capture of central Andean headwaters but still fragmented drainage. Finally, stage III (4–0.6 Ma) stabilizes into Solimões–Madeira dual dominance and high sedimentation, reflecting a mature transcontinental river system punctuated by short-lived perturbations from ~2.4–2.2 Ma following the onset of the Northern Hemisphere glaciation. These results reconcile long-standing discrepancies between continental and marine archives, demonstrating that the Amazon's transcontinentalization was a protracted, stepwise process shaped by tectonics, climate, and foreland dynamics.

7.1. Introduction

Submarine fans serve as important sedimentary archives that record past fluvial discharge, sea-level variations, ocean circulation, and long-term geodynamic and climatic changes (Clift et al., 2008). Notably, the submarine Amazon Fan, situated at the mouth of the Amazon River, is among the world's largest deep-sea sedimentary systems (approximately 375,000 km^2; **Fig. 7.1**; Figueiredo et al., 2009). It accumulates substantial volumes of terrigenous sediments and organic matter transported from the Amazon Basin (**Fig. 7.1A,B**; Cruz et al., 2019; Gorini et al., 2014), making it a long-term sink for terrestrial organic carbon on geological timescales (Hage et al., 2022).

Since its inception, the Amazon Fan has served as the primary depocenter for sediment transported along the Brazilian Equatorial Margin (Figueiredo et al., 2009; Gorini et al., 2014; Hoorn et al., 2017), accumulating tremendous amounts of terrigenous material transported from the Amazon Basin. The development of the Amazon Fan is commonly linked to the establishment of an east-flowing transcontinental drainage system, marked by the arrival and sustained delivery of Andean-derived sediments to the Brazilian Equatorial Margin (Figueiredo et al., 2009; Hoorn et al., 2017; van Soelen et al., 2017). The timing of this transition, however, remains highly debated, with estimates ranging from the Early Miocene to as late as the Pleistocene, depending on whether evidence derives from continental (Campbell et al., 2006; Cremon et al., 2016; Horbe et al., 2019, 2013; Jaramillo et al., 2017; Nogueira et al., 2013; Rossetti et al., 2015) or marine sedimentary archives (Dobson et al., 2001; Figueiredo et al., 2009; Gorini et al., 2014; Heinrich and Zonneveld, 2013; Hoorn et al., 2017; Lammerstma et al. 2018). Nonetheless, the large-scale drainage reorganization that produced this system, and its subsequent evolution into the modern Amazon, remains incompletely resolved.

Several key uncertainties continue to complicate basin-scale reconstructions, including: widespread development of wetlands (Hoorn et al., 2022, 2010) with growing evidence of marine incursions in Western Amazonia during the Miocene (MMI; **Fig. 7.1A**; (Jaramillo et al., 2017; Leandro et al., 2022; Salamanca Villegas et al., 2016), the role of structural arches on preventing basin-wide connectivity (Figueiredo et al., 2009; Rossetti et al., 2023), continuous uplift events across northern South America (Horton, 2018; Japsen et al.,

2025; Moizinho et al., 2024), and the absence of a substantial increase in Amazon Fan sedimentation rates until the Pliocene (**Moizinho et al. 2026**; Figueiredo et al., 2009). Together, these factors underscore the complexity of constructing integrated models of Amazon Basin evolution, particularly regarding the chronology of continental-scale drainage integration and the sediment-routing pathways involved (e.g., Albert et al., 2021; Sacek, 2014; Sacek et al., 2023).

Rare earth elements (REEs) and Nd isotopes are widely used provenance tracers owing to their coherent behavior during weathering, transport, and sedimentation (Bayon et al. 2015; Tiper et al., 2025). In detrital sediments, REE distribution patterns help constrain the nature of the source rocks, while εNd values differentiate inputs from old cratonic sources (e.g., the Amazonian Craton or reworked Phanerozoic sediments) versus more juvenile, radiogenic sediment contributions (e.g, Mesozoic volcano-sedimentary sequences from the Andes). Over the past decades, these geochemical tracers have been extensively applied to provenance studies across the Amazon source-to-sink system (Custódio et al., 2024; Figueiredo et al., 2009; Hoorn et al., 2017; Höppner et al., 2018; Hurtado et al., 2018; Louterbach et al., 2018; Moizinho et al., 2024, 2022; Roddaz et al., 2021, 2014, 2005; Rodrigues et al., 2023; Rousseau et al., 2019; van Soelen et al., 2017; Viers et al., 2008).

Here, we analyze 91 sediment samples from cuttings recovered in the BP-3 industry well (3°02'58.660" N, 47°44'45.801" W; 754 mbsl), drilled in the upper Amazon Fan. Located at the main depocenter of the Brazilian Equatorial Margin since the Early Miocene (Rouby et al., 2022), BP-3 preserves one of the most continuous Neogene archives of Amazon Fan sedimentation and has been widely referenced in previous studies (Figueiredo et al., 2009; Hoorn et al., 2017; Lammerstma et al., 2018; Gorini et al., 2014; Reis et al., 2016; Souza et al., 2020, 2025). In this study, we present new clay mineralogical data together with REE concentrations and Nd isotopic compositions from separated clay fractions. These results are integrated with previously published datasets from BP-3, anchored to a newly developed astronomically tuned age model (Moizinho et al., 2025), and further compared with a broad suite of continental archives from northern South America (**Fig. 7.1**). Collectively, they refine constraints on the timing of the onset of the transcontinental Amazon River and shed new light on sediment-routing dynamics across the Earth's largest watershed, with implications for geodynamic reorganizations, climatic shifts, and biotic exchanges since the Late Miocene.

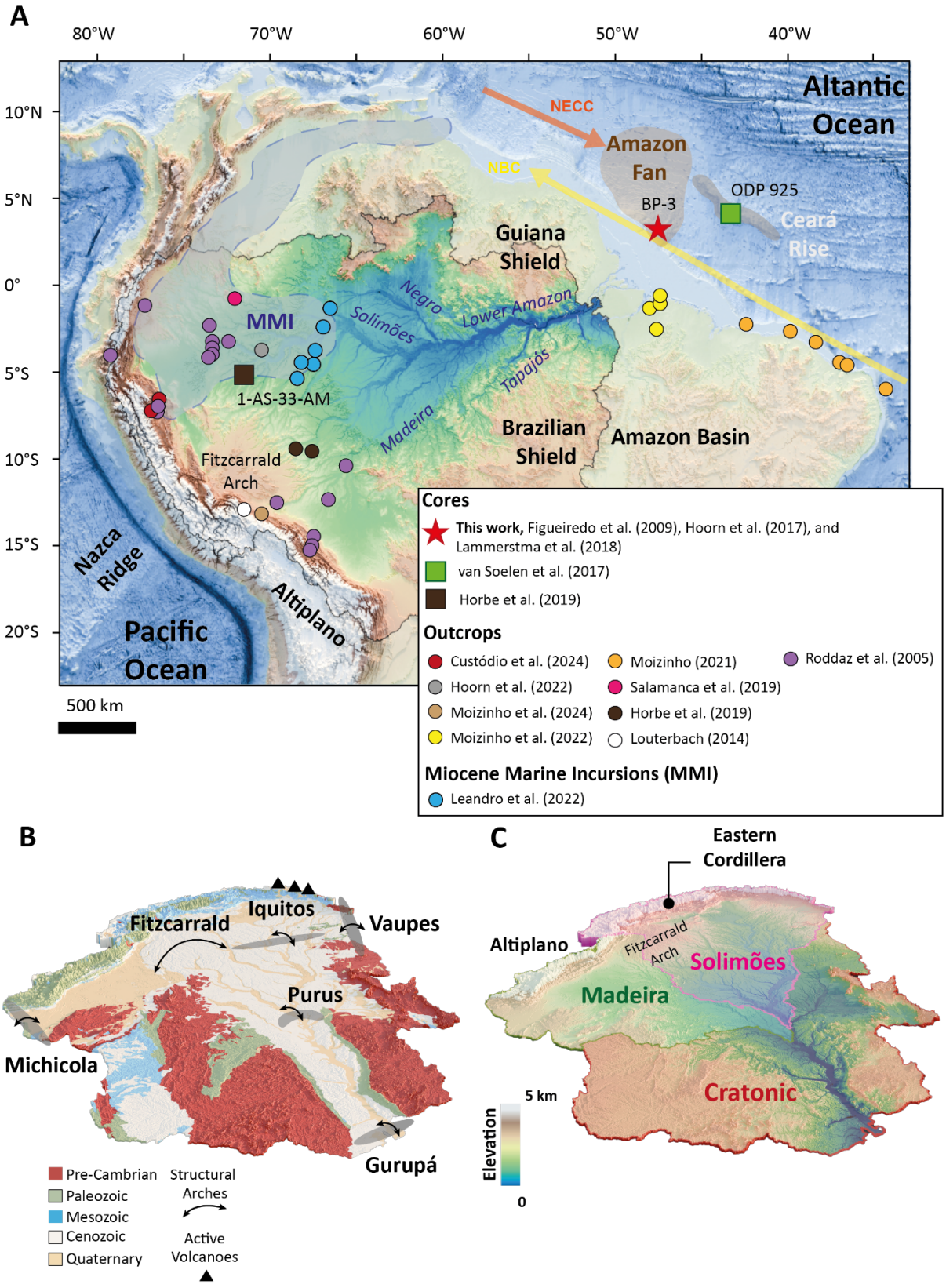

Figure 7.1. (A) Physiographic map of the Amazon Basin showing major tectonic features and topographic domains, including the Fitzcarrald Arch, Pastaza–Marañon Basin, and areas influenced by Miocene marine incursions (MMI; Jaramillo et al., 2017; Leandro et al., 2022). **(B)** Location of the Amazon Fan along the Brazilian Equatorial Margin with the BP-3 exploration well (this study) and ODP Leg 154 site 925 (white circle), showing the main outflow of

the Amazon and Pará rivers, the North Brazil Current (NBC), and the North Equatorial Counter Current (NECC). **(C)** Simplified geological map of northern South America highlighting the main lithotectonic provinces of the Amazon Basin and surrounding shields, foreland, and intraplate basins, as well as major structural arches and the Nazca Ridge (after Roddaz et al., 2005; Espurt et al., 2007). **(D)** Simplified subdivision of the Amazon Basin into the three main geochemical domains (Solimões, Madeira, Cratonic) used in this study, based on differences in lithology, weathering regime, and isotopic signatures (Viers et al., 2008; Moquet et al., 2011; Chapter III).

7.2. Results and Discussion

1.4.1. Onset of Andean sediment supply in the Amazon Fan

From the Amazon Fan's perspective, the establishment of the transcontinental drainage system in the Amazon Basin has long been debated. Early estimates based on extrapolated sedimentation rates suggested an onset between 16.5 and 8.0 Ma (Damuth et al., 1977), later refined to 11.8–10.0 Ma through seismic, biostratigraphy, and isotopic correlations (Figueiredo et al., 2007, 2009), and more recently to ~9.4–9.0 Ma (Hoorn et al., 2017). This transcontinentalization event has been interpreted as the merging of two previously disconnected river systems, one in eastern Amazonia and the other in western Amazonia (Hoorn, 1994, 2017; Wesselingh, 2006; Figueiredo et al., 2009), yet the why and how this event took place is still unclear (see discussion in the next section). Previous works have suggested that the Purus Arch, a prominent structural high in Central Amazonia, may have acted as a critical barrier preventing the eastern drainage from connecting to the Western Amazon Basin until the late Miocene (Figueiredo et al., 2009; Hoorn et al., 2010, 2017; van Soelen et al., 2018).

Our new data show that prior to 12.2 (± 1.3), detrital clays delivered to the BP-3 site were dominated by kaolinite (**Chapter V, Fig. 5.4, 7.3A**) and displayed WRAS-normalized REE patterns characterized by LREE enrichment over MREE and HREE (**Fig. 7.2**), an overall distribution consistent with clay derived from rivers draining igneous/metamorphic terrains (Bayon et al., 2015). It is important to mention that all of the samples on this interval are anomalously depleted in LREE in relation to WRAS. These patterns are comparable to those observed in glauconitic pellets formed by marine authigenesis on the Congo shelf (Bayon et al., 2023), raising the possibility that early fan sediments incorporated an authigenic component (**Chapter VI**). While such processes may modify the REE distribution pattern of the resulting clay assemblages, the underlying fluvial Nd isotopic signal still remained preserved due to the

comparatively very low Nd contents of ambient pore waters (Bayon et al., 2023). During this phase, $\varepsilon Nd(0)_{clay}$ values were consistently unradiogenic (−19.1 ± 1.8 (2σ), n = 24; **Chapter VI; Fig., 7.3B**), clearly pointing towards a dominant cratonic provenance. Modern analogues are provided by the Maroni, Negro, and Tapajós rivers, which drain the Brazilian and Guiana shields in eastern Amazonia, and whose suspended and dissolved loads are likewise dominated by craton-derived clays (**Chapter III**; **Fig. 7.2**; Höppner et al., 2018; Viers et al., 2008; Rousseau et al., 2019). Therefore, our data reinforces the interpretation that the BP-3 site prior to 12 Ma was mainly supplied by a riverine system exclusively draining cratonic domains in Eastern Amazonia (**Fig. 7.4**).

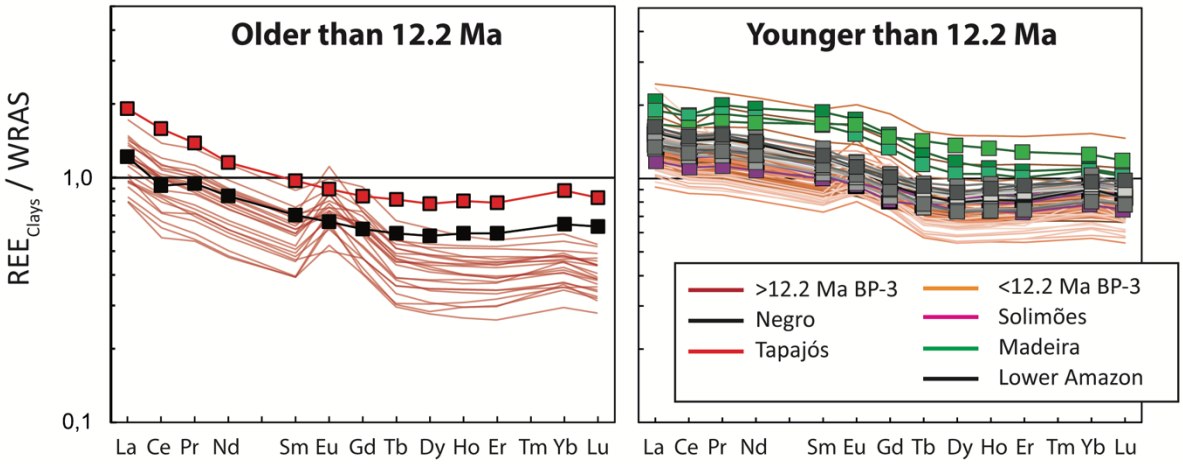

Figure 7.2. WRAS-normalized REE distribution pattern for the clay and FeOOH fractions of BP-3 and modern Amazon Basin sediments. Please note that REE distribution for FeOOH Is also normalized to Gd to avoid dilution effects.

At 12.2 ± 1.3 Ma, however, a marked provenance shift occurs at the BP-3 site. Clay mineralogy transitions from kaolinite to illite+chlorite dominated assemblages, reflecting the input of freshly eroded detritus (**Fig. 7.3A**). The REE distribution patterns show LREE and MREE enrichment and flat HREE distributions, characteristic of large river basins draining diverse lithologies (Bayon et al., 2015). In parallel, εNd(0) values rise sharply (+ 7 ε units), reaching a significantly more radiogenic signature (**Fig. 7.3B**). These geochemical changes coincide with a major increase in fluvial input (Lammertsma et al., 2018) and pollen assemblages with Andean taxa (Hoorn et al., 2017) in the BP-3 (**Fig. 7.3C**), reflecting the westward expansion of the Amazon Basin and capture of *white-water* fluvial systems carrying Andean-derived sediments that once were restricted to Western Amazonia (Albert et al., 2018, 2021).

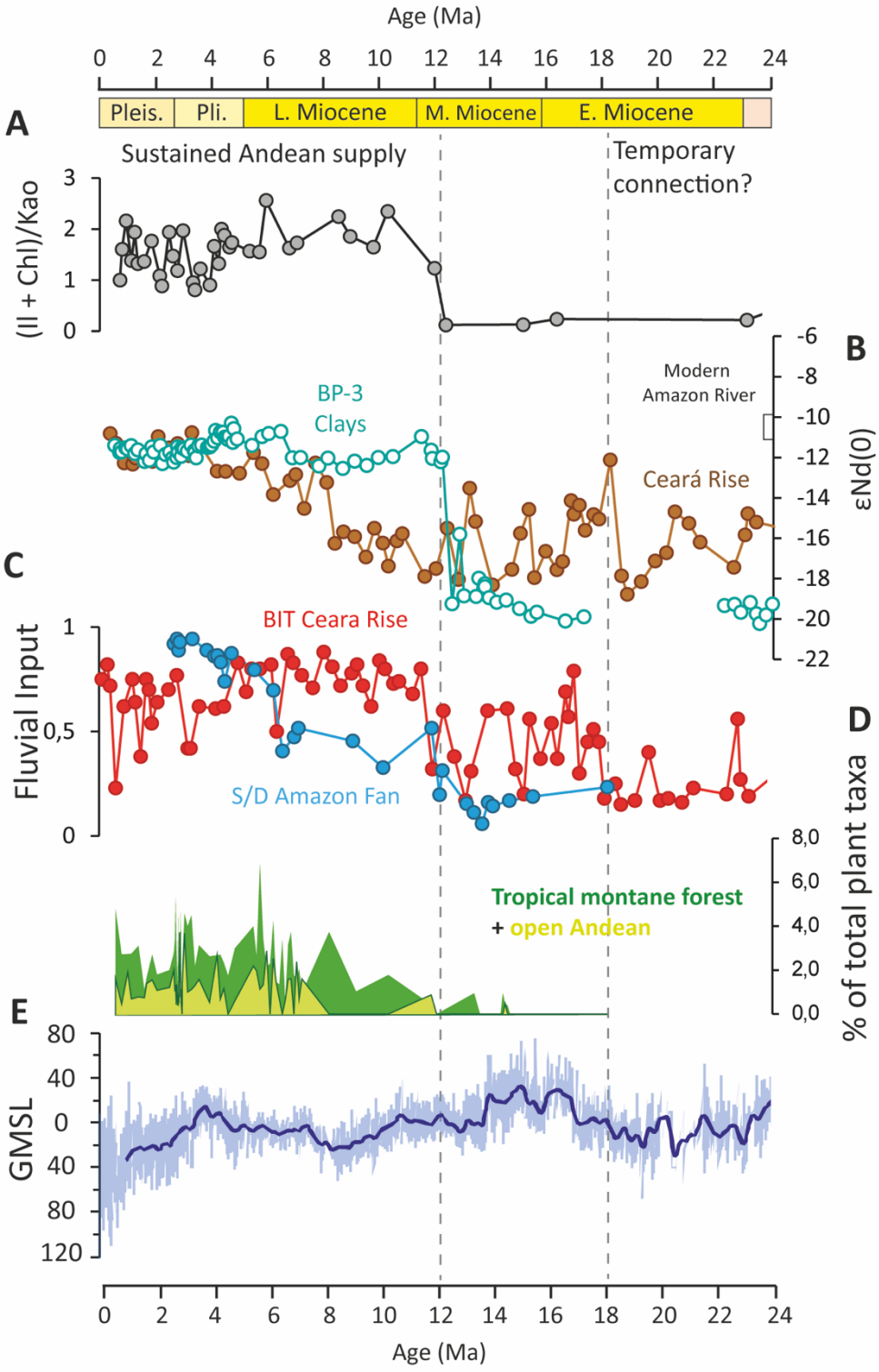

Figure 7.3. Multiproxy records from the Amazon Fan and Ceará Rise documenting the timing of transcontinental Amazon River establishment. (A) Clay mineral assemblages showing the ratio of illite+chlorite to kaolinite (Il+Chl/Kao) in the Amazon Fan. **(B)** εNd(0) values for Amazon Fan clays (black), Amazon Fan FeOOH leachates (red), and comparison with Ceará Rise sediments (brown; van Soelen et al., 2017) and the modern Amazon River range (color bar; Chapter III). **(C)** Fluvial input proxies from the Ceará Rise (BIT index, red; van Soelen et al., 2017) and Amazon Fan (S/D ratio, blue; Lammerstma et al., 2018). **(D)** Palynological record showing percentages of tropical montane forest and open Andean taxa (Hoorn et al., 2017). **(E)** Global mean sea-level variations (Miller et al., 2020).

Our new chronology predates the widely cited ~9.4–9.0 Ma biostratigraphic estimate and tightens the previously proposed 16–10 Ma window for the first arrival of Andean sediment to the Amazon Fan. In doing so, it establishes a clearer temporal framework for the onset of Andean influence along the Brazilian Equatorial Margin and for evaluating how river integration unfolded at the basin scale. At the same time, we cannot rule out older, short-lived episodes of Andean sediment export routed through alternative or transient pathways. More radiogenic Nd isotopic compositions reported from the Ceará Rise at ~18 Ma (ODP Site 925; **Fig. 7.3B**; Dobson et al., 2001; van Soelen et al., 2017) hint at such a possibility. However, this particular time interval coincides with a 22–17.7 Ma hiatus in the BP-3 records (Moizinho et al., 2026), which precludes direct testing of whether an early Miocene pulse may have reached the fan itself. These signals occurred during a time when global mean sea level was substantially lower, on the order of ~40 m below present (**Fig. 7.3E;** Miller et al., 2020), favoring shelf exposure and glacio-eustatically driven valley incision. Such conditions could have temporarily linked portions of western and eastern Amazonia, enabling episodic bypass of cratonic sinks and short-lived export of Andean-sourced material to the Equatorial Atlantic. As the sea level rose and accommodation was re-established on the shelf, the radiogenic fingerprint would be expected to wane, consistent with the transient nature of this mechanism. Crucially, beyond these potential brief connections, our record demonstrates that the sustained and continuous delivery of Andean material to the Amazon Fan at 12.2 ± 1.3 Ma. This timing supports a mid-Miocene consolidation of a through-going, transcontinental Amazon River and significantly reduces the uncertainty surrounding when persistent Andean provenance became established. By distinguishing between ephemeral lowstand pathways and the onset of continuous Andean supply, these results provide a sharper chronological anchor for integrating marine and continental records of Amazon Basin evolution.

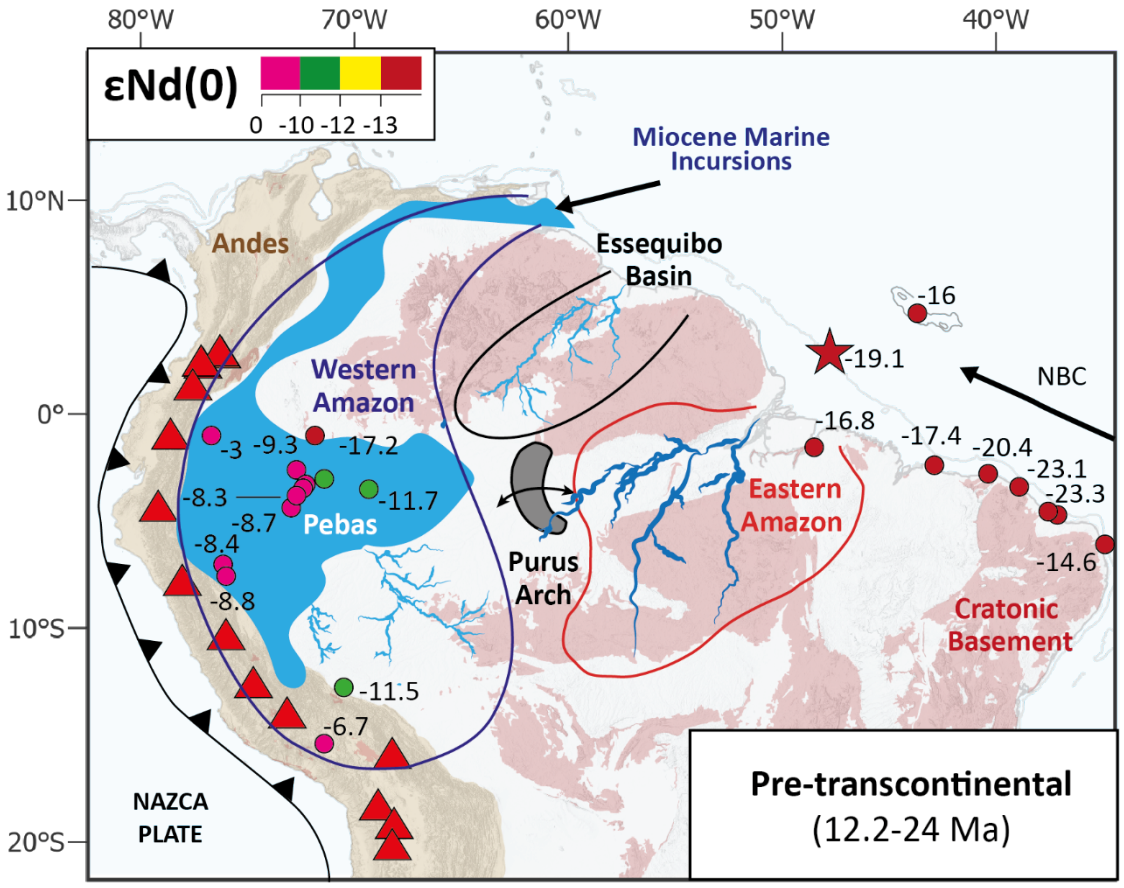

Figure 7.4. Nd isotopic signatures (εNd(0)) and drainage configuration before sustained Andean sediment reached the Atlantic. The Amazon Fan site (BP-3; red star) records highly unradiogenic values (−19.1), reflecting exclusive cratonic input from eastern Amazonia. Offshore Ceará Rise sediments (−16) also indicate shield-derived sources, while western Amazonia shows more radiogenic values (−3 to −9), confined within foreland depocenters and Miocene wetlands. Marine incursions further enhanced west–east compartmentalization. This phase reflects a segmented basin with the Purus Arch acting as a persistent divide that prevented Andean detritus from reaching the margin.

1.4.2. Stages of a transcontinental Amazon Fan

The establishment of a transcontinental Amazon River left an indelible mark on the provenance signatures preserved in the Amazon Fan. Downcore variations in clay isotopic compositions capture not only the timing of the arrival of Andean detritus to the Atlantic margin, but also the progressive reorganization of sediment-routing pathways within the Amazon Basin since the Late Miocene. To quantify these changes, we applied a three-endmember mixing model that integrates both εNd and Sm/Nd compositions of fine-grained sediment sources across the basin (**Fig. 7.5**). For the Andean sources, we used clay compositions from the Solimões and Madeira rivers (see **Chapter III**), which today represent the two principal tributaries delivering sediment from the central and southern Andes, respectively. As a cratonic counterpart, we adopted values from Amazon Fan clays older than 12.2 Ma, which have consistently been interpreted as reflecting a purely cratonic supply prior to the onset of transcontinental drainage integration (see the above discussion; Figueiredo et al., 2009; Hoorn et al., 2017). This approach allows us to decompose the provenance evolution of the Amazon Fan into three main isotopic stages, each reflecting distinct phases in the development of the basin's sediment-routing system (**Fig. 7.6**).

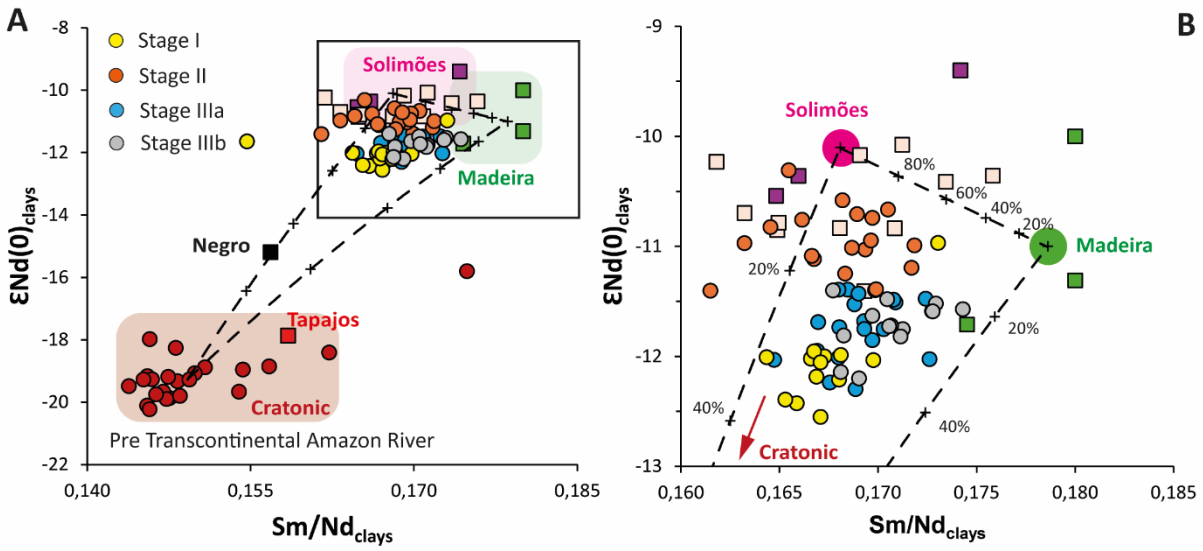

Figure 7.5. Mixing model results constraining the stepwise integration of Andean and cratonic sources into the Amazon Fan. **(A)** Cross-plot of $\varepsilon Nd(0)_{clays}$ versus Sm/Nd_{clays} showing Amazon Fan samples from three isotopic stages (Stage I–III; colored circles) compared with modern river endmembers (squares: Negro, Tapajós, Solimões, Madeira) and pre-transcontinental Amazon Fan sediments (red field). **(B)** Mixing polygons illustrating relative contributions from Solimões, Madeira, and cratonic sources; dashed lines represent modeled mixing trajectories.

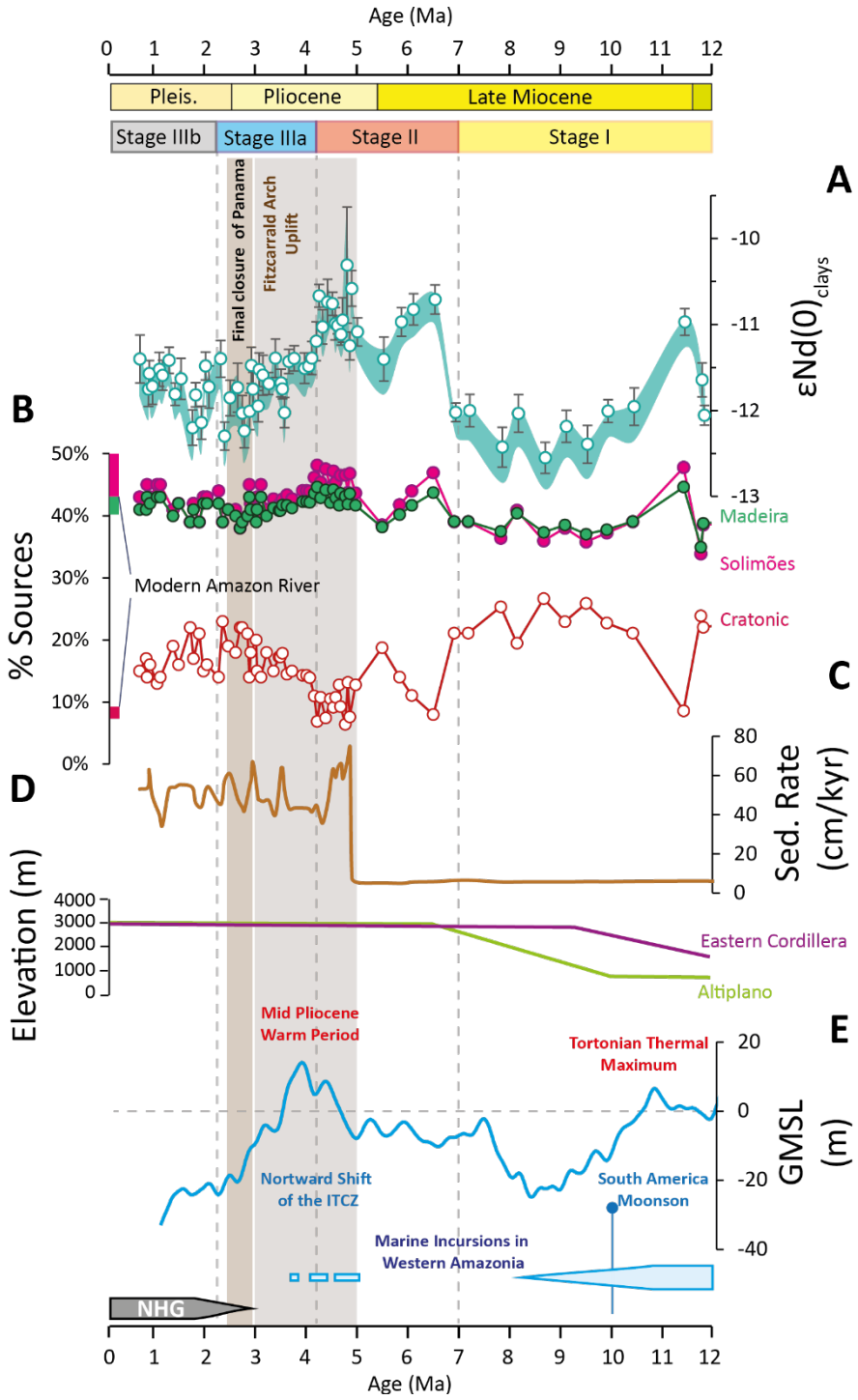

Figure 7.6. Multiproxy reconstruction of Amazon Fan provenance and drainage evolution over the last 12 Myr. **(A)** εNd(0) values of detrital clays, with fields indicating modern Solimões, Madeira, and Lower Amazon River signatures. **(B)** Contributions of analogues to modern Solimões, Madeira, and Cratonic sources. **(C)** Amazon Fan sedimentation rates (Moizinho et al., 2026). **(D)** Global mean sea level (GMSL; Miller et al., 2020), events of Miocene (MMI) and Pliocene Marine influences in Western Amazonia (Leandro et al., 2022), and the onset of the Northern Hemisphere Glaciation (NHG; Bartoli et al., 2005). Colored bars on top highlight three isotopic stages defined in this study: Stage I (12.2–7 Ma), Stage II (6.9–4.1 Ma), and Stage III (4.0–0.6 Ma). Key geodynamic events are highlighted by shaded areas, including: Altiplano (Boschman et al., 2021) and Fitzcarrald Arch (Espurt et al, 2005, 2009) uplifts, and the final closure of the Panama Isthmus (Bartoli et al., 2005)

Stage I (12.2–7 Ma) is characterized by $\varepsilon Nd(0)_{clay}$ values between −12.7 and −11.8 (Figs. 7.5 and 7.6), which indicate a mixed provenance. End-member mixing model results suggest a substantial cratonic contribution (~22%) coexisting with near-equal proportions from Solimões (~39%) and Madeira (~39%) sources (**Fig. 7.6B**). The persistence of the cratonic component during this interval suggests that, although Andean input dominated the sediment budget exported to the Atlantic Ocean, sediment routing was still strongly influenced by long-lived cratonic tributaries. This balance reflects the embryonic phase of a transcontinental drainage system, when Andean detritus was first delivered to the Equatorial Margin but had not yet established full dominance over the sediment budget.

The second stage (7–4 Ma) is marked by the most radiogenic $\varepsilon Nd(0)_{clay}$ values in the entire record (−11.2 to −10.5; **Fig. 7.6A**), which approach modern Amazon Fan compositions (−10.5; Bayon et al., 2015). Mixing model outputs reveal a sharp reduction in cratonic input (~11%) and a slight predominance of Solimões-like sources (~45%) over Madeira (~42%; **Fig. 7.6B**). This shift signals a critical reorganization of the drainage network, with Andean tributaries taking bigger control of sediment delivery to the Atlantic. The isotopic convergence with modern values strongly suggests that by this time the Amazon River had reached a configuration broadly similar to today, with Andean sediment supply dominating over cratonic inputs.

Stage III, the final stage in our record, spans from 4 to 0.6 Ma and is subdivided into two distinct phases: Stage IIIa and Stage IIIb (**Fig. 7.6**). Stage IIIa is characterized by a strong declining trend in $\varepsilon Nd(0)_{clays}$, until circa 2.4Ma. Mixing model results indicate that this evolution correlates with a progressive increase in cratonic contributions (**Fig. 7.6B**). The transition between Stage IIIa and IIIB is marked by a short-lived but coherent perturbation between 2.4 and 2.2 Ma, where $\varepsilon Nd(0)_{clays}$ shift to more radiogenic values. After that, in Stage IIIb, all three proxies shift toward higher values, converging toward the modern Amazon River range (**Fig. 7.6**). This evolution highlights the resilience of the Andean signal despite periodic fluctuations in cratonic supply, pointing to a fully consolidated sediment-routing system by the mid-Pleistocene.

Overall, our Nd isotopic record from the Amazon Fan demonstrates that Andean-derived sediments have overwhelmingly dominated fine-grained delivery to the Brazilian Equatorial Margin since the Late Miocene. More importantly, the record captures not only the onset of sustained Andean input, but also subsequent reorganizations in source contributions that

reflect broader tectonic, geomorphic, and climatic forcings. In the following section, we situate these findings within a wider paleogeographic, geodynamic, and paleoclimatic context. By integrating our isotopic record with an astronomically tuned age model and comparing it to compiled Neogene Nd isotopic data from across northern South America (**Table 7.1**), we highlight how Andean uplift, foreland basin dynamics, and global climate shifts jointly shaped the long-term evolution of the world's largest river system.

Table 7.1. Compilation of Nd isotopic composition for Late Neogene sedimentary deposits in Northern South America. SAZ: Sub Andean Zone; BEM: Brazilian Equatorial Margin. The data from Miriam (2018) and Moizinho (2021) are from their Master's degree dissertations.

Epoch	Western Amazonia				Eastern Amazonia				Marine/Coastal Records			
	Sed. Basin	Lith. Unit	εNd(0)	Ref.	Sed. Basin	Lith. Unit	εNd(0)	Ref.	Sed. Basin	Lith. Unit	εNd(0)	Ref.
Pleistocene												
					Marajó	Post Barreiras Fm.	-17.4 (n=2)	*Moizinho et al. (2022)*	Amazon Fan	Orange Fm.	-10.8 (n=5)	*Figueiredo et al. (2009) and Hoorn et al. (2018)*
									Ceará Rise	n/a	-11.6 (n=11)	*van Soelen et al. (2017)*
Pliocene												
	Madre de Dios	Madre de Dios Fm.	-11.8 (n=1)	*Moizinho et al. (2024)*					Amazon Fan	Orange Fm.	-9.2 (n=3)	*Figueiredo et al. (2009) and Hoorn et al. (2017)*
	Iquitos Forebulge	Amazon Fm.	-5.8 (n=3)	*Roddaz et al. (2005)*					Ceará Rise	n/a	-11.9 (n=6)	*van Soelen et al. (2018)*
		Nauta Member	-9.8 (n=2)	*Roddaz et al. (2005)*					BEM	n/a		Moizinho (2021)
		White Sand Fm.	-13 (n=2)	*Roddaz et al. (2005)*								*Miriam (2018)*
Late Miocene												
	Solimões	Iça Fm.	-9.5 (n=15)	*Horbe et al. (2019)*	Marajó	Barreiras Fm.	-17.5 (n=2)	*Moizinho et al. (2022)*	Amazon Fan	Orange Fm.	-12 (n=11)	*Figueiredo et al. (2009) and Hoorn et al. (2017)*
	Acre	Solimões/Pebas Fm.	-9.6 (n=11)	*Horbe et al. (2019)*					Ceará Rise	n/a	-14.7 (n=18)	*van Soelen et al. (2018)*
	Beni SAZ	SAZ Terranes	-10.4 (n=2)	*Roddaz et al. (2005)*					BEM	n/a		Moizinho (2021)
	Beni-Marmore	Iñapari Fm.	-11.8 (n=2)	*Roddaz et al. (2005)*								*Miriam (2018)*
	Beni-Marmore	Madre de Dios Fm.	-12.5 (n=1)	*Roddaz et al. (2005)*								
	Iquitos Forebulge	Solimões/Pebas Fm.	-10.3 (n=5)	*Roddaz et al. (2005)*								
	Madre de Dios	Madre de Dios Fm. (Inambari)	-12.3 (n=3)	*Moizinho et al. (2024)*								
	Madre de Dios	Madre de Dios Fm. (Punquiri)	-10.2 (n=2)	*Roddaz et al. (2005)*								

1.4.3. Reconciling continental and marine records of basin evolution

Stage I (12.2 – 7 Ma) – Embryonic transcontinental system

The upper Amazon Fan record shows the first sustained Andean input by ~12.2 Ma, marking the embryonic phase of a transcontinental system (**Fig. 7.7**). This phase would be the equivalent of the *"Acre"* phase proposed in previous basin reconstructions (e.g., Albert et al., 2019; Hoorn et al., 2010). Our mixing model (**Section 4**) indicates near equal proportions from Solimões and Madeira-like, alongside persistent cratonic sources, resulting in an average -12 $\varepsilon Nd(0)_{clay}$ isotopic signature at the BP-3 site (**Fig. 7.7,** yellow star). Comparable isotopic values are observed in coeval successions of the South Andean Foreland Basins (SAFB), such as Madre de Dios and Beni (Louterbach et al., 2014; Roddaz et al., 2005; Moizinho et al., 2024; **Table 7.1**).

By contrast, central Amazonian records paint a different picture. Late Miocene/Pliocene sediments deposited near the Iquitos Forebulge (**Fig. 7.1C and 7.7**) show significantly more radiogenic εNd(0) values (~−9; **Fig. 7.6A**; Roddaz et al., 2005), while the deposits of the Solimões Formation (west of the Purus Arch) record different signatures, depending on which intracratonic basin the samples were recovered from. In the eastern limit of the Solimões Basin, near the west flank of the Purus Arch, the Solimões Formation shows westward-directed paleoflow, cratonic zircon ages, and only sparse Andean palynomorphs (Dino et al., 2012; Nogueira et al., 2013; Mapes, 2009). On the other hand, borehole samples recovered in the western portion of the Solimões Basin and on river outcrops in the Acre Basin show predominantly radiogenic Andean-like εNd(0) signature (-9.9; Horbe et al., 2019; **Fig. 7.7**). These observations point to a proto-Amazon drainage that remained segmented, with the Purus Arch still acting as a major divide in Central Amazonia (Rossetti et al., 2023). Stage I in the Amazon Fan also coincides with repeated marine incursions into central western Amazonia (**Fig. 7.1A, 7.6, 7.7**; Leandro et al., 2022), probably associated with the waning phases of the Pebas mega-wetland (>1 Mkm^2; Salas-Gismondi et al., 2015, 2016; Jaramillo et al., 2017), highlighting high accommodation space generated by foreland flexural subsidence and further underscoring the incomplete nature of eastward integration.

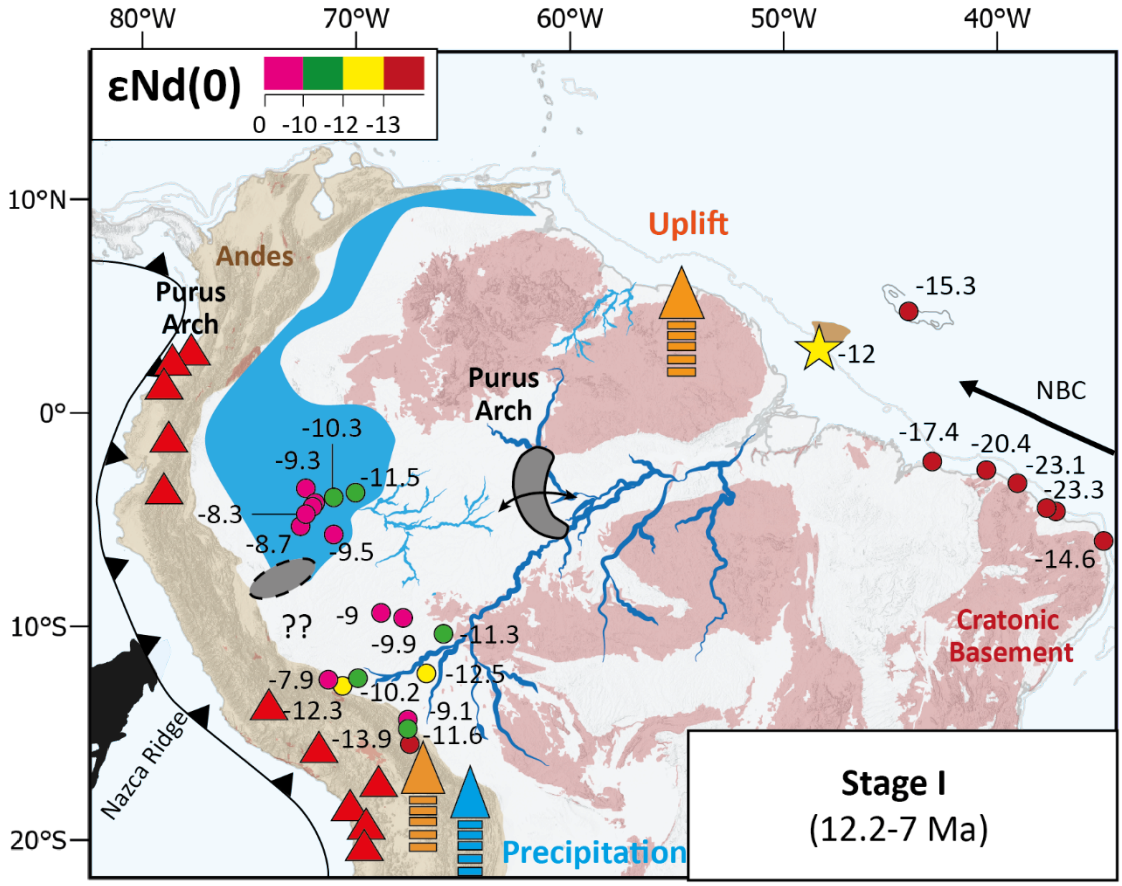

Figure 7.7. Nd isotopic signatures during the first sustained arrival of Andean detritus to the Amazon Fan (yellow star, εNd ≈ −12). While cratonic inputs remained significant, radiogenic contributions from western Amazonia (−7 to −10) signal initial Andean export, likely routed through southern corridors bypassing the Purus Arch. Meanwhile, Ceará Rise and equatorial margin sites continued to record unradiogenic cratonic values (−15 to −23), underscoring incomplete basin integration. Tectono-climatic drivers, including Fitzcarrald Arch uplift, Nazca Ridge subduction, and intensified Andean precipitation, enhanced erosion but could not fully overcome central divides. Stage I thus represents an incipient but fragmented transcontinental system.

Perhaps the greatest challenge in reconciling continental and marine records of Amazon transcontinentalization lies in the long-standing assumption that the river could only have become transcontinental through breaching the Purus Arch and integrating the Solimões sub-basin tributaries. Here we propose an alternative scenario: Andean detritus may have bypassed the Purus Arch through independent southern corridors, without requiring full basin-wide connectivity at first (**Fig. 7.7**). Both tectonic and climatic evidence tend to support this hypothesis.

Geochronological and thermochronological studies indicate that the northern Altiplano experienced rapid uplift between 9.1 and 5.4 Ma, reaching near-modern elevations during this interval (Boschman et al., 2021 and references therein). The rise of the Bolivian Altiplano strengthened the South American Low-Level Jet and helped establish the South American Monsoon System (**Fig. 7.6F**; Poulsen et al., 2010). This climatic reorganization intensified humidity across the Andes, boosting central Altiplano rainfall by up to 400% after the mid-Miocene (Martínez et al., 2020). In turn, denudation rates of the Bolivian Eastern Cordillera sharply increased (Sacek et al., 2023). Although much of the resulting sediment was initially trapped in foreland depocenters such as the Madre de Dios Basin (Roddaz et al., 2005, 2006; Louterbach et al., 2018; Moizinho et al., 2024), the modern Madeira River system demonstrates how material could eventually bypass such storage. Once beyond the foreland, the Madeira and its tributaries cut directly into crystalline basement, unimpeded by thick sedimentary covers (e.g., Solimoes Basin), thereby establishing an efficient routing system. Such basement-controlled entrenchment likely facilitated rapid eastward sediment transport along structural valleys, creating a direct connection to eastern Amazonia and ultimately the Atlantic margin.

Neotectonics provided a further mechanism for establishing this bypass. Seismic surveys and satellite image analyses show that tectonic reactivation has profoundly shaped the paleogeography of Amazonia (Campos and Teixeira, 1988; Costa et al., 2001; Rosseti, 2014). In particular, NE–SW strike-slip fault systems are widespread in eastern Amazonia and exert strong structural control over the Madeira River (Costa et al., 2001). Although the exact zone of influence of the Purus Arch is difficult to delimit, the confluence of the Madeira with the lower Amazon River occurs more than 100 km east of the arch itself, highlighting how regional tectonics could redirect sediment pathways. During Stage I, global sea level stood ~20 m below present (**Fig. 7.6F**; Miller et al., 2020), conditions that would have enhanced valley incision in a Madeira-like fluvial system. The combined effects of Miocene neotectonic reactivation and lowstand incision could thus have opened an efficient eastward sediment-routing corridor, bypassing the Purus divide.

By framing the bypass hypothesis within this tectonic–climatic–sea-level context, we can resolve a key inconsistency: marine records register the arrival of Andean material earlier than many continental reconstructions allow. Rather than a contradiction, this mismatch reveal different sensitivities: the fan archives the products of even transient export events, while

continental basins may record only longer-term drainage reorganizations. Thus, the earliest Andean signal at the Brazilian Equatorial Margin does not imply full Solimões integration, but can instead be explained by a southern bypass corridor around the Purus Arch. This interpretation challenges a central tenet of existing models and underscores the need to envision transcontinentalization not as a single threshold event, but as a multi-phased process involving both transient pathways and permanent drainage reconfigurations.

Stage II (7 – 4 Ma) – Solimões capture and a transitional mosaic drainage

Stage II is marked by a decisive isotopic shift toward more radiogenic values, reflecting a growing dominance of Solimões-like contributions that brought Amazon Fan signatures closer to those of the modern Amazon Delta (−10.5; **Fig. 7.8**; Bayon et al., 2015). This event is concomitant with a 1-3 northward displacement of the ITCZ during the Middle Pliocene Warm Period (MPWP; Pontes et al., 2020, 2022). We interpret this transition as evidence for the progressive capture of tributaries draining Mesozoic volcano-sedimentary sequences in the central Andes (0–10°S; **Fig. 7.8**). Yet, while the marine record signals stronger Andean influence, continental archives suggest that full integration of the basin was not yet achieved. The Içá and Remanso formations preserve contrasting paleoflow directions across the Purus region, with evidence of both west- and east-directed drainage (Rozo et al., 2005; Nogueira et al., 2013), and the absence of Andean palynomorphs in eastern facies (Dino et al., 2012) points to limited eastward connectivity. This incomplete integration is reflected in differing interpretations of sediment supply. Latrubesse et al. (2010) attributed relatively low Fan sedimentation rates during this interval to a continued dominance of shield-derived flux, arguing against the existence of a fully developed Amazon River. However, our mixing models contradict this view, indicating progressively larger Andean contributions despite the modest accumulation rates. The discrepancy highlights the transitional nature of Stage II, when Andean material increasingly reached the Atlantic, but drainage remained fragmented and buffered by internal sediment sinks.

At the same time, profound tectono-environmental changes were reshaping western Amazonia. The collapse of the Pebas megawetland and its replacement by the fluvial sands of the Ipururo Formation, together with regional exhumation of the Huallaga Basin (Eude et al.,

2015), testify to large basin-scale reorganization (Baby et al., 2025). Numerical models of flexural subsidence and dynamic topography (Bicudo et al., 2019, 2020) nevertheless suggest that a central megawetland may have persisted into the Late Miocene, maintaining compartmentalized drainage and delaying full eastward connectivity. Superimposed on this tectonic evolution, global mean sea level (GMSL) highstands in the Early Pliocene, up to 10 m above Tortonian levels (**Fig. 7.6F**; Miller et al., 2020), triggered episodes of marine incursion into western Amazonia. Such events, recorded at 4.7, 4.2–4.1, and 3.8 Ma (Leandro et al., 2022), may have temporarily revived wetland conditions and further postponed the establishment of a unified eastward-flowing system.

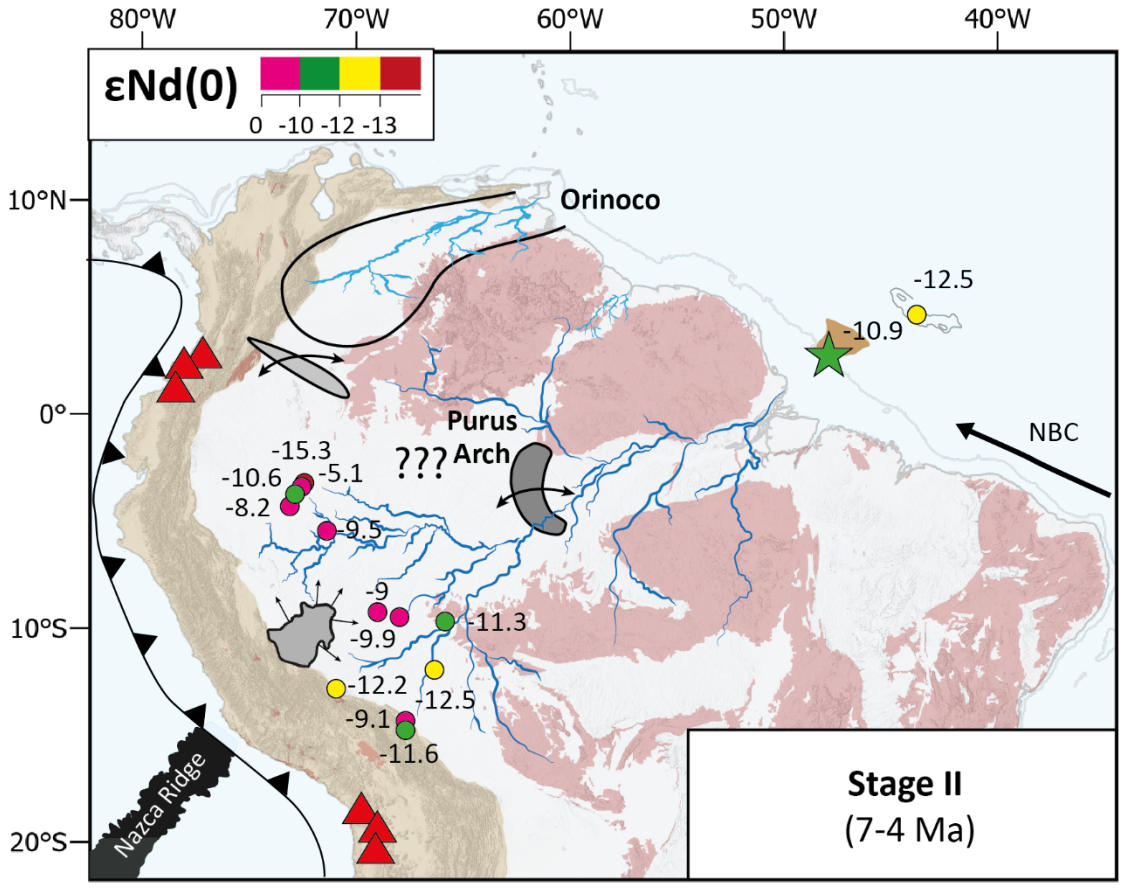

Figure 7.8. Isotopic signatures at the Amazon Fan converge toward modern values (εNd ≈ −10.5), marking growing Andean dominance. Mixing models reveal increased Solimões-like input, reflecting progressive capture of central Andean tributaries. Nonetheless, continental records show contrasting paleoflow directions and persistent wetlands in western Amazonia, indicating incomplete drainage integration. The sharp rise in Fan sedimentation rates at ~5 Ma coincides with Fitzcarrald Arch uplift and Nazca Ridge subduction, which reduced accommodation space and enhanced erosion. Stage II thus records a mosaic landscape of foreland basins, wetlands, and emerging transcontinental connections.

The end of Stage II is distinguished by a dramatic, nearly ninefold increase in Fan sedimentation rates, reaching up to ~80 cm kyr^{-1} (**Fig. 7.7D**). This sharp acceleration coincided with the onset of Nazca Ridge subduction beneath South America and the uplift of the Fitzcarrald Arch, which generated a ~400,000 km^2 positive relief in the Peruvian–Brazilian retroarc basins (Espurt et al., 2007; Regard et al., 2009). The emergence of this topographic high reduced accommodation space, accelerated erosion of foreland sediments, and promoted widespread denudation across western Amazonia (Baby et al., 2025). Continued uplift of the Fitzcarrald Arch ultimately subdivided western Amazonia into the Solimões and Madeira sub-basins (Espurt et al., 2007, 2011), reinforcing the dual provenance patterns observed today and fueling a major biodiversification of the region (Albert et al., 2019).

Taken together, Stage II represents an intermediate phase of Amazon watershed expansion and drainage reorganization. The marine fan record documents steadily increasing Andean contributions after 7 Ma, but the continental interior still reflects a fragmented landscape of wetlands, foreland depocenters, erosion zones, and only partially integrated river systems. The turning point came after ~5 Ma, when sedimentation rates in the Fan surged nearly ninefold, coinciding with the Nazca Ridge subduction and subsequent uplift of the Fitzcarrald Arch. This tectonic pulse reduced accommodation space, mobilized foreland sediments, and subdivided western Amazonia into the Solimões and Madeira sub-basins, reinforcing dual provenance patterns and driving widespread denudation. The collapse of internal sediment sinks, combined with these structural reorganizations, established more direct sediment-routing pathways to the Atlantic. In this sense, the late Stage II reorganization was not merely transitional but transformative, dismantling barriers that had long compartmentalized the basin and setting the foundation for the fully integrated, high-throughput Amazon River system that emerged in Stage III.

Stage III (4 - 0.6 Ma) – Towards modern configuration

By the onset of Stage III, the Amazon Fan had already experienced a dramatic and sustained increase in accumulation rates (40–80 cm kyr^{-1}), signaling the emergence of a high-throughput sediment-routing system capable of efficiently transferring vast amounts of material from the continent to the Atlantic. Yet, despite this apparent stability, provenance proxies reveal

important variability that speaks to the continued sensitivity of the basin to climatic and tectonic forcing. Stage IIIa (4–2.4 Ma) is characterized by a pronounced increase in cratonic contributions to the Fan. This trend developed coincidently with a fundamental global regional climate reorganization linked to the progressive cooling of the eastern equatorial Pacific (Fedorov et al., 2015; Liu et al., 2019, 2022) and the establishment of a more persistent La Niña–like state (Wara et al., 2005). At the same time, mountain belts worldwide, including the Alps, Himalaya, Rockies, and Andes, underwent accelerated erosion after ~3–4 Ma (Herman et al., 2013; Wilkinson, 2005; Larsen et al., 2014; Molnar, 2017; Zhang et al., 2001). In the Andes, pollen and climate records point to persistently wet Pliocene conditions (Grimmer et al., 2018), consistent with intensified hydrological cycling under high sea levels (Miller et al., 2020). These combined climatic and tectonic drivers enhanced erosion in the Eastern Cordillera (Fisher et al., 2023) and fueled the progradation of massive gravel deposits in foreland basins such as the Llanos (Parra et al., 2010) and Madre de Dios (Moizinho et al., 2024). However, the BP-3 provenance record suggests that much of this Andean-derived sediment was stored within continental depocenters rather than exported to the Fan (**Fig. 7.6B**).

Global sea-level fluctuations provide a coherent mechanism for this partitioning. Studies of Pleistocene sediments demonstrate that highstands favor sediment trapping in foreland basins and on continental shelves, whereas lowstands steepen river gradients, reduce floodplain storage, and enhance sediment bypass to the margin (Abouchami and Zabel, 2003; Damuth et al., 1995; Mason et al., 2019; Mertz and Dunne, 2007; Irion and Kalliola, 2010). Comparable dynamics can be observed today in the lower Amazon Basin, where discharge variability is strongly modulated by the South American Summer Monsoon (SASM) and latitudinal shifts of the Intertropical Convergence Zone (ITCZ; Garreaud et al., 2009; Marengo, 2004). Atlantic and Pacific sea-surface temperature (SST) variability further controls moisture transport into Amazonia, influencing discharge of the Amazon and its tributaries (Marengo & Espinoza, 2016). Under these conditions, tributaries such as the Xingu and Negro often act as temporary sediment traps, where ria-like deposits accumulate in flooded valleys (Bertassoli Jr., 2019). Taken together, these observations suggest that climate-driven alternation between continental trapping during highstands and margin delivery during lowstands was already a defining feature of the Amazon system by the mid-Pliocene.

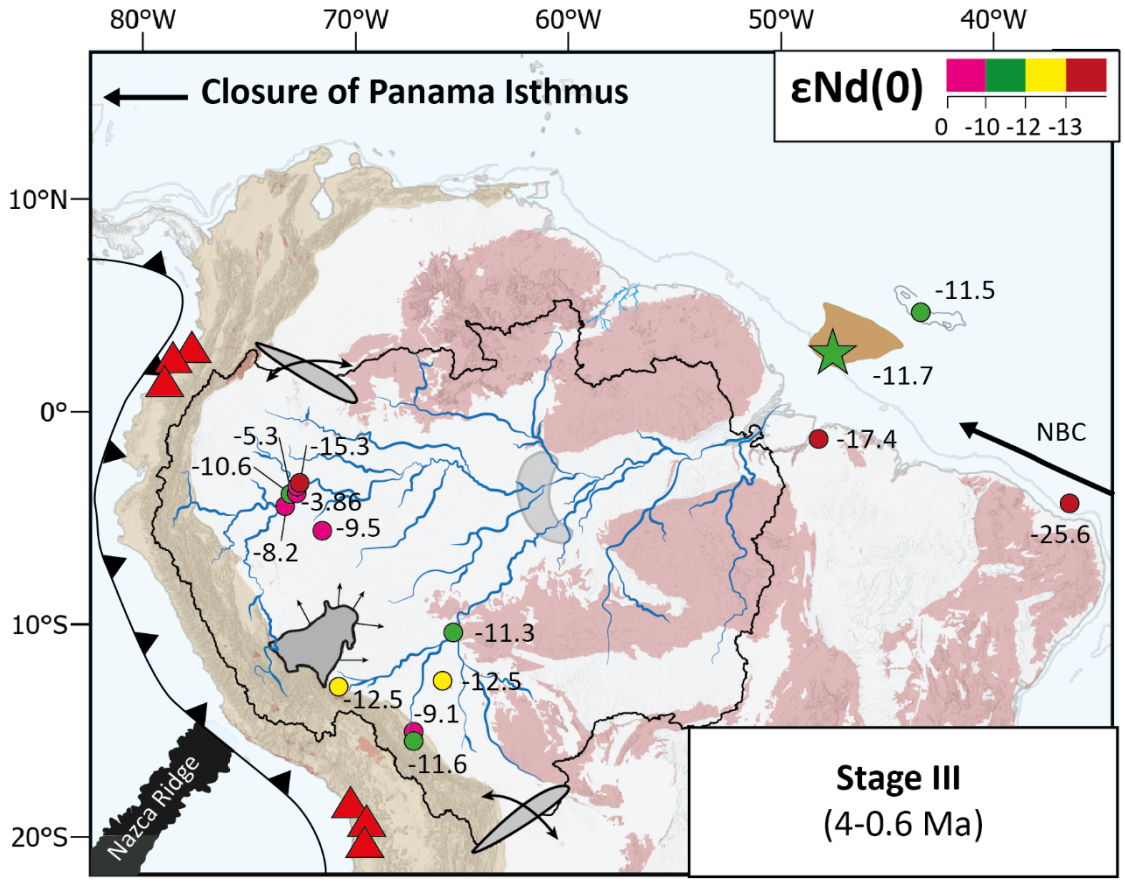

Figure 7.9. The Amazon Fan records persistently high sedimentation rates (40–70 cm kyr^{-1}) and dual Solimões–Madeira dominance, reflecting a mature high-throughput system. Early in this stage (Stage IIIa), increased cratonic contributions and less radiogenic εNd values coincide with Pliocene warmth and high sea levels, implying enhanced upstream sediment trapping. A short-lived perturbation at 2.4–2.2 Ma, characterized by unradiogenic clays, collapsed $\Delta\varepsilon Nd_{FeOOH-clay}$, and low concavity indices, indicates a temporary cutoff of Andean supply, likely linked to the onset of Northern Hemisphere glaciation. After this event (Stage IIIb), proxies converge toward modern values, although our youngest sample (0.56 Ma) suggests the fully integrated Amazon system was only attained in the Holocene.

The transition from Stage IIIa to Stage IIIb coincides with the Pliocene–Pleistocene boundary and is marked by a short-lived but coherent perturbation between 2.4 and 2.2 Ma (**Figs. 7.6**). This interval overlaps with the final closure of the Isthmus of Panama and the onset of Northern Hemisphere glaciation (Bartoli et al., 2005). We propose that the combined effects of sea-level fall and the expansion of colder climates reorganized sediment pathways through enhanced channel incision. This interpretation is consistent with geomorphic evidence for Negro paleovalley incision (Rossetti et al., 2023) and terrace development across the Purus region (Bezerra, 2018), suggesting that the perturbation recorded at the Fan was the marine counterpart of late-stage continental reorganizations in central Amazonia.

Stage IIIb (2.2–0.6 Ma) represents the final approach toward the modern Amazon configuration. During this interval, the system became increasingly shaped by the climatic oscillations introduced by Northern Hemisphere glaciation (**Fig. 7.9**). Our youngest sample, dated to 0.56 Ma, indicates that none of the proxies yet reproduce modern values, implying that the present-day configuration of the Amazon system was only fully achieved during the Holocene. Numerous studies have shown that glacial–interglacial cycles imposed strong climatic oscillations across Amazonia (Akabane et al., 2024; Grigolato et al., 2025; Häggi et al., 2017; Zhang et al., 2017), modulating the balance between Andean and cratonic contributions without fundamentally reorganizing drainage pathways (Govin et al., 2014; Höppner et al., 2017). This pattern underscores the resilience of the mature transcontinental Amazon: once established, the system withstood major climatic oscillations without reverting to a fragmented configuration.

In sum, Stage III captures the final transition toward a fully integrated Amazon River system. While sedimentation rates and provenance contributions fluctuated in response to tectonics, sea-level change, and climatic oscillations, the overarching trajectory was one of increasing stability and efficiency in sediment routing from the Andes to the Atlantic, culminating in the modern configuration of the world's largest river basin.

7.8. Conclusions

Our multiproxy geochemical record from the Amazon Fan, integrated within a newly astronomically tuned age model, refines the chronology of transcontinental drainage integration in northern South America and, importantly, provides the first high-resolution reconstruction of how the system evolved after transcontinentalization. Whereas previous marine studies concentrated mainly on the initial establishment of a through-going river, our dataset demonstrates that sediment routing, source contributions, and weathering dynamics continued to reorganize throughout the late Neogene. We show that the first sustained arrival of Andean-derived sediments occurred at ~12.2 Ma, predating the widely cited ~9.4–9.0 Ma estimate and narrowing the previously broad 16–10 Ma window. Provenance reconstructions reveal a stepwise trajectory: Stage I (12.2–7 Ma) captures an embryonic phase, with incipient Andean input superimposed on a strong cratonic background; Stage II (6.9–4.1 Ma) manifest the

decisive capture of northern and central Andean sources, tipping the balance toward Andean dominance but within a still transitional, compartmentalized basin; and Stage III (4.0–0.6 Ma) records the stabilization of a mature, high-throughput sediment-routing system, with persistently high accumulation rates and a drainage configuration converging on that of the modern Amazon. By extending the focus beyond the threshold of transcontinentalization, our record provides new resolution on how the interplay of Andean uplift, foreland basin dynamics, sea-level oscillations, and global climate change progressively shaped the Amazon system. This long-term perspective bridges the gap between marine and continental archives, revealing that the present-day Amazon River was not the outcome of a single event but rather the product of successive reorganizations and feedbacks operating across tectonic, climatic, and geomorphic timescales.

Ultimately, the Amazon Fan archive reveals a river system that became geomorphically integrated, sedimentologically efficient, and ecologically interconnected, while remaining sensitive to tectonic activity along structural highs and to sea-level–driven alternations between sediment trapping and bypass. The emergence of this fully transcontinental river not only reconfigured South America's sediment fluxes but also established the physical and ecological foundations of the basin's extraordinary biodiversity and its central role in global biogeochemical cycles. Crucially, these reorganizations also reshaped continental weathering regimes by redistributing drainage networks and erosional hotspots—an aspect further explored in the following chapter, where we move from provenance toward the chemical weathering evolution of the Amazon Basin.

VIII

Late Cenozoic co-evolution of tectonics, climate, and weathering in the Amazon Basin

Declaration/ Declaração/ Déclaration

Understanding the evolution of chemical weathering in the Amazon Basin is fundamental to evaluating its role in long-term carbon cycle regulation. While previous studies have emphasized provenance and drainage integration, the contribution of silicate versus sedimentary rock weathering over Neogene timescales remains poorly constrained. In this chapter, we present a multiproxy record from the Amazon Fan (12–0.6 Ma), combining REE patterns with Nd–Hf isotopes in paired clay and Fe-(oxyhydr)oxide fractions to track weathering processes through time. These data allow us to assess the balance between CO_2 sources and sinks as uplift, hydroclimate, and sediment storage reshaped the basin.

[PT] Compreender a evolução do intemperismo químico na Bacia Amazônica é essencial para avaliar seu papel na regulação do ciclo do carbono em longo prazo. Embora estudos anteriores tenham enfatizado a proveniência e a integração da drenagem, a contribuição relativa entre intemperismo de silicatos e de rochas sedimentares ao longo do Neógeno permanece pouco conhecida. Neste capítulo, apresentamos um registro multiproxy do Leque do Amazonas (12–0,6 Ma), combinando padrões de ETR com isótopos de Nd–Hf em frações pareadas de argilas e Fe-(óxi-hidróxidos) para rastrear os processos de intemperismo ao longo do tempo. Esses dados permitem avaliar o balanço entre fontes e sumidouros de CO_2 à medida que o soerguimento, o hidroclima e o armazenamento sedimentar remodelaram a bacia.

[FR] Comprendre l'évolution de l'altération chimique dans le bassin amazonien est essentiel pour évaluer son rôle dans la régulation du cycle du carbone à long terme. Bien que les études précédentes aient surtout mis l'accent sur la provenance et l'intégration du drainage, la contribution relative de l'altération des silicates et des roches sédimentaires au cours du Néogène reste mal contrainte. Dans ce chapitre, nous présentons un enregistrement multiproxy du cône de l'Amazone (12–0,6 Ma), combinant les distributions des REE et les isotopes Nd–Hf dans les fractions appariées d'argiles et de Fe-(oxyhydro)xydes afin de retracer les processus d'altération au cours du temps. Ces données permettent d'évaluer l'équilibre entre sources et puits de CO_2 à mesure que le soulèvement, l'hydroclimat et le stockage sédimentaire remodelaient le bassin.

Abstract

Chemical weathering plays a central role in regulating Earth's long-term climate through its influence on the global carbon cycle. Yet, uncertainties remain about how mountain uplift, lithology, and sediment storage shape the balance between CO_2 sources and sinks. Here, we present a 12–0.6 Ma multiproxy weathering record from the Amazon Fan (BP-3 well), integrating rare earth element (REE) distributions and Nd–Hf isotopes from paired clay and Fe-(oxyhydr)oxide fractions, together with bulk geochemical indices. Our results reveal a fundamental shift in the weathering regime of the Amazon Basin: during the Late Miocene, rapid uplift of the Central Andes exposed pyrite- and organic carbon–rich black shales, enhancing oxidative weathering and net CO_2 release. In contrast, from ~4.5 Ma onward, intensified silicate weathering under warm and humid Pliocene climates, coupled with efficient floodplain "reactors," transformed the lowlands of the Amazon Basin into a significant CO_2 sink. The Late Pliocene–Pleistocene shows that high weathering fluxes persisted despite global cooling, sustained by ENSO-driven rainfall variability and glacial–interglacial sediment recycling. Together, these findings highlight the Amazon source-to-sink system as a critical, previously underestimated contributor to Neogene CO_2 drawdown. By documenting the transition from a CO_2 source to a sink, our study refines the uplift–weathering hypothesis and underscores the importance of tropical floodplains in amplifying global climate feedbacks.

8.1. Introduction

On continents, rocks are dissolved through chemical weathering, a process that consumes substantial amounts of carbon dioxide (CO_2) and plays a major role in regulating Earth's climate through time (Walker et al., 1981; Berner et al., 1983). A contentious view is that mountain-building events during Earth's history were followed by enhanced physical erosion and accelerated dissolution of crystalline silicate rocks, resulting in a net drawdown of atmospheric CO_2 and global climate cooling (Raymo and Ruddiman, 1992). Although high-relief regions generally display elevated silicate weathering rates (West et al., 2005), several studies argue that global silicate fluxes remained relatively invariant even as erosion intensified (e.g., Willenbring & von Blanckenburg, 2010).

A major source of uncertainty surrounding the Earth's climate sensitivity to continental weathering arises from the challenge of distinguishing the individual contributions of igneous/metamorphic and sedimentary rocks to overall weathering rates during mountain erosion. Over geological timescales spanning millions of years, weathering of crystalline silicate rocks acts as a sink for atmospheric CO_2, while the alteration of sedimentary rocks may instead act as a net source of CO_2 (e.g., Bufe et al., 2021; Hilton and West, 2020; Horan et al., 2017). For instance, sulfide oxidation coupled with carbonate dissolution has been identified as a significant CO_2 source during orogeny (Torres et al., 2014). Recent global syntheses show that oxidation of ancient organic carbon preserved in sedimentary rocks (OC_{petro}) could release on the order of 68 MtC yr^{-1}, comparable to the carbon uptake from silicate weathering, making some mountain belts net CO_2 sources rather than sinks (Zondervan et al., 2023). This recognition has shifted attention toward lithological controls on weatherability and CO_2 mobilization. In parallel, the spatial variability of chemical weathering across catchments has gained particular attention over recent years. While high-elevation regions in the Andes supply vast quantities of reactive minerals, silicate weathering prevails in floodplains located downstream, which act as dynamic reactors where substantial atmospheric CO_2 fluxes can be consumed (Bouchez et al., 2012; Torres et al., 2016). A similar process has been also documented in Quaternary sediment records from the Bay of Bengal, with evidence for climate-driven alternations between highland- and floodplain-dominated weathering (Yu et al., 2020). In the Amazon Basin, foreland floodplains also account for more than half of OC_{petro} oxidation , effectively doubling CO_2 release compared with the Andes alone (Dellinger et al., 2023). Thus,

the balance of sources and sinks cannot be understood without considering both highland inputs and lowland transformations at the catchment scale (Trapp-Müller et al., 2025).

Once considered as the dominant driver of Cenozoic cooling (Raymo and Ruddiman, 1992; France-Lanord and Derry, 1999), the Himalayan–Tibetan system now appears less effective than previously assumed, as Neogene silicate weathering fluxes from large Himalayan river basins remained relatively invariant despite sustained uplift (e.g., Clift and Jonell, 2021; Clift et al., 2024; Zhang et al., 2025). Instead, the emergence of mafic and ultramafic terrains in tropical arc–continent collision zones has been highlighted as a critical CO_2 sink. Ophiolite exposures in Papua New Guinea and Southeast Asia, when subjected to warm and humid climates, weather rapidly and have been suggested to disproportionately enhance CO_2 consumption (Macdonald et al., 2019; Bayon et al., 2023; Clift et al., 2024). Paleogeographic reconstructions further show that low-latitude arc-continent collisions in the geological past coincided with and the occurrence of major glacial periods, underscoring their central role in setting Earth's background climate (Macdonald et al., 2019). Modern global carbon flux driven by silicate weathering and its spatiotemporal distribution show that the highest CO_2 consumption occurs in tropical regions, accounting for 88 % of the global total (Zhang et al., 2021). Taken alone, mafic weathering in Southeast Asia could represent up to 70% of global silicate weathering fluxes annually (Hartmann et al., 2014). However, despite growing evidence of the importance of tropical arc-continent collision in driving global glaciation, modelling studies have suggested that this process may not have been sufficient to reach the atmospheric CO_2 threshold required for the initiation of the Northern Hemisphere Glaciation (Park et al., 2020).

Building on these global insights, this chapter investigates the coupled evolution of uplift, hydroclimate, and weathering in the Amazon Basin over the past 12 million years using sediments recovered from a well drilled in the upper Amazon Fan (BP-3 Well). Since 12.2 ± 1.3 Ma, the Fan has received a dominant Andean sediment supply, making it an exceptional archive of mountain uplift, drainage integration, and associated weathering processes (see previous chapter). To disentangle silicate from sedimentary weathering contributions, we combine rare earth element (REE) distributions with Nd isotopic compositions of paired clay and Fe-(oxyhydr)oxide fractions (FeOOH; Bayon et al., 2020; Jang et al., 2024; Moizinho et al., under review at *Chemical Geology*). To further constrain the evolution of silicate weathering in sediments delivered to the Fan, we integrate Hf–Nd isotopes of clays (Bayon et al., 2016) with

classical indices such as the Chemical Index of Alteration (CIA; Nesbitt & Young, 1982) and K/Al ratios. Together, these multiproxy datasets provide a robust framework to reconstruct how the balance between silicate and sedimentary weathering evolved as Andean uplift, monsoon dynamics, and foreland floodplain storage reshaped the Amazon source-to-sink system.

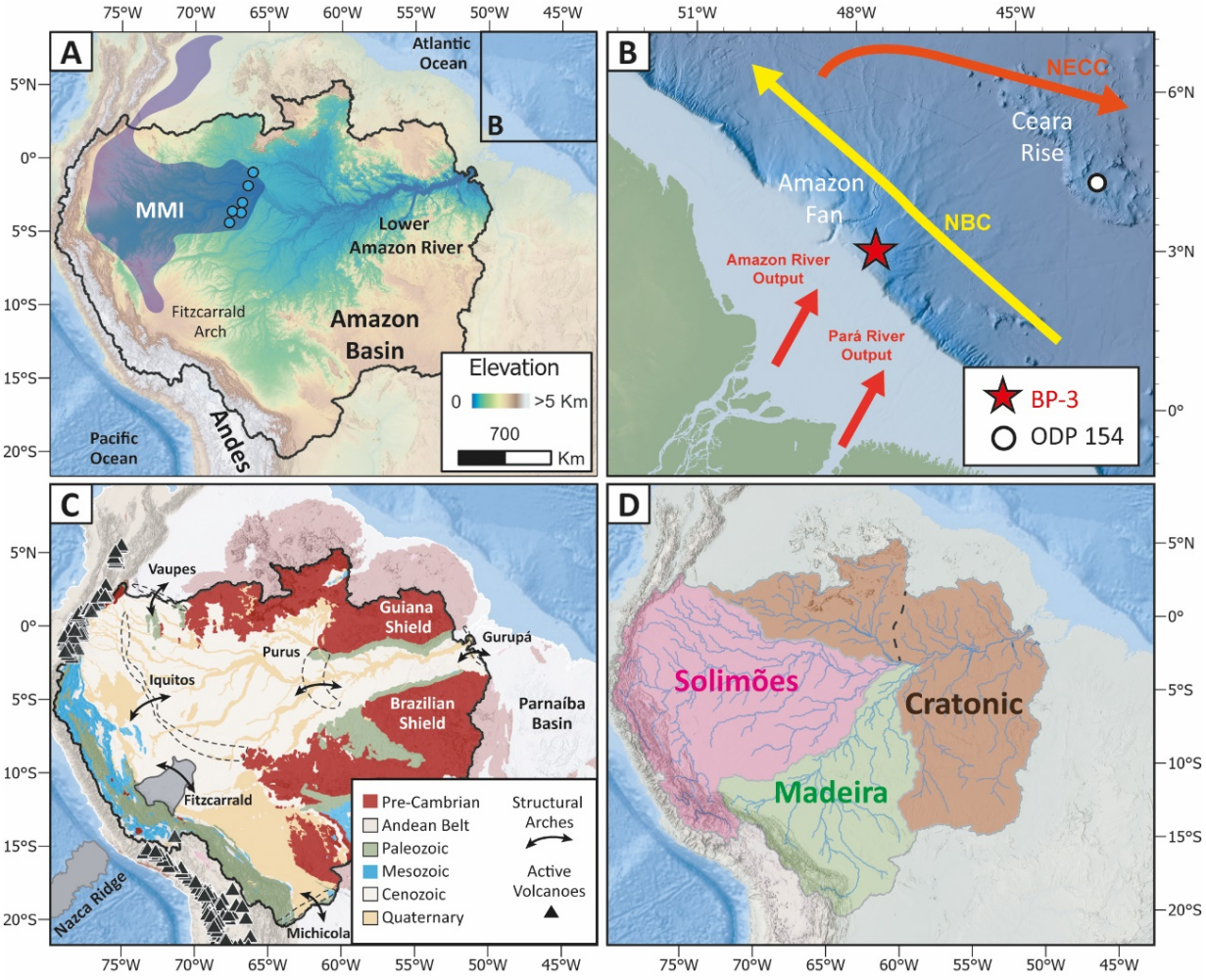

Figure 8.1. (A) Physiographic map of the Amazon Basin showing major tectonic features and topographic domains, including the Fitzcarrald Arch, Pastaza–Marañon Basin, and areas influenced by Miocene marine incursions (MMI; Jaramillo et al., 2017; Leandro et al., 2022). **(B)** Location of the Amazon Fan along the Brazilian Equatorial Margin with the BP-3 exploration well (this study) and ODP Leg 154 site 925 (white circle), showing the main outflow of the Amazon and Pará rivers, the North Brazil Current (NBC), and the North Equatorial Counter Current (NECC). **(C)** Simplified geological map of northern South America highlighting the main lithotectonic provinces of the Amazon Basin and surrounding shields, foreland, and intraplate basins, as well as major structural arches and the Nazca Ridge (after Roddaz et al., 2005; Espurt et al., 2007). **(D)** Simplified subdivision of the Amazon Basin into the three main geochemical domains (Solimões, Madeira, Cratonic) used in this study, based on differences in lithology, weathering regime, and isotopic signatures (Viers et al., 2008; Moquet et al., 2011; Chapter III).

8.2. Materials and methods

8.2.1. Study site, age model, and sedimentation rates

The 1-BP-3-APS well (hereafter BP-3) was drilled in the upper Amazon Fan (3°02'58.660" N, 47°44'45.801" W; 754 m water depth; Figs. 4.1B, 4.2A) and reaches a maximum depth of 5655 m below sea level. This site has been referred to under different names in previous studies, including *Well 2* (Figueiredo et al., 2009; Hoorn et al., 2017; Lammerstma et al., 2018), *Well 4* (Gorini et al., 2014), and *Well P1* (Reis et al., 2016). Recently, a new astronomically tuned age-depth model was established for BP-3 using gamma-ray logs calibrated with calcareous nannofossil biostratigraphy as tie points (Moizinho et al., 2025). The present study focuses on the interval between 12.2 and 0.6 Ma, during which sedimentation rates varied markedly from ~5–13 cm kyr^{-1} in the Late Miocene to more than 50 cm kyr^{-1} in the Early Pliocene.

8.2.2. Sample preparation and grain size separation

A total of 91 ditch-cutting samples were recovered from BP-3 and processed following a sequential leaching protocol designed to remove carbonate phases, easily reducible Fe-(oxyhydr)oxides, and organic matter (Bayon et al., 2002). Bulk powders were first disaggregated in an agate mortar, after which ~1 g of dried material was placed in 50-ml polyethylene centrifuge tubes with 20 ml of 5% (v/v) acetic acid and shaken mechanically for three hours to dissolve carbonate phases. The residues were then treated with 20 ml of a 15% (v/v) acetic acid–0.5 M hydroxylamine hydrochloride solution for two days to extract more resistant carbonate phases together with Fe–Mn oxides. The resulting leachates were filtered through 0.20 µm cellulose acetate membranes, evaporated to dryness, redissolved in concentrated HNO_3 to remove hydroxylamine, and finally taken up in 4 M HCl for analysis. The residual detrital fraction was subsequently treated with 20 ml of 35% (v/v) H_2O_2 for two days to remove organic matter. After leaching, detrital residues were separated by differential centrifugation into silt (63–4 µm) and fine clay (<2 µm) fractions following the procedure of Bayon et al. (2015). For comparison, clay-size fractions separated from modern Amazon River sediments (n = 10) were also analyzed for Hf–Nd isotopes.

8.2.3. Disentangling silicate vs. sedimentary rock weathering in the geological record

Recent studies have shown that the application of rare earth element (REE) distributions and neodymium (Nd) isotopic compositions measured in paired detrital fractions and labile Fe-(oxyhydr)oxide (FeOOH) phases leached from river sediments provide a powerful framework for distinguishing bedrock lithologies and associated weathering processes in modern watersheds (Jang et al., 2020, 2024; Larkin et al., 2021; Bayon et al., 2020; Süfke et al., 2019; Hindshaw et al., 2018; Von Blanckenburg et al., 2015; Moizinho et al., under review at *Chemical Geology*). In the Amazon Basin, modern FeOOH phases display diagnostic REE fractionation patterns that directly reflect their origin: (i) silicate weathering in cratonic lowlands, (ii) oxidative pyrite weathering (OPW) in the Eastern Cordillera of the Central Andes associated with Paleozoic black shale erosion, and (iii) reworking of ancient marine Fe oxides Domain draining Mesozoic sedimentary rocks (Chapter III). These geochemical fingerprints are intrinsic to each province and provide a means of disentangling provenance signals that may remain ambiguous in the detrital fraction alone. Additional insights emerge from comparing Nd isotopic signatures of FeOOH and coexisting clays. Secondary FeOOH phases formed directly from weathering typically inherit the isotopic composition of the underlying bedrock. In contrast, in sedimentary or mixed-lithology watersheds, Nd isotopic compositions of riverine Fe oxides commonly diverge from the εNd values of detrital clays (Bayon et al., 2020; Hindshaw et al., 2018; Jang et al., 2020). This isotopic decoupling is best explained by the incorporation of REE contributions derived from non-silicate sources, such as ancient marine Fe oxides eroded from sedimentary successions (Bayon et al., 2020; Jang et al., 2020).

Although Fe-oxide phases in marine sediments are potentially sensitive to post-depositional redox conditions and diagenesis (Michalopoulos & Aller, 1995, 2004), our results demonstrate that leached fractions retain robust terrestrial signatures (Chapter VI). This opens the way for applying FeOOH REE–Nd systematics beyond modern rivers to deep-time records, providing a novel means of disentangling silicate and sedimentary weathering contributions in ancient source-to-sink systems.

8.2.4. Tracing silicate weathering intensity

Combining radiogenic Hf and Nd isotopes in detrital clay fractions provides a sensitive proxy for silicate weathering (Bayon et al., 2009a, 2016). Both isotopic systems behave similarly during magmatic differentiation. As a consequence, most igneous and sedimentary rocks align along a global "Terrestrial array" in εNd–εHf space (Vervoort et al., 1999), in which radiogenic and unradiogenic values, respectively, characterize mantle-derived juvenile rocks and old crustal rocks. Earth surface processes, however, can decouple Hf-Nd isotopic systems. During sediment transport, mineral sorting preferentially enriches zircons (low εHf) in coarse fractions, whereas fine-grained clay fractions, typically zircon-poor, tend to display more radiogenic εHf values and define a distinct "Clay array" (Bayon et al., 2016). Within this framework, departures of clay εHf from the Clay array, expressed as $\Delta\varepsilon Hf_{clay,}$ are controlled by varying relative contributions of unweathered detrital minerals (with low, unradiogenic, εHf values) versus secondary clays formed during chemical weathering (with high, radiogenic, εHf). This decoupling arises because Lu-bearing minerals dissolve preferentially during continental weathering, releasing radiogenic Hf that is subsequently incorporated into newly formed secondary clays (Bayon et al., 2006). Intensified silicate weathering, therefore, both increase the release of radiogenic dissolved Hf and enhance the formation of radiogenic secondary clays, leading to higher $\Delta\varepsilon Hf_{clay}$ values.

It's important to note that the clay fractions analyzed in this study are zircon-poor, with Zr concentrations averaging 133 ppm (maximum 191 ppm), within the range of modern zircon-depleted river clays (Bayon et al., 2016). No significant correlation is observed between εHf(t) values and Zr concentrations, nor between $\Delta\varepsilon Hf(0)_{clay}$ and Zr (**see chapter V, section 5.3**), confirming that the observed isotopic trends primarily reflect chemical weathering processes rather than zircon contamination. As such, $\Delta\varepsilon Hf(0)_{clay}$ provides a robust proxy for silicate weathering intensity in the Amazon Fan record.

In addition, the Chemical Index of Alteration (CIA; Nesbitt & Young, 1982) is a widely used proxy for assessing silicate weathering intensity (eg., McLennan et al., 1993, Clift et al., 2024). It is calculated as:

$$CIA = \frac{Al_2O_3}{Al_2O_3 + Na_2O + K_2O + CaO^*} \times 100$$

where CaO* represents the content of CaO in the silicate component. CIA values increase with progressive leaching of mobile cations (Na, K, Ca) relative to the relatively immobile Al.

8.3. Results

Chapters V and VI and tables XX XX have reported a detailed description of the results (e.g., elemental concentrations and Hf-Nd isotopic compositions), alongside temporal variations. Hafnium isotopes for modern Amazon River clays are reported in Table S3.3 and represented as a yellow bar on Figure 8.2B. CIA_{Bulk} values stay ~66–69 in Stage I–II, peaks in the mid-Pliocene (~3.5 Ma) at ~72–74, then falls back to ~66 by ~2.4 Ma and rises again in Stage IIIb (**Fig. 8.2A**). $\Delta\varepsilon Hf(0)_{clays}$ is near-zero to mildly negative in Stages I–II (around −2 to −3), climb to a mid-Pliocene maximum (up to ~+4–5 between ~4 and 3 Ma), and then drop steeply to strongly negative values by ~0.6 Ma (≈ −9 to −10; Fig. **8.2B**). $\Delta\varepsilon Nd_{FeOOH-clays}$ is low in Stage I (≤ 1.5), reaches ~4 ε units in Stage II, declines during Stage IIIa, collapses to ~0 at 2.4–2.2 Ma, and rises again in Stage IIIb (**Fig. 8.2C**). The FeOOH % relative to the bulk rock stays mostly ~0.5–1.0 wt% through Stage I, increasing toward 1.2-2 wt% in early Stage II. After 5 Ma, it starts to constantly increase, oscillating between 2 and 3% (**Fig. 8.1D**). Calculated concativity indexes (CI) values in leached Fe-oxyhydroxide fractions are high in Stage I (≈ 3.0–3.6), decrease to ~2.2–2.8 through Stage II and much of Stage IIIa, and keep descending toward lower values in Stage IIIb (1.8-2.1; **Fig. 8.1E**). Finally, sedimentation rate is ~5 cm kyr^{-1} during Stage I and most of Stage II, rises sharply near ~5 Ma (~80cm kyr^{-1}), and remains high (60–70 cm kyr^{-1}) throughout Stage III (**Fig. 8.1F**).

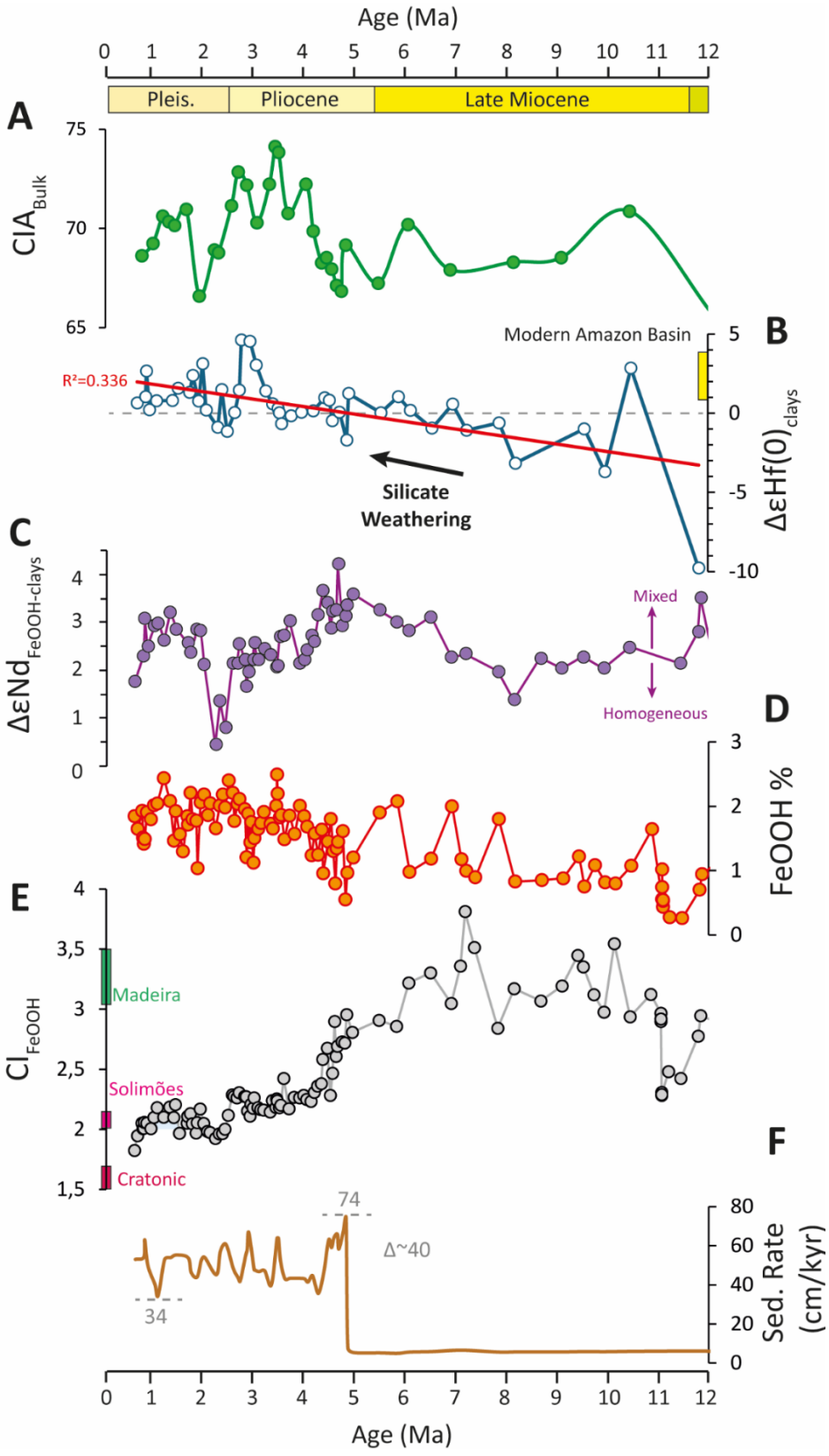

Figure 8.2. Evolution of weathering proxies in Amazon Fan sediments (BP-3 well) from 12 to 0.5 Ma. Silicate weathering indicators include **(A)** bulk CIA and **(B)** $\Delta\varepsilon Hf(0)_{clays}$. **(C)** $\Delta\varepsilon Nd_{FeOOH-clays}$ indicate the silicate vs. sedimentary rock weathering **(D)** FeOOH wt% tracks the abundance of easily reducible iron phases. **(E)** Concativity index (CI), a quantitative measure of the degree of MREE enrichment, of the FeOOH phases (CIFeOOH). **(F)** Sedimentation rates derived from an astronomically tunned age model (Moizinho et al., 2025).

8.4. Discussion

8.4.1. Late Cenozoic co-evolution of tectonics, weathering, and climate in the Amazon Basin

Late Miocene (12-5Ma): Central Andes uplift and oxidative weathering

The Late Miocene (12.2 ± 1.3 Ma) marks the first sustained export of Andean-derived sediments to the Atlantic margin, with over 70% of their source traced to the Andes (see previous chapter). From this point onward, the Amazon submarine fan became an exceptional archive, directly recording the geodynamic evolution of the Andes and the associated erosional and weathering patterns. The rapid rise of the central Andes (**Fig. 8.3F**) was a first-order driver of hydroclimatic, erosional, and weathering changes in South America. As the southern Peruvian and Bolivian Eastern Cordillera rose (10°-20°s), thick Paleozoic sedimentary successions, abundant in black shales enriched in organic carbon and diagenetic pyrite, were exhumed (Moizinho et al., 2024 and references therein). These highly reactive lithologies created landscapes prone to oxidative weathering, analogous to conditions observed today in the Madeira Basin (Moizinho et al., submitted; Chapter III) and in other high-elevation regions where glacial or periglacial processes accelerate sulfide breakdown (Jang et al., 2024; Larkin et al., 2021). While silicate weathering in these cold, steep environments was likely subdued, rapid sulfide oxidation would have produced sulfuric acid, enhanced carbonate dissolution, and promoted the formation of secondary Fe-(oxyhydr)oxide phases (Torres et al., 2016; Bufe et al., 2021). This mechanism is well recorded in our Amazon Fan dataset. Leached Fe-oxide fractions display the characteristic MREE-enriched REE patterns (**Fig. 8.1F**) that reflect pyrite-derived FeOOH phases (Jang et al., 2024). The persistence of these signals provides a geochemical fingerprint of Central Andean uplift in the offshore record. In contrast, proxies of silicate weathering intensity remain moderate, with CIA values fluctuating around 65–67 in the bulk and 77-85 in the clays, and $\Delta\varepsilon Hf(0)_{clays}$ near-zero to mildly negative (**Figs. 8.1B–C**). These results indicate that oxidative weathering of black shales was pervasive and silicate dissolution had not yet reached the higher-intensity regime.

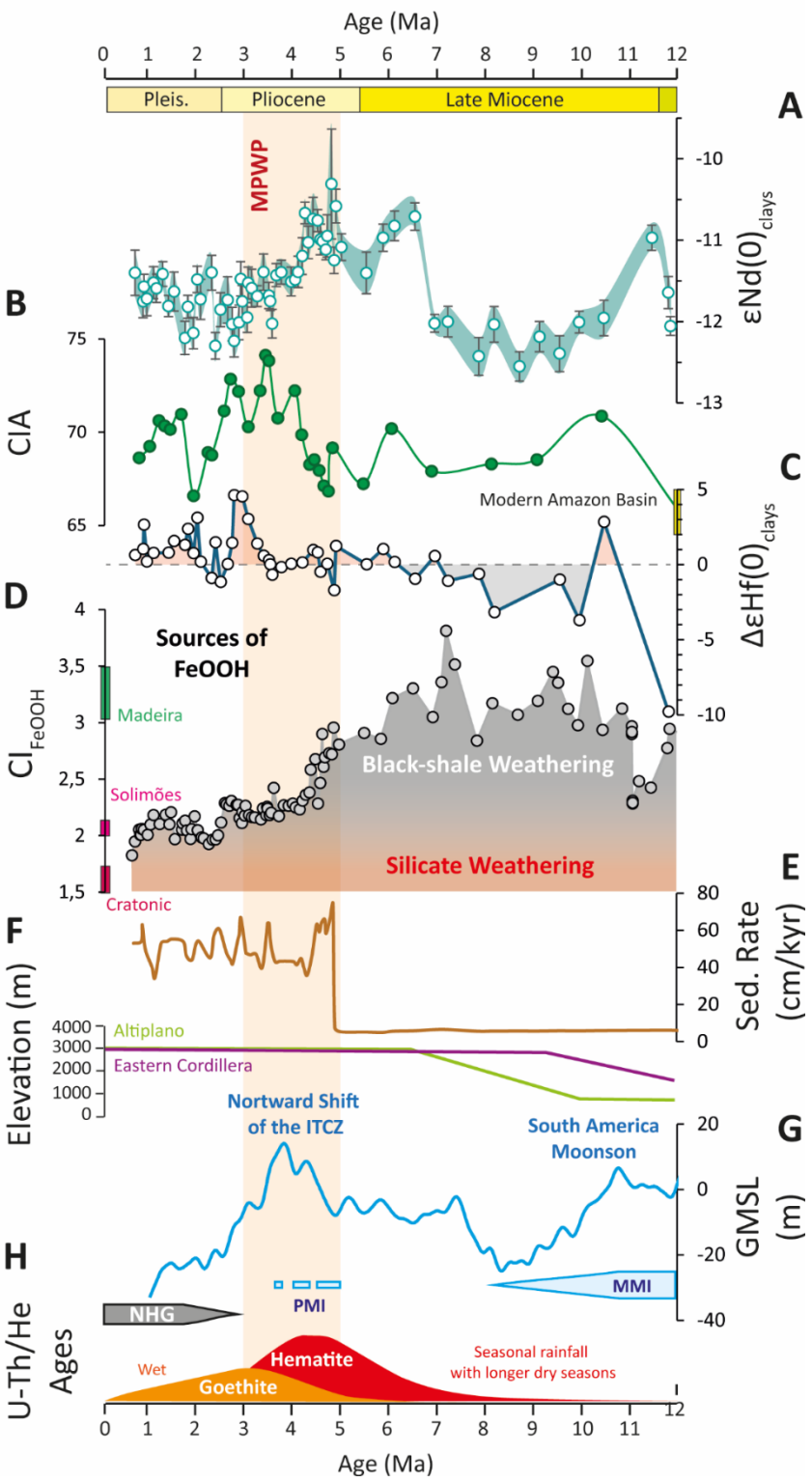

Figure 8.3. Evolution of provenance, weathering, and climate proxies from the Amazon Fan and key events in the Amazon Basin over the past 12 Myr. (A) Clay εNd(0) values. **(B)** Bulk CIA. **(C)** $\Delta\varepsilon Hf(0)_{clays}$. **(D)** Concavity Index (CI_{FeOOH}) with reference fields for Madeira, Solimões, and cratonic sources. (E) Sedimentation rates from the BP-3 age model. **(F)** Uplift histories of the Altiplano and Eastern Cordillera (Boschman et al., 2021). **(G)** Global mean sea level (GMSL; Westerhold et al., 2020) and regional hydroclimate forcings. **(H)** U–Th/He ages of Amazonian laterites (Gautheron et al., 2023). Shaded intervals highlight the Mid-Pliocene Warm Period (MPWP), Pliocene Marine Incursion (PMI), Miocene Marine Incursion (MMI), and the onset of Northern Hemisphere Glaciation (NHG).

Nd isotopic relationships further support this interpretation. ΔεNd offsets between FeOOH and clays remain relatively small during this interval (mean = 2.46 ± 1 2σ; **Fig. 8.1D**), consistent with Fe-oxides forming directly from freshly eroded Andean material during rapid exhumation, which limited isotopic decoupling between phases. Yet, binary mixing models reveal a persistent cratonic contribution of ~30%, suggesting that the Fe-oxide pool exported to the Fan was a composite of (i) pyrite-derived phases formed in uplifted shales and (ii) craton-sourced Fe-oxides. Notably, the concavity index (CI) values observed (~3–3.5) may underestimate the true signal of Andean pyrite oxidation. Modern analogues such as Taiwan, where shale-rich terrains are rapidly exhumed, yield riverine Fe-oxides with CI values as high as 8 (Bayon et al., in preparation), underscoring the capacity of fast-uplifting mountain belts to generate exceptionally concave REE patterns even when mixed with other sources.

Despite the rapid exhumation of the Central Andes, sediment accumulation on the Amazon Fan remained modest, with rates below 10 cm kyr^{-1} (**Fig. 8.1G**). Much of the eroded material was trapped in Andean foredeep depozones of the retroarc foreland basins rather than exported to the Atlantic margin (see previous chapter). Modern analogues provide a parallel: the Madeira Basin today experiences some of the highest denudation rates in the Andes due to ITCZ-driven rainfall seasonality, yet much of its sediment is stored in floodplains before reaching the lower Amazon (Baby et al., 2009; Vauchel et al., 2017). Yet, the Fan record still preserves a clear geochemical imprint of uplift. MREE-enriched patterns in the FeOOH fractions point to oxidative weathering of pyrite-rich Paleozoic shales in the Eastern Cordillera. These microcrystalline phases are typically associated with clays and thus less prone to hydraulic sorting than coarser detrital silicates, making them more likely to escape foreland storage and reach the margin. Thus, even a limited flux of suspended material was sufficient to transmit the oxidative weathering signal offshore. In this sense, the Late Miocene represents a transitional stage: uplift-driven erosion generated abundant reactive phases, but large-scale sediment bypass and intensified silicate weathering only developed later in the Pliocene, once transcontinental routing became fully established.

Early-Mid Pliocene (5-3 Ma): Warmth, ITCZ shift, and intensifying chemical weathering

The Early to Mid-Pliocene marks a turning point in the Amazon weathering system, as chemical weathering proxies rise to their highest levels of the Neogene. CIA values peak between ~4 and 2 Ma at ~72–74 (**Fig. 8.1B**), while $\Delta\varepsilon Hf(0)_{clays}$ climbs to strongly radiogenic values of +4 to +5 (**Fig. 8.1C**). These converging signals indicate that silicate dissolution intensified markedly during this interval, in contrast to the comparatively weaker silicate weathering regime of the Late Miocene. Offshore sediment accumulation rates also jumped nearly tenfold (60–80 cm kyr^{-1}; **Fig. 8.1G**), pointing to the establishment of a high-throughput sediment-routing system that continuously delivered fresh silicates to the lowlands and to the margin.

This rise in weathering intensity coincides with the global warmth of the Pliocene, particularly the Mid-Pliocene Warm Period (MPWP, 3.3–3.0 Ma), when mean annual temperatures were 2–3 °C above preindustrial levels and atmospheric CO_2 reached ~400 ppm (Haywood et al., 2020; McClymont et al., 2020). Proxy data and climate simulations show that the ITCZ was displaced northward by 1–3° during this interval (Pontes et al., 2020; 2022; Zhang et al., 2021), producing wetter conditions across northern Amazonia and drier conditions to the south. These hydroclimatic changes, coupled with warm and humid background conditions, would have favored both enhanced physical erosion in the Andes and stronger silicate weathering in retroarc foreland basins and lowland settings.

Importantly, the geochemical signals suggest that retroarc foreland basins were no longer just passive depocenters but had become active chemical weathering “reactors.” As sediment storage expanded in the floodplains, freshly eroded material underwent intense chemical alteration before being exported to the margin, amplifying the CIA and $\Delta\varepsilon Hf(0)_{clays}$ signals recorded offshore. This interpretation is consistent with continental archives: lateritic profiles in central Amazonia record a coeval phase of Fe-oxide precipitation and clay formation, with hematite dominating under more seasonal climates before ~3 Ma and goethite prevailing under wetter mid-Pliocene conditions (Gautheron et al., 2023). These marine and continental datasets demonstrate that the Amazon Basin responded coherently to mid-Pliocene warmth, with intensified silicate weathering expressed from the Andes to the Fan.

At the same time, shifts in FeOOH behavior reveal that this period of silicate weathering intensification coincided with changes in Fe-oxide sources. FeOOH % stabilized at relatively high levels (2–3 wt%; **Fig. 8.1E**), but the Concavity Index fell from ~2.8 to ~1.8 (**Fig. 8.1F**), reflecting a declining role of oxidative pyrite weathering (OPW) phases together with increasing contribution of secondary oxides formed via silicate weathering. This observation is supported by the ΔεNd offset, which, after rising during the Late Miocene, also began to decrease, collapsing to near-zero by 2.4–2.2 Ma (**Fig. 8.1D**). This pattern is consistent with progressively increasing silicate weathering from that time onward across the Amazon basin.

In sum, the Early–Mid Pliocene represents the peak of Amazonian chemical weathering, fueled by global warmth, northward ITCZ displacement, and the emergence of floodplains as powerful weathering reactors. This interval highlights the strong coupling between climate state and weathering intensity: unlike the Late Miocene, when tectonics and foreland trapping muted silicate dissolution, the Pliocene warmth created the hydroclimatic and geomorphic conditions for maximum chemical alteration across the basin.

Late Pliocene-Pleistocene (3-0.6 Ma): High weathering under a cooling world

At the Pliocene–Pleistocene transition, our geochemical proxies record a short-lived but pronounced weakening of chemical weathering. Between 3.0 and 2.2 Ma, CIA declines from ~74 to ~66 (**Fig. 8.2A**), $\Delta\varepsilon Hf(0)_{clays}$ drops from +5 to –1 (**Fig. 8.2B**), the Concavity Index falls from ~2.5 to ~2.0 (**Fig. 8.3D**), and $\Delta\varepsilon Nd_{FeOOH-clays}$ collapses to near zero (**Fig. 8.2C**). This pattern is difficult to reconcile at first glance: Nd isotopes (unradiogenic clays and muted ΔεNd offsets) suggest stronger cratonic input, whereas weathering proxies indicate a shift toward less chemically altered sources. A plausible explanation is that this interval reflects an influx of freshly eroded crystalline basement, rather than more recycled or pre-weathered cratonic detritus. The onset of Northern Hemisphere glaciation (NHG) brought significant glacial and periglacial advances in the tropical Andes, producing large volumes of unweathered detritus. Such an input would dilute radiogenic secondary clays, lowering CIA and ΔεHf, while also reducing isotopic decoupling between FeOOH and clays, consistent with the muted ΔεNd observed at this time.

After ~2.2 Ma, all proxies rebound: CIA and $\Delta\varepsilon Hf(0)_{clays}$ rise again, and CI stabilizes towards FeOOH phases sourced by silicate weathering processes, indicating that the Amazon weathering engine quickly re-establishes a vigorous silicate weathering regime. The apparent resilience of silicate weathering during the Late Pliocene–Pleistocene is paradoxical, given that this period was marked by progressive global cooling and the intensification of NHG (Westerhold et al., 2020).

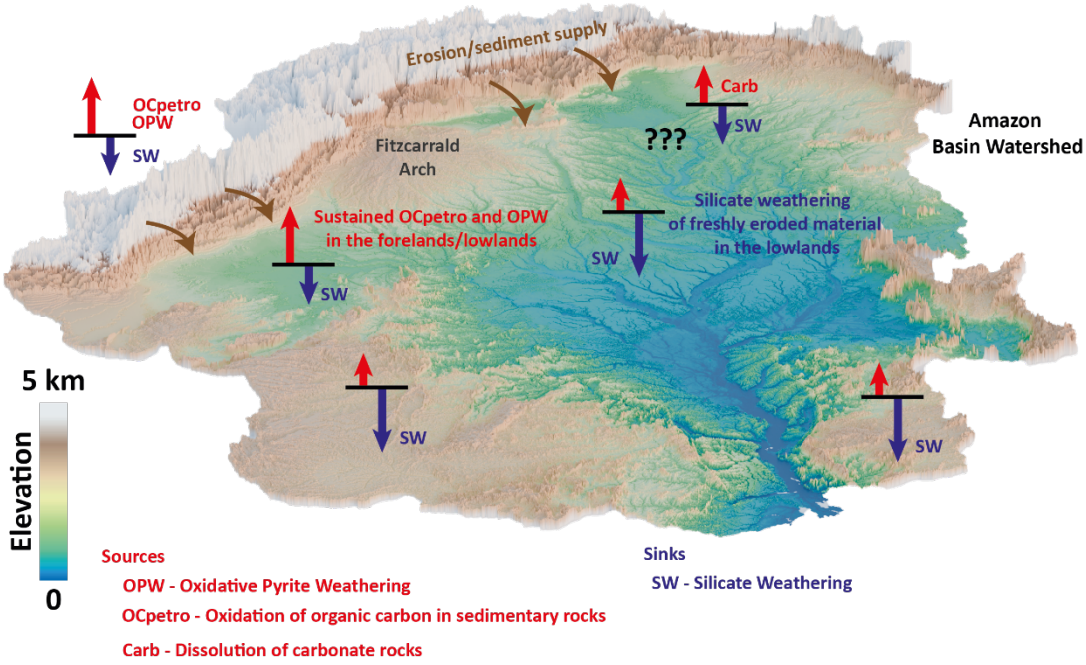

Figure 8.4. Schematic 3D topographic map of the Amazon Basin highlighting major physiographic units and sediment-routing pathways. Andean uplift and erosion supply material to foreland basins (Madeira and Solimões), where silicate weathering of freshly eroded sediments acts as a CO_2 sink. Cratonic areas (Brazilian and Guiana shields) contribute more stable, weathered material, while the Fitzcarrald Arch influences drainage partitioning.

This paradox can be resolved by considering the erosion–weathering coupling under new climatic forcing. The onset of NHG steepened equatorial–polar temperature gradients and reinforced Walker and Hadley circulations (Etourneau et al., 2010; Westerhold et al., 2020). Two processes likely sustained high weathering fluxes despite cooler conditions (**Fig. 8.4**). First, stronger ENSO variability and a more vigorous Walker circulation after ~4.5 Ma (Fedorov et al., 2015; Liu et al., 2019) enhanced rainfall seasonality over the Andes, generating repeated pulses of erosion and sediment export. Second, the emergence of glacial–interglacial cyclicity produced large volumes of fresh detritus through glacial and periglacial erosion

during glacials, followed by interglacial intervals during which previously stored sediments in Amazonian floodplains underwent intense chemical alteration under warm, humid monsoonal conditions (Yu et al., 2020).

Viewed in comparison with the mid-Pliocene warm period (4.5–3 Ma), this interval underscores a fundamental shift in the controls on Amazon weathering. During the mid-Pliocene warmth, high CIA and radiogenic ΔεHf reflected vigorous silicate weathering under favorable climatic conditions—warmth and humidity amplified chemical reactions. In contrast, during the cooler Late Pliocene–Pleistocene, equally high weathering fluxes were maintained through a different pathway: the tight coupling of erosion and floodplain weathering under ENSO-driven rainfall variability and glacial–interglacial cycles. In this framework, Late Pliocene–Pleistocene weathering was not sustained in spite of global cooling, but because of it. Alternating erosional and weathering regimes created a highly effective coupling between physical erosion and silicate dissolution, with glaciers, ENSO variability, and floodplain reactors working in concert to maintain high chemical weathering fluxes. Offshore geochemical records thus capture the integrated outcome of a resilient Amazon weathering engine, demonstrating how tropical source-to-sink systems can sustain vigorous silicate weathering under both warm and cool global states, but through different mechanisms.

8.4.2. Implications for the CO_2 cycle

The uplift–weathering hypothesis (Raymo & Ruddiman, 1992) proposed that mountain building during the late Cenozoic accelerated the exposure and hydrolysis of silicate minerals, driving a net sink of atmospheric CO_2 and initiating global cooling and ice-sheet expansion. However, recent studies have shown that this framework is too simple. Global climate models and geochemical records suggest that Himalayan weathering fluxes alone were insufficient to account for Neogene CO_2 decline (e.g., Park et al., 2020). Instead, additional mechanisms must have contributed.

As mentioned above, one major candidate is the collision and emergence of arc–continent systems in Southeast Asia. Geochemical records from the Indian and Pacific Oceans demonstrate that after ~4 Ma, erosion and chemical weathering of exposed ophiolites in Indonesia and New Guinea intensified sharply, enhancing global CO_2 consumption (**Fig. 8.5**;

Bayon et al., 2023; Clift et al., 2024). Modeling shows that without this late Neogene increase in mafic weathering, atmospheric pCO_2 would have remained too high to permit the onset of Northern Hemisphere glaciation (Park et al., 2020). Beyond simple silicate hydrolysis, weathering of ophiolites also produces smectite-rich clays with high surface areas, which strongly promote organic carbon burial and thereby amplify CO_2 sequestration (Murray & Jagoutz, 2024).

Our Amazon Fan record provides the first long-term evidence that the Andes played a central role in the Neogene carbon cycle, a role that has been largely overlooked compared to Southeast Asia and the Himalayas. During the Late Miocene, uplift of the Eastern Cordillera exposed Paleozoic black shales rich in pyrite and petrogenic organic carbon. Their oxidative weathering likely released large amounts of CO_2, tipping the carbon balance toward a source despite rapid Andean exhumation (Torres et al., 2014; Zondervan et al., 2023). In sharp contrast, after ~4.5 Ma, our silicate weathering proxies rise steeply, signaling a transition to intense silicate weathering under warm and humid Pliocene conditions. This shift effectively transformed the Andes from a net CO_2 source into a significant CO_2 sink, synchronizing with global Pliocene cooling and the onset of Northern Hemisphere glaciation. In this light, the Andes emerges as a critical but underappreciated driver of Late Cenozoic climate evolution, complementing the better-known contribution of Southeast Asian ophiolite weathering and helping to explain how atmospheric CO_2 ultimately fell to levels low enough to sustain Quaternary ice ages.

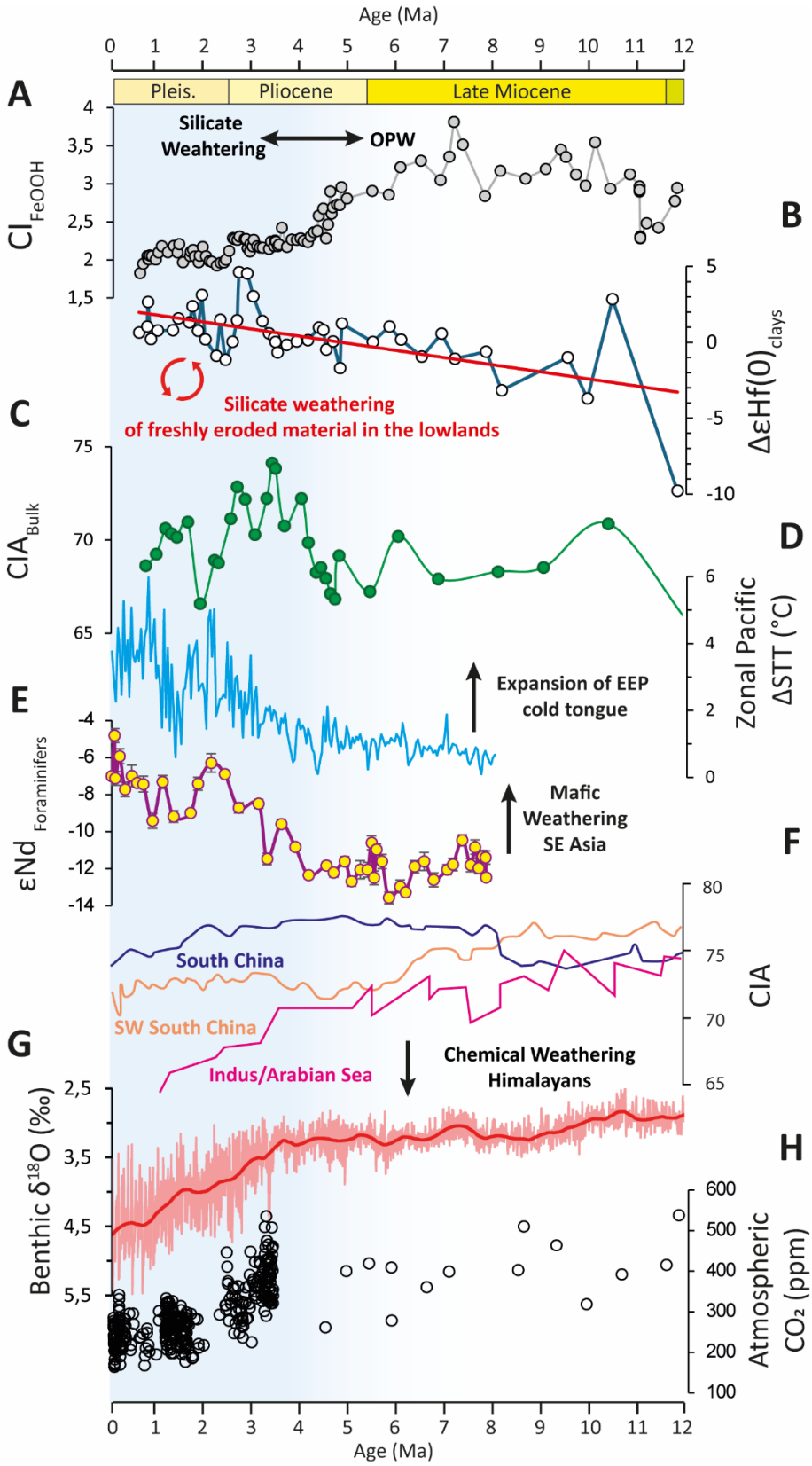

Figure 8.5. Comparison of Amazon Fan weathering proxies with global and regional climate records over the past 12 Myr. (A) Concavity Index (CI_{FeOOH}) of Fe-(oxyhydr)oxides distinguishing oxidative pyrite weathering (OPW) from silicate-derived phases. **(B)** $\Delta\varepsilon Hf(0)_{clays}$ reflecting the degree of silicate dissolution and secondary clay

formation. **(C)** Bulk CIA values as an additional measure of silicate weathering intensity. **(D)** Eastern equatorial Pacific (EEP) zonal sea-surface temperature gradient (ΔSST) showing the development of the Pacific cold tongue (Fedorov et al., 2019). **(E)** εNd of foraminifera from the Indian Ocean recording enhanced mafic weathering in Southeast Asia (Bayon et al., 2023). **(F)** CIA records from South China, SW South China, and the Indus/Arabian Sea reflecting chemical weathering of the Himalayas (Clift and Jonell, 2021, and references therein). **(G)** Benthic $\delta^{18}O$ stack (red; Lisiecki & Raymo, 2004) with individual records, indicating global cooling. **(H)** Atmospheric CO_2 concentrations from marine proxies and ice cores (Rae et al., 2021).

Crucially, our results highlight the role of tropical floodplains in amplifying this sink. Acting as vast silicate weathering reactors, tropical foreland and lowland floodplains in the Amazon Basin repeatedly stored freshly eroded Andean sediments and subjected them to prolonged alteration under warm, humid conditions before export to the margin. This mechanism aligns with the emerging concept of a silicate weathering continuum (Trapp-Müller et al., 2025), in which downstream environments extend and magnify the weathering signal initiated in mountain headwaters. The Andes-Amazon source-to-sink system provides the first long-term demonstration of this process, showing that floodplain reworking can sustain high silicate weathering fluxes even under global cooling and sediment trapping conditions.

Viewed globally, the Neogene CO_2 decline was likely sustained by a combination of processes: enhanced mafic weathering in Southeast Asia, increased organic carbon burial linked to ophiolite clays, and the transition of the Andes from a source to a sink of CO_2 after ~4 Ma. A common feature between these different processes is that they are all linked to silicate weathering occurring under warm and humid tropical climates. Taken together, these mechanisms refine the uplift–weathering hypothesis, showing that mountain building can either destabilize or stabilize climate depending on the lithologies exposed and the efficiency of sediment storage and recycling along the source-to-sink pathway but also, importantly, depending on regional climate conditions.

9. Conclusions

Our multiproxy record identifies the Andes as a previously underestimated piece of the Late Cenozoic CO_2 drawdown puzzle. By capturing the switch from CO_2 source (oxidative shale weathering) to CO_2 sink (silicate hydrolysis amplified by floodplain reactors), the Amazon Fan record demonstrates that Andean uplift was not a passive background process but an active driver of global climate evolution. While the timing and direction of this transition are now clear, the magnitude of Andean CO_2 fluxes remains uncertain. Quantifying these fluxes is the essential next step; without it, the true weight of the Andes in the global carbon budget cannot be assessed. Integrating this long-overlooked mountain belt, together with its floodplains, into Earth system models is critical to fully resolve the mechanisms of Late Cenozoic cooling.

IX

Conclusions and perspectives

This thesis applied a consistent set of geochemical tools, rare earth element (REE) patterns and neodymium isotopic compositions in paired clay and Fe-(oxyhydr)oxide (FeOOH) fractions, to a diverse suite of archives from the Amazon Basin and Fan. The overarching aim was to reconstruct the co-evolution of tectonics, climate, and weathering in northern South America during the late Cenozoic. To achieve this, I calibrated new proxies in modern river sediments, developed an astronomically tuned age model for the Amazon Fan, tested the integrity of FeOOH leachates in deep-marine sequences, and reconstructed sediment provenance and weathering regimes across the past 24 Myr. Together, these approaches yielded insights into the mechanisms that governed sediment routing, chemical weathering, and carbon cycling in the world's largest river basin.

Calibration of geochemical proxies in the modern Amazon Basin

Analyses of river sediments collected during the AMANAUS cruise established the foundation for interpreting the Amazon Fan record. Nd isotopes and REE patterns in clays and FeOOH fractions display distinct responses to lithology and weathering mode. $\Delta\varepsilon Nd_{FeOOH-clay}$ proved a robust tracer of silicate vs. sedimentary rock weathering, while REE concativity indexes capture the source of FeOOH phases. These findings validate the use of paired clays and FeOOH to disentangle lithology-dependent chemical weathering processes in a tropical setting. These findings reinforce the powefull application of such proxies for future studies of source-to-sink weathering fluxes.

Chronology and integrity of the Amazon Fan record

A new astronomically tuned age model for the BP-3 well extended the Amazon Fan chronology back to ~24 Ma, providing one of the longest continuous orbitally resolved archives of tropical sedimentation. Gamma-ray cyclicity enabled direct correlation to global sea-level changes, showing that sedimentation rates on the fan were strongly modulated by both orbital climate variability and tectonic reorganizations. Importantly, the late Miocene was characterized by persistently low accumulation rates despite Andean uplift and intensified rainfall, implying major sediment trapping in the Pebas wetlands. In contrast, the Early Pliocene

marked an order-of-magnitude increase in sedimentation rates, synchronous with global sea-level rise and ITCZ shifts. Evaluation of drilling mud impacts and FeOOH preservation showed that most intervals are reliable archives, although extreme Ba enrichments highlight the need for caution in interpreting REE systematics at some depths. These results establish the Amazon Fan as a robust, orbitally tuned source-to-sink record of Andean uplift, climate change, and sediment flux.

Provenance and drainage integration of the Amazon Basin

Clay Nd isotopes from BP-3 revealed three main stages of transcontinental drainage integration. Stage I (12–7 Ma) records the first sustained Andean export, dominated by Madeira-like sources routed around the Purus Arch. Stage II (7–4 Ma) reflects partial capture of central Andean headwaters, producing the most radiogenic signatures yet still fragmented drainage. Stage III (4–0.6 Ma) shows stabilization into Solimões–Madeira dual dominance and high sediment throughput to the Atlantic. These findings place the onset of transcontinental sediment export significantly earlier than many previous estimates, and they demonstrate a progressive, stepwise integration of the basin. The results highlight how tectonic barriers, wetland dynamics, and headwater capture controlled the delivery of sediments to the Atlantic margin.

Weathering regimes and long-term carbon cycle implications

Integration of CIA, $\Delta\varepsilon Hf_{clays}$, $\Delta\varepsilon Nd_{FeOOH\text{-}clays}$, and REE indices revealed intense oxidative weathering of organic-rich shales during the Late Miocene until Early Pliocene, representing a persistent CO_2 source, traceable through REE distribution patterns of FeOOH phases. Then, silicate weathering intensified after ~4.5 Ma, coincident with accelerated fresh mineral supply and continuous silicate weathering in the Amazonian floodplains representing a growing CO_2 sink. This multiproxy framework demonstrates that the balance of lithologies, rather than uplift alone, modulated CO_2 fluxes over million-year timescales. In doing so, the thesis refines the "uplift–weathering" theory of Raymo and Ruddiman (1992) by explicitly distinguishing between silicate sinks and sedimentary-rock sources.

Concluding Remarks and Future Perspectives

The paired analysis of clays and FeOOH emerges as a powerful methodological contribution, enabling the disentangling of silicate versus sedimentary rock weathering. The astronomically tuned age model for BP-3 provides a chronological backbone for integrating orbital, climatic, and tectonic controls on sedimentation. Provenance reconstructions have redefined the timing of Amazon River integration, while multiproxy weathering records have clarified the dual role of the basin as both a CO_2 sink and source.

Looking forward, several avenues stand out:

Quantifying CO_2 budgets. The next frontier in resolving Late Cenozoic global cooling is to quantify the net CO_2 consumption of the Amazon source-to-sink system through the late Neogene. While this thesis identified the competing roles of silicate versus sedimentary rock weathering, constraining flux magnitudes remains a missing piece essential for evaluating Cenozoic cooling.

Revisiting Miocene climate puzzles. Could the uplift of the central Andes during the mid–late Miocene have delayed global cooling? Did oxidative weathering of OC_{petro} and black shales contribute additional CO_2 to sustain warmth during the Middle Miocene Climatic Optimum? Testing these hypotheses requires coupling geochemical reconstructions with Earth System Models.

Constraining floodplain archives. Amazonian floodplains played a pivotal role in sediment storage and weathering during the Neogene, yet their chronologies remain poorly resolved due to limited fossil preservation. Cyclostratigraphy, particularly in intervals with marine incursions that can be tied to global $\delta^{18}O$ stacks, offers a promising pathway to refine depositional ages and integrate floodplains into source-to-sink reconstructions.

The Amazon of tomorrow. Atmospheric pCO_2 is projected to reach levels comparable to the Pliocene, a period when the Amazon Basin operated under warm and humid conditions with intensified weathering and sediment export. Future research should explore how the basin's hydrological and geochemical systems responded then, to anticipate how they may respond in the coming century.

In summary, this thesis provides new constraints on the evolution of Amazonian weathering, provenance, and sedimentation over the past 24 Myr. It underscores the Amazon Basin's dual role in regulating Earth's climate: as a driver of long-term CO_2 sequestration through silicate weathering and as a potential source of CO_2 through oxidative weathering of organic-rich sediments. Beyond regional insights, the findings demonstrate the necessity of source-to-sink perspectives for evaluating the links between tectonics, climate, and the carbon cycle on geological timescales.

References

Akabane, T.K., Chiessi, C.M., Hirota, M., Bouimetarhan, I., Prange, M., Mulitza, S., Bertassoli Jr, D.J., Häggi, C., Staal, A., Lohmann, G., Boers, N., Daniau, A.L., Oliveira, R.S., Campos, M.C., Shi, X., De Oliveira, P.E., 2024. Weaker Atlantic overturning circulation increases the vulnerability of northern Amazon forests. Nat. Geosci. https://doi.org/10.1038/s41561-024-01578-z

Albarède, F., Goldstein, S.L., Dautel, D., 1997. The neodymium isotopic composition of manganese nodules from the Southern and Indian oceans, the global oceanic neodymium budget, and their bearing on deep ocean circulation. Geochimica et Cosmochimica Acta 61, 1277–1291. https://doi.org/10.1016/S0016-7037(96)00404-8

Albert, J.S., Bernt, M.J., Fronk, A.H., Fontenelle, J.P., Kuznar, S.L., Lovejoy, N.R., 2021. Late Neogene megariver captures and the Great Amazonian Biotic Interchange. Global and Planetary Change 205, 103554. https://doi.org/10.1016/j.gloplacha.2021.103554

Albert, J.S., Val, P., Hoorn, C., 2018. The changing course of the Amazon River in the Neogene: center stage for Neotropical diversification. Neotrop. ichthyol. 16, e180033. https://doi.org/10.1590/1982-0224-20180033

Allègre, C.J., Dupré, B., Négrel, P., Gaillardet, J., 1996. Sr□Nd□Pb isotope systematics in Amazon and Congo River systems: constraints about erosion processes. Chemical Geology 131, 93–112. https://doi.org/10.1016/0009-2541(96)00028-9

Alvim, A.M.V., Santos, R.V., Roddaz, M., Antoine, P.-O., Ramos, M.I.F., Do Carmo, D.A., Linhares, A.P., Negri, F.R., 2021. Fossil isotopic constraints (C, O and 87Sr/86Sr) on Miocene shallow-marine incursions in Amazonia. Palaeogeography, Palaeoclimatology, Palaeoecology 573, 110422. https://doi.org/10.1016/j.palaeo.2021.110422

Ansart, C., Guinoiseau, D., Quantin, C., Calmels, D., Gautheron, C., Agrinier, P., Bouchez, J., Fekiacova, Z., Pinna-Jamme, R., Demri, D., Balan, E., Heller, B., Bollaert, Q., Ataytür, Ö., Allard, T., 2025. Lateritic Cenozoic paleoenvironmental and paleoclimatic conditions in the Central Amazon basin, Brazil, inferred from mineralogy, geochemistry and geochronology. Palaeogeography, Palaeoclimatology, Palaeoecology 662, 112674. https://doi.org/10.1016/j.palaeo.2024.112674

Armijos, E., Crave, A., Vauchel, P., Fraizy, P., Santini, W., Moquet, J.-S., Arevalo, N., Carranza, J., Guyot, J.-L., 2013. Suspended sediment dynamics in the Amazon River of Peru. Journal of South American Earth Sciences 44, 75–84. https://doi.org/10.1016/j.jsames.2012.09.002

Baby, P., Prudhomme, A., Brusset, S., Robert, A., Roddaz, M., Calderon, Y., Eude, A., Gil, W., Hermoza, W., Hurtado, C., Brichau, S., Calvès, G., Antoine, P.-O., Salas-Gismondi, R., 2025. The Northern Central Andes and Andean tectonic evolution revisited: An integrated stratigraphic and structural model of three superimposed orogens. Earth-Science Reviews 260, 104998. https://doi.org/10.1016/j.earscirev.2024.104998

Barnes, J.B., Ehlers, T.A., Insel, N., McQuarrie, N., Poulsen, C.J., 2012. Linking orography, climate, and exhumation across the central Andes. Geology 40, 1135–1138. https://doi.org/10.1130/G33229.1

Barrat, J.-A., Bayon, G., 2024. Practical guidelines for representing and interpreting rare earth abundances in environmental and biological studies. Chemosphere 352, 141487. https://doi.org/10.1016/j.chemosphere.2024.141487

Barrat, J.-A., Bayon, G., Lalonde, S., 2023. Calculation of cerium and lanthanum anomalies in geological and environmental samples. Chemical Geology 615, 121202. https://doi.org/10.1016/j.chemgeo.2022.121202

Barrat, J.A., Keller, F., Amossé, J., Taylor, R.N., Nesbitt, R.W., Hirata, T., 1996. DETERMINATION OF RARE EARTH ELEMENTS IN SIXTEEN SILICATE REFERENCE SAMPLES BY ICP-MS AFTER TM ADDITION AND ION EXCHANGE SEPARATION. Geostandards Newsletter 20, 133–139. https://doi.org/10.1111/j.1751-908X.1996.tb00177.x

Barrat, J.A., Zanda, B., Moynier, F., Bollinger, C., Liorzou, C., Bayon, G., 2012. Geochemistry of CI chondrites: Major and trace elements, and Cu and Zn Isotopes. Geochimica et Cosmochimica Acta 83, 79–92. https://doi.org/10.1016/j.gca.2011.12.011

Barroux, G., Sonke, J.E., Boaventura, G., Viers, J., Godderis, Y., Bonnet, M., Sondag, F., Gardoll, S., Lagane, C., Seyler, P., 2006. Seasonal dissolved rare earth element dynamics of the Amazon River main stem, its tributaries, and the Curuaí floodplain. Geochem Geophys Geosyst 7, 2006GC001244. https://doi.org/10.1029/2006GC001244

Bayon, G., Dennielou, B., Etoubleau, J., Ponzevera, E., Toucanne, S., Bermell, S., 2012. Intensifying Weathering and Land Use in Iron Age Central Africa. Science 335, 1219–1222. https://doi.org/10.1126/science.1215400

Bayon, G., Douglas, G.B., Denton, G.J., Monin, L., De Deckker, P., 2020a. Preferential Riverine Export of Fine Volcanogenic Particles to the Southeast Australian Margin. Front. Mar. Sci. 7, 89. https://doi.org/10.3389/fmars.2020.00089

Bayon, G., Garzanti, E., Dinis, P., Beaufort, D., Barrat, J.-A., Germain, Y., Trinquier, A., Barbarano, M., Overare, B., Adeaga, O., Braquet, N., 2024. Contribution of Saharan dust to chemical weathering fluxes and associated phosphate release in West Africa. Earth and Planetary Science Letters 641, 118845. https://doi.org/10.1016/j.epsl.2024.118845

Bayon, G., Lambert, T., Vigier, N., De Deckker, P., Freslon, N., Jang, K., Larkin, C.S., Piotrowski, A.M., Tachikawa, K., Thollon, M., Tipper, E.T., 2020b. Rare earth element and neodymium isotope tracing of sedimentary rock weathering. Chemical Geology 553, 119794. https://doi.org/10.1016/j.chemgeo.2020.119794

Bayon, G., Patriat, M., Godderis, Y., Trinquier, A., De Deckker, P., Kulhanek, D.K., Holbourn, A., Rosenthal, Y., 2023. Accelerated mafic weathering in Southeast Asia linked to late Neogene cooling. Science Advances 9, eadf3141. https://doi.org/10.1126/sciadv.adf3141

Bayon, G., Skonieczny, C., Delvigne, C., Toucanne, S., Bermell, S., Ponzevera, E., André, L., 2016. Environmental Hf–Nd isotopic decoupling in World river clays. Earth and Planetary Science Letters 438, 25–36. https://doi.org/10.1016/j.epsl.2016.01.010

Bayon, G., Toucanne, S., Skonieczny, C., André, L., Bermell, S., Cheron, S., Dennielou, B., Etoubleau, J., Freslon, N., Gauchery, T., Germain, Y., Jorry, S.J., Ménot, G., Monin, L., Ponzevera, E., Rouget, M.-L., Tachikawa, K., Barrat, J.A., 2015. Rare earth elements and neodymium isotopes in world river sediments revisited. Geochimica et Cosmochimica Acta 170, 17–38. https://doi.org/10.1016/j.gca.2015.08.001

Bayon, G., Vigier, N., Burton, K.W., Jean Carignan, A.B., Etoubleau, J., Chu, N.-C., 2006. The control of weathering processes on riverine and seawater hafnium isotope ratios. Geol 34, 433. https://doi.org/10.1130/G22130.1

Berger, A., Loutre, M.F., 1994. Astronomical Forcing through Geological Time, in: De Boer, P.L., Smith, D.G. (Eds.), Orbital Forcing and Cyclic Sequences. Wiley, pp. 15–24. https://doi.org/10.1002/9781444304039.ch2

Berner, R.A., 1999. Atmospheric oxygen over Phanerozoic time. Proc. Natl. Acad. Sci. U.S.A. 96, 10955–10957. https://doi.org/10.1073/pnas.96.20.10955

Berner, R.A., Lasaga, A.C., Garrels, R.M., 1983. The carbonate-silicate geochemical cycle and its effect on atmospheric carbon dioxide over the past 100 million years. American Journal of Science 283, 641–683. https://doi.org/10.2475/ajs.283.7.641

Bicudo, T.C., Sacek, V., De Almeida, R.P., Bates, J.M., Ribas, C.C., 2019. Andean Tectonics and Mantle Dynamics as a Pervasive Influence on Amazonian Ecosystem. Sci Rep 9, 16879. https://doi.org/10.1038/s41598-019-53465-y

Blattmann, T.M., Wang, S.-L., Lupker, M., Märki, L., Haghipour, N., Wacker, L., Chung, L.-H., Bernasconi, S.M., Plötze, M., Eglinton, T.I., 2019. Sulphuric acid-mediated weathering on Taiwan buffers geological atmospheric carbon sinks. Sci Rep 9, 2945. https://doi.org/10.1038/s41598-019-39272-5

Blichert-Toft, J., Chauvel, C., Albarède, F., 1997. Separation of Hf and Lu for high-precision isotope analysis of rock samples by magnetic sector-multiple collector ICP-MS. Contributions to Mineralogy and Petrology 127, 248–260. https://doi.org/10.1007/s004100050278

Boschman, L.M., 2021. Andean mountain building since the Late Cretaceous: A paleoelevation reconstruction. Earth-Science Reviews 220, 103640. https://doi.org/10.1016/j.earscirev.2021.103640

Bouchez, J., Gaillardet, J., France-Lanord, C., Maurice, L., Dutra-Maia, P., 2011. Grain size control of river suspended sediment geochemistry: Clues from Amazon River depth profiles. Geochem Geophys Geosyst 12, 2010GC003380. https://doi.org/10.1029/2010GC003380

Bouvier, A., Vervoort, J.D., Patchett, P.J., 2008. The Lu–Hf and Sm–Nd isotopic composition of CHUR: Constraints from unequilibrated chondrites and implications for the bulk composition of terrestrial planets. Earth and Planetary Science Letters 273, 48–57. https://doi.org/10.1016/j.epsl.2008.06.010

Brady, P.V., 1991. The effect of silicate weathering on global temperature and atmospheric CO_2. J. Geophys. Res. 96, 18101–18106. https://doi.org/10.1029/91JB01898

Brantley, S.L., Lebedeva, M., Bazilevskaya, E., 2014. Relating Weathering Fronts for Acid Neutralization and Oxidation to pCO2 and pO2, in: Treatise on Geochemistry. Elsevier, pp. 327–352. https://doi.org/10.1016/B978-0-08-095975-7.01317-6

Calmels, D., Gaillardet, J., Brenot, A., France-Lanord, C., 2007. Sustained sulfide oxidation by physical erosion processes in the Mackenzie River basin: Climatic perspectives. Geol 35, 1003. https://doi.org/10.1130/G24132A.1

Campbell, K.E., Frailey, C.D., Romero-Pittman, L., 2006. The Pan-Amazonian Ucayali Peneplain, late Neogene sedimentation in Amazonia, and the birth of the modern Amazon River system. Palaeogeography, Palaeoclimatology, Palaeoecology 239, 166–219. https://doi.org/10.1016/j.palaeo.2006.01.020

Caves Rugenstein, J.K., Ibarra, D.E., Von Blanckenburg, F., 2019. Neogene cooling driven by land surface reactivity rather than increased weathering fluxes. Nature 571, 99–102. https://doi.org/10.1038/s41586-019-1332-y

Chalk, T.B., Hain, M.P., Foster, G.L., Rohling, E.J., Sexton, P.F., Badger, M.P.S., Cherry, S.G., Hasenfratz, A.P., Haug, G.H., Jaccard, S.L., Martínez-García, A., Pälike, H., Pancost, R.D., Wilson, P.A., 2017. Causes of ice age intensification across the Mid-Pleistocene Transition. Proc. Natl. Acad. Sci. U.S.A. 114, 13114–13119. https://doi.org/10.1073/pnas.1702143114

Clift, P.D., Du, Y., Mohtadi, M., Pahnke, K., Sutorius, M., Böning, P., 2024a. The erosional and weathering response to arc–continent collision in New Guinea. JGS 181, jgs2023-207. https://doi.org/10.1144/jgs2023-207

Clift, P.D., Jonell, T.N., Du, Y., Bornholdt, T., 2024b. The impact of Himalayan-Tibetan erosion on silicate weathering and organic carbon burial. Chemical Geology 656, 122106. https://doi.org/10.1016/j.chemgeo.2024.122106

Colin, C., Siani, G., Liu, Z., Blamart, D., Skonieczny, C., Zhao, Y., Bory, A., Frank, N., Duchamp-Alphonse, S., Thil, F., Richter, T., Kissel, C., Gargani, J., 2014. Late Miocene to early Pliocene climate variability off NW Africa (ODP Site 659). Palaeogeography, Palaeoclimatology, Palaeoecology 401, 81–95. https://doi.org/10.1016/j.palaeo.2014.02.015

Cremon, É.H., Rossetti, D. de F., Sawakuchi, A. de O., Cohen, M.C.L., 2016. The role of tectonics and climate in the late Quaternary evolution of a northern Amazonian River. Geomorphology 271, 22–39. https://doi.org/10.1016/j.geomorph.2016.07.030

Cruz, A.M., Reis, A.T., Suc, J.P., Silva, C.G., Praeg, D., Granjeon, D., Rabineau, M., Popescu, S.M., Gorini, C., 2019. Neogene evolution and demise of the Amapá carbonate platform, Amazon continental margin, Brazil. Marine and Petroleum Geology 105, 185–203. https://doi.org/10.1016/j.marpetgeo.2019.04.009

Custódio, M.A., Roddaz, M., Santos, R.V., Dantas, E.L., Brusset, S., Louterbach, M., Hurtado, C., Gonçalves, G.O., 2024. Maastrichtian-Cenozoic erosional history of the northern Peruvian Amazonian Andes implications for the Eastern Cordillera evolution (Huallaga Basin, northern Peru). Global and Planetary Change 242, 104584. https://doi.org/10.1016/j.gloplacha.2024.104584

Dai, A., Trenberth, K.E., 2002. Estimates of Freshwater Discharge from Continents: Latitudinal and Seasonal Variations. J. Hydrometeor 3, 660–687. https://doi.org/10.1175/1525-7541(2002)003%253C0660:EOFDFC%253E2.0.CO;2

Damuth, J.E., 1977. Late Quaternary sedimentation in the western equatorial Atlantic. Geol Soc America Bull 88, 695. https://doi.org/10.1130/0016-7606(1977)88%253C695:LQSITW%253E2.0.CO;2

Dellinger, M., Gaillardet, J., Bouchez, J., Calmels, D., Louvat, P., Dosseto, A., Gorge, C., Alanoca, L., Maurice, L., 2015. Riverine Li isotope fractionation in the Amazon River basin controlled by the weathering regimes. Geochimica et Cosmochimica Acta 164, 71–93. https://doi.org/10.1016/j.gca.2015.04.042

Dellinger, M., Hilton, R.G., Baronas, J.J., Torres, M.A., Burt, E.I., Clark, K.E., Galy, V., Ccahuana Quispe, A.J., West, A.J., 2023. High rates of rock organic carbon oxidation sustained as Andean sediment transits the Amazon foreland-floodplain. Proc. Natl. Acad. Sci. U.S.A. 120, e2306343120. https://doi.org/10.1073/pnas.2306343120

DePaolo, D.J., 1988. Neodymium Isotope Geochemistry: an Introduction. Springer Berlin Heidelberg, Berlin, Heidelberg.

DePaolo, D.J., Wasserburg, G.J., 1976. Inferences about magma sources and mantle structure from variations of ^{143}Nd/^{144}Nd. Geophys. Res. Lett. 3, 743–746. https://doi.org/10.1029/GL003i012p00743

Dobson, D.M., Dickens, G.R., Rea, D.K., 2001. Terrigenous sediment on Ceara Rise: a Cenozoic record of South American orogeny and erosion. Palaeogeography, Palaeoclimatology, Palaeoecology 165, 215–229. https://doi.org/10.1016/S0031-0182(00)00161-9

Dos Santos Albuquerque, M.F., Horbe, A.M.C., Danišík, M., 2020. Episodic weathering in Southwestern Amazonia based on (U Th)/He dating of Fe and Mn lateritic duricrust. Chemical Geology 553, 119792. https://doi.org/10.1016/j.chemgeo.2020.119792

Dos Santos Albuquerque, M.F., Horbe, A.M.C., Gautheron, C., Vieira, J.G.C., Val, P., Pinna-Jamme, R., Salazar, C.A., 2025. (U Th)/He Geochronology of Fe and Fe Al Lateritic Duricrusts and Bauxites in Central-Northern Amazonia: Implications for Paleoclimate and Landscape Evolution. Chemical Geology 689, 122835. https://doi.org/10.1016/j.chemgeo.2025.122835

Dosseto, A., Bourdon, B., Gaillardet, J., Allègre, C.J., Filizola, N., 2006. Time scale and conditions of weathering under tropical climate: Study of the Amazon basin with U-series. Geochimica et Cosmochimica Acta 70, 71–89. https://doi.org/10.1016/j.gca.2005.06.033

Ehlers, T.A., Poulsen, C.J., 2009. Influence of Andean uplift on climate and paleoaltimetry estimates. Earth and Planetary Science Letters 281, 238–248. https://doi.org/10.1016/j.epsl.2009.02.026

Eldrett, J.S., Harding, I.C., Wilson, P.A., Butler, E., Roberts, A.P., 2007. Continental ice in Greenland during the Eocene and Oligocene. Nature 446, 176–179. https://doi.org/10.1038/nature05591

Espurt, N., Baby, P., Brusset, S., Roddaz, M., Hermoza, W., Regard, V., Antoine, P.-O., Salas-Gismondi, R., Bolaños, R., 2007. How does the Nazca Ridge subduction influence the modern Amazonian foreland basin? Geol 35, 515. https://doi.org/10.1130/G23237A.1

Etourneau, J., Schneider, R., Blanz, T., Martinez, P., 2010. Intensification of the Walker and Hadley atmospheric circulations during the Pliocene–Pleistocene climate transition. Earth and Planetary Science Letters 297, 103–110. https://doi.org/10.1016/j.epsl.2010.06.010

Fedorov, A.V., Brierley, C.M., Lawrence, K.T., Liu, Z., Dekens, P.S., Ravelo, A.C., 2013. Patterns and mechanisms of early Pliocene warmth. Nature 496, 43–49. https://doi.org/10.1038/nature12003

Figueiredo, J., Hoorn, C., van der Ven, P., Soares, E., 2009. Late Miocene onset of the Amazon River and the Amazon deep-sea fan: Evidence from the Foz do Amazonas Basin. Geology 37, 619–622. https://doi.org/10.1130/G25567A.1

Fisher, G.B., Luna, L.V., Amidon, W.H., Burbank, D.W., De Boer, B., Stap, L.B., Bookhagen, B., Godard, V., Oskin, M.E., Alonso, R.N., Tuenter, E., Lourens, L.J., 2023. Milankovitch-paced erosion in the southern Central Andes. Nat Commun 14, 424. https://doi.org/10.1038/s41467-023-36022-0

France-Lanord, C., Derry, L.A., 1997. Organic carbon burial forcing of the carbon cycle from Himalayan erosion. Nature 390, 65–67. https://doi.org/10.1038/36324

Gaillardet, J., Dupre, B., Allegre, C.J., Négrel, P., 1997. Chemical and physical denudation in the Amazon River Basin. Chemical Geology 142, 141–173. https://doi.org/10.1016/S0009-2541(97)00074-0

Gaillardet, J., Dupré, B., Louvat, P., Allègre, C.J., 1999. Global silicate weathering and CO2 consumption rates deduced from the chemistry of large rivers. Chemical Geology 159, 3–30. https://doi.org/10.1016/S0009-2541(99)00031-5

Garçon, M., Chauvel, C., 2014. Where is basalt in river sediments, and why does it matter? Earth and Planetary Science Letters 407, 61–69. https://doi.org/10.1016/j.epsl.2014.09.033

Garzione, C.N., McQuarrie, N., Perez, N.D., Ehlers, T.A., Beck, S.L., Kar, N., Eichelberger, N., Chapman, A.D., Ward, K.M., Ducea, M.N., Lease, R.O., Poulsen, C.J., Wagner, L.S., Saylor, J.E., Zandt, G., Horton, B.K., 2017. Tectonic Evolution of the Central Andean Plateau and Implications for the Growth of Plateaus. Annu. Rev. Earth Planet. Sci. 45, 529–559. https://doi.org/10.1146/annurev-earth-063016-020612

Gautheron, C., Sawakuchi, A.O., Dos Santos Albuquerque, M.F., Cabriolu, C., Parra, M., Ribas, C.C., Pupim, F.N., Schwartz, S., Kern, A.K., Gómez, S., De Almeida, R.P., Horbe, A.M.C., Haurine, F., Miska, S., Nouet, J., Findling, N., Riffel, S.B., Pinna-Jamme, R., 2022. Cenozoic weathering of fluvial terraces and emergence of biogeographic boundaries in Central Amazonia. Global and Planetary Change 212, 103815. https://doi.org/10.1016/j.gloplacha.2022.103815

Gerard, M., Seyler, P., Benedetti, M.F., Alves, V.P., Boaventura, G.R., Sondag, F., 2003. Rare earth elements in the Amazon basin. Hydrological Processes 17, 1379–1392. https://doi.org/10.1002/hyp.1290

Goddéris, Y., François, L.M., 1996. Balancing the Cenozoic carbon and alkalinity cycles: Constraints from isotopic records. Geophysical Research Letters 23, 3743–3746. https://doi.org/10.1029/96GL03575

Gorini, C., Haq, B.U., dos Reis, A.T., Silva, C.G., Cruz, A., Soares, E., Grangeon, D., 2014. Late Neogene sequence stratigraphic evolution of the *Foz do Amazonas* Basin, Brazil. Terra Nova 26, 179–185. https://doi.org/10.1111/ter.12083

Grigolato, J., Chiessi, C.M., Bertassoli, D.J., Campos, M.C., Shimizu, M.H., Magalhães, R.H., Nace, T., Sawakuchi, A.O., Wahnfried, I.D., Neri, R., Cunha, A.C., Silva, C.G., Baker, P.A., Govin, A., Zabel, M., 2025. Past Amazon precipitation under different Atlantic Meridional Overturning Circulation and sea surface temperature scenarios of the last deglaciation. Quaternary Science Reviews 362, 109425. https://doi.org/10.1016/j.quascirev.2025.109425

Guyot, J.L., Jouanneau, J.M., Soares, L., Boaventura, G.R., Maillet, N., Lagane, C., 2007. Clay mineral composition of river sediments in the Amazon Basin. CATENA 71, 340–356. https://doi.org/10.1016/j.catena.2007.02.002

Häggi, C., Chiessi, C.M., Merkel, U., Mulitza, S., Prange, M., Schulz, M., Schefuß, E., 2017. Response of the Amazon rainforest to late Pleistocene climate variability. Earth and Planetary Science Letters 479, 50–59. https://doi.org/10.1016/j.epsl.2017.09.013

Harris, S.E., Mix, A.C., 2002. Climate and tectonic influences on continental erosion of tropical South America, 0–13 Ma. Geol 30, 447. https://doi.org/10.1130/0091-7613(2002)030%253C0447:CATIOC%253E2.0.CO;2

Haywood, A.M., Tindall, J.C., Dowsett, H.J., Dolan, A.M., Foley, K.M., Hunter, S.J., Hill, D.J., Chan, W.-L., Abe-Ouchi, A., Stepanek, C., Lohmann, G., Chandan, D., Peltier, W.R., Tan, N., Contoux, C., Ramstein, G., Li, X., Zhang, Z., Guo, C., Nisancioglu, K.H., Zhang, Q., Li, Q., Kamae, Y., Chandler, M.A., Sohl, L.E., Otto-Bliesner, B.L., Feng, R., Brady, E.C., Von Der Heydt, A.S., Baatsen, M.L.J., Lunt, D.J., 2020. The Pliocene Model Intercomparison Project Phase 2: large-scale climate features and climate sensitivity. Clim. Past 16, 2095–2123. https://doi.org/10.5194/cp-16-2095-2020

Heinrich, S., Zonneveld, K.A.F., 2013. Influence of the Amazon River development and constriction of the Central American Seaway on Middle/Late Miocene oceanic conditions at the Ceara Rise. Palaeogeography, Palaeoclimatology, Palaeoecology 386, 599–606. https://doi.org/10.1016/j.palaeo.2013.06.026

Henderson, P., 1984. General Geochemical Properties and Abundances of the Rare Earth Elements, in: Developments in Geochemistry. Elsevier, pp. 1–32. https://doi.org/10.1016/B978-0-444-42148-7.50006-X

Hilley, G.E., Porder, S., 2008. A framework for predicting global silicate weathering and CO_2 drawdown rates over geologic time-scales. Proc. Natl. Acad. Sci. U.S.A. 105, 16855–16859. https://doi.org/10.1073/pnas.0801462105

Hilton, R.G., West, A.J., 2020. Mountains, erosion and the carbon cycle. Nat Rev Earth Environ 1, 284–299. https://doi.org/10.1038/s43017-020-0058-6

Hindshaw, R.S., Aciego, S.M., Piotrowski, A.M., Tipper, E.T., 2018. Decoupling of dissolved and bedrock neodymium isotopes during sedimentary cycling. Geochem. Persp. Let. 43–46. https://doi.org/10.7185/geochemlet.1828

Holbourn, A.E., Kuhnt, W., Clemens, S.C., Kochhann, K.G.D., Jöhnck, J., Lübbers, J., Andersen, N., 2018. Late Miocene climate cooling and intensification of southeast Asian winter monsoon. Nat Commun 9, 1584. https://doi.org/10.1038/s41467-018-03950-1

Hoorn, C., Bogotá-A, G.R., Romero-Baez, M., Lammertsma, E.I., Flantua, S.G.A., Dantas, E.L., Dino, R., do Carmo, D.A., Chemale, F., 2017. The Amazon at sea: Onset and stages of the Amazon River from a marine record, with special reference to Neogene plant turnover in the drainage basin. Global and Planetary Change 153, 51–65. https://doi.org/10.1016/j.gloplacha.2017.02.005

Hoorn, C., Palazzesi, L., Silvestro, D., 2022. Editorial Preface to Special Issue: Exploring the impact of Andean uplift and climate on life evolution and landscape modification: From Amazonia to Patagonia. Global and Planetary Change 211, 103759. https://doi.org/10.1016/j.gloplacha.2022.103759

Hoorn, C., Wesselingh, F.P. (Eds.), 2010. Amazonia--landscape and species evolution: a look into the past. Wiley-Blackwell, Chichester, UK ; Hoboken, NJ.

Hoorn, C., Wesselingh, F.P., Ter Steege, H., Bermudez, M.A., Mora, A., Sevink, J., Sanmartín, I., Sanchez-Meseguer, A., Anderson, C.L., Figueiredo, J.P., Jaramillo, C., Riff, D., Negri, F.R., Hooghiemstra, H., Lundberg, J., Stadler, T., Särkinen, T., Antonelli, A., 2010. Amazonia Through Time: Andean Uplift, Climate Change, Landscape Evolution, and Biodiversity. Science 330, 927–931. https://doi.org/10.1126/science.1194585

Höppner, N., Lucassen, F., Chiessi, C.M., Sawakuchi, A.O., Kasemann, S.A., 2018. Holocene provenance shift of suspended particulate matter in the Amazon River basin. Quaternary Science Reviews 190, 66–80. https://doi.org/10.1016/j.quascirev.2018.04.021

Horan, K., Hilton, R.G., Selby, D., Ottley, C.J., Gröcke, D.R., Hicks, M., Burton, K.W., 2017. Mountain glaciation drives rapid oxidation of rock-bound organic carbon. Sci. Adv. 3, e1701107. https://doi.org/10.1126/sciadv.1701107

Horbe, A.M.C., Albuquerque, M.F.D.S., Dantas, E.L., 2022. Nd and Sr Isotopes and REE Investigation in Tropical Weathering Profiles of Amazon Region. Front. Earth Sci. 10, 845224. https://doi.org/10.3389/feart.2022.845224

Horbe, A.M.C., da Trindade, I.R., Dantas, E.L., Santos, R.V., Roddaz, M., 2014. Provenance of quaternary and modern alluvial deposits of the Amazonian floodplain (Brazil) inferred from major and trace elements and Pb–Nd–Sr isotopes. Palaeogeography, Palaeoclimatology, Palaeoecology 411, 144–154. https://doi.org/10.1016/j.palaeo.2014.06.019

Horbe, A.M.C., Motta, M.B., De Almeida, C.M., Dantas, E.L., Vieira, L.C., 2013. Provenance of Pliocene and recent sedimentary deposits in western Amazônia, Brazil: Consequences for the paleodrainage of the Solimões-Amazonas River. Sedimentary Geology 296, 9–20. https://doi.org/10.1016/j.sedgeo.2013.07.007

Horbe, A.M.C., Roddaz, M., Gomes, L.B., Castro, R.T., Dantas, E.L., do Carmo, D.A., 2019. Provenance of the Neogene sediments from the Solimões Formation (Solimões and Acre Basins), Brazil. Journal of South American Earth Sciences 93, 232–241. https://doi.org/10.1016/j.jsames.2019.05.004

Horton, B.K., 2018. Sedimentary record of Andean mountain building. Earth-Science Reviews 178, 279–309. https://doi.org/10.1016/j.earscirev.2017.11.025

Hurtado, C., Roddaz, M., Santos, R.V., Baby, P., Antoine, P.-O., Dantas, E.L., 2018. Cretaceous-early Paleocene drainage shift of Amazonian rivers driven by Equatorial Atlantic Ocean opening and Andean uplift as deduced from the provenance of northern Peruvian sedimentary rocks (Huallaga basin). Gondwana Research 63, 152–168. https://doi.org/10.1016/j.gr.2018.05.012

Hyeong, K., Lee, J., Seo, I., Lee, M.J., Yoo, C.M., Khim, B.-K., 2014. Southward shift of the Intertropical Convergence Zone due to Northern Hemisphere cooling at the Oligocene-Miocene boundary. Geology 42, 667–670. https://doi.org/10.1130/G35664.1

Jacobsen, S.B., Wasserburg, G.J., 1980. Sm-Nd isotopic evolution of chondrites. Earth and Planetary Science Letters 50, 139–155. https://doi.org/10.1016/0012-821X(80)90125-9

Jang, K., Bayon, G., Han, Y., Joo, Y.J., Kim, Ji-Hoon, Ryu, J.-S., Woo, J., Forwick, M., Szczuciński, W., Kim, Jung-Hyun, Nam, S.-I., 2020. Neodymium isotope constraints on chemical weathering and past glacial activity in Svalbard. Earth and Planetary Science Letters 542, 116319. https://doi.org/10.1016/j.epsl.2020.116319

Jang, K., Bayon, G., Pourret, O., Joe, Y.J., Kim, J.-H., Byun, E., Forwick, M., León, R., Nam, S.-I., 2024. A distinctive rare earth element signature for pyrite oxidation and glacial weathering. Chemical Geology 660, 122167. https://doi.org/10.1016/j.chemgeo.2024.122167

Japsen, P., Green, P.F., Bonow, J.M., 2025. Ups and downs of the Guiana Shield and Amazon Basin over the last 500 Myr. Gondwana Research S1342937X25002163. https://doi.org/10.1016/j.gr.2025.06.020

Jaramillo, C., Romero, I., D'Apolito, C., Bayona, G., Duarte, E., Louwye, S., Escobar, J., Luque, J., Carrillo-Briceño, J.D., Zapata, V., Mora, A., Schouten, S., Zavada, M., Harrington, G., Ortiz, J., Wesselingh, F.P., 2017. Miocene flooding events of western Amazonia. Sci. Adv. 3, e1601693. https://doi.org/10.1126/sciadv.1601693

Joshua West, A., Bickle, M.J., Collins, R., Brasington, J., 2002. Small-catchment perspective on Himalayan weathering fluxes. Geol 30, 355. https://doi.org/10.1130/0091-7613(2002)030%253C0355:SCPOHW%253E2.0.CO;2

Kaandorp, R.J.G., Vonhof, H.B., Wesselingh, F.P., Pittman, L.R., Kroon, D., Van Hinte, J.E., 2005. Seasonal Amazonian rainfall variation in the Miocene Climate Optimum. Palaeogeography, Palaeoclimatology, Palaeoecology 221, 1–6. https://doi.org/10.1016/j.palaeo.2004.12.024

Konhauser, K.O., Lalonde, S.V., Planavsky, N.J., Pecoits, E., Lyons, T.W., Mojzsis, S.J., Rouxel, O.J., Barley, M.E., Rosìere, C., Fralick, P.W., Kump, L.R., Bekker, A., 2011. Aerobic bacterial pyrite oxidation and acid rock drainage during the Great Oxidation Event. Nature 478, 369–373. https://doi.org/10.1038/nature10511

Kraft, L., Campos, M.C., Nascimento, R.A., Dias, B.B., Crivellari, S., Kochhann, M.V.L., Bertassoli, D.J., Venancio, I.M., Santos, T.P., Baker, P.A., Silva, C.G., Chiessi, C.M., 2025. AMOC-forced southward migration of the ITCZ under a warm climate background. Palaeogeography, Palaeoclimatology, Palaeoecology 661, 112705. https://doi.org/10.1016/j.palaeo.2024.112705

Kump, L.R., Brantley, S.L., Arthur, M.A., 2000. Chemical Weathering, Atmospheric CO_2 , and Climate. Annu. Rev. Earth Planet. Sci. 28, 611–667. https://doi.org/10.1146/annurev.earth.28.1.611

Lacan, F., Tachikawa, K., Jeandel, C., 2012. Neodymium isotopic composition of the oceans: A compilation of seawater data. Chemical Geology 300–301, 177–184. https://doi.org/10.1016/j.chemgeo.2012.01.019

Lammertsma, E.I., Troelstra, S.R., Flores, J.-A., Sangiorgi, F., Chemale Jr., F., Do Carmo, D.A., Hoorn, C., 2018. Primary productivity in the western tropical Atlantic follows Neogene Amazon River evolution. Palaeogeography, Palaeoclimatology, Palaeoecology 506, 12–21. https://doi.org/10.1016/j.palaeo.2018.05.048

Larkin, C.S., Piotrowski, A.M., Hindshaw, R.S., Bayon, G., Hilton, R.G., Baronas, J.J., Dellinger, M., Wang, R., Tipper, E.T., 2021. Constraints on the source of reactive phases in sediment from a major Arctic river using neodymium isotopes. Earth and Planetary Science Letters 565, 116933. https://doi.org/10.1016/j.epsl.2021.116933

Latrubesse, E.M., Cozzuol, M., Da Silva-Caminha, S.A.F., Rigsby, C.A., Absy, M.L., Jaramillo, C., 2010. The Late Miocene paleogeography of the Amazon Basin and the evolution of the Amazon River system. Earth-Science Reviews 99, 99–124. https://doi.org/10.1016/j.earscirev.2010.02.005

Lawrence, M.G., Greig, A., Collerson, K.D., Kamber, B.S., 2006. Rare Earth Element and Yttrium Variability in South East Queensland Waterways. Aquat Geochem 12, 39–72. https://doi.org/10.1007/s10498-005-4471-8

Leandro, L.M., Linhares, A.P., De Lira Mota, M.A., Fauth, G., Santos, A., Villegas-Martín, J., Vieira, C.E.L., Bruno, M.D.R., Lee, B., Baecker-Fauth, S., Lopes, F.M., Ramos, M.I.F., 2022. Multi-proxy evidence of Caribbean-sourced marine incursions in the Neogene of Western Amazonia, Brazil. Geology. https://doi.org/10.1130/G49544.1

Lee, T., Rand, D., Lisiecki, L.E., Gebbie, G., Lawrence, C., 2023. Bayesian age models and stacks: combining age inferences from radiocarbon and benthic δ^{18}O stratigraphic alignment. Clim. Past 19, 1993–2012. https://doi.org/10.5194/cp-19-1993-2023

Li, S., Goldstein, S.L., Raymo, M.E., 2021. Neogene continental denudation and the beryllium conundrum. Proc. Natl. Acad. Sci. U.S.A. 118, e2026456118. https://doi.org/10.1073/pnas.2026456118

Ling, S., Wu, X., Ren, Y., Sun, C., Liao, X., Li, X., Zhu, B., 2015. Geochemistry of trace and rare earth elements during weathering of black shale profiles in Northeast Chongqing, Southwestern China: Their mobilization, redistribution, and fractionation. Geochemistry 75, 403–417. https://doi.org/10.1016/j.chemer.2015.07.004

Lisiecki, L.E., Raymo, M.E., 2005a. A Pliocene-Pleistocene stack of 57 globally distributed benthic δ^{18}O records. Paleoceanography 20, 2004PA001071. https://doi.org/10.1029/2004PA001071

Lisiecki, L.E., Raymo, M.E., 2005b. A Pliocene-Pleistocene stack of 57 globally distributed benthic ??18O records. Paleoceanography 20, 1–17. https://doi.org/10.1029/2004PA001071

Liu, X., Herold, N., Huber, M., 2024. Atlantic Meridional Overturning Circulation Influence on the Annual Mean Intertropical Convergence Zone Location in the Miocene. Geophysical Research Letters 51, e2024GL109159. https://doi.org/10.1029/2024GL109159

Louterbach, M., Roddaz, M., Antoine, P.-O., Marivaux, L., Adnet, S., Bailleul, J., Dantas, E., Santos, R.V., Chemale, F., Baby, P., Sanchez, C., Calderon, Y., 2018. Provenance record of late Maastrichtian-late Palaeocene Andean Mountain building in the Amazonian retroarc foreland basin (Madre de Dios basin, Peru). Terra Nova 30, 17–23. https://doi.org/10.1111/ter.12303

Lupker, M., France-Lanord, C., Galy, V., Lavé, J., Gaillardet, J., Gajurel, A.P., Guilmette, C., Rahman, M., Singh, S.K., Sinha, R., 2012. Predominant floodplain over mountain weathering of Himalayan sediments (Ganga basin). Geochimica et Cosmochimica Acta 84, 410–432. https://doi.org/10.1016/j.gca.2012.02.001

Ma, L., Jin, L., Brantley, S.L., 2011. How mineralogy and slope aspect affect REE release and fractionation during shale weathering in the Susquehanna/Shale Hills Critical Zone Observatory. Chemical Geology 290, 31–49. https://doi.org/10.1016/j.chemgeo.2011.08.013

Macdonald, F.A., Swanson-Hysell, N.L., Park, Y., Lisiecki, L., Jagoutz, O., 2019. Arc-continent collisions in the tropics set Earth's climate state. Science 364, 181–184. https://doi.org/10.1126/science.aav5300

Maslin, M.A., Li, X.S., Loutre, M.-F., Berger, A., 1998. THE CONTRIBUTION OF ORBITAL FORCING TO THE PROGRESSIVE INTENSIFICATION OF NORTHERN HEMISPHERE GLACIATION. Quaternary Science Reviews 17, 411–426. https://doi.org/10.1016/S0277-3791(97)00047-4

McCulloch, M.T., WasseXrburg, G.J., 1978. fractionated mantle-derived materials are determiined. 200, 9.

McGee, D., Moreno-Chamarro, E., Green, B., Marshall, J., Galbraith, E., Bradtmiller, L., 2018. Hemispherically asymmetric trade wind changes as signatures of past ITCZ shifts. Quaternary Science Reviews 180, 214–228. https://doi.org/10.1016/j.quascirev.2017.11.020

Meade, R.H., 1994. Suspended sediments of the modern Amazon and Orinoco rivers. Quaternary International 21, 29–39. https://doi.org/10.1016/1040-6182(94)90019-1

Meade, R.H., Dunne, T., Richey, J.E., Santos, U.D.M., Salati, E., 1985. Storage and Remobilization of Suspended Sediment in the Lower Amazon River of Brazil. Science 228, 488–490. https://doi.org/10.1126/science.228.4698.488

Merschel, G., Bau, M., Schmidt, K., Münker, C., Dantas, E.L., 2017. Hafnium and neodymium isotopes and REY distribution in the truly dissolved, nanoparticulate/colloidal and suspended loads of rivers in the Amazon Basin, Brazil. Geochimica et Cosmochimica Acta 213, 383–399. https://doi.org/10.1016/j.gca.2017.07.006

Miller, K.G., Browning, J.V., John Schmelz, W., Kopp, R.E., Mountain, G.S., Wright, J.D., 2020. Cenozoic sea-level and cryospheric evolution from deep-sea geochemical and continental margin records. Science Advances 6. https://doi.org/10.1126/sciadv.aaz1346

Misra, S., Froelich, P.N., 2012. Lithium Isotope History of Cenozoic Seawater: Changes in Silicate Weathering and Reverse Weathering. Science 335, 818–823. https://doi.org/10.1126/science.1214697

Moizinho, G.R., Roddaz, M., Brichau, S., Louterbach, M., Dantas, E.L., Santos, R.V., Bayon, G., Bailleul, J., Vink, J., Hoorn, C., 2024. New constraints on the Late Miocene-Pliocene deformational and depositional evolution of the Eastern Cordillera and Sub-Andean Zone in Southern Peru. Journal of South American Earth Sciences 133, 104700. https://doi.org/10.1016/j.jsames.2023.104700

Moizinho, G.R., Vieira, L.C., Santos, R.V., Nogueira, A.C.R., Dantas, E.L., Roddaz, M., 2022. Provenance of Miocene-Pleistocene siliciclastic deposits in the Eastern Amazonia coast (Brazil) and paleogeographic implications. Palaeogeography, Palaeoclimatology, Palaeoecology 587, 110799. https://doi.org/10.1016/j.palaeo.2021.110799

Moquet, J.-S., Crave, A., Viers, J., Seyler, P., Armijos, E., Bourrel, L., Chavarri, E., Lagane, C., Laraque, A., Casimiro, W.S.L., Pombosa, R., Noriega, L., Vera, A., Guyot, J.-L., 2011. Chemical weathering and atmospheric/soil CO2 uptake in the Andean and Foreland Amazon basins. Chemical Geology 287, 1–26. https://doi.org/10.1016/j.chemgeo.2011.01.005

Moquet, J.-S., Guyot, J.-L., Crave, A., Viers, J., Filizola, N., Martinez, J.-M., Oliveira, T.C., Sánchez, L.S.H., Lagane, C., Casimiro, W.S.L., Noriega, L., Pombosa, R., 2016. Amazon River dissolved load:

temporal dynamics and annual budget from the Andes to the ocean. Environ Sci Pollut Res 23, 11405–11429. https://doi.org/10.1007/s11356-015-5503-6

Mora, A., Parra, M., Strecker, M.R., Sobel, E.R., Hooghiemstra, H., Torres, V., Jaramillo, J.V., 2008. Climatic forcing of asymmetric orogenic evolution in the Eastern Cordillera of Colombia. Geological Society of America Bulletin 120, 930–949. https://doi.org/10.1130/B26186.1

Moreira-Turcq, P., Seyler, P., Guyot, J.L., Etcheber, H., 2003. Exportation of organic carbon from the Amazon River and its main tributaries. Hydrological Processes 17, 1329–1344. https://doi.org/10.1002/hyp.1287

Mulch, A., Uba, C.E., Strecker, M.R., Schoenberg, R., Chamberlain, C.P., 2010. Late Miocene climate variability and surface elevation in the central Andes. Earth and Planetary Science Letters 290, 173–182. https://doi.org/10.1016/j.epsl.2009.12.019

Nogueira, A.C.R., Silveira, R., Guimarães, J.T.F., 2013. Neogene–Quaternary sedimentary and paleovegetation history of the eastern Solimões Basin, central Amazon region. Journal of South American Earth Sciences 46, 89–99. https://doi.org/10.1016/j.jsames.2013.05.004

O'Dea, A., Lessios, H.A., Coates, A.G., Eytan, R.I., Restrepo-Moreno, S.A., Cione, A.L., Collins, L.S., De Queiroz, A., Farris, D.W., Norris, R.D., Stallard, R.F., Woodburne, M.O., Aguilera, O., Aubry, M.-P., Berggren, W.A., Budd, A.F., Cozzuol, M.A., Coppard, S.E., Duque-Caro, H., Finnegan, S., Gasparini, G.M., Grossman, E.L., Johnson, K.G., Keigwin, L.D., Knowlton, N., Leigh, E.G., Leonard-Pingel, J.S., Marko, P.B., Pyenson, N.D., Rachello-Dolmen, P.G., Soibelzon, E., Soibelzon, L., Todd, J.A., Vermeij, G.J., Jackson, J.B.C., 2016. Formation of the Isthmus of Panama. Sci. Adv. 2, e1600883. https://doi.org/10.1126/sciadv.1600883

Ohr, M., Halliday, A.N., Peacor, D.R., 1994. Mobility and fractionation of rare earth elements in argillaceous sediments: Implications for dating diagenesis and low-grade metamorphism. Geochimica et Cosmochimica Acta 58, 289–312. https://doi.org/10.1016/0016-7037(94)90465-0

Oldeman, A.M., Baatsen, M.L.J., Von Der Heydt, A.S., Dijkstra, H.A., Tindall, J.C., Abe-Ouchi, A., Booth, A.R., Brady, E.C., Chan, W.-L., Chandan, D., Chandler, M.A., Contoux, C., Feng, R., Guo, C., Haywood, A.M., Hunter, S.J., Kamae, Y., Li, Q., Li, X., Lohmann, G., Lunt, D.J., Nisancioglu, K.H., Otto-Bliesner, B.L., Peltier, W.R., Pontes, G.M., Ramstein, G., Sohl, L.E., Stepanek, C., Tan, N., Zhang, Q., Zhang, Z., Wainer, I., Williams, C.J.R., 2021. Reduced El Niño variability in the mid-Pliocene according to the PlioMIP2 ensemble. Clim. Past 17, 2427–2450. https://doi.org/10.5194/cp-17-2427-2021

Parra, M., Mora, A., Jaramillo, C., Strecker, M.R., Sobel, E.R., Quiroz, L., Rueda, M., Torres, V., 2009. Orogenic wedge advance in the northern Andes: Evidence from the Oligocene-Miocene sedimentary record of the Medina Basin, Eastern Cordillera, Colombia. Geological Society of America Bulletin 121, 780–800. https://doi.org/10.1130/B26257.1

Patchett, P.J., White, W.M., Feldmann, H., Kielinczuk, S., Hofmann, A.W., 1984. Hafnium/rare earth element fractionation in the sedimentary system and crustal recycling into the Earth's mantle. Earth and Planetary Science Letters 69, 365–378. https://doi.org/10.1016/0012-821X(84)90195-X

Pepin, E., Guyot, J.L., Armijos, E., Bazan, H., Fraizy, P., Moquet, J.S., Noriega, L., Lavado, W., Pombosa, R., Vauchel, P., 2013. Climatic control on eastern Andean denudation rates (Central Cordillera from Ecuador to Bolivia). Journal of South American Earth Sciences 44, 85–93. https://doi.org/10.1016/j.jsames.2012.12.010

Pérez-López, R., Delgado, J., Nieto, J.M., Márquez-García, B., 2010. Rare earth element geochemistry of sulphide weathering in the São Domingos mine area (Iberian Pyrite Belt): A proxy for fluid–rock interaction and ancient mining pollution. Chemical Geology 276, 29–40. https://doi.org/10.1016/j.chemgeo.2010.05.018

Piper, D.Z., 1974. Rare earth elements in the sedimentary cycle: A summary. Chemical Geology 14, 285–304. https://doi.org/10.1016/0009-2541(74)90066-7

Pontes, G.M., Taschetto, A.S., Sen Gupta, A., Santoso, A., Wainer, I., Haywood, A.M., Chan, W.-L., Abe-Ouchi, A., Stepanek, C., Lohmann, G., Hunter, S.J., Tindall, J.C., Chandler, M.A., Sohl, L.E., Peltier, W.R., Chandan, D., Kamae, Y., Nisancioglu, K.H., Zhang, Z., Contoux, C., Tan, N., Zhang, Q., Otto-Bliesner, B.L., Brady, E.C., Feng, R., Von Der Heydt, A.S., Baatsen, M.L.J., Oldeman, A.M., 2022. Mid-Pliocene El Niño/Southern Oscillation suppressed by Pacific intertropical convergence zone shift. Nat. Geosci. 15, 726–734. https://doi.org/10.1038/s41561-022-00999-y

Pontes, G.M., Wainer, I., Taschetto, A.S., Sen Gupta, A., Abe-Ouchi, A., Brady, E.C., Chan, W.-L., Chandan, D., Contoux, C., Feng, R., Hunter, S.J., Kame, Y., Lohmann, G., Otto-Bliesner, B.L., Peltier, W.R., Stepanek, C., Tindall, J., Tan, N., Zhang, Q., Zhang, Z., 2020. Drier tropical and subtropical Southern Hemisphere in the mid-Pliocene Warm Period. Sci Rep 10, 13458. https://doi.org/10.1038/s41598-020-68884-5

Poulsen, C.J., Ehlers, T.A., Insel, N., 2010. Onset of Convective Rainfall During Gradual Late Miocene Rise of the Central Andes. Science 328, 490–493. https://doi.org/10.1126/science.1185078

Rae, J.W.B., Zhang, Y.G., Liu, X., Foster, G.L., Stoll, H.M., Whiteford, R.D.M., 2021. Atmospheric CO_2 over the Past 66 Million Years from Marine Archives. Annu. Rev. Earth Planet. Sci. 49, 609–641. https://doi.org/10.1146/annurev-earth-082420-063026

Raymo, M.E., Ruddiman, W.F., 1992. Tectonic forcing of late Cenozoic climate. Nature 359, 117–122. https://doi.org/10.1038/359117a0

Ribas, C.C., Aleixo, A., Nogueira, A.C.R., Miyaki, C.Y., Cracraft, J., 2012. A palaeobiogeographic model for biotic diversification within Amazonia over the past three million years. Proc. R. Soc. B. 279, 681–689. https://doi.org/10.1098/rspb.2011.1120

Richey, J.E., Nobre, C., Deser, C., 1989. Amazon River Discharge and Climate Variability: 1903 to 1985. Science 246, 101–103. https://doi.org/10.1126/science.246.4926.101

Rickli, J., Frank, M., Stichel, T., Georg, R.B., Vance, D., Halliday, A.N., 2013. Controls on the incongruent release of hafnium during weathering of metamorphic and sedimentary catchments. Geochimica et Cosmochimica Acta 101, 263–284. https://doi.org/10.1016/j.gca.2012.10.019

Roddaz, M., Dera, G., Mourlot, Y., Calvès, G., Kim, J.-H., Chaboureau, A.-C., Mounic, S., Raisson, F., 2021. Provenance constraints on the Cretaceous-Paleocene erosional history of the Guiana Shield as determined from the geochemistry of clay-size fraction of sediments from the Arapaima-1 well (Guyana-Suriname basin). Marine Geology 434, 106433. https://doi.org/10.1016/j.margeo.2021.106433

Roddaz, M., Viers, J., Brusset, S., Baby, P., Hérail, G., 2005. Sediment provenances and drainage evolution of the Neogene Amazonian foreland basin. Earth and Planetary Science Letters 239, 57–78. https://doi.org/10.1016/j.epsl.2005.08.007

Roddaz, M., Viers, J., Moreira-Turcq, P., Blondel, C., Sondag, F., Guyot, J.-L., Moreira, L., 2014. Evidence for the control of the geochemistry of Amazonian floodplain sediments by stratification of suspended sediments in the Amazon. Chemical Geology 387, 101–110. https://doi.org/10.1016/j.chemgeo.2014.07.022

Rodrigues, M.D.A., Roddaz, M., Santos, R.V., Louterbach, M., D'Apolito, C., Brusset, S., Dantas, E.L., Negri, F.R., 2023. New insights into the Cretaceous evolution of the Western Amazonian paleodrainage system. Sedimentary Geology 453, 106434. https://doi.org/10.1016/j.sedgeo.2023.106434

Rohrmann, A., Sachse, D., Mulch, A., Pingel, H., Tofelde, S., Alonso, R.N., Strecker, M.R., 2016. Miocene orographic uplift forces rapid hydrological change in the southern central Andes. Sci Rep 6, 35678. https://doi.org/10.1038/srep35678

Rossetti, D.F., Cohen, M.C.L., Tatumi, S.H., Sawakuchi, A.O., Cremon, É.H., Mittani, J.C.R., Bertani, T.C., Munita, C.J.A.S., Tudela, D.R.G., Yee, M., Moya, G., 2015. Mid-Late Pleistocene OSL chronology in western Amazonia and implications for the transcontinental Amazon pathway. Sedimentary Geology 330, 1–15. https://doi.org/10.1016/j.sedgeo.2015.10.001

Rossetti, D.F., Valeriano, M.M., Vasconcelos, D.L., 2023. A different path to the Negro River in the Chibanian as a window to temporalize the eastward-flowing transcontinental Amazon. Journal of South American Earth Sciences 122, 104187. https://doi.org/10.1016/j.jsames.2022.104187

Rousseau, T.C.C., Roddaz, M., Moquet, J.-S., Handt Delgado, H., Calves, G., Bayon, G., 2019. Controls on the geochemistry of suspended sediments from large tropical South American rivers (Amazon, Orinoco and Maroni). Chemical Geology 522, 38–54. https://doi.org/10.1016/j.chemgeo.2019.05.027

Sacek, V., 2014. Drainage reversal of the Amazon River due to the coupling of surface and lithospheric processes. Earth and Planetary Science Letters 401, 301–312. https://doi.org/10.1016/j.epsl.2014.06.022

Sacek, V., Mutz, S.G., Bicudo, T.C., De Almeida, R.P., Ehlers, T.A., 2023. The Amazon paleoenvironment resulted from geodynamic, climate, and sea-level interactions. Earth and Planetary Science Letters 605, 118033. https://doi.org/10.1016/j.epsl.2023.118033

Salamanca Villegas, S., Van Soelen, E.E., Teunissen Van Manen, M.L., Flantua, S.G.A., Santos, R.V., Roddaz, M., Dantas, E.L., Van Loon, E., Sinninghe Damsté, J.S., Kim, J., Hoorn, C., 2016. Amazon forest dynamics under changing abiotic conditions in the early Miocene (Colombian Amazonia). Journal of Biogeography 43, 2424–2437. https://doi.org/10.1111/jbi.12769

Santos, J.O.S., Hartmann, L.A., Gaudette, H.E., Groves, D.I., Mcnaughton, N.J., Fletcher, I.R., 2000. A New Understanding of the Provinces of the Amazon Craton Based on Integration of Field Mapping and U-Pb and Sm-Nd Geochronology. Gondwana Research 3, 453–488. https://doi.org/10.1016/S1342-937X(05)70755-3

Santos, R.V., Sondag, F., Cochonneau, G., Lagane, C., Brunet, P., Hattingh, K., Chaves, J.G.S., 2015. Source area and seasonal $^{87}Sr/^{86}Sr$ variations in rivers of the Amazon basin: AMAZON RIVERS SOURCE SEDIMENTS. Hydrol. Process. 29, 187–197. https://doi.org/10.1002/hyp.10131

Scholz, S.R., Petersen, S.V., Escobar, J., Jaramillo, C., Hendy, A.J.W., Allmon, W.D., Curtis, J.H., Anderson, B.M., Hoyos, N., Restrepo, J.C., Perez, N., 2020. Isotope sclerochronology indicates enhanced seasonal precipitation in northern South America (Colombia) during the Mid-Miocene Climatic Optimum. Geology 48, 668–672. https://doi.org/10.1130/G47235.1

Soulet, G., Hilton, R.G., Garnett, M.H., Roylands, T., Klotz, S., Croissant, T., Dellinger, M., Le Bouteiller, C., 2021. Temperature control on CO2 emissions from the weathering of sedimentary rocks. Nat. Geosci. 14, 665–671. https://doi.org/10.1038/s41561-021-00805-1

Stallard and Edmon, 1987. Geochemistry of the Amazon: 3. Weathering chemistry and limits to dissolved inputs. J. Geophys. Res. 92, 8293–8302. https://doi.org/10.1029/JC092iC08p08293

Stallard, R.F., Edmond, J.M., 1983. Geochemistry of the Amazon: 2. The influence of geology and weathering environment on the dissolved load. J. Geophys. Res. 88, 9671–9688. https://doi.org/10.1029/JC088iC14p09671

Süfke, F., Gutjahr, M., Gilli, A., Anselmetti, F.S., Glur, L., Eisenhauer, A., 2019. Early stage weathering systematics of Pb and Nd isotopes derived from a high-Alpine Holocene lake sediment record. Chemical Geology 507, 42–53. https://doi.org/10.1016/j.chemgeo.2018.12.026

Sundell, K.E., Saylor, J.E., Lapen, T.J., Horton, B.K., 2019. Implications of variable late Cenozoic surface uplift across the Peruvian central Andes. Sci Rep 9, 4877. https://doi.org/10.1038/s41598-019-41257-3

Tanaka, T., Togashi, S., Kamioka, H., Amakawa, H., Kagami, H., Hamamoto, T., Yuhara, M., Orihashi, Y., Yoneda, S., Shimizu, H., Kunimaru, T., Takahashi, K., Yanagi, T., Nakano, T., Fujimaki, H., Shinjo, R., Asahara, Y., Tanimizu, M., Dragusanu, C., 2000. JNdi-1: a neodymium isotopic reference in consistency with LaJolla neodymium. Chemical Geology 168, 279–281. https://doi.org/10.1016/S0009-2541(00)00198-4

Taylor, S.R., McLennan, S.M., 1985. The continental crust: its composition and evolution: an examination of the geochem. record preserved in sedimentary rocks, Geoscience texts. Blackwell, Oxford.

Torres, M.A., Moosdorf, N., Hartmann, J., Adkins, J.F., West, A.J., 2017. Glacial weathering, sulfide oxidation, and global carbon cycle feedbacks. Proc. Natl. Acad. Sci. U.S.A. 114, 8716–8721. https://doi.org/10.1073/pnas.1702953114

Torres, M.A., West, A.J., Clark, K.E., 2015. Geomorphic regime modulates hydrologic control of chemical weathering in the Andes–Amazon. Geochimica et Cosmochimica Acta 166, 105–128. https://doi.org/10.1016/j.gca.2015.06.007

Torres, M.A., West, A.J., Clark, K.E., Paris, G., Bouchez, J., Ponton, C., Feakins, S.J., Galy, V., Adkins, J.F., 2016. The acid and alkalinity budgets of weathering in the Andes–Amazon system: Insights into the erosional control of global biogeochemical cycles. Earth and Planetary Science Letters 450, 381–391. https://doi.org/10.1016/j.epsl.2016.06.012

Torres, M.A., West, A.J., Li, G., 2014. Sulphide oxidation and carbonate dissolution as a source of CO2 over geological timescales. Nature 507, 346–349. https://doi.org/10.1038/nature13030

Trapp-Müller, G., Caves Rugenstein, J., Conley, D.J., Geilert, S., Hagens, M., Hong, W.-L., Jeandel, C., Longman, J., Mason, P.R.D., Middelburg, J.J., Milliken, K.L., Navarre-Sitchler, A., Planavsky, N.J., Reichart, G.-J., Slomp, C.P., Sluijs, A., Van Hinsbergen, D.J.J., Zhang, X.Y., 2025. Earth's silicate weathering continuum. Nat. Geosci. 18, 691–701. https://doi.org/10.1038/s41561-025-01743-y

van Soelen, E.E., Kim, J.-H., Santos, R.V., Dantas, E.L., Vasconcelos de Almeida, F., Pires, J.P., Roddaz, M., Sinninghe Damsté, J.S., 2017. A 30 Ma history of the Amazon River inferred from terrigenous sediments and organic matter on the Ceará Rise. Earth and Planetary Science Letters 474, 40–48. https://doi.org/10.1016/j.epsl.2017.06.025

Vervoort, J.D., Patchett, P.J., Blichert-Toft, J., Albarède, F., 1999. Relationships between Lu–Hf and Sm–Nd isotopic systems in the global sedimentary system. Earth and Planetary Science Letters 168, 79–99. https://doi.org/10.1016/S0012-821X(99)00047-3

Viers, J., Roddaz, M., Filizola, N., Guyot, J.-L., Sondag, F., Brunet, P., Zouiten, C., Boucayrand, C., Martin, F., Boaventura, G.R., 2008. Seasonal and provenance controls on Nd–Sr isotopic compositions of Amazon rivers suspended sediments and implications for Nd and Sr fluxes exported to the Atlantic Ocean. Earth and Planetary Science Letters 274, 511–523. https://doi.org/10.1016/j.epsl.2008.08.011

Viers, J., Wasserburg, G.J., 2004. Behavior of Sm and Nd in a lateritic soil profile. Geochimica et Cosmochimica Acta 68, 2043–2054. https://doi.org/10.1016/j.gca.2003.10.034

Von Blanckenburg, F., Bouchez, J., Ibarra, D.E., Maher, K., 2015. Stable runoff and weathering fluxes into the oceans over Quaternary climate cycles. Nature Geosci 8, 538–542. https://doi.org/10.1038/ngeo2452

Wadham, J.L., Hawkings, J.R., Tarasov, L., Gregoire, L.J., Spencer, R.G.M., Gutjahr, M., Ridgwell, A., Kohfeld, K.E., 2019. Ice sheets matter for the global carbon cycle. Nat Commun 10, 3567. https://doi.org/10.1038/s41467-019-11394-4

West, A., Galy, A., Bickle, M., 2005. Tectonic and climatic controls on silicate weathering. Earth and Planetary Science Letters 235, 211–228. https://doi.org/10.1016/j.epsl.2005.03.020

Westerhold, T., Marwan, N., Drury, A.J., Liebrand, D., Agnini, C., Anagnostou, E., Barnet, J.S.K., Bohaty, S.M., De Vleeschouwer, D., Florindo, F., Frederichs, T., Hodell, D.A., Holbourn, A.E., Kroon, D., Lauretano, V., Littler, K., Lourens, L.J., Lyle, M., Pälike, H., Röhl, U., Tian, J., Wilkens, R.H., Wilson, P.A., Zachos, J.C., 2020. An astronomically dated record of Earth's climate and its predictability over the last 66 million years. Science 369, 1383–1388. https://doi.org/10.1126/SCIENCE.ABA6853

White, A.F., Blum, A.E., 1995. Effects of climate on chemical_ weathering in watersheds. Geochimica et Cosmochimica Acta 59, 1729–1747. https://doi.org/10.1016/0016-7037(95)00078-E

Willenbring, J.K., von Blanckenburg, F., 2010. Long-term stability of global erosion rates and weathering during late-Cenozoic cooling. Nature 465, 211–214. https://doi.org/10.1038/nature09044

Wittmann, H., Von Blanckenburg, F., Maurice, L., Guyot, J.-L., Filizola, N., Kubik, P.W., 2011. Sediment production and delivery in the Amazon River basin quantified by in situ-produced cosmogenic nuclides and recent river loads. Geological Society of America Bulletin 123, 934–950. https://doi.org/10.1130/B30317.1

Yu, Z., Colin, C., Bassinot, F., Wan, S., Bayon, G., 2020. Climate-Driven Weathering Shifts Between Highlands and Floodplains. Geochem Geophys Geosyst 21, e2020GC008936. https://doi.org/10.1029/2020GC008936

Zachos, J., 2001. Trends, Rhythms, and Aberrations in Global Climate 65 Ma to Present. Science 292, 686–693. https://doi.org/10.1126/science.1059412

Zhang, J., Wan, S., Clift, P.D., Jin, H., Song, Z., Tang, Y., Yu, Z., Zhang, K., Lu, J., Jiao, W., Li, A., 2025. Evolution of silicate weathering in the Yangtze River Basin since 3.5 Ma as archived in the East China Seas: Controlling factors and global significance. Global and Planetary Change 250, 104807. https://doi.org/10.1016/j.gloplacha.2025.104807

Zhang, K., Shields, G.A., 2023. Early diagenetic mobilization of rare earth elements and implications for the Ce anomaly as a redox proxy. Chemical Geology 635, 121619. https://doi.org/10.1016/j.chemgeo.2023.121619

Zhang, S., Bai, X., Zhao, C., Tan, Q., Luo, G., Wang, J., Li, Q., Wu, L., Chen, F., Li, C., Deng, Y., Yang, Y., Xi, H., 2021. Global CO_2 Consumption by Silicate Rock Chemical Weathering: Its Past and Future. Earth's Future 9, e2020EF001938. https://doi.org/10.1029/2020EF001938

Zhao, Y., Wei, W., Santosh, M., Hu, J., Wei, H., Yang, J., Liu, S., Zhang, G., Yang, D., Li, S., 2022. A review of retrieving pristine rare earth element signatures from carbonates. Palaeogeography, Palaeoclimatology, Palaeoecology 586, 110765. https://doi.org/10.1016/j.palaeo.2021.110765

Zondervan, J.R., Hilton, R.G., Dellinger, M., Clubb, F.J., Roylands, T., Ogrič, M., 2023. Rock organic carbon oxidation CO2 release offsets silicate weathering sink. Nature 623, 329–333. https://doi.org/10.1038/s41586-023-06581-9

APPENDIX 1

New constraints on the Late Miocene-Pliocene deformational and depositional evolution of the Eastern Cordillera and Sub-Andean Zone in Southern Peru

Journal of South American Earth Sciences 133 (2024) 104700

Contents lists available at ScienceDirect

Journal of South American Earth Sciences

journal homepage: www.elsevier.com/locate/jsames

New constraints on the Late Miocene-Pliocene deformational and depositional evolution of the Eastern Cordillera and Sub-Andean Zone in Southern Peru

G.R. Moizinho [a,b,c,*], M. Roddaz [a], S. Brichau [a], M. Louterbach [d], E.L. Dantas [b], R.V. Santos [b], G. Bayon [c], J. Bailleul [e], J. Vink [f], C. Hoorn [g]

[a] Géosciences-Environnement Toulouse, Université de Toulouse, Toulouse, France
[b] Instituto de Geociências, Universidade de Brasília, Brasília, Brazil
[c] IFREMER, Geo-ocean, Plouzané, France
[d] Harvard Graduate School of Design, Department of Landscape Architecture, Cambridge, USA
[e] Bassins-Réservoirs-Ressources, Institut Polytechnique Lasalle Beauvais, Beauvais Cedex, France
[f] Centre for Biodiscovery School of Biological Sciences Victoria University of Wellington Wellington, New Zealand
[g] Institute of Biodiversity and Ecossistem Dynamics, University of Amsterdam, Netherlands

ARTICLE INFO

Keywords:
Andes
Miocene-Pliocene
Uplift
Thermochronology
Chronostratigraphy
Provenance

ABSTRACT

The deformation history of the Eastern Cordillera (EC) and Sub-Andean Zone (SAZ) of southern Peru is critical for understanding the roles that tectonics and climate played in the erosional exhumation of bedrock and the associated sediment flux delivered to the Amazon drainage basin. In this study, we report new field and subsurface data, apatite fission track (AFT) and (U–Th)/He thermochronological ages, U–Pb ages on detrital zircon grains, Sr–Nd isotopic compositions of fine sediments, which combined with previously published data, provide new constraints on the Neogene deformation and deposition history across the southern Peruvian EC and SAZ between 12° and 14°S. Late Miocene-Pliocene deformation is recorded by AFT and AHe ages in both the EC and SAZ and by growth strata geometry in the SAZ. This period is characterized by the development of piggy-back synclines and duplexes in the SAZ, overthrusting of the EC, and input of recycled sedimentary rocks of the SAZ and first cycle sediments from Triassic Plutonic rocks from the EC to the late Miocene-Pleistocene piggy-back syncline sediments. We report a transition from low-energy sand-dominated to high-energy conglomerate-dominated deposits in the Plio-Pleistocene marking an increase in sedimentation rates, indicating that the thrust wedge has continued to propagate. Our data agrees with that of previously published studies and indicate that the Late Miocene-Pliocene was a period of tectonic uplift and deformation in both the EC and SAZ.

1. Introduction

The Andes, the longest and second largest continental mountain range on Earth, constitute an important barrier to atmospheric fluxes in the Southern Hemisphere and affect the regional-scale climate by blocking zonal flows, influencing regional wind patterns, and precipitation rates (Fig. 1; Lenters and Cook, 1995; Campetella and Vera, 2002; Garreaud et al., 2003; Insel et al., 2010; Espinoza et al., 2020). Hence, the rise of the Andes is thought to have affected the climate in the eastern Pacific Ocean, besides moisture transport, and precipitation patterns in the adjacent Amazon Basin (Uba et al., 2006; Sepulchre et al., 2009; Insel et al., 2010; Poulsen et al., 2010).

The Eastern Cordillera (EC) and the Sub-Andean Zone (SAZ) define the Eastern Andean Orogenic wedge of Bolivia and Peru and constitute an orographic barrier to the moisture flux from the Amazon (e.g., Bookhagen and Strecker, 2018; Chavez and Takahashi, 2017). Most of the studies indicate that the EC experienced deformation, exhumation, and surface uplift during the Miocene (e.g., Horton et al., 2022; McQuarrie et al., 2008; Eude et al., 2015; Sundell et al., 2019). In Bolivia, by comparing the shape of the wedge assimilated to a Coulomb wedge and the present climatic zones, Horton (1999) interpreted precipitation-induced erosion to be responsible for a lesser propagation of the wedge in the north. Similarly, the decrease in width of the northern Bolivian Eastern Orogenic wedge has been interpreted as the

* Corresponding author. Géosciences-Environnement Toulouse, Université de Toulouse, Toulouse, France.
E-mail address: gabriel.ribeiro-moizinho@univ.tlse3.fr (G.R. Moizinho).

https://doi.org/10.1016/j.jsames.2023.104700
Received 12 August 2023; Received in revised form 27 October 2023; Accepted 15 November 2023
Available online 24 November 2023
0895-9811/© 2023 Elsevier Ltd. All rights reserved.

result of a wetter climate of northern Bolivia since ca. 19 Ma (McQuarrie et al., 2008). Alternatively, weakening of the retroarc lithosphere and development of a crustal-scale detachment due to strain accumulation in the Central Andes (13–22°C; Oncken et al., 2012) as well as inherited properties of the retroarc lithosphere or flat slab subduction (Horton et al., 2022) may explain accelerated shortening in the SAZ since the Middle Miocene.

The SAZ defines the eastern limit of the Central Andes, and it provides an example of an active fold and thrust belt in a retro-arc, non-collisional setting (Fig. 2). The onset of the SAZ deformation of the Central Andes and its Neogene history varies. Pliocene thrusting and forward propagation of the deformation have been documented in the SAZ in central and northern Peru (4–12.5 Lat S°, Espurt et al., 2011; Gautheron et al., 2013; Eude et al., 2015). However, in northern Bolivia and southern Peru (12.5–17 Lat S°), the absence of deformation in the EC and a "limited deformation in the Subandes" for the past 4 Ma in northern Bolivia and southern Peru have been used to advocate for a Pliocene climatic control on the exhumation and erosion of the terrain, (Lease and Ehlers, 2013).

In this paper, we revisited the Late Miocene-Pliocene exhumation history of the Amazonian southern Peruvian SAZ based on the correlation of previously published seismic sections (Baby et al., 2018b; Zamora et al., 2019), thermochronology (Mora et al., 2011; Baby et al., 2018b) and biostratigraphic ages (Marivaux et al., 2012; Antoine et al., 2013) with new AFT and AHe ages. Additionally, we report new sedimentological, provenance (Sr–Nd isotopic compositions of fine sediments and U–Pb ages of detrital zircon in sandstones), biostratigraphic and chronostratigraphic ($^{40}Ar/^{39}Ar$ in biotite ages) data sets to better understand the basin-fill evolution of the Madre de Dios retroarc foreland basin in response to the forward propagation of the Eastern Andean Orogenic wedge.

2. Geological background

2.1. Structural setting

The studied area is located between 12° and 14° S latitudes on the eastern side of the Peruvian Andes, and it comprises the EC and the Madre de Dios Basin. The basin is part of the southern Amazonian foreland basin systems and can be divided into the SAZ and the Madre de Dios foredeep (Gil, 2001; Hermoza, 2004; Roddaz et al., 2005; Fig. 2). The Madre de Dios basin is bounded in the southwest by the Azulmayo

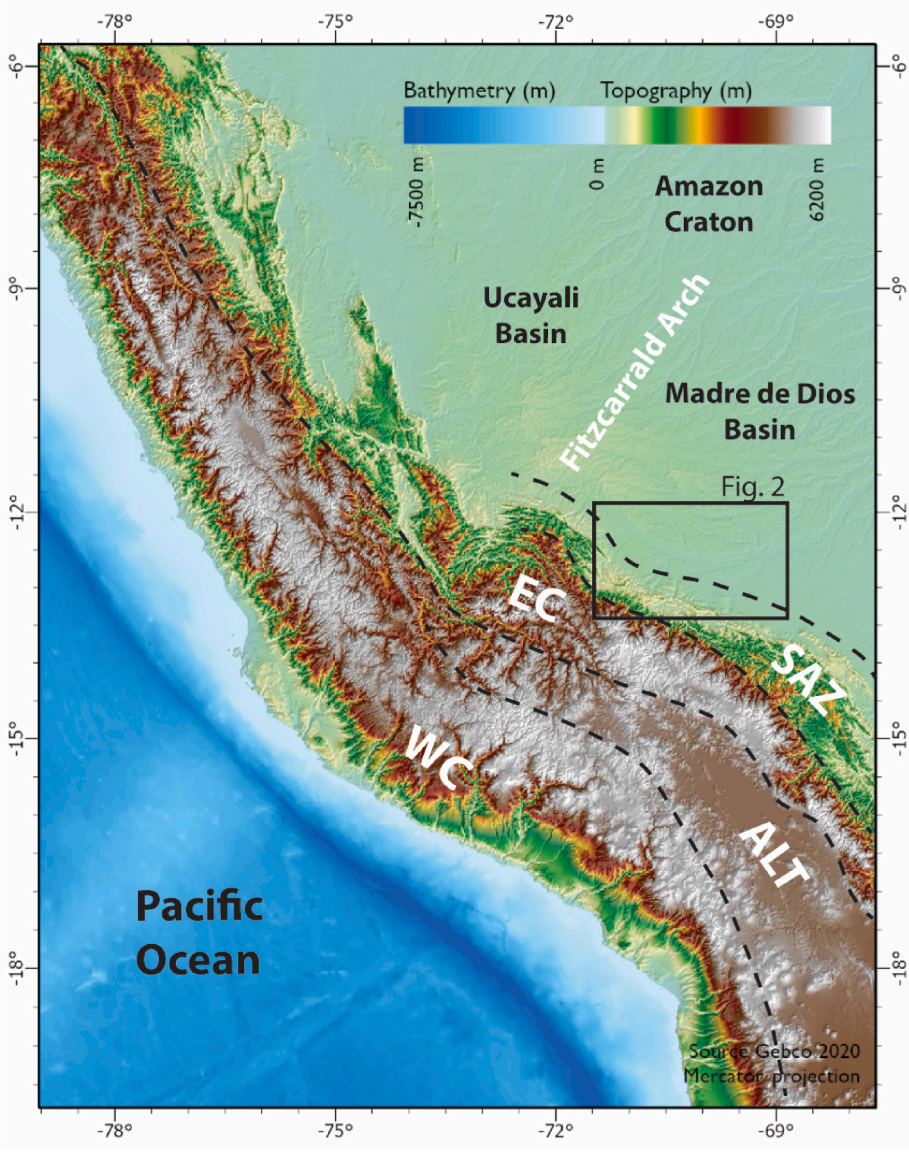

Fig. 1. Topographic and bathymetric map of the central Andes showing the location of the studied area (thick black outline, Fig. 2).

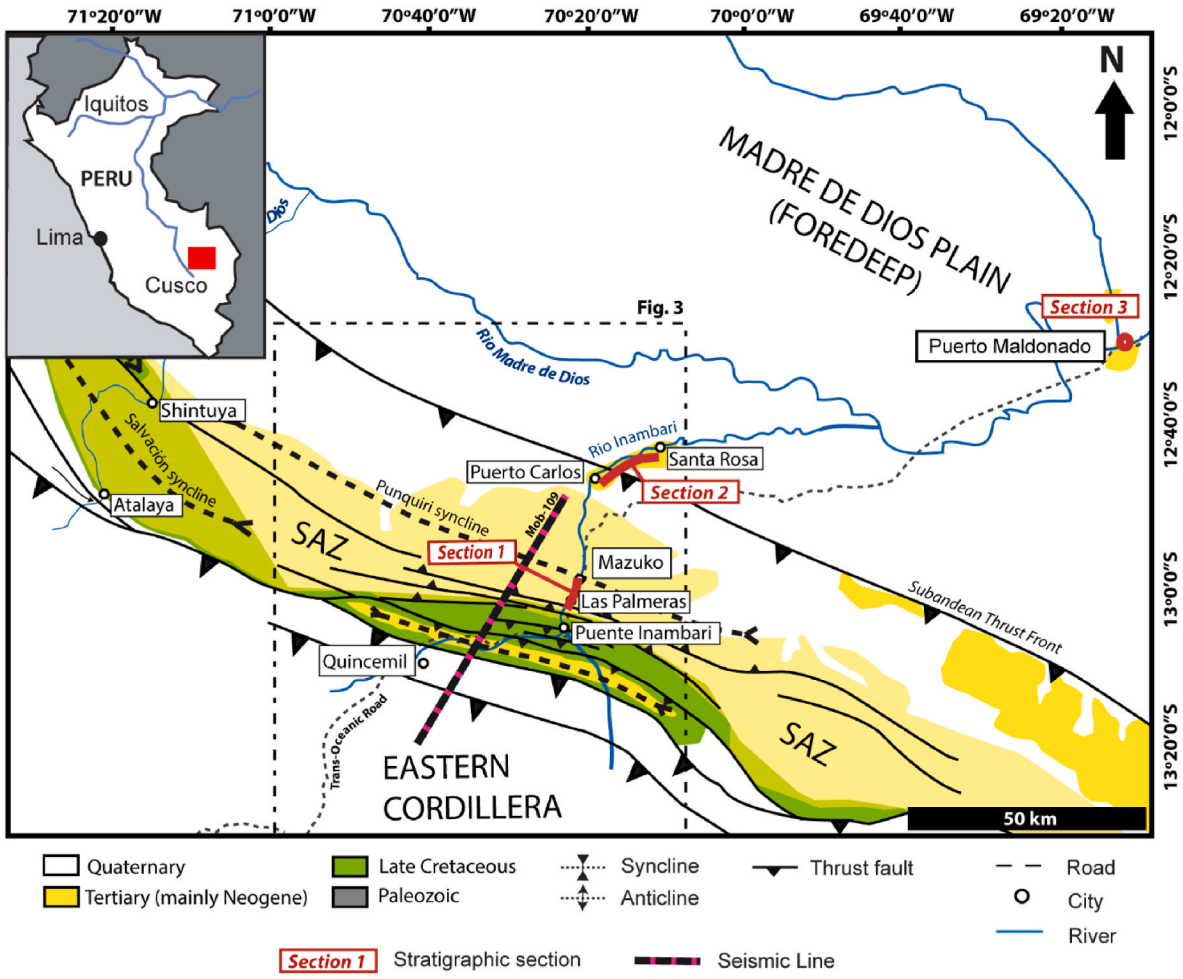

Fig. 2. Simplified geological and structural map of the Madre de Dios foreland basin. The sedimentary sections described in this study are located along the Inambari River in the SAZ (Sections 1 and 2) and in Puerto Maldonado for the foredeep zone (Section 3). The seismic line MOB-109 utilized to interpret the Inambari transect is represented by the black, pink-dashed line.

thrust, which places pre-Mesozoic rocks of the EC over the Mesozoic sedimentary rocks of the SAZ, north and northeast by the Brazilian Shield, and north and northwest by the Fitzcarrald Arch. The southern Peruvian EC is a double verging thrust wedge consisting, in its inner part, of an SW-verging system of thrust faults and folds of the Central Andean back thrust belt involving Paleozoic and Mesozoic sedimentary strata (McQuarrie and DeCelles, 2001). In its outer part, Permo-Triassic plutons and metamorphosed Precambrian and Paleozoic strata (Dalmayrac et al., 1980; Kontak et al., 1990; Mišković et al., 2009) overthrusting the SAZ. The oldest rocks outcropping in the studied area are the metamorphic rocks of the "Iscaybamba Complex". The exact age of these metamorphic rocks is unknown, but they could be Cambrian or older (Marocco, 1978; Megard, 1978; Dalmayrac et al., 1980; Dalmayrac and Molnar, 1981; Laubacher and Megard, 1985). In this section (see location in Fig. 3), the EC is interpreted as a large crustal-scale ramp anticline above a footwall ramp. Additional east-verging faults to the west of the anticline are interpreted to repeat the Ordovician section (i.e., Marcapata and Ollachea thrust faults, Figs. 2 and 3).

In the Madre de Dios Basin, the SAZ is separated from the EC by the Azulmayo thrust, also known as the "Main thrust" (Perez et al., 2016), and from the foredeep by the Tambopata thrust, which corresponds to the Sub-Andean thrust front (Figs. 3 and 4). The SAZ is interpreted as being constituted of a hinterland dipping duplex developed either in the Paleogene sedimentary infill (Fig. 4, Baby et al., 2018b; Gil Rodriguez et al., 2001) or in the Ordovician to Cretaceous series (Perez et al., 2016). On the other hand, Mora et al. (2014) have interpreted it as a thin-skinned passive-roof duplex. This duplex is overthrust by an imbricate system of Cretaceous strata as observed in seismic lines (see Fig. 17B in Baby et al., 2018b), and field relationships (see Figure 18 in Baby et al., 2018b and Figure 38 in Louterbach, 2014). The propagation of the deformation towards the Madre de Dios foredeep is partly controlled by the development of the deep duplexes. Their shortening is accommodated at the surface by tectonic imbricates and by the Tambopata frontal thrust (Gil Rodriguez et al., 2001; Baby et al., 2018a), which transported eastwards the Punquiri piggyback syncline consisting of Cenozoic sediments (Baby et al., 2018a). The strata involved in the Punquiri syncline are Paleogene through to Plio-Pleistocene in age, as shown by biostratigraphic evidence (Antoine et al., 2013; Louterbach, 2014; this study).

The balanced cross-section published by Baby et al. (2018b) shows that the shortening in the SAZ is kinematically linked to the displacement of the EC over a crustal-scale ramp, linking the development of the EC crustal anticline to the documented shortening in the SAZ. This link has also been recognized in other parts of the eastern Andes (Echavarria et al., 2003; Espurt et al., 2011; Eude et al., 2015). Since this transport of the EC along a crustal ramp implies a tectonic uplift, it follows that it was also contemporary with the deformation of the SAZ.

2.2. Neogene stratigraphic framework

The Madre de Dios Basin sedimentary infill consists of approximately 3.3 km of siliciclastic sediments that overlie the marine Cretaceous

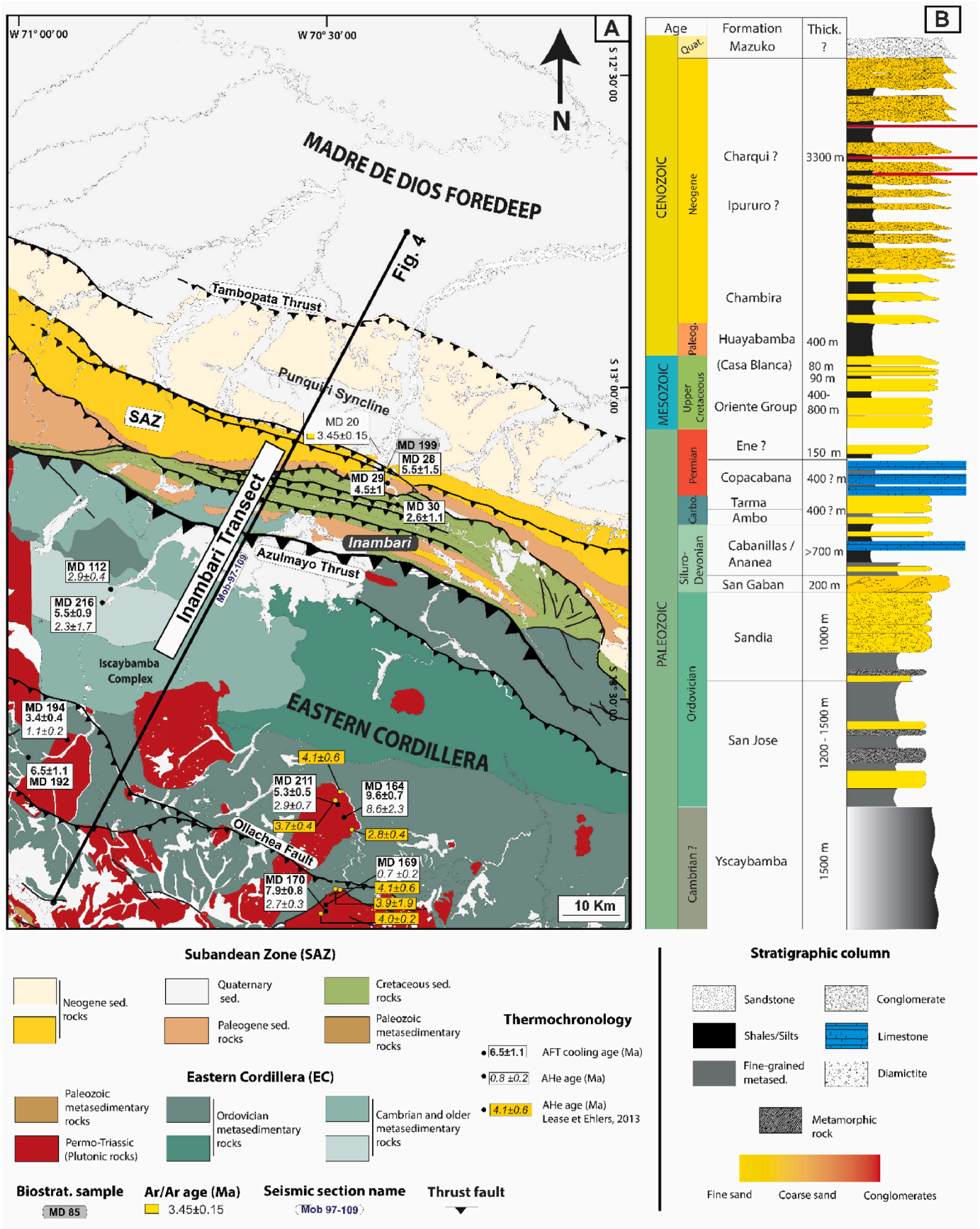

Fig. 3. A) Geological map of the study area (modified after INGEMMET) with the main section. New biostratigraphic and thermochronological (AFT and AHe ages). **B)** Synthetic sedimentary column for the SAZ of the Madre de Dios foreland basin. Thickness and lithologies are taken from (Gil Rodriguez et al., 2001; Gil Rodriguez, 2002; Hermoza, 2004; Louterbach, 2014) and confidential reports. Simplified from Louterbach (2014).

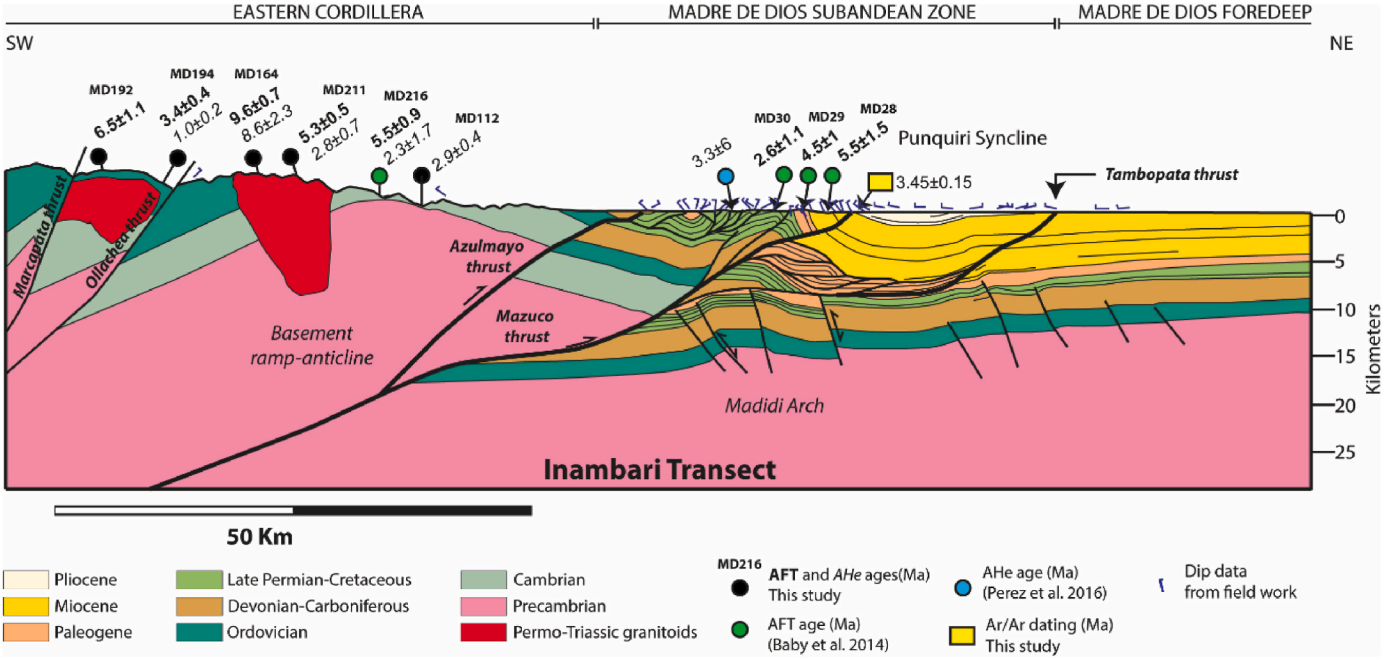

Fig. 4. Inambari structural cross-section interpreted in depth. See Fig. 3 for location. This section has been constructed using field data and MOB-97-109 and MD-56 seismic lines. Local geochronological constraints, as well as nearby thermochronological results, have been projected onto this section (modified after Baby et al., 2018b).

Cachiayacu Formation. Its stratigraphic record has been described regarding both the SAZ and foredeep compartments (Gil Rodriguez et al., 2001; Hermoza, 2004; Roddaz et al., 2010). In the SAZ, three units are recognized: the Paleocene Huayabamba Formation, the Miocene Ipururo Group, and the Plio-Pleistocene Mazuko Formation. In the foredeep, the two older units are also observed, and the Plio-Pleistocene Mazuko Formation is absent. These depositional ages are supported by palynological data (Carpenter and Berumen, 1999; Cooperación Técnica Peruana-Alemana, 1982; Gutierrez, 1982; Valdivia, 1974), thermochronological analysis (Apatite to Zircon Inc, 2004; Hermoza, 2004) and radiometry ($^{40}Ar/^{39}Ar$ on volcanic feldspar and biotite; Campbell et al., 2001; Gil Rodriguez et al., 2001; Mobil Oil Corporation, 1998).

In the SAZ, the Ipururo Group consists of Miocene deposits divided into three formations: the Bala, Quendeque, and Charqui formations (Roddaz et al., 2010). At first, these formations were thought to be fluvial to alluvial in nature (Gil Rodriguez et al., 2001; Hermoza, 2004; Roddaz et al., 2010). Alluvial, deltaic, and estuarine coastal plain facies have been reported in the Miocene Bolivian Quendeque Formation (Hovikoski et al., 2007b, 2007c). Miocene tidal-influenced deposits were also described in the Bolivian Beni-Mamoré Basin, which is adjacent to the Madre de Dios Basin (Roddaz et al., 2006).

In the Peruvian foredeep, the Ipururo Group encompasses the Ipururo Formation and Units A and B of the Madre de Dios Formation (Campbell et al., 2001). The Ipururo Formation is thought to be Miocene in age based on stratigraphic correlations (Hermoza, 2004). The Madre de Dios Formation is Late Miocene ($^{40}Ar/^{39}Ar$ dating on feldspars at 9.01 ± 0.28 Ma, Campbell et al., 2001) and thus considered as a lateral equivalent of the Bolivian Charqui Formation (Roddaz et al., 2010). Overall, the Madre de Dios Formation has been interpreted as formed by tide-dominated estuarine deposits (Hovikoski et al., 2005; Roddaz et al., 2006).

3. Sampling and methodologies

3.1. Low temperature thermochronology

Eight samples were collected along two vertical profiles in the eastern flank of the EC for Apatite Fission Track (AFT) and Apatite U–Th/He (AHe) analyses: six Permo-Triassic plutonic rocks (MD164, MD169, MD170, MD192, MD194, and MD211) and two metasedimentary rocks belonging to the Paleozoic (Cambrian?) Iscabambay Complex (MD112 and MD216; see Tables 1 and 2). The AFT age of MD216 was previously presented by Baby et al. (2018b) but the dataset was never published. In the SAZ, we provide the full dataset for three AFT ages of three Cretaceous to Paleogene sedimentary rocks (MD30, MD29, and MD28). These AFT ages were reported by Mora et al. (2011) and Baby et al. (2018b) but the dataset was never published. The locations of the samples are shown in Fig. 3 and projected onto the cross-section in Fig. 4.

The AFT analysis of the SAZ was carried out by Apatite to Zircon Inc. (former Donnelick Analytical LabAFT analyses). Sample preparation and the rest of the AFT and AHe analyses were performed at Geoscience Environment Toulouse (GET, France) and Caltech (USA), respectively, following the methodology described in Eude et al. (2015). Detailed analytical procedures can be found in the supplementary data material.

3.1.1. Thermal modeling

To understand the significance of the results, thermal histories need to be extracted from the data. This process requires modeling software that incorporates numerical descriptions of thermal resetting in both the FT and (U–Th)/He systems. For this study, sample thermal histories were obtained using the modeling package HeFTy v2.0.9.85 of Ketcham (2005), which includes the multi-compositional AFT annealing algorithm of Ketcham et al. (2007). HeFTy software excels in reverse modeling of both AFT and AHe data. It uses a Monte Carlo approach to seek optimal cooling paths, governed by user-specified t–T boundaries. The software predicts thermal histories that align closely with the actual data collected. The modeling of each sample considers various input parameters, such as central AFT ages, track length distribution, Dpar values, and average AHe dates. When available, grain sizes and chemical attributes are also included (Table 1). The annealing multi-kinetic model of Ketcham et al. (2007) has been used for the AFT data and the radiation damage accumulation model of Gautheron and Tassan-Got (2009) for the AHe data. Comprehensive results from the thermal modeling are

Table 1
Fission track data. Abbreviations are as follows: EC: Eastern Cordillera; SAZ Subandean Zone; PC: Pongo de Coneq; IN: Inambari; ρs, spontaneous track density (× 10^6 tracks per cm^2); Ns, number of spontaneous tracks counted in apatite grains; ρi, induced track density in external detector (muscovite)(× 106 tracks per cm2); Ni, number of induced tracks counted in micas; ρd, density of tracks on the neutron monitor; Nd, number of tracks counted in the dosimeter; Pχ2 (%), probability of obtaining χ2 value for n degrees of freedom (where n = number of crystals - 1): if the probability is less than 5%, it is likely that the grains counted represent a mixed age population and in this case the best-fit peak age (P1–P2) were determined with BINOMFIT (Brandon, 1996, 2002) and are given in Ma ± 1SE; TL, mean length of measured confined tracks; ML: Mélanie Louterbach; D: Donelick; SB: Stéphanie Brichau. See supplementary material for detail in analytical procedures.

Area	Sample Name	Age	Lithology	Longitude	Latitute	Elevation (m)	ρS	Ns	ρi	Ni	ρd	Nd	P(χ^2) (%)
EC	MD 170	Permo-Triassic	Plutonic rock	−7,049,500	−1,384,040	3213	231600	114	6134000	3124	1423000	41768	99,43
	MD 192	Permo-Triassic	Plutonic rock	−7,098,110	−1,359,570	3000	45540	39	1433000	1234	1367000	13741	92,44
	MD 194	Permo-Triassic	Plutonic rock	−7,091,780	−1,356,870	2385	82870	70	4796000	4283	1367000	13741	99,52
	MD 164	Permo-Triassic	Plutonic rock	−7,046,680	−1,368,790	1883	394400	186	9080000	4115	1406000	13542	81,83
	MD 211	Permo-Triassic	Plutonic rock	−7,047,750	−1,366,790	1733	180712	107	7281816	4364	1438300	14485	99,94
	MD 216	Paleozoic (Cambrian?)	Metasediment	−7,086,083	−1,334,566	986	89265	37	3508563	1403	1377758	13741	75,39
SAZ	MD 30	Late Cretaceous	Sandstone	−7,038,383	−1,318,562	382	15000	51	3085000	1051	3122000	5154	1,4
	MD 29	Late Cretaceous	Sandstone	−7,040,074	−1,314,935	371	265000	131	3787000	1875	3124000	5154	0,0
	MD 28	Miocene	Sandstone	−7,039,736	−1,312,999	366	266000	126	2413000	1142	3126000	5154	0

Area	Sample Name	Mean U (ppm)	Central Age (Ma)	Pooled age (Ma)	Mean Age (Ma)	P1 (Ma)	P2 (Ma)	Ng	TL	of Tracks	Dpar (μm)	Std (μm)	Analysts
EC	MD 170	53,9	7.9 ± 0.8	**7.9 ± 0.8**	8.1 ± 1.3			28	11.03 ± 0.5	50	2,03	1,95	ML
	MD 192	13,1	6.5 ± 1.1	**6.5 ± 1.1**	6.1 ± 0.9			19	12,8	1	NO	NO	ML
	MD 194	43,9	3.4 ± 0.4	**3.4 ± 0.4**	3.4 ± 0.4			26	11.15 ± 0.6	26	2,48	1,84	ML
	MD 164	80,8	9.6 ± 0.7	**9.6 ± 0.7**	9.0 ± 0.6			20	11.45 ± 0.2	80	1,77	1,54	ML
	MD 211	63,3	5.3 ± 0.5	**5.3 ± 0.5**	5.4 ± 0.3			20	11.37 ± 0.2	103	2,17	1,8	ML
	MD 216	31,8	5.5 ± 0.9	**5.5 ± 0.9**	5.5 ± 1.0			19	10.62 ± 0.87	4	2,43	1,74	ML
SAZ	MD 30			**7.91 ± 1.16**	13.9 ± 3.8	**2.6 ± 1.1 (5)**	1.6 ± 2.0	17	13.96 ± 0.22	21	1,84	0,99	D
	MD 29			**11.4 ± 1.1**	11.4 ± 1.1	**4.5 ± 1.0 (16)**	1.9 ± 2.1	26	13.96 ± 0.21	53	1,69	1,51	D
	MD 28			**18.0 ± 1.8**	13.4 ± 3.0	**5.5 ± 1.5 (15)**	1.6 ± 3.5	25	13.67 ± 0.34	18	1,8	0	D

available in the supplementary dataset.

Initial constraints used for sedimentary samples are the estimated stratigraphic deposit age (Paleogene for MD28, and Cretaceous for MD29, and 30; Louterbach, 2014) and a large box from 40 °C to 200 °C from the older stratigraphic age to the actual to leave maximum freedom to the software to find solutions and because of the lack of geological constraints. For the crystalline samples (MD112, 164, 169, 170, 194, 211, and 216), initial parameters were established within a temperature range of 0 °C–200 °C. This range begins from an age marginally older than the previously recorded thermochronological age and concludes between 10 and 20 Ma, based on the specific thermochronological ages. This approach was chosen since the available geological data doesn't provide sufficient detail to pinpoint the thermal history prior to acquiring its AFT ages. For each sample, we tested between 10,000 and 20,000 paths. The model either continued until it found 50 suitable paths or stopped if identifying these paths proved easy for the software. Pink shading highlights the group of 50 optimal cooling paths (based on a 0.5 criterion) derived from a broader set of Monte Carlo trials (usually exceeding 1000). The green shading indicates the range of "acceptable" paths (more than 30) within the same set, determined by a more relaxed goodness-of-fit criterion of 0.05.

3.2. Facies analyses

In the studied area Neogene deposits outcrop almost continuously along the Inambari River, from the south-western flank of the Punquiri syncline towards the Madre de Dios foredeep. Three stratigraphic sections were studied at locations I, II, and III (Fig. 2). These sections were reported in Louterbach (2014, http://thesesups.ups-tlse.fr/2530/) but have never been published. The sedimentary logs corresponding to the studied stratigraphic sections have been measured at a 1:500m scale during several field works between 2010 and 2012 following the methodology of Miall (1996).

3.3. Chronostratigraphy: $^{40}Ar/^{39}Ar$ step heating method

We collected a sample at a tuffaceous level dated by Gil Rodriguez et al. (2001) at 3.23 ± 0.3 Ma (by Ar/Ar dating on biotite) and 2.96 ± 0.34 Ma (Ar/Ar dating on plagioclase). This sample (sample MD 157; longitude: −70.409 and latitude −13.1115) is stratigraphically located at ~ 2.5 km to the top of the exposed Plio-Pleistocene series between seismic horizons T3 and T4 (Louterbach, 2014). In the studied area, the tuff and enclosing layers are significantly deformed with steeply dipping beds N90E, 84 (Fig. S8).

The selected sample was crushed, sieved and single grains of biotite were handpicked under a binocular microscope and cleaned in an ultrasonic bath using acetone and distilled water. The minerals were packaged in aluminum foils and irradiated for 50 h in the core of the Triga Mark II nuclear reactor of Pavia (Italia) with several aliquots of the Taylor Creek sanidine standard (28.34 ± 0.10 Ma) as flux monitor.

Table 2
(U–Th)/He ages were performed by laser heating for He extraction and ICP-MS for U–Th determinations at Caltech. The estimated analytical uncertainty for He ages is about 15% (2σ) due to multi-grain aliquots. Standard deviation on ages is used as error when higher than the analytical uncertainty. n = number of grains per aliquot. Multiple grain aliquots have been used due to young ages and consequently low He concentration. C*probably affected by implantation see AHe ages vs eU and Th/U.

		Sample no.	Aliquot name	Mineral	n	Rs (μm)	weight (μg)	F_T	He nmol/g	U (ppm)	Th (ppm)	Sm (ppm)	eU (ppm)	Th/U	He raw age (Ma)	He corr. age (Ma)	error Abs	Std dev	Longitude (Decimal degrees)	Latitude (Decimal degrees)	Elevation (m)
EC	INAMBARI	**MD112**	A B	Apatite	2	55,2	7,48	0,77	0,76	54,35	9,72	162,39	57,46	0,18	2,4	3,2	0,5		−70,8422	−13,3242	843
		mean		Apatite	2	41	2,89	0,68	0,48	48,40	7,98	128,00	50,93	0,16	1,8	2,6	0,4				
								0,72	**0,62**	**51,38**	**8,85**	**145,20**	**54,19**	**0,17**	**2,1**	**2,9**	**0,3**	**0,4**			
		MD164	A B C	Apatite	3	35,6	3,3	0,64	2,63	69,22	5,66	200,95	71,52	0,08	6,8	10,7	1,6		−70,4668	−13,6879	1883
		mean		Apatite	3	40,4	4,33	0,71	2,52	72,12	3,47	212,23	73,94	0,05	6,3	9,0	1,3				
				Apatite	2	45,5	4,54	0,72	2,48	100,44	3,83	240,85	102,48	0,04	4,5	6,2	0,9				
								0,69	**2,54**	**80,60**	**4,32**	**218,01**	**82,65**	**0,06**	**5,9**	**8,6**	**0,8**	**2,3**			
		MD169	A	Apatite	4	68,7	20,31	0,78	0,93	34,95	1035,75	472,39	288,81	29,64	0,6	0,8	0,12		−70,4865	−13,8273	2994
		mean	B C	Apatite	4	42,5	4,07	0,64	0,91	43,68	1996,70	666,90	531,95	45,71	0,3	0,5	0,08				
				Apatite	4	67,5	15,25	0,77	0,25	7,43	257,34	92,49	70,39	34,64	0,7	0,9	0,13				
								0,73	**0,69**	**28,69**	**1096,60**	**410,59**	**297,05**	**36,66**	**0,5**	**0,7**	**0,06**	**0,2**			
		MD170	A B C	Apatite	3	34,6	2,8	0,60	1,04	57,21	356,86	328,09	145,43	6,24	1,4	2,3	0,3		−70,495	−13,8404	3213
		mean		Apatite	3	34,3	2,95	0,59	1,01	46,11	264,82	283,42	111,76	5,74	1,7	2,9	0,4				
				Apatite	3	42,6	5,15	0,67	0,96	42,12	217,25	299,77	96,29	5,16	1,9	2,8	0,4				
								0,62	**1,00**	**48,48**	**279,64**	**303,76**	**117,83**	**5,71**	**1,6**	**2,7**	**0,2**	**0,3**			
		MD194	A	Apatite	4	45,8	8,45	0,72	0,24	46,38	27,01	115,96	53,48	0,58	0,8	1,1	0,2		−70,9178	−13,5687	2385
		mean	B C	Apatite	3	54,8	13,53	0,76	0,15	37,91	33,19	134,75	46,60	0,88	0,6	0,8	0,1				
				Apatite	3	35,9	2,98	0,71	0,16	28,02	39,21	126,31	38,13	1,40	0,8	1,1	0,2				
								0,73	**0,18**	**37,44**	**33,14**	**125,67**	**46,07**	**0,95**	**0,7**	**1,0**	**0,09**	**0,2**			
		MD211	A	Apatite	3	32,5	2,69	0,62	1,08	82,51	23,13	194,71	89,02	0,28	2,3	3,6	0,5		−70,4775	−13,6679	1733
		mean	B C	Apatite	4	36,4	4,92	0,68	0,79	79,45	30,41	260,81	88,04	0,38	1,7	2,5	0,4				
				Apatite	4	34,5	3,76	0,66	0,43	47,67	13,49	255,86	52,12	0,28	1,5	2,3	0,3				
								0,65	**0,77**	**69,87**	**22,34**	**237,13**	**76,39**	**0,32**	**1,8**	**2,8**	**0,2**	**0,7**			
		MD216	A	Apatite	3	39,4	4,21	0,62	0,53	17,50	531,40	249,32	147,78	30,36	0,7	1,1	0,2		−70,86083	−13,34566	986
		mean	C	Apatite	4	28,3	2,23	0,52	0,16	10,14	26,37	89,46	16,96	2,60	1,8	3,5	0,5				
								0,57	**0,35**	**13,82**	**278,89**	**169,39**	**82,37**	**16,48**	**1,3**	**2,3**	**0,3**	**1,7**			

Argon isotopic interferences on K and Ca were determined by irradiation of KF and CaF_2 pure salts from which the following correction factors were obtained: ($^{40}Ar/^{39}Ar$) K = 0.00969 ± 0.00038, ($^{38}Ar/^{39}Ar$) K = 0.01297 ± 0.00045, ($^{39}Ar/^{37}Ar$)Ca = 0.0007474 ± 0.000021 and ($^{36}Ar/^{37}Ar$)Ca = 0.000288 ± 0.000016. Argon analyses were performed at Geosciences Montpellier (France) with an analytical system that consists of: (a) an IR-CO2 laser of 100 kHz used at 5–15% during 30 s for step-heating experiments, (b) a lenses system for beam focusing, (c) a steel sample chamber, maintained at 10-8 - 10-9 bar, with a drilled copper plate and samples on, (d) an inlet line for purification of gases including two Zr–Al getters, (e) a multi-collector mass spectrometer (Argus VI from Thermo-Fisher). Custom-made software controls the laser intensity, the timing of extraction/purification, and the data acquisition. To measure the argon background within the system, one blank analysis was performed in every three sample analyses. The ArArCalc software© v2.5.2 was used for data reduction and plotting. The one-sigma errors reported on plateau, isochron, and total gas ages include the error on the irradiation factor J. Atmospheric ^{40}Ar was estimated using a value of the initial $^{40}Ar/^{36}Ar$ of 295.5. Results are summarized in Table S1.

3.4. Biostratigraphy

We provide two new biostratigraphic constraints from samples MD199 and MD202, collected along the Inambari River. Chunks (approximately 1 kg) of clay were collected and transported in plastic bags. For the preparation, a standard procedure (dense liquid separation) of the University of Amsterdam was followed (see Hoorn, 1993). With a knife, small blocks of approximately 1 cm^3 were cut from the middle part of the clay. This sample was sieved at 212 μm. The samples were then treated with a 10% sodium pyrophosphate solution ($Na_4P_2O_7 \cdot 10H_20$). Bromoform was used to separate the inorganic/organic layers. Glycerin was used to stick the grains on the slide and paraffin was used to seal it.

Pollen and spores were counted for a maximum of two slides if the sum was less than 200, and only one slide if it contained more than 200 palynomorphs. Photographs were taken of each of the different pollen and spore types with an Optikam B5- microscope camera at a magnification of 1000× and were identified with a palynological database (Jaramillo and Rueda, 2023) and s literature (da Silva-Caminha et al., 2010; Germeraad et al., 1968; Hoorn, 1993; Lorente, 1986). Additional identifications were provided by Millerlandy Romero-Baez, and where identification was not possible, we listed taxa as an unknown type. The samples were dated based on the presence of biostratigraphic markers and using the stratigraphical zonations from Venezuela and Colombia (Jaramillo et al., 2011).

3.5. 2-D seismic data

The two-dimensional seismic section Mob-97-109, acquired and processed by the Hunt Oil Exploration and Production Company of Peru and their partner Repsol Exploration Company (2009–2010), was used for stratigraphic correlation and structural interpretation in the SAZ (Fig. 8). We used the software Move® to project the seismic lines, the biostratigraphic and thermochronological ages, and our field data onto the section.

3.6. Provenance analyses

3.6.1. Sr–Nd isotopes

The Nd–Sr isotopic compositions were measured at Geosciences Environment Toulouse (GET) and were incorporated in the Master thesis of Sanchez (2012). The analyzed samples were first digested in hydrogen peroxide for 24 h at ambient temperature and then digested in HNO_3 for 24 h at 80 °C followed by HF– HNO_3 for 24 h at 80 °C, and finally HCl + HNO_3 for 24 h at 115 °C. Blank tests were performed to estimate the level of contamination induced by the acid digestion, but it was found to be negligible. Aliquots containing about 1000 ng of Sr and Nd were loaded into the ion exchange columns. Sr and Nd were separated using the Sr-SPEC, TRU-SPEC, and LN-SPEC resins (Eichrom). Nd and Sr isotopic ratios were measured using a Finnigan Mat 261 thermal ionization mass spectrometer in dynamic mode. During the Nd run, the $^{146}Nd/^{144}Nd$ (=0.7219) was used to correct the signal for mass fractionation. For each sample, checks were made for the absence of samarium (Sm). The accuracy of the measurements was estimated on the Rennes University standard for Nd (=0.511961 ± 14). This value was calibrated relative to the La Jolla standard by the Brest, Toulouse, and Rennes laboratories (Lacan, 2002). During the Sr run, $^{86}Sr/^{88}Sr$ (=0.1194) was used to correct the signal for mass fractionation. The accuracy of the measurements was checked against the NBS 987 standard (=0.710240). The average values fall within the range given for these standards so that no instrumental bias needs to be considered. The repeatability of these standards is around 15 ppm. This value is adopted for the overall uncertainty of all measurements, even if some individual samples yield results with a lower internal precision. Total blanks (acid digestion plus column chemistry) for Nd and Sr were checked by ICP-MS and found to be negligible compared to the Nd and Sr amounts loaded onto the columns.

The measured $^{143}Nd/^{144}Nd$ ratios are expressed as the fractional deviation in parts per 10^4 (units) from $^{143}Nd/^{144}Nd$ in a Chondritic Uniform Reservoir (CHUR) as measured at the present day:

$$\varepsilon Nd(0) = (((^{143}Nd/^{144}Nd)S / ICHUR(0) - 1)*10^4$$

where $(^{143}Nd/^{144}Nd)_S$ is the present-day ratio measured in the sample and ICHUR(0) is the $^{143}Nd/^{144}Nd$ in the CHUR reference reservoir at the present (ICHUR(0) = 0.512638 (Jacobsen and Wasserburg, 1980).

3.6.2. Detrital zircon

3.6.2.1. U–Pb geochronology. 10 Neogene sandstone samples were collected on river outcrops along the Punquiri syncline. Figs. S4–S7 show their stratigraphic position and Figs. S9–S13 the outcrops where the samples were collected. Zircon grain separation and U–Pb analysis were conducted at the University of Brasília, Brazil. For each sample, about 7 kg of sedimentary rocks were first processed in a rock crusher, producing chips roughly 3–5 cm in size. We used a SELFRAG with a voltage of 130 kV and a frequency of 3 Hz to defragment the samples liberating the mineral phases. Heavy minerals were concentrated by panning and the magnetic fraction was removed using a FRANZ isodynamic magnetic separator. After randomly hand-picked, mounted in epoxy resin mounts, and polished, back-scattered electron (BSE) images of the detrital zircon grains were obtained using a FEI QUANTA 450 Scanning Electron Microscope (SEM). The BSE images were used to identify the growth areas and zoning in zircon grains, to select suitable areas for U–Pb analysis, and to perform qualitative morphological analysis of detrital zircon grains (Fig. S14). The mounts were then cleaned with 3% nitric acid before ICP-MS analysis.

About 150–200 grains were analyzed per sample with a 25 μm beam using a Teledyne Iridia ablation system coupled to a Thermo Finnigan Element XR SF-ICP-MS (See Supplementary Table S3 for details). Analyses were carried out with the standard-sample bracketing method (Albarède et al., 2004). To calibrate downhole fractionation and instrument drift, zircon GJ1 (608 ± 1; Jackson et al., 2004) was used as primary reference material, and zircons 91500 (1065.4 ± 0.3 Ma; Wiedenbeck et al., 1995) and Plešovice (337 ± 0.37 Ma; Sláma et al., 2008) as secondary/validation. Data processing and correction of laser-induced fractionation (LIEF) were performed using IOLITE v4.0 (Paton et al., 2011) and VizualAge (Petrus and Kamber, 2012).

In general, measured U–Pb ages were filtered considering the quality of individual grain analysis, eliminating zircon grains with the following features: (1) high individual ^{204}Pb value; (2) high individual errors for

isotopic ratios (>3%); (3) discordances higher than 10%. For clarity, all the generated data is presented in Supplementary Table 3. Finally, the "best age" for a given zircon grain was chosen using $^{206}Pb/^{238}U$ for zircons younger than 1.5 Ga and $^{206}Pb/^{207}Pb$ ages were provided for grains older than 1.5 Ga (Spencer et al., 2016). Detrital zircon age data is visualized and compared qualitatively using kernel density estimations (KDE) diagrams and probability density plots (PDP)

To quantify the degree of dissimilarity between the detrital age distributions of the analyzed samples and investigate the contribution of recycled sedimentary units, we used the standard statistical technique called multidimensional scaling (MDS) popularized by Vermeesch (2013). The MDS method is a superset of principal component analysis that, given a table of pairwise 'dissimilarities' between samples, produces a 'map' of points on which 'similar' samples cluster closely together, and 'dissimilar' samples plot far apart (Vermeesch, 2013). Following the latest recommendations by Vermeesch (2018), we used the Kolmogorov-Smirnov test to produce an MDS map comparing the analyzed samples. The closest and second closest neighbors are linked by solid and dashed lines, respectively, and the goodness of fit was evaluated using the "stress" value of the configuration (0.2 = poor; 0.1 = fair; 0.05 = good; Vermeesch, 2013). The MDS maps were produced using the provenance package of Vermeesch et al. (2016).

3.6.2.2. Morphology. In this study, we adopted the roundness and elongation classifications proposed by Augustsson et al. (2018). This method applies solely to intact grains that display consistent U–Pb ages. For roundness, we utilized a streamlined version of Powers (1953) framework, categorizing grains as euhedral, subangular to subrounded, or rounded. As for elongation, we used the length-to-width ratios to distinguish between round (below 1.3), oval (ranging from 1.3 to 1.8), and elongated (exceeding 1.8) crystals.

4. Deformation, exhumation, and erosion of the Southern Peruvian EC and SAZ

4.1. Eastern Cordillera

All EC AFT ages passed the $\chi 2$ test ($P(\chi 2)>5\%$) indicating that they have concordant grain age distributions (Table 1). The AFT central ages range from 3.4 ± 0.4 to 9.6 ± 0.7 Ma with MTL ranging from 10.62 ± 0.9–12.8 μm. AHe ages range from 0.8 ± 0.2 to 8.8 ± 2.3 Ma (Table 2). Overall, the AHe ages are younger or like their associated AFT ages. When comparing the AHe and AFT ages with elevation (Fig. 5), two trends can be observed. The AFT and AHe ages increase from elevations of 986 ± 10 to 1883 ± 15 m above sea level (m.a.s.l.). Our AHe ages are like those of Lease and Ehlers (2013) collected at the same elevation (e.g., MD211 sampled at ~1733 m.a.s.l. and 11PR04 sampled at ~1759 m.a.s.l., Fig. 5, Table 2). Above ~1900 m.a.s.l. a marked shift toward younger AHe and AFT ages is observed. The lowest samples and those which are in the footwall of the Ollachea fault (MD 211 and MD164, Figs. 2 and 4) have older AHe and AFT ages than the samples located in the hanging wall of the fault (MD 194 and MD169). The thermochronological ages might indicate a large Plio-Pleistocene uplift of the Ollachea hanging wall (Figs. 4 and 5). Additionally, the thermal histories derived from the inverse modeling of thermochronometer ages using the HeFTY software (Fig. 6) further indicate rapid Plio-Pleistocene cooling between 1 and 3 Ma while before the samples may have stayed in the Partial Annealing/Retention Zone during an extended period (probably at least 4–5 Ma).

4.1.1. Sub-Andean zone

The Punquiri syncline may show a late Miocene-Pleistocene growth strata. These growth strata are highlighted by dip data projected onto seismic line Mob-97-109 (Fig. 7). The growth strata from the Punquiri syncline can thus be correlated with those that are located above the late Miocene marker T2 registered in the Pongo de Coñeq area and are interpreted to be mostly late Miocene to Pliocene in age (Louterbach, 2014). Pliocene deformation is further attested by the presence of significantly deformed tuff and enclosing layers with steeply dipping beds (N90, 84E). This tuffaceous level, situated between seismic horizons T3 and T4 was dated to 3.45 ± 0.15 Ma using the Ar–Ar method.

In the SAZ, the three sandstones (MD28, MD29, and MD30) dated with the AFT method failed the $\chi 2$ test with $P(\chi 2)$ being less than 1.4% (Table 1; Fig. 6b). The best-fit peaks in each fission track grain age distribution were determined based on a binomial model described by Galbraith (1988) and Galbraith and Green (1990) using the BINOMFIT program (Brandon, 1992, 1996, 2002; Fig. S2). The youngest peak ages for samples MD28, MD29, and MD30 are 5.5 ± 1.5 Ma, 4.5 ± 1 Ma, and 2.6 ± 1.1 Ma, respectively (Table 1). The youngest peak age is the dominant component for samples MD28 and MD29 containing 60% and 64% of the distribution, respectively. The youngest peak age of sample MD30, although not dominant, represents a significant part of the grain ages (~30%). The HeFTy of these samples suggests that the AFT ages are reset AFT ages (Fig. 8).

5. Late Miocene-Pleistocene depositional evolution in the Madre de Dios Basin

In summary, the approximately 3300m thick late Miocene-Pleistocene deposits can be divided into lower and upper intervals. The lower ~2000 m are interpreted as sand-dominated deposits. The upper ~1300 m are characterized by an abrupt change to conglomerate-

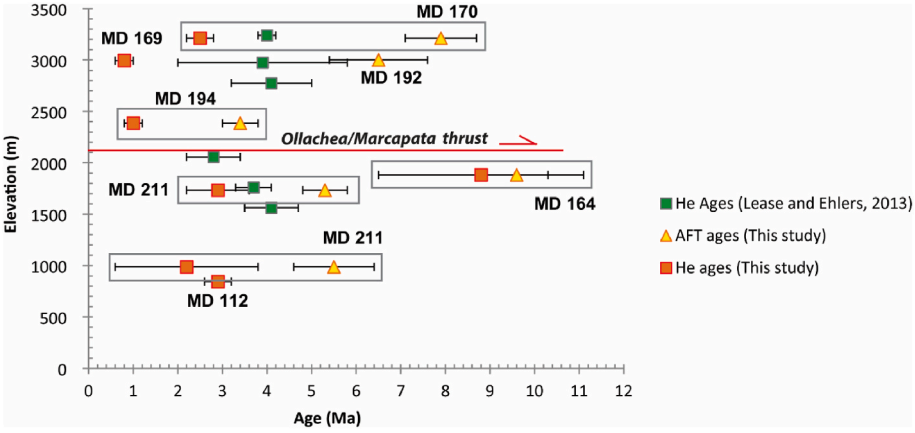

Fig. 5. A) Cooling ages versus elevation. AHe, apatite (U–Th)/He; AFT, apatite Fission Track; AHe and AFT age errors are at 1σ standard for Eastern Cordillera samples.

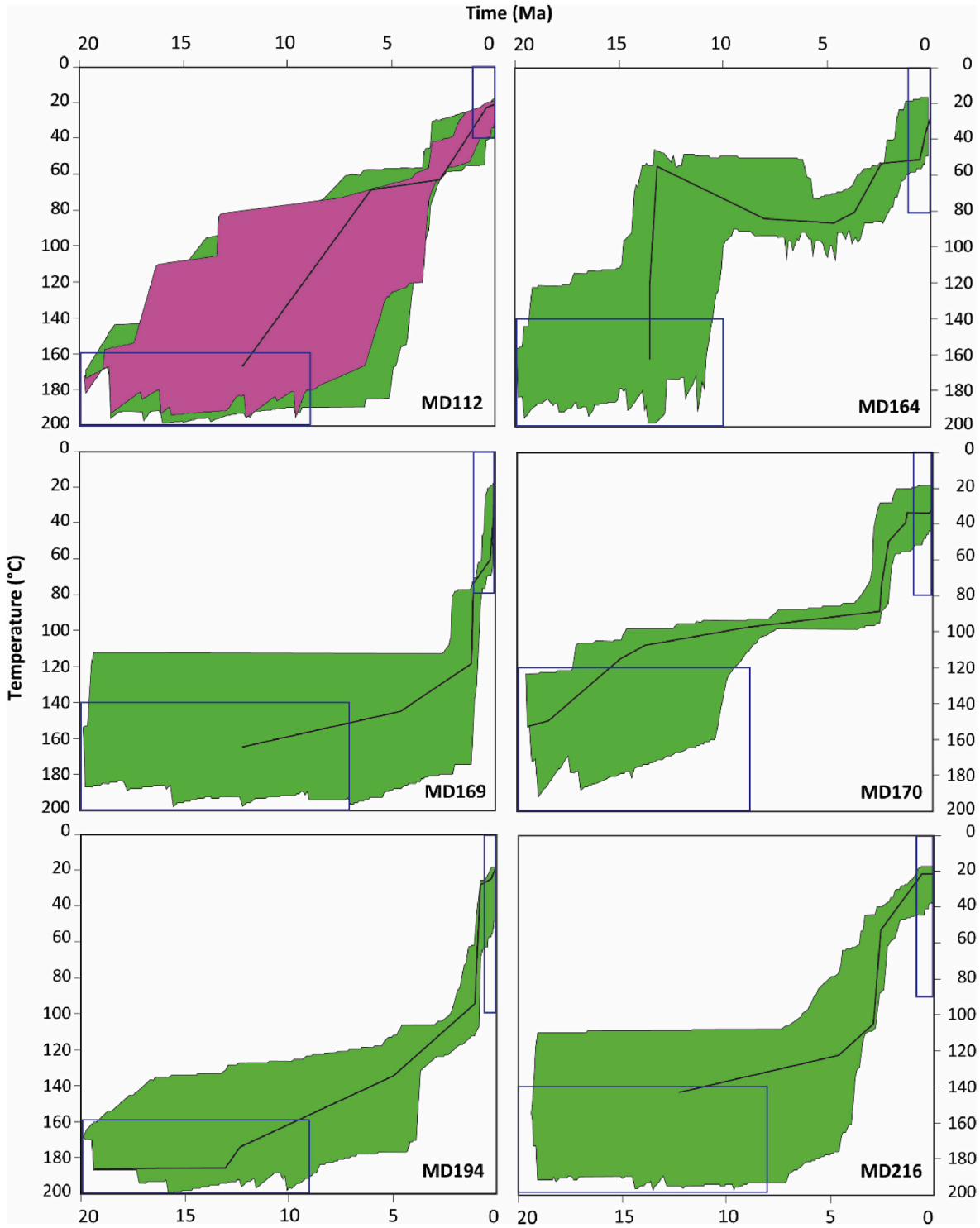

Fig. 6. Modeled t-T paths for the crystalline EC samples (MD 112, MD164, MD169, MD170, MD194, and MD216) using 'HeFTy' software (see section 3.1.1. Thermal Modeling for detail on data input). Green: Thermal history with an acceptable fit (criterion of 0.05). Purple: Thermal history with a good fit (criterion of 0.5). Black line: best-fit models. Note that MD112, 164,169, 170, 194, 211, and 216 records almost all the same exhumation histories with a main period of exhumation between 1 and 3 Ma while before the samples seem to stay in the PAZ during a long period of time (probably at least 4–5 Myr).

dominated deposits. The two sections are separated by erosive unconformities or by a stratigraphic gap. The full composite stratigraphic section can be found in detail in the Supplementary Dataset (Figs. S4–S7) and is summarized in Fig. 9. The sedimentary facies and facies association for these deposits are found in Tables 3 and 4, respectively.

We also report two new biostratigraphic ages and one $^{40}Ar/^{39}Ar$ age on biotite from a tuffaceous level in the Punquiri syncline (MD204). Samples MD199 and MD202 were dated based on their palynological content. The presence of *Echitricolporites spinosus* (17.41–0.14 Ma, Jaramillo et al., 2011), *Proteacidites triangulates* (24.13–3.41 Ma, Jaramillo et al., 2011) and *Cyatheacidites annulatus* (7.15–0.11 Ma, after Jaramillo et al., 2011) in the MD199 and MD202 samples suggest a late Miocene to Pliocene (ranging between 7.15 and 3.41 Ma) depositional age

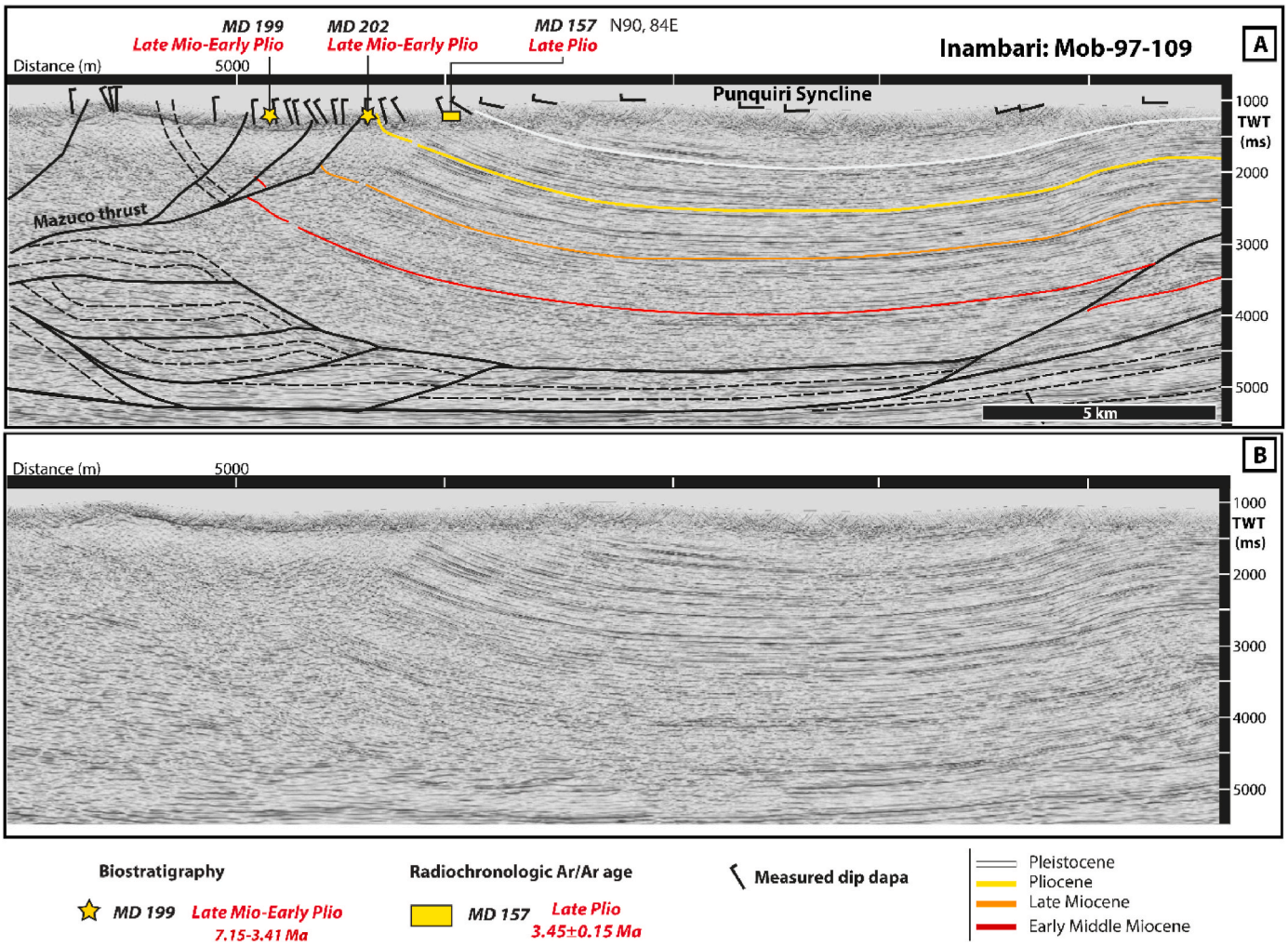

Fig. 7. A) Interpreted profile of seismic section MOB-97-109 (see Figs. 2 and 3 for location) illustrating the sedimentary infilling of the Punquiri syncline (modified from Louterbach, 2014). Dated outcrops were projected onto the seismic profile. The structural style of the SAZ duplex has been simplified. Dip values of analyzed outcrops projected onto the seismic line (black thick hyphens) show a progressive decrease toward the center of the syncline indicating syntectonic sedimentation associated with the duplex growth and Punquiri syncline formation (i.e., "growth strata deposits"); Late Mio: Late Miocene; Early Plio: Early Pliocene. B) Non-interpreted seismic line MOB-97-109.

(Table S1; Fig. S8). Our new radiometric age documented for outcrop MD 157 (3.45 ± 0.15 Ma; Table S2; Fig. S9) is consistent with the radiometric age obtained by Gil Rodriguez et al. (2001) in the same area (3.23 ± 0.3 Ma).

5.1. Lower section: sandstone-dominated interval

5.1.1. Fluvial channel sandy deposits (FCs)

Description: Facies association FCs is mainly made up of arkosic fine- to coarse-grained sandstones fining upsection into fine-grained to silty deposits (Fig. 9). Sandy to gravelly conglomeratic facies may be occasionally present at the base of the fining-upward units. The base of facies association FCs is characterized by a slightly deeply erosive and channelized surface. A 10 to 30-cm-thick mud breccia (Gm, Table 1) can also occur at the base of the facies association. Clasts (<2 cm) are angular to subrounded and consist of reworked mud clasts and extraformational ferruginous clasts (Gmf, e.g., in Section 1, at 1175 m, Fig. S4). These Gm deposits can be either clast- or matrix-supported. The basal parts of the channel infillings can also be constituted by Gt, Gh, or Gp facies (Table 3). Gt facies corresponds to conglomeratic deposits, 30 cm-to more than 3 m-thick, with trough crossbedding. Gh and Gp facies correspond to horizontally and planar bedded conglomerates, respectively, with normal to inverse grading and occasional pebble imbrications. The channel fillings typically evolve upsection into fine-to medium-grained sandstones. These sandstones are 10 cm to pluri-metric thick and can be massive (Sm), with trough cross-stratification (St), with planar (Sp), or horizontal bedding (Sh). Frequent mud clasts commonly highlight the sedimentary structures, particularly the trough cross-bedding structures situated at the base of the sandy channel-shaped bodies (Stmc). The top of Facies association FCs is characterized by 10 cm–100 cm thick finer deposits such as fine-grained rippled sandstones (Sr) or laminated siltstones to mudstone (Fl). Facies Sfu corresponds to 50-300 cm-thick fining-upward sandstones. Overall, facies association FCs corresponds to a single thick channelized sedimentary unit ranging in thickness between 50 cm and 5m, or a series of 1m–30m sandy stacked channel filling units (vertically stacked CH components). There are no lateral accretion characteristics.

Interpretation: The channel-shape geometries and fining-upward sequences show that facies association FCs is mostly generated by sandy stream floods at the end of significant flow episodes in the channels. The repeated vertical stacking patterns of the fining-upward units suggest that flow velocity fluctuates regularly. The presence of facies Sp, St, and Sh (Fig. 10), as well as the lack of lateral accretion features, imply that sand bodies are the result of limited, high-energy stream floods and record deposition linked with subaqueous dunes and upper-stage flat beds (Miall, 1996). Facies Sm corresponds to massive sandstones

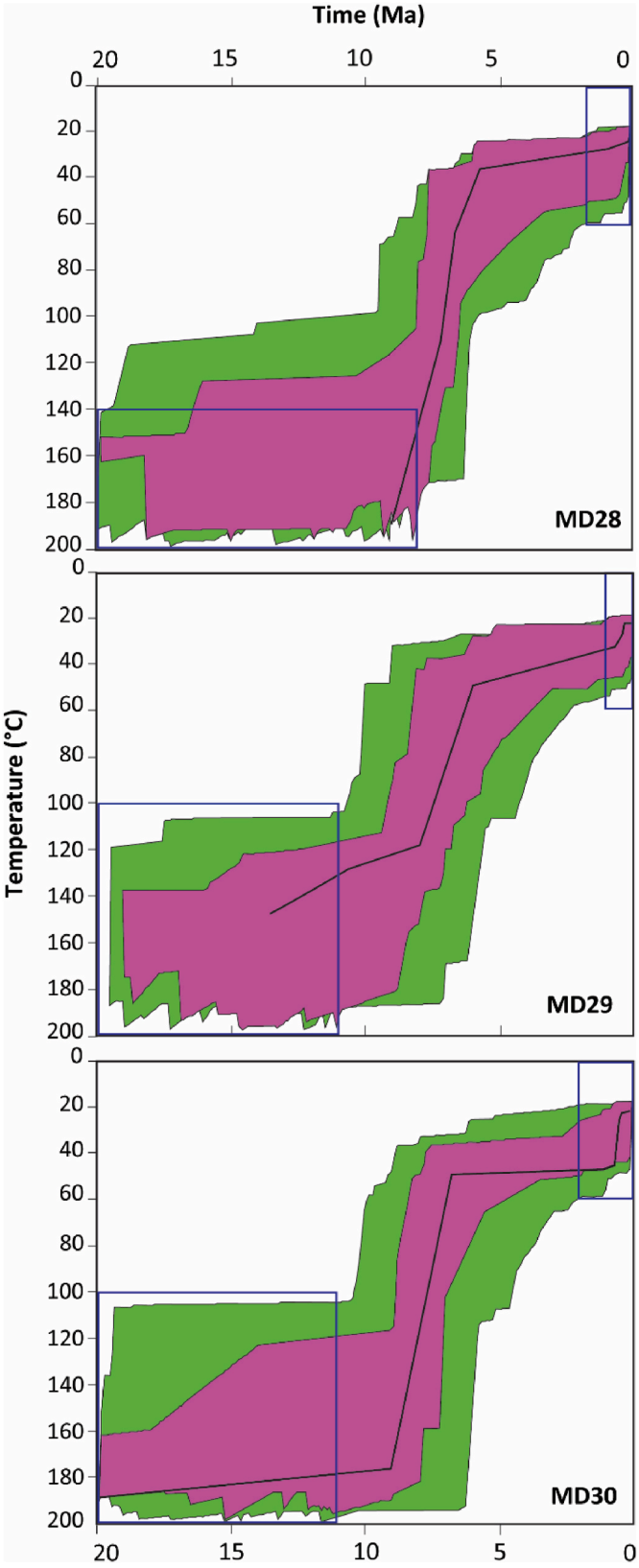

Fig. 8. Modeled t-T paths for the SAZ samples (MD 30 (Cretaceous, SAZ), MD 29 (Cretaceous, SAZ) and MD 28 (Paleogene? SAZ) samples, using 'HeFTy' program (see section 3.1.1. Thermal Modeling for detail). Green: Thermal history with an acceptable fit (criterion of 0.05). Purple: Thermal history with a good fit (criterion of 0.5). Black line: best-fit models.

deposited during sediment gravity flow or rapid deposition. Facies Sfu, Sr, and Fl, situated at the top of the channel filling sequences, are associated with a loss of stream flood energy during the channel abandonment phase. The poorly developed, disorganized, and matrix-supported conglomeratic bedforms (Gm-Gmf) described at the base of the sequences suggest high sedimentation fallout rates and/or shallow flow depth (e.g., in Jo et al., 1997; Uba et al., 2005). We interpret facies Gt, Gh, and Gp as being deposited by occasional high energy stream floods equivalent to those produced by gravel-laden streams in poorly to well-confined channels (e.g., in Ridgway and DeCelles, 1993; Uba et al., 2005). Because facies association FCs is associated with continental fine-grained overbank deposits (O) the sandy facies of FCs have been interpreted as fluvial channel-filling deposits. Depending on the geometry of the sandy units and their vertical stacking pattern, deposits can be associated with a single-story fluvial channel (single fining-up sandy unit) or multi-story channel complex (sandy units displaying an important vertical stacking).

5.1.2. *Overbank deposits (O)*

Description: Facies association O is common in the studied sedimentary sections (Supplementary Figs. S4–S7) and frequently overly the FCs and FCg associations. It consists of massive mudstone or siltstone (facies Fm, Table 3), laminated mud or silt deposits (facies Fl, Table 3), bioturbated reddish or varicolored mudstone to siltstone (facies Fb, Table 3) or blue to dark structureless or rippled mudstone to siltstone (Facies Fbl, Table 3) occasionally interbedded with silty or sandy bodies. Facies Fb can also present occasional desiccation traces. In muddy Root traces, carbonate nodules, and bioturbations can often be observed in muddy to silty layers these fine-grained overbank deposits range from 20 cm-to 20 m in thickness. Coarser-grained sandy deposits with thicknesses ranging from 20 to 200 cm of massive or fining-upwards fine-grained to medium-grained sandstones (Sm or Sfu), rippling sandstones (Sr), or coarsening-upwards sandstone (Scu) can be intercalated within the fine-grained overbank deposits. Additionally, within the overbank fine-grained sequences of the Inambari transect, two tuffaceous layers have been described (outcrop MD 2019-08 at 1615 m in Fig. S2 and outcrop MD 2019-09 at 2465 m in Fig. S5). These tuffaceous layers range in thickness from 30 to 100 cm and may exhibit ripples or flat horizontal sedimentary features (T, Fig. 11-C). These facies are rich in wood pieces and leaf remnants.

Interpretation: Palynomorphs determined in MD 199 and MD 202 suggest a continental paleoenvironment for this facies association (Table S1). Furthermore, the facies of facies association O are usually strongly associated with facies associations FCs and FCcg, both of which are interpreted as continental. We interpreted that facies association O represents deposition in a floodplain environment (Fm, Fb, Fbl, P) occasionally disturbed by waning flow deposits (Sr, Sm, Fl) and crevasse sand bodies (Scu). Facies Fm represents deposition from low-energy flows or from standing water pools after channel abandonment (Miall, 1996). The absence of desiccation cracks, the existence of sporadic root traces, and the general reddish-to-purple color of Facies Fb imply oxidizing circumstances (e.g., Turner, 1980; Miall, 1996; Retallack, 1997) with common subaerial exposure (e.g., Esteban and Klappa, 1983). The dark color of facies Fbl and its proximity to a fluvial system are consistent with deposition in an anoxic environment such as an oxbow lake or continental swamp (Miall, 1996). The thin carbonate layers, occasional carbonate nodules, numerous root traces, and continental bioturbation of facies P show pedogenic alteration following deposition (e.g., Wright and Tucker, 1991; Retallack, 1997) and are linked with a well-developed paleosol horizon. Thin layers of fine-grained silty to sandy deposits organized by thin lamination and occasional ripples (Fl and Sr) might be suggestive of low-energy streams (waning floods) linked with deposition in remote floodplains (e.g., Uba et al., 2006). The sporadic coarsening-upward and massive sandstones of facies Sm and Scu can be attributed to crevasse splay deposits and crevasse-channel fills that occur in a proximate floodplain environment.

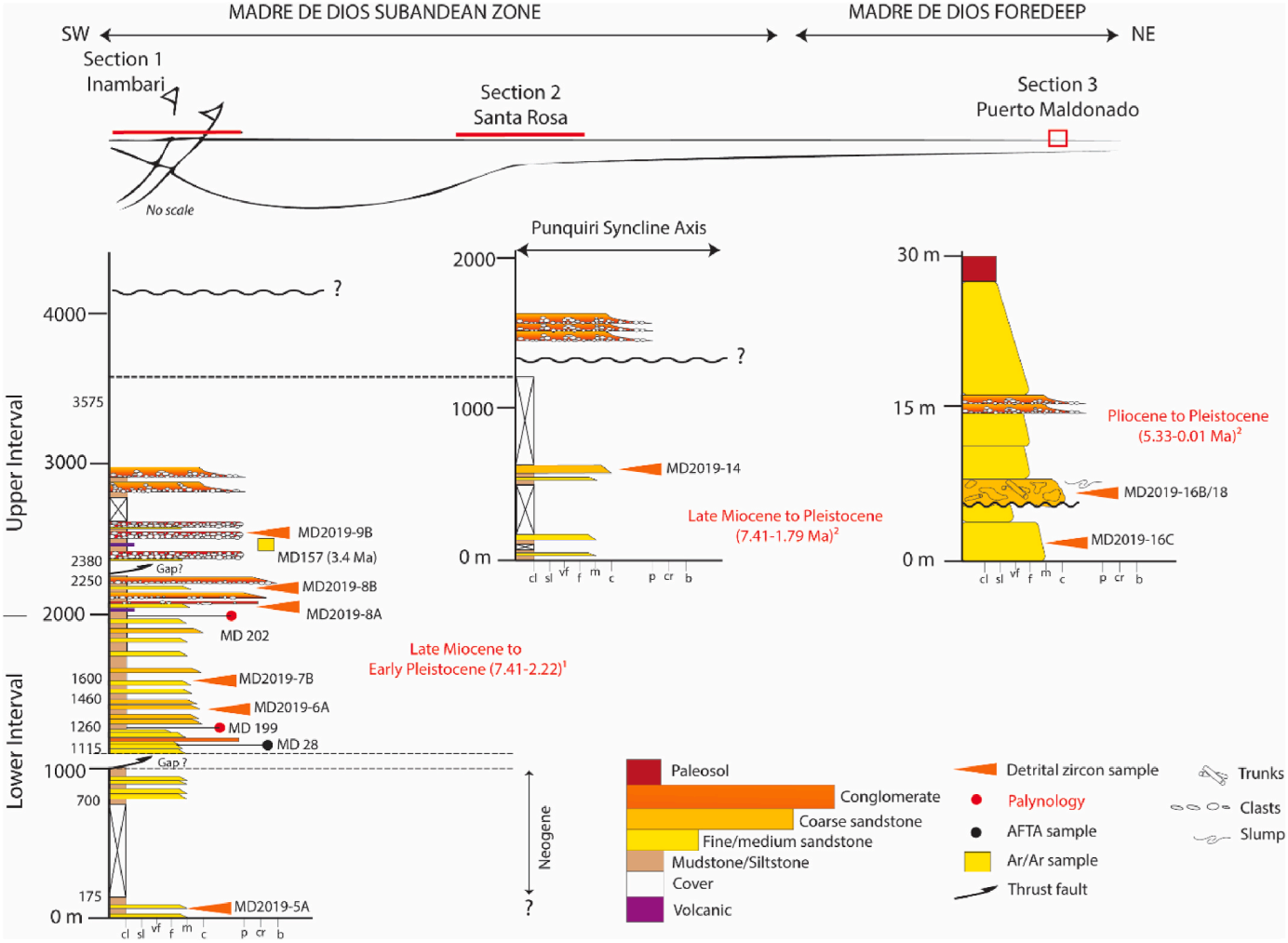

Fig. 9. Simplified stratigraphic sections for the Neogene deposits in the Inambari Transect of the Madre de Dios Basin. Biostratigraphic ages are from [1]This work and [2] Louterbach (2014).

It should be noted that these sandy units can be found in some sedimentary successions regarded as overbank deposits and may represent evidence of active channel avulsion processes at the time (e.g., DeCelles and Horton, 2003).

5.2. *Upper interval: conglomerate-dominated deposits*

5.2.1. *Fluvial channel conglomerate deposits (FCcg)*

Description: Facies association FCcg occurred mostly in the Plio-Pleistocene deposits although it can be present in the Miocene sedimentary rocks (Fig. S6). It is associated with facies associations O (overbank) and FCs (Fluvial channel sandy deposits). Its thickness ranges between 2 and 15 m. Facies association FCcg always starts with an erosive surface overlaid by the conglomerate deposits with trough cross-bedding (Gt, see Table 1 for detailed facies descriptions) and planar or horizontal bedding (Gp and Gh, respectively). The matrix of the clast-supported conglomerate facies consists of medium to very coarse-grained arkosic sandstone. Conglomerate bodies are 1m–3 m thick. They can evolve upwards into finer-grained deposits, displaying an overall fining-up trend, or be eroded by another conglomerate body forming an important stacking pattern (see Figs. S5 and S6, from 2309 to 2407m). Clasts are dominated by metamorphic and granitic, can be up to >40 cm in diameter, are sub-rounded to well-rounded, and are moderately sorted. The clast-size distribution is polymodal and shows inverse to normal grading. Imbricated clasts are present. Finer-grained deposits of facies association FCcg can be massive or fine upward from very coarse to fine-grained sandstones (Sm, Fig. 11-D and Sfu, respectively), sandstones with trough cross-bedding (St, Fig. 11-E) occasionally highlighted by mud clasts (Stmc), and sandstones with planar bedding (Sp). Outcrop MD 206 shows this fining-up trend from conglomerates to sandstone facies (Fig. S6, from 2805 to 2825 m).

Interpretation: Occasional cross-stratification and rare clast imbrications of the clast-supported pebble-to-boulder conglomerates facies associated with basal erosive surfaces suggest deposition from high-energy floods such as those produced by gravel-laden streams in poorly to well-confined channels (e.g., in Ridgway and DeCelles, 1993; Uba et al., 2005). The organized clast-supported conglomerate facies (Gt, Gh, and Gp) with weak imbrications may be the result of incised-channel gravel bedload sedimentation under low-to waning-energy flows (Jo et al., 1997; Uba et al., 2005). This interpretation is supported by the presence of frequent erosive surfaces associated with overall stacking patterns. Consequently, Gt, Gh, and Gp facies may correspond to transverse or lingoid bars (Miall, 1996). Trough cross-bedded sand (St) and conglomerate bodies (Gt) mainly represent channel deposits (Miall, 1996). Sandy facies such as Sfu, Sm, Sp, or Sh deposits are less frequent and mainly situated at the top of the fining-up sequences. They are interpreted to have been deposited following a loss of energy from the stream floods. Because facies association FCcg is strongly associated with the Overbank facies association (O), where only continental palynomorphs have been found (Table S1), it is interpreted

Table 3
Summary of the Neogene lithofacies and interpreted depositional environments in the Madre de Dios retroarc foreland basin (modified from Miall, 1996).

Facies Code	Lithofacies	Sedimentary structures/other characteristics	Interpretation
Gh	Clast-supported conglomerates. Granule to boulder, subrounded to well-rounded	Trough cross-stratification, normal grading with imbrications	Transverse bar, minor channel fill
Gm-Gmf	"Mud-breccias". Matrix-supported to clast-supported conglomerates (Gravel to pebble)	Planar cross-stratification	Linguoid bar, transverse bar
Sr	Sandstones. Very fine to medium-grained, occasionally pebbly. Moderate sorting	Rippled cross-stratification (climbing ripples)	2D or 3D ripples, upper flow regime
Sp	Sandstones. Very fine to medium-grained, occasionally pebbly. Moderate sorting	Planar cross-bedded, possible mud clasts at the base	Linguoid, transverse bar
Sh	Siltstones or very fine- to coarse-grained sandstones	Horizontal lamination	Planar bed flow (lower or upper flow regime)
St	Very fine- to coarse-grained sandstones	Trough cross-stratification	3D dune migration
Stmc	Very fine- to very coarse-grained sandstones, with scattered to aligned pebbles	Trough cross-stratification, highlighted by mud clasts or occasional lithoclasts (mm to pluri-cm). Occasional wood fragments.	Seasonal regime. 3D dune migration
Sm	Massive sandstones (fine to coarse-grained, with possible scattered to aligned pebbles) moderate to well sorted	No structure. Occasional wood fragments	Rapid deposition, gravity flow
Sfu	Massive sandstones (fine to very coarse-grained), finning upward	Frequently aligned mudclasts and lithoclasts at the base. Occasional wood fragments.	Fluvial bedforms and bars, waning flood
Scu	Massive sandstones (fine to very coarse-grained), coarsening upward	Frequently aligned mudclasts and lithoclasts at the base. Occasional wood fragments	Crevasse splay
Sb	Very fine- to medium-grained sandstones (reddish-yellow)	Bioturbation (continental)	
Fl	Siltstones, mudstones	Lamination, very small ripples. Occasional flame-structure. Occasionally calcareous	Overbank or waning flood deposits
Fm	Siltstones, mudstones	Structureless. Occasionally calcareous	Overbank or waning flood deposits
Fb	Mudstones to siltstones (red to purple)	Bioturbated (continental). Red to green.	Overbank or abandoned channel, incipient soil
Fbl	Mudstones to siltstones (blue to grey/dark grey)	Structureless or some ripples	Backswamp, oxbow-lake, anoxic environment
P	Mudstones to siltstones (red to purple). Carbonaceous nodular, gypsum levels	Frequent bioturbation and rootlets, carbonaceous nodules, and stratified gypsum. Possible ferruginous pisoliths	Paleosoil
T	Tuffaceous deposit. May be micaceous	Structureless, rippled, or with planar lamination. Some wood debrites	Volcanoclastic lacustrine deposits

Table 4
Facies association for the Neogene deposits in the Madre de Dios retroarc foreland basin.

Interpretation		Facies
FCcg	Braided (?) river. Mainly gravelly to conglomeratic fluvial channel filling	Gh, Gp, Gt, Stmc, St, Sm, Sh, Sfu
FCs	Meandering fluvial channel filling with conglomeratic levels at the base	Sfu, Sm, Sr, Sh, Sp, St, Stmc, Fl, Gt, Gh, Gp, Gm-Gmf, (Fb)
O	Overbank: abandoned channel, waning flow deposit and paleosol, continental swamp or oxbow lake (Osw). Possible coarsening upward sandy crevasse splays (Ocp)	Fm, Fl, Fb, P, Sfu, Sm, Scu, Sr, T

to be deposited by high-energy braided fluvial rivers deposits laterally changing into a fine-grained fluvial floodplain environment.

5.3. Provenance

5.3.1. Sr–Nd isotopes

The $^{87}Sr/^{86}Sr$ isotopic composition of five fine-grained Neogene samples analyzed ranges from 0.72475 to 0.73358, and the ƐNd is between −11.7 and −12.6 (Table 5). The Sr–Nd isotopic fingerprint of suspended particulate matter (SPM; Allègre et al., 1996; Viers et al., 2008; Santos et al., 2015; Rousseau et al., 2019) and bulk mudstone (Roddaz et al., 2005; Hoorn et al., 2017; van Soelen et al., 2017; Hurtado et al., 2018; Chavez et al., 2022; Moizinho et al., 2022) has been extensively used as provenance tracer to distinguish between Andean and cratonic sources in different Amazonian rivers. In Fig. 12 we plotted the $^{87}Sr/^{86}Sr$ and ƐNd(0) composition of relevant Andean sources and the SPM from the main tributaries in the Amazon drainage basin. Our data highlights that all analyzed Neogene mudstone samples from the Madre de Dios Basin fall into the Sub Andean Zone isotopic fingerprint. This is the same field of the present-day SPM transported by the Madeira River, and of other sedimentary rocks from the south Amazonian foreland basin (SAFB; Roddaz et al., 2005b).

5.3.2. Detrital zircon U–Pb ages and morphology

Of the ten samples examined, three originate from the lower sand-dominated interval, while the remaining seven hail from the upper conglomerate-dominated interval (refer to Fig. 9). Results of the U–Pb isotope analyses are detailed in Table S3 and showcased in Fig. 13. Predominantly, the principal zircon age groups fall between 900 and 1300 Ma (Grenville/Sunsás) and 500–700 Ma (Brasiliano/Pampean), together making up an average of 53% of all grains studied. Another discernible group, spanning 250-130 Ma (Triassic-Jurassic), appears in every sample and constitutes an average of 15.2% of the grains. Additionally, less dominant populations from both the Precambrian and Phanerozoic eras are evident, particularly within the 1300–1540 Ma (Rondonia-San Ignácio), 500-400 Ma (Famatinian), and 400-250 Ma (Paleozoic) clusters. While these age groups are consistently present across the section, a minor fluctuation in the proportion of Triassic ages can be noticed from sample MD2019-5A to MD2019-16B. It seems that during periods of increased Triassic on the detrital zircon population, there was a corresponding decrease from other age groups.

Zircon grains generated during the Grenville/Sunsás and Brasiliano/Pampean orogenies can be found elsewhere in the Coastal Cordillera, Altiplano, Eastern Cordillera, or Amazonian Craton, and thus are not useful to discriminate between Andean and cratonic sources (Chavez et al., 2022). The presence of zircon grains younger than 500 Ma in all analyzed samples typifies an Andean provenance (Chavez et al., 2022 and references therein). Famatinian (500-400 Ma) rocks occur in isolated Ordovician intrusions of the Marañon and Arequipa massifs (Ramos, 2009; Loewy and ConnelyDalziel, 2004). Perez and Horton (2014) also reported Famatinian detrital zircon populations in the Oligocene-Miocene sedimentary rocks from the Ayaviri Basin, a

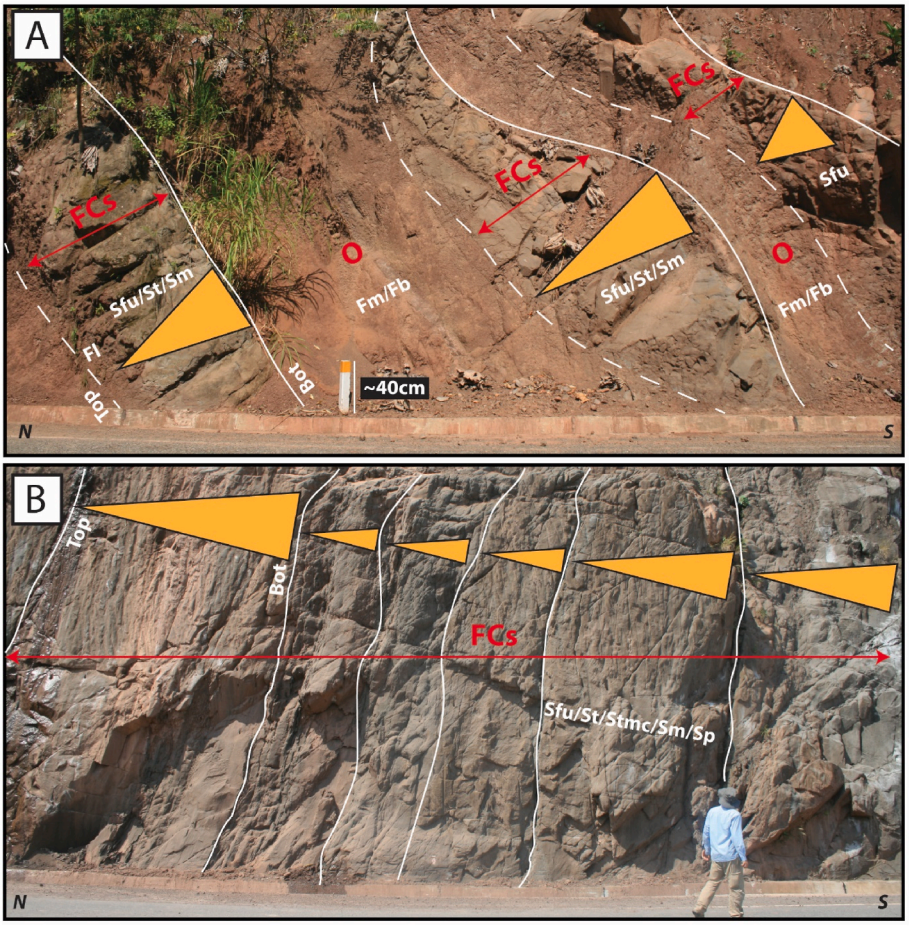

Fig. 10. Two distinct vertical organizations (stacking) of alternating FCs and O facies associations. The Punquiri syncline's axis is located at the left in both images (towards the North and stratigraphic top). A) Outcrop MD 197 showing overturned strata. Isolated meter-thick and fining-upward fluvial channels (FCs) are separated by thick fine-grained overbank deposits (O). B) Outcrop MD 209 showing vertically stacked fluvial sandstones presenting a fining-upward pattern. Sandstones are mainly made up of facies Sfu, St, Stmc, Sm, and Sp. Because of the important thickness of facies association FCs (range between 10 and 15m), lower and upper contacts with facies association O are not visible here. Martin Roddaz for scale (1.76m).

hinterland basin in the northern Altiplano Plateau, approximately 200 km southwest of the studied area. Permo-Triassic (290-216 Ma) magmatism was active along the entire length of the Peruvian Eastern Cordillera (Kontak et al., 1985; Clark et al., 1990; Soler and Bonhomme, 1990; Sempere et al., 2002; Mišković et al., 2009; Boekhout et al., 2013). Several Permo-Triassic plutons have been mapped in the southwest portion of the studied area (Fig. 3). Middle to Late Triassic (245-220 Ma) ages are recorded by the volcano-sedimentary rocks of the Mitu Formation (Spikings et al., 2016) and batholiths (Sempere et al., 2002) in the Cordillera de Carabaya region. Jurassic (201-145 Ma) rocks in the Central Andes are associated with the Jurassic magmatic arc and attributed to extensional processes across the western Gondwana margin (Oliveros et al., 2012; Boekhout et al., 2013). Finally, zircon grains younger than 130 Ma, are characterized as the Andean arc (Chocolate and Toquepala arcs) and typify a Coastal Cordillera provenance (Chavez et al., 2022).

We compared our dataset with Paleozoic metasedimentary rocks from the Eastern Cordillera (Reimann et al., 2010; Bahlburg et al., 2011), the Middle to Late Triassic Mitu Group (Perez and Horton, 2014; Spikings et al., 2016), the Cretaceous Huancané Formation (Spikings et al., 2016) and the Paleocene sedimentary rocks from the Madre de Dios Formation (Louterbach et al., 2018). In the MDS map (Fig. 14A) the upper Miocene-Pliocene samples plot scattered, and no cluster can be discriminated, even between samples of similar depositional ages. However, our samples plot right in between the compiled detrital zircon ages dataset. This configuration might indicate a continuous input of recycled sediments in the Madre de Dios Basin and that although the proportion of the contribution of each source might oscillate over the Late Miocene-Pliocene, the sources were kept the same. On the other hand, even though connected by a solid line with one of the Neogene samples (MD2019-14A), the overall high dissimilarity with the Mitu Group might suggest that the reworking of this unit was either discrete or unlikely.

Zircon morphological analyses were performed on unbroken grains with concordant ages. The results are summarized in Table S3 and illustrated in Figs. 15 and 16. Overall, the zircon grains exhibited a diverse range of lengths, spanning from 73 μm to 228 μm, and most were categorized as rounded and elongated. There seems to be a noticeable trend of a rise in the percentage of euhedral grains between samples MD2019-09B and MD2019-14A, which might indicate an increase on first-cycle sediments (Augustsson et al., 2018, Zavaleta et al., 2023). Furthermore, we explored the correlation between zircon grain shape, U–Pb ages, and potential zircon-producing events (Fig. 16a). In our dataset, the prevalent zircon populations - Grenville, Brasiliano, and Triassic – are consistently present in both oval and elongated shapes forms across samples. Notably, zircons with elongation exceeding 3 are more prevalent in the Triassic populations than in the Brasiliano and Grenville (Fig. 16b).

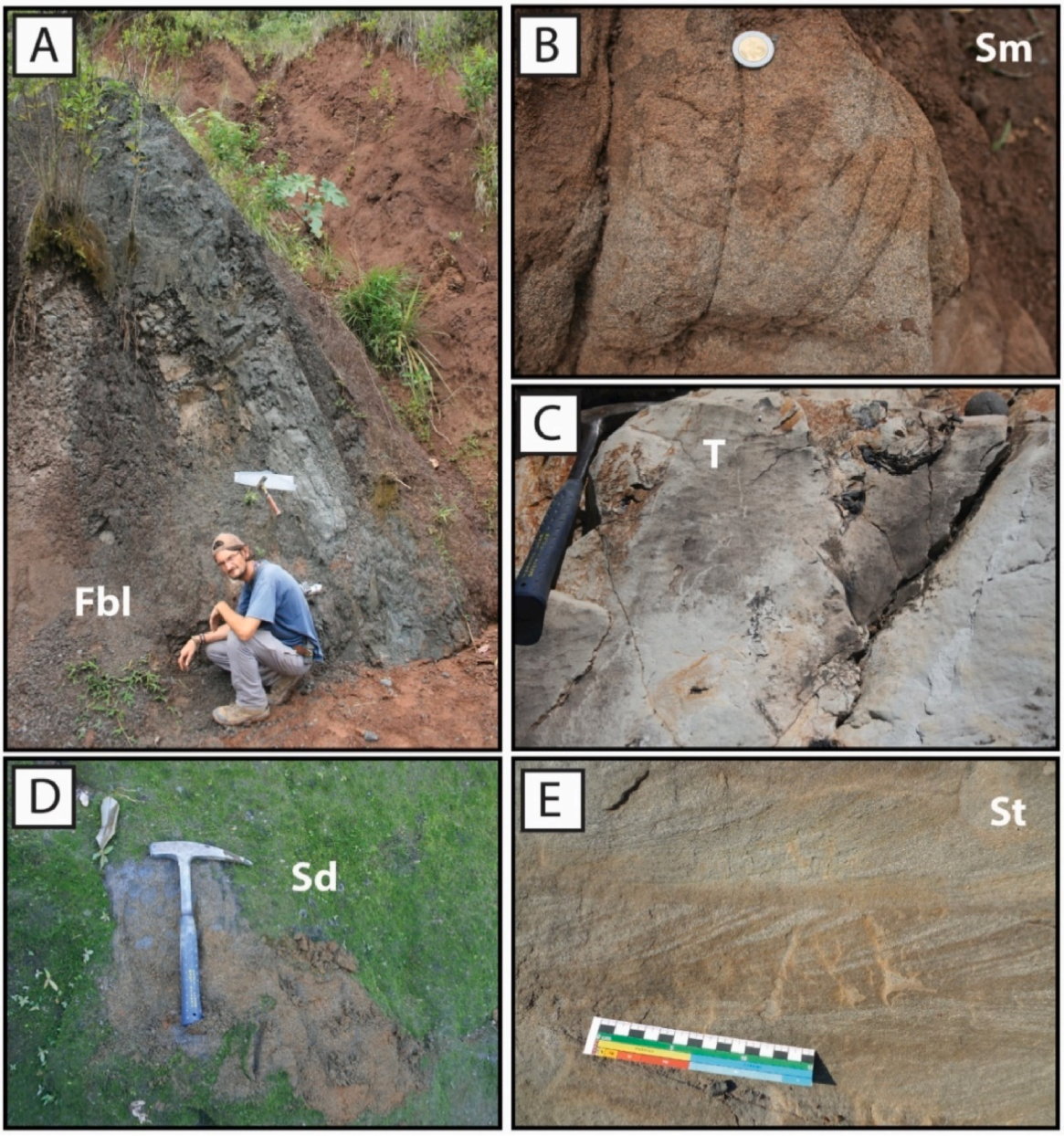

Fig. 11. Examples of facies found in the Neogene of the Madre de Dios foreland basin. A) Facies Fbl showing grey mudstones to siltstones. B) Facies Sm showing structureless medium-grained massive sandstones. C) Facies T showing a tuffaceous rock with plant fragments and some ripples. D) Facies Sd showing shaly fine-grained sandstone E) Facies St showing trough cross-bedded in fine-to medium-grained sandstones.

Table 5
Sr–Nd isotopic compositions of the analyzed Neogene sedimentary rocks from the Madre de Dios foreland basin.

Sample	Age	Sr (ppm)	Nd (ppm)	$^{87}Sr/^{86}Sr$	$\pm 2\sigma$	$^{143}Nd/^{144}Nd$	$\pm 2\sigma$	$\varepsilon Nd(0)$
MD197	Early Miocene	113,2	51,37	0,724753	9	0,512038	6	−11,7
MD199	Late Miocene- Pliocene	102,4	44,17	0,733581	7	0,511991	5	−12,6
MD 200B	Late Miocene- Pliocene	117,9	41,65	0,728020	11	0,511997	5	−12,5
MD 202D	Late Miocene- Pliocene	86,33	38,49	0,728579	8	0,512011	6	−12,2
MD 204B	Pliocene	106	40,16	0,729826	12	0,512023	7	−12

6. Discussion

6.1. Neogene deformation of the sub-Andean zone

The Oligocene-middle Miocene period of thrust deformation has been recorded in the EC and Altiplano zones adjacent to the study area (Perez and Horton, 2014; Horton et al., 2022). Growth strata recorded along the footwall of the Ayaviri thrust fault indicate that thrust deformation along the southwest-directed, northeastern basin margin of the Ayaviri thrust fault, was active at around 28-26 Ma at the EC/Altiplano boundary (Perez and Horton, 2014). Additionally, an abrupt middle Miocene shift to coarse alluvial fan deposition sourced from the

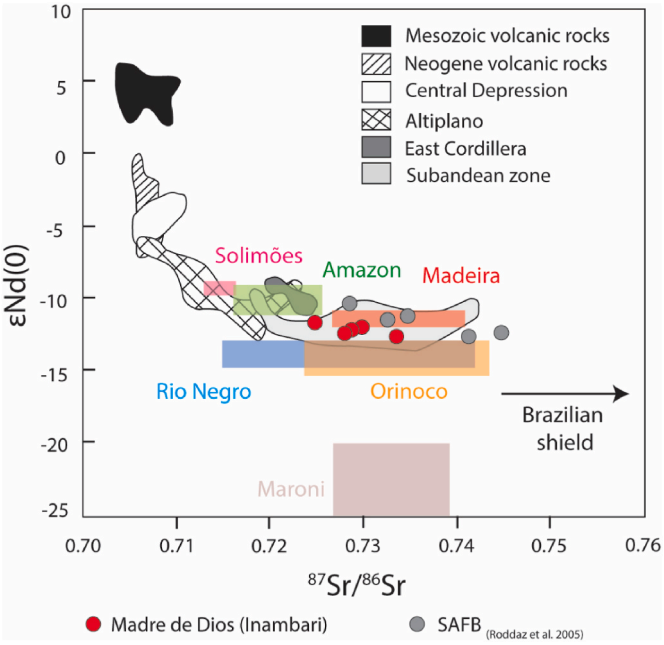

Fig. 12. $^{87}Sr/^{86}Sr$-εNd (0) diagram for Neogene Madre de Dios foreland basin sedimentary rocks compared with several relevant source areas and modern suspended particulate material in western Amazonia. Quaternary Ecuadorian volcanic lavas are from Barragan et al. (1998); the Mesozoic and Neogene volcanic rocks are from Kay et al. (1994); data for the Central depression, the Altiplano, the Eastern Cordillera, and the Subandean zone are taken from Pinto (2003) and Roddaz et al. (2005). SPM from the Tapajós, Negro, Urucara, and Trompetas (Allègre et al., 1996), Madeira and Solimões rivers (Viers et al., 2008), and the Amazon, Orinoco, and Maroni rivers (Rousseau et al., 2019).

Western Cordillera is interpreted to have been driven by out-of-sequence deformation along the northeast-directed, southwestern basin margin of the Pasani thrust at 18–16 Ma (Perez and Horton, 2014). This northern Altiplano out-of-sequence deformation was coincident with the structurally driven exhumation of the EC at 15–16 Ma as recorded by the He dates of zircon grains from the Coasa pluton and Rio San Gabán transect located in the EC (Perez et al., 2016). Paleo elevation models based on hydrogen isotopic compositions of hydrated volcanic glasses and modern stream waters suggest that the EC was slowly elevated 1.5–2 km between 25 and 10 Ma, which rate is interpreted to be consistent with crustal shortening as the dominant driver of surface uplift (Sundell et al., 2019). In our study area, there is no thermochronological or sedimentary record of deformation before the late Miocene.

6.2. Late Miocene-Pliocene

Overall, our dataset suggests that the southern Peruvian EC and SAZ have been deforming, uplifting, and propagating forward since the late Miocene as evidenced by late Miocene to Pliocene AFT and AHe ages related to out-of-sequence thrusting in the EC; and by the presence of growth strata geometry in the SAZ (Punquiri syncline) in response to the duplex formation and development of piggyback synclines (Fig. 15). Similar piggyback basins associated with duplexes in the hinterland have been documented in the Bolivian and Peruvian SAZ (Baby et al., 1995; Espurt et al., 2011; Mora et al., 2014; Parra et al., 2010). Analog modeling of the Bolivian SAZ suggests that the dominance of sedimentation over erosion in the foreland basin favors the forward propagation of the frontal thrust and development of piggy-back basins (active depositional basins between thrust structures; Leturmy et al., 2000). Mora et al. (2014) proposed that a period of late Miocene topographic growth and an associated increase in accommodation and sedimentation rates favor the development of duplexes in the Inambari area of the southern Peruvian SAZ. Our data agree with these findings, especially regarding the Plio-Pleistocene units, in which syntectonic growth strata are associated with the development of duplexes, piggy-back synclines, and the forward propagation of the SAZ and input of recycled sedimentary rocks of the SAZ to the late Miocene-Pleistocene piggy-back syncline sediments.

Our provenance proxies show that the source of sediments being eroded in the southern portion of the Madre de Dios basin did not change significantly throughout the Neogene (Fig. 13). Besides the always present Precambrian ages from the crystalline basement found elsewhere in the Andes and Western Amazonia, the Permian, Triassic, and Jurassic were the main detrital zircon ages populations observed. These ages represent different extensional magmatic events, and their distribution varies across strike in the Eastern Cordillera (Chavez et al., 2022). In fact, our data reveals a high similarity between the detrital zircon populations and Sr–Nd isotopic compositions of Late Miocene -Pliocene sedimentary rocks and older SAZ sedimentary successions which supports the input of recycled Paleozoic to Cretaceous sediments from the SAZ (Figs. 14 and 15). This hypothesis is further supported by the rounded nature of most grains observed, signaling longer transportation processes or sediment recycling.

However, the observed increase in the proportion of Triassic-aged zircons, together with the reduced presence of Grenville and Brasiliano zircons and an increase in euhedral grains between samples from the upper interval (MD2019-09B–16B), might indicate that, for a time, a Triassic terrain was more fertile and sourced the Madre de Dios basin with first cycle zircon grains. Permo-Triassic plutonic rocks crop out extensively on the EC (see Fig. 3a), which we interpret to suggest erosion of the EC.

These results are consistent with what is recorded in the central Peruvian SAZ, north of our study area, where the Pliocene reactivation of Paleozoic thrusts has also been observed (Gautheron et al., 2013). In that region, 23 km of shortening affecting the Camisea SAZ (12°S) has accumulated since 6 Ma (Espurt et al., 2011), demonstrating that a significant amount of deformation has affected the EC-SAZ since the Pliocene. This is also consistent with the Ecuadorian, Bolivian and Argentinian Andes where the Sub-Andean thrust wedge has continued propagating until the present and notably during the Plio-Pleistocene (Horton and DeCelles, 1997; Echavarria et al., 2003; Uba et al., 2009a; Espurt et al., 2011; Gautheron et al., 2013; Eude et al., 2015; Anderson et al., 2018; Margirier et al., 2023). Additionally, the propagation of the Sub-Andean thrust wedge could also be supported by the overall coarsening-up trend of the Madre de Dios SAZ's Neogene sedimentary infill, which we interpret as a depositional megasequence characterized by a significant rise in sedimentation rates. This is demonstrated by the presence of distal sand-dominated deposits in the Neogene (lower interval), which evolved into conglomerate-dominated deposits in the Late Miocene to Pleistocene (upper interval) periods (Figs. 9 and 15).

6.3. Tectonic vs. Climatic controls in the erosion of the EC and SAZ

Large scale kinematics of fold and thrust belts obey the theory of a tapered orogenic wedge (Chapple, 1978; Davis et al., 1983; Dahlen, 1984, 1990; Dahlen et al., 1984; DeCelles and Mitra, 1995). This suggests that the fronts of orogenic wedges develop taper toward their undeformed forelands and advance when the sum (θ) of their basal (β) and upper (α) slopes reach a critical value θc. When changes in (β) and (α) force the wedge out of the critical state into a "supercritical" or "subcritical" state, the wedge responds by deforming to alter its geometry until the critical condition is regained (DeCelles and Mitra, 1995; Horton et al., 2022). For instance, an orogenic wedge that becomes subcritical may attempt to regain a critical state through internal deformation by out-of-sequence thrusting, synchronous thrusting, or duplexing (e.g., Boyer, 1992; DeCelles and Mitra, 1995; Mitra and Sussman, 1997; Horton et al., 2022; Uba et al., 2009b). In turn, processes

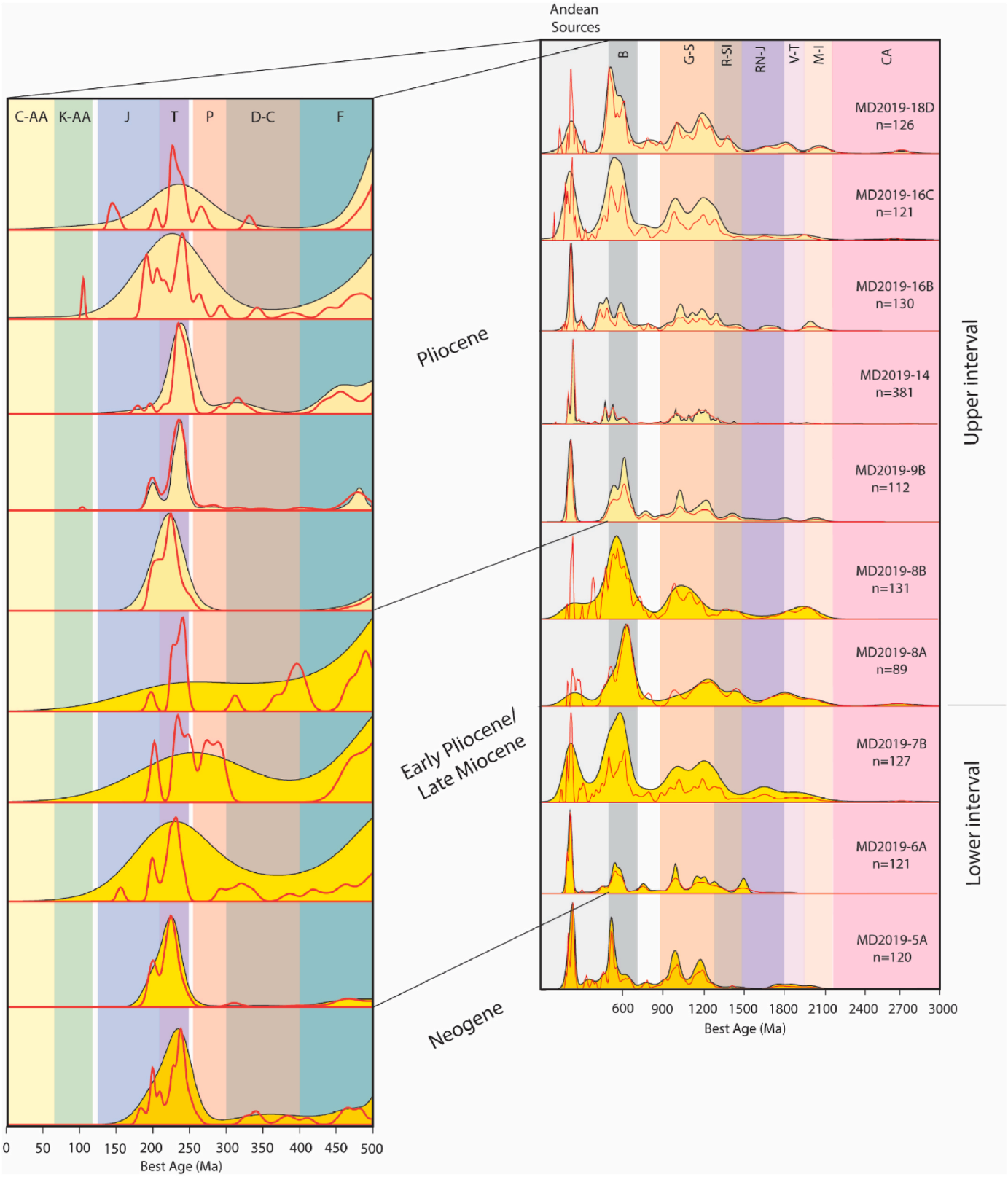

Fig. 13. Stratigraphic evolution of U–Pb ages on zircon grains with age distributions displayed by their Kernel Density Estimation (KDE) and Probability Density Plots (PDP; red line). C-AA: Cenozoic Andean Arc (Less than 60 Ma); K-AA: Cretaceous Andean Arc (66–120 Ma); J: Jurassic Extension & Chocolate Arc (130–216 Ma); T: Triassic rift (216–250 Ma); P: Permian magmatism (252–290 Ma); D–C: Devonian & Carboniferous magmatism (300–400 Ma); F: Famatinian (400–500 Ma); B: Brasiliano (500–700 Ma); G–S: Greenville-Sunsás (900–1300 Ma); R–SI: Rondonia-San Ignácio (1300–1540 Ma); RN-J: Rio Negro-Juruena (1540–1820 Ma); V–T: Ventuari-Tapajós (1820–2000 Ma); M–I: Maroni-Itacaiunas (2000–2200 Ma); CA: Central Amazon (>2200 Ma). Age ranges are from Tassinari and Macambira (1999), Reimann et al. (2010), and Chavez et al. (2022).

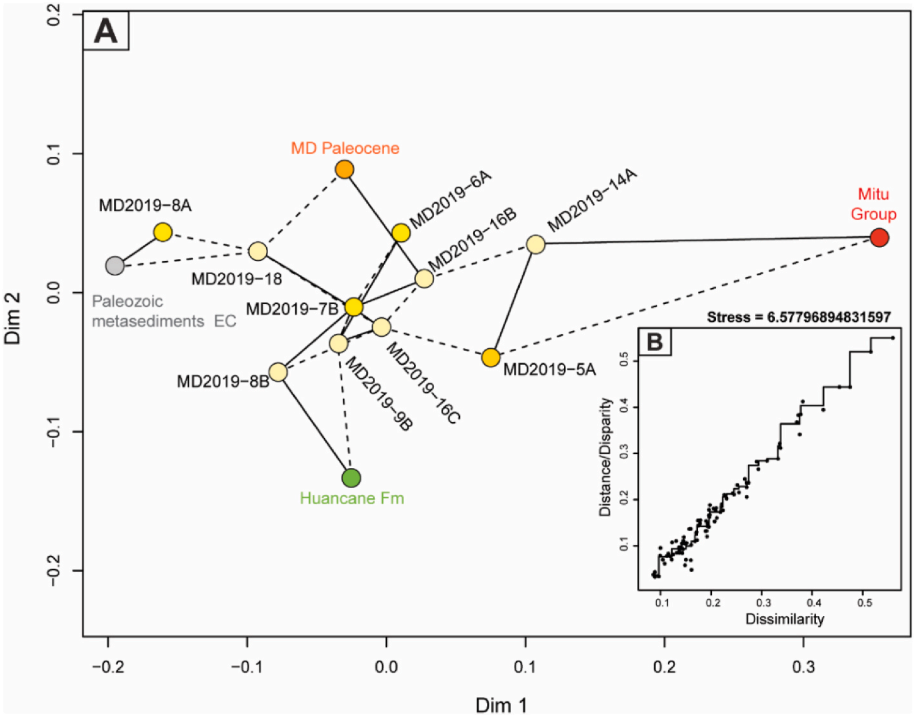

Fig. 14. A) MDS map based on the U–Pb age distributions of detrital zircons grains using the Kolmogorov-Smirnov test. The closest and second closest neighbors are linked by solid and dashed lines, respectively. Data for MD Paleocene (combination of samples MD85, 176, 177, 239, 255, and 256) can be found in Louterbach et al. (2018); Mitu Group, Triassic magmatic rocks, and Huancané formation are from Spikings et al. (2016). Paleozoic metasedimentary rocks EC consist of the combination of the metasedimentary rocks analyzed in Reimann et al. (2010) and Bahlburg et al. (2011). B) Sherpard plot of the U–Pb data showing the transformation from dissimilarity to distances and disparities (Vermeesch, 2013).

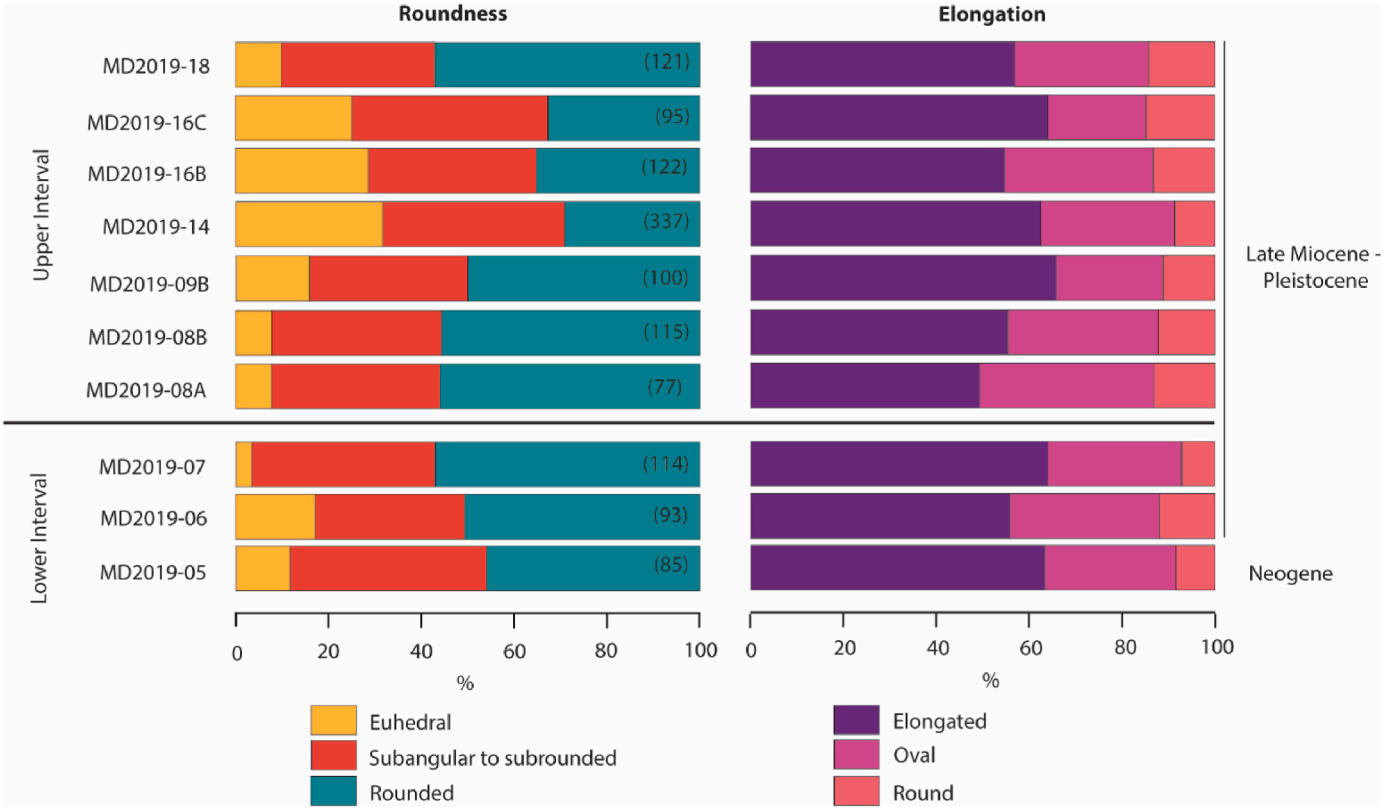

Fig. 15. Roundness and elongation for detrital zircons with concordant ages. Broken grains without a clear shape in the BSE images were not included.

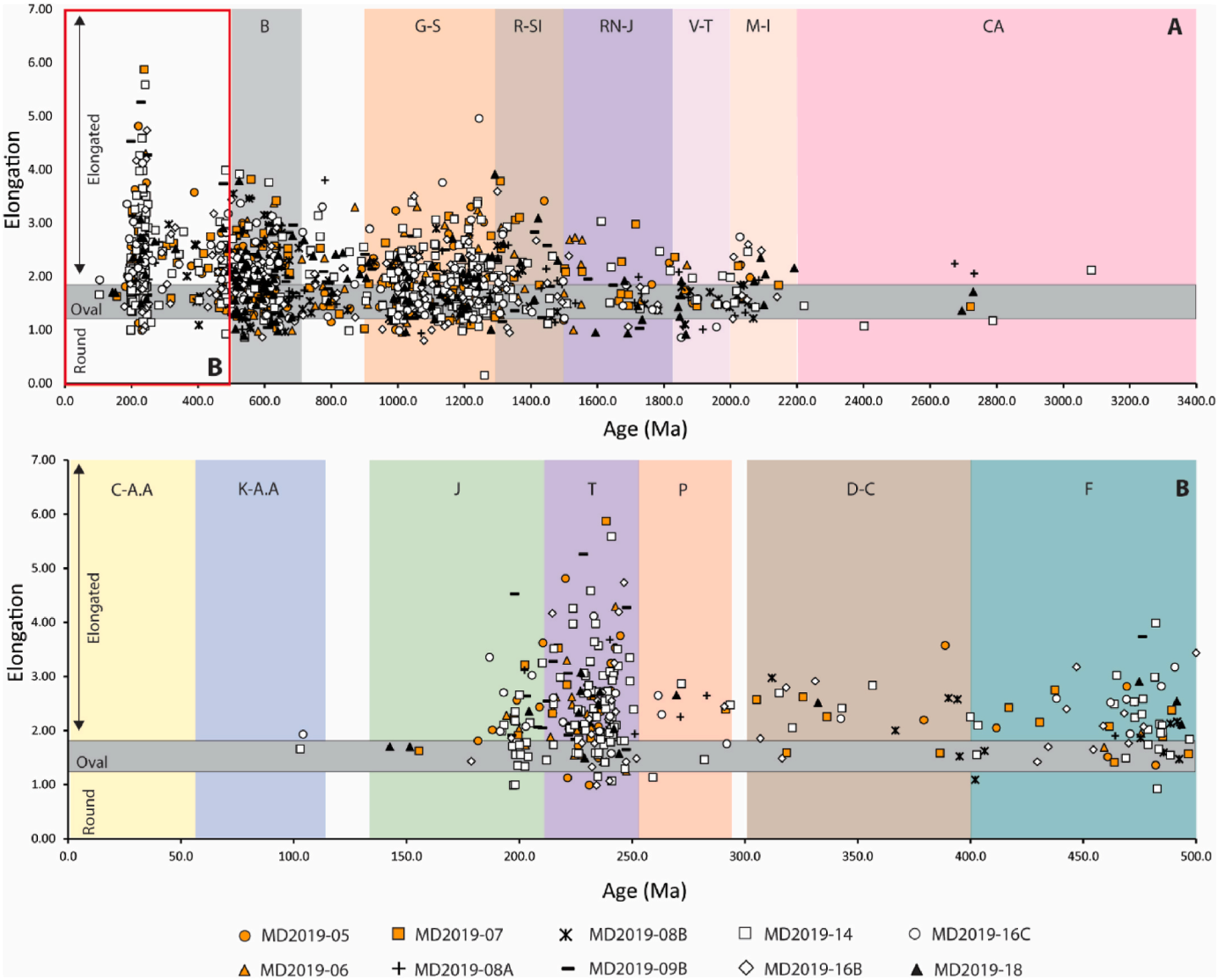

Fig. 16. Detrital zircon shape vs. concordant age. The field for oval grains (length/width = 1.3/1.8) is marked by a horizontal grey bar. **A)** Plot covering all the ages observed. **B)** Close-up on detrital zircon ages younger than 500 Ma, characteristics of Andean provenance.

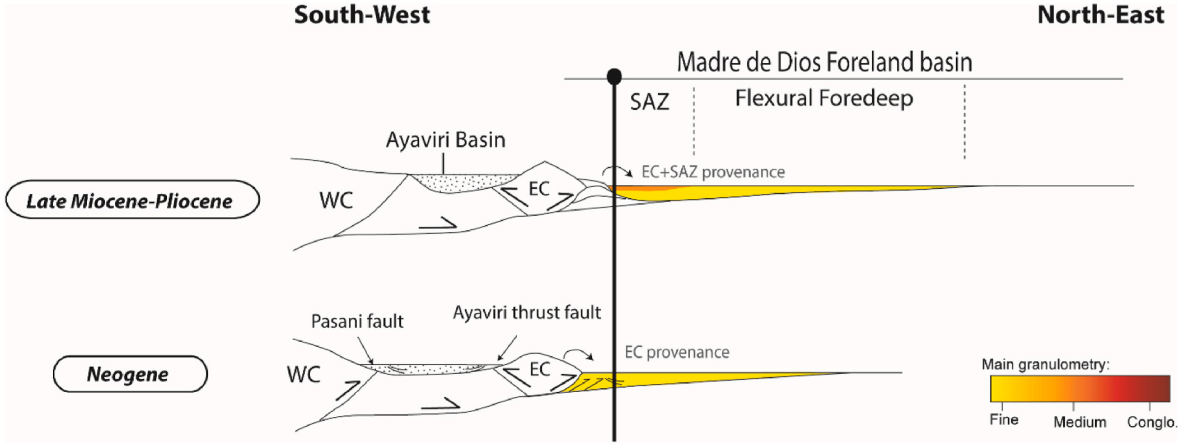

Fig. 17. Sketch showing the evolution of the Southern Amazonian retro arc foreland basin system from the Early Miocene to the present day. The black line indicates the approximate location of the studied area. Early Miocene activities and related growth strata of the Pasani and Ayaviri thrust faults are reported in Perez and Horton (2014). WC: Western Cordillera; EC: Eastern Cordillera; SAZ: Sub-Andean Zone. Modified from DeCelles and Horton (2003). See text for details.

such as erosion, which reduce surface slope, may ultimately tend to induce internal deformation within the wedge (DeCelles, 1994; DeCelles and Mitra, 1995). We interpret the surface uplift of the EC, as the presence of out of sequence thrusting and the EC provenance of Neogene sedimentary rock as indicating that the southern Peruvian Amazonian EC and SAZ orogenic wedge existed under subcritical conditions. This is consistent with previous studies suggesting that the propagation and width of the Andean orogenic wedge have been limited by focused erosion (Horton et al., 2022) on the EC, potentially driven by a wetter climate since the Miocene (McQuarrie et al., 2008).

Many studies have emphasized the potential climatic controls on the Neogene erosion, exhumation, and deformation in the EC and SAZ (McQuarrie et al., 2008; Uba et al., 2009b; Lease and Ehlers, 2013). In the studied area, Plio-Pleistocene climatic forcing has previously been inferred based on the presence of widespread Pliocene AHe erosional cooling ages in the EC and from the assumption that tectonic activity has been lacking for the past 4 My both in the EC and SAZ (Lease and Ehlers, 2013). This Pliocene erosion of the Bolivian and southern Peruvian EC has been interpreted as being controlled by a "shift in global climate from early Pliocene warmth to late Pliocene cooling driven by sea surface temperature changes". It is possible that after having reached a critical elevation in the Miocene leading to higher rainfall and erosion gradients across the EC, focused erosion led to accelerated exhumation and increasing deformation in the adjacent SAZ. Such a climatic forcing has been invoked in the EC of Colombia to explain the differences in exhumation and deformation rates between a drier western flank and a humid eastern flank (Mora et al., 2011) although this view has recently been challenged (Pérez-Consuegra et al., 2021). Our thermochronological cooling ages advocate for Plio-Pleistocene uplift and related erosion both in the EC and the SAZ, consistent with the ~4 Ma cooling age data presented by Lease and Ehlers (2013). In contrast with the climatic driver of exhumation proposed by these authors, coeval uplift induced the exhumation of the SAZ, the EC, and Pliocene growth strata, which all support the 4 Ma to present tectonic uplift in the EC as an important driver of exhumation; these also provide evidence against the assumption that deformation was absent in the SAZ during this time.

7. Conclusions

The combination of fieldwork, structural and stratigraphic sections interpretation of depositional environments, AFT and AHe ages, interpretations of a new subsurface dataset, and provenance data from the Eastern Cordillera and Sub Andean Zone show that significant deformation occurred in the Amazonian orogenic wedge of southern Peru during the Late Miocene-Pliocene, even though climatic changes may have enhanced erosion or modified erosional processes. The late Miocene to Pliocene deformation is recorded by AFT and AHe ages in both the EC and SAZ and by growth strata geometry in the SAZ. This period is characterized by 1) the development of piggy-back synclines and duplexes in the SAZ, as well as the overthrusting of the EC and input of recycled sedimentary rocks of the SAZ to the late Miocene-Pleistocene piggy-back syncline sediments. Additionally, the transition from distal low energy fluvial system in the Early Miocene (lower section), to a high energy proximal fluvial system in the Late Miocene to Pleistocene (upper section) indicates an increase in sedimentation rates, thus our data show that the thrust wedge has continued propagating until the present, following a period of notably active propagation during the Plio-Pleistocene.

CRediT authorship contribution statement

G.R. Moizinho: Writing - original draft, Investigation, Formal analysis. **M. Roddaz:** Writing - review & editing, Visualization, Supervision, Resources, Funding acquisition, Conceptualization. **S. Brichau:** Investigation, Formal analysis. **M. Louterbach:** Writing - original draft, Investigation, Formal analysis. **E.L. Dantas:** Supervision, Resources, Funding acquisition, Conceptualization. **R.V. Santos:** Supervision, Resources, Funding acquisition, Conceptualization. **G. Bayon:** Supervision. **J. Bailleul:** Investigation, Formal analysis. **J. Vink:** Investigation, Formal analysis. **C. Hoorn:** Investigation, Formal analysis.

Declaration of competing interest

The authors declare that they have no known competing financial interests or personal relationships that could have appeared to influence the work reported in this paper.

Data availability

Data will be made available on request.

Acknowledgments

This work received financial and institutional support from Repsol S. A., Perupetro, and the IRD (Institut pour la Recherche et le Développement). Patrick Monié is thanked for his help and interpretation of Ar dating results. We thank Jean-Claude Soula, Patrice Baby, and Stéphane Brusset for their helpful comments and discussions on previous drafts of this paper. This paper is also dedicated to the memory of Jean-Claude Soula who passed away in 2020. This work was part of the Ph.D. project of Melanie Louterbach which has been sponsored by Repsol. This study was also supported and funded by CAPES-COFECUB program Te 924/18/88881.143095/2017–01 "Paléo-Amazone: evolution Neogene de l'Amazonie Brésilienne/O PALEO AMAZONAS: evolução neogênica da Amazônia Brasileira"" and by the joint Brazilian-European facility for climate and geodynamic research on the Amazon River Basin sediment (CLIM-AMAZON) project. We thank German Bayona and Mauricio Parra as well as the editor Andres Folguera for valuable reviews that improved this contribution.

Appendix A. Supplementary data

Supplementary data to this article can be found online at https://doi.org/10.1016/j.jsames.2023.104700.

References

Albarède, F., Telouk, P., Blicheret-Toft, J., Boyet, M., Agranier, A., Nelson, B., 2004. Precise and accurate isotopic measurements using multiple-collector ICPS. Geochem. Cosmochim. Acta 68 (12), 2725–2744.

Allègre, C.J., Dupré, B., Négrel, P., Gaillardet, J., 1996. Sr-Nd-Pb isotope systematics in Amazon and Congo River systems: constraints about erosion processes. Chem. Geol. 131, 93–112. https://doi.org/10.1016/0009-2541(96)00028-9.

Anderson, R.B., Long, S.P., Horton, B.K., Thomson, S.N., Calle, A.Z., Stockli, D.F., 2018. Orogenic wedge evolution of the central Andes, Bolivia (21°S): implications for cordilleran cyclicity. Tectonics 37, 3577–3609. https://doi.org/10.1029/2018TC005132.

Antoine, P.-O., Roddaz, M., Brichau, S., Tejada-Lara, J., Salas-Gismondi, R., Altamirano, A., 2013. Middle Miocene vertebrates from the Amazonian Madre de Dios Subandean zone, Perú. J. South Am. Earth Sci. 42, 91–102. https://doi.org/10.1016/j.jsames.2012.07.008.

Augustsson, C., Voigt, T., Bernhart, K., Kreißler, M., Gaupp, R., Gärtner, A., Hofmann, M., Linnemann, U., 2018. Zircon size-age sorting and source-area effect: the German Triassic Buntsandstein Group. Sediment. Geol. 375, 218–231, 161.10.1016/j.sedgeo.2017.11.004.

Apatite to Zircon Inc, 2004. Peru Samples: Apatite and Zircon Fission-Tracks Data.

Baby, P., Calderon, Y., Hurtado, C., Bandach, A., 2018a. *Atlas of the Peruvian Subandean petroleum systems From source to trap*. Perupetro and IRD. Lima Available at: https://www.researchgate.net/publication/334042013_ATLAS_OF_THE_PERUVIAN_SUBANDEAN_PETROLEUM_SYSTEMS_-_From_source_to_trap.

Baby, P., Calderón, Y., Hurtado, C., Louterbach, M., Espurt, N., Brusset, S., et al., 2018b. The Peruvian sub-andean foreland basin system: structural overview, geochronologic constraints, and unexplored plays. In: *Petroleum Basins and Hydrocarbon Potential of the Andes of Peru and Bolivia* AAPG Memoirs. AAPG), pp. 91–121.

Baby, P., Colletta, B., Zubieta, D., 1995. Etude geometrique et experimentale d'un bassin transporte; exemple du synclinorium de l'Alto Beni (Andes centrales). Bull. Société Géologique Fr. 166, 797–811.

Bahlburg, H., Vervoort, J.D., Andrew DuFrane, S., Carlotto, V., Reimann, C., Cárdenas, J., 2011. The U–Pb and Hf isotope evidence of detrital zircons of the Ordovician Ollantaytambo Formation, southern Peru, and the Ordovician provenance and paleogeography of southern Peru and northern Bolivia. J. South Am. Earth Sci. 32, 196–209. https://doi.org/10.1016/j.jsames.2011.07.002.

Barragan, R., Geist, D., Hall, M., Larson, P., Kurz, M., 1998. Subduction controls on the compositions of lavas from the Ecuadorian Andes. Earth Planet. Sci. Lett. 154, 153–166.

Boekhout, F., Sempere, T., Spikings, R., Schaltegger, U., 2013. Late Paleozoic to Jurassic chronostratigraphy of coastal southern Peru: temporal evolution of sedimentation along an active margin. J. South Am. Earth Sci. 47, 179–200. https://doi.org/10.1016/j.jsames.2013.07.003.

Bookhagen, B., Strecker, M.R., 2018. Orographic barriers, high-resolution TRMM rainfall, and relief variations along the eastern Andes. Geophys. Res. Lett. 35, L06403 https://doi.org/10.1029/2007GL032011.

Boyer, S.E., 1992. Geometric evidence for synchronous thrusting in the southern Alberta and northwest Montana thrust belts. In: McClay, K.R. (Ed.), Thrust Tectonics. Springer Netherlands, Dordrecht, pp. 377–390. https://doi.org/10.1007/978-94-011-3066-0_34.

Brandon, M.T., 1992. Decomposition of fission-track grain-age distributions. Am. J. Sci. 292, 535–564. https://doi.org/10.2475/ajs.292.8.535.

Brandon, M.T., 1996. Probability density plot for fission-track grain-age samples. Radiat. Meas. 26, 663–676. https://doi.org/10.1016/S1350-4487(97)82880-6.

Brandon, M.T., 2002. Decomposition of mixed grain age distributions using Binomfit. Track 24, 13–18.

Campbell, K.E., Heizler, M., Frailey, C.D., Romero-Pittman, L., Prothero, D.R., 2001. Upper cenozoic chronostratigraphy of the southwestern Amazon Basin. Geology 29 (7), 595–598.

Campetella, C.M., Vera, C.S., 2002. The influence of the Andes mountains on the South American low-level flow. Geophys. Res. Lett. 29 https://doi.org/10.1029/2002GL015451, 7-1-7–4.

Carpenter, D., Berumen, M., 1999. Geological and Geochemical Modeling of the Fold and Thrust Belt of the Southeastern, INGEPET Exploration and Exploration of Petroleum and Gas.

Chapple, W.M., 1978. Mechanics of thin-skinned fold-and-thrust belts. GSA Bull 89, 1189–1198. https://doi.org/10.1130/0016-7606(1978)89<1189. MOTFB>2.0.CO;2.

Chavez, C., Roddaz, M., Dantas, E.L., Santos, R.V., Alván, A.A., 2022. Provenance of the middle jurassic-cretaceous sedimentary rocks of the Arequipa basin (south Peru) and implications for the geodynamic evolution of the central Andes. Gondwana Res. 101, 59–76. https://doi.org/10.1016/j.gr.2021.07.018.

Chavez, S.P., Takahashi, K., 2017. Orographic rainfall hot spots in the Andes-Amazon transition according to the TRMM precipitation radar and in situ data. J. Geophys. Res. Atmos. 122 (11), 5870–5882. https://doi.org/10.1002/2016JD026282.

Cooperación Técnica Peruana-Alemana, 1982. Evaluación de las cuencas Ucayali y Madre de Dios.

Clark, A.H., Farrar, E., Kontak, D.J., Langridge, R.J., M.J.A, F., France, L.J., McBride, S. L., Woodman, P.L., Wasteneys, H.A., Sandeman, H.A., Archibald, D.A., 1990. Geologic and geochronologic constraints on the metallogenic evolution of the Andes of southeastern Peru. Econ. Geol. 85, 1520–1583. https://doi.org/10.2113/gsecongeo.85.7.1520.

da Silva-Caminha, S.A.F., Jaramillo, C.A., Absy, M.L., 2010. Neogene palynology of the Solimões basin, Brazilian Amazonia. Palaeontograph. Abteilung B 13–79. https://doi.org/10.1127/palb/284/2010/13.

Dahlen, F.A., 1984. Noncohesive critical Coulomb wedges: an exact solution. J. Geophys. Res. Solid Earth 89, 10125–10133. https://doi.org/10.1029/JB089iB12p10125.

Dahlen, F.A., 1990. Critical taper model of fold-AND-THRUST belts and accretionary wedges. Annu. Rev. Earth Planet Sci. 18, 55–99. https://doi.org/10.1146/annurev.ea.18.050190.000415.

Dahlen, F.A., Suppe, J., Davis, D., 1984. Mechanics of fold-and-thrust belts and accretionary wedges: cohesive Coulomb Theory. J. Geophys. Res. Solid Earth 89, 10087–10101. https://doi.org/10.1029/JB089iB12p10087.

Dalmayrac, B., Laubacher, G., Marocco, R., Martinez, C., Tomasi, P., 1980. La chaine hercynienne d'amerique du sud structure et evolution d'un orogene intracratonique. Geol. Rundsch. 69, 1–21. https://doi.org/10.1007/BF01869020.

Dalmayrac, B., Molnar, P., 1981. Parallel thrust and normal faulting in Peru and constraints on the state of stress. Earth Planet Sci. Lett. 55, 473–481. https://doi.org/10.1016/0012-821X(81)90174-6.

Davis, D., Suppe, J., Dahlen, F.A., 1983. Mechanics of fold-and-thrust belts and accretionary wedges. J. Geophys. Res. Solid Earth 88, 1153–1172. https://doi.org/10.1029/JB088iB02p01153.

DeCelles, P.G., 1994. Late Cretaceous-Paleocene synorogenic sedimentation and kinematic history of the Sevier thrust belt, northeast Utah and southwest Wyoming. GSA Bull 106, 32–56. https://doi.org/10.1130/0016-7606(1994)106<0032:LCPSSA>2.3.CO;2.

DeCelles, P.G., Horton, B.K., 2003. Early to middle Tertiary foreland basin development and the history of Andean crustal shortening in Bolivia. GSA Bull 115, 58–77. https://doi.org/10.1130/0016-7606(2003)115<0058:ETMTFB>2.0.CO;2.

DeCelles, P.G., Mitra, G., 1995. History of the Sevier orogenic wedge in terms of critical taper models, northeast Utah and southwest Wyoming. GSA Bull 107, 454–462. https://doi.org/10.1130/0016-7606(1995)107<0454:HOTSOW>2.3.CO;2.

Echavarria, L., Hernndez, R., Allmendinger, R., Reynolds, J., 2003. Subandean thrust and fold belt of northwestern Argentina: geometry and timing of the Andean evolution. AAPG Bull. 87, 965–985.

Espinoza, J.C., Garreaud, R., Poveda, G., Arias, P.A., Molina-Carpio, J., Masiokas, M., et al., 2020. Hydroclimate of the Andes Part I: main climatic features. Front. Earth Sci. 8. Available at: https://www.frontiersin.org/article/10.3389/feart.2020.00064. (Accessed 6 April 2022).

Espurt, N., Barbarand, J., Roddaz, M., Brusset, S., Baby, P., Saillard, M., et al., 2011. A scenario for late Neogene Andean shortening transfer in the Camisea Subandean zone (Peru, 12°S): implications for growth of the northern Andean Plateau. Geol. Soc. Am. Bull. 123, 2050–2068. https://doi.org/10.1130/B30165.1.

Esteban, M., Klappa, C., 1983. Carbonate depositional environments. AAPG Memoir 33, 1–54.

Eude, A., Roddaz, M., Brichau, S., Brusset, S., Calderon, Y., Baby, P., et al., 2015. Controls on timing of exhumation and deformation in the northern Peruvian eastern Andean wedge as inferred from low-temperature thermochronology and balanced cross section. Tectonics 34. https://doi.org/10.1002/2014TC003641, 2014TC003641.

Galbraith, R.F., 1988. Graphical display of estimates having differing standard errors. Technometrics 30, 271–281. https://doi.org/10.2307/1270081.

Galbraith, R.F., Green, P.F., 1990. Estimating the component ages in a finite mixture. Int. J. Radiat. Appl. Instrum. Part Nucl. Tracks Radiat. Meas. 17, 197–206. https://doi.org/10.1016/1359-0189(90)90035-V.

Gautheron, C., Tassan-Got, L., 2009. A Monte Carlo approach to diffusion applied to noble gas/helium thermochronology. Chem. Geol. 273, 212–224.

Garreaud, R., Vuille, M., Clement, A.C., 2003. The climate of the Altiplano: observed current conditions and mechanisms of past changes. Palaeogeogr. Palaeclimatol. Palaecolo. 194, 5–12. https://doi.org/10.1016/S0031-0181(03)00269-4.

Gautheron, C., Espurt, N., Barbarand, J., Roddaz, M., Baby, P., Brusset, S., et al., 2013. Direct dating of thick- and thin-skin thrusts in the Peruvian Subandean zone through apatite (U–Th)/He and fission track thermochronometry. Basin Res. 25, 419–435. https://doi.org/10.1111/bre.12012.

Germeraad, J.H., Hopping, C.A., Muller, J., 1968. Palynology of tertiary sediments from tropical areas. Rev. Palaeobot. Palynol., Palinology of Tertiary Sediments from Tropical Areas 6, 189–348. https://doi.org/10.1016/0034-6667(68)90051-1.

Gil Rodriguez, W., 2002. Evolucion Lateral de la deformacion de un frente orogenico : ejemplo de las cuencas sunandinas entre 0°Y y 16°S, 3. Université Paul Sabatier Toulouse.

Gil Rodriguez, W., Baby, P., Ballard, J.-F., 2001. Structure et contrôle paléogéographique de la zone subandine péruvienne. Comptes Rendus Académie Sci. - Ser. IIA - Earth Planet. Sci. 333, 741–748. https://doi.org/10.1016/S1251-8050(01)01693-7.

Gil, W.F., 2001. Evolution latérale de la déformation d'un front orogénique : exemple des bassins subandins entre 0° et 16°S. Available at: http://www.theses.fr/2001TOU30045. (Accessed 19 August 2021).

Gutierrez, M., 1982. Evaluacion potential petrolifero cuencas Huallaga, Ucayali y Madre de Dios. Zonacion bioestratigrafica del intervalo Cretacico superior-Tertiario inferior, Petroperu. Internal Report, Lima.

Hermoza, W., 2004. Dynamique tectono-sédimentaire et restauration séquentielle du rétro-bassin d'avant-pays des Andes centrales. theses.fr. Available at: http://www.theses.fr/2004TOU30134. (Accessed 10 January 2022).

Hoorn, C., 1993. Marine incursions and the influence of Andean tectonics on the Miocene depositional history of northwestern Amazonia: results of a palynostratigraphic study. Palaeogeogrp. Palaeoclimatol. Palaeocol 105, 267-209.

Hoorn, C., Bogotʹa-A, G.R., Romero-Baez, M., Lammertsma, E.I., Flantua, S.G.A., Dantas, E.L., Dino, R., do Carmo, D.A., Chemale, F., 2017. The Amazon at sea: onset and stages of the Amazon River from a marine record, with special reference to Neogene plant turnover in the drainage basin. Global Planet. Change 153, 51–65. https://doi.org/10.1016/j.gloplacha.2017.02.005.

Horton, B.K., 1999. Erosional control on the geometry and kinematics of thrust belt development in the central Andes. Tectonics 18, 1292–1304. https://doi.org/10.1029/1999TC900051.

Horton, B.K., DeCelles, P.G., 1997. The modern foreland basin system adjacent to the Central Andes. Geology 25, 895–898. https://doi.org/10.1130/0091-7613(1997)025<0895:TMFBSA>2.3.CO;2.

Horton, B.K., Capaldi, T.N., Perez, N.D., 2022. The role of flat slab subduction, ridge subduction, and tectonic inheritance in Andean deformation. Geology 50 (9), 1007–1012. https://doi.org/10.1130/G50094.1.

Hovikoski, J., Räsänen, M., Gingras, M., Roddaz, M., Brusset, S., Hermoza, W., Pittman, L.R., Lertola, K., 2005. Miocene semidiurnal tidal rhythmites in Madre de Dios, Peru. Geology 33 (3), 177–180.

Hovikoski, J., Gingras, M., Räsänen, M., Rebata, L.A., Guerrero, J., Ranzi, A., Melo, J., Romero, L., del Prado, H.N., Jaimes, F., 2007b. The nature of Miocene Amazonian epicontinental embayment: high-frequency shifts of the low-gradient coastline. Geol. Soc. Am. Bull. 119 (11–12), 1506–1520.

Hovikoski, J., Räsänen, M., Gingras, M., Lopéz, S., Romero, L., Ranzi, A., Melo, J., 2007c. Palaeogeographical implications of the Miocene Quendeque Formation (Bolivia) and tidally influenced strata in southwestern Amazonia. Science Direct 243, 23–41.

Hurtado, C., Roddaz, M., Santos, R.V., Baby, P., Antoine, P.-O., Dantas, E.L., 2018. Cretaceous-early Paleocene drainage shift of Amazonian rivers driven by Equatorial Atlantic Ocean opening and Andean uplift as deduced from the provenance of northern Peruvian sedimentary rocks (Huallaga basin). Gondwana Res. 63, 152–168. https://doi.org/10.1016/j.gr.2018.05.012.

Insel, N., Poulsen, C.J., Ehlers, T.A., 2010. Influence of the Andes Mountains on South American moisture transport, convection, and precipitation. Clim. Dynam. 35, 1477–1492. https://doi.org/10.1007/s00382-009-0637-1.

Jacobsen, S.B., Wasserburg, G., 1980. Sm-Nd isotopic evolution of chondrites. Earth Planet Sci. Lett. 50 (1), 139–155.

Jackson, S., Pearson, N.J., Griffin, W., Belousova, E.A., 2004. The application of laser ablation-inductively coupled plasma-mass spectrometry to in situ U-Pb zircon geochronology. Chem. Geol. 211, 47–69.

Jaramillo, C.A., Rueda, M., Torres, V., 2011. A palynological zonation for the Cenozoic of the llanos and llanos foothills of Colombia. Palynology 35, 46–84. https://doi.org/10.1080/01916122.2010.515069.

Jaramillo, C., Rueda, M., 2023. A Morphological Electronic Database of Cretaceous-Cenozoic and Extant pollen, spores and dinoflagellates from Northern South America, v. 2023. Last consulted 28th of November 2023. http://biogeodb.stri.si.edu/jaramillosdb/web/morphological/.

Jo, H., Rhee, C., Chough, S., 1997. Distinctive characteristics of a streamflow-dominated alluvial fan deposit: Sanghori area, Kyongsang Basin (Early Cretaceous), southeastern Korea. Sediment. Geol. 110 (1), 51–79.

Kay, S.M., Coira, B., Viramonte, J., 1994. Young mafic back arc volcanic rocks as indicators of continental lithospheric delamination beneath the argentine Puna Plateau, Central Andes. J. Geophys. Res. Solid Earth 99, 24323–24339. https://doi.org/10.1029/94JB00896.

Ketcham, R.A., 2005. Forward and inverse modeling of low-temperature thermochronometry data. Rev. Mineral. Geochem. 58, 275–314. https://doi.org/10.2138/rmg.2005.58.11.

Ketcham, R.A., Carter, A., Donelick, R., Barbarand, J., Hurford, A., 2007. Improved modeling of fission-track annealing in apatite. Am. Mineral. 92, 799–810. https://doi.org/10.2138/am.2007.2281.

Kontak, D.J., Clark, A.H., Farrar, E., Archibald, D.A., Baadsgaard, H., 1990. Late paleozoic-early mesozoic magmatism in the Cordillera de Carabaya, puno, southeastern Peru: geochronology and petrochemistry. J. South Am. Earth Sci. 3, 213–230. https://doi.org/10.1016/0895-9811(90)90004-K.

Kontak, D.J., Clark, A.H., Farrar, E., Strong, D.F., 1985. The rift-associated Permo-Triassic magmatism of the Eastern Cordillera: a precursor to the Andean orogeny. Rift-Assoc. Permo-Triassic Magmat. East. Cordill. Precursor Andean Orogeny 36–44.

Lacan, F., 2002. Masses d'eau des Mers Nordiques et de l'Atlantique Subarctique tracées par les isotopes du néodyme. Université Paul Sabatier-Toulouse III.

Laubacher, Gérard, Megard, F., 1985. The Hercynian basement: a review. In: Pitcher, W. S., Atherton, M.P., Cobbing, E.J., Beckinsale, R.D. (Eds.), Magmatism at a Plate Edge: the Peruvian Andes, pp. 29–35.

Lease, R.O., Ehlers, T.A., 2013. Incision into the eastern andean plateau during Pliocene cooling. Science 341, 774–776. https://doi.org/10.1126/science.1239132.

Lenters, J.D., Cook, K.H., 1995. Simulation and diagnosis of the regional summertime precipitation climatology of south America. J. Clim. 8, 2988–3005.

Leturmy, P., Mugnier, J.L., Vinour, P., Baby, P., Colletta, B., Chabron, E., 2000. Piggyback basin development above a thin-skinned thrust belt with two detachment levels as a function of interactions between tectonic and superficial mass transfer: the case of the Subandean Zone (Bolivia). Tectonophysics 320, 45–67.

Loewy, J.N., Connely, Dalziel, I.W.D., 2004. An orphaned basement block: the Arequipa-Antofalla Basement of the central Andean margin of South America. GSA Bull 116, 171–187. https://doi.org/10.1130/B25226.1.

Lorente, M.A., 1986. Palynology and palynofacies of the upper Tertiary in Venezuela. https://www.schweizerbart.de/publications/detail/isbn/9783443640118/Dissertat_Botanicae_Band_99. (Accessed 2 December 2019).

Louterbach, M., 2014. Propagation du front orogénique Subandin et réponse sédimentaire associée dans le bassin d'avant-pays amazonien (Madre de Dios, Pérou). Available at: http://thesesups.ups-tlse.fr/2530/.

Louterbach, M., Roddaz, M., Antoine, P.-O., Marivaux, L., Adnet, S., Bailleul, J., et al., 2018. Provenance record of late Maastrichtian–late Palaeocene Andean Mountain building in the Amazonian retroarc foreland basin (Madre de Dios basin, Peru). Terra. Nova 30, 17–23. https://doi.org/10.1111/ter.12303.

Margirier, A., Strecker, M.R., Reiners, P.W., Thomson, S.N., Casado, I., George, S.W.M., Alvarado, A., 2023. Late Miocene exhumation of the western Cordillera, Ecuador, driven by increased coupling between the subducting carnegie ridge and the south American continent. Tectonics 42, e2022TC007344. https://doi.org/10.1029/2022TC007344.

Marivaux, L., Salas-Gismondi, R., Tejada, J., Billet, G., Louterbach, M., Vink, J., et al., 2012a. A platyrrhine talus from the early Miocene of Peru (Amazonian Madre de Dios sub-Andean zone). J. Hum. Evol. 63, 696–703. https://doi.org/10.1016/j.jhevol.2012.07.005.

Marivaux, L., Salas-Gismondi, R., Tejada, J., Billet, G., Louterbach, M., Vink, J., et al., 2012b. A platyrrhine talus from the early Miocene of Peru (Amazonian Madre de Dios sub-Andean zone). J. Hum. Evol. 63, 696–703. https://doi.org/10.1016/j.jhevol.2012.07.005.

Marocco, R., 1978. Estudio geológico de la Cordillera de Vilcabamba-.

McQuarrie, N., DeCelles, P., 2001. Geometry and structural evolution of the central Andean backthrust belt, Bolivia. Tectonics 20, 669–692. https://doi.org/10.1029/2000TC001232.

McQuarrie, N., Ehlers, T.A., Barnes, J.B., Meade, B., 2008. Temporal variation in climate and tectonic coupling in the central Andes. Geology 36, 999–1002. https://doi.org/10.1130/G25124A.1.

Megard, F., 1978. Etude geologique des Andes du Perou central; contribution a l'etude geologique des Andes N. Mem. ORSTOM.

Miall, A.D., 1996. The Geology of Fluvial Deposits: Sedimentary Facies, Basin Analysis, and Petroleum Geology. Springer-Verlag Inc Berlin, p. 582.

Mišković, A., Spikings, R.A., Chew, D.M., Košler, J., Ulianov, A., Schaltegger, U., 2009. Tectonomagmatic evolution of Western Amazonia: geochemical characterization and zircon U-Pb geochronologic constraints from the Peruvian Eastern Cordilleran granitoids. Geol. Soc. Am. Bull. 121, 1298–1324. https://doi.org/10.1130/B26488.1.

Mitra, G., Sussman, A.J., 1997. Structural evolution of connecting splay duplexes and their implications for critical taper: an example based on geometry and kinematics of the Canyon Range culmination, Sevier Belt, Central Utah. J. Struct. Geol. 19, 503–521. https://doi.org/10.1016/S0191-8141(96)00108-3.

Mobil Oil Corporation, 1998. Phase I Technical Synthesis Tambopata Lot 78, Peru.

Moizinho, G.R., Vieira, L.C., Santos, R.V., Nogueira, A.C.R., Dantas, E.L., Roddaz, M., 2022. Provenance of Miocene-Pleistocene siliciclastic deposits in the Eastern Amazonia coast (Brazil) and paleogeographic implications. Palaeogeogrp. Palaeoclimatol. Palaeocol. 587, 110799.

Mora, A., Baby, P., Roddaz, M., Parra, M., Brusset, S., Hermoza, W., et al., 2011. Tectonic history of the Andes and sub-Andean zones: implications for the development of the Amazon drainage basin. In: Amazonia: Landscape and Species Evolution. Wiley-Blackwell, pp. 38–60. https://doi.org/10.1002/9781444306408.ch4.

Mora, A., Ketcham, R.A., Higuera-Diaz, I.C., Bookhagen, B., Jimenez, L., Rubiano, J., 2014. Formation of passive-roof duplexes in the Colombian Subandes and Peru. Lithosphere 6, 456–472. https://doi.org/10.1130/L340.1.

Oliveros, V., Labbé, M., Rossel, P., Charrier, R., Encinas, A., 2012. Late Jurassic paleogeographic evolution of the Andean back-arc basin: new constrains from the Lagunillas Formation, northern Chile (27°30'–28°30'S). J. South Am. Earth Sci. 37, 25–40. https://doi.org/10.1016/j.jsames.2011.12.005.

Oncken, O., Boutelier, D., Dresen, G., Schemmann, K., 2012. Strain accumulation controls failure of a plate boundary zone: linking deformation of the Central Andes and lithosphere mechanics. G-cubed 13, Q12007. https://doi.org/10.1029/2012GC004280.

Parra, M., Mora, A., Jaramillo, C., Torres, V., Zeilinger, G., Strecker, M.R., 2010. Tectonic controls on Cenozoic foreland basin development in the north-eastern Andes, Colombia. Basin Res. 22 (6), 874–903. https://doi.org/10.1111/j.1365-2117.2009.00459.x.

Paton, C., Hellstrom, J., Paul, B., Woodhead, J., Hergt, J., 2011. Iolite: Freeware for the visualization and processing of mass spectrometric data. J. Anal. Atom. Spect. 26 (12), 2508–2518.

Perez, N.D., Horton, B.K., 2014. Oligocene-Miocene deformational and depositional history of the Andean hinterland basin in the northern Altiplano plateau, southern Peru. Tectonics 33, 1819–1847. https://doi.org/10.1002/2014TC003647.

Perez, N.D., Horton, B.K., McQuarrie, N., Stubner, K., Ehlers, T.A., 2016. Andean shortening, inversion and exhumation associated with thin- and thick-skinned deformation in southern Peru. Geol. Mag. 153, 1013–1041. https://doi.org/10.1017/S0016756816000121.

Pérez-Consuegra, N., Hoke, G.D., Mora, A., Fitzgerald, P., Sobel, E.R., Sandoval, J.R., et al., 2021. The case for tectonic control on erosional exhumation on the tropical northern Andes based on thermochronology data. Tectonics 40, e2020TC006652. https://doi.org/10.1029/2020TC006652.

Petrus, J.A., Kamber, B.S., 2012. VizualAge: a novel approach to laser ablation ICP-MS UPb geochronology data reduction. Geostand. Geoanal. Res. 36, 247–270. https://doi.org/10.1111/j.1751-908X.2012.00158.x.

Pinto, L., 2003. Traçage de l'erosion Cénozoique des Andes Centrales 'a l'aide dela minéralogie et de la géochimie des sédiments (Nord du Chili et Nord-Ouest de la Bolivie) (PhD thesis). Université Paul Sabatier, Toulouse, p. 196.

Poulsen, C.J., Ehlers, T.A., Insel, N., 2010. Onset of convective rainfall during gradual Late Miocene rise of the Central Andes. Science 328, 490–493. https://doi.org/10.1126/science.1185078.

Powers, M.C., 1953. A new roundness scale for sedimentary particles. J. Sediment. Res., 23117 https://doi.org/10.1306/D4269567-2B26-11D7-8648000102C1865D. –119.

Ramos, V.A., 2009. Anatomy and global context of the Andes: main geologic features and the Andean orogenic cycle. Geological Society of America Memoirs 204, 31–65. https://doi.org/10.1130/2009.1204(02).

Reimann, C.R., Bahlburg, H., Kooijman, E., Berndt, J., Gerdes, A., Carlotto, V., et al., 2010. Geodynamic evolution of the early Paleozoic Western Gondwana margin 14°–17°S reflected by the detritus of the Devonian and Ordovician basins of southern Peru and northern Bolivia. Gondwana Res. 18, 370–384. https://doi.org/10.1016/j.gr.2010.02.002.

Retallack, G., 1997. Palaeosols in the upper Narrabeen group of New South Wales as evidence of Early Triassic palaeoenvironments without exact modern analogues. Aust. J. Earth Sci. 44 (2), 185–201.

Ridgway, K.D., DeCelles, P.G., 1993. Stream-dominated alluvial fan and lacustrine depositional systems in Cenozoic strike-slip basins, Denali fault system, Yukon Territory, Canada. Sedimentology 40 (4), 645–666.

Roddaz, M., Viers, J., Brusset, S., Baby, P., Herail, G., 2005. Sediment provenances and drainage evolution of the Neogene Amazonian foreland basin. Earth Planet Sci. Lett. 239, 57–78. https://doi.org/10.1016/j.epsl.2005.08.007.

Roddaz, M., Brusset, S., Baby, P., Herail, G., 2006. Miocene tidal influenced sedimentation to continental Pliocene sedimentation in the forebulge–backbulge depozones of the Beni–Mamore foreland Basin (northern Bolivia). J. S. Am. Earth Sci. 20 (4), 351–368.

Roddaz, M., Hermoza, W., Mora, A., Baby, P., Parra, M., Christophoul, F., Brusset, S., Espurt, N., 2010. Cenozoic Sedimentary Evolution of the Amazonian Foreland Basin System, pp. 61–88.

Rousseau, T.C.C., Roddaz, M., Moquet, J.-S., Handt Delgado, H., Calves, G., Bayon, G., 2019. Controls on the geochemistry of suspended sediments from large tropical South American rivers (Amazon, Orinoco, and Maroni). Chem. Geol. 522, 38–54. https://doi.org/10.1016/j.chemgeo.2019.05.027.

Sanchez, C., 2012. Reconstitution de l'exhumation cénozoique des Andes Centrales à partir de l'étude de la provenance des sédiments du bassin amazonien (analyses géochimique (majeurs, trace et isotopie Nd-Sr) et minéralogique (RX et minéraux lourds) (Master thesis), vol. 3. Univeristé Paul Sabatier Toulouse, Toulouse.

Santos, R.V., Sondag, F., Cochonneau, G., Lagane, C., Brunet, P., Hattingh, K., Chaves, J. G.S., 2015. Source area and seasonal 87 Sr/86 Sr variations in rivers of the Amazon basin: amazon rivers source sediments. Hydrol. Process. 29, 187–197. https://doi.org/10.1002/hyp.10131.

Sepulchre, P., Sloan, L.C., Fluteau, F., 2009. Modelling the response of amazonian climate to the uplift of the andean mountain range. In: Amazonia: Landscape and Species Evolution. John Wiley & Sons, Ltd), pp. 211–222. https://doi.org/10.1002/9781444306408.ch13.

Sempere, T., Carlier, C., Soler, P., Fornari, M., Carlotto, V., Jacay, J., Arispe, O., Néraudeau, D., Cárdenas, J., Rosas, S., Jiménez, N., 2002. Late Permian-Middle Jurassic lithospheric thinning in Peru and Bolivia, and it's bearing on Andean-age tectonics. Tectonophys., Andean Geodyn. ISAG 4 (345), 153–181. https://doi.org/10.1016/S0040-1951(01)00211-6.

Sláma, J., et al., 2008. Plezovice zircon A new natural reference material for U–Pb and Hf isotopic microanalysis. Chemical Geology, Chemical Geology 249, 1–35. https://doi.org/10.1016/j.chemgeo.2007.11.005.

Soler, P., Bonhomme, M.G., 1990. Relation of magmatic activity to plate dynamics in central Peru from Late Cretaceous to present. https://doi.org/10.1130/SPE241-p173.

Spencer, C.J., Kirkland, C.L., Taylor, R.J.M., 2016. Strategies towards statistically robust interpretations of *in situ* U-Pb zircon geochronology. Geosci. Front. 7 (4), 581–589.

Spikings, R., Reitsma, M.J., Boekhout, F., Mišković, A., Ulianov, A., Chiaradia, M., et al., 2016. Characterisation of Triassic rifting in Peru and implications for the early disassembly of western Pangaea. Gondwana Res. 35, 124–143. https://doi.org/10.1016/j.gr.2016.02.008.

Sundell, K.E., Saylor, J.E., Lapen, T.J., et al., 2019. Implications of variable late Cenozoic surface uplift across the Peruvian central Andes. Sci. Rep. 9, 4877. https://doi.org/10.1038/s41598-019-41257-3.

Tassinari, C.C.G., Macambira, E.M.B., 1999. Geochronological provinces of the Amazonian Craton. Episodes 22 (3), 174–182.

Turner, P., 1980. Continental Red Beds. Elsevier.

Uba, C.E., Heubeck, C., Hulka, C., 2005. Facies analysis and basin architecture of the Neogene Subandean synorogenic wedge, southern Bolivia. Sediment. Geol. 180, 91–123.

Uba, C.E., Heubeck, C., Hulka, C., 2006. Evolution of the late cenozoic chaco foreland basin, southern Bolivia. Basin Res. 18 (2), 145–170.

Uba, C.E., Kley, J., Strecker, M.R., Schmitt, A.K., 2009a. Unsteady evolution of the Bolivian Subandean thrust belt: the role of enhanced erosion and clastic wedge progradation. Earth Planet Sci. Lett. 281, 134–146. https://doi.org/10.1016/j.epsl.2009.02.010.

Uba, C.E., Kley, J., Strecker, M.R., Schmitt, A.K., 2009b. Unsteady evolution of the Bolivian Subandean thrust belt: the role of enhanced erosion and clastic wedge progradation. Earth Planet Sci. Lett. 281, 134–146. https://doi.org/10.1016/j.epsl.2009.02.010.

Valdivia, H., 1974. Estratigrafia de la Faja Subandina de la region de Madre de Dios.

van Soelen, E.E., Kim, J.-H., Santos, R.V., Dantas, E.L., Vasconcelos de Almeida, F., Pires, J.P., Roddaz, M., Sinninghe Damste, J.S., 2017. A 30 Ma history of the Amazon River inferred from terrigenous sediments and organic matter on the Ceará rise. Earth Planet Sci. Lett. 474, 40–48. https://doi.org/10.1016/j.epsl.2017.06.025.

Vermeesch, P., 2013. Multi-sample comparison of detrital age distributions. Chem. Geol. 341, 140–146. https://doi.org/10.1016/j.chemgeo.2013.01.010.

Vermeesch, P., 2018. Dissimilarity measures in detrital geochronology. Earth Sci. Rev. 178, 310–321. https://doi.org/10.1016/j.earscirev.2017.11.027.

Vermeesch, P., Resentini, A., Garzanti, E., 2016. An R package for statistical provenance analysis. Sediment. Geol. 336, 14–25. https://doi.org/10.1016/j.sedgeo.2016.01.009.

Viers, J., Roddaz, M., Filizola, N., Guyot, J.-L., Sondag, F., Brunet, P., Zouiten, C., Boucayrand, C., Martin, F., Boaventura, G.R., 2008. Seasonal and provenance controls on Nd-Sr isotopic compositions of Amazon rivers suspended sediments and implications for Nd and Sr fluxes exported to the Atlantic Ocean. Earth Planet Sci. Lett. 274, 511–523.

Wiedenbeck, M., Alle, P., Corfu, F., Grif fin, W.L., Meier, M., Oberli, F., Von Quadt, A., Roddick, J.C., Spiegel, W., 1995. Three natural zircon standards for U-ThePb, Lu-Hf, trace element and REE analysis. Geostand. Newsl. 19, 1–23.

Wright, V., Tucker, M., 1991. Calcretes. Reprint Series Volume 2 of the International Association of Sedimentologists. Blackwell Scientific Publications.

Zamora, G., Louterbach, M., Arriola, P., 2019. Chapter 12 - structural controls along the Peruvian Subandes. In: Horton, B.K., Folguera, A. (Eds.), Andean Tectonics. Elsevier, pp. 333–362. https://doi.org/10.1016/B978-0-12-816009-1.00015-0.

Zavaleta, A.G., Hauser, N., Roddaz, M., Gonçalves, G.O., González, P.A., Baby, P., Reimold, W.U., Puma, F., Bravo, P., Humerez, M., 2023. Provenance of Devonian-Carboniferous sedimentary rocks of the Tarija Basin, southern Bolivia: implications for the geodynamic evolution of the southwestern margin of Gondwana. GSA Bullet. https://doi.org/10.1130/B36701.1.

APPENDIX 2

Neogene paleo-drainage divide in Western Amazonia (Madre de Dios Basin, Peru): provenance evidence and implications

Martin Roddaz[1*], Mélanie Louterbach[2], Elton Luiz Dantas[3], Roberto Ventura Santos[3], **Gabriel Ribeiro Moizinho[1,3,4]**, Germain Bayon[4], Jochem Vink[5], and Carina Hoorn[6]

[1]Géosciences-Environnement Toulouse, Université de Toulouse; UPS (SVT-OMP);; CNRS; IRD; 14 Avenue Édouard Belin, F-31400 Toulouse, France

[2] Harvard Graduate School of Design, Department of Landscape Architecture, 48 Quincy Street, MA 02138 Cambridge, USA

[3] *Laboratório de Geocronologia, Instituto de Geociências, Universidade de Brasília, Brasília, DF 70910-000, Brazil*.

[4]*Geo-Ocean, Univ. Brest, CNRS, Ifremer, UMR6538, F-29280, Plouzané, France*

[5] Centre for Biodiscovery School of Biological Sciences Victoria University of Wellington Wellington 6012, New Zealand

[6] *Institute for Biodiversity and Ecosystem Dynamics, University of Amsterdam, the Netherlands*

Abstract

Reconstructing the geological history of the Amazon River and its paleodrainage is of prime importance for constraining the geological evolution of the Amazonian landscape and for understanding the control of tectonics and geodynamics processes on Amazonian landscape dynamics. In addition, it can provide important constraints on the origin of Amazonian Biodiversity. Many studies have focused on the Neogene timing of the transcontinentalization of the Amazon River and on geodynamic mechanisms that may have driven this process. The Neogene geological history of the western Amazonian paleodrainage is viewed as homogenous. In this study, we report new stratigraphic and sedimentological constraints on the Neogene sedimentary rocks of the northern part of the Madre de Dios Basin (South Peru) and determine the provenance of these sedimentary rocks based on major and trace element geochemistry, Sr-Nd isotopes, and U-Pb detrital zircon ages. The multidisciplinary dataset presented here shows that the Neogene sedimentary rocks of the northern part (12.5°-13° lat S) have a different provenance than those of the southern part (13°-14° lat S) of the Madre de Dios Basin. The sedimentary rocks of the northern part of the Basin are characterized by Solimoes like ƐNd (0) values (between -9.8 and -5.2) for fined grained sedimentary rocks and U-Pb age distribution of a dominated by zircon ages between 0.9-1.3 Ga (Grenville/Sunsas), 0.5-0.7 Ga (Brasilian/Pampean), 290-252 Ma (Permian magmatism) and to a lesser extent by zircons ages younger than 130 Ma (Andean Arc) zircon. We interpret these sedimentary rocks to be sourced by the Altiplano and the Eastern Cordillera (EC) whereas the Neogene sedimentary rocks of the southern part were sourced by the EC and Subandean Zone (SAZ). Combined with previous studies, this implies the existence of a paleogeographic barrier within the Madre de Dios Basin that existed since the Cretaceous. Hence, we propose that the southern limit of the Maastrichtian to Plio-Pleistocene Amazonian paleodrainage basin was located within the Madre de Dios Basin and also speculate that this intrabasinal drainage divide might be a driver for endemism and species diversification within the Madre de Dios Basin.

1. Introduction

Big Rivers are the main arteries of continent and are important for landscape evolution, elemental fluxes and biotic communities including human (Wohl, 2015). They are defined as the "trunk" rivers which either drain a large drainage basin, have a long course, or transport a large amount of sediment and water (Potter, 1978). Constraining the geological history of Big rivers and their drainage basins is important for understanding landscape evolution and past biogeochemical cycles because they play a key role in present-day geochemical cycles, particularly in the CO2 cycle (Gaillardet et al., 1999; Galy et al., 2007). Big rivers are long term features, ten to hundred millions years, that may result from major geological processes (Miall, 2006). However, identifying and reconstructing the geological evolution of Big rivers and their drainage basin remain challenging (Miall, 2006).

The Amazon River is the greatest supplier of materials to the oceans, providing about 20% of the water (Callède et al., 2004), ~10% of the dissolved load (Gaillardet et al., 2003), and ~3% of the suspended load (Milliman and Syvitski, 1992) to the world's oceans. The Andean Amazonian rivers are the dominant contributors transporting more than 95% of the mean annual suspended sediment flux delivered (2/3 and 1/3 from the Solimões and Madeira rivers, respectively (Filizola and Guyot, 2004). The geological history of the Amazon paleodrainage is the result of the interaction of geodynamic mechanisms acting in the South American plate with climate and sea-level fluctuations (Sacek et al., 2023). Recent studies have shown the existence of continent wide cratonic paleodrainage originated in the Amazon craton between the Cenomanian and the Maastrichtian in Western Amazonia (Hurtado et al., 2018; Rodrigues et al., 2023). Western Amazonia started to be sourced by the Andes between the late Maastrichtian and the Paleocene (Hurtado et al., 2018; Louterbach et al., 2018) whereas the Paleogene eastern Amazonian paleodrainage was cratonic in provenance (Stewart et al., 2016; van Soelen et al., 2017) The Neogene configuration of the Amazonian paleodrainage is a much-discussed subject (Albert et al., 2018; Hoorn et al., 2017, 2010; Roddaz et al., 2011, 2005; Sacek et al., 2023; van Soelen et al., 2017). Most previous studies have focused on the timing of the establishment of the transcontinental Amazon River (Figueiredo et al., 2009; Gorini et al., 2014; Hoorn et al., 2017; van Soelen et al., 2017) and on the geodynamic processes (Andean mountain building, flat-slab subduction or dynamic topography) responsible for this

transcontinentalization process (Bicudo et al., 2020, 2019; Eakin et al., 2014; Rodríguez Tribaldos V. et al., 2017; Sacek, 2014; Shephard et al., 2010).The Neogene geological history of the western Amazonian paleodrainage is viewed as homogenous (Roddaz et al., 2011).

The tropical Andes and the adjacent Amazon Basin are the world's most biodiverse regions (Hoorn et al., 2022; Rahbek et al., 2019). The present-day biodiversity of the Amazon region is inherited from the Neogene and the Andean mountain building was the main factor for the evolution of Amazonian landscapes and ecosystems (Hoorn et al., 2010). Major rivers and their drainage dynamics, tectonically driven Amazonian river megacaptures, landscape dynamics caused by topographic barrier migration are suspected to play a major role in Amazonian vertebrates diversification since the Neogene (Albert et al., 2021; Oberdorff et al., 2019; Ribas et al., 2011) and even since the Paleogene (Cassemiro et al., 2023; Musher et al., 2022). Hence, constraining the Neogene history of Amazonian paleodrainage is not only important for understanding the Andean uplift but may also provide important temporal milestones for understanding the origin of the Amazonian biodiversity making it of special interest not only to geoscientist but also to other scientific communities including to biologists and paleontologists.

In this study, we provide new stratigraphic constraints, seismic interpretations based on the interpretation of a new subsurface seismic dataset, sedimentological sections, major and trace element geochemistry, Sr-Nd isotopes and U-Pb detrital zircon ages on the Neogene sedimentary infill of the Salvación syncline of the northern part of the Madre de Dios Basin (South Peru), one of the highest biodiversity hot spot of Amazonia (Torre-Marin Rando et al., 2021). We revised the Neogene stratigraphy of the Salvación syncline and determine the provenance of the Neogene sedimentary rocks. We show that the Neogene sedimentary rocks of the northern part of the Madre de Dios Basin are sourced by the Eastern Cordillera (EC) and the Altiplano and that they have a different provenance to coeval sedimentary rocks of the southern part of the Basin analyzed in (Moizinho et al., 2023). Associated with results of recent studies, our dataset indicates that a long lived intrabasinal drainage barrier existed possibly since the Cretaceous.

2. Geological setting

2.1 Structural Setting

The Madre de Dios Basin is located between 12º and 14º S latitudes in the south-eastern part of the Peruvian Andes and Amazonian Basin (Figs. 1 and 2). The Madre de Dios Basin is constituted by the Madre de Dios Subandean zone (SAZ) and the Madre de Dios foredeep and is included in the southern Amazonian retroarc foreland basin (Roddaz et al., 2005). The SAZ is separated from the Eastern Cordillera (EC) by the Azulmayo thrust named "Main thrust" in Perez et al., (2016) and from the Madre de Dios foredeep by the Tambopata thrust which corresponds to the Subandean thrust front (Fig. 1 and 2). The Madre de Dios foredeep is limited north and northeast by the Brazilian Shield, and north and northwest by the Fitzcarrald Arch. In the northern part of the Madre de Dios area (Pongo de Coñeq area, Figs. 1 and 2), the piggy-back basin (Salvación syncline) is transported by the Subandean thrust front (Louterbach et al., 2014; Perez et al., 2016). The Salvación syncline comprises late Cretaceous-Cenozoic marine, tide-influenced and fluvial deposits (Gil Rodriguez, 2002, 2001; Louterbach et al., 2014).

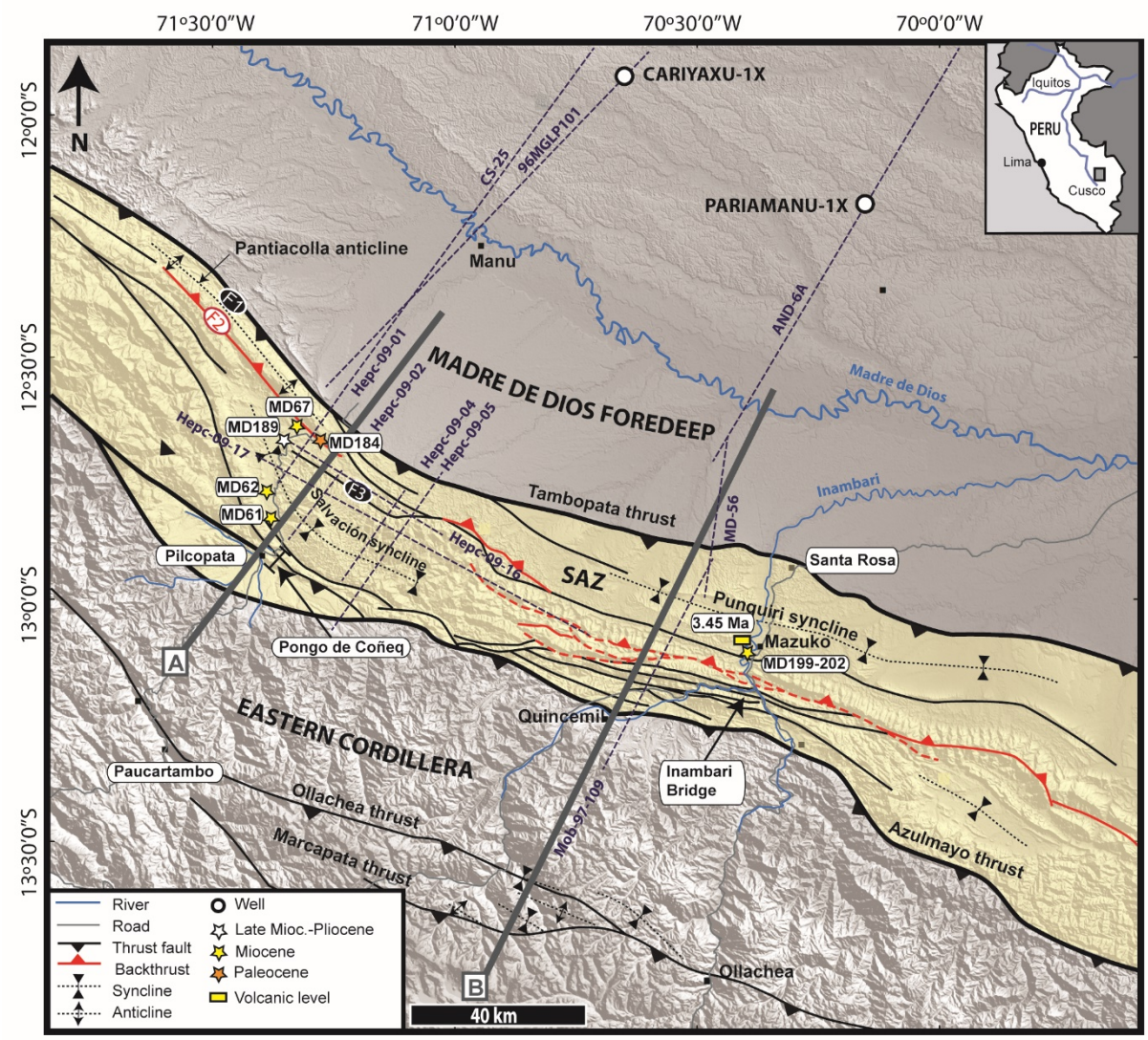

Figure 1: Structural map of the studied area. Seismic lines used by Mélanie Louterbach (Louterbach, 2014) are indicated by dark blue dashed lines. F1 to F3 refer to the faults identified in seismic lines. Red lines correspond to back-thrust faults. The main outcrops used for stratigraphic review are located on the map, depicted by a star (biostratigraphy) or a yellow rectangle (geochronology).

2.2 Neogene sedimentary infill and stratigraphy of the Madre de Dios Basin

The Cenozoic sedimentary infill of the Madre de Dios Basin is composed of about 3.3km of siliciclastic sediments (Gil Rodriguez, 2002; Louterbach, 2014; Moizinho et al., 2023). The detailed stratigraphic record of both the SAZ and foredeep depozones can be found elsewhere (i.e. Gil Rodriguez, 2001; Hermoza, 2004; Roddaz et al., 2011). The sedimentary succession of the SAZ consists of the sedimentary rocks of the Paleocene Huayabamba Formation, the Miocene Ipururo Group, and the Plio-Pleistocene Mazuko Formation. The Huayabamba Formation and the Ipururo Group are present in the foredeep but the Plio-Pleistocene Mazuko Formation is absent. The stratigraphic ages of the Cenozoic sedimentary succession are supported by palynological data (Caldas and Kehrer, 1982; Carpenter and Berumen, 1999; Gutierrez, 1982; Valdivia, 1974), thermochronological analysis (Hermoza, 2004) and radiometry (40Ar/39Ar dating, Campbell et al., 2001; Gil Rodriguez, 2001; Moizinho et al., 2023). The Paleocene Huayabamba Formation consists of estuarine tide-dominated sedimentary rocks of Andean origin (Louterbach et al., 2018, 2014). The Ipururo Group of the SAZ consists of three formations: the Bala, Quendeque, and Charqui formations (Roddaz et al., 2011). The deposits of these formations are predominantly fluvial to alluvial (Gil Rodriguez, 2002, 2001; Hermoza, 2004; Roddaz et al., 2011) although some coastal facies have been recognized in the Bolivian Quendeque Formation (Hovikoski et al., 2007b, 2007a). The Ipururo Group of the Peruvian foredeep depozone includes the Ipururo Formation and Units A and B of the Madre de Dios Formation (Campbell et al., 2001). The Miocene age of the Ipururo Formation has been established based on stratigraphic correlations (Hermoza, 2004). The Late Miocene age of the Madre de Dios Formation is supported by 40Ar/39Ar dating on feldspars at 9.01 ± 0.28 Ma (Campbell et al. 2001. The depositional environment of the Madre de Dios Formation was interpreted as tide-dominated estuaries (Hovikoski et al., 2005; Roddaz et al., 2006).

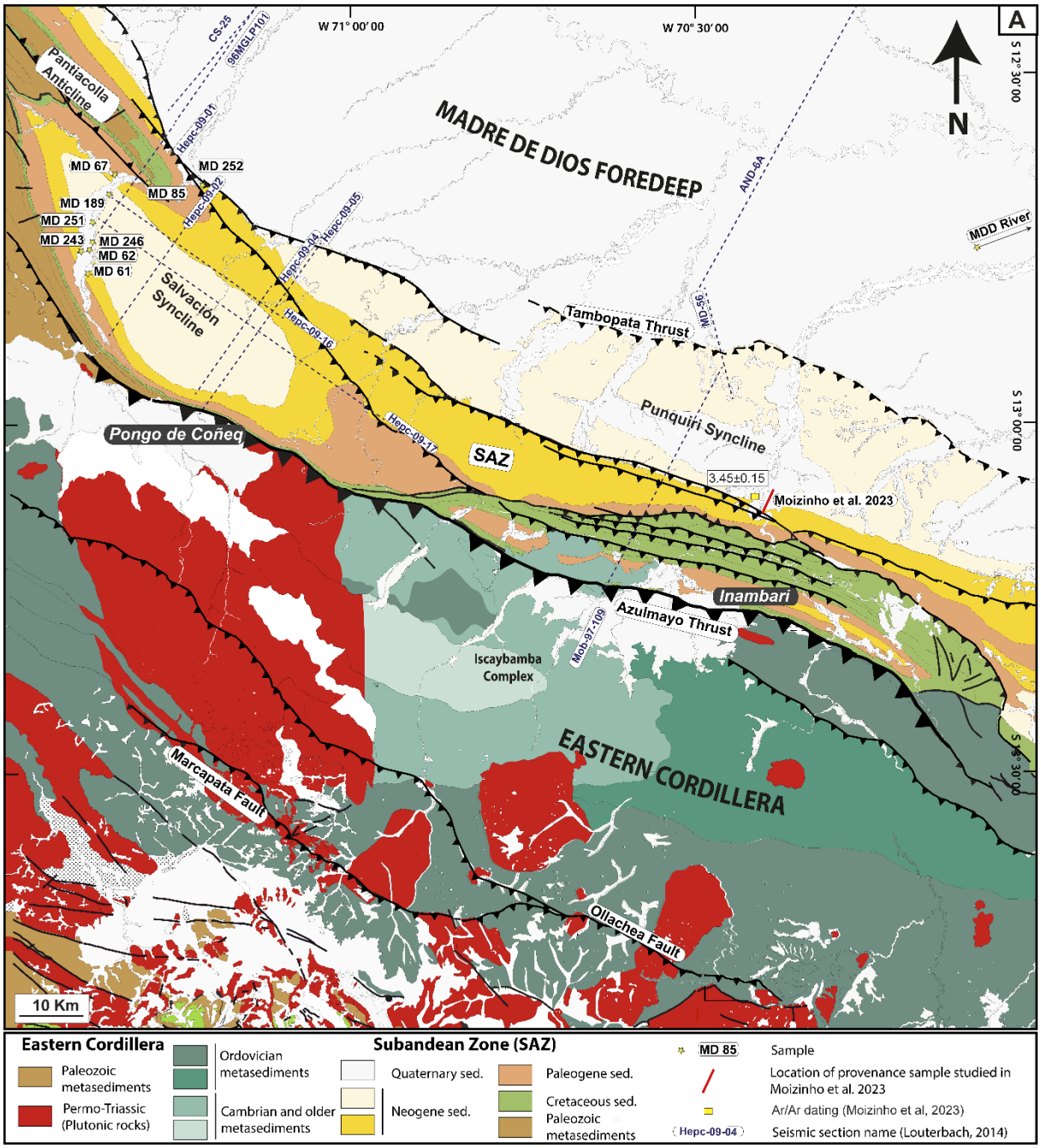

Figure 2: Geological map of the study area (modified after INGEMMET maps of (Chávez V. et al., 1997; Vargas Vilchez and Hipólito Romero, 1998). The samples analyzed in this study are located in this map with a yellow star. The arrows indicate the direction (Puerto Maldonado town) where the modern river sands of the Madre de Dios River have been sampled.

3. Materials and Methods

3.1. Sampling and sedimentary sections

The Salvación syncline provides relatively good outcrop conditions for Western Amazonia. Three composite sections were constructed during the PhD thesis of Mélanie Louterbach at 1/500 scale based on three field work campaigns made between 2010 and 2012 (Louterbach, 2014) across the Salvación syncline. The outcrops of the composite sections were only accessible by pirogue. Rock descriptions were reported at the decimeter scale. Sedimentary hiatuses were estimated using GPS locations and dip measurements. In this study, we only provide the thicknesses of the sections. For details on the sedimentary facies and depositional environment, the reader is referred to (Antoine et al., 2013; Louterbach, 2014; Louterbach et al., 2014; Marivaux et al., 2012). The stratigraphic datum is set to the base of the Cretaceous series. The location of all samples collected in this study can be found in the Supplementary Table 1.

3.2. Biostratigraphy constraints seismic stratigraphic correlations

The stratigraphic dating of the Salvación syncline (Pongo de Coñeq area), is based on published studies (Antoine et al., 2013; Louterbach et al., 2014; Marivaux et al., 2012) which dated Paleogene and Neogene outcrops. In addition, we provide in this paper one new stratigraphic constraint on one of the outcrops (MD 189, see details in the supplementary dataset). Three seismic sections that image the Pongo de Coñeq SAZ and Madre de Dios foredeep (seismic lines Hepc-09-02, Hepc-09-01 and 96MGLP101) were used to make correlations within the Salvación syncline. The seismic facies were identified in the Cenozoic infill based on amplitude characteristics and correlate with the Cariyacu-1X well, seismic sections Hepc-09-01 and Hepc-09-02. The definition of seismic facies and seismic correlations within the northern part of the Madre de Dios Basin was made by Mélanie Louterbach during her phd thesis (Louterbach, 2014).

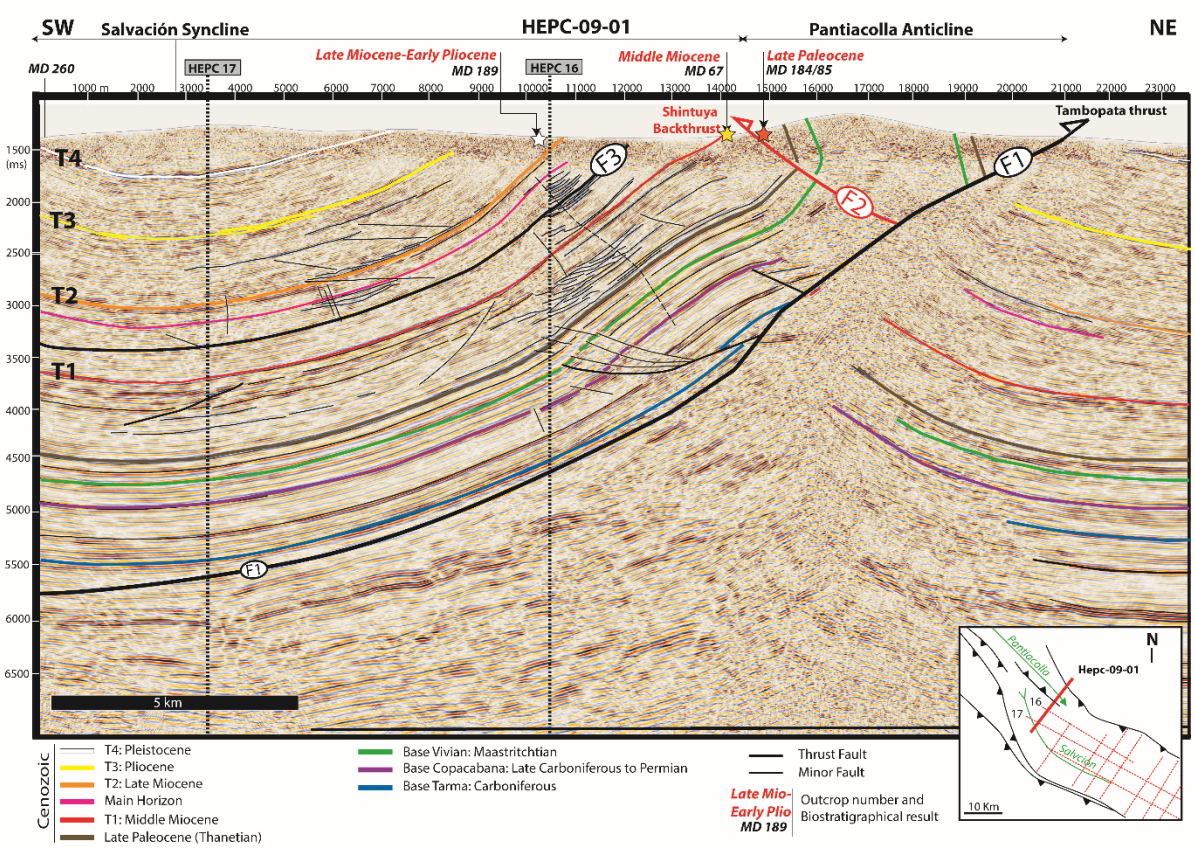

Figure 3: Interpretation of seismic profile HEPC-09-01 across the Salvación syncline and Pantiacolla anticline. Seismic line location is shown on Figure 1. The Neogene reflectors (T1 to T4) were calibrated using dated outcrops (MD66/189, MD 67, MD 184/85, see Supplementary dataset for details). Faults are indicated by thick black lines.

3.3. Major and Trace element concentrations and Sr-Nd Isotopes

3.3.1. Bulk rock

Six Neogene fine-grained sedimentary rocks were collected on river outcrops along the Salvación syncline (see Fig. 2 and Table S1 for location). The major and trace element concentrations were measured at the Service d'Analyse des Roches et Mineraux (SARM, INSU facility, Vandoeuvre-Les-Nancy, France) by ICP-OES (Na, Mg, K, Ca, Sc, Ti, Mn, Fe, Al, Si, and P) and ICP-MS (Rb, Cs, Ba, Sr, Th, U, Y, Zr, Nb, Hf, Cr, V, Co, Cu, Ni, Zn, La, Ce, Pr, Nd, Sm, Eu, Gd, Tb, Dy, Ho, Er, Tm, Yb, Lu, and Ta) after alkali fusion. Analytical details are available on http://helium.crpg.cnrs-nancy.fr/SARM/ and in (Carignan et al., 2001). Precision is better than 5% for elements measured by ICP-OES, and 10% for elements measured by ICP-MS. It is possible to use the Chemical Index of Alteration (CIA) to assess the degree of source-area weathering and the paleo weathering conditions of ancient sediments (Fedo et al., 1995; Nesbitt and Young, 1982). This index measures the weathering intensity of feldspars relative to unaltered protoliths, and is defined as CIA = [Al2O3/(Al2O3+CaO*+Na2)+K2O)] x 100 (in molar proportions), in which CaO* represents the CaO content in the silicate fraction. We do not have CO2 data for our analyses, and thus we cannot correct for Ca in carbonates to obtain CaO*. To calculate CaO*, we have assumed the value of CaO if CaO ≤ Na2O or CaO = Na2O if CaO>Na2O (Bock et al., 1998). The Eu anomaly is calculated relative to chondrites: Eu/Eu* = EuN/(SmN x GdN)½, where N refers to the chondrite-normalized concentration value (Condie, 1993). This facilitates comparisons with sediments derived from basic or felsic sources (Cullers, 2000) and the PAAS (Pourmand et al., 2012; Taylor and McLennan, 1985). The Cerium anomaly (ΩCe) normalized to PAAS is calculated following (De Baar et al., 1985): ΩCe = 2 x (Ce sample/CePAAS)/ [(Lasample/LaPAAS) + (Prsample/PrPAAS)], where Xsample is the concentration of samples and XPAAS refers to the concentration of the PAAS standard.

The Nd-Sr isotopic compositions were measured at Geosciences Environment Toulouse (GET) and were incorporated in the Master thesis of Caroline Sanchez (Sanchez, 2012). Details regarding the analytical procedures and measurement of Sr-Nd isotopes at GET (Toulouse, France) can be found in the supplementary dataset.

The measured 143Nd/144Nd ratios are expressed as the fractional deviation in parts per 104 (units) from 143Nd/144Nd in a Chondritic Uniform Reservoir (CHUR) as measured at the present day:

$$\varepsilon Nd(0) = ((143Nd/144Nd)S / ICHUR(0) - 1)*104$$

where (143Nd/144Nd)S is the present-day ratio measured in the sample and ICHUR(0) is the 143Nd/144Nd in the CHUR reference reservoir at the present (ICHUR(0)=0.512638 (Jacobsen and Wasserburg, 1980).

3.3.2. Labile Fe-oxides

The rare earth element (REE) composition of labile Fe-oxide phases (e.g., ferrihydrite, lepidocrocite) leached from sediments serves as a valuable proxy for distinguishing bedrock lithology and weathering processes in modern river basins (Bayon et al., 2020; Jang et al., 2024). Given the well-defined lithological contrasts within the Madre de Dios Basin (Fig. 2), we applied this approach by analyzing Fe-oxide leachates from ten sediment samples, four from the northern Pongo de Coneq section and six from the southern Inambari section (Fig. S1, Table S1). For a detailed tectono-stratigraphic evolution discussion for the Inambari the reader is referred to Moizinho et al. (2023).

Bulk sediment samples were first sieved to obtain the <63 μm fraction and then subjected to a stepwise leaching protocol following the method described by Bayon et al. (2022). Carbonates were initially removed using 5% acetic acid (AA). Subsequently, easily reducible iron oxyhydroxides—such as ferrihydrite and lepidocrocite—were extracted using a mixture of 15% AA and 0.05 M hydroxylamine hydrochloride (HH). The leachate was then filtered through a 0.20 μm membrane, evaporated at 120°C for 24 hours, redissolved in nitric acid to eliminate residual HH, evaporated again at 110°C, and finally dissolved in 4 M hydrochloric acid.

Major and trace element abundances were determined at the Pôle Spectrométrie Océan (Brest, France) using a Thermo Scientific Element XR sector field (SF) ICP-MS operated in low-resolution mode. Elemental concentrations were calculated using the Tm addition method, following procedures outlined by (Barrat et al., 1996, 2012). To assess the precision and

accuracy of our data, a series of certified reference materials (BCR-2, DNC-1, GSPN-2, GSPN-3, and GSMC-3) were analyzed. The precision for major and trace elements was better than 3 %, and the accuracy of measured concentrations was typically <5 %. The REE concentrations are reported relative to the initial mass of bulk sediment. were normalized to values for the PAAS (Pourmand et al., 2012; Taylor and McLennan, 1985), denoted by the subscript "N".

3.4. U-Pb dating

Five Neogene sandstones were collected on river outcrops along the Salvación syncline (see Fig. 2 and Table S1 for locations), and one present-day sand sample was obtained at Puerto Maldonado to determine their U-Pb zircon age distribution (see Table S1 for locations). Details regarding the LA-ICP-MS U-Th-Pb dating of the analyzed samples at the Laboratory of Geochronology of the University of Brasilia (Brazil) can be found in Table S4 (supplementary dataset).

To statistically compare the detrital age distributions of the analyzed samples, we used the standard statistical technique called multidimensional scaling (MDS) popularized by Vermeesch (2013). The MDS method is a "superset of principal component analysis" that, given a table of pairwise 'dissimilarities' between samples, produces a 'map' of points on which 'similar' samples cluster closely together, and 'dissimilar' samples plot far apart (Vermeesch, 2013). Following the latest recommendations by Vermeesch (2018), we used the Kolmogorov-Smirnov test to produce a MDS map comparing the analyzed samples. The closest and second closest neighbors are linked by solid and dashed lines, respectively, and the goodness of fit was evaluated using the "stress" value of the configuration (0.2 = poor; 0.1 = fair; 0.05 = good; Vermeesch, 2013). The MDS map was generated using the provenance package of Vermeesch et al. (2016).

We also reported the maximum depositional ages (MDA) for one sample (MD61), selecting at least three analyses in the youngest cluster of ages and, the YC2σ[3+] was defined as the weighted mean average of the three youngest overlapping analyses and associated 2σ uncertainty of this cluster (Dickinson and Gehrels, 2009; Sharman et al., 2018; Sharman and Malkowski, 2020).

4. Results

4.1. Stratigraphic constraints

Sample MD 189 (Fig. 1 and tables S2) was dated based on its palynological content (see supplementary dataset for details). The presence of Cichoreacidites longispinosus from 10.06-1.18 Ma (Jaramillo et al., 2011) and Retipollenites crotonicollumelatus from 13.94-3.56 Ma (Jaramillo et al., 2011) suggest that sample MD 189 may have belonged to the zone F. longispinosus (sensu (Lorente, 1986) and is late Miocene to Pliocene in age. The extremely high abundance of reworked Paleozoic megaspores further suggests these sediments were sourced in a Paleozoic hinterland.

The results obtained from sample MD 189 presented above, as well as outcrops dated in published studies (MD 61 “Pinturan” biochronological unit, between 18.75 and 16.5 Ma, Marivaux et al., 2012; MD 67 Colloncuran-early Laventan age, between 15.6 and 13.0 Ma, Antoine et al., 2013; and MD 184 (Thanetian, between 59.2 and 56 Ma, Louterbach et al., 2014) were projected along seismic section Hepc-09-01 (Fig. 3). Four seismic markers (T1 to T4) were interpreted for the Neogene sedimentary infill based on their proximity to biostratigraphic dating at the surface (Fig S1) by M. Louterbach during her Phd (Louterbach, 2014). The T1 marker corresponds to the outcrop MD67 sample at surface, dated to the late early to late middle Miocene and referred to as belonging to the middle Miocene in this study for simplification. The T2 marker is close to the late Miocene to early Pliocene MD 189 outcrop, located just stratigraphically below (Fig 3). For this reason, we ascribed a late Miocene age to the T2 seismic marker. Based on to its stratigraphic position and lithostratigraphic correlation with the base of the Plio-Pleistocene correlation of the Mazuko Formation, we assigned a Pliocene age to the T3 marker. The T4 marker is the stratigraphically youngest seismic marker identified in the Salvación syncline. It correspond to the uppermost erosive surface documented in this syncline. Based on the INGEMMET geological map (Fig. 3), we interpret it as having a Pleistocene age.

The synthetic sedimentary sections showing the thickness, the stratigraphic constraints, the stratigraphic position of each sample analyzed for Sr-Nd isotopes and U-Pb dating, and the approximate projection of seismic reflectors T1 to T4 are shown in Fig. 4. A

stratigraphic age was ascribed to the Neogene samples analyzed for their Sr-Nd isotopes and U-Pb zircon age distribution based on their position of these sedimentary sections.

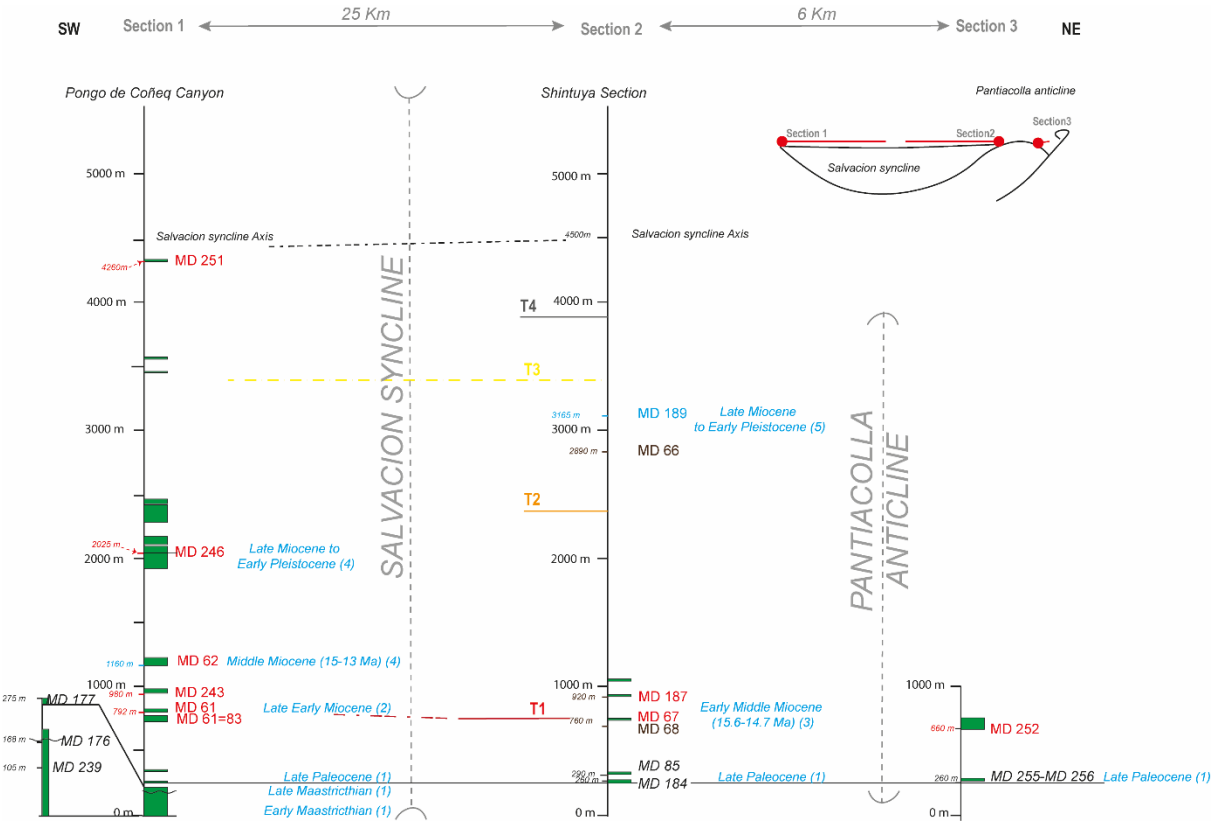

Figure 4: Synthetic sedimentary log sections measured in the Salvación syncline and in the Pantiacolla anticline, along the Pongo de Coñeq area showing the position of each sample studied for its biostratigraphic content (in blue) and its U-Pb zircon ages or Sr-Nd isotopic compositions (in red). Green rectangles correspond to the outcrop observations made on the field. The location of each seismic marker identified from 2D seismic line Hepc-09-01 is shown in red (T1), orange (T2), yellow (T3) and grey (T4). MD=Samples/Outcrops. Biostratigraphic and provenance results of samples/outcrops MD239, MD176, MD177, MD184, MD85, MD255 and MD256 were published in (Louterbach et al., 2018b). Biostratigraphic results of outcrops MD 61 and MD 67 were published in (Marivaux et al., 2012) and in (Antoine et al., 2013) respectively. (1) refers to (Louterbach et al., 2018), (2) to (Marivaux et al., 2012), (3) to (Antoine et al., 2013) and (4) to (Louterbach, 2014) and (5) to this study. Modified from (Louterbach, 2014).

The samples MD 83 and MD 61 were collected at MD 61 outcrop and are late early Miocene in age, between 18.75 and 16.5 Ma, (Marivaux et al., 2012). The samples MD 62A and MD 62B were collected at MD 62 outcrop estimated to be between 15 and 13 Myr old (Louterbach, 2014). The sample MD 67 was collected at MD67 outcrop (760 m above the stratigraphic datum) which was dated between 15.6 and 14.7 Ma (Antoine et al., 2013). Sample MD 187 was collected 920 m above the stratigraphic datum, 160 m above sample MD 67 in the Shituya section. It is located between seismic marker T1 (Middle Miocene) and T2. Stratigraphically, MD 187 is at a deepest stratigraphic level than MD 62 (middle Miocene, between 15 and 13 Ma). So we ascribed a middle Miocene age for MD 187 sample.

Sample MD 252 was collected at 600 m above the stratigraphic datum, located between the Paleocene samples analyzed in (Louterbach et al., 2018, 2014) and sample MD 61. This sample is thought to be of early to middle Miocene age and is considered to be the oldest analyzed sample. Sample MD 61 was obtained at 792 m above the stratigraphic datum and is the second oldest analyzed sample, dated as having deposited between 18.75 and 16.5 Ma, (Marivaux et al., 2012). Sample MD 243was obtained 980 m above the stratigraphic datum between MD 61 and MD 62 (15 and 13 Ma, see Louterbach, 2014). Hence, sample MD243 is middle Miocene in age. Sample MD 246 is stratigraphically above MD 243 and is located 2025 m above the stratigraphic datum. Based on its palynological content (see Louterbach (2014) for details), it is late Miocene to Pleistocene in age. However, because it is stratigraphically located between seismic markers T2 (late Miocene) and T3 (middle Miocene), we favor a late Miocene age for sample MD 243. Sample MD 251 was obtained from the top of the first sedimentary section (Fig. 4), 4200 m above the stratigraphic datum in the Salvación syncline axis. It was sampled at the center of the syncline and is stratigraphically situated above seismic marker T4 (Pleistocene). Hence, we ascribed a Pleistocene age for sample MD251.

4.2. Major and trace element concentrations and Sr-Nd isotopes

The concentrations of major and trace elements of the bulk rock analyzed samples (Table 1, 2) were normalized against the Post Archean Australian Shales (PAAS) concentration (Pourmand et al., 2012; Taylor and McLennan, 1985, see Supplementary Figure S2t) because they are considered representative shales of the upper continental crust (Taylor and McLennan,

1985). All samples show depletion in Cs, Cr, V, Co, Cu, and Ni and enrichment in P2O5, Zr, Nb, Hf, and Y. Enrichment in CaO can be noted in MD62B and MD67, while other samples are depleted. The Al/Si (in moles) ratios of analyzed samples range from 0.24 to 0.36 (Table 1). The CIA values of the bulk samples range from 64 to 76.

The analyzed samples have slightly lower Cr/Th ratios (5.04-6.60) than those of PAAS (7.53) and quite similar Th/Sc ratios (0.81-0.99) as those of PAAS (0.92). When normalized against PAAS (see supplementary Fig/ S2), the REE patterns of the analyzed samples are relatively flat with positive Eu anomalies (Eu/Eu* between 0.67 and 0.80), higher than the that of the PAAS (Eu/Eu* = 0.58, Pourmand et al. 2012). The Ce anomalies range between 1.03 and 1.08 and quite similar to that of the PAAS (i.e., ΩCe = 1). They are higher to the Ce anomalies of the authigenic smectites and seawater (ΩCe < 0.50), (De Baar et al., 1985). The analyzed samples have radiogenic Nd isotopic composition with ƐNd (0) values between -9.8 and -5.2 and a small range of 87Sr/86Sr isotopic compositions (0.710571-0.718402, Table 3).

The REE concentrations of Fe-oxide leachates from the southern (Inambari) and northern (Pongo de Coneq) sectors of the Madre de Dios Basin reveal distinct compositional differences (Table 4). In the Inambari section, Nd concentrations range from 1.15 to 17.81 µg/g, with the majority of samples falling between 1 and 5 µg/g. By comparison, Nd concentrations in the Pongo de Coneq samples are lower, ranging from 0.98 to 3.66 µg/g. When normalized to Post-Archean Australian Shale (PAAS) and further normalized to Gd to minimize dilution effects, the REE patterns highlight a clear mid-REE (MREE) enrichment in the northern Pongo de Coneq samples (Fig. 5a). In contrast, the Inambari samples exhibit relatively elevated light REE (LREE) concentrations compared to heavy REEs (HREE), consistent with flatter or gently LREE-enriched profiles (Fig. 5b).

4.3. U-Pb dating results

The U-Pb zircon age distributions of analyzed samples of the Salvación syncline and modern sands of the Madre de Dios River as well as the percentages of U-Pb zircon ages representing orogenic events of Amazon craton and Andes are shown in Figure 6 and Table 4 respectively. Details on individual U-Pb zircon ages for each sample can be found in the supplementary material (Table S4). The U-Pb age distribution of all analyzed samples is

dominated by zircon ages between 0.9-1.3 Ga (Grenville/Sunsas), 0.5-0.7 Ga (Brasilian/Pampean), 290-252 Ma (Permian magmatism) and to a lesser extent by zircons ages younger than 130 Ma (Andean Arc) (Table 5 and Fig. 6). In the MDS graph (Fig.7), the early to middle Miocene samples (MD 61 and MD 252) and the modern Madre de Dios River sediments are connected by solid lines suggesting that they have quite similar U-Pb zircon age distributions. The middle Miocene samples (MD 243 and MD 61) are also connected by solid and dashed lines with the Permian Mitu sandstones analyzed in Spikings et al. (2016). The late Miocene (MD 246) sample is connected by solid lines with the Paleocene samples analyzed in Louterbach et al. (2018b) suggesting a good degree of similarity. The Pleistocene sample (MD 251) is connected by dashed lines to the Paleozoic metasediments of the EC analyzed in Reimann et al. (2010) and Bahlburg et al.(2011). The Maastrichtian samples analyzed in Louterbach et al. (2018) plot apart from the analyzed samples, suggesting that they are dissimilar. Hence, based on Table 5 and Figs. 6 and 7, two main difference in U-Pb zircon age distributions can be found along the stratigraphic succession. indicate two main changes in zircon distributions along the succession. The early to middle Miocene samples are characterized by an important contribution of Paleozoic magmatic, especially Permian, zircons. This Permian contribution is dominant for the middle Miocene sample MD 243 (55.1%, Table 5). The first change was observed between the Middle and Late Miocene. The late Miocene sample MD 246 is characterized by an increase of Cretaceous Andean Arc and Grenville/Sunsas zircon (13.9%, and 56.3% respectively) and a strong decrease in the Paleozoic magmatic zircon contribution (3.8%) when compared with the early to middle Miocene samples. The second change is seen between the Pleistocene and the Late Miocene. The youngest Pleistocene sample (MD 251) has fewer contributions of Cretaceous Andean Arc (1.2%) and Grenville/Sunsas (31.8%) zircons, and a higher contribution of Brazilian/Pampean and Rondonia-San Ignacio zircons (20.0% and 15.3%, respectively) than the late Miocene sample (MD 246). When compared with the Neogene sandstones of the southern part of the Madre de Dios Basin (Moizinho et al., 2023), most of the analyzed samples plot apart from the “Neogene Inambari” field and show no connection with these samples with the exception of the Pleistocene sample (MD 251) and to a lesser extent early Miocene MD 252 sample.

5. Discussion

5.1. Provenance interpretation

Sedimentary sorting, weathering and diagenesis might influence the concentrations of major and trace element and prevent the use of Eu anomalies, Cr/Th and Th/Sc ratios as well as Nd isotopic compositions for determining the provenance of sedimentary rock (McLennan et al., 1993). The effect of sedimentary sorting may be evaluated using the Al/Si ratios which is a proxy of grain size (Bouchez et al., 2011). Absence of correlation between the Al/Si ratios and the Eu/Eu*, Cr/Th, and ƐNd (0) (Supplementary Table 5) suggests that sedimentary sorting has not modified these provenance proxies. In addition, flat REE patterns against PAAS and the fact that CIA values are closed to that of the PAAS suggest that weathering did not significantly affect the major and trace elements concentrations of the analyzed samples. Ce anomalies (ΩCe) higher than 0.99 (Table 2), further indicate no incorporation of authigenic smectites during the early diagenetic process (e.g. (Rodrigues et al., 2023). Hence, the Eu anomalies, Cr/Th and Th/Sc ratios as well as Nd isotopic compositions of analyzed samples may be use as provenance proxies. The Eu anomalies, the Cr/Th and the Th/Sc ratios are in favor of a silicic/felsic source sensu (Cullers, 2000) because fine-grained sedimentary rocks derived from silicic/felsic sources are characterized by low Eu/Eu* ratios (0.3 to 0.94), high Th/Sc (> 0.64), and low Cr/Th (< 15) (Cullers, 2000). Additional constraints can be obtained by the Nd Isotopic composition. The provenance of Amazonian sedimentary rocks can be distinguished using their Nd isotopic compositions (Basu et al., 1990; Roddaz et al., 2005). Sedimentary rocks sourced by Cratonic paleo drainage are characterized by more negative ƐNd (0) values, between -12.7 to -20, than those of Andean-derived sediments (Figueiredo et al., 2009; Hoorn et al., 2017; Horbe et al., 2013; Nie et al., 2012a; Roddaz et al., 2005; Rodrigues et al., 2023). The ƐNd (0) values of analyzed samples being higher than -9.8, this suggests an Andean source for the Neogene sediments of the Salvación syncline. Modern Sr-Nd isotopic compositions of Suspended Particulate Matter (SPM) transported by tropical south American rivers have different isotopic compositions as a function of their drainage basin (e.g; (Allègre et al., 1996; Rousseau et al., 2019; Santos et al., 2015; Viers et al., 2008), suggesting that these Sr-Nd isotopic composition can be used for the reconstruction of Amazonian past drainage basin. In the 87Sr/86Sr vs Nd(0) diagram (Fig. 8), the Neogene analyzed samples of the northern part of

the Madre de Dios Basin plot close to the Altiplano and Solimões SPM fields indicating a similar Andean source and a lithologically similar drainage basin as that of the Solimões. In this diagram (Fig. 8), the analyzed samples can be distinguished from the Neogene samples of the northern Bolivian SAZ (Roddaz et al., 2005) and the southern part of the Madre de Dios Basin (Moizinho et al., 2023), which plot closer to the SAZ and Madeira SPM fields. These findings suggest that the Neogene fine-grained sedimentary rocks of the northern part of the Madre de Dios basin have a different Andean source than those of the southern part of the Madre de Dios Basin.

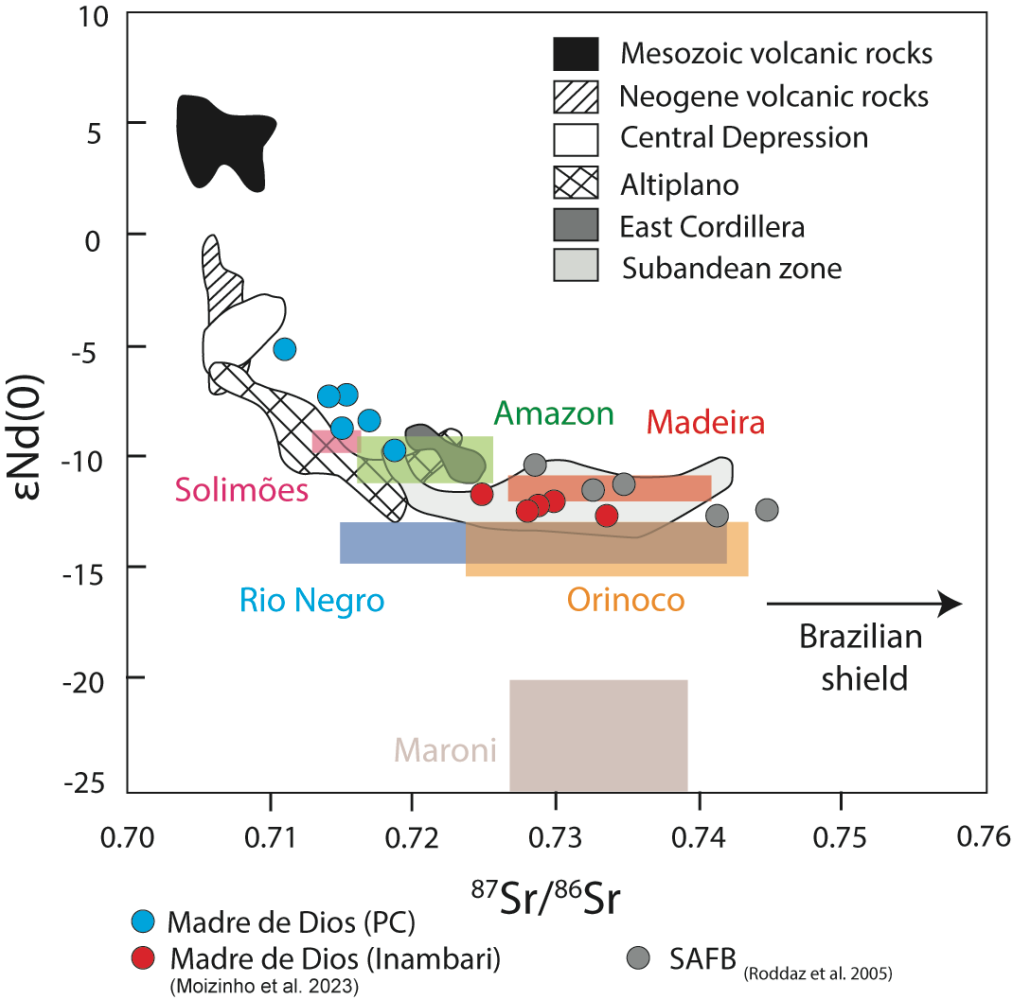

Figure 8: $^{87}Sr/^{86}Sr$-εNd(0) diagram for the Neogene Madre de Dios foreland basin sedimentary rocks compared with several relevant source areas and modern suspended particulate material in western Amazonia. Quaternary Ecuadorian volcanic lavas are from (Barragan et al., 1998); the Mesozoic and Neogene volcanic rocks are from (Kay et al., 1994); data for the Central depression, the Altiplano, the Eastern Cordillera, and the Subandean zone are taken from

(Pinto, 2003; Roddaz et al., 2005). SPM from the Tapajos, Negro, Urucara, and Trompetas (Allègre et al., 1996), Madeira and Solimões rivers (Viers et al., 2008), and the Amazon, Orinoco, and Maroni rivers (Rousseau et al., 2019). The red circles correspond to the Sr-Nd isotopic compositions of the sedimentary rocks of the Southern part of the Madre de Dios Basin analyzed in (Moizinho et al., 2023). The blue circles show the Sr-Nd isotopic compositions of the sedimentary rocks of the Southern part of the Madre de Dios Basin (this study). The grey circles indicate the Sr-Nd isotopic composition of the Neogene sedimentary rock of the Beni Basin (north Bolivia) analyzed in Roddaz et al. (2005). SAFB and PC refer to South Amazonian Foreland Basin (Roddaz et al., 2005) and Pongo de Coneq area (Louterbach, 2014).

The REE composition of leached Fe-oxide fractions from sediments in the Madre de Dios Basin further reveals clear provenance differences between its northern and southern sectors. Recent studies have shown that mid-REE (MREE) enrichment in Fe-oxides—expressed using the concavity index ($CI = GdN / (La_6N \times Yb_7N)^{1/13}$; Barrat and Bayon, 2024; Bayon et al., 2020; Lawrence et al., 2006)—is a sensitive tracer of lithological contrasts. In the northern Pongo de Coneq section (Upper Madeira sub-basin), Fe-oxides exhibit markedly elevated CI values (4.1 ± 2.6, n = 4; Fig. 8A). In contrast, samples from the southern Inambari region show much lower CI values (1.3 ± 0.4, n = 6; Fig. 8B). High CI values (>2.5) are characteristic of regions where oxidative weathering of sulfide-bearing rocks—particularly black shales—drives the formation of Fe-oxides under low-pH conditions. These settings favor the release and mobilization of REEs, with MREEs preferentially scavenged by authigenic Fe-oxides (Bayon et al., 2020; Jang et al., 2024; Moizinho et al., under review). Although the geochemical mechanisms driving this process are explored in detail elsewhere (Jhang et al., 2024; Moizinho et al., under review), it is noteworthy that the Upper Madeira region, where the Pongo de Coñec samples were collected, is widely recognized as a hotspot for sulfide oxidation in the Amazon headwaters (Moquet et al., 2011, 2016; Torres et al., 2015, 2016; Dellinger et al., 2023). In contrast, the Inambari samples lack significant MREE enrichment, suggesting limited influence from sulfide weathering processes. Instead, their REE signatures are more typical of Fe-oxides derived from silicate lithologies (CI = 1.6 ± 0.3, n = 24; Bayon et al., 2020). Given the high rates of physical erosion and limited chemical weathering in the Andean and sub-Andean zones (Stallard and Edmond,

1987), these Fe-oxides likely reflect the recycling of Paleozoic and Precambrian siliciclastic sediments rather than in situ soil formation.

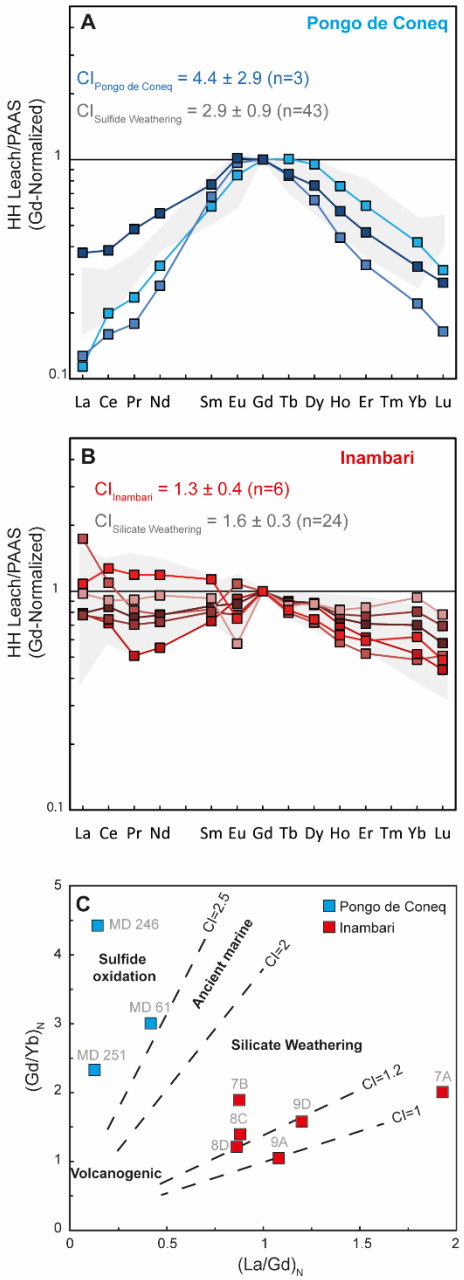

Figure 5: Shale-normalized REE patterns (PAAS; Pourmand et al., 2012; Taylor and McLennan, 1985) for leached Fe-oxide from Neogene sediments of the (a) Pongo de Coneq and (b) Inambari sections. REE concentrations are reported relative to the initial mass of bulk sediment. For clarity, REE data were also normalized Gd_{PAAS} to avoid any dilution effect. Concativity indices (CI) were calculated using the weighted geometric means of shale-normalized La and Yb (see text for details). (c) Plot of shale-normalized $(Gd/Yb)_N$ versus $(La/Gd)_N$ used to discriminate between sources of Fe-oxides in sediments, including secondary Fe-oxides from sulfide oxidation, ancient marine Fe-oxides from sedimentary rock weathering, secondary Fe-oxides from silicate rock weathering, and volcanogenic Fe-oxides (Bayon et al., 2020; Jang et al., 2024).

Finally, a difference in provenance between the Neogene sedimentary rocks of the northern and southern part of the Madre de Dios Basin is also evidenced by the U-Pb zircon age distributions. The U-Pb zircon age distribution of the northern part of the Madre de Dios are characterized by the presence of Cretaceous to Cenozoic Andean arc zircons whereas these zircons are absent from the Neogene samples of the southern part of the Madre de Dios Basin

(Moizinho et al., 2023). The difference in provenance is also confirmed by the statistical analysis of the U-Pb zircon distributions of the Neogene samples as shown in the MDS maps (Fig. 7 and Supplementary Figures S3 and S4). In these maps, the Neogene sedimentary rocks of the southern part of the Madre de Dios Basin, which were interpreted to be sourced by the EC and SAZ (Moizinho et al., 2023) define a distinct group when compared with our analyzed early to Pliocene sedimentary rocks and sediments of the northern part of the Madre de Dios Basin.

Regarding the provenance of the analyzed samples, all the samples are characterized by a significant proportion of zircons younger than 500 Ma which typifies an Andean provenance (see Chavez et al., 2022; Hurtado et al., 2018). The presence of Cretaceous and Cenozoic zircons further suggests subordinate contribution from the Altiplano in all samples (Table 5) Note that the dominant to significant proportion of Grenville/Sunsas U-Pb zircon ages (0.9-1.3 Ga) in all analyzed samples is not useful for differentiating Andean and cratonic sources as the Grenville/Sunsas zircons can be found elsewhere in the Andes (Coastal Cordillera, Altiplano, and EC) orin the Amazon craton (Table 5). In addition, the MDS map shows different contributions of the source area during the Neogene. The most early to middle Miocene sample (MD 252) plots close to the modern sands of the Madre de Dios river sampled at Puerto Maldonado (MDD River) indicating similar contribution of the different Andean sources. The middle Miocene samples (MD 243 and MD 61) are connected by solid and dashed lines with the Permian Mitu sandstones analyzed in Spikings et al. (2016) indicating a similar provenance. We interpret a dominant EC source because the Permo-Triassic plutonic rocks and the volcanic rocks of the Mitu Fm are in the EC (Spikings et al., 2016). In addition, we suggest that the strong increase in Permian zircon contributions and the decrease in Brazilian/Pampean zircon contribution, as well as the absence of Cenozoic Andean Arc zircons in the MD 243 sample may be the result of the increasing erosion of the EC. The late Miocene (MD 246) and Pleistocene (MD 251) samples plot apart from the middle Miocene samples. The late Miocene sample (MD 246) is connected by a by solid lines with the Paleocene samples analyzed in Louterbach et al. (2018), thus suggesting a similar provenance. The Pleistocene sample (MD 251) is connected with solid line with the Plio-Pleistocene sample of the southern part of the Madre de Dios Basin suggesting a shared provenance. This sample is also connected with dashed line to the Paleozoic metasediments of the Eastern Cordillera analyzed in Reimann et al. (2010) and Bahlburg et al. (2011). We thus suggest that this Pleistocene samples has greater contributions

from the recycled sedimentary rocks of the SAZ, indicating the increasing erosion and deformation of the SAZ. This latter hypothesis is supported by the high content of reworked Paleozoic megaspores found in sample MD 189 which is stratigraphically between MD 246 and MD 251 (Fig. 4).

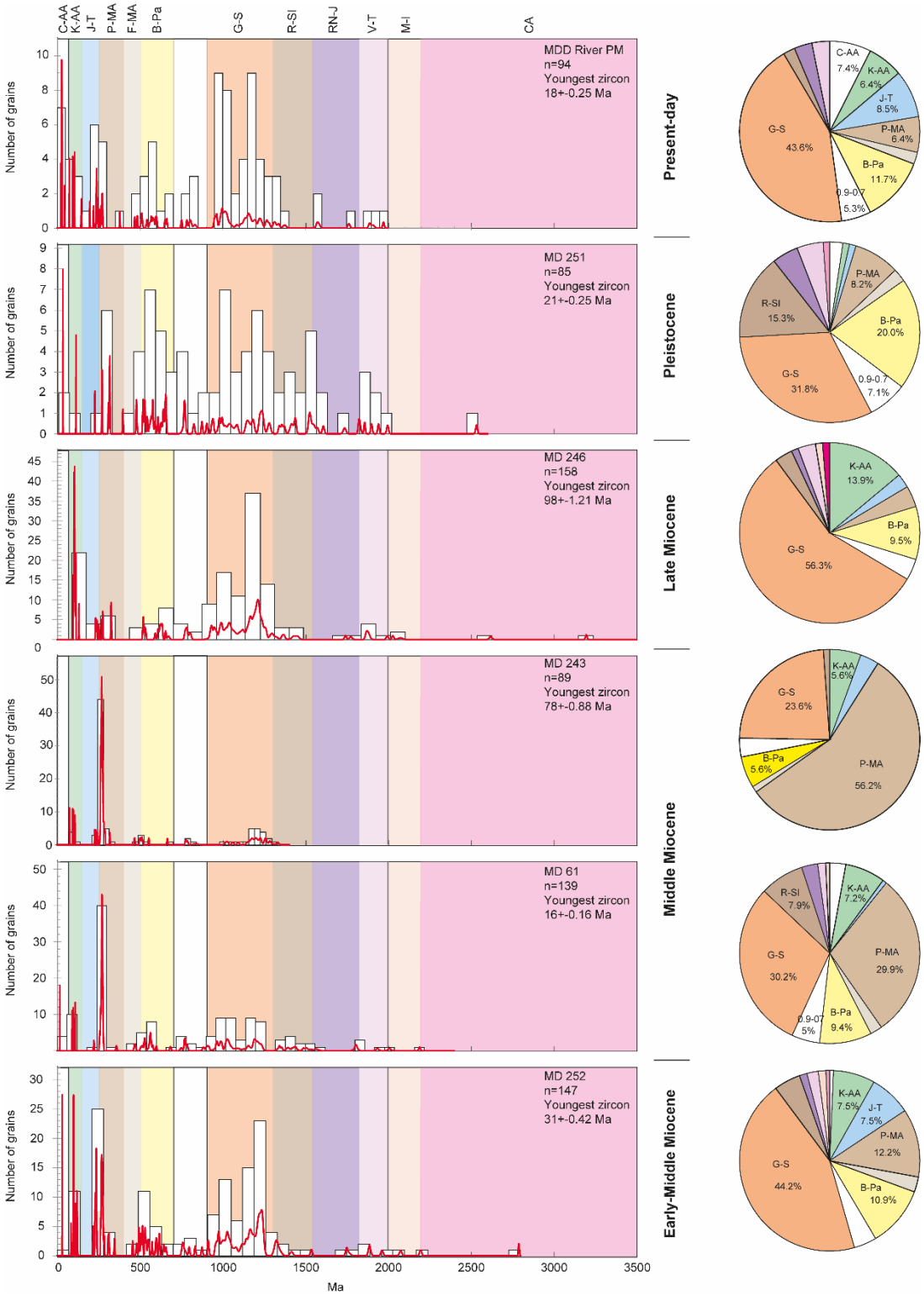

Figure 6: Stratigraphic evolution of U-Pb ages on zircon grains with the age probability (red line) and age histogram (white bars). AA: Andean Arc (less than130 Ma); JA: Jurassic Arc (216–130 Ma); TR: Triassic Rift (250–216 Ma); PMA: Paleozoic Magmatic Arc (0.4–0.25 Ga); FA: Famatinian (0.5–0.4 Ga); B-P: Brazilian-Pampean (0.7–0.5 Ga); G-S: Grenville – Sunsás (1.3 Ga-0.9 Ga); R-SI: Rondonia - San Ignacio mobile belt (1.54–1.3 Ga); RN-J: Rio Negro - Juruena mobile belt (1.82–1.54 Ga); V-T: Ventuari-Tapajós (Trans-amazonian) mobile belt (2.0–1.82 Ga); MI: Maroni - Itacaiúnas Province (2.2–2.0 Ga); Central Amazonian: Central Amazonian province (>2.2 Ga).

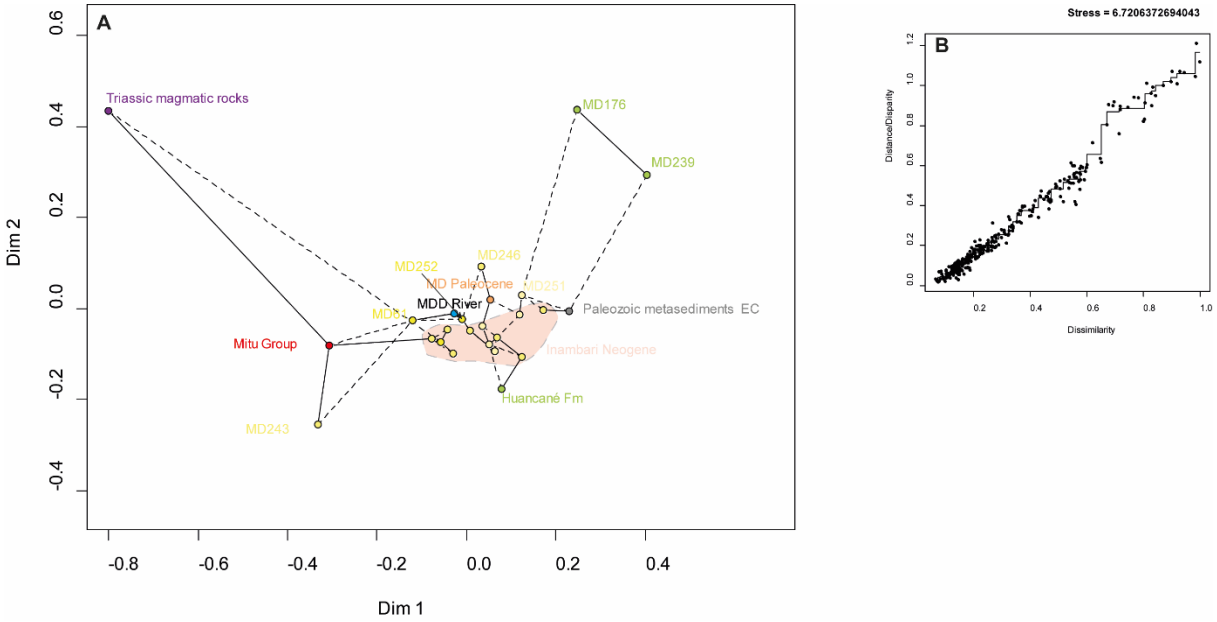

Figure 7: A) MDS map based on the U-Pb age distributions of detrital zircons of the analyzed samples using the Kolmogorov–Smirnov test. Closest and second closest neighbors are linked by solid and dashed lines, respectively; Data for MD Paleocene (sum of MD85, MD177, MD255, and MD256), MD239 and MD176 can be found in (Louterbach et al., 2018); Mitu Group refers to the Mitu sandstones, Triassic magmatic rocks and Cretaceous sandstone of the Huancané Formation analyzed in (Spikings et al., 2016); Paleozoic metasediments EC consists of the sum of the zircon ages of the metasedimentary rocks of the Eastern Cordillera analyzed in (Reimann et al., 2010) and in (Bahlburg et al., 2011). The “Inambari Neogene” field encompasses all the Neogene sandstones of the southern part of the Madre de Dios Basin analyzed in (Moizinho et al., 2023); For convenience, the labels of these samples have been removed but they are shown in supplementary figures S3 and S4; B) Shepard plot of the U-Pb data showing the

transformation from dissimilarity to distances and disparities. The low stress value of 0.067 (~6.7%) indicates a good transformation (Vermeesch, 2013).

5.2. Paleogeography and biological implications

Our provenance results indicate that two different drainage basins with different Andean sources coexisted during the Neogene in the Madre de Dios Basin (Fig. 9). The northern part of the Basin is characterized by Solimoes like ƐNd (0) values for fined grained sedimentary rocks, authigenic Fe-oxides formed from sulfide oxidation processes and zircons sourced by the Altiplano, EC and SAZ whereas the southern part has fined grained sedimentary rocks with Madeira like ƐNd (0) values, Fe-oxides formed via silicate weathering processes and zircon sourced by the EC and SAZ (Moizinho et al., 2023). Several mechanisms/processes may account for the coexistence of two drainage basins in the same retroarc foreland basin system during the Neogene. Differential erosion linked to focused precipitation (rainfall) in the source area might account for the difference in provenance between the northern and southern parts of the Madre de Dios Basin during the Neogene. We found this hypothesis unlikely because there is no evidence of a difference in the rainfall or climatic regimes during the Neogene between the two studied areas. Rather, available studies suggest that the Madre de Dios Basin experienced a similar climatic regime as the northern Bolivian Beni Basin (e.g. (McQuarrie et al., 2008) and that the EC adjacent to both basins was affected by widespread Pliocene incision likely due to a combine effect of change in paleoclimate (Falkowski et al., 2023; Lease and Ehlers, 2013) and tectonic surface uplift and deformation in both the EC and SAZ (Moizinho et al., 2023). Difference in surface uplift of the EC and Altiplano due to difference in deformation might also explain the difference in provenance found between the northern and southern parts of the Madre de Dios Basins. We also found this hypothesis unlikely because no significant difference in the Neogene deformation of the SAZ is found south to latitude 12°S is found (Baby et al., 2018b, 2018a; Mora et al., 2011) and available paleoelevation model also suggest no difference in surface uplift between the northern and southern parts of the Madre de Dios Basin (Sundell et al., 2019).

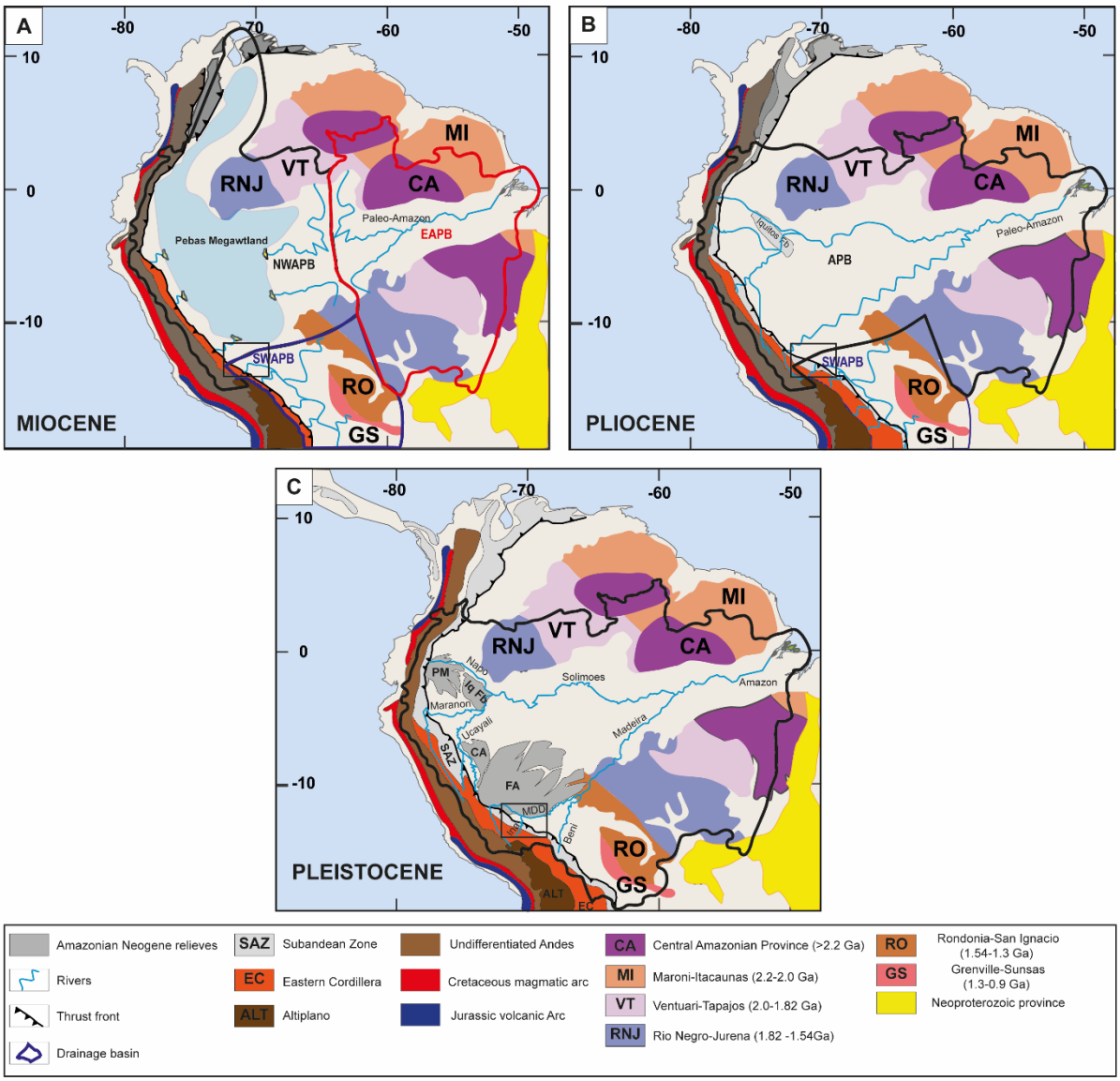

Figure 9: Neogene Paleogeographic maps of the studied area. For all maps, the position and extent of the Jurassic and Cretaceous volcanic Andean arcs are based on (Hurtado et al., 2018 and references therein). The location and extent of major tectonic provinces and the ages of their more recent metamorphic events of the Amazon craton are modified and adapted from (Cordani et al., 2000). The location of the studied area is indicated by a black rectangle in each map A) Middle Miocene Paleogeographic map. The extent of the Pebas megawetland is based on (Boonstra et al., 2015; Hoorn et al., 2010). The position of the thrust front is approximate and based on sequential reconstruction and structural mapping of (Baby et al., 2018a, 2018b; Espurt et al., 2011b; Eude et al., 2015; Gautheron et al., 2013; Gil Rodriguez et al., 2001; Moizinho et al., 2023; Mora et al., 2008). The red, blue and black curves delimit the extent of the Eastern Amazonian Paleodrainage Basin (EAPB), the South Western Amazonian Paleodrainage

Basin (SWAPB) and the North Western Amazonian Paleodrainage Basin (NWAPB). The extent of Andes and Eastern Cordillera domains are based on (Roddaz et al., 2011). B) Pliocene paleogeographic map. The blue and black curves delimit the extent of the South Western Amazonian Paleodrainage Basin (SWAPB) and the Amazonian Paleodrainage Basin (APB). The location and extent of the Iquitos Forebulge (Iquitos Fb) is based on (Roddaz et al., 2005). The position of the thrust front is approximate and based on sequential reconstruction and structural mapping of (Baby et al., 2018a, 2018b; Espurt et al., 2011b; Eude et al., 2015; Gautheron et al., 2013; Gil Rodriguez et al., 2001; Moizinho et al., 2023; Mora et al., 2008). C) Pleistocene to present-day configuration of the Amazon Basin. Ina: Inambari River; MDD: Madre de Dios River; FA: Fitzcarrald Arch; CA: Contamana Arch; Iq Fb: Iquitos forebulge; PM: Pastaza Megafan.

Rather, we do believe that the difference in provenance is best explained by the presence of a paleogeographic barrier within the Madre de Dios retroarc foreland Basin (Fig. 9). The exact location and the mechanisms responsible for the presence of this paleogeographic barrier during the Neogene remain unclear. A potential candidate might be the intrabasinal Madidi Arch, which is located somewhere in the Madre de Dios SAZ, but this structure may not have affected the Neogene sedimentary record (Fig. 2 in McGroder et al., 2015). Interestingly, different provenances are found for Cretaceous sedimentary rocks of the northern and southern parts of the Madre de Dios Basin (Rodrigues et al., 2023). Maastrichtian sedimentary rocks of the northern part of the Madre de Dios were sourced by the central part of the Amazonian craton and were part of the same paleodrainage system as those located in the other Peruvian and Ecuadorian Amazonian basins (Rodrigues et al., 2023). In contrast, coeval Cretaceous rocks of the southern part of the Madre de Dios Basin were sourced by local cratonic sources and were not connected with this cratonic-wide paleodrainage system. Although Paleogene provenance data are lacking for the southern part of the Madre de Dios Basin, we speculate that the drainage divide highlighted in this study might be inherited from the Cretaceous times. Given the fact that the sedimentary rocks of the northern part of Madre de Dios have Solimoes-like □Nd(0) values and that those of the southern part have Madeira-like □Nd(0) values, we propose that the southern limit of the Maastrichtian to Mio-Pliocene Amazonian paleodrainage basin was located within the Madre de Dios Basin (Fig. 9). Finally, following this scenario, it follows that

the Pliocene uplift of the Fitzcarrald Arch (Espurt et al., 2007, 2011a) is the mechanism at the origin of the modern configuration of the Amazonian drainage (Fig. 9).

The presence of this long-lived Cretaceous to Pliocene drainage divide between the northern and southern part of the Madre de Dos Basin might have promoted endemism and species diversification. Major rivers and their drainage dynamics are suspected to significantly affect allopatric speciation of Amazonian vertebrates in the Plio-Pleistocene (Ribas et al., 2011). Recent studies have also highlighted the role of landscape dynamics in shaping the geological history of drainage basin connections on assembly and diversifications of Amazonian "basin-wide fish faunas" since the Paleogene (Cassemiro et al., 2023). For instance, (Musher et al., 2022) ascribed the Cenozoic diversification of the Tityridae (bird) families in the Amazon Basin to be partly caused by barrier displacement and dynamic spatially heterogenous landscape. Similarly, tectonically driven Amazonian river megacaptures such as the transcontinentalization of the Amazon River that connected eastern and western Amazonia or the Pliocene Fitzcarrald Arch uplift (Espurt et al., 2007, 2011a) during the Neogene are suspected that to be an important driver of lineage diversification of taxa in the lowlands of the Amazon Basin (see (Albert et al., 2021) and references therein). The region of the Fitzcarrald Arch, including the Madre de Dios Basin, has high fish diversity with relatively ancient fish species that originated before the uplift of the Fitzcarrald Arch (Albert et al., 2011). The fish species richness of the Amazon Basin is higher in the western part with fish dispersal progressing eastward (Oberdorff et al., 2019) after the Amazon River became transcontinental during the late Miocene (Figueiredo et al., 2009; Gorini et al., 2014; van Soelen et al., 2017) and the Pliocene uplift of the Fitzcarrald Arch (Espurt et al., 2007, 2011a). Interestingly, the Madre de Dios Basin has one of the highest fish species richness and the fish highest endemic richness of western Amazonian basins (Oberdorff et al., 2019) that probably originated from the Miocene times and might be due to geographic isolation (dispersal limitation). We therefore suggest that the long lived drainage divide within the Madre de Dios Basin might be one of the driver for the inherited high diversity and rich endemism of the fish species.

6. Conclusions

The combination of field work, stratigraphic correlation using a new subsurface dataset and provenance data (major and trace element concentrations, Sr-Nd isotopes, and zircon U-Pb dating) from the Madre de Dios Basin yields the following conclusions:

- The Neogene fine-grained sedimentary rocks of the northern part of the Madre de Dios Basin have trace element ratios (Cr/Th and Th/Sc) and REE patterns that typify felsic/silicic source;
- They are characterized Solimões like ƐNd (0) values for fine-grained sedimentary rocks and zircons sourced by the Altiplano and EC;
- Contrasting REE composition of leached Fe-oxides in the Pongo de Coneq and Inambari sections indicates different lithological sources for sediments
- The zircon age distribution of the Neogene sedimentary rocks indicates sources located in the Altiplano, EC and SAZ;
- The Neogene sedimentary rocks of the northern part of the Madre de Dios Basin have a different provenance than the Neogene sedimentary rocks of the southern part of the Madre de Dios Basin which are characterized by Madeira like ƐNd (0) values and zircon sourced by the EC and SAZ (Moizinho et al., 2023);
- The difference in provenance is likely due to the existence of a paleogeographic barrier within the Madre de Dios retroarc foreland Basin, but the exact location and the mechanisms responsible for the presence of this paleogeographic barrier during the Neogene remain unclear;

Finally, given that the Cretaceous sedimentary rocks of the northern and southern part de Madre de Dios Basin have different provenance (Rodrigues et al., 2023), we propose that the southern limit of the Maastrichtian to Plio-Pleistocene Amazonian paleodrainage basin was located within the Madre de Dios Basin. We also speculate that this long-lived intrabasinal drainage divide might be a driver for endemism and species diversification within the Madre de Dios Basin.

Acknowledgements

This work received financial and institutional supports by Repsol S.A., Perupetro and the IRD (Institut pour la recherche et le Développement). The field works and sedimentological analyses were undertaken during the PhD of ML. This study was also supported and funded by CAPES-COFECUB program Te 924/18 “Paléo-Amazone: evolution Néogène de l’Amazonie Brésilienne” and by the joint Brazilian-European facility for climate and geodynamic research on the Amazon River Basin sediment (CLIM-AMAZON) project.

APPENDIX 3

Major and Trace Elements Modern Amazon Basin

Table S3.1. Major elements for modern Amazon Basin river sediments in different size-fractions.

Sample River	Type	Na_2O %	MgO %	Al_2O_3 %	P_2O_5 %	K_2O %	CaO %	TiO_2 %	MnO %	Fe_2O_3 %
Negro										
Sand (>63 µm)	Bedload		0,02	0,63	0,01	0,07		1,47	0,04	1,41
Coarse to Medium Silt	Bedload	0,10	0,08	3,04	0,02	0,42		1,13	0,02	1,37
Fine Silt	Bedload	0,43	0,51	22,5	0,06	1,83	0,00	1,45	0,02	5,22
Clay	Bedload	0,18	0,50	27,5	0,08	1,21	0,00	1,11	0,01	8,04
Fe-Mn Oxides	Bedload	0,00	0,00	0,09	0,00	0,00	0,03	0,00	0,00	0,32
Solimões										
Sol-1										
Coarse to Medium Silt	SPM	2,07	1,31	14,9	0,03	2,48	0,99	0,81	0,04	3,71
Fine Silt	SPM	1,54	1,74	17,6	0,05	2,75	0,33	1,03	0,04	5,25
Clay	SPM	0,37	1,93	23,7	0,07	2,64	0,18	1,01	0,03	6,63
Fe-Mn Oxides	SPM		0,08	0,36	0,10	0,01	0,16	0,00	0,07	1,83
Sol-2										
Coarse to Medium Silt	SPM	2,09	1,21	13,2	0,03	2,24	1,07	0,74	0,04	3,37
Fine Silt	SPM	1,63	1,70	18,6	0,04	3,24	0,68	0,97	0,04	5,04
Clay	SPM	0,42	1,96	21,2	0,07	2,89	0,22	1,05	0,04	6,79
Fe-Mn Oxides	SPM		0,08	0,37	0,11	0,01	0,19	0,00	0,07	1,83
Sol-3 (Catalão Lake)										
Sand (>63 µm)	Bedload	1,60	1,38	14,9	0,06	2,56	0,98	0,89	0,04	4,37
Coarse to Medium Silt	Bedload	2,09	1,15	12,6	0,03	2,00	1,05	0,83	0,03	3,38
Fine Silt	Bedload	1,59	1,79	18,0	0,05	3,06	0,51	0,92	0,04	5,35
Clay	Bedload	0,52	1,85	21,8	0,08	2,71	0,12	0,85	0,03	6,98
Fe-Mn Oxides	Bedload	0,00	0,07	0,3	0,08	0,01	0,21	0,00	0,03	1,16
Madeira										
Mad-1										
Coarse to Medium Silt	SPM	1,06	0,89	14,1	0,04	2,71		0,72	0,02	3,24
Fine Silt	SPM	0,85	1,27	20,5	0,07	3,41		0,95	0,03	5,24
Clay	SPM	0,39	1,35	22,0	0,14	3,89	0,04	0,77	0,03	7,56
Fe-Mn Oxides	SPM		0,05	0,27	0,04	0,01	0,12	0,00	0,04	1,63

Mad-2										
Sand (>63 µm)	Bedload	0,47	0,42	5,71	0,03	1,45	0,19	0,43	0,02	2,03
Coarse to Medium Silt	Bedload	0,94	0,82	10,4	0,04	2,09	0,06	0,94	0,03	3,52
Fine Silt	Bedload	0,79	1,49	20,6	0,09	4,25	0,06	1,16	0,04	6,45
Clay	Bedload	0,34	1,61	23,4	0,16	4,28	0,02	0,95	0,04	9,12
Fe-Mn Oxides	Bedload	0,00	0,03	0,16	0,04	0,01	0,07	0,00	0,04	0,84
Mad-3										
Clays		0,33	1,65	23,0	0,21	3,03	0,14	1,08	0,05	9,88
Fe-Mn Oxides		0,00	0,02	0,13	0,04	0,01	0,06	0,00	0,02	0,41
Tapajós										
Sand (>63 µm)	Bedload		0,00	0,22	0,00	0,03		0,06	0,00	0,09
Coarse to Medium Silt	Bedload	0,36	0,26	2,63	0,02	0,44	0,18	0,86	0,02	2,16
Fine Silt	Bedload	0,01	0,63	16,7	0,07	0,67		1,40	0,02	5,88
Clay	Bedload		0,37	31,5	0,10	0,67		1,12	0,01	5,56
Fe-Mn Oxides	Bedload		0,01	0,17	0,19	0,00	0,05	0,00	0,00	1,43
Amazon River (Post-Madeira)										
AMZ-1 (Camaleão Island)										
Coarse to Medium Silt	SPM	1,88	1,25	12,65	0,02	2,12	0,91	0,77	0,03	3,51
Fine Silt	SPM	1,42	1,90	19,21	0,05	3,34	0,48	1,09	0,04	5,67
Clay	SPM	0,30	1,96	22,87	0,07	2,77	0,14	1,05	0,03	7,15
Fe-Mn Oxides	SPM	-0,01	0,08	0,36	0,09	0,01	0,14	0,00	0,05	1,29
AMZ-2 (Pre Madeira)										
Coarse to Medium Silt	SPM	2,12	1,26	15,32	0,03	2,54	1,05	0,78	0,04	3,56
Fine Silt	SPM	1,51	1,75	19,36	0,05	2,87	0,36	0,94	0,04	5,18
Clay	SPM	0,43	1,89	23,26	0,08	2,87	0,18	0,98	0,03	6,96
Fe-Mn Oxides	SPM		0,07	0,35	0,09	0,01	0,19	0,00	0,07	1,82
AMZ-3										
Coarse to Medium Silt	SPM	1,97	1,17	13,01	0,03	2,38	0,89	0,78	0,03	3,39
Fine Silt	SPM	1,36	1,41	18,01	0,05	2,73	0,30	0,88	0,03	4,50
Clay	SPM	0,51	1,81	24,38	0,10	3,62	0,16	1,03	0,03	7,62
Fe-Mn Oxides	SPM		0,06	0,33	0,06	0,01	0,19	0,00	0,02	1,14
AMZ-4 (Serpa)										
Sand (>63 µm)	Bedload	1,30	1,24	13,58	0,05	2,67	0,71	0,84	0,04	4,11
Coarse to Medium Silt	Bedload	1,67	1,05	11,10	0,03	2,23	0,65	0,80	0,03	3,31
Fine Silt	Bedload	1,32	1,56	17,14	0,06	3,44	0,36	1,04	0,04	5,26
Clay	Bedload	0,45	1,90	22,95	0,10	3,44	0,10	0,93	0,04	7,74
Fe-Mn Oxides	Bedload	0,00	0,06	0,23	0,06	0,01	0,17	0,00	0,03	0,90
AMZ-5 (Mocambo)										
Sand (>63 µm)	Bedload	0,92	0,35	5,61	0,03	1,58	0,45	0,21	0,02	1,57

Coarse to Medium Silt	SPM	1,89	1,18	13,91	0,03	2,37	0,94	0,80	0,03	3,53
Fine Silt	SPM	1,53	1,80	19,21	0,06	3,61	0,53	1,08	0,04	5,67
Clay	SPM	0,45	1,91	23,64	0,10	3,28	0,15	1,01	0,04	7,83
Fe-Mn Oxides	SPM	0,00	0,06	0,28	0,07	0,01	0,18	0,00	0,07	1,48
AMZ-6 (Parintins)										
Sand (>63 µm)	Bedload	1,13	0,68	7,76	0,02	1,72	0,81	0,44	0,02	2,24
Coarse to Medium Silt	Bedload	1,27	0,86	9,03	0,03	1,60	0,79	1,12	0,05	3,62
Fine Silt	Bedload	0,98	1,65	16,60	0,05	2,59	0,36	1,16	0,04	5,91
Clay	Bedload	0,12	2,00	22,88	0,09	2,66		1,15	0,04	7,84
Fe-Mn Oxides	Bedload		0,04	0,15	0,07	0,00	0,08	0,00	0,02	0,62
AMZ-7 (Juruti)										
Sand (>63 µm)	Bedload	1,32	0,87	10,03	0,03	2,22	0,79	0,45	0,03	2,90
Coarse to Medium Silt	Bedload	1,52	0,86	9,02	0,02	1,75	0,78	0,77	0,03	2,81
Fine Silt	Bedload	1,40	1,91	19,43	0,06	3,53	0,35	1,14	0,04	6,66
Clay	Bedload	0,44	1,95	24,16	0,09	3,01	0,06	0,97	0,04	8,13
Fe-Mn Oxides	Bedload	0,00	0,04	0,14	0,07	0,00	0,10	0,00	0,02	0,57
AMZ-8 (Óbidos)										
Coarse to Medium Silt	SPM	1,85	1,04	14,61	0,03	2,75	0,67	0,70	0,03	3,16
Fine Silt	SPM	1,40	1,53	18,82	0,05	3,70	0,42	0,94	0,03	4,87
Clay	SPM	0,43	1,83	23,15	0,08	3,47	0,14	1,00	0,03	7,21
Fe-Mn Oxides	SPM		0,06	0,33	0,09	0,01	0,18	0,00	0,10	2,09
AMZ-9 (Óbidos)										
Sand (>63 µm)	Bedload	1,29	0,72	8,46	0,03	1,88	0,82	0,43	0,02	2,34
Coarse to Medium Silt	Bedload	1,49	0,98	10,67	0,03	2,00	0,74	0,83	0,03	3,17
Fine Silt	Bedload	1,20	1,86	19,60	0,06	3,47	0,25	1,03	0,04	6,31
Clay	Bedload	0,48	1,74	22,90	0,10	2,84	0,07	0,91	0,04	8,10
Fe-Mn Oxides	Bedload	0,00	0,06	0,25	0,10	0,01	0,15	0,00	0,04	1,22
AMZ-10 (AMA-8)										
Sand (>63 µm)	Bedload	1,10	0,69	7,54	0,02	1,68	0,80	0,52	0,03	2,41
Coarse to Medium Silt	Bedload	1,44	0,90	9,67	0,03	1,99	0,64	0,89	0,03	3,20
Fine Silt	Bedload	1,28	1,65	18,02	0,05	3,38	0,31	1,02	0,04	5,73
Clay	Bedload	0,46	1,70	21,92	0,11	2,96	0,05	0,82	0,03	8,46
Fe-Mn Oxides	Bedload	0,00	0,04	0,16	0,07	0,00	0,09	0,00	0,02	0,98
Post Tapajós										
AMZ-11										
Coarse to Medium Silt	SPM	1,62	1,13	13,83	0,03	2,42	0,58	0,78	0,03	3,36
Fine Silt	SPM	1,22	1,91	18,32	0,06	3,46	0,49	1,12	0,04	5,75
Clay	SPM	0,22	1,90	23,15	0,08	2,91	0,07	1,12	0,03	7,16
Fe-Mn Oxides	SPM		0,07	0,30	0,07	0,01	0,11	0,00	0,07	1,71

Table S3.2. Trace elements for modern Amazon Basin river sediments in different size-fractions.

Sample	Type	Li	Rb	Sr	Y	Zr	La	Ce	Pr	Nd	Sm	Eu	Gd	Tb	Dy	Ho	Er	Yb	Lu	Hf	Th	U	Ni	Cu	Zn
River		ppm	ppm	ppm	ppm	ppm	ppm	ppm	ppm	ppm	ppm	ppm	ppm	ppm	ppm	ppm	ppm	ppm	ppm	ppm	ppm	ppm	ppm	ppm	ppm
Negro																									
Sand (>63 µm)	Bedload	4,20	2,37	7,00	9,89	668	18,1	34,7	3,86	13,5	2,28	0,30	1,74	0,26	1,49	0,33	1,09	1,78	0,32	18,4	7,28	3,42	1,22	2,46	48,1
Coarse to Medium Silt		9,95	16,6	19,2	38,7	985	23,4	47,9	5,52	20,6	3,99	0,54	4,07	0,78	5,30	1,24	4,00	5,06	0,81	26,5	11,7	5,66	3,35	3,72	37,3
Fine Silt		37,0	83,7	75,8	31,4	311	52,5	84,3	10,7	36,9	6,08	1,04	4,68	0,80	5,05	1,08	3,11	3,41	0,51	8,44	15,6	4,48	28,96	11,78	73,6
Clay		38,9	66,9	58,7	17,0	146	46,0	72,0	8,29	27,5	4,31	0,78	3,19	0,48	2,86	0,60	1,75	1,94	0,29	4,04	17,4	3,37	26,76	11,53	68,3
Fe-Mn Oxides			0,49	1,91	1,47	0,11	2,85	6,40	0,54	1,91	0,31	0,06	0,29	0,04	0,23	0,05	0,12	0,10	0,01	0,01	0,07	0,07	0,42	0,21	13,46
Solimões																									
Sol-1																									
Coarse to Medium Silt	SPM	38,1	86,2	233	25,0	130	27,0	53,6	6,22	23,4	4,30	0,60	3,81	0,62	3,90	0,85	2,43	2,44	0,36	3,67	8,16	2,41	19,8	15,7	55,9
Fine Silt		59,9	125	187	25,6	127	42,3	81,0	9,37	34,0	5,65	0,75	4,31	0,64	4,07	0,88	2,60	2,63	0,38	3,57	11,48	2,96	30,2	24,1	79,0
Clay		75,3	129	119	23,4	136	50,6	94,6	10,9	38,2	6,33	1,11	4,19	0,64	3,96	0,81	2,35	2,65	0,39	3,91	15,73	3,28	36,53	24,44	125
Fe-Mn Oxides			3,45	8,19	8,91	0,98	6,73	18,4	2,10	8,94	2,01	0,44	2,07	0,29	1,57	0,30	0,76	0,57	0,07	0,04	0,09	0,24	3,55	2,53	15,3
Sol-2																									
Coarse to Medium Silt	SPM	33,0	81,24	231,77	22,74	113,30	24,39	48,34	5,62	21,07	3,87	0,56	3,40	0,57	3,62	0,76	2,27	2,27	0,32	3,14	7,39	2,17	17,99	15,40	47,43
Fine Silt		63,4	123,45	190,60	24,07	126,51	38,27	74,06	8,58	30,50	5,18	0,93	3,96	0,63	3,84	0,82	2,35	2,53	0,35	3,56	10,89	2,70	29,48	22,47	85,21
Clay		75,3	134,95	130,85	25,09	151,65	54,70	104,23	11,85	41,48	6,84	1,18	4,82	0,68	4,04	0,87	2,56	2,85	0,41	4,11	16,60	3,41	38,80	26,58	106,45
Fe-Mn Oxides			3,61	8,43	8,62	0,59	6,35	17,53	1,98	8,51	1,92	0,42	1,94	0,28	1,50	0,28	0,72	0,55	0,07	0,02	0,09	0,23	3,41	2,55	15,80
Sol-3 (Catalão Lake)																									
Sand (>63 µm)	Bedload	41,92	93,09	198,55	28,28	142,06	32,20	64,74	7,53	27,8	5,18	1,02	4,41	0,72	4,57	0,96	2,86	2,85	0,39	4,11	10,06	2,57	22,57	22,13	70,11

Coarse to Medium Silt		33,13	79,44	223,07	26,72	132,87	27,59	54,74	6,34	23,5	4,38	0,65	3,90	0,66	4,22	0,89	2,66	2,59	0,37	3,72	8,10	2,40	16,94	13,43	43,92
Fine Silt		65,60	121,89	156,52	22,70	118,53	38,04	73,11	8,50	29,8	5,05	0,91	3,81	0,59	3,62	0,79	2,24	2,37	0,33	3,34	11,47	2,62	31,01	21,66	87,30
Clay		69,49	133,37	88,59	22,53	136,31	44,54	86,11	9,87	35,3	6,15	1,15	4,61	0,65	3,67	0,75	2,16	2,36	0,34	3,94	14,50	2,91	34,65	23,53	106,36
Fe-Mn Oxides			1,71	9,04	7,32	0,18	5,10	13,35	1,57	6,7	1,54	0,33	1,58	0,24	1,27	0,24	0,60	0,45	0,05	0,01	0,09	0,18	2,70	1,72	16,74
Madeira																									
Mad-1																									
Coarse to Medium Silt		65,45	116,79	82,10	27,54	115,10	29,55	59,32	6,83	25,7	4,65	0,62	3,91	0,68	4,42	0,94	2,64	2,64	0,38	3,16	8,40	2,32	20,24	13,78	67,46
Fine Silt	SPM	97,99	169,23	111,68	26,49	104,91	48,51	96,12	11,14	40,9	7,09	0,96	5,08	0,74	4,43	0,91	2,62	2,69	0,38	2,90	12,57	2,78	33,90	19,21	85,81
Clay		116,56	205,22	117,50	32,00	118,11	77,37	139,47	17,35	62,5	11,40	2,05	7,76	1,04	5,71	1,11	3,13	3,27	0,47	3,32	22,30	3,21	41,07	24,98	73,76
Fe-Mn Oxides			3,31	6,10	7,18	0,56	3,64	11,26	1,34	6,2	1,66	0,40	1,93	0,27	1,40	0,25	0,58	0,38	0,05	0,03	0,10	0,21	2,78	2,19	11,88
Mad-2																									
Sand (>63 µm)		27,78	49,39	53,92	13,19	106,28	19,23	39,86	4,65	17,4	3,21	0,58	2,54	0,37	2,25	0,46	1,32	1,31	0,19	2,96	4,96	1,25	11,58	6,92	25,30
Coarse to Medium Silt		55,01	95,24	75,21	35,36	282,69	38,76	78,76	9,20	34,2	6,29	0,94	5,40	0,90	5,63	1,19	3,42	3,46	0,50	7,72	11,17	3,38	18,58	9,93	48,22
Fine Silt	Bedload	124,19	184,92	116,82	33,58	137,33	58,24	114,18	13,38	48,4	8,43	1,46	6,25	0,95	5,59	1,16	3,29	3,35	0,47	3,82	16,70	3,40	40,15	21,67	89,77
Clay		125,33	198,26	123,36	29,05	140,19	70,93	138,17	15,95	57,5	10,03	1,78	6,85	0,92	5,10	1,05	2,95	3,20	0,46	3,90	24,35	3,73	47,27	29,00	89,21
Fe-Mn Oxides			2,16	3,28	5,21	0,14	2,48	7,62	0,91	4,3	1,19	0,28	1,40	0,20	1,04	0,18	0,42	0,29	0,03	0,01	0,07	0,12	2,20	1,41	9,63
Mad-3																									
Clays	Bedload	122,3	159,33	126,49	36,78	184,46	62,39	124,08	14,79	54,61	10,15	1,95	7,58	1,15	6,68	1,34	3,76	3,74	0,53	5,22	24,24	4,14	52,60	56,30	124,00
Fe-Mn Oxides		0,5	0,82	5,31	3,04	0,05	1,68	4,83	0,56	2,6	0,69	0,16	0,76	0,11	0,58	0,10	0,24	0,17	0,02	0,01	0,03	0,10	2,19	2,99	5,00
Tapajós																									
Sand (>63 µm)		1,82	0,41	1,75	1,46	15,94	2,97	6,35	0,66	2,2	0,39	0,07	0,26	0,04	0,25	0,05	0,15	0,17	0,03	0,44	0,97	0,20	0,19	1,28	3,78
Coarse to Medium Silt		8,49	14,34	41,34	62,40	2475,87	40,01	86,32	9,64	35,9	7,29	1,01	6,80	1,22	8,47	2,01	6,86	10,12	1,69	66,43	33,81	10,14	4,84	4,11	28,68
Fine Silt	Bedload	25,69	65,64	67,16	34,40	368,04	44,16	76,46	8,43	28,3	5,12	0,98	4,28	0,73	5,32	1,17	3,69	4,60	0,61	9,96	17,95	5,07	27,28	12,57	122,58
Clay		31,02	48,82	36,58	22,29	208,42	72,25	122,94	12,11	37,7	5,97	1,06	4,35	0,67	3,87	0,82	2,34	2,67	0,38	5,94	23,86	3,32	21,31	12,89	62,75
Fe-Mn Oxides			0,60	2,45	6,33	0,49	10,38	25,29	2,98	11,3	2,02	0,36	1,64	0,23	1,24	0,23	0,58	0,47	0,06	0,02	0,05	0,16	1,32	1,70	68,31

Amazon River (Post-Madeira)																									
AMZ-1 (Camaleão Island)																									
Coarse to Medium Silt		36,7	85,2	197	21,9	107,10	24,81	49,5	5,68	21,3	3,90	0,54	3,39	0,56	3,49	0,75	2,19	2,19	0,30	2,97	7,43	2,15	21,21	13,58	50,01
Fine Silt	SPM	70,4	135	153	27,45	132,69	43,75	83,9	9,73	34,9	5,91	1,04	4,51	0,72	4,47	0,93	2,75	2,87	0,40	3,75	12,32	3,07	38,11	22,19	118,28
Clay		72,5	132	101	24,45	150,13	54,24	102	11,69	40,6	6,69	1,22	4,65	0,68	4,03	0,85	2,51	2,78	0,40	4,13	17,11	3,43	42,35	23,95	109,42
Fe-Mn Oxides			3,42	6,81	6,83	0,88	6,28	17,19	1,83	7,53	1,61	0,34	1,59	0,23	1,22	0,23	0,57	0,44	0,06	0,04	0,14	0,16	2,80	0,94	24,04
AMZ-2 (Pre Madeira)																									
Coarse to Medium Silt		37,4	86,5	235	24,7	139	26,1	52,1	6,03	22,5	4,12	0,57	3,52	0,60	3,85	0,82	2,40	2,43	0,35	3,76	8,02	2,33	20,3	15,4	59,1
Fine Silt	SPM	60,7	127	172	22,6	118	38,8	75,4	8,62	31,1	5,27	0,67	3,89	0,59	3,73	0,78	2,29	2,36	0,34	3,30	10,7	2,70	31,7	23,6	89,9
Clay		79,0	138	114	23,9	145	50,6	96,8	11,0	38,5	6,50	1,15	4,40	0,66	3,92	0,83	2,50	2,70	0,38	3,96	16,5	3,33	38,2	24,2	115
Fe-Mn Oxides			3,10	8,56	7,69	1,03	5,89	17,0	1,82	7,68	1,70	0,37	1,77	0,25	1,34	0,26	0,65	0,49	0,06	0,04	0,10	0,22	2,85	1,45	13,95
AMZ-3																									
Coarse to Medium Silt		41,2	91	213	24	121	26	51	6	22	4,0	0,55	3,56	0,6	3,90	0,83	2,38	2,39	0,34	3,35	7,70	2,29	19	14	60
Fine Silt	SPM	66,5	130	157	23	105	39	75	9	32	5,34	0,68	3,91	0,59	3,66	0,77	2,26	2,28	0,33	2,87	10,4	2,57	28	20	87
Clay		97,9	168	129	26	149	60	114	13	46	7,85	1,40	5,44	0,76	4,44	0,92	2,73	2,93	0,43	4,13	19,3	3,66	42	26	114
Fe-Mn Oxides			3,23	8,58	7,74	0,53	5,48	15,5	1,71	7,29	1,67	0,38	1,75	0,25	1,36	0,25	0,64	0,46	0,06	0,02	0,06	0,18	2,24	1,56	11,8
AMZ-4 (Serpa)																									
Sand (>63 µm)		50,1	97,6	155	28,5	161	31	62	7	27	4,88	0,95	4,31	0,71	4,54	0,96	2,80	2,88	0,41	4,61	9,72	2,53	24	19	66
Coarse to Medium Silt		42,3	86,1	165	28,6	153	28	56	7	24	4,55	0,66	4,10	0,69	4,48	0,97	2,76	2,78	0,41	4,30	8,33	2,52	20	12	53
Fine Silt	Bedload	77,0	138	142	28,9	141	47	90	11	38	6,45	1,16	4,73	0,75	4,66	0,99	2,80	2,91	0,41	3,91	13,0	3,00	30	19	76
Clay		89,0	162	102	25,5	146	53	103	12	42	7,32	1,32	5,14	0,74	4,27	0,88	2,52	2,81	0,40	4,15	19,6	3,38	40	27	105
Fe-Mn Oxides			1,75	7,33	5,84	0,12	3,80	10,5	1,21	5,25	1,26	0,28	1,32	0,20	1,03	0,19	0,48	0,35	0,04	0,01	0,07	0,13	2,34	1,16	13

AMZ-5 (Mocambo)																								
Sand (>63 µm)	Bedload	17,0	46,2	94,4	8,84	37,3	12,9	26,5	3,03	11,3	2,14	0,50	1,76	0,27	1,53	0,30	0,81	0,81	0,11	1,09	3,16	0,67	9,07	5,06	18,4
Coarse to Medium Silt		40,3	85,5	205	23,5	122	27	54	6	23	4,26	0,59	3,64	0,60	3,78	0,79	2,27	2,34	0,33	3,43	8,16	2,29	18,3	13,1	51,7
Fine Silt		167	142	162	27,0	134	44	85	10	35	6,08	1,09	4,56	0,71	4,35	0,91	2,67	2,81	0,39	3,76	13,3	3,0	34,9	23,6	97
Clay		89,6	149	114	25,9	149	56	107	12	43	7,48	1,33	5,44	0,74	4,38	0,90	2,66	2,84	0,42	4,20	19,2	3,6	40,5	26,3	115
Fe-Mn Oxides			2,55	8,24	6,58	0,88	4,81	13,8	1,47	6,29	1,42	0,32	1,49	0,22	1,16	0,22	0,55	0,41	0,05	0,03	0,13	0,20	2,79	1,00	14,0
AMZ-6 (Parintins)																									
Sand (>63 µm)	Bedload	22,7	53,2	143	14,9	86,5	17,1	34,3	3,93	14,4	2,60	0,58	2,30	0,38	2,40	0,50	1,43	1,41	0,20	2,24	4,60	1,12	13,4	7,46	37,9
Coarse to Medium Silt		28,1	54,9	141	40,3	520	42,5	85,2	9,86	36,5	6,75	1,00	5,98	1,00	6,17	1,33	3,95	4,32	0,66	14,50	14,6	4,56	15,2	8,81	39,0
Fine Silt		77,0	132	140	31,4	192	47,1	93,4	10,8	39,3	6,95	1,28	4,98	0,79	4,95	1,10	3,16	3,44	0,50	5,29	12,4	3,48	44,3	21,4	112
Clay		89,4	153	118	28,0	136	61,6	119	13,6	48,8	8,27	1,39	5,47	0,79	4,65	0,98	2,80	3,15	0,43	3,84	17,9	3,58	53,6	24,8	89,3
Fe-Mn Oxides			2,11	2,83	4,92	0,24	3,60	9,37	1,16	5,04	1,19	0,24	1,24	0,18	0,93	0,17	0,42	0,31	0,04	0,01	0,08	0,09	2,02	1,40	11,3
AMZ-7 (Juruti)																									
Sand (>63 µm)	Bedload	31,4	71,6	161	12,6	67,9	18,1	35,6	4,07	15,1	2,77	0,57	2,29	0,35	2,08	0,43	1,24	1,24	0,18	1,94	5,34	1,22	18,9	11,1	47,7
Coarse to Medium Silt		31,2	63,4	158	24,3	180	31,8	63,6	7,32	27,0	4,91	0,74	4,08	0,64	3,88	0,82	2,35	2,37	0,35	4,96	8,61	2,39	14,6	8,66	30,8
Fine Silt		86,8	156	137	30,3	161	49,0	97,1	11,0	39,2	6,76	1,20	5,01	0,80	4,88	1,04	3,03	3,13	0,44	4,49	14,9	3,24	44,3	24,1	103
Clay		84,1	155	100	24,3	145	58,2	112	12,9	45,9	7,43	1,30	4,92	0,70	3,98	0,84	2,42	2,75	0,38	4,14	16,4	3,36	44,7	23,7	127
Fe-Mn Oxides			1,51	3,41	4,25	0,15	2,86	7,57	0,93	4,03	0,98	0,21	1,03	0,15	0,80	0,14	0,36	0,26	0,03	0,01	0,07	0,08	1,91	1,16	11,6
AMZ-8 (Óbidos)																									
Coarse to Medium Silt	SPM	44,4	94,8	183	23,2	102	25	49,1	5,62	21,1	3,79	0,49	3,35	0,57	3,63	0,79	2,23	2,24	0,32	2,88	7,08	2,08	37,9	12,7	47,8
Fine Silt		82,4	152	160	24,6	118	42	83,1	9,51	34,5	5,89	1,02	4,32	0,65	4,02	0,83	2,44	2,58	0,36	3,35	11,9	2,76	35,3	20,1	85,5
Clay		95,3	163	122	25,1	141	58	110	12,6	44,0	7,39	1,28	5,04	0,73	4,20	0,89	2,64	2,77	0,40	3,96	19,6	3,44	42,4	26,4	108
Fe-Mn Oxides			3,33	8,35	7,66	0,85	5,56	16,1	1,74	7,47	1,71	0,39	1,77	0,26	1,38	0,26	0,64	0,48	0,06	0,03	0,13	0,25	10,1	2,76	16,6

AMZ-9 (Óbidos)																								
Sand (>63 µm)	Bedload	25,9	58,8	159	12,9	79,2	19,6	39,1	4,50	16,4	2,96	0,63	2,29	0,35	2,17	0,43	1,30	1,26	0,18	2,29	4,56	1,14	14,1	8,60	39,0
Coarse to Medium Silt		35,6	71,0	152	29,0	225	34,5	68,9	8,07	30,0	5,57	0,85	4,64	0,76	4,63	0,97	2,86	2,91	0,43	6,21	9,54	2,81	17,1	9,85	36,3
Fine Silt		90,0	152	122	25,6	136	47,1	93,7	10,7	38,3	6,53	1,12	4,67	0,70	4,22	0,89	2,50	2,66	0,38	3,86	14,2	2,99	40,7	22,5	87,0
Clay		78,8	143	89,5	22,4	138	54,7	104	12,0	42,3	6,90	1,21	4,70	0,63	3,70	0,77	2,24	2,51	0,36	3,96	17,2	3,19	38,7	23,9	101
Fe-Mn Oxides			2,38	5,46	7,48	0,28	5,22	14,2	1,64	7,05	1,69	0,36	1,75	0,26	1,35	0,25	0,63	0,46	0,05	0,01	0,14	0,17	2,91	1,50	16,7
AMZ-10 (AMA-8)																								
Sand (>63 µm)	Bedload	23,2	54	137	14,8	86,5	22,2	44,0	4,94	18,1	3,29	0,67	2,68	0,42	2,52	0,49	1,43	1,43	0,20	2,55	5,00	1,34	13,2	7,85	29,3
Coarse to Medium Silt		36,6	73	145	37,0	349	38,1	77,3	9,00	33,7	6,33	0,90	5,52	0,92	5,79	1,24	3,66	3,76	0,55	9,64	11,3	3,58	16,0	9,45	33,2
Fine Silt		86,1	142	130	27,8	152	44,7	87,4	10,1	36,2	6,28	1,13	4,77	0,73	4,46	0,96	2,74	2,89	0,39	4,33	13,3	2,90	37,9	19,58	87,3
Clay		84,7	148	86,0	22,1	128	51,4	100	11,5	41,1	7,04	1,24	4,76	0,65	3,65	0,76	2,23	2,44	0,36	3,62	16,9	2,97	40,3	21,40	110,6
Fe-Mn Oxides			1,69	3,32	4,64	0,17	2,96	8,15	0,97	4,26	1,05	0,23	1,10	0,16	0,87	0,16	0,40	0,29	0,03	0,01	0,08	0,11	1,76	1,32	9,90
Post Tapajós																								
AMZ-11																								
Coarse to Medium Silt	SPM	45,8	95,2	161	24,7	126	27,2	55,3	6,29	23,7	4,29	0,59	3,72	0,62	3,91	0,83	2,40	2,44	0,35	3,46	8,43	2,34	20,8	13,1	54,3
Fine Silt		87,1	150	149	28,2	128	46,1	89,2	10,4	37,3	6,49	1,12	4,81	0,75	4,54	0,95	2,80	2,93	0,41	3,63	12,8	3,00	36,9	21,4	96,8
Clay		87,36	154	119	26,5	145	62,3	117	13,4	46,8	7,73	1,34	5,31	0,77	4,38	0,94	2,81	2,95	0,45	3,98	19,0	3,61	42,6	22,4	95,9
Fe-Mn Oxides			4,21	5,50	7,94	1,22	6,61	17,4	2,01	8,44	1,87	0,41	1,91	0,27	1,45	0,27	0,66	0,49	0,06	0,05	0,12	0,23	3,17	1,66	15,4

Table S3.3. Hf-Nd isotopic compositions of modern amazon basin river sediments.

Sample	Type	$^{143}Nd/^{144}Nd$	2se	εNd(0)	2 σ	$^{176}Hf/^{177}Hf$	2se	εHf(0)	2 σ	ΔεHf
River										
Negro										
Sand (>63 µm)	Bedload	0,512150	0,000010	-9,4	0,2					
Coarse to Medium Silt		0,511961	0,000007	-13,0	0,1					
Fine Silt		0,511857	0,000006	-15,1	0,1					
Clay		0,511852	0,000006	-15,19	0,1	0,282715	0,000008	-2,47	0,27	4,1
Fe-Mn Oxides		0,511859	0,000005	-15,0	0,1					
Solimões										
Sol-1										
Coarse to Medium Silt	SPM	0,512180	0,000011	-8,8	0,2					
Fine Silt		0,512093	0,000008	-10,5	0,2					
Clay		0,512099	0,000009	-10,36	0,2	0,282747	0,000011	-1,34	0,38	1,4
Fe-Mn Oxides		0,512381	0,000008	-4,9	0,2					
Sol-2										
Coarse to Medium Silt	SPM	0,512159	0,000005	-9,2	0,1					
Fine Silt		0,512100	0,000005	-10,3	0,1					
Clay		0,512090	0,000009	-10,54	0,2	0,282917	0,000009	4,68	0,30	6,7
Fe-Mn Oxides		0,512362	0,000009	-5,2	0,2					
Sol-3 (Catalão Lake)										
Sand (>63 µm)	Bedload	0,512155	0,000008	-9,3	0,2					
Coarse to Medium Silt		0,512181	0,000010	-8,8	0,2					
Fine Silt		0,512108	0,000006	-10,2	0,1					
Clay		0,512148	0,000005	-9,40	0,1					
Fe-Mn Oxides		0,512378	0,000005	-4,9	0,1					
Madeira										
Mad-1										
Coarse to Medium Silt	SPM	0,512039	0,000016	-11,5	0,3					
Fine Silt		0,512015	0,000034	-12,0	0,7					
Clay		0,512050	0,000006	-11,31	0,1	0,282685	0,000008	-3,53	0,27	0,0
Fe-Mn Oxides		0,512219	0,000007	-8,0	0,1					
Mad-2										
Sand (>63 µm)	Bedload	0,512056	0,000010	-11,2	0,2					
Coarse to Medium Silt		0,512043	0,000006	-11,5	0,1					
Fine Silt		0,512024	0,000006	-11,8	0,1					
Clay		0,512030	0,000007	-11,71	0,1	0,282737	0,000009	-1,68	0,33	2,1
Fe-Mn Oxides		0,512231	0,000007	-7,8	0,1					

Mad-3										
Clays	Bedload									
Fe-Mn Oxides										
Tapajós										
Sand (>63 µm)		0,511754	0,000014	-17,1	0,3					
Coarse to Medium Silt		0,511812	0,000004	-16,0	0,1					
Fine Silt	Bedload	0,511782	0,000013	-16,5	0,3					
Clay		0,511714	0,000007	-17,87	0,1					
Fe-Mn Oxides		0,511758	0,000005	-17,0	0,1					
Amazon River (Post-Madeira)										
AMZ-1 (Camaleão Island)										
Coarse to Medium Silt		0,512156	0,000007	-9,2	0,1					
Fine Silt	SPM	0,512076	0,000005	-10,8	0,1					
Clay		0,512074	0,000007	-10,9	0,1	0,282746	0,000011	-1,37	0,38	1,8
Fe-Mn Oxides		0,512254	0,000010	-7,3	0,2					
AMZ-2 (Pre Madeira)										
Coarse to Medium Silt		0,512160	0,000010	-9,2	0,2					
Fine Silt	SPM	0,512088	0,000006	-10,6	0,1					
Clay		0,512109	0,000007	-10,2	0,1	0,282754	0,000011	-1,11	0,39	1,5
Fe-Mn Oxides		0,512325	0,000007	-5,9	0,1					
AMZ-3										
Coarse to Medium Silt		0,512138	0,000007	-9,6	0,1					
Fine Silt	SPM	0,512061	0,000006	-11,1	0,1					
Clay		0,512075	0,000004	-10,8	0,1	0,282760	0,000007	-0,87	0,26	2,3
Fe-Mn Oxides		0,512314	0,000006	-6,2	0,1					
AMZ-4 (Serpa)										
Sand (>63 µm)		0,512088	0,000007	-10,6	0,1					
Coarse to Medium Silt		0,512107	0,000004	-10,2	0,1					
Fine Silt	Bedload	0,512055	0,000004	-11,2	0,1					
Clay		0,512099	0,000005	-10,4	0,1	0,282987	0,000009	7,13	0,32	9,9
Fe-Mn Oxides		0,512319	0,000007	-6,1	0,1					
AMZ-5 (Mocambo)										
Sand (>63 µm)		0,512221	0,000007	-8,0	0,1					
Coarse to Medium Silt		0,512197	0,000011	-8,4	0,2					
Fine Silt	Bedload	0,512079	0,000006	-10,8	0,1					
Clay		0,512096	0,000004	-10,4	0,1	0,282906	0,000014	4,28	0,50	7,1
Fe-Mn Oxides		0,512310	0,000007	-6,2	0,1					
AMZ-6 (Parintins)										

Sand (>63 µm)		0,512203	0,000006	-8,3	0,1					
Coarse to Medium Silt		0,512076	0,000005	-10,8	0,1					
Fine Silt	Bedload	0,512026	0,000009	-11,8	0,2					
Clay		0,512045	0,000012	-11,4	0,2					
Fe-Mn Oxides		0,512347	0,000006	-5,5	0,1					
AMZ-7 (Juruti)										
Sand (>63 µm)		0,512144	0,000007	-9,5	0,1					
Coarse to Medium Silt		0,512095	0,000005	-10,4	0,1					
Fine Silt	Bedload	0,512067	0,000007	-11,0	0,1					
Clay		0,512106	0,000009	-10,2	0,2					
Fe-Mn Oxides		0,512353	0,000005	-5,4	0,1					
AMZ-8 (Óbidos)										
Coarse to Medium Silt		0,512115	0,000010	-10,0	0,2					
Fine Silt	SPM	0,512063	0,000004	-11,1	0,1					
Clay		0,512075	0,000004	-10,8	0,1	0,282867	0,000008	2,89	0,28	6,0
Fe-Mn Oxides		0,512277	0,000007	-6,9	0,1					
AMZ-9 (Óbidos)										
Sand (>63 µm)		0,512150	0,000009	-9,4	0,2					
Coarse to Medium Silt		0,512080	0,000006	-10,7	0,1					
Fine Silt	Bedload	0,512047	0,000014	-11,4	0,3					
Clay		0,512082	0,000010	-10,7	0,2	0,282867	0,000008	2,89	0,28	5,9
Fe-Mn Oxides		0,512298	0,000007	-6,5	0,1					
AMZ-10 (AMA-8)										
Sand (>63 µm)		0,512146	0,000007	-9,4	0,1					
Coarse to Medium Silt		0,512085	0,000004	-10,6	0,1					
Fine Silt	Bedload	0,512059	0,000008	-11,1	0,1					
Clay		0,512113	0,000006	-10,1	0,1	0,282984	0,000018	7,05	0,65	9,6
Fe-Mn Oxides		0,512318	0,000006	-6,1	0,1					
Post Tapajós										
AMZ-11										
Coarse to Medium Silt		0,512125	0,000020	-9,9	0,4					
Fine Silt	SPM	0,512107	0,000030	-10,2	0,6					
Clay		0,512077	0,000027	-10,8	0,5					
Fe-Mn Oxides		0,512189	0,000013	-8,6	0,3					

APPENDIX 4

Orbital and sea-level controls on long-term sediment deposition in the Amazon Fan

Contents lists available at ScienceDirect

Global and Planetary Change

journal homepage: www.elsevier.com/locate/gloplacha

Research Article

Orbital and sea-level controls on long-term sediment deposition in the Amazon Fan

Gabriel R. Moizinho [a,b,c,*], Thiago P. Santos [d], Germain Bayon [a], Martin Roddaz [b], Natalia Vázquez Riveiros [a], Marina Rabineau [a], Daniel Aslanian [a], Victor Carreira [e], Elton L. Dantas [c], Roberto V. Santos [c]

[a] Geo-Ocean, Univ. Brest, CNRS, Ifremer, UMR6538, F-29280 Plouzané, France
[b] Géosciences-Environnement Toulouse, Université de Toulouse, Toulouse, France
[c] Instituto de Geociências, Universidade de Brasília (UnB), Brasília, DF, Brazil
[d] School of Arts, Sciences and Humanities, University of São Paulo, São Paulo, Brazil
[e] Programa de Pós-Graduação em Dinâmica dos Oceanos e da Terra, Universidade Federal, Fluminense, Niterói, Brazil

ARTICLE INFO

Editor: Dr. Fabienne Marret-Davies

Keywords:
Amazon Fan
Cyclostratigraphy
Orbital control
Neogene
Andes
Climate

ABSTRACT

The Amazon Fan, one of the largest deep-sea fans on Earth, is a vital archive of the Amazon Basin's long-term climate and tectonic evolution. However, the factors driving sediment deposition patterns during the Neogene remain poorly understood. Here, we present an astronomical age model for a 4800 m-long sedimentary record (BP-3 well), spanning the past ~24 million years, a key interval encompassing the Amazon River's evolution into a transcontinental system. Gamma-ray (GR) data reveal strong Milankovitch cyclicity, highlighting the fan's sensitivity to orbital climate variability and enabling correlations with global mean sea level (GMSL). Our analysis shows persistently low sedimentation rates (~5–13 cm/kyr) during the late Miocene, despite Andean uplift and increased precipitation, likely due to sediment trapping by mega-wetlands in Western Amazonia. A marked increase in sedimentation (~50 cm/kyr) during the Early Pliocene (5.1–4.8 ± 1.78 Ma) reflects the collapse of these barriers, facilitating sediment transport to the Atlantic despite high GMSL. The GR record also captures the transition from obliquity- to eccentricity-dominated glacial-interglacial cycles during the mid-Pleistocene Transition (~1.3 Ma). These findings align with GMSL and benthic $\delta^{18}O$ data, supporting a minimal tuning approach and emphasizing the Amazon Fan's sensitivity to global climate changes. Our revised chronology provides a robust framework for understanding the Neogene evolution of the Amazon River and its links to Andean tectonics and climate variability.

1. Introduction

Continental margins host unique sediment records of past fluvial discharge to the oceans, sea-level fluctuations, oceanic circulation, geodynamic and climate change (Clift et al., 2008). Submarine fans are particularly significant among these deposits, representing continental margins' largest deep-water sedimentary systems that can be used to reconstruct the interplay of terrestrial climate, regional tectonics, and sea-level variations over geological timescales (Flood and Piper, 1995). The Amazon Fan, situated at the mouth of the Amazon River, ranks among the world's largest deep-sea fan systems, spanning an area of approximately 375,000 km^2 (Fig. 1; Figueiredo et al., 2009). The Amazon Fan developed in the mid-to-late Miocene, driven by Andean orogeny and dynamic topography, which reorganized river systems across the Amazon Basin to flow eastward toward the Atlantic Ocean (Hoorn et al., 2017; Shephard et al., 2010). Since its inception, the Amazon Fan has served as the primary depocenter for sediments along the Brazilian Equatorial Margin (Figueiredo et al., 2009; Gorini et al., 2014; Hoorn et al., 2017), accumulating tremendous amounts of terrigenous material transported from the Amazon Basin. This scenario places the Amazon Fan as an exceptional repository for reconstructing northern South America's geodynamic and climatic evolution during the Neogene.

Previous efforts in this direction were conducted on sediment records drilled during the Ocean Drilling Program (ODP) Leg 155 Expedition (Fig. 1b), leading to various investigations exploring terrestrial organic

* Corresponding author.
E-mail address: gabriel.ribeiro.moizinho@ifremer.fr (G.R. Moizinho).

https://doi.org/10.1016/j.gloplacha.2025.105068
Received 23 April 2025; Received in revised form 10 September 2025; Accepted 10 September 2025

carbon accumulation in the fan, the interplay between surface and deep ocean circulation, regional moisture availability and freshwater discharge, and the evolution of the Amazon rainforest (Burns and Maslin, 1999; Maslin et al., 2000). The ODP Leg 154, while located in a more distal setting on the Ceará Rise, has been instrumental in documenting the onset of the Amazon River as a transcontinental system and the far-reaching impact of riverine discharge on the western Atlantic over million-year timescales (Stewart et al., 2016; Van Soelen et al., 2017). Recent high-resolution reconstructions of the last glacial-interglacial cycle have further emphasized the interactions between the Amazon climate and high-latitude regions, highlighting their potential impact on vegetation via changes in the Atlantic Meridional Overturning Circulation (Akabane et al., 2024 and references therein).

Seismic analyses indicate that cyclic sedimentation in the Amazon Fan comprises successions of pelagic interglacial calcareous oozes, channel-levee systems, and regionally extensive mass-transport deposits (Manley and Flood, 1988; Maslin et al., 1998). During the past 11,000 years (and likely during older interglacials), the Amazon Fan was temporarily inactive as Amazon River sediments were mostly trapped on the inner continental shelf due to high sea level and surface water circulation (Maslin et al., 2005). In contrast, fan growth was most pronounced during periods of low sea level, when the Amazon River extended across the exposed continental shelf and discharged terrigenous sediments directly into the Amazon Fan complex through the canyon and distributary channels (Figueiredo et al., 2007).

The interpretation of sedimentary sequences in the Amazon Fan is complicated by the interplay between global mean sea level (GMSL) variability and autocyclic processes like channel avulsion or mass transport deposits. Simultaneously, GMSL carries a strong imprint of orbital signals driven by Milankovitch forcing (Miller et al., 2005). Under progressively colder climate conditions since the mid-Oligocene, the growth of massive ice sheets has been highly sensitive to the

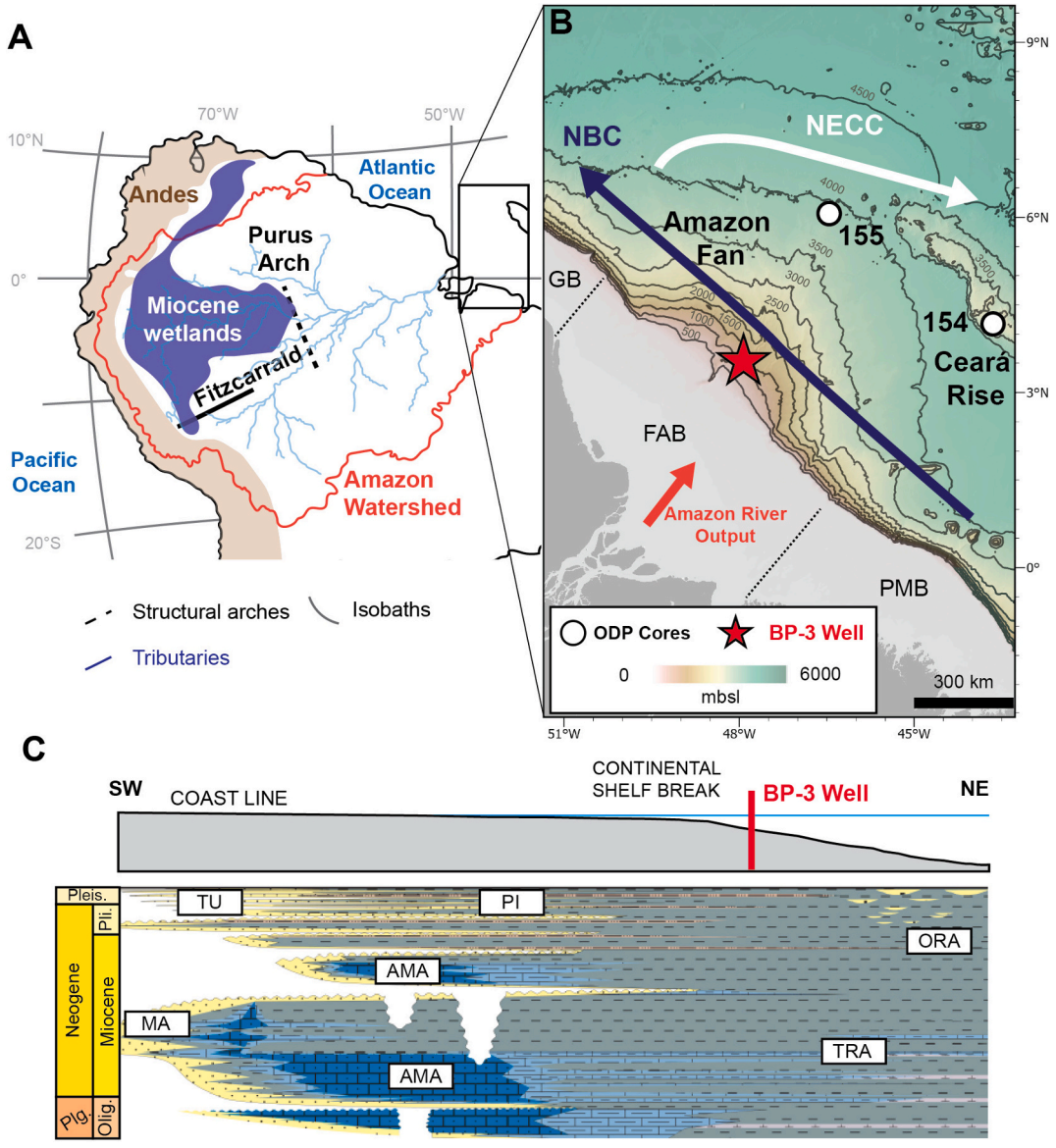

Fig. 1. (a) Map of South America illustrating the modern drainage configuration of the Amazon Basin and the sediment transport pathways of the Amazon source-to-sink system. The purple area indicates the approximate extent of the Miocene mega-wetlands in Western Amazonia (b) The offshore sedimentary basins of the Brazilian Equatorial Margin are indicated as follows: GB: Guyana Basin, FAB: Foz do Amazonas Basin, PMB: Pará-Maranhão Basin. Arrows indicate the positions of the Northern Brazilian Current (NBC) and Northern Equatorial Counter Current (NECC) (c) Upper Paleogene-Neogene stratigraphic chart of the FAB central shelf, simplified from Cruz (2019). TU: Tucunaré, PI: Pirarucu, ORA: Orange, AMA: Amapá, MA: Marajó, and TA: Travosas Formations. (For interpretation of the references to colour in this figure legend, the reader is referred to the web version of this article.)

interaction of precession, obliquity, and eccentricity, directly influencing GMSL and the formation of third-order eustatic sequences worldwide (Boulila et al., 2011; Laskar et al., 2004; Pälike et al., 2006; Westerhold et al., 2020). Astronomical forcing also plays a significant role in controlling long-term tropical hydroclimate variability and the positioning of precipitation belts, as seasonal rainfall and temperature gradients are significantly modulated by insolation, which can largely be predicted by precession and obliquity (Clement et al., 2004; Laskar et al., 2004). The well-established periodicity of precession, obliquity, and eccentricity for the last 40 million years provides an opportunity to use their sedimentary imprints as geochronometers, enabling the refinement of geological timescales and the development of high-resolution astronomically tuned chronologies (Hinnov, 2013). Such efforts have advanced our understanding of the evolution of the Neogene and the broader Cenozoic climate (Westerhold et al., 2020).

Surprisingly, cyclostratigraphy and astronomical tuning have yet to be thoroughly applied to the Neogene Amazon Fan record. Although an astronomical age model was developed for the Cretaceous Limoeiro Formation, it pertains to a period predating the Amazon River's establishment (Boulila et al., 2020). Cyclic sediment deposition, likely influenced by obliquity, has been proposed as a driver of floodplain fill packages in the Miocene wetlands of western Amazonia (Hoorn et al., 2022b). However, this hypothesis did not explicitly test the presence or absence of astronomical variability. This study recasts well-log data from the 1-BP-3-APS exploration well drilled in the upper Amazon Fan. Using the boundaries established by previous nannofossil biostratigraphic analyses (Figueiredo et al., 2009; Hoorn et al., 2017), we construct an astronomical timescale with uncertainties derived from gamma-ray (GR) well-log data. Our study uncovers previously unrecognized details of Amazon Fan deposition, offering the first explicit comparison with GMSL for the past ~24 million years. Despite the relatively consistent correlation between GMSL and long-term GR patterns, we propose that the exceptional sedimentation rate from the Plio-Pleistocene cannot be attributed solely to the decline in GMSL during this period.

2. Regional setting

The Foz do Amazonas Basin (FAB), the westernmost segment of the Brazilian Equatorial Margin, is bordered by the Guiana Basin to the west and the Pará-Maranhão Basin to the east (Fig. 1b). Covering an area of approximately 360,000 km^2, the FAB hosts sedimentary deposits up to 9000 m thick. Between the late Paleocene and late Miocene (ca. 61.7–8.0 Ma), carbonate platforms were the dominant depositional environment in the basin, resulting in the accumulation of around 4000 m of mixed carbonate-siliciclastic shelf sediments (Marajó and Amapá Formations) and deep-water calcilutites and mudstones (Fig. 1c; Figueiredo et al., 2007). During the Langhian stage of the mid-Miocene (~15.2 Ma), a globally warm climate led to high sea levels, marked in the FAB by a maximum flooding surface on the Amapá Platform. This transgressive event caused the Marajó Formation coastal systems to retreat and promoted carbonate platform development on the outer shelf (Figueiredo et al., 2007). However, subsequent sea-level decline during the Tortonian (~9.5–8.0 Ma), coupled with an increase in siliciclastic sediment supply, heightened water turbidity and drove shoreline progradation. These processes led to the exposure and erosion of carbonate platforms, effectively terminating carbonate deposition in the FAB (Figueiredo et al., 2009; Gorini et al., 2014). Cruz et al. (2019) further revealed a south-to-north sedimentary filling pattern in the FAB, with siliciclastic deposition beginning in the southeast around ~8 Ma and reaching the northwest by ~3.7 Ma. This progressive sedimentation preserved carbonate deposition in the northwest FAB for extended periods, reflecting spatial variability in sediment delivery and deposition dynamics.

The Neogene sedimentary history of the Amazon Fan reflects the interplay of Andean orogeny, dynamic topography, climate variability, and sea-level changes (Shephard et al., 2010; Hoorn et al., 2017; Albert et al., 2018). During the mid-Miocene (~16–11.5 Ma), Andean surface uplift induced flexural subsidence, resulting in the formation of the Pebas system, a long-lived mega-wetland composed of swamps, lakes, and fluvial systems influenced by marine incursions (Jaramillo et al., 2017; Leandro et al., 2022). At that time, the Purus Arch, a prominent structural high in Central Amazonia, may have acted as a critical barrier preventing the western drainage from connecting to the eastern Amazon Basin until the late Miocene (Figueiredo et al., 2009). However, other authors have suggested that the Purus Arch only breached during the Pleistocene, following the deposition of the Iça Formation (Nogueira et al., 2013; Horbe et al., 2013; Rossetti et al., 2015). While the significance of the Purus Arch remains debated, alternative scenarios suggest that the Amazon fluvial system may have bypassed this barrier during the Neogene (Hoorn et al., 2017). Eventually, the interplay of tectonics and long-term climate change led to the demise of these mega-wetlands, the bypass of the Purus Arch, and the connection of eastern and western Amazonia, facilitating the development of the modern transcontinental Amazon River.

Finally, the formation of the Amazon Fan, commonly linked to the onset of the transcontinental Amazon River, remains a topic of ongoing debate. The Amazon Fan initially formed on the continental slope, becoming the primary depocenter for siliciclastic input from the late Miocene onward. Early estimates, based on extrapolated Quaternary sedimentation rates from core samples, placed the onset of the transcontinental Amazon River between 16.5 and 8.0 Ma (Damuth and Kumar, 1975). Subsequent studies correlating well data, seismic profiles, and isotopic data suggested a later age of 11.8–10.0 Ma (Figueiredo et al., 2007, 2009). More recently, Hoorn et al. (2017), using nannofossil zonation calibrated to GTS 2012, proposed that Andean-derived sediments were first exported to the Amazon Fan between ~9.4 and 9.0 Ma.

3. Methodology

3.1. 1-BP-3-APS well-log data

The 1-BP-3-APS (hereafter BP-3) is an industry well drilled in the upper Amazon Fan (3° 2′ 58.660″ N, 47° 44′ 45.801″ W; 754 m below sea level – mbsl – Figs. 1b and 2a) reaching a max depth of 5655 mbsl. This well has been referenced under various names in prior studies, including Well 2 (Figueiredo et al., 2009; Hoorn et al., 2017; Lammerstma et al., 2018), Well 4 (Gorini et al., 2014), and Well P1 (Reis et al., 2016). The GR well-log data was acquired by Schlumberger and provided by the Brazilian Petroleum and Gas Agency (ANP). GR data have a vertical resolution of 15–20 cm, and values are presented in API (American Petroleum Institute) units. This study focuses on the interval between 1450 and 4800 mbsl. The lithology of this interval includes alternating limestone and mudstone from 4800 to 4080 mbsl, transitioning to siltstone and fine sandstone until 3620 mbsl, and intercalated mudstone and siltstone down to 1450 mbsl. Due to drilling-related artifacts, the GR well-log is discontinuous; therefore, we divided it into three internally consistent intervals (Fig. 2a): Section 3 (S3, 4425–4800 mbsl), Section 2 (S2, 3680–4415 mbsl), and Section 1 (S1, 1480–3670 mbsl). It should be noted that these 10 m non-measurement segments are not caused by stratigraphic discontinuities. The break between S1 and S2 coincides with a total mud loss at 3679 m during casing and cementing operations. This caused a baseline shift in the GR record by reducing the attenuation typically provided by drilling mud. Similarly, the break between S2 and S3 corresponds to a sequence of severe mud losses during casing operations. These events altered the absolute magnitude of the GR baseline but did not affect the relative variability of the signal, which remains consistent with lithological changes. For this reason, S1, S2, and S3 are treated as independent GR segments that can be interpreted stratigraphically within each interval but are not directly comparable in absolute values across boundaries.

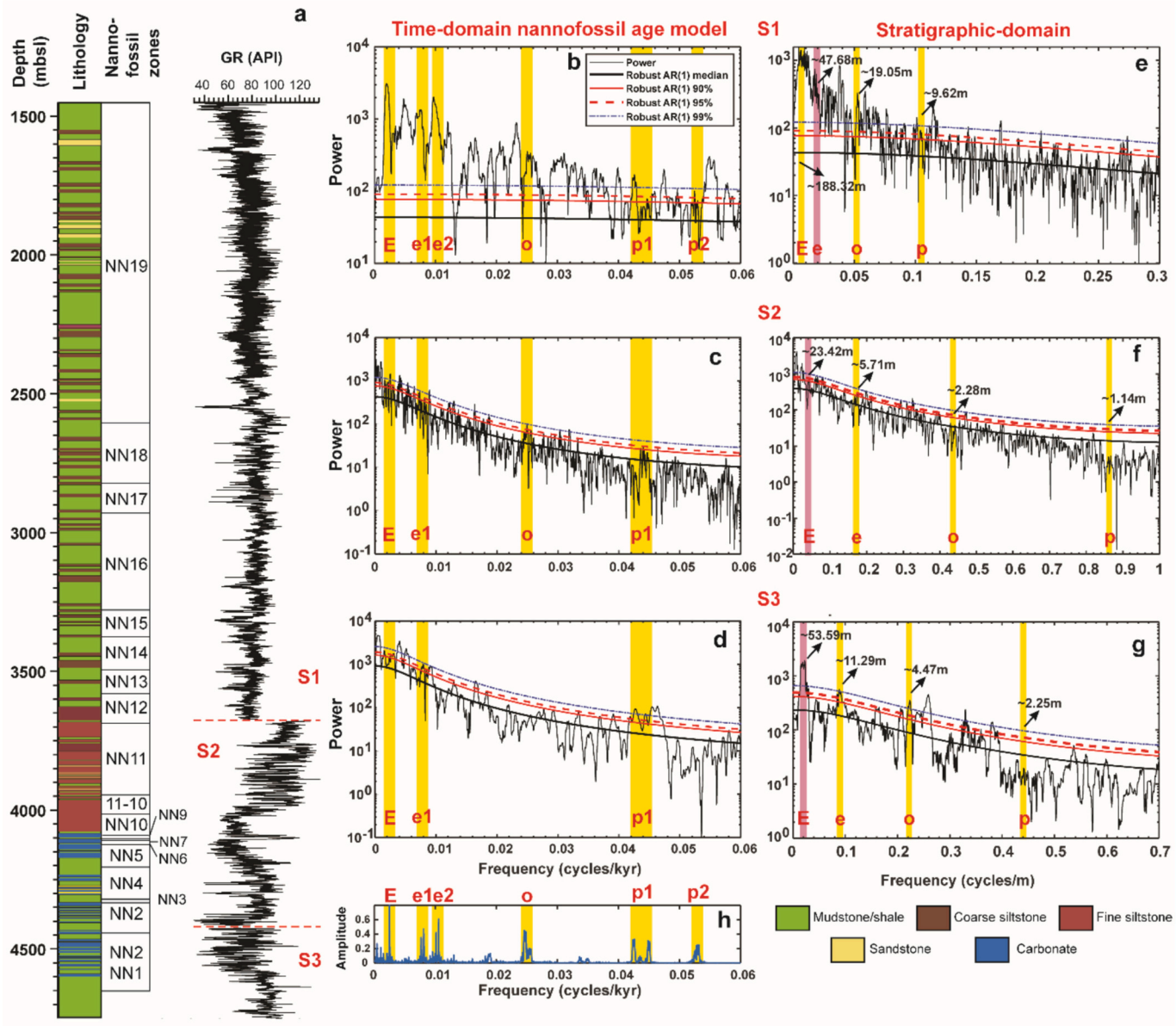

Fig. 2. Multi-taper spectral analysis of gamma-ray (GR) data from the BP3 well for sections S3, S2, and S1. (a) GR data from the BP3 well plotted alongside lithological information and Nannofossil zonation from previous studies (Figueiredo et al., 2009; Hoorn et al., 2017). (b), (c), and (d) Multi-taper spectral analysis of GR data in the time domain, tuned to the biostratigraphic age model. Yellow bars highlight spectral bands corresponding to 405-kyr long eccentricity (E), ~100-kyr short eccentricity (e1 and e2), 41-kyr obliquity (o), and ~ 21-kyr precession (p1 and p2) cycles. (e), (f), and (g) Multi-taper spectral analysis of GR data in the stratigraphic domain, with yellow bars indicating filtered wavelengths associated with orbital signals. (h) The spectral amplitude of the orbital solution (Laskar et al., 2004) for the past ~24 Myr. (For interpretation of the references to colour in this figure legend, the reader is referred to the web version of this article.)

3.2. *Prior biochronology of BP-3 well and a novel astronomical time scale*

An age model for BP-3 was initially developed using calcareous nannofossil biostratigraphy on ditch-cutting samples (Varol Research, 2004; Figueiredo et al., 2009) and was subsequently updated to the GTS2012 timescale (Hoorn et al., 2017). According to this prior biostratigraphic evaluation, the 1450 to 4800 mbsl interval encompasses the Late Oligocene (NP25) to Pleistocene (NN19) period. Unlike the continental shelf or deeper fan regions, sedimentation on the upper fan has remained relatively uninterrupted during past sea-level fluctuations. However, stratigraphic breaks have been reported immediately above 4145, 3338, and 2654 mbsl. The first hiatus above 4145 m (Section S2) corresponds at least to the complete absence of biozone NN8. The hiatuses at 3338 and 2654 mbsl are associated with the partial absence of the lower parts of biozones NN16 and NN19, spanning ~1.0 and 0.73 Ma, respectively (Varol Research, 2004; Hoorn et al., 2017). It should be recognized that chronological inferences within a given biozone based on sparse biostratigraphic data remain problematic, as the limited temporal resolution imposes serious constraints on any refined internal interpretation. In addition, short-term intervals of poor preservation, whether caused by carbonate dissolution, dilution from the sudden influx of siliciclastic material, or other ecological factors, may further bias such analyses. Later in the manuscript (Section 3.3), based on the suite of statistical analyses conducted here, we challenge these earlier interpretations and, within the bounds of our uncertainty evaluation, argue instead for a largely complete chronostratigraphic succession in Section S1.

The nannofossil biostratigraphy published by Figueiredo et al. (2009) was accompanied by a portion of the GR data employed in the current study. However, to date, the potential of these data for

constructing a coherent astronomical time scale has not been explored. We investigated the eventual expression of orbital forcing using statistical cyclostratigraphic methods, applying these techniques to the GR data from the BP-3 well. GR data reflect the combined radiogenic emission of potassium, thorium, and uranium, typically present in minerals such as feldspar, mica, clays, and organic-rich particles. Consequently, higher GR values are likely associated with clay- or organic-rich sediments, while lower GR values generally correspond to coarser carbonate and sandstone components (Cantalejo and Pickering, 2015). The balance between these sediment fractions within a basin is strongly influenced by the surrounding climate, which enhances the GR signal-to-noise ratio and enables more efficient detection of astronomical signals from stratigraphic noise (Li et al., 2019; Weedon, 2003). Limitations on this assumption rely on the non-climatic factors influencing the radiogenic signatures of the mentioned elements, possibly linked to high concentrations of heavy minerals, such as zircons (Šimíček et al., 2012).

Our approach begins with an independent verification of astronomical periodicities before orbital tuning. We leveraged nannofossil biostratigraphic published by Figueiredo et al. (2009) and subsequently updated by Hoorn et al. (2017) as a prior age-depth control. This biostratigraphic age model was applied across the three segments where the GR data were collected, placing the intervals S3, S2, and S1 between the late Oligocene and late Pleistocene. At present, biostratigraphy remains the only viable means of anchoring this well to an absolute timescale. The use of biostratigraphic constraints to guide subsequent cyclostratigraphic refinement is a well-established strategy in astrochronological studies (e.g., Groeneveld et al., 2021; Koutsodendris et al., 2021; Raffi and Backman, 2022).

After applying the nannofossil age-depth model to each GR section, we performed a linear interpolation based on their respective mean temporal resolution and detrended the data using a LOWESS regression with a 35 % window. This process was designed to remove very long, non-astronomical frequencies mixed in the data. The significant frequencies preserved in each GR section were verified using power spectral analysis through the prolate multi-taper spectral estimator (MTM) (Thomson, 1982). The analysis was performed with 2π tapers and a robust red noise null hypothesis model supported by a theoretical first-order autoregressive process fitted to the data and reported regarding the 90 %, 95 %, and 99 % spectral confidence levels (Fig. 2).

Subsequently, we searched for the respective orbital cycle found in the first step, but in the stratigraphic domain, choosing the one that best fit in terms of number of cycles. A Gaussian bandpass filter was used to isolate the most appropriate wavelength in each section. We followed a minimum tuning approach, aligning each minimum in our filtered data with a corresponding minimum in the target astronomical signal for the chronological interval yielded by the biostratigraphic age model (Hinnov, 2013; Laskar et al., 2004). For intervals S3 and S2, the target astronomical frequency was the $g_2 - g_5$ 405-kyr cycle, also known as the 'metronome'. The 405-kyr cycle is considered the most stable astronomical cycle (Laskar, 2020). For sections S3 and S2, we filtered frequencies corresponding to 1/0.01866 and 1/0.04269 cycle/m (wavelengths of ~53.59 m and ~ 23.42 m, respectively) (Figs. 2f and g). For interval S1, the target astronomical frequency was the $g_4 - g_5$ ~ 95-kyr short eccentricity cycle. Among the various eccentricity cycles within this band, the ~95-kyr cycle exhibits the highest power spectrum during the Plio-Pleistocene interval (Laskar et al., 2004). For Section S1, we filtered the frequency at 1/0.02097 cycles/m (wavelength of ~47.68 m). In Figs. 2e-g, we indicated additional frequencies with respect to the distribution related to the frequency ratio method (20:5:2:1) (Laskar et al., 2004); however, we reinforce that they were not used for tuning purposes since some of them do not overcome the spectral confidence levels.

Uncertainty evaluation remains a topic of ongoing debate in cyclostratigraphy, with no standardized methodology for quantifying it (Sinnesael et al., 2019). Age uncertainty can arise from various factors, including the non-linear response of the climate system, which can distort climate signals, the effects of sampling and statistical methods, resolution limitations, and the inherently incomplete nature of the stratigraphic record (Meyers, 2019). Insights from stochastic sedimentation modeling suggest that the average deviation in total duration when tuning to the 405-kyr and ~ 100-kyr cycles is approximately 14.5 % and 21.5 %, respectively (Wang et al., 2024). We directly incorporated the average deviation of 14.5 % for interval S3. For intervals S2 and S1, in addition to the average deviation for the 405-kyr and ~ 100-kyr cycles, we accounted for an additional uncertainty of approximately 1.2 Ma and 0.19 Ma due to the potential absence of three 405-kyr and two ~95-kyr cycles, respectively (Figs. 3 and 4). Ultimately, our age model did not diverge significantly from previous efforts based on biostratigraphic data (Figueiredo et al., 2009; Hoorn et al., 2017) (Supplementary Fig. 1). Still, it substantially improves chronostratigraphic control while addressing more realistic uncertainties not previously assumed (Supplementary Fig. 1). Supplementary Tables 1–3 present the age models for intervals S1, S2, and S3, including their uncertainty estimates and the Gaussian band-pass filters used for astronomical tuning.

3.3. A bayesian age model approach for the Plio-Pleistocene interval

An additional experiment was conducted in the upper part of section S1 (upper ~3000 mbsl). In this interval, we examined the capabilities of Integrated Prediction Error Filter Analysis (INPEFA), a feature within Cyclolog® software (Djin Nio et al., 2005). INPEFA calculates prediction error by creating new data points based on prior samples, with each point representing the numerical error between predicted and observed values at corresponding depths. A 10 m moving window was applied to the data. Assuming the record exhibits cyclic patterns due to climatic variations, INPEFA leverages these patterns to assess continuity and discontinuity in the dataset by quantifying spectral changes. The approach generates new sample points where each value represents either a positive or negative prediction error, indicating overestimation or underestimation of the GR values. Overestimation (negative error) suggests a "sandy" and more regressive segment, while underestimation (positive error) suggests a "muddy" and more transgressive trend. We interpret that significant changes in the depositional system occur at inflection points between predominantly negative and positive trends (Djin Nio et al., 2005). In this study, we worked exclusively on the mid-term INPEFA output.

Then, we attempt a probabilistic tuning between the results of the INPEFA analysis and the reference deep-ocean benthic oxygen isotope ($\delta^{18}O$) LR04 stack (Lisiecki and Raymo, 2005) to generate an alternative age model for the upper part of section S3. This experiment employed Bayesian Inference Gaussian Process regression and Multiproxy Alignment for Continuous Stacks (BIGMACS) (Lee et al., 2023). BIGMACS is a newly developed software package designed to probabilistically align ocean sediment core data and construct multiproxy age models. It formally incorporates multiple sources of age uncertainty to produce probabilistic alignments that are more informative and less subjective than traditional tie-point approaches (Lee et al., 2023). Median age models and their uncertainties are derived from the distribution of Markov chain Monte Carlo samples. Lastly, the correlation between mid-term INPEFA and GMSL was assessed using Pyleoclim, a Python 3.9 application (Khider et al., 2022). Both datasets were interpolated to their mean resolution and standardized using Pyleoclim tools. We applied time-series correlation with the default isospectral method, supported by 5000 Monte Carlo simulations. As mentioned in Section 3.2 and later discussed in Section 5.3, the exceptional results obtained through the combined application of INPEFA and BIGMACS indicate a nearly complete stratigraphic succession for the upper ~3000 mbsl. This evidence leads us to question the existence of the hiatus associated with the partial absence of biozone NN19 at 2654 mbsl. A similar reasoning may be applied to the reported hiatus for biozone NN16 at 3338 mbsl,

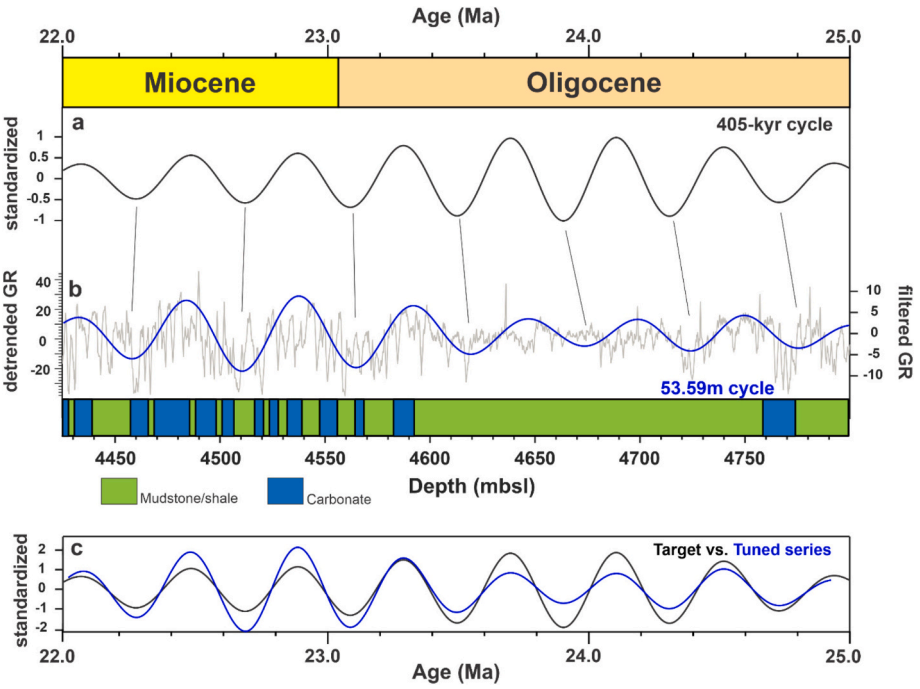

Fig. 3. Astronomical tuning for interval S3 of BP3 well. (a) Representation of the 405-kyr long eccentricity cycle (Laskar et al., 2004). (b) LOWESS-detrended gamma ray (GR) data from BP3 well (light grey) together with the Gaussian bandpass filter applied to GR data (blue), with cutoff frequencies of 0.0149–0.0224 cycles/m, in the stratigraphic domain. Thin black lines indicate the alignment of each eccentricity minimum in filtered GR data. (c) Target 405-kyr cycle (black) compared with filtered GR data (black) in the time domain. (For interpretation of the references to colour in this figure legend, the reader is referred to the web version of this article.)

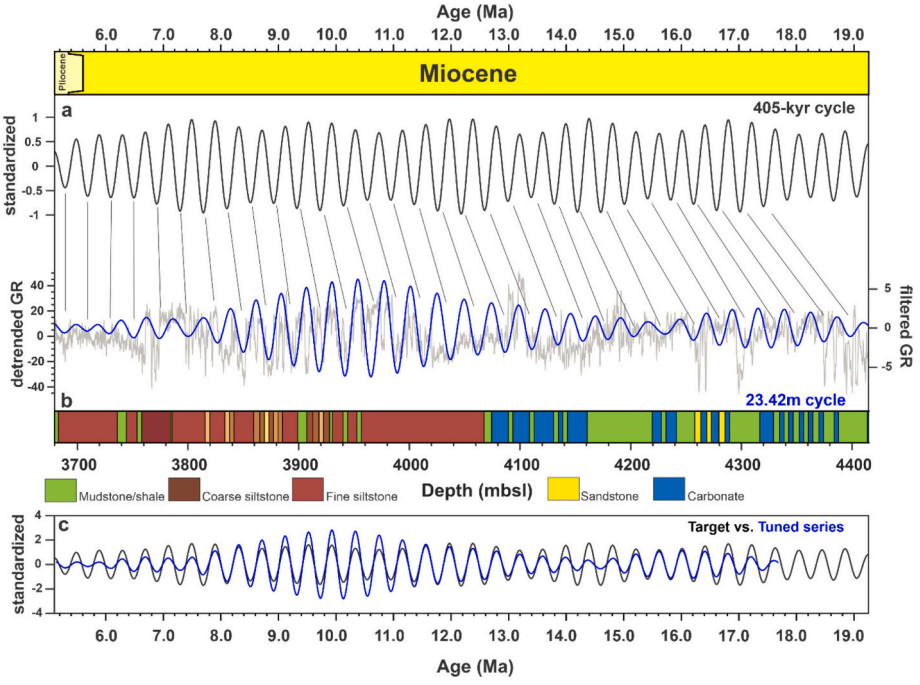

Fig. 4. Astronomical tuning for interval S2 of BP3 well. (a) Representation of the 405-kyr long eccentricity cycle (Laskar et al., 2004). (b) LOWESS-detrended gamma ray (GR) data from BP3 well (light grey) together with the Gaussian bandpass filter applied to GR data (blue), with cutoff frequencies of 0.03869–0.04669 cycles/m, in the stratigraphic domain. Thin black lines indicate the alignment of each eccentricity minimum within the filtered GR data. (c) The target 405-kyr cycle (black) compared with the filtered GR data (black) in the time domain. (For interpretation of the references to colour in this figure legend, the reader is referred to the web version of this article.)

given its comparable nature.

4. Results

The GR values of the BP-3 well range from 40 to 130 API, with the maximum values occurring near the top of interval S2 (~ 4000–3600 mbsl; Fig. 2a). An abrupt change in mean values marks the transition between intervals S2 and S3 (~3600 mbsl), where GR decreases from approximately 120 to 80 API. In interval S1, a noticeable shift to higher frequency variability is observed around ~2450 mbsl, accompanied by a gradually decreasing trend toward the top of the well (Fig. 2a).

Aligned with the nannofossil biostratigraphic age model, intervals S3, S2, and S1 are constrained to 24.8–19.6 Ma, 19.2–5.09 Ma, and 5.03–0.43 Ma, respectively. The MTM power spectral analysis indicates that intervals S3 and S2 are predominantly characterized by lower frequency variability (>1/100 cycles/ka) (Fig. 2c and d). Within this frequency band, the 405-kyr cycle was identified, exceeding the 90 % and 99 % confidence levels for intervals S3 and S2, respectively. Lower frequency variability is also observed in interval S1, with well-defined 405-kyr-long eccentricity and ~ 100 and ~ 130-kyr short eccentricity cycles (99 % confidence level) (Fig. 2b). Additionally, higher-frequency variability within obliquity and precession bands is thoroughly represented in section S1, while in sections S3 and S2, their representation is not constant (Figs. 2c and d). It is crucial to highlight that no orbital tuning was conducted at this stage, underscoring the significant influence of orbitally induced climate modulation on this dataset.

In the stratigraphic domain, the equivalent long eccentricity cycles for intervals S3 and S2, and the short eccentricity cycle for interval S1, were isolated using Gaussian bandpass filtering. For intervals S3 and S2, the long eccentricity cycle corresponds to wavelengths of approximately 53.5 and 23.4 cycles/m, respectively. In interval S1, the short eccentricity cycle is associated with a frequency of about 47.68 cycles/m (Fig. 2e-g). The minimal tuning approach aligned each minimum in the filtered wavelengths with the corresponding orbital cycle within the periods indicated by the biostratigraphic data (Figs. 3–5). For intervals S3 and S2, the orbital solution suggests the presence of seven and 35 minima in the 405-kyr band, while seven and 31 sedimentary cycles are likely associated with the 405-kyr band, respectively (Figs. 4 and 5). We interpret that no missing beats occur in interval S3, while approximately 1.2 Ma may be absent in interval S2. For interval S1, the orbital solution indicates the existence of 49 minima in the ~95-kyr eccentricity band, while 46 sedimentary cycles are correlated. The caveats listed in Section 3.2, plus the potential existence of hiatuses, as outlined in Figueiredo et al. (2009) and Hoorn et al. (2017), result in final astronomical age models with root mean square error constrained between 24.9 and 22.0 ± 0.003 Ma, 17.6–5.1 ± 2.0 Ma and 4.81–0.42 ± 0.65 Ma for sections S3, S2 and S1, respectively (Figs. 3–5; Supplementary Fig. 1).

5. Discussion

5.1. Orbital Pacing and Global mean Sea Level in the Amazon Fan

The Neogene history of sediment deposition in the Amazon Fan is highly complex, driven by the interaction between Andean orogeny, dynamic topography, climate variability, and sea-level fluctuations (Hoorn et al., 1995). The interplay of these processes is believed to have facilitated the formation of diverse environments, ranging from shallow marine conditions to extensive fluvio-lacustrine mega-lakes in the western Amazon during the early- to mid-Miocene (Boonstra et al., 2015; Jaramillo et al., 2017; Leandro et al., 2022). Over time, these geological and climatic factors contributed to the development of the transcontinental Amazon River and played a crucial role in shaping the remarkable biodiversity of the Amazon Basin (Sawakuchi et al., 2022).

A numerical model developed to investigate the formation of the Amazon River, incorporating tectonic activities, climate variations, and global mean sea level (GMSL) changes, indicates that sea level played a critical role in controlling intermittent marine incursions in the western Amazon (Sacek et al., 2023). Additionally, in coastal regions, periods of sea level drop were generally associated with increased sedimentation rates (Sacek et al., 2023). Furthermore, the application of detrital zircon geochronology indicates that sea-level fluctuations played a critical role in controlling sediment sources in the Amazon Fan in the Pleistocene (Mason et al., 2019). During warm periods, sea-level highstands promoted a greater influx of craton-derived sediments. In contrast, cold

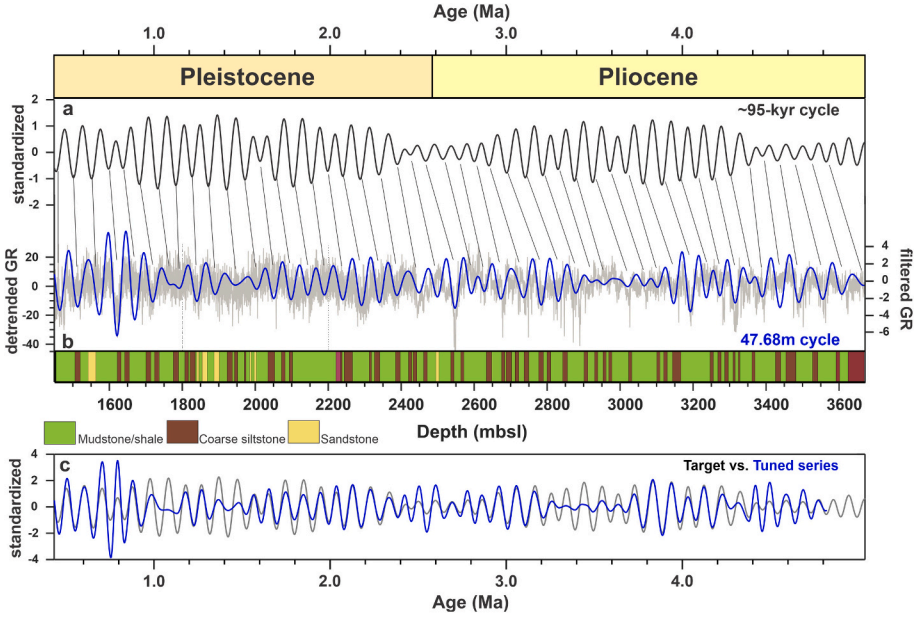

Fig. 5. Astronomical tuning for interval S1 of the BP3 well. (a) Representation of the ~95-kyr short eccentricity cycle (Laskar et al., 2004). (b) LOWESS-detrended gamma ray (GR) data from the BP3 well (light grey) alongside the Gaussian bandpass filter applied to the GR data (blue), with cutoff frequencies of 0.01697–0.02497 cycles/m, in the stratigraphic domain. Thin black lines indicate the alignment of each eccentricity minimum within the filtered GR data. (c) The target ~95-kyr cycle (black) compared with the filtered GR data (black) in the time domain. (For interpretation of the references to colour in this figure legend, the reader is referred to the web version of this article.)

intervals were marked by shelf incision, base-level lowering, and enhanced connectivity between terrestrial, shelf, and deep-sea environments. These conditions facilitated the downslope transport of Andean-sourced zircons (Mason et al., 2019). Gamma ray (GR) data from sedimentary records spanning the continental shelf to the upper slope further reflect the impact of sea-level oscillations (Li et al., 2018; Tortarolo, 2023). Transgressive phases and sea-level highstands typically coincide with increased deposition of fine-grained pelagic sediments, terrigenous clay minerals, and organic matter—resulting in elevated GR values (Wagreich and Koukal, 2020). In contrast, regressive phases and sea-level lowstands are associated with the preferential accumulation of coarser siliciclastic and carbonate sediments, reflected by lower GR values.

Fig. 6 compares the GR data for the BP-3 well, aligned with the developed astronomical timescale, to the GMSL of Miller et al. (2020). A general agreement is observed between the long-term trends in GR and GMSL, both during periods above and below present-day sea level. Notable correlations are evident in intervals S3 and S1 (Figs. 6a and c), while in interval S2, the relationship is stronger during the near ice-free conditions of the Miocene Climatic Optimum. In the mid-Miocene, the GMSL declines in two distinct steps, although this pattern is not precisely mirrored in the GR data. However, during the late Miocene, both proxies exhibit a similar upward trend toward the Pliocene (Fig. 6b). The Plio-Pleistocene is characterized by a gradual GR increase in the BP-3 well from ~4.7 to 2.6 Ma, aligning with periods of high sea level during the Pliocene Climatic Optimum. Subsequently, both proxies display a gradual decline throughout the Pleistocene. The mechanism unifying GR and GMSL is likely the dynamic interplay between the growth and decay of continental-scale glaciations, which began in Antarctica during the early Oligocene and was later intensified by Northern Hemisphere glaciation (Miller et al., 2020). Eustatic sea-level fluctuations driven by ice volume changes ultimately influence depositional dynamics and the nature of sediments in deltaic, upper slope, and deep-sea fan environments, all affecting the GR signal.

The waxing and waning of ice sheets since the late Oligocene exhibit strong orbital pacing, with GMSL responding to 21-kyr precession, 41-kyr obliquity, ~100-kyr, and 405-kyr eccentricity cycles, along with amplitude modulation of obliquity and eccentricity at ~1.2- and ~ 2.4-Myr rhythms, respectively (Boulila et al., 2011; Miller et al., 2020; Pälike et al., 2006). A wavelet transform analysis (Torrence and Compo, 1998) of the GR data reveals that deposition in the Amazon Fan also preserves a wide range of Milankovitch frequencies (Fig. 6). During the sea-level fall associated with the Mi1 event at the Oligo-Miocene transition (~23 Ma), spectral power in the 405-kyr band is prominent in both GR and GMSL records. Benthic $\delta^{18}O$ and $\delta^{13}C$ records from the western equatorial Atlantic (ODP Site 926 – Ceará Rise) indicate an increase in the 405-kyr cycle amplitude across the Mi1 event, suggesting a pivotal shift in the global climate system driven by positive feedback mechanisms on the global carbon cycle (Zachos, 2001). In the early Miocene, the GMSL lowstand is further marked by strong spectral power in the 21-kyr precession and 41-kyr obliquity bands in the BP-3 data (Fig. 6c). Additionally, a longer temporal variability at Myr-scale (~1.2/2.4-Myr cycle) is evident in interval S2 (early to mid-Miocene), agreeing with GMSL (Fig. 6b). Continental margin deposition may act as a low-pass filter, amplifying Myr-scale variability and aliasing higher-frequency signals, particularly under low sedimentation rates (<6 cm/kyr) (Miller et al., 2020). Like the early Miocene, higher frequencies in the 41-kyr and ~ 100-kyr bands are also observed in the GR data, corresponding with the series of GMSL falls (Mi2–Mi4) marking the end of the Miocene Climatic Optimum (Fig. 6b).

The GMSL record exhibits a weak expression of the 405-kyr cycle during the Plio-Pleistocene interval, and the underlying cause remains

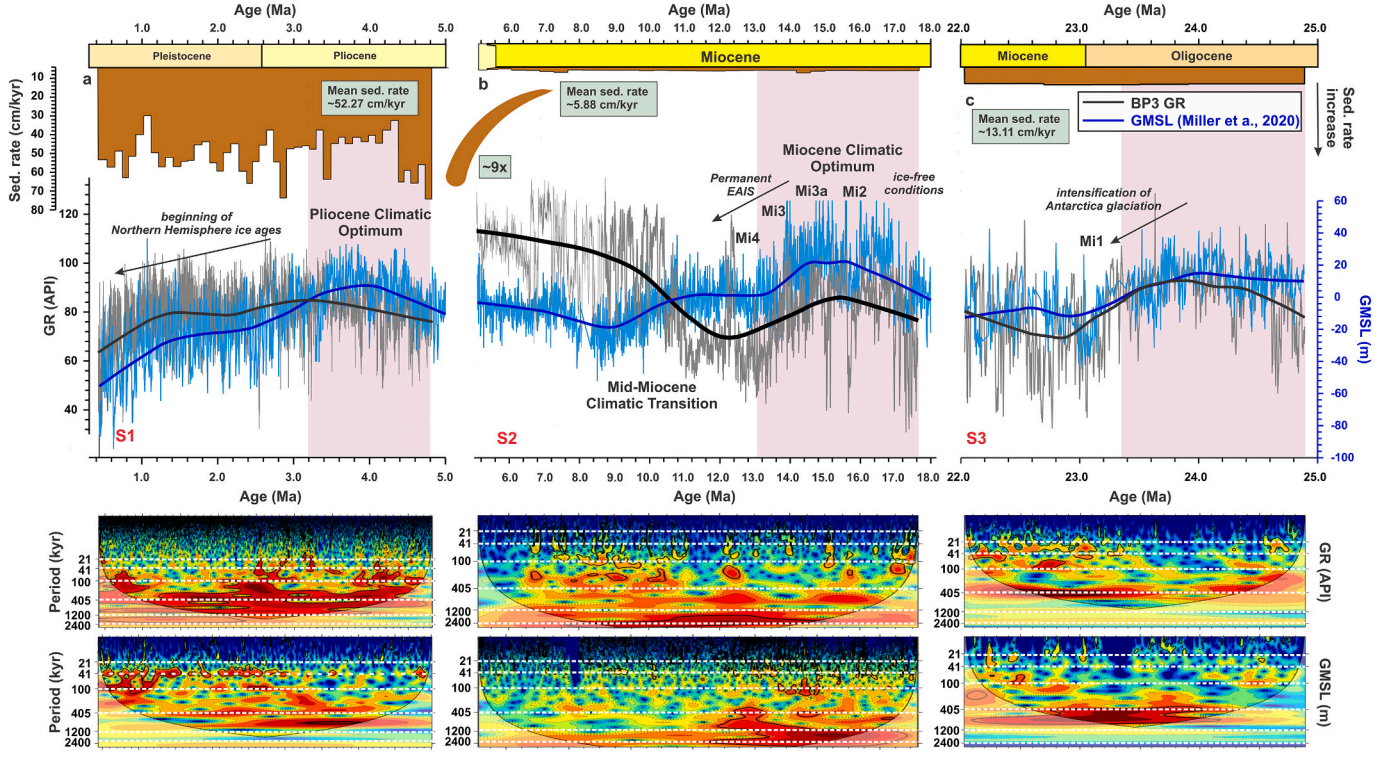

Fig. 6. Estimated sedimentation rates derived from the astronomical age model, and comparison of gamma-ray (GR) data with global mean sea level (GMSL) (Miller et al., 2020). Panels (a-c) from top to bottom: sedimentation rate (cm/kyr; shaded brown area); GR data (thin black line) with a 35 % LOWESS regression (thick black line); GMSL (thin blue line) with a 35 % LOWESS regression (thick blue line); and wavelet transform (Torrence and Compo, 1998) of standardized GR data. Dashed white lines denote the positions of obliquity (1.2-Myr) and eccentricity (2.4-Myr) amplitude modulations, long eccentricity (405-kyr), short eccentricity (~100-kyr), obliquity (41-kyr), and precession (21-kyr). (For interpretation of the references to colour in this figure legend, the reader is referred to the web version of this article.)

uncertain (Miller et al., 2020). Conversely, the 405-kyr cycle is clearly preserved in the GR data (Fig. 6a). Coupled simulations of global ice volume over the past 5 million years suggest that the 405-kyr modulation is present in Plio-Pleistocene ice volume variability but becomes obscured due to the dominant influence of Northern Hemisphere ice sheets linked to the 41- and ~ 100-kyr cycles since 2.9 Ma (De Boer et al., 2014). Cosmogenic radionuclide data from the southern Andes provide direct evidence of a 405-kyr cyclic control over erosion rates (Fisher et al., 2023). This may reflect a direct influence of the long eccentricity cycle on moisture transport from the Atlantic or, more likely, an indirect effect through amplitude modulation of the 21-kyr precession. Such mechanisms could explain the consistent expression of the 405-kyr cycle in the GR data, as tropical hydroclimate is notably sensitive to seasonal insolation changes, particularly within the precession band (e.g., Cheng et al., 2013; Marzocchi et al., 2015). The nonlinear interaction of orbitally driven climatic factors, such as continental precipitation, with GMSL variability may account for the observed discrepancies between the GR data and GMSL at this point.

Furthermore, geochemical and environmental magnetic proxy records on the northwest Australian shelf show strong modulation of the monsoon dynamics by the 405-kyr cycle between 2.9 and 1.6 Ma, providing direct support for the preservation of this cycle in certain Quaternary sedimentary records (Zhao et al., 2024). Thus, the persistence of the 405-kyr cycle within the last ~4.8 Myr section of BP-3 is consistent with other records. The last ~1.3 Myr period also displays an enhanced expression of the ~100-kyr cycle, which will be examined in detail in the subsequent section (Section 5.3; Fig. 6a). Detecting multiple astronomical signals in the BP-3 GR spectrograms ultimately validates our minimal tuning approach and suggests no inherent bias toward the selected target frequency for each interval (Fig. 6).

5.2. *The imprint of orbital forcing on sedimentation rates at the Amazon Fan*

The novel astronomical age model for the BP-3 well also enables a reassessment of Neogene sedimentation rates in the Amazon Fan. Figueiredo et al. (2009) proposed three stages of development that led to the exceptionally high sedimentation rates observed in the most recent period: 1) before approximately 6.8 Ma, when sedimentation rates were relatively low (<5 cm/kyr); 2) between ~6.8 and 2.4 Ma when sediment discharge increased sixfold despite a general rise in GMSL; and finally, 3) from 2.4 Ma to the present, a period characterized by a notable increase in sedimentation rates with a mean value of 122 cm/kyr, but punctually peaking at 1116 cm/kyr (Figueiredo et al., 2009). Our revised estimate for the sedimentation rate during the Plio-Pleistocene interval is more moderate, as the regular placement of tie-points by cyclostratigraphy avoids abrupt time compressions. In our model, the substantial increase in sediment discharge occurred between 5.1 and 4.8 ± 1.78 Ma (Fig. 6a and b and Supplementary fig. 1), slightly later than Figueiredo et al. (2009) suggested, but still consistent when considering the full uncertainty range. Paleogeographic reconstructions based on 2D and 3D seismic data (Rouby et al., 2022) show that the BP-3 site remained within the main depocenter of the Brazilian Equatorial Margin throughout the 23–0 Ma interval. Thus, the marked increase in sedimentation rates after ~5 Ma is best interpreted as reflecting an overall increase in sediment supply to the Amazon Fan system, consistent with the regional signal documented by Figueiredo et al. (2009), rather than a lateral migration of fan lobes. This increased sedimentation rate is also consistent with observations of a Messinian worldwide tectonic revolution, as summarized by Leroux et al. (2018).

Notably, despite the evident influence of GMSL on the GR signal, no comparable effect on sedimentation rates is observed. In the S3 section, the calculated sedimentation rate changes are minimal (<1 cm/kyr). The transition from S3 to S2 is marked by a two-fold decrease in sedimentation rates, and although S2 exhibits more significant fluctuations (~2 cm/kyr), these variations are unlikely to be attributed to the ~30 m GMSL drop from the late Oligocene to the late Miocene (Figs. 6b and c). The early Pliocene in section S1 is a critical period for this evaluation. When approaching the Pliocene Climatic Optimum, the sea level was approximately 20 m above the present, and, despite this, the Amazon Fan experienced significant sediment discharge of ~50 cm/kyr. This suggests that the sea-level highstand of the early Pliocene did not impede substantial sediment transport to the Atlantic Ocean.

This persistently low sedimentation rate in the Amazon Fan until approximately 5 Ma may be attributed to the presence of mega-wetland systems in the western Amazon Basin (Boonstra et al., 2015; Hoorn et al., 2022a). This system, known as the Pebas system, comprised a complex mosaic of swamps, lakes, and fluvial networks influenced by episodic marine incursions. Acting as a sediment trap, the Pebas system likely retained the majority of Andean and cratonic sediments within the Amazon Basin. While the Pebas System is considered to have existed no later than ~13 Ma (Hoorn et al., 2022a; Jaramillo et al., 2017), other findings suggest that a connection between western Amazonia and the Caribbean region may have persisted longer (Aguilera et al., 2013; Espinosa et al., 2021). Minor marine influences have been identified in the early Pliocene (~4.7, 4.2–4.1, and 3.8 Ma) (Leandro et al., 2022), potentially contributing to the observed low sedimentation rates during this time. If such marine incursions impacted sediment discharge to the Amazon Fan, they might explain why sedimentation rates remained low until the early Pliocene. However, it should be noted that this scenario of prolonged marine incursions in western Amazonia is not supported in all models (Sacek et al., 2023). Applying our astronomical age model in conjunction with previously published neodymium (Nd) isotopic data from the same well (Hoorn et al., 2017), we observe the influx of Andean-derived sediment as early as 12.2 ± 1.3 Ma. This transition is marked by an abrupt shift in εNd values from highly negative (−18.8 ± 1.7, n = 9) to more radiogenic signatures (−10.7 ± 1.8, n = 15), reflecting the increased contribution of juvenile material sourced from Andean volcano-sedimentary Cenozoic deposits. This finding indicates that while sediment traps such as the Pebas System significantly delayed sediment export, they did not entirely hinder the onset of transcontinental drainage and sediment delivery to the deep sea during the Late Miocene.

If GMSL decline was not the primary driver of the massive sediment discharge starting in the early Pliocene, another mechanism must have been at play. Geochemical proxies indicate that the northern Altiplano experienced rapid uplift between 9.1 and 5.4 Ma, likely reaching its modern elevation during this period (Kar et al., 2016). This surface uplift facilitated the organization and intensification of the South American Low-Level Jet, leading to substantial (>400 %) increases in precipitation across the central Altiplano. This increase was due to convective activity triggered by latent heat release as air masses converged on the plateau (Poulsen et al., 2010). Fossil flora evidence suggests that precipitation in the central Altiplano was nearly three times higher than current levels during the mid-Miocene, with these wet conditions persisting into the early Pliocene (Martínez et al., 2020). Additionally, pollen records from equatorial South America indicate continuously wet conditions during the early Pliocene, supporting the idea of a southward displacement of the Intertropical Convergence Zone, which would have transported moisture from the Atlantic across Amazonia (Grimmer et al., 2018). This increase in humidity from the mid-Miocene onward likely intensified the denudation rates of Andean rocks due to enhanced precipitation (Sacek et al., 2023). In addition, the Pliocene uplift of the Fitzcarrald Arch (Espurt et al., 2007), a positive topographic area that covers 400,000 km^2 of the Peruvian-Brazilian retroarc basins (Regard et al., 2009), may have been an additional trigger in favoring erosion of the Amazonian retroarc foreland basin sediments and in reducing the accommodation space in the Amazon retroarc foreland basins. Therefore, we propose that the resulting sediments were initially retained within wetland systems in western Amazonia, acting as efficient sediment traps. With the disappearance of these barriers during the early Pliocene, sediments produced by these processes found an unrestricted pathway to the

Atlantic Ocean. This sediment flush was so substantial that it exceeded the influence of high GMSL during the early Pliocene.

To summarize, the spectral analysis of BP-3 GR data reveals a comprehensive archive of orbital-induced climate variability influencing sedimentation at the Amazon Fan and, consequently, the stacking of sedimentary units from Amazon River-derived material. The developed astronomical timescale enables a detailed comparison between Amazon Fan dynamics and GMSL over the past ~24 million years, facilitating the identification of the factors that led to an exceptional sedimentation rate in this region.

5.3. *The Quaternary Ice Ages and the mid-Pleistocene transition*

The middle portion of section S1, corresponding to the last ~3.5 Myr (upper ~3000 mbsl), is marked by a shift to a high-frequency variability in GR data. This shift is unrelated to the astronomical tuning, as observed in the stratigraphic domain (Figs. 1 and 2). Globally, the late Pliocene to early Pleistocene transition is characterized by a fundamental shift in Earth's climate, as inferred from benthic foraminifera $\delta^{18}O$ marine records (Lisiecki and Raymo, 2005; Westerhold et al., 2020). During this period, the oxygen isotopic composition of the global oceans became progressively heavier, indicating an expansion in global ice volume with a concomitant sea-level decrease and a reduction in global temperature (Shackleton, 1987). The amplitude of benthic $\delta^{18}O$ variability also gradually increased, leading to the series of ice ages that punctuated the Quaternary period. These changes significantly impacted GMSL, with amplitude variability reaching approximately 120 m during more recent glacial intervals (Miller et al., 2020).

To further quantify the linkages between global climate change and Amazon Fan dynamics, we applied INPEFA over the upper ~3000 m. The inflection points of the INPEFA curves indicate significant shifts in depositional regimes, likely influenced by GMSL and climate change (Djin Nio et al., 2005). INPEFA outputs successfully identified the depositional changes associated with GMSL in the Espírito Santo basin (western South Atlantic) from the late Paleocene to the early Miocene (Santos et al., 2023). When aligned to the developed astronomical model for section S1 and compared with the GMSL, we found a striking visual association, mainly from the Pleistocene onset at 2.58 Ma (Fig. 7a). The sequence of peaks in the mid-term INPEFA nearly corresponds to elevated GMSL (and lower benthic foraminifera $\delta^{18}O$) constrained during the brief Pleistocene interglacials.

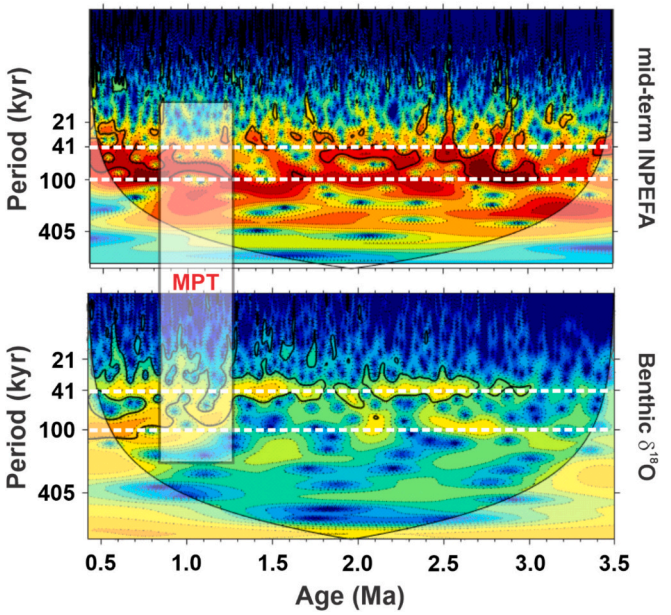

Fig. 8. Wavelet transform of the standardized mid-term Integrated Prediction Error Filter (INPEFA) applied to BP3 gamma ray (GR) data in the time domain for the upper part of the S3 section (upper panel) and the benthic foraminifera oxygen isotope record ($\delta^{18}O$) from the LR04 reference stack (lower panel) (Lisiecki and Raymo, 2005). The white rectangle highlights the interval associated with the mid-Pleistocene Transition (MPT). Dashed white lines indicate the spectral bands corresponding to 41-kyr and ~100-kyr orbital cycles.

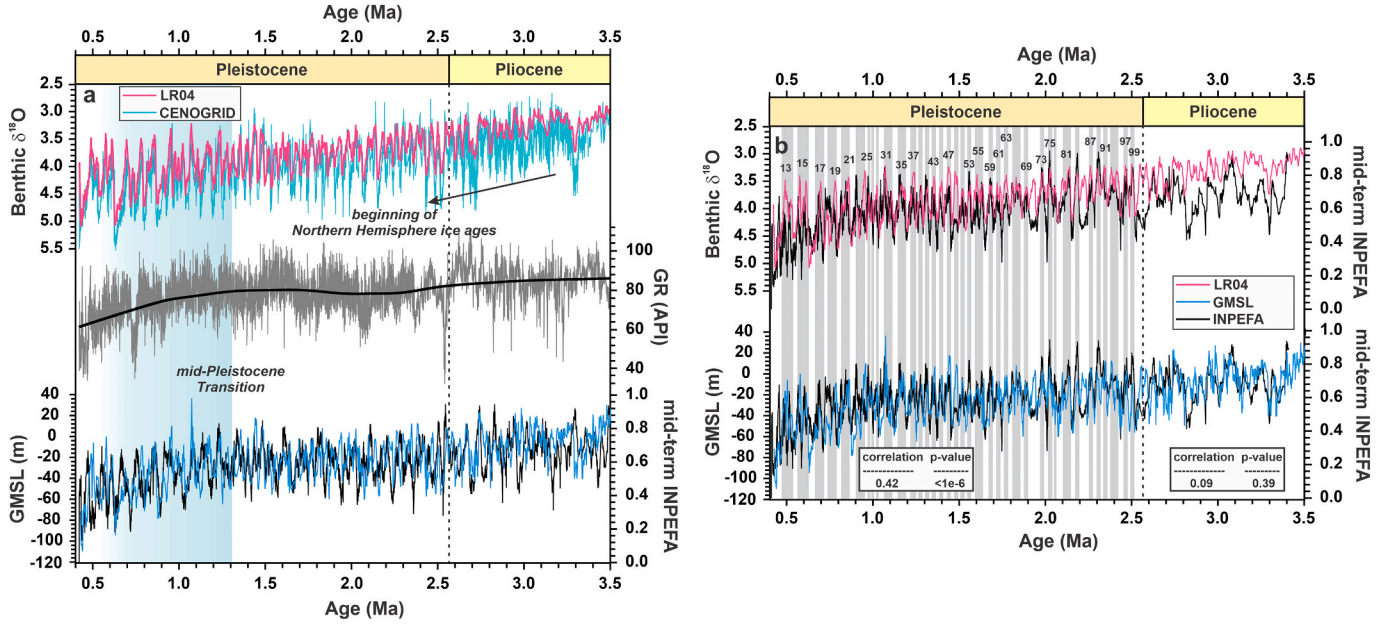

Fig. 7. Comparison of gamma ray (GR) data and the mid-term Integrated Prediction Error Filter Analysis (INPEFA) results for the upper ~3600 mbsl of the BP3 well. (a) from top to bottom: reference benthic oxygen isotope ($\delta^{18}O$) records from CENOGRID (light blue line) (Westerhold et al., 2020) and LR04 (pink line) (Lisiecki and Raymo, 2005); GR data (thin black line) with a 35 % LOWESS regression (thick black line); GMSL (blue line) (Miller et al., 2020) and mid-term INPEFA signal summed with the 35 % LOWESS regression used for GR data. (b) same as (a), but the mid-term INPEFA signal is plotted using the probabilistic age model developed with BIGMACS (Lee et al., 2023). Vertical grey bars highlight interglacial periods, and numbers indicate selected Marine Isotope Stages between ~0.5–2.58 Ma. (For interpretation of the references to colour in this figure legend, the reader is referred to the web version of this article.)

Interestingly, the distribution of spectral content in mid-term INPEFA exhibits strong power, mainly at the obliquity band during the early to mid-Pleistocene (Fig. 8). From ~1.3–1.2 Ma, there is a clear increment in the ~100-kyr frequency that prevailed until the uppermost part of the record. These features are consistent with the glacial-interglacial variability observed in benthic foraminiferal $\delta^{18}O$ records, which shifts from obliquity- to eccentricity-dominated signal at ~1.3–1.2 Ma (Fig. 8). This transition is known as the mid-Pleistocene Transition and is characterized by an increased resilience of northern hemisphere ice caps, making ice ages spent longer (Berends et al., 2021; Clark and Pollard, 1998) (Fig. 7a). Why Earth's climate responded so strongly to a weak forcing in eccentricity at that time remains fiercely debated in the literature (e.g., Barker et al., 2022). However, identifying these Pleistocene climate shifts in our GR series tuned to ~100-kyr eccentricity demonstrates that the same climate variability was recorded in the Amazon Fan sedimentary system.

To further explore the apparent coupling between mid-term INPEFA and both GMSL and benthic foraminiferal $\delta^{18}O$ records, we applied a probabilistic tuning approach for the upper part of the S1 section, aligning our data directly with the benthic foraminifera LR04 reference (Lisiecki and Raymo, 2005) using the routine of BIGMACS software (Lee et al., 2023). In our case, BIGMACS facilitated a probabilistic stratigraphic alignment of benthic $\delta^{18}O$ with mid-term INPEFA. The resulting age model was slightly compressed (~0.42–3.40 Ma) relative to that generated by minimal tuning with the ~100-kyr cycle (~0.42–3.50 Ma) but with an order of magnitude lower uncertainty, ranging ±0.01–0.025 Ma (Supplementary Fig. 2). Interestingly, the association between mid-term INPEFA and GMSL was notably robust, with a clear imprint of Marine Isotope Stages (MIS) in the variability of the well-log data (Fig. 7b). This is not easily found, but when available, it supports building accurate high-resolution age models (e.g., Dearing Crampton-Flood et al., 2020; Zhang et al., 2019).

In the late Pliocene (~ 2.6–3.5 Ma), visual alignment between INPEFA and GMSL remains consistent. However, the isospectral correlation test indicates a lack of statistical significance in this portion ($R = 0.09$, $p = 0.39$), likely due to the software's limited capacity to match finer-scale variability between GMSL and mid-term INPEFA. A marked shift occurs at 2.6 Ma, where INPEFA cyclicity aligns closely with individual MIS, with peaks (lows) in INPEFA matching interglacial (glacial) periods characterized by higher (lower) sea levels and lower (higher) benthic $\delta^{18}O$ values (Fig. 7b). Exceptions to this alignment are solely observed during MIS 101, 85, and 71. We argue that the identification of nearly all MIS between ~2.5 and 0.5 Ma provides strong evidence that the upper ~3000 mbsl of BP-3 constitutes an essentially complete stratigraphic section, rendering the hiatus inferred from the partial absence of biozone NN19 more unlikely (Hoorn et al., 2017). A similar interpretation may be extended to the lower hiatus associated with the partial absence of biozone NN16. However, this inference should be approached carefully, as this lower interval was not examined with the same set of analytical tools. Ultimately, this fourth to fifth-order stratigraphic analysis reveals that the BP-3 site holds a continuous sediment record spanning the last ~3.0 Myr, making it a compelling target for scientific coring to investigate Plio-Pleistocene variability in the Amazon River system. The statistically significant correlation ($R = 0.42$, $p < 0.05$) between mid-term INPEFA and GMSL underscores the Amazon Fan's high sensitivity to the onset of early Pleistocene glaciations. This sensitivity initially structured sedimentary architecture in response to the 41-kyr glacial-interglacial cycles and later to the 100-kyr cycles (Figs. 7 and 8).

6. Conclusions

This study underscores the interplay between orbital forcing, sea-level changes, and regional geodynamic events in controlling sediment deposition in the Amazon Fan. Our reassessment of the GR data for the BP-3 well reveals a strong imprint of Milankovitch cycles over the last 24 million years, emphasizing the fan's sensitivity to orbital climate variability. Our new astronomically tuned age model refined prior chronologies, enabling robust correlations between sedimentary cycles and GMSL. We show that low sedimentation rates prevailed during the Miocene, at a time when the combination of active Andean tectonics, uplift of the Fitzcarrald Arch, and enhanced regional precipitation in the Amazon Basin was most likely associated with high erosion rates. This discrepancy is best interpreted as reflecting efficient sediment trapping by mega-lake systems in western Amazonia. The subsequent drastic increase in sediment discharge to the Atlantic starting from the Early Pliocene indicates a major drainage reorganization across the Amazon Basin at that time, most likely caused by the breach of the Purus Arch, leading to enhanced sediment export to the Atlantic Ocean. Finally, in the Plio-Pleistocene, the GR record captures a major sensitivity of the fan to the GMSL changes imposed by the glacial-interglacial variability seen through the expression of isotopic stages. In this sense, the glaciation of the northern hemisphere has become a major force in fan sedimentary architecture. The shift from obliquity- to eccentricity-dominated glacial-interglacial cycles characterizing the mid-Pleistocene Transition (~1.3 Ma) further highlights the Amazon Fan's responsiveness to global climatic shifts. These findings provide a new framework for future high-resolution proxy investigations of the detailed evolution of the Amazon Basin during the Neogene and its link to global climate.

CRediT authorship contribution statement

Gabriel R. Moizinho: Writing – original draft, Visualization, Investigation, Data curation, Conceptualization. **Thiago P. Santos:** Writing – original draft, Investigation, Funding acquisition, Formal analysis, Conceptualization. **Germain Bayon:** Writing – review & editing, Supervision, Project administration. **Martin Roddaz:** Writing – review & editing, Supervision, Resources. **Natalia Vázquez Riveiros:** Writing – review & editing, Supervision, Project administration. **Marina Rabineau:** Writing – review & editing, Validation, Supervision. **Daniel Aslanian:** Writing – review & editing, Validation, Supervision. **Victor Carreira:** Software, Methodology. **Elton L. Dantas:** Writing – review & editing. **Roberto V. Santos:** Writing – review & editing, Supervision, Resources, Project administration.

Declaration of competing interest

The authors declare that they have no known competing financial interests or personal relationships that could have appeared to influence the work reported in this paper.

Data availability

The authors confirm that all data necessary for supporting the scientific findings of this paper have been provided.

Acknowledgments

This research had financial support from the Coordination for the Improvement of Higher Personnel – Brazil (CAPES) – Finance Code 001, the Agence Nationale de Recherche ECLIP-SED project (ANR-20-01CE-0003), and the CAPES-COFECUB program through their funding of actions 32/2022 and Te 1003/23 (project numbers 8881.712022/2022-1 and 49558SM). TPS also thanks the Programa de Apoio a Novos Docentes (process 22.1.09345.01.2) of the University of São Paulo. We acknowledge the Brazilian Oil and Gas Agency (ANP) for giving access to the BP-3 well data (SAA 48610.204116/2022-88). We are very gratefull for Dr. Fabienne Marret-Davis for her editorial handling and an anonimous reviewer for their constructive comments and review.

Appendix A. Supplementary data

Supplementary data to this article can be found online at https://doi.org/10.1016/j.gloplacha.2025.105068.

References

Aguilera, O., Lundberg, J., Birindelli, J., Sabaj Pérez, M., Jaramillo, C., Sánchez-Villagra, M.R., 2013. Palaeontological evidence for the last Temporal Occurrence of the Ancient Western Amazonian River Outflow into the Caribbean. PloS One 8, e76202. https://doi.org/10.1371/journal.pone.0076202.

Akabane, T.K., Chiessi, C.M., Hirota, M., Bouimetarhan, I., Prange, M., Mulitza, S., Bertassoli Jr., D.J., Häggi, C., Staal, A., Lohmann, G., Boers, N., Daniau, A.L., Oliveira, R.S., Campos, M.C., Shi, X., De Oliveira, P.E., 2024. Weaker Atlantic overturning circulation increases the vulnerability of northern Amazon forests. Nat. Geosci. https://doi.org/10.1038/s41561-024-01578-z.

Albert, J.S., Val, P., Hoorn, C., 2018. The changing course of the Amazon River in the Neogene: center stage for Neotropical diversification. Neotropic. Ichthyol. 16. https://doi.org/10.1590/1982-0224-20180033.

Barker, S., Starr, A., Conn, S., Lordsmith, S., Owen, L., Nederbragt, A., Hemming, S., Hall, I., Levay, L., 2022. Persistent influence of precession on northern ice sheet variability since the early. Pleistocene 376, 961–967. https://doi.org/10.1126/science.abm4033.

Berends, C.J., Köhler, P., Lourens, L.J., Wal, R.S.W., 2021. On the Cause of the Mid-Pleistocene transition. Rev. Geophys. 59. https://doi.org/10.1029/2020RG000727.

Boulila, S., Galbrun, B., Miller, K.G., Pekar, S.F., Browning, J.V., Laskar, J., Wright, J.D., 2011. On the origin of Cenozoic and Mesozoic "third-order" eustatic sequences. Earth-Sci. Rev. 109, 94–112. https://doi.org/10.1016/j.earscirev.2011.09.003.

Boonstra, M., Ramos, M.I.F., Lammertsma, E.I., Antoine, P.O., Hoorn, C., 2015. Marine connections of Amazonia: evidence from foraminifera and dinoflagellate cysts (early to middle Miocene, Colombia/Peru). Palaeogeogr. Palaeoclimatol. Palaeoecol. 417, 176–194.

Boulila, S., Brange, C., Cruz, A.M., Laskar, J., Gorini, C., Reis, T.D., Silva, C.G., 2020. Astronomical pacing of late cretaceous third- and second-order sea-level sequences in the Foz do Amazonas Basin. Marine Petrol. Geol. 117, 104382. https://doi.org/10.1016/j.marpetgeo.2020.104382.

Burns, S.J., Maslin, M.A., 1999. Composition and circulation of bottom water in the western Atlantic Ocean during the last glacial, based on pore-water analyses from the Amazon Fan. Geol 27, 1011. https://doi.org/10.1130/0091-7613(1999)027<1011:CACOBW>2.3.CO;2.

Cantalejo, B., Pickering, K.T., 2015. Orbital forcing as principal driver for fine-grained deep-marine siliciclastic sedimentation, Middle-Eocene Ainsa Basin, Spanish Pyrenees. Palaeogeogr. Palaeoclimatol. Palaeoecol. 421, 24–47. https://doi.org/10.1016/j.palaeo.2015.01.008.

Cheng, H., Sinha, A., Cruz, F.W., Wang, X., Edwards, R.L., d'Horta, F.M., Ribas, C.C., Vuille, M., Stott, L.D., Auler, A.S., 2013. Climate change patterns in Amazonia and biodiversity. Nat. Commun. 4, 1411. https://doi.org/10.1038/ncomms2415.

Clark, P.U., Pollard, D., 1998. Origin of the Middle Pleistocene transition by ice sheet erosion of regolith. Paleoceanography 13, 1–9. https://doi.org/10.1029/97PA02660.

Clement, A.C., Hall, A., Broccoli, A.J., 2004. The importance of precessional signals in the tropical climate. Climate Dynam. 22, 327–341. https://doi.org/10.1007/s00382-003-0375-8.

Clift, P., Hodges, K., Heslop, D., Hannigan, R., Van Long, H., Calves, G., 2008. Correlation of Himalayan exhumation rates and Asian monsoon intensity. Nat. Geosci. 1 (12), 875–880. https://doi.org/10.1038/ngeo351.

Cruz, A.M., Reis, A.T., Suc, J.P., Silva, C.G., Praeg, D., Granjeon, D., Raibneau, M., Popescu, S.M., Gorini, C., 2019. Neogene evolution and demise of the Amapá carbonate platform, Amazon continental margin, Brazil. Marine Petrol. Geol. 105, 185–203. https://doi.org/10.1016/j.marpetgeo.2019.04.009.

Damuth, J.E., Kumar, N., 1975. Amazon Cone: morphology, sediments, age, and growth pattern. Geologic. Soc. Am. Bull. 86 (6), 863–878.

De Boer, B., Lourens, L.J., Van De Wal, R.S.W., 2014. Persistent 400,000-year variability of Antarctic ice volume and the carbon cycle is revealed throughout the Plio-Pleistocene. Nat. Commun. 5, 2999. https://doi.org/10.1038/ncomms3999.

Dearing Crampton-Flood, E., Noorbergen, L.J., Smits, D., Boschman, R.C., Donders, T.H., Munsterman, D.K., Ten Veen, J., Peterse, F., Lourens, L., Sinninghe Damsté, J.S., 2020. A new age model for the Pliocene of the southern North Sea basin: a multi-proxy climate reconstruction. Clim. Past 16, 523–541. https://doi.org/10.5194/cp-16-523-2020.

Djin Nio, S., Brouwer, J.H., Smith, D., de Jong, M., Böhm, A.R., 2005. Spectral trend attribute analysis: applications in the stratigraphic analysis of wireline logs. First Break 23. https://doi.org/10.3997/1365-2397.23.4.26503.

Espinosa, B.S., D'Apolito, C., Da Silva-Caminha, S.A.F., 2021. Marine influence in western Amazonia during the late Miocene. Global Planet. Change 205, 103600. https://doi.org/10.1016/j.gloplacha.2021.103600.

Espurt, N., Baby, P., Brusset, S., Roddaz, M., Hermoza, W., Regard, V., Antoine, P.O., Salas-Gismondi, R., Bolanos, R., 2007. How does the Nazca Ridge subduction influence the modern Amazonian foreland basin? Geology 35, 515–518. https://doi.org/10.1130/G23237A.1.

Figueiredo, J., Zalán, P., Soares, E., 2007. Bacia da Foz do Amazonas. Boletim de Geociências da Petrobras 15, 299–309.

Figueiredo, J., Hoorn, C., Van Der Ven, P., Soares, E., 2009. Late Miocene onset of the Amazon River and the Amazon deep-sea fan: evidence from the Foz do Amazonas Basin. Geology 37, 619–622. https://doi.org/10.1130/G25567A.1.

Fisher, G.B., Luna, L.V., Amidon, W.H., Burbank, D.W., De Boer, B., Stap, L.B., Bookhagen, B., Godard, V., Oskin, M.E., Alonso, R.N., Tuenter, E., Lourens, L.J., 2023. Milankovitch-paced erosion in the southern Central Andes. Nat. Commun. 14, 424. https://doi.org/10.1038/s41467-023-36022-0.

Flood, R.D., Piper, D.J.W., 1995. Proceeding of the Ocean Drilling Program. Initial Rep. 155, 1233. https://doi.org/10.2973/odp.proc.ir.155.1995.

Gorini, C., Haq, B.U., dos Reis, A.T., Silva, C.G., Cruz, A., Soares, E., Grangeon, D., 2014. Late Neogene sequence stratigraphic evolution of the *Foz do Amazonas* Basin, Brazil. Terra Nova 26, 179–185. https://doi.org/10.1111/ter.12083.

Grimmer, F., Dupont, L., Lamy, F., Jung, G., González, C., Wefer, G., 2018. Early Pliocene vegetation and hydrology changes in western equatorial South America. Clim. Past 14, 1739–1754. https://doi.org/10.5194/cp-14-1739-2018.

Groeneveld, J., De Vleeschouwer, D., McCaffrey, J.C., Gallagher, S.J., 2021. Dating the northwest shelf of Australia since the Pliocene. Geochem. Geophys. Geosyst. 22 (3), e2020GC009418.

Hinnov, L.A., 2013. Cyclostratigraphy and its revolutionizing applications in the earth and planetary sciences. Bull. Geol. Soc. Am. 125, 1703–1734. https://doi.org/10.1130/B30934.1.

Hoorn, C., Bogotá-A, G.R., Romero-Baez, M., Lammertsma, E.I., Flantua, S.G.A., Dantas, E.L., Dino, R., Do Carmo, D.A., Chemale, F., 2017. The Amazon at sea: Onset and stages of the Amazon River from a marine record, with special reference to Neogene plant turnover in the drainage basin. Global Planet. Change 153, 51–65. https://doi.org/10.1016/j.gloplacha.2017.02.005.

Hoorn, C., Boschman, L.M., Kukla, T., Sciumbata, M., Val, P., 2022a. The Miocene wetland of western Amazonia and its role in Neotropical biogeography. Bot. J. Linn. Soc. 199, 25–35. https://doi.org/10.1093/botlinnean/boab098.

Hoorn, C., Kukla, T., Bogotá-Angel, G., Van Soelen, E., González-Arango, C., Wesselingh, F.P., Vonhof, H., Val, P., Morcote-Rios, G., Roddaz, M., Dantas, E.L., Santos, R.V., Sinninghe Damsté, J.S., Kim, J.-H., Morley, R.J., 2022b. Cyclic sediment deposition by orbital forcing in the Miocene wetland of western Amazonia? New insights from a multidisciplinary approach. Global Planet. Change 210, 103717. https://doi.org/10.1016/j.gloplacha.2021.103717.

Horbe, A.M.C., Motta, M.B., Almeida, C.M., Dantas, E.L., Vieira, L.C., 2013. Provenance of Pliocene and recent sedimentary deposits in western Amazônia, Brazil: Consequences for the paleodrenage of the Solimões-Amazonas River. Sedimentary Geol. 296, 9–20. https://doi.org/10.1016/j.sedgeo.2013.07.007.

Jaramillo, C., Romero, I., D'Apolito, C., Bayona, G., Duarte, E., Louwye, S., Escobar, J., Luque, J., Carrillo-Briceño, J.D., Zapata, V., Mora, A., Schouten, S., Zavada, M., Harrington, G., Ortiz, J., Wesselingh, F.P., 2017. Miocene flooding events of western Amazonia. Sci. Adv. 3, e1601693. https://doi.org/10.1126/sciadv.1601693.

Kar, N., Garzione, C.N., Jaramillo, C., Shanahan, T., Carlotto, V., Pullen, A., Moreno, F., Anderson, V., Moreno, E., Eiler, J., 2016. Rapid regional surface uplift of the northern Altiplano plateau revealed by multiproxy paleoclimate reconstruction. Earth Planet. Sci. Lett. 447, 33–47. https://doi.org/10.1016/j.epsl.2016.04.025.

Khider, D., Emile-Geay, J., Zhu, F., James, A., Landers, J., Ratnakar, V., Gil, Y., 2022. Pyleoclim: paleoclimate timeseries analysis and visualization with python. Paleoceanog Paleoclimatol. 37. https://doi.org/10.1029/2022PA004509.

Koutsodendris, A., Nakajima, K., Kaboth-Bahr, S., Berke, M.A., Franzese, A.M., Hall, I.R., Hemming, S.R., Just, J., LeVay, L.J., Pross, J., Robinson, R., 2021. A Plio-Pleistocene (c. 0–4 Ma) cyclostratigraphy for IODP Site U1478 (Mozambique Channel, SW Indian Ocean): exploring an offshore record of paleoclimate and ecosystem variability in SE Africa. nos 54, 159–181. https://doi.org/10.1127/nos/2020/0608.

Lammerstma, E.I., Troelstra, S.R., Flores, J.-A., Sangiorgi, F., Chemale Jr., F., do Carmo, D.A., Hoorn, C., 2018. Primary productivity in the western tropical Atlantic follows Neogene Amazon River evolution. Palaeogeogr. Palaeoclimatol. Palaecol. 506, 12. https://doi.org/10.1016/j.palaeo.2018.05.048.

Laskar, J., 2020. Astrochronology. In: Geologic Time Scale 2020. Elsevier, pp. 139–158. https://doi.org/10.1016/B978-0-12-824360-2.00004-8.

Laskar, J., Robutel, P., Joutel, F., Gastineau, M., Correia, A.C.M., Levrard, B., 2004. A long-term numerical solution for the insolation quantities of the Earth. Astron. Astrophys. 428, 261–285. https://doi.org/10.1051/0004-6361:20041335.

Leandro, L.M., Linhares, A.P., De Lira Mota, M.A., Fauth, G., Santos, A., Villegas-Martín, J., Vieira, C.E.L., Bruno, M.D.R., Lee, B., Baecker-Fauth, S., Lopes, F.M., Ramos, M.I.F., 2022. Multi-proxy evidence of Caribbean-sourced marine incursions in the Neogene of Western Amazonia, Brazil. Geology. https://doi.org/10.1130/G49544.1.

Lee, T., Rand, D., Lisiecki, L.E., Gebbie, G., Lawrence, C., 2023. Bayesian age models and stacks: combining age inferences from radiocarbon and benthic δ^{18} O stratigraphic alignment. Clim. Past 19, 1993–2012. https://doi.org/10.5194/cp-19-1993-2023.

Leroux, E., Aslanian, D., Rabineau, M., Pellen, R., Moulin, M., 2018. The late Messianian Event 6 Ma ago: a worldwide tectonic revolution. Terra Nova 30, 207–214. https://doi.org/10.1111/ter.12327.

Li, M., Hinnov, L.A., Huang, C., Ogg, J.G., 2018. Sedimentary noise and sea levels linked to land–ocean water exchange and obliquity forcing. Nat. Commun. 9, 1004. https://doi.org/10.1038/s41467-018-03454-y.

Li, M., Huang, C., Ogg, J., Zhang, Y., Hinnov, L., Wu, H., Chen, Z.Q., Zou, Z., 2019. Paleoclimate proxies for cyclostratigraphy: Comparative analysis using a lower Triassic marine section in South China. Earth-Sci. Rev. 189, 125–146. https://doi.org/10.1016/j.earscirev.2019.01.011.

Lisiecki, L.E., Raymo, M.E., 2005. A Pliocene-Pleistocene stack of 57 globally distributed benthic?? 18O records. Paleoceanography 20, 1–17. https://doi.org/10.1029/2004PA001071.

Manley, P.L., Flood, R.D., 1988. Cyclic sediment deposition within amazon deep-sea fan. Bulletin 72. https://doi.org/10.1306/703C910E-1707-11D7-8645000102C1865D.
Martínez, C., Jaramillo, C., Correa-Metrío, A., Crepet, W., Moreno, J.E., Aliaga, A., Moreno, F., Ibañez-Mejia, M., Bush, M.B., 2020. Neogene precipitation, vegetation, and elevation history of the Central Andean Plateau. Sci. Adv. 6, eaaz4724. https://doi.org/10.1126/sciadv.aaz4724.
Marzocchi, A., Lunt, D.J., Flecker, R., Bradshaw, C.D., Farnsworth, A., Hilgen, F.J., 2015. Orbital control on late Miocene climate and the North African monsoon: insight from an ensemble of sub-precessional simulations. Clim. Past 11, 1271–1295. https://doi.org/10.5194/cp-11-1271-2015.
Maslin, M., Mikkelsen, N., Vilela, C., Haq, B., 1998. Sea-level –and gas-hydrate–controlled catastrophic sediment failures of the Amazon Fan. Geol 26, 1107. https://doi.org/10.1130/0091-7613(1998)026<1107:SLAGHC>2.3.CO;2.
Maslin, M., Vilela, C., Mikkelsen, N., Grootes, P., 2005. Causes of catastrophic sediment failures of the Amazon Fan. Quat. Sci. Rev. 24, 2180–2193. https://doi.org/10.1016/j.quascirev.2005.01.016.
Maslin, M.A., Durham, E., Burns, S.J., Platzman, E., Grootes, P., Greig, S.E.J., Nadeau, M.-J., Schleicher, M., Pflaumann, U., Lomax, B., Rimington, N., 2000. Palaeoreconstruction of the Amazon River freshwater and sediment discharge using sediments recovered at Site 942 on the Amazon Fan. J. Quaternary Sci. 15, 419–434. https://doi.org/10.1002/1099-1417(200005)15:4<419::AID-JQS541>3.0.CO;2-L.
Mason, C.C., Romans, B.W., Stockli, D.F., Mapes, R.W., Fildani, A., 2019. Detrital zircons reveal sea-level and hydroclimate controls on Amazon River to deep-sea fan sediment transfer. Geology 47, 563–567. https://doi.org/10.1130/G45852.1.
Miller, K.G., Kominz, M.A., Browning, J.V., Wright, J.D., Mountain, G.S., Katz, M.E., Sugarman, P.J., Cramer, B.S., Christie-Blick, N., Pekar, S.F., 2005. The phanerozoic record of global sea-level change. Science 310, 1293–1298. https://doi.org/10.1126/science.1116412.
Meyers, S.R., 2019. Cyclostratigraphy and the problem of astrochronologic testing. Earth-Sci. Rev. 190, 190–223.
Miller, K.G., Browning, J.V., John Schmelz, W., Kopp, R.E., Mountain, G.S., Wright, J.D., 2020. Cenozoic Sea-level and cryospheric evolution from deep-sea geochemical and continental margin records. Sci. Adv. 6. https://doi.org/10.1126/sciadv.aaz1346.
Nogueira, A.C.R., Silveira, R., Guimarães, J.T.F., 2013. Neogene-Quaternary sedimentary and paleovegetation history of the eastern Solimões Basin, Central Amazon region. J. South Am. Earth Sci. 46, 89–99. https://doi.org/10.1016/j.jsames.2013.05.004.
Pälike, H., Norris, R.D., Herrle, J.O., Wilson, P.A., Coxall, H.K., Lear, C.H., Shackleton, N. J., Tripati, A.K., Wade, B.S., 2006. The heartbeat of the Oligocene climate system. Science 314, 1894–1898. https://doi.org/10.1126/science.1133822.
Poulsen, C.J., Ehlers, T.A., Insel, N., 2010. Onset of Convective Rainfall during Gradual late Miocene rise of the Central Andes. Science 328, 490–493. https://doi.org/10.1126/science.1185078.
Raffi, I., Backman, J., 2022. The role of calcareous nannofossils in building age models for Cenozoic marine sediments: a review Rendiconti Lincei. Scienze Fisiche e Naturali 33 (1), 25–38.
Regard, V., Lagnous, R., Espurt, N., Darrozes, J., Baby, P., Roddaz, M., Calderon, Y., Hermoza, Y., 2009. Geomorphic evidence for recent uplift of the Fitzcarrald Arch (Peru): A response to the Nazca Ridge subduction. Geomorphology 107, 107–117. https://doi.org/10.1016/j.geomorph.2008.12.003.
Reis, A.T., Araújo, E., Silva, C.G., Cruz, A.M., Gorini, C., Droz, L., Migeon, S., Perovano, R., King, I., Bache, F., 2016. Effects of a regional décollement level for gravity tectonics on late Neogene to recent large-scale slope instabilities in the Foz do Amazonas Basin, Brazil. Mar. Pet. Geol. 75, 29–52. https://doi.org/10.1016/j.marpetgeo.2016.04.011.
Rossetti, D.F., Cohen, M.C.L., Tatumi, S.H., Sawakuchi, A.O., Cremon, E.H., Mittani, J.C. R., Bertani, T.C., Munita, C.J., Tudela, D.R.G., Yee, M., Moya, G., 2015. Mid-late Pleistocene OSL chronology in western Amazonia and implications for the transcontinental Amazon pathway. Sediment. Geol. 330, 1–15. https://doi.org/10.1016/j.sedgeo.2015.10.001.
Rouby, D., Loparev, A., Chardon, D., Bajolet, F., Dall'Asta, M., Paquet, F., Fillon, C., Roig, J.Y., Ye, J., 2022. Sediment routing systems to the Atlantic rifted margin of the Guiana Shield. Geosphere 19 (3), 957–974. https://doi.org/10.1130/GES02561.1.
Sacek, V., Mutz, S.G., Bicudo, T.C., De Almeida, R.P., Ehlers, T.A., 2023. The Amazon paleoenvironment resulted from geodynamic, climate, and sea-level interactions. Earth Planet. Sci. Lett. 605, 118033. https://doi.org/10.1016/j.epsl.2023.118033.
Santos, T.P., Lisboa, L.P., Carreira, V., Bione, F.R.A., Venancio, I.M., Bernardes, M.C., Belem, A.L., Díaz, R.A., Moreira, M., Lopes, A.A.O., Santos, T.L., Souza, I.V., Spigolon, A.L.D., Albuquerque, A.L.S., 2023. Orbitally-driven Palaeogene to Neogene deposition in the western South Atlantic (Espírito Santo Basin) and its correlation with global sea level. Sedimentology, 13104. https://doi.org/10.1111/sed.13104.
Sawakuchi, A.O., Schultz, E.D., Pupim, F.N., et al., 2022. Rainfall and sea level drove the expansion of seasonally flooded habitats and associated bird populations across Amazonia. Nat Commun 13, 4945. https://doi.org/10.1038/s41467-022-32561-0.
Shackleton, N.J., 1987. Oxygen isotopes, ice volume and sea level. Quat. Sci. Rev. 6, 183–190. https://doi.org/10.1016/0277-3791(87)90003-5.
Shephard, G.E., Müller, R.D., Liu, L., Gurnis, M., 2010. Miocene drainage reversal of the Amazon River driven by plate-mantle interaction. Nat. Geosci. 3, 870–875. https://doi.org/10.1038/ngeo107.
Šimíček, D., Bábek, O., Leichmann, J., 2012. Outcrop gamma-ray logging of siliciclastic turbidites: Separating the detrital provenance signal from facies in the foreland-basin turbidites of the Moravo-Silesian basin, Czech Republic. Sedimentary Geol. 261–262, 50–64. https://doi.org/10.1016/j.sedgeo.2012.03.003.
Sinnesael, M., De Vleeschouwer, D., Zeeden, C., Batenburg, S.J., Da Silva, A.C., de Winter, N.J., Dinarès-Turell, J., Drury, A.J., Gambacorta, G., Hilgen, F.J., Hinnov, L. A., Hudson, A.J.L., Kemp, D.B., Lantink, M.L., Laurin, J., Li, M., Liebrand, D., Ma, C., Meyers, S.R., Monkenbusch, J., Montanari, A., Nohl, T., Pälike, H., Pas, D., Ruhl, M., Thibault, N., Vahlenkamp, M., Valero, L., Wouters, S., Wu, H., Claeys, P., 2019. The Cyclostratigraphy Intercomparison Project (CIP): consistency, merits and pitfalls. Earth Sci. Rev. 199, 102965. https://doi.org/10.1016/j.earscirev.2019.102965.
Stewart, J.A., Gutjahr, M., James, R.H., Anand, P., Wilson, P.A., 2016. Influence of the Amazon River on the Nd isotope composition of deep water in the western equatorial Atlantic during the Oligocene–Miocene transition. Earth Planet. Sci. Lett. 454, 132–141. https://doi.org/10.1016/j.epsl.2016.08.037.
Thomson, D.J., 1982. Spectrum estimation and harmonic analysis. Proc. IEEE 70, 1055–1096. https://doi.org/10.1109/PROC.1982.12433.
Torrence, C., Compo, G.P., 1998. A practical guide to wavelet analysis. Bull. Am. Meteorol. Soc. 79, 61–78. https://doi.org/10.1175/1520-0477(1998)079<0061:APGTWA>2.0.CO;2.
Tortarolo, L., 2023. Shelf Edge Evolution of the Brazilian Equatorial Margin Since 4 Ma: Impact of Amazonian Siliciclastic Sediments, Orbitally Controlled Sea-Level Changes, Subsidence, and Oceanographic Currents. https://theses.hal.science/tel-04614728.
Van Soelen, E.E., Kim, J.-H., Santos, R.V., Dantas, E.L., Vasconcelos De Almeida, F., Pires, J.P., Roddaz, M., Sinninghe Damsté, J.S., 2017. A 30 Ma history of the Amazon River inferred from terrigenous sediments and organic matter on the Ceará rise. Earth Planet. Sci. Lett. 474, 40–48. https://doi.org/10.1016/j.epsl.2017.06.025.
Varol Research, 2004. Varol Research Nannofossil Biostratigraphy of BP Offshore Well. Internal ReportAgência Nacional do Petróleo. Gás Natural e Biocombustíveis, Brazil.
Wagreich, M., Koukal, V., 2020. The pelagic archive of short-term sea-level change in the cretaceous: a review of proxies linked to orbital forcing. SP 498, 39–56. https://doi.org/10.1144/SP498-2019-34.
Wang, M., Li, M., Hajek, E.A., Kemp, D.B., Wu, Y., Zhu, H., Huang, C., Zhang, H., Ji, K., Zhang, R., Wei, R., Jin, Z., 2024. Assessing the preservation of orbital signals across different sedimentary environments: Insights from stochastic sedimentation modeling. Earth Planet. Sci. Lett. 642, 118866. https://doi.org/10.1016/j.epsl.2024.118866.
Weedon, G.P., 2003. *Time-series analysis and cyclostratigraphy: examining stratigraphic records of environmental cycles*. Cambridge University Press.
Westerhold, T., Marwan, N., Drury, A.J., Liebrand, D., Agnini, C., Anagnostou, E., Barnet, J.S.K., Bohaty, S.M., De Vleeschouwer, D., Florindo, F., Frederichs, T., Hodell, D.A., Holbourn, A.E., Kroon, D., Lauretano, V., Littler, K., Lourens, L.J., Lyle, M., Pälike, H., Röhl, U., Tian, J., Wilkens, R.H., Wilson, P.A., Zachos, J.C., 2020. An astronomically dated record of Earth's climate and its predictability over the last 66 million years. Science 369, 1383–1388. https://doi.org/10.1126/SCIENCE.ABA6853.
Zachos, J.C., 2001. Climate response to orbital forcing across the oligocene-miocene boundary. Science 292, 274–278. https://doi.org/10.1126/science.1058288.
Zhang, Y., Yi, L., Ogg, J.G., 2019. Pliocene-Pleistocene magneto-cyclostratigraphy of IODP Site U1499 and implications for climate-driven sedimentation in the northern South China Sea. Palaeogeogr. Palaeoclimatol. Palaeoecol. 527, 118–132. https://doi.org/10.1016/j.palaeo.2019.04.029.
Zhao, S., Grant, K.M., Heslop, D., Gallagher, S.J., Bolton, C.T., Auer, G., 2024. Early pleistocene orbital-scale variability in australian northwest shelf sediments. Paleoceanog Paleoclimatol. 39, e2024PA005015. https://doi.org/10.1029/2024PA005015.

View publication stats

Table S4.1. Age depth model of 1-BP-3-APS well log tuned to short eccentricity ~95kyr cycle for section1 and long eccentricity 405-kyr cycle for sections 2 and 3 from LA04 (Laskar et al., 2004).

Gamma Ray Section	Depth (mbsl)	Age (ka)	Error upper	Error lower
Section 1				
	1464	447	763	132
	1514	541	862	219
	1574	644	975	314
	1622	743	1083	403
	1672	822	1171	474
	1722	919	1278	559
	1763	1022	1394	650
	1794	1123	1508	738
	1841	1217	1615	819
	1892	1307	1718	896
	1946	1411	1837	984
	2005	1514	1957	1071
	2053	1602	2058	1145
	2099	1687	2158	1216
	2145	1789	2277	1301
	2191	1893	2399	1388
	2242	1986	2507	1464
	2293	2071	2608	1534
	2342	2169	2724	1615
	2390	2276	2850	1702
	2451	2379	2972	1786
	2501	2455	3062	1848
	2549	2543	3167	1920
	2594	2641	3283	1999
	2629	2734	3394	2074
	2675	2818	3494	2142
	2737	2903	3596	2211
	2785	3004	3716	2291
	2834	3108	3841	2376
	2880	3208	3960	2456
	2922	3294	4064	2525
	2957	3387	4174	2599
	3023	3491	4299	2683
	3068	3590	4418	2762
	3104	3677	4523	2832
	3149	3776	4641	2910
	3194	3885	4772	2997
	3238	3984	4892	3077
	3275	4076	5002	3149
	3317	4170	5116	3225
	3358	4277	5244	3310
	3391	4377	5365	3390
	3441	4454	5457	3450
	3492	4541	5562	3520
	3557	4639	5681	3598
	3608	4731	5792	3671
	3663	4805	5881	3729
Section 2				
	3688	5272	6695	3849
	3708	5665	7119	4211
	3728	6068	7556	4580
	3751	6466	7989	4943

	3774	6870	8429	5310
	3800	7276	8874	5678
	3827	7667	9303	6031
	3850	8087	9765	6409
	3873	8493	10213	6774
	3895	8898	10660	7136
	3918	9302	11107	7497
	3941	9705	11555	7856
	3965	10113	12008	8218
	3989	10527	12469	8586
	4013	10936	12924	8947
	4037	11342	13378	9306
	4062	11748	13832	9664
	4086	12156	14288	10024
	4111	12566	14748	10384
	4134	12975	15206	10743
	4157	13375	15656	11095
	4180	13776	16107	11446
	4202	14178	16558	11797
	4231	14579	17010	12148
	4257	14994	17478	12511
	4280	15398	17932	12863
	4303	15801	18387	13215
	4327	16196	18833	13559
	4351	16596	19285	13907
	4374	16993	19734	14253
	4399	17409	20203	14614
Section 3				
	4458	22281	25511	19050
	4510	22695	25986	19405
	4565	23098	26447	19749
	4620	23503	26911	20095
	4674	23910	27377	20443
	4724	24313	27839	20788
	4775	24731	28317	21145

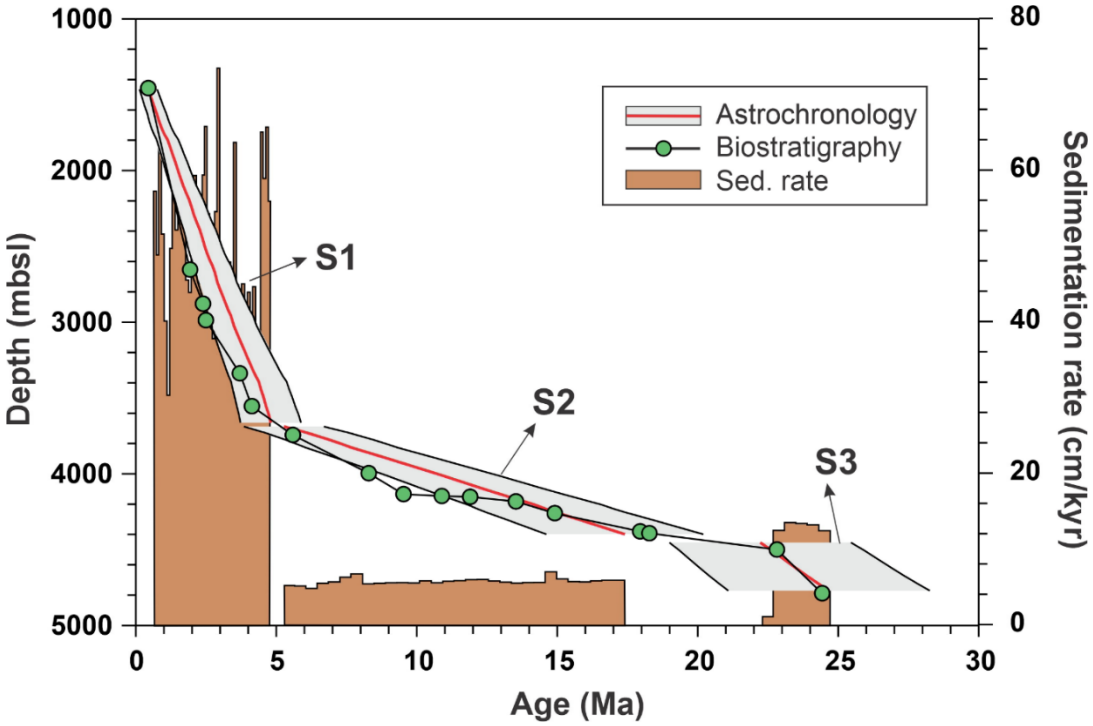

Figure S4.1 – Comparison of the previously published age model for the BP3 well, based on nannofossil biostratigraphy data (Figueiredo et al., 2009; Hoorn et al., 2017), with the astrochronological age model developed in this study for sections S3, S2, and S1. The biostratigraphic age model is represented by green dots and a black line, while yellow dots indicate depths where multiple ages were assigned in the input age model of Hoorn et al. (2017), attributed to brief sediment disturbances. The mean age model derived from cyclostratigraphy is depicted as a thick red line, with the associated 1σ uncertainty shown as a grey shaded area. Also shown are the sedimentation rates (in cm/kyr) for sections S3, S2, and S1, illustrating temporal changes in sediment deposition across the analyzed intervals.

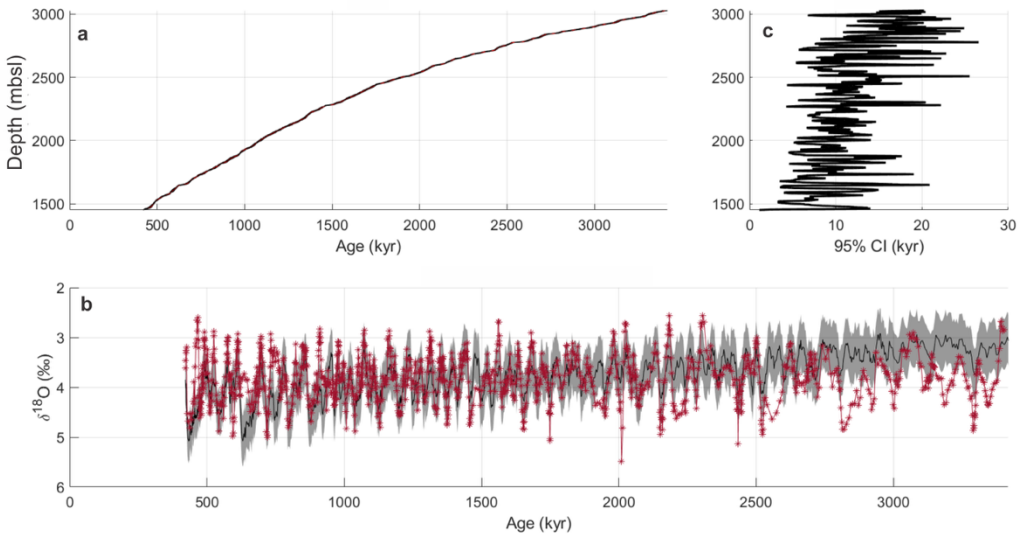

Figure S4.2 – Results of Bayesian Inference Gaussian Process regression and Multiproxy Alignment for Continuous Stacks (BIGMACS) (Lee et al., 2023) applied to tune the mid-term INPEFA to the LR04 reference stack (Lisiecki and Raymo, 2005) for the upper portion of the S3 section. (a) Age-depth model derived from probabilistic alignment. (b) Alignment of the mid-term INPEFA (red line) with the LR04 δ18O stack (black line), with 1σ uncertainty represented by the shaded grey area. (c) Chronological uncertainty associated with the probabilistic tuning, expressed as the 95% confidence interval.

APPENDIX 5

Bulk geochemistry and clay-sized fraction mineralogy, major and trace elements, and Nd isotopes of clay-sized sediments of the Amazon Fan

Table S5.1. Bulk sediment major element concentrations measured via XRF.

Depth	Age	P.F. 1050°C	SiO_2	TiO_2	Al_2O_3	Fe_2O_3	MnO	MgO	CaO	Na_2O	K_2O	P_2O_5	SO_3	BaO	Total	CIA
mbsl	Ma		% m/m	% m/m	% m/m	% m/m	% m/m	% m/m	% m/m	% m/m	% m/m	% m/m	% m/m	% m/m	% m/m	
1617	0,7	19,7	38,09	0,57	11,49	5,04	< 0,05	1,08	5,91	1,06	1,63	0,13	4,9	11	101	69
1735	1,0	16,3	43,83	0,64	14,57	5,94	0,05	1,37	4,72	1,23	2,24	0,17	2,8	6,31	100	69
1806	1,1	15,6	47,05	0,73	17,74	6,96	0,05	1,49	2,28	1,41	2,53	0,19	1,3	3,19	101	71
1870	1,3	16,5	48,22	0,74	16,85	6,66	0,05	1,46	2,32	1,33	2,52	0,18	1,1	2,86	101	70
1932	1,4	11,8	51,74	0,81	17,62	6,87	0,06	1,6	3,13	1,4	2,67	0,19	< 1,0	1,54	100	70
2060	1,6	18,2	44,94	0,66	14,46	5,5	< 0,05	1,29	5,06	1,11	2,09	0,16	2,5	5	101	71
2184	1,9	13,6	52,59	0,73	13,06	5,21	0,06	1,25	1,68	1,3	2,1	0,13	2,2	6,32	100	67
2346	2,2	15,5	53,44	0,79	14,55	5,55	0,08	1,27	2,27	1,31	2,08	0,14	1,2	2,76	101	69
2382	2,3	14,9	47,76	0,7	12,83	5,23	0,06	1,32	5,73	1,06	2,16	0,11	2,8	5,63	101	69
2535	2,5	13,4	54,58	0,84	15,55	6,01	0,09	1,32	1,74	1,15	2,33	0,15	< 1,0	2,35	101	71
2598	2,7	10,3	55,55	0,87	18,18	6,82	0,11	1,54	1,46	1,23	2,52	0,16	< 1,0	1,07	100	73
2679	2,8	15,4	52,46	0,81	15,89	6,09	0,08	1,42	3,43	1,12	2,25	0,17	< 1,0	1,38	101	72
2796	3,0	15,6	52,21	0,75	14,41	5,39	0,07	1,28	2,76	1,17	2,07	0,14	1,3	3,63	101	70
2913	3,3	10,5	55,67	0,89	17,32	6,41	0,07	1,56	2,98	1,26	2,32	0,13	< 1,0	1,13	100	72
2958	3,4	15,4	49,17	0,81	17,41	6,46	0,07	1,4	1,65	1,12	2,21	0,15	1,4	3,57	101	74
3003	3,5	16,8	47,27	0,8	16,82	6,12	0,07	1,37	2,01	1,12	2,1	0,15	1,4	4,29	100	74
3093	3,7	14,2	48,4	0,73	14	5,78	0,08	1,46	3,54	1,1	2	0,15	3,1	6,62	101	71
3246	4,0	15,8	44,95	0,71	14,39	5,59	0,07	1,28	5,1	1,04	1,95	0,13	3,1	6,66	101	72
3309	4,2	16,5	44,75	0,64	12,55	4,93	0,05	1,27	6,15	1,03	1,87	0,13	3,5	7,49	101	70
3372	4,3	15,4	46,51	0,67	12,61	4,94	0,06	1,29	5,17	1,13	1,98	0,14	3,4	7,41	101	68
3417	4,4	10,8	55,88	0,79	15,12	5,77	0,07	1,48	4,04	1,32	2,4	0,13	1	2,43	101	69
3480	4,5	15,6	47,63	0,68	12,38	4,8	0,05	1,22	3,61	1,14	1,93	0,12	3,6	8,33	101	68
3543	4,6	13,6	49,26	0,67	11,97	4,85	0,05	1,29	3,43	1,15	1,92	0,12	3,7	9,64	102	67

3597	4,7	14,6	50,24	0,7	12,3	4,83	0,05	1,27	2,92	1,21	1,96	0,12	2,9	7,37	101	67
3660	4,8	26,4	38,04	0,52	9,11	3,5	0,05	1,19	12,81	0,84	1,2	0,1	2,1	4,12	100	69
3697	5,4	14,1	48,53	0,7	12,97	5,36	0,05	1,28	1,82	1,25	2,04	0,13	3,5	8,69	101	67
3727	6,0	13,9	55,95	0,84	16,24	6,09	0,08	1,46	1,47	1,32	2,36	0,15	< 1,0	1,15	101	70
3775	6,9	14,2	49,6	0,76	14,02	5,59	0,07	1,38	2,67	1,24	2,35	0,12	2,5	5,74	100	68
3853	8,1	32,2	38,27	0,53	9,57	3,69	< 0,05	0,96	9,61	0,83	1,58	0,07	1,2	1,75	100	68
3907	9,1	22,4	45,82	0,65	11,5	4,45	0,06	1,12	7,49	0,97	1,93	0,09	1,5	2,87	101	69
3985	10,5	18,0	52,6	0,83	16,02	6,06	0,1	1,3	1,51	1,3	2,13	0,14	< 1,0	0,95	101	71
4087	12,2	16,6	54,59	0,5	9,68	3,96	< 0,05	0,97	6,12	0,98	1,73	0,08	1,8	3,76	101	66
4111	12,6	19,0	38,38	0,63	15,73	5,24	< 0,05	1,37	9,77	0,71	1,21	0,09	3,8	5,28	101	81
4279	15,4	25,3	26,02	0,4	9,94	3,41	< 0,05	0,93	14,62	0,54	0,58	0,09	7,3	10,57	100	81
4390	17,3	25,9	30,01	0,47	11,97	4,03	< 0,05	1,19	16,62	0,59	0,73	0,08	4,2	4,14	100	81
4606	23,4	24,8	32,45	0,46	11,43	3,88	< 0,05	1,27	15,27	0,59	0,83	0,09	4,4	4,96	101	80
4681	24,0	25,9	31,69	0,52	12,57	4,32	< 0,05	1,19	12,77	0,59	0,96	0,07	4	5,18	100	81
4711	24,2	25,6	32,57	0,51	12,01	4,47	< 0,05	1,19	12,57	0,63	1,07	0,09	4,1	5,7	101	79

Table S5.2. Semi-quantitative estimation of clay mineral abundances using the MacDiff software.

Depth	Age Model	Smectite	Kaolinite	Chlorite	Illite
mbsl	Ma	%	%	%	%
1617	0,7	2	49	15	34
1665	0,8	1	38	19	42
1735	1,0	2	31	20	47
1806	1,1	0	43	15	43
1870	1,3	0	34	18	48
1932	1,4	7	40	12	41
2060	1,6	3	41	16	40
2184	1,9	17	30	11	42
2346	2,2	0	48	14	38
2382	2,3	0	53	16	31
2535	2,5	3	33	15	49
2590	2,6	6	38	9	47
2679	2,8	17	38	9	36
2796	3,0	2	33	18	47
2958	3,4	14	44	13	29
3003	3,5	6	52	9	33
3093	3,7	0	45	14	41
3248	4,0	18	43	10	29
3309	4,2	4	36	16	44
3372	4,3	0	43	14	43
3417	4,4	1	33	14	52
3480	4,5	2	34	22	42
3597	4,7	2	37	13	48
3660	4,8	18	30	12	40
3697	5,4	22	31	12	35
3715	5,8	26	29	12	33
3727	6,0	11	25	22	42
3775	6,9	8	35	15	42
3853	8,1	6	29	15	50
3957	10,0	10	34	13	43
3985	10,5	13	26	14	47
4005	10,8	10	36	12	42
4087	12,2	4	43	11	42
4111	12,6	0	89	0	11
4279	15,4	21	62	7	10
4312	15,9	10	79	6	5
4351	16,6	27	59	7	7
4375	17,0	17	68	6	9
4621	23,5	22	64	4	10
4711	24,2	20	59	7	14

Table S5.3. Major element concentrations of the clay-sized fraction of Amazon Fan (BP-3) samples analyzed via SF-ICP-MS.

Depth	Age Model	NaO	MgO	Al_2O_3	P_2O_5	K_2O	CaO	TiO_2	MnO	Fe_2O_3
mbsl	Ma	%	%	%	%	%	%	%	%	%
1527	0,6	0,6	1,9	24,1	0,1	3,8	0,2	1,1	0,0	7,0
1617	0,7	0,6	1,5	20,4	0,1	5,0	0,2	0,7	0,0	5,0
1626	0,7	0,6	1,6	20,1	0,1	5,1	0,2	0,8	0,0	5,3
1665	0,8	0,7	1,6	19,6	0,1	5,2	0,1	0,7	0,0	4,6
1735	1,0	1,0	1,9	22,7	0,1	8,3	0,2	0,8	0,0	5,6
1761	1,0	1,6	2,3	32,5	0,1	8,4	0,2	1,5	0,0	8,0
1806	1,1	2,7	1,6		0,2	3,8	0,5	2,1	0,1	13,5
1870	1,3	0,7	1,7	21,8	0,1	5,0	0,1	0,8	0,0	5,5
1932	1,4	1,2	1,9	23,9	0,1	5,4	0,1	0,9	0,0	6,0
2060	1,6	0,8	1,8	22,0	0,1	7,0	1,0	0,8	0,0	5,2
2094	1,7	0,8	1,9	22,4	0,1	5,3	0,1	0,8	0,0	5,0
2148	1,8	1,3	2,2	24,5	0,1	8,9	0,1	1,0	0,0	5,6
2184	1,9	2,1	1,9	23,8	0,1	5,9	0,4	0,8	0,0	5,8
2220	1,9	0,6	1,8	21,5	0,1	4,6	0,3	0,9	0,0	5,6
2346	2,2	0,6	1,7	21,4	0,1	3,4	0,3	0,8	0,0	5,5
2382	2,3	0,6	1,6	22,1	0,1	4,1	0,4	0,8	0,0	5,3
2445	2,4	0,9	1,8	21,7	0,1	6,3	0,4	0,9	0,0	5,2
2535	2,5	0,6	1,7	21,8	0,1	3,9	0,2	0,9	0,0	5,1
2580	2,6	1,0	2,2	25,2	0,1	8,2	0,5	1,1	0,0	6,1
2598	2,7	1,6	1,5	21,3	0,1	3,4	0,2	0,8	0,0	5,6
2643	2,8	0,3	0,9	11,9	0,0	1,8	0,2	0,4	0,0	3,0
2661	2,8	3,2	3,5		0,2	6,7	0,4	1,7	0,1	13,4
2679	2,8	0,9	1,3	19,0	0,1	2,6	0,2	0,6	0,0	4,7
2751	2,9	2,0	2,1	28,9	0,1	3,4	0,2	1,0	0,0	7,7
2760	3,0	1,5	1,6	20,9	0,1	2,4	0,0	0,8	0,0	5,6
2796	3,0	0,7	1,4	17,0	0,1	2,5	0,2	1,0	0,0	4,3
2850	3,1	0,5	1,5	19,8	0,1	2,3	0,1	0,8	0,0	4,8
2913	3,3	1,5	1,5	21,5	0,1	2,2	0,0	0,8	0,0	5,7
2958	3,4	0,4	1,4	20,9	0,1	2,1	0,1	0,8	0,0	4,9
2976	3,4	0,5	1,5	21,6	0,1	2,2	0,1	0,8	0,0	5,3
3003	3,5	0,5	1,5	22,1	0,1	2,1	0,1	0,8	0,0	4,9
3048	3,5	0,9	3,2		0,1	4,5	0,1	1,7	0,0	11,2
3093	3,7	0,5	1,7	20,0	0,1	2,4	0,1	0,8	0,0	5,0
3183	3,9	0,6	1,6	20,0	0,1	2,6	0,1	0,9	0,0	5,6
3219	3,9	0,5	1,5	19,4	0,1	2,3	0,1	0,9	0,0	4,9
3246	4,0	0,4	1,5	20,9	0,1	2,4	0,1	0,9	0,0	4,9
3282	4,1	0,5	1,6	18,9	0,1	2,4	0,1	0,8	0,0	5,0
3309	4,2	0,6	1,8	20,2	0,1	2,8	0,1	0,9	0,0	5,2

3336	4,2	0,4	1,7	19,6	0,1	2,6	0,1	0,8	0,0	5,1
3372	4,3	0,5	1,8	21,4	0,1	2,7	0,0	0,8	0,0	5,8
3417	4,4	0,8	1,8	22,2	0,1	2,6	0,0	0,7	0,0	5,8
3453	4,5	0,6	1,7	20,2	0,1	2,6	0,1	0,9	0,0	5,1
3480	4,5	0,5	1,6	16,8	0,1	2,4	0,1	0,8	0,0	4,7
3525	4,6	0,4	1,6	16,3	0,1	2,6	0,1	0,8	0,0	4,7
3543	4,6	0,4	1,7	18,9	0,1	2,7	0,1	0,8	0,0	4,7
3597	4,7	0,3	1,5	17,3	0,0	2,3	0,1	0,7	0,0	4,2
3633	4,8	0,3	1,2	12,9	0,1	1,7	0,2	0,6	0,0	3,7
3660	4,8	1,8	2,0	21,6	0,1	2,8	0,1	0,8	0,0	6,2
3669	4,9	0,3	1,4	15,2	0,0	2,2	0,1	0,8	0,0	4,3
3697	5,4	0,5	1,7	20,3	0,1	2,8	0,1	0,9	0,0	4,6
3715	5,8	0,6	1,9	21,6	0,1	3,0	0,1	0,9	0,0	5,2
3727	6,0	0,9	1,8	20,9	0,1	2,8	0,1	0,8	0,0	6,0
3751	6,5	0,7	1,9	20,8	0,1	2,9	0,1	0,8	0,0	6,0
3775	6,9	0,5	1,9	22,0	0,1	3,4	0,1	1,0	0,0	5,3
3793	7,2	0,9	2,0	23,2	0,1	3,4	0,1	0,9	0,0	6,7
3835	7,8	0,5	1,7	20,6	0,1	3,2	0,1	0,9	0,0	4,9
3853	8,1	0,2	1,1	14,0	0,0	2,1	0,1	0,6	0,0	3,3
3883	8,7	0,3	1,1	12,9	0,1	2,1	0,1	0,6	0,0	3,9
3907	9,1	0,3	1,4	16,8	0,1	2,5	0,1	0,7	0,0	4,1
3931	9,5	0,3	1,2	14,8	0,1	2,3	0,1	0,6	0,0	3,7
3955	9,9	0,3	1,3	14,8	0,1	2,3	0,2	0,7	0,0	4,0
3985	10,5	0,4	1,4	16,2	0,1	2,5	0,1	0,8	0,0	4,0
4045	11,5	0,6	1,3	14,4	0,1	2,6	0,2	0,8	0,0	4,1
4066	11,8	0,4	1,3	13,4	0,0	10,3	0,2	0,6	0,0	3,6
4069	11,9	0,4	1,6	19,6	0,1	3,0	0,1	0,9	0,0	4,3
4087	12,2	0,4	1,4	17,7	0,0	2,5	0,1	0,7	0,0	4,1
4090	12,2	0,6	1,3	14,5	0,0	2,5	0,2	0,9	0,0	3,8
4111	12,6	0,3	1,2	22,9	0,0	1,3	0,0	1,0	0,0	4,2
4126	12,8	0,2	0,8	12,8	0,1	1,4	0,2	0,6	0,0	2,7
4135	13,0	0,1	0,9	14,4	0,0	1,3	0,2	0,6	0,0	3,3
4159	13,4	0,1	0,6	12,8	0,1	1,1	0,2	0,7	0,0	2,4
4165	13,5	0,2	1,2	25,7	0,1	1,9	0,0	1,0	0,0	4,4
4177	13,7	0,1	1,4	24,1	0,1	1,9	0,0	1,0	0,0	4,7
4177	13,7	0,1	0,9	17,9	0,0	1,4	0,2	0,7	0,0	3,0
4186	13,9	0,1	1,2	18,9	0,0	1,4	0,2	0,7	0,0	3,7
4201	14,2	0,1	1,2	21,1	0,1	1,2	0,1	0,8	0,0	4,0
4225	14,5	0,1	0,9	16,8	0,0	1,2	0,1	0,7	0,0	3,2
4255	15,0	0,1	1,0	19,8	0,0	1,1	0,1	0,7	0,0	3,1
4279	15,4	2,1	1,2	22,7	0,0	1,2	0,1	0,8	0,0	4,3
4291	15,6	0,1	1,1	24,2	0,1	1,2	0,0	1,1	0,0	3,9
4351	16,6	0,1	1,1	21,1	0,0	1,0	0,1	0,8	0,0	3,0

4390	17,3	0,1	1,2	21,0	0,1	1,3	0,1	0,9	0,0	3,5
4456	22,3	0,1	1,3	20,3	0,1	1,3	0,1	0,7	0,0	3,1
4501	22,6	0,1	1,1	16,5	0,0	1,3	0,1	0,6	0,0	3,4
4531	22,8	0,1	1,2	18,4	0,1	1,3	0,1	0,6	0,0	3,1
4576	23,2	0,1	1,2	18,1	0,1	1,1	0,1	0,6	0,0	2,9
4606	23,4	0,3	1,0	19,3	0,0	0,9	0,1	0,8	0,0	3,9
4621	23,5	0,0	1,2	19,2	0,0	1,1	0,1	0,7	0,0	3,0
4651	23,7	0,1	1,0	18,2	0,1	1,1	0,1	0,6	0,0	2,9
4681	24,0	0,1	1,2	21,5	0,0	1,3	0,1	0,8	0,0	3,4
4711	24,2	0,2	1,3	19,3	0,0	1,6	0,1	0,8	0,0	4,2

Table S5.4. Trace element concentrations of clay-sized fraction of Amazon Fan (BP-3) samples analyzed via SF-ICP-MS.

Depth	Age Model	Li	Sr	Zr	Ba	Hf	Th	U	Ni	Cu	Zn	Sc	V	Cr	La	Ce	Pr	Nd	Sm	Eu	Gd	Tb	Dy	Ho	Er	Yb	Lu	Y
mbsl	Ma	ppm	ppm	ppm	ppm	ppm	ppm	ppm	ppm	ppm	ppm	ppm	ppm	ppm	ppm	ppm	ppm	ppm	ppm	ppm	ppm	ppm	ppm	ppm	ppm	ppm	ppm	ppm
1527	0,6	90,3	131,7	166,5	2652	4,7	17,1	3,3	44,8	25,5	114,4	19,0	166,8	100,6	55,7	108,4	11,9	42,3	7,1	1,3	5,0	0,7	4,3	0,9	2,6	2,7	0,4	24,8
1617	0,7	100,1	374,7	77,7	8025	2,3	11,5	2,6	33,7	25,7	101,8	14,7	139,0	75,2	42,1	79,4	9,0	32,0	5,5	1,0	4,0	0,6	3,3	0,7	2,0	2,0	0,3	18,9
1626	0,7	93,1	321,8	41,7	15842	1,4	10,1	2,6	33,3	24,9	104,8	14,7	144,2	81,4	44,3	81,8	9,4	33,0	5,8	1,2	4,5	0,6	3,5	0,7	2,1	2,2	0,3	19,2
1665	0,8	109,4	183,8	141,0	10254	4,2	14,5	2,8	29,7	20,4	97,8	15,0	136,2	70,1	48,1	90,4	10,2	36,0	6,1	1,2	4,6	0,6	3,7	0,7	2,2	2,3	0,3	20,9
1735	1,0	114,1	201,6	127,2	11305	3,8	13,6	2,9	34,3	22,8	112,6	15,6	159,5	85,4	46,3	87,7	10,0	35,4	6,1	1,1	4,4	0,6	3,6	0,7	2,2	2,3	0,3	21,1
1761	1,0	158,3	184,5		911	6,3	21,6	4,5	50,4	20,3	154,0	21,7	224,9	118,4	80,1	125,9	17,1	60,4	10,4	1,9	7,4	1,0	5,7	1,2	3,4	3,4	0,5	24,5
1806	1,1	274,9	251,0		217	10,9	11,1	7,2	82,6	58,2	236,0	11,7	395,4	213,1	12,7	36,2	4,7	19,2	4,0	0,8	3,0	0,4	2,7	0,6	1,8	2,1	0,3	15,5
1870	1,3	95,5	153,3	128,3	6540	3,8	14,3	2,7	32,8	20,5	108,3	16,9	154,3	78,4	52,4	98,5	11,1	39,2	6,6	1,2	4,6	0,7	3,9	0,8	2,4	2,5	0,4	20,0
1932	1,4	107,0	113,1	146,9	771	4,2	16,9	2,9	35,9	14,2	107,5	17,8	170,5	92,3	58,6	101,4	12,0	42,2	7,2	1,4	5,1	0,7	4,1	0,8	2,5	2,6	0,4	20,5
2060	1,6	117,7	202,0	131,9	11854	3,8	15,0	2,8	33,2	25,8	147,9	16,4	150,7	78,8	47,5	89,3	10,0	35,2	5,9	1,1	4,3	0,6	3,5	0,7	2,2	2,2	0,3	20,6
2094	1,7	110,9	121,6	148,4	737	4,2	23,8	2,9	30,5	13,1	91,6	21,4	142,9	74,8	50,5	99,7	11,6	41,1	7,0	1,3	5,0	0,7	3,9	0,8	2,4	2,6	0,4	23,6
2148	1,8	149,5	229,1	152,9	11863	4,4	14,3	3,1	42,0	28,0	143,1	18,3	172,1	87,0	49,3	91,7	10,5	36,9	6,2	1,2	4,6	0,6	3,6	0,7	2,2	2,2	0,3	22,3
2184	1,9	118,3	102,7	143,4	803	4,1	17,7	2,7	36,0	15,8	267,6	18,9	164,1	85,3	44,6	83,1	9,5	33,5	5,7	1,0	4,1	0,6	3,4	0,7	2,1	2,2	0,3	19,2
2220	1,9	92,9	142,2	128,9	5821	3,8	14,2	2,7	37,2	20,3	246,0	16,9	150,3	79,4	49,4	92,7	10,6	37,2	6,3	1,2	4,6	0,6	3,8	0,8	2,3	2,3	0,3	20,4
2346	2,2	76,8	125,0	134,4	4914	4,0	14,3	2,7	32,0	20,8	186,0	16,1	146,5	79,3	50,2	92,8	10,6	37,4	6,4	1,2	4,8	0,7	3,9	0,8	2,4	2,4	0,4	20,8
2382	2,3	91,0	100,5	132,0	2310	3,9	15,5	2,5	34,9	27,8	267,9	16,2	148,4	78,8	45,2	80,1	9,2	32,4	5,5	1,0	4,1	0,6	3,4	0,7	2,1	2,1	0,3	18,2
2445	2,4	104,3	150,9	134,6	5920	4,0	13,0	2,7	38,2	21,1	298,9	17,0	146,3	79,4	50,8	93,3	10,7	37,6	6,4	1,2	4,7	0,7	3,9	0,8	2,3	2,3	0,4	20,1
2535	2,5	88,3	136,8	125,5	5278	3,7	13,6	2,7	34,9	16,8	194,3	17,4	151,7	82,2	54,2	103,9	11,7	41,8	7,0	1,3	5,1	0,7	4,0	0,8	2,4	2,4	0,4	21,1
2580	2,6	140,1	160,5	139,9	4892	4,1	15,0	3,0	48,2	22,5	339,2	21,1	178,4	95,4	68,6	125,3	14,2	52,8	8,7	1,6	6,4	0,8	4,9	1,0	3,0	2,9	0,5	22,1
2598	2,7	90,8	88,6	128,0	638	3,7	17,3	2,6	30,0	11,8	182,2	17,4	151,0	83,5	49,5	94,4	10,5	37,1	6,2	1,1	4,4	0,6	3,6	0,7	2,2	2,3	0,3	19,6
2643	2,8	47,8	60,8	60,6	3041	1,8	6,8	1,3	18,7	8,2	136,9	9,0	82,7	47,0	58,5	111,7	12,5	44,7	7,5	1,4	5,5	0,7	4,3	0,9	2,6	2,7	0,4	10,4
2661	2,8	167,5	161,5		1367	7,6	34,1	5,1	67,3	26,6	358,4	38,6	353,8	195,0	49,4	101,4	10,8	38,7	6,7	1,3	4,9	0,7	3,8	0,8	2,2	2,2	0,3	38,0
2679	2,8	70,9	63,4	109,4	376	3,2	12,8	2,1	25,8	9,5	144,9	14,0	136,2	72,8	47,2	88,9	9,9	35,0	6,0	1,1	4,3	0,6	3,5	0,7	2,2	2,2	0,3	16,9

2751	2,9	91,0	106,4	168,1	1310	4,9	20,9	3,3	38,9	17,5	214,7	23,0	213,6	110,1	55,2	106,5	11,7	41,5	6,9	1,3	5,3	0,7	4,3	0,9	2,6	2,7	0,4	25,2
2760	3,0	68,6	80,5	127,8	987	3,7	16,0	2,6	27,9	12,6	89,2	16,9	162,9	81,2	42,2	80,9	9,0	31,7	5,3	1,0	4,0	0,6	3,2	0,7	2,0	2,1	0,3	19,1
2796	3,0	54,1	365,1	183,7	24581	5,2	12,2	3,0	26,5	14,9	88,2	14,7	127,6	65,5	44,2	83,6	9,7	34,7	6,0	1,2	4,8	0,7	4,3	0,9	2,6	2,8	0,4	26,2
2850	3,1	63,0	131,5	137,5	6427	3,9	15,4	2,8	27,8	14,8	90,1	16,1	156,6	78,5	45,7	82,7	9,4	32,7	5,5	1,1	4,2	0,6	3,4	0,7	2,1	2,2	0,3	20,4
2913	3,3	64,8	76,1	140,0	677	4,0	16,8	2,5	27,9	12,0	88,9	17,1	155,3	82,7	42,2	79,9	8,9	31,4	5,3	1,0	4,1	0,6	3,4	0,7	2,1	2,1	0,3	19,9
2958	3,4	58,6	122,4	148,0	6031	4,3	15,9	2,6	26,2	19,4	84,4	16,1	143,3	76,4	42,8	77,4	8,8	30,9	5,2	1,0	4,1	0,6	3,4	0,7	2,1	2,2	0,3	20,1
2976	3,4	59,7	154,0	106,5	8213	3,3	13,6	2,8	26,7	19,4	87,9	16,1	146,0	74,6	44,5	82,8	9,3	32,8	5,6	1,1	4,5	0,6	3,6	0,7	2,2	2,3	0,3	21,4
3003	3,5	56,9	162,8	146,8	10529	4,3	13,8	2,7	25,5	17,4	87,5	15,6	138,1	71,5	44,4	83,1	9,3	32,7	5,6	1,1	4,5	0,6	3,7	0,8	2,2	2,3	0,3	21,7
3048	3,5	141,7	157,0		1194	8,3	28,6	5,3	55,3	23,3	188,0	34,0	318,0	171,8	92,1	183,0	19,7	70,1	11,8	2,4	9,5	1,3	7,4	1,5	4,4	4,6	0,7	43,9
3093	3,7	64,4	232,6	125,3	12369	3,6	12,0	2,8	27,5	19,1	96,6	16,1	148,4	76,6	48,1	94,2	10,3	36,8	6,2	1,2	4,8	0,6	3,5	0,7	2,1	2,3	0,3	21,1
3183	3,9	66,0	169,9	141,4	7275	4,1	15,5	2,9	28,6	15,3	97,6	16,7	155,3	73,7	50,2	97,0	10,8	38,3	6,5	1,3	5,0	0,7	4,0	0,8	2,4	2,5	0,4	23,3
3219	3,9	62,7	246,8	114,4	13984	3,3	12,6	2,9	27,5	16,7	93,1	15,8	148,0	73,8	49,5	95,5	10,7	38,0	6,5	1,3	5,0	0,7	3,7	0,8	2,2	2,4	0,3	22,1
3246	4,0	62,6	210,3	199,1	13642	5,5	14,8	2,8	26,4	18,2	92,9	16,3	152,7	79,6	46,6	88,0	9,8	34,8	5,9	1,2	4,7	0,6	3,6	0,7	2,2	2,3	0,3	21,5
3282	4,1	60,6	316,4	93,8	6428	2,8	11,6	2,8	27,5	17,7	98,3	15,5	154,8	75,6	45,8	89,2	10,0	35,5	6,1	1,2	4,8	0,6	3,6	0,7	2,1	2,3	0,3	21,6
3309	4,2	71,6	312,8		41263	12,1	19,0	3,2	31,4	19,5	103,2	17,9	158,6	76,4	53,1	102,9	11,5	40,8	7,0	1,7	5,5	0,7	4,0	0,8	2,4	2,8	0,4	24,6
3336	4,2	67,9	176,6	131,0	9012	3,7	12,2	2,8	27,8	20,2	95,5	16,1	155,2	76,8	44,8	83,8	9,5	33,7	5,7	1,1	4,5	0,6	3,3	0,7	2,0	2,2	0,3	20,2
3372	4,3	71,2	79,7	124,9	585	3,6	13,7	2,6	27,5	10,7	90,5	17,0	164,4	82,5	43,4	83,6	9,3	32,9	5,6	1,1	4,4	0,6	3,4	0,7	2,1	2,2	0,3	19,9
3417	4,4	68,5	84,7	120,4	1473	3,4	15,3	2,6	28,0	10,6	89,3	17,1	42,4	81,1	49,3	92,8	10,2	35,6	5,9	1,1	4,5	0,6	3,4	0,7	2,0	2,1	0,3	19,7
3453	4,5	67,1	172,0	139,6	7823	4,0	13,3	2,9	28,2	16,1	98,6	16,8	154,7	77,4	48,6	92,7	10,4	36,8	6,3	1,3	5,0	0,7	3,8	0,8	2,2	2,3	0,3	22,2
3480	4,5	62,9	451,9	30,1	6842	0,9	6,9	3,0	25,4	19,4	92,2	14,3	138,7	70,3	45,5	87,8	10,0	35,9	6,1	1,2	4,8	0,6	3,7	0,8	2,2	2,3	0,3	21,6
3525	4,6	66,0	594,7	29,4	9808	0,9	10,4	3,1	27,7	19,7	90,4	14,4	135,1	68,9	48,0	92,8	10,4	37,2	6,2	1,2	4,7	0,6	3,7	0,8	2,2	2,4	0,3	21,5
3543	4,6	71,2	386,2	152,5	23787	4,4	14,6	2,9	26,5	18,7	95,5	16,1	147,1	73,6	48,4	93,1	10,3	36,7	6,2	1,4	4,9	0,6	3,7	0,8	2,2	2,4	0,3	21,7
3597	4,7	63,8	243,5	116,9	14070	3,4	13,6	2,5	23,1	15,7	81,9	14,1	136,9	68,0	42,6	78,8	8,9	31,3	5,2	1,1	4,1	0,5	3,1	0,7	2,0	2,1	0,3	18,7
3633	4,8	48,9	663,4	35,7	8755	1,1	8,4	2,3	20,4	16,9	72,6	11,0	145,4	53,2	34,9	67,5	7,5	26,6	4,5	0,9	3,6	0,5	2,7	0,6	1,6	1,7	0,2	16,0
3660	4,8	76,8	90,4	131,2	1241	3,7	16,1	2,7	29,3	11,2	94,6	18,5	158,3	85,3	47,3	95,2	10,5	37,3	6,3	1,2	4,9	0,6	3,6	0,7	2,2	2,2	0,3	21,0
3669	4,9	57,5	562,3	67,4	17279	2,0	11,2	2,7	23,6	15,6	85,3	13,6	140,5	63,1	42,6	81,2	9,2	32,4	5,4	1,2	4,2	0,6	3,3	0,7	2,0	2,2	0,3	19,2
3697	5,4	76,0	368,7	84,8	7655	2,5	13,9	2,9	26,5	11,9	84,8	16,7	151,2	78,8	50,4	95,4	10,5	37,1	6,0	1,2	4,6	0,6	3,5	0,7	2,2	2,4	0,3	21,1
3715	5,8	82,2	220,3	145,2	7946	4,2	15,5	3,0	29,8	14,0	95,6	18,4	161,4	83,5	53,5	102,3	11,3	39,7	6,5	1,3	5,0	0,7	3,8	0,8	2,4	2,6	0,4	22,9

3727	6,0	76,9	158,1	124,6	5985	3,6	14,5	2,6	28,6	9,8	93,1	16,2	159,5	84,7	45,7	89,1	9,8	34,5	5,7	1,1	4,4	0,6	3,3	0,7	2,1	2,1	0,3	19,3
3751	6,5	78,3	359,9	126,3	20477	3,6	14,3	2,6	29,3	11,3	100,7	16,3	160,6	86,4	45,4	89,3	9,8	35,0	5,9	1,3	4,6	0,6	3,4	0,7	2,1	2,3	0,3	20,4
3775	6,9	103,6	231,9	148,3	7591	4,3	17,5	3,0	32,9	12,5	98,7	18,7	158,9	89,9	60,3	116,9	12,8	45,4	7,6	1,5	5,8	0,7	4,2	0,9	2,6	2,7	0,4	24,3
3793	7,2	102,4	131,4	151,7	1576	4,3	20,7	3,2	31,7	12,4	91,4	19,5	164,3	96,5	63,6	121,3	13,4	47,8	8,0	1,5	6,2	0,8	4,4	0,9	2,7	2,8	0,4	25,4
3835	7,8	97,4	226,6	134,8	8112	3,9	16,4	2,9	29,6	11,5	85,6	16,7	149,9	83,8	55,8	107,4	11,7	41,4	6,9	1,4	5,3	0,6	3,7	0,8	2,3	2,4	0,4	21,7
3853	8,1	61,7	257,4	103,0	10573	2,9	12,0	2,0	18,0	7,9	53,1	11,4	121,4	58,0	38,5	72,1	8,0	28,2	4,8	1,0	3,9	0,5	2,7	0,6	1,7	1,8	0,3	15,7
3883	8,7	61,0	524,2	26,4	8121	0,8	9,0	2,3	20,1	10,3	70,8	11,2	145,8	58,3	39,1	74,2	8,3	29,2	4,9	1,0	3,9	0,5	2,9	0,6	1,8	1,9	0,3	16,7
3907	9,1	72,8	359,8	61,6	12913	1,9	14,0	2,4	20,8	10,7	66,6	14,1	140,3	71,8	44,4	82,4	9,1	31,6	5,3	1,1	4,2	0,5	3,1	0,6	2,0	2,1	0,3	18,0
3931	9,5	63,0	307,3	100,6	13019	2,9	11,7	2,2	18,7	8,7	63,3	12,5	142,1	63,3	40,9	76,6	8,5	29,7	4,9	1,1	4,0	0,5	2,7	0,6	1,7	1,9	0,3	16,0
3955	9,9	64,9	808,2	107,0	7327	3,1	11,3	2,3	20,4	11,0	74,0	12,6	141,2	62,4	40,9	77,7	8,6	30,4	5,0	1,0	4,0	0,5	2,9	0,6	1,8	2,0	0,3	17,2
3985	10,5	70,9	470,4	160,2	26799	4,6	13,9	2,5	22,0	10,9	73,6	13,9	134,2	66,0	44,6	83,3	9,2	32,3	5,4	1,4	4,4	0,5	3,2	0,7	2,0	2,3	0,3	19,1
4045	11,5	53,9	637,3		35477	6,3	14,2	2,3	22,5	11,1	77,7	11,7	129,5	64,1	36,6	70,8	7,8	28,0	4,8	1,3	4,3	0,5	3,2	0,7	2,0	2,2	0,3	19,6
4066	11,8	51,8	754,8	119,7	135483	3,6	27,8	1,8	17,1	9,5	65,9	13,3	117,2	59,2	88,6	137,7	12,4	39,3	6,1	1,2	5,7	0,6	3,2	0,7	1,9	2,5	0,3	26,4
4069	11,9	84,1	478,7		64704	19,2	27,8	3,1	25,3	9,4	77,5	17,5	155,2	77,6	59,9	114,9	12,5	43,9	7,3	1,3	5,9	0,7	4,2	0,9	2,6	3,0	0,4	25,3
4087	12,2	80,4	238,2	124,7	8382	3,7	15,2	2,3	19,3	11,0	69,3	14,3	144,4	74,8	41,6	77,9	8,6	30,3	5,1	1,0	4,2	0,5	3,1	0,6	1,8	2,0	0,3	17,8
4090	12,2	65,2	604,3	34,2	10141	1,1	10,8	2,6	21,6	8,0	70,5	11,9	126,2	61,8	41,7	79,8	8,9	31,5	5,3	1,1	4,3	0,6	3,4	0,7	2,1	2,2	0,3	20,0
4111	12,6	96,8	88,6	141,1	1517	4,2	16,7	2,3	18,3	3,9	40,3	12,5	114,9	112,8	51,4	88,3	9,0	28,8	4,2	0,8	3,4	0,4	2,6	0,5	1,5	1,5	0,2	14,2
4126	12,8	54,0	859,2	97,9	131368	2,8	10,1	1,9	12,0	7,1	46,1	8,1	115,7	57,1	32,5	52,6	5,9	19,7	3,4	1,4	3,4	0,3	1,8	0,4	1,1	2,1	0,2	11,4
4135	13,0	65,5	819,3	36,5	7970	1,2	5,4	1,7	12,7	8,0	50,0	8,1	102,7	78,1	30,0	44,3	4,8	15,4	2,4	0,6	2,1	0,2	1,4	0,3	0,8	0,9	0,1	7,2
4159	13,4	55,7	910,5	102,6	9864	2,9	6,7	2,2	12,3	4,9	37,0	7,3	106,5	61,1	38,1	56,2	6,3	20,1	3,0	0,8	2,7	0,3	1,7	0,3	1,0	1,1	0,2	8,9
4165	13,5	125,2	155,4	159,4	3273	4,8	11,1	2,4	22,4	7,2	63,2	13,0	151,6	124,8	55,2	83,8	8,8	27,5	4,0	0,8	3,4	0,4	2,2	0,4	1,3	1,4	0,2	11,7
4177	13,7	101,2	91,5	147,7	1118	4,4	14,6	2,2	21,1	7,8	58,9	12,8	132,7	114,9	56,3	87,4	9,4	29,6	4,4	0,9	3,8	0,5	2,7	0,5	1,6	1,7	0,2	14,1
4177	13,7	65,2	1038,4		179710	22,5	31,5	1,8	14,5	5,5	47,2	10,8	110,8	76,2	44,2	67,1	7,2	23,0	3,7	1,2	3,7	0,4	2,0	0,4	1,2	2,1	0,2	12,6
4186	13,9	76,6	444,2		37048	9,1	18,9	1,7	14,1	7,2	52,2	10,6	108,2	95,9	46,2	80,5	8,6	28,3	4,4	1,3	3,8	0,4	2,4	0,5	1,3	1,5	0,2	12,3
4201	14,2	79,0	227,5	135,6	8043	3,9	14,0	2,2	18,4	8,0	57,4	11,4	113,2	108,1	49,1	77,5	8,2	26,1	3,8	0,8	3,3	0,4	2,4	0,5	1,4	1,4	0,2	12,9
4225	14,5	74,1	551,7	104,2	26003	3,2	11,3	1,8	17,4	7,4	46,1	9,6	104,5	85,9	42,3	69,5	7,5	24,3	3,6	1,1	3,1	0,4	2,0	0,4	1,2	1,3	0,2	10,8
4255	15,0	87,6	397,4	160,2	18858	4,7	12,9	1,8	12,1	3,2	38,9	9,9	100,5	97,2	46,3	78,5	8,4	27,2	3,9	1,0	3,3	0,4	2,1	0,4	1,1	1,3	0,2	10,9
4279	15,4	103,5	241,8	116,1	10098	3,7	16,5	2,0	14,3	5,5	50,8	11,7	109,4	121,8	47,2	77,0	8,1	25,7	3,8	0,9	3,3	0,4	2,1	0,4	1,2	1,2	0,2	10,7

4291	15,6	102,4	118,4	159,8	2349	4,7	17,4	2,6	17,1	5,4	42,4	12,0	105,2	112,1	65,5	108,1	11,6	37,3	5,5	1,2	4,8	0,5	3,1	0,6	1,7	1,8	0,2	15,3
4351	16,6	95,3	368,0	121,8	15555	3,7	16,9	2,7	12,1	2,7	37,0	10,7	95,9	103,5	53,9	93,9	9,9	32,1	4,7	1,1	3,9	0,5	2,5	0,5	1,4	1,4	0,2	13,0
4390	17,3	96,3	273,9	122,4	10347	3,7	13,7	2,5	17,5	3,1	41,9	11,6	99,9	101,8	52,6	85,3	9,1	29,2	4,3	1,0	3,6	0,4	2,4	0,5	1,3	1,4	0,2	12,5
4456	22,3	95,5	395,7	92,5	17594	2,8	10,1	2,9	12,4	4,1	47,6	10,0	125,8	110,3	39,0	66,5	6,8	21,9	3,2	1,0	3,0	0,3	1,9	0,4	1,1	1,4	0,2	10,4
4501	22,6	71,3	490,7	105,2	25472	3,1	8,7	2,2	15,2	7,9	46,1	9,2	125,2	83,8	34,7	55,8	5,8	18,7	2,8	0,9	2,4	0,3	1,5	0,3	0,9	1,1	0,1	8,3
4531	22,8	79,4	349,9	81,4	15942	2,5	9,7	2,1	13,1	6,9	41,3	9,2	109,4	93,3	30,3	48,6	4,9	15,7	2,4	0,7	2,2	0,2	1,4	0,3	0,9	1,0	0,1	8,2
4576	23,2	80,7	340,9	83,5	16440	2,5	9,6	2,2	13,8	5,7	39,2	8,8	112,3	93,0	31,6	51,6	5,2	16,5	2,4	0,8	2,1	0,3	1,5	0,3	0,9	1,1	0,1	8,7
4606	23,4	88,0	302,6	121,9	2838	3,7	10,6	2,5	15,0	7,7	45,5	9,7	115,3	99,7	36,1	64,2	6,1	19,4	2,8	0,6	2,4	0,3	1,7	0,4	1,0	1,1	0,2	9,3
4621	23,5	79,6	331,8	96,6	16518	3,0	13,6	2,1	11,7	4,4	43,0	9,2	92,9	93,9	36,6	62,0	6,3	20,1	2,9	0,7	2,4	0,3	1,7	0,4	1,0	1,1	0,2	9,5
4651	23,7	72,5	388,6	99,2	16513	3,0	14,1	2,0	11,3	4,6	99,5	8,7	102,9	91,9	36,8	65,4	6,5	21,1	3,1	0,8	2,7	0,3	1,9	0,4	1,1	1,2	0,2	10,5
4681	24,0	88,3	351,6	161,3	18294	4,6	17,2	2,1	14,5	5,4	41,7	11,1	109,6	107,2	43,5	77,2	7,6	24,4	3,6	0,9	3,0	0,4	2,2	0,5	1,3	1,5	0,2	12,5
4711	24,2	71,6	317,1	108,9	13833	3,3	13,8	2,3	16,2	7,7	47,7	11,8	130,4	110,8	44,9	77,0	7,8	25,2	3,7	0,9	3,1	0,4	2,2	0,4	1,3	1,4	0,2	12,3

Table S5.5. Lanthanum, Cerium, and Europium anomalies of the clay-sized fraction of BP-3 sediments. Anomalies were calculated using geometrical extrapolations of WRAS-normalized values.

Depth	Age	Ce/Ce*	La/La*	Eu/Eu*
1527	0,6	1,0	0,7	1,0
1617	0,7	0,9	0,7	1,0
1626	0,7	0,9	0,9	1,2
1665	0,8	0,9	0,8	1,1
1735	1,0	0,9	0,8	1,1
1761	1,0	0,8	0,7	1,1
1806	1,1	0,9	1,4	1,1
1870	1,3	0,9	0,7	1,0
1932	1,4	0,9	0,7	1,1
2060	1,6	1,0	0,7	1,1
2094	1,7	0,9	0,8	1,1
2148	1,8	0,9	0,8	1,1
2184	1,9	0,9	0,7	1,1
2220	1,9	0,9	0,7	1,1
2346	2,2	0,9	0,8	1,1
2382	2,3	0,9	0,8	1,1
2445	2,4	0,9	0,8	1,1
2535	2,5	1,0	0,8	1,1
2580	2,6	1,0	0,8	1,1
2598	2,7	1,0	0,7	1,1
2643	2,8	1,0	0,8	1,1
2661	2,8	1,0	0,8	1,1
2679	2,8	1,0	0,7	1,1
2751	2,9	1,0	0,8	1,1
2760	3,0	1,0	0,8	1,1
2796	3,0	0,9	0,9	1,1
2850	3,1	0,9	0,7	1,1
2913	3,3	1,0	0,8	1,1
2958	3,4	0,9	0,8	1,1
2976	3,4	1,0	0,8	1,1
3003	3,5	1,0	0,8	1,1
3048	3,5	1,0	0,8	1,1
3093	3,7	1,0	0,8	1,2
3183	3,9	1,0	0,8	1,1
3219	3,9	1,0	0,8	1,2
3246	4,0	1,0	0,8	1,2
3282	4,1	1,0	0,8	1,1
3309	4,2	1,0	1,0	1,4
3336	4,2	0,9	0,8	1,1
3372	4,3	1,0	0,8	1,1

3417	4,4	1,0	0,7	1,1
3453	4,5	1,0	0,8	1,1
3480	4,5	0,9	0,8	1,1
3525	4,6	1,0	0,8	1,1
3543	4,6	1,0	0,9	1,3
3597	4,7	0,9	0,8	1,2
3633	4,8	1,0	0,8	1,2
3660	4,8	1,0	0,8	1,1
3669	4,9	0,9	0,9	1,3
3697	5,4	1,0	0,8	1,1
3715	5,8	1,0	0,8	1,1
3727	6,0	1,0	0,8	1,1
3751	6,5	1,0	0,9	1,3
3775	6,9	1,0	0,8	1,1
3793	7,2	1,0	0,8	1,1
3835	7,8	1,0	0,8	1,2
3853	8,1	1,0	0,8	1,2
3883	8,7	1,0	0,8	1,2
3907	9,1	1,0	0,8	1,2
3931	9,5	1,0	0,9	1,3
3955	9,9	1,0	0,8	1,2
3985	10,5	1,0	1,0	1,5
4045	11,5	1,0	1,2	1,5
4066	11,8	1,1	0,5	1,1
4069	11,9	1,0	0,7	1,0
4087	12,2	1,0	0,8	1,2
4090	12,2	1,0	0,8	1,2
4111	12,6	1,0	0,5	1,1
4126	12,8	0,9	1,4	2,3
4135	13,0	0,9	0,7	1,5
4159	13,4	0,9	0,7	1,5
4165	13,5	0,9	0,5	1,2
4177	13,7	0,9	0,5	1,2
4177	13,7	0,9	0,9	1,9
4186	13,9	0,9	0,9	1,7
4201	14,2	0,9	0,5	1,2
4225	14,5	0,9	0,8	1,7
4255	15,0	0,9	0,7	1,5
4279	15,4	0,9	0,6	1,3
4291	15,6	0,9	0,6	1,2
4351	16,6	0,9	0,6	1,3
4390	17,3	0,9	0,6	1,3
4456	22,3	1,0	0,8	1,8
4501	22,6	0,9	0,8	1,8
4531	22,8	1,0	0,8	1,8
4576	23,2	1,0	0,8	1,8

4606	23,4	1,0	0,5	1,2
4621	23,5	0,9	0,6	1,4
4651	23,7	1,0	0,7	1,5
4681	24,0	1,0	0,7	1,5
4711	24,2	1,0	0,6	1,4

Table S5.6. Hf-Nd isotopes measured via MC-ICPS-MS on the clay fraction of BP-3 sediments.

Depth	$^{143}Nd/^{144}Nd$	2se	εNd(0)	2 σ	$^{176}Hf/^{177}Hf$	2se	εHf(0)	2 σ	ΔεHf
1527	0,512046	0,000014	-11,40	0,28	0,282702	0,000012	-2,95	0,42	0,64
1617	0,512028	0,000010	-11,75	0,20	0,282705	0,000009	-2,83	0,31	1,04
1626	0,512037	0,000008	-11,57	0,15	0,282755	0,000013	-1,07	0,47	2,66
1665	0,512029	0,000011	-11,72	0,21	0,282682	0,000008	-3,63	0,27	0,21
1735	0,512039	0,000010	-11,52	0,20	0,282703	0,000006	-2,90	0,21	0,79
1761	0,512036	0,000009	-11,59	0,17	0,282744	0,000007	-1,45	0,25	2,29
1806	0,512045	0,000008	-11,42	0,15	0,282768	0,000007	-0,61	0,25	2,99
1870	0,512025	0,000007	-11,81	0,13	0,282697	0,000006	-3,12	0,20	0,80
1932	0,512034	0,000012	-11,63	0,24	0,282723	0,000008	-2,21	0,27	1,57
2060	0,512005	0,000010	-12,20	0,20	0,282703	0,000008	-2,90	0,28	1,32
2094	0,512024	0,000007	-11,82	0,14	0,282741	0,000009	-1,54	0,33	2,38
2148	0,512008	0,000010	-12,14	0,19	0,282689	0,000006	-3,40	0,20	0,77
2184	0,512041	0,000008	-11,48	0,16	0,282770	0,000008	-0,52	0,28	3,13
2220	0,512029	0,000013	-11,73	0,25	0,282682	0,000005	-3,65	0,17	0,20
2346	0,512046	0,000011	-11,40	0,21	0,282658	0,000007	-4,49	0,24	-0,90
2382	0,512000	0,000008	-12,30	0,16	0,282705	0,000005	-2,81	0,17	1,48
2445	0,512022	0,000011	-11,85	0,21	0,282641	0,000006	-5,10	0,21	-1,15
2535	0,512028	0,000015	-11,73	0,28	0,282677	0,000009	-3,81	0,32	0,04
2580	0,512013	0,000011	-12,03	0,21	0,282711	0,000006	-2,63	0,22	1,45
2598	0,512003	0,000010	-12,24	0,20	0,282796	0,000008	0,38	0,29	4,63
2643	0,512014	0,000011	-12,01	0,21	0,282661	0,000007	-4,40	0,26	-0,33
2661	0,512042	0,000011	-11,48	0,21	0,282716	0,000006	-2,43	0,20	1,22
2679	0,512028	0,000010	-11,75	0,20	0,282804	0,000010	0,68	0,36	4,55
2751	0,512017	0,000009	-11,95	0,18	0,282701	0,000005	-2,97	0,17	1,05
2760	0,512039	0,000010	-11,53	0,20	0,282766	0,000006	-0,66	0,21	3,03
2796	0,512036	0,000012	-11,59	0,23	0,282542	0,000007	-8,58	0,23	-4,84
2850	0,512031	0,000007	-11,69	0,13	0,282717	0,000010	-2,42	0,34	1,40
2913	0,512046	0,000011	-11,39	0,22	0,282700	0,000007	-2,99	0,26	0,60
2958	0,512031	0,000008	-11,68	0,16	0,282686	0,000007	-3,50	0,25	0,31
2976	0,512028	0,000006	-11,75	0,11	0,282677	0,000006	-3,83	0,20	0,03
3003	0,512014	0,000009	-12,02	0,18	0,282651	0,000005	-4,75	0,18	-0,67
3048	0,512044	0,000007	-11,43	0,14	0,282670	0,000005	-4,05	0,19	-0,44

3093	0,512046	0,000008	-11,39	0,15	0,282679	0,000003	-3,76	0,12	-0,17
3183	0,512040	0,000009	-11,51	0,18	0,282683	0,000006	-3,62	0,21	0,06
3219	0,512041	0,000005	-11,48	0,09	0,282531	0,000007	-8,97	0,25	-5,32
3246	0,512046	0,000010	-11,39	0,19	0,282784	0,000008	-0,04	0,27	3,55
3282	0,512056	0,000012	-11,19	0,23	0,282692	0,000005	-3,29	0,18	0,14
3309	0,512083	0,000007	-10,67	0,13					
3336	0,512065	0,000010	-11,03	0,20					
3372	0,512079	0,000014	-10,74	0,27	0,282725	0,000003	-2,11	0,11	0,97
3417	0,512078	0,000007	-10,76	0,13	0,282721	0,000005	-2,28	0,17	0,81
3453	0,512067	0,000010	-10,99	0,19	0,282679	0,000006	-3,74	0,20	-0,47
3480	0,512065	0,000005	-11,01	0,10					
3525	0,512060	0,000006	-11,11	0,12					
3543	0,512069	0,000013	-10,95	0,26	0,282695	0,000006	-3,18	0,21	0,06
3597	0,512102	0,000035	-10,31	0,67					
3633	0,512053	0,000008	-11,25	0,16	0,282638	0,000013	-5,18	0,44	-1,71
3660	0,512088	0,000011	-10,58	0,21	0,282737	0,000006	-1,71	0,21	1,24
3669	0,512062	0,000008	-11,09	0,16					
3697	0,512045	0,000013	-11,40	0,26	0,282684	0,000007	-3,57	0,26	0,03
3715	0,512068	0,000009	-10,97	0,17	0,282722	0,000005	-2,21	0,16	1,05
3727	0,512075	0,000009	-10,82	0,18	0,282701	0,000005	-2,97	0,18	0,17
3751	0,512081	0,000009	-10,71	0,17	0,282672	0,000004	-4,00	0,14	-0,95
3775	0,512014	0,000006	-12,02	0,11	0,282686	0,000005	-3,51	0,19	0,57
3793	0,512015	0,000010	-12,00	0,19	0,282640	0,000005	-5,13	0,19	-1,07
3835	0,511993	0,000012	-12,43	0,23	0,282643	0,000006	-5,01	0,20	-0,61
3853	0,512013	0,000011	-12,03	0,22	0,282580	0,000005	-7,25	0,18	-3,16
3883	0,511987	0,000009	-12,55	0,18					
3907	0,512005	0,000010	-12,19	0,19					
3931	0,511995	0,000011	-12,39	0,22	0,282633	0,000006	-5,36	0,23	-0,99
3955	0,512014	0,000007	-12,01	0,13	0,282566	0,000005	-7,76	0,17	-3,69
3985	0,512017	0,000011	-11,96	0,22	0,282752	0,000013	-1,18	0,48	2,85
4045	0,512068	0,000008	-10,97	0,16	0,282515	0,000010	-9,54	0,36	-6,28
4066	0,512033	0,000010	-11,64	0,20	0,282401	0,000006	-13,57	0,22	-9,79
4069	0,512012	0,000006	-12,05	0,11					
4087	0,512004	0,000010	-12,21	0,20	0,282591	0,000004	-6,88	0,14	-2,65
4090	0,512015	0,000007	-11,99	0,13	0,282657	0,000004	-4,52	0,14	-0,47
4111	0,511643	0,000009	-19,2	0,18	0,282459	0,000004	-11,54	0,15	-1,83
4126	0,511820	0,000007	-15,8	0,14	0,282489	0,000016	-10,47	0,58	-3,44
4135	0,511664	0,000009	-18,9	0,18	0,282334	0,000005	-15,95	0,18	-6,54
4159	0,511662	0,000011	-18,9	0,21	0,282454	0,000014	-11,70	0,49	-2,27
4165	0,511708	0,000011	-18,0	0,21	0,282361	0,000014	-14,98	0,50	-6,25
4177	0,511694	0,000018	-18,3	0,36	0,282403	0,000016	-13,52	0,56	-4,58
4177	0,511686	0,000006	-18,4	0,11	0,282447	0,000013	-11,96	0,45	-2,90
4186	0,511658	0,000007	-19,0	0,13	0,282495	0,000008	-10,24	0,30	-0,76
4201	0,511648	0,000007	-19,2	0,14	0,282482	0,000005	-10,71	0,19	-1,06
4225	0,511653	0,000010	-19,1	0,19	0,282408	0,000011	-13,33	0,38	-3,76
4255	0,511631	0,000006	-19,5	0,12	0,282368	0,000006	-14,74	0,20	-4,85

4279	0,511612	0,000010	-19,9	0,20	0,282485	0,000006	-10,61	0,21	-0,42
4291	0,511622	0,000010	-19,7	0,19					
4351	0,511599	0,000008	-20,1	0,16					
4390	0,511610	0,000006	-19,9	0,11	0,282500	0,000006	-10,06	0,20	0,16
4456	0,511639	0,000013	-19,3	0,26	0,282417	0,000018	-13,00	0,62	-3,23
4501	0,511642	0,000009	-19,3	0,18	0,282529	0,000018	-9,04	0,65	0,69
4531	0,511622	0,000014	-19,7	0,26	0,282452	0,000013	-11,78	0,46	-1,74
4576	0,511647	0,000009	-19,2	0,18	0,282448	0,000012	-11,91	0,42	-2,25
4606	0,511618	0,000009	-19,7	0,18	0,282452	0,000007	-11,76	0,25	-1,66
4621	0,511593	0,000010	-20,2	0,20	0,282405	0,000007	-13,44	0,25	-2,96
4651	0,511615	0,000009	-19,8	0,17	0,282458	0,000015	-11,56	0,53	-1,42
4681	0,511642	0,000005	-19,3	0,10	0,282438	0,000010	-12,29	0,36	-2,56
4711	0,511642	0,000010	-19,3	0,20	0,282422	0,000006	-12,84	0,21	-3,11

Table S5.7. Barium excess calculation outputs

Depth	Age	Ba Excess
1527	0,6	2225
1617	0,7	7664
1626	0,7	15486
1665	0,8	9907
1735	1,0	10903
1761	1,0	335
1806	1,1	217
1870	1,3	6155
1932	1,4	348
2060	1,6	11464
2094	1,7	340
2148	1,8	11430
2184	1,9	382
2220	1,9	5441
2346	2,2	4534
2382	2,3	1919
2445	2,4	5536
2535	2,5	4892
2580	2,6	4445
2598	2,7	260
2643	2,8	2831
2661	2,8	1367
2679	2,8	40
2751	2,9	798
2760	3,0	618
2796	3,0	24281

2850	3,1	6077
2913	3,3	297
2958	3,4	5661
2976	3,4	7832
3003	3,5	10137
3048	3,5	1194
3093	3,7	12016
3183	3,9	6920
3219	3,9	13641
3246	4,0	13273
3282	4,1	6094
3309	4,2	40906
3336	4,2	8666
3372	4,3	206
3417	4,4	1080
3453	4,5	7466
3480	4,5	6544
3525	4,6	9519
3543	4,6	23451
3597	4,7	13764
3633	4,8	8527
3660	4,8	858
3669	4,9	17010
3697	5,4	7296
3715	5,8	7564
3727	6,0	5615
3751	6,5	20109
3775	6,9	7201
3793	7,2	1165
3835	7,8	7747
3853	8,1	10326
3883	8,7	7894
3907	9,1	12615
3931	9,5	12757
3955	9,9	7066
3985	10,5	26511
4045	11,5	35222
4066	11,8	135247
4069	11,9	64358
4087	12,2	8069
4090	12,2	9884
4111	12,6	1111
4126	12,8	131141
4135	13,0	7715
4159	13,4	9637
4165	13,5	2818

4177	13,7	690
4177	13,7	179393
4186	13,9	36713
4201	14,2	7669
4225	14,5	25706
4255	15,0	18507
4279	15,4	9697
4291	15,6	1921
4351	16,6	15182
4390	17,3	9974
4456	22,3	17235
4501	22,6	25179
4531	22,8	15616
4576	23,2	16120
4606	23,4	2496
4621	23,5	16178
4651	23,7	16191
4681	24,0	17913
4711	24,2	13492

APPENDIX 6

Major and trace elements, and Nd isotopes of leached FeOOH fractions of the Amazon Fan

Table S6.1. Major element concentrations of leached FeOOH fraction of Amazon Fan (BP-3) samples analyzed via SF-ICP-MS.

Depth	Age	Na_2O	MgO	Al_2O_3	P_2O_5	CaO	TiO_2	MnO	Fe_2O_3	K_2O
mbsl	(Ma)	%	%	%	%	%	%	%	%	%
1527	0,56	0,08	0,13	0,29	0,03	0,70	0,00	0,05	1,66	0,07
1563	0,63	0,05	0,15	0,17	0,03	1,14	0,00	0,05	1,48	0,04
1608	0,71	0,05	0,15	0,23	0,04	0,81	0,00	0,04	1,73	0,04
1617	0,73	0,04	0,15	0,20	0,03	1,10	0,00	0,04	1,36	0,03
1626	0,75	0,04	0,14	0,21	0,04	0,86	0,00	0,04	1,27	0,03
1635	0,76	0,04	0,16	0,21	0,03	1,45	0,00	0,03	1,34	0,03
1665	0,81	0,04	0,15	0,21	0,04	0,74	0,00	0,03	1,72	0,04
1707	0,89	0,04	0,15	0,25	0,04	0,70	0,00	0,04	1,62	0,03
1735	0,95	0,04	0,16	0,30	0,04	0,83	0,00	0,03	1,81	0,03
1761	1,02	0,08	0,12	0,35	0,04	0,55	0,00	0,02	1,84	0,07
1806	1,15	0,05	0,14	0,31	0,04	0,64	0,00	0,02	2,19	0,03
1870	1,27	0,05	0,14	0,26	0,04	0,75	0,00	0,03	1,87	0,03
1914	1,35	0,04	0,17	0,20	0,04	1,32	0,00	0,03	1,32	0,03
1932	1,38	0,07	0,14	0,36	0,05	0,69	0,00	0,02	1,73	0,06
1977	1,46	0,04	0,16	0,19	0,03	1,28	0,00	0,05	1,41	0,04
2013	1,53	0,05	0,12	0,22	0,03	1,30	0,00	0,03	1,17	0,03
2060	1,61	0,04	0,18	0,28	0,04	1,20	0,00	0,04	1,66	0,03
2067	1,63	0,04	0,17	0,27	0,04	1,49	0,00	0,03	1,54	0,02
2094	1,68	0,07	0,14	0,45	0,05	0,62	0,00	0,02	1,99	0,07
2112	1,72	0,04	0,16	0,24	0,04	1,30	0,00	0,04	1,62	0,03
2148	1,80	0,04	0,16	0,21	0,04	1,11	0,00	0,04	1,60	0,03
2157	1,82	0,02	0,13	0,16	0,02	1,02	0,00	0,03	0,93	0,02
2184	1,88	0,07	0,14	0,42	0,05	0,37	0,00	0,03	1,85	0,06
2220	1,95	0,07	0,16	0,30	0,05	0,93	0,00	0,05	1,96	0,04
2265	2,02	0,05	0,14	0,25	0,04	0,73	0,00	0,04	1,68	0,03
2292	2,07	0,04	0,13	0,23	0,04	0,55	0,00	0,04	1,84	0,02
2346	2,18	0,04	0,12	0,24	0,02	0,64	0,00	0,04	1,49	0,03
2382	2,26	0,04	0,13	0,26	0,04	0,56	0,00	0,04	1,81	0,03
2418	2,32	0,05	0,15	0,29	0,04	0,80	0,00	0,05	1,96	0,03
2445	2,37	0,05	0,12	0,22	0,03	0,45	0,00	0,04	1,78	0,03

2490	2,44	0,05	0,14	0,28	0,06	0,60	0,00	0,05	2,16	0,03
2535	2,52	0,04	0,15	0,29	0,05	0,75	0,00	0,04	1,99	0,03
2553	2,55	0,03	0,18	0,25	0,05	1,40	0,00	0,04	1,59	0,03
2580	2,61	0,04	0,18	0,27	0,04	0,75	0,00	0,04	1,83	0,03
2598	2,65	0,07	0,18	0,41	0,04	0,50	0,00	0,05	1,90	0,07
2643	2,76	0,04	0,14	0,28	0,04	0,66	0,00	0,04	1,76	0,03
2661	2,79	0,04	0,11	0,26	0,04	0,98	0,00	0,04	1,09	0,06
2679	2,82	0,07	0,17	0,41	0,04	0,71	0,00	0,03	1,69	0,07
2715	2,87	0,07	0,14	0,35	0,05	0,98	0,00	0,03	1,29	0,07
2724	2,88	0,05	0,16	0,37	0,06	1,05	0,00	0,02	1,58	0,04
2751	2,93	0,06	0,13	0,30	0,09	1,10	0,00	0,02	1,01	0,04
2760	2,95	0,06	0,14	0,40	0,05	0,79	0,00	0,03	1,35	0,07
2796	3,03	0,04	0,13	0,29	0,05	0,73	0,00	0,03	1,48	0,03
2823	3,08	0,04	0,14	0,25	0,05	1,15	0,00	0,03	1,57	0,03
2850	3,14	0,04	0,13	0,30	0,05	0,83	0,00	0,03	1,72	0,03
2913	3,28	0,06	0,16	0,48	0,04	0,70	0,00	0,02	1,55	0,07
2931	3,32	0,04	0,15	0,33	0,04	0,79	0,00	0,04	1,49	0,03
2958	3,39	0,05	0,14	0,39	0,04	0,59	0,00	0,03	1,81	0,03
2967	3,40	0,09	0,27	2,63	0,03	0,31	0,00	0,04	2,24	0,29
2976	3,42	0,05	0,16	0,44	0,04	0,64	0,00	0,03	1,98	0,03
3003	3,46	0,04	0,14	0,37	0,04	0,63	0,00	0,03	1,64	0,03
3021	3,49	0,04	0,22	0,37	0,05	0,97	0,00	0,05	1,67	0,03
3048	3,55	0,06	0,14	0,38	0,04	0,55	0,00	0,04	1,34	0,04
3093	3,65	0,04	0,20	0,45	0,06	0,97	0,00	0,04	1,67	0,03
3138	3,75	0,03	0,16	0,37	0,05	0,64	0,00	0,04	1,41	0,03
3183	3,86	0,04	0,14	0,42	0,03	0,55	0,00	0,03	1,80	0,03
3219	3,94	0,04	0,19	0,38	0,05	1,54	0,00	0,04	1,66	0,04
3246	4,00	0,03	0,14	0,28	0,06	1,95	0,00	0,04	1,51	0,03
3282	4,09	0,03	0,13	0,26	0,06	1,51	0,00	0,03	1,11	0,03
3309	4,15	0,04	0,18	0,37	0,07	1,72	0,00	0,04	1,42	0,04
3336	4,22	0,02	0,14	0,29	0,05	1,08	0,00	0,03	1,12	0,02
3363	4,29	0,03	0,20	0,38	0,06	1,43	0,00	0,04	1,47	0,04
3372	4,32	0,06	0,10	0,24	0,05	0,96	0,00	0,04	0,86	0,04
3417	4,42	0,07	0,17	0,53	0,06	1,03	0,00	0,03	1,31	0,08
3453	4,47	0,04	0,16	0,33	0,05	0,93	0,00	0,04	1,62	0,03
3480	4,52	0,04	0,16	0,32	0,05	1,03	0,00	0,05	1,17	0,03
3507	4,56	0,07	0,09	0,23	0,04	0,60	0,00	0,04	0,72	0,03
3525	4,59	0,03	0,18	0,34	0,05	0,85	0,00	0,04	1,21	0,03
3543	4,62	0,03	0,18	0,36	0,05	0,83	0,00	0,04	1,30	0,02
3597	4,71	0,03	0,19	0,41	0,06	0,81	0,00	0,03	1,45	0,03
3633	4,76	0,01	0,14	0,15	0,03	3,70	0,00	0,03	0,50	0,01
3660	4,80	0,06	0,12	0,36	0,04	0,56	0,00	0,03	0,87	0,07
3669	4,92	0,03	0,16	0,31	0,05	1,17	0,00	0,03	1,08	0,02

3697	5,45	0,04	0,18	0,36	0,06	0,56	0,00	0,04	1,71	0,03
3715	5,80	0,06	0,21	0,47	0,07	0,77	0,00	0,05	1,87	0,04
3727	6,04	0,06	0,12	0,36	0,04	0,40	0,00	0,03	0,88	0,07
3751	6,47	0,04	0,15	0,44	0,05	0,57	0,00	0,02	1,07	0,07
3775	6,89	0,07	0,22	0,49	0,06	1,01	0,00	0,04	1,80	0,04
3787	7,08	0,04	0,12	0,34	0,04	0,43	0,00	0,03	1,06	0,05
3793	7,17	0,05	0,09	0,25	0,03	0,44	0,00	0,05	0,90	0,03
3805	7,35	0,03	0,15	0,34	0,02	0,93	0,00	0,03	0,81	0,08
3835	7,82	0,03	0,15	0,45	0,09	1,49	0,00	0,03	1,62	0,03
3853	8,14	0,04	0,15	0,26	0,02	2,41	0,00	0,02	0,75	0,03
3883	8,68	0,03	0,15	0,26	0,04	1,99	0,00	0,02	0,77	0,02
3907	9,10	0,02	0,11	0,26	0,03	1,70	0,00	0,02	0,79	0,02
3925	9,42	0,03	0,16	0,28	0,04	1,81	0,00	0,02	1,10	0,03
3931	9,53	0,02	0,19	0,19	0,03	1,92	0,00	0,02	0,68	0,02
3943	9,74	0,03	0,14	0,25	0,05	1,56	0,00	0,02	0,98	0,03
3955	9,94	0,02	0,15	0,20	0,03	1,10	0,00	0,03	0,73	0,02
3967	10,14	0,05	0,09	0,18	0,02	1,03	0,00	0,04	0,72	0,04
3985	10,46	0,03	0,16	0,28	0,04	1,50	0,00	0,03	0,97	0,03
4009	10,87	0,03	0,26	0,34	0,05	1,42	0,00	0,03	1,48	0,03
4021	11,08	0,01	0,11	0,19	0,03	1,40	0,00	0,01	0,50	0,03
4021	11,08	0,02	0,14	0,26	0,03	1,51	0,00	0,01	0,67	0,03
4021	11,08	0,01	0,15	0,33	0,04	0,63	0,00	0,01	0,92	0,02
4022	11,09	0,01	0,15	0,24	0,01	1,60	0,00	0,01	0,39	0,03
4022	11,09	0,02	0,16	0,27	0,01	1,74	0,00	0,01	0,48	0,03
4022	11,09	0,01	0,16	0,27	0,01	1,53	0,00	0,01	0,49	0,03
4030	11,23	0,01	0,13	0,09	0,01	3,98	0,00	0,01	0,25	0,01
4045	11,48	0,01	0,14	0,07	0,01	5,61	0,00	0,01	0,24	0,01
4066	11,82	0,01	0,13	0,21	0,03	2,39	0,00	0,01	0,63	0,02
4069	11,87	0,01	0,16	0,26	0,03	1,24	0,00	0,01	0,85	0,02
4087	12,17	0,02	0,14	0,27	0,04	1,85	0,00	0,02	1,00	0,03
4090	12,22	0,02	0,20	0,28	0,04	1,52	0,00	0,01	1,05	0,03
4099	12,37	0,04	0,07	0,11	0,40	4,38	0,00	0,02	0,39	0,02
4111	12,57	0,06	0,11	0,23	0,06	1,90	0,00	0,01	0,49	0,07
4126	12,83	0,01	0,25	0,04	0,01	9,69	0,00	0,01	0,16	0,01
4135	12,99	0,01	0,43	0,06	0,03	7,54	0,00	0,01	0,23	0,01
4141	13,10	0,04	0,37	1,48	0,05	6,37	0,00	0,01	0,49	0,16
4141	13,10	0,04	0,32	0,97	0,04	7,30	0,00	0,01	0,45	0,14
4141	13,10	0,04	0,31	0,95	0,03	8,34	0,00	0,01	0,45	0,14
4141	13,10	0,05	0,33	0,99	0,03	8,17	0,00	0,01	0,47	0,15
4159	13,42	0,01	0,31	0,04	0,02	7,40	0,00	0,01	0,15	0,01
4165	13,52	0,01	0,26	0,04	0,02	7,89	0,00	0,01	0,22	0,01
4177	13,73	0,03	0,11	0,12	0,07	2,23	0,00	0,01	0,25	0,02
4177	13,73	0,01	0,33	0,06	0,03	6,12	0,00	0,01	0,18	0,02

4186	13,89	0,02	0,20	0,07	0,03	3,12	0,00	0,01	0,23	0,02
4195	14,05	0,03	0,25	0,13	0,04	6,38	0,00	0,01	0,29	0,03
4201	14,15	0,07	0,20	2,66	0,04	2,62	0,00	0,00	1,01	0,25
4201	14,15	0,08	0,15	1,71	0,03	3,46	0,00	0,01	0,63	0,21
4213	14,33	0,04	0,12	0,17	0,03	1,83	0,00	0,01	0,50	0,04
4225	14,50	0,02	0,19	0,06	0,03	5,97	0,00	0,01	0,22	0,01
4255	14,97	0,00	0,08	0,07	0,01	0,26	0,00	0,00	0,31	0,01
4279	15,38	0,04	0,17	0,09	0,04	5,21	0,00	0,01	0,37	0,03
4291	15,59	0,03	0,12	0,07	0,03	2,81	0,00	0,01	0,35	0,02
4312	15,95	0,03	0,15	0,14	0,04	2,30	0,00	0,00	0,37	0,03
4336	16,35	0,03	0,19	0,12	0,03	7,01	0,00	0,01	0,22	0,02
4351	16,60	0,03	0,15	0,12	0,04	2,07	0,00	0,01	0,48	0,02
4375	17,00	0,04	0,16	0,12	0,05	2,06	0,00	0,01	0,62	0,03
4390	17,26	0,04	0,24	0,14	0,05	2,86	0,00	0,01	0,66	0,03
4456	22,12	0,01	0,24	0,06	0,01	5,90	0,00	0,01	0,18	0,01
4501	22,62	0,02	0,32	0,08	0,03	5,99	0,00	0,00	0,22	0,01
4531	22,85	0,03	0,35	0,08	0,02	7,95	0,00	0,01	0,22	0,02
4576	23,18	0,02	0,39	0,10	0,04	4,29	0,00	0,01	0,26	0,02
4606	23,40	0,03	0,27	0,12	0,04	2,91	0,00	0,00	0,37	0,02
4621	23,51	0,02	0,37	0,12	0,03	2,69	0,00	0,00	0,35	0,02
4651	23,74	0,01	0,25	0,05	0,01	6,37	0,00	0,00	0,15	0,01
4681	23,97	0,03	0,18	0,15	0,03	2,05	0,00	0,01	0,61	0,03
4711	24,21	0,03	0,15	0,13	0,03	2,26	0,00	0,01	0,54	0,02

Table S6.2 Trace element concentrations of the leached FeOOH fraction of Amazon Fan (BP-3) samples analyzed via SF-ICP-MS.

Depth	Age	Li	Sr	Ba	V	Cr	Co	Ni	Cu	Zn	La	Ce	Pr	Nd	Sm	Eu	Gd	Tb	Dy	Ho	Er	Yb	Lu	Y
mbsl	(Ma)	ppm	ppm	ppm	ppm	ppm	ppm	ppm	ppm	ppm	ppm	ppm	ppm	ppm	ppm	ppm	ppm	ppm	ppm	ppm	ppm	ppm	ppm	ppm
1527	0,56	3,6	31,7	150	7,16	2,01	12,7	9,16	3,26	19,2	4,01	10,27	1,23	4,84	1,12	0,26	1,20	0,18	1,05	0,20	0,54	0,44	0,05	6,12
1563	0,63	2,7	27,9	129	6,33	2,78	2,84	3,83	2,30	20,6	2,85	7,56	0,91	3,68	0,89	0,21	0,98	0,15	0,87	0,17	0,44	0,37	0,04	4,97
1608	0,71	3,0	28,4	89	11,36	3,46	2,76	4,36	3,62	21,9	3,03	8,40	1,02	4,11	0,99	0,23	1,08	0,16	0,93	0,18	0,46	0,38	0,05	5,05
1617	0,73	3,6	36,2	118	9,18	3,02	2,84	6,19	5,24	17,0	1,87	5,29	0,62	2,49	0,60	0,14	0,68	0,10	0,58	0,11	0,30	0,25	0,03	3,31
1626	0,75	3,6	31,0	153	8,29	3,26	2,78	3,71	4,31	17,3	2,09	5,79	0,68	2,75	0,67	0,16	0,75	0,11	0,65	0,13	0,33	0,27	0,03	3,65
1635	0,76	3,3	43,7	112	10,57	3,20	2,59	3,26	2,99	17,8	1,99	5,55	0,67	2,72	0,67	0,16	0,74	0,11	0,63	0,12	0,32	0,27	0,04	3,51
1665	0,81	3,7	28,8	127	10,86	3,30	3,11	5,15	3,12	19,5	2,99	8,24	1,00	4,02	0,98	0,23	1,06	0,16	0,90	0,17	0,45	0,37	0,04	4,88
1707	0,89	3,6	27,5	95	10,67	4,39	2,92	4,63	4,22	19,3	3,46	9,32	1,13	4,53	1,08	0,26	1,18	0,18	1,01	0,19	0,50	0,41	0,05	5,57
1735	0,95	4,3	29,0	110	14,40	4,60	2,97	4,37	3,65	22,5	3,10	8,37	1,05	4,25	1,03	0,24	1,11	0,17	0,93	0,18	0,45	0,37	0,04	5,02
1761	1,02	3,6	27,2	105	13,01	3,19	10,7	4,55	2,38	17,3	4,77	12,62	1,60	6,48	1,57	0,37	1,66	0,25	1,36	0,25	0,64	0,50	0,06	7,01
1806	1,15	3,0	28,3	57	18,33	4,00	3,04	4,73	4,29	22,5	3,55	9,88	1,22	4,93	1,20	0,28	1,30	0,20	1,10	0,21	0,54	0,44	0,05	5,89
1870	1,27	3,3	26,1	58	14,67	3,22	3,08	4,68	3,34	20,6	3,64	9,96	1,26	5,11	1,25	0,30	1,34	0,20	1,11	0,21	0,53	0,42	0,05	5,85
1914	1,35	3,2	33,8	107	9,66	2,58	2,69	3,34	2,20	16,5	2,28	6,39	0,78	3,18	0,78	0,19	0,84	0,13	0,71	0,14	0,35	0,28	0,04	3,82
1932	1,38	4,1	34,6	131	11,66	2,99	6,41	4,59	2,03	17,7	4,19	11,20	1,45	5,87	1,44	0,34	1,53	0,23	1,27	0,24	0,60	0,47	0,06	6,48
1977	1,46	3,0	31,9	123	7,79	2,56	2,99	3,95	2,47	19,2	2,49	6,74	0,81	3,29	0,80	0,19	0,89	0,14	0,79	0,15	0,40	0,33	0,04	4,55
2013	1,53	2,6	28,4	74	9,46	2,04	2,12	2,72	4,54	14,6	1,81	5,70	0,71	3,05	0,78	0,20	1,34	0,15	0,69	0,13	0,33	0,30	0,04	3,43
2060	1,61	3,5	30,7	83	13,18	3,40	3,40	4,44	4,05	20,9	2,94	8,18	1,00	3,97	0,95	0,22	1,02	0,15	0,86	0,16	0,42	0,35	0,04	4,63
2067	1,63	2,9	29,1	68	13,54	4,05	3,01	4,15	4,11	18,6	2,14	5,95	0,72	2,94	0,72	0,17	0,80	0,12	0,67	0,13	0,33	0,27	0,04	3,69
2094	1,68	4,0	26,3	116	16,47	4,03	8,79	4,98	2,67	20,4	5,04	13,49	1,68	6,73	1,62	0,38	1,72	0,26	1,41	0,26	0,67	0,53	0,06	7,25
2112	1,72	2,8	30,0	100	10,06	2,64	3,23	4,51	3,27	19,2	2,90	8,10	0,98	3,92	0,95	0,23	1,02	0,16	0,87	0,17	0,43	0,35	0,04	4,79
2148	1,80	2,5	28,3	136	7,88	2,27	3,11	4,14	2,17	18,3	3,45	9,47	1,13	4,50	1,07	0,25	1,13	0,17	0,97	0,18	0,48	0,39	0,05	5,35
2157	1,82	2,0	23,7	103	5,18	1,78	2,43	2,87	1,91	14,8	1,62	4,52	0,54	2,16	0,52	0,13	0,59	0,09	0,49	0,10	0,25	0,21	0,03	2,82
2184	1,88	3,4	25,3	125	8,56	2,59	9,40	5,23	2,69	19,7	5,05	13,47	1,68	6,77	1,64	0,38	1,76	0,26	1,45	0,27	0,69	0,54	0,06	7,63
2220	1,95	3,1	36,8	140	9,24	2,92	3,91	5,22	2,93	25,9	4,44	12,17	1,46	5,85	1,42	0,34	1,55	0,24	1,33	0,25	0,66	0,53	0,06	7,59
2265	2,02	2,2	29,0	130	7,65	2,72	3,25	4,05	2,16	21,8	3,86	10,63	1,24	4,94	1,17	0,27	1,27	0,19	1,09	0,21	0,54	0,44	0,05	6,21
2292	2,07	2,1	25,8	147	7,68	3,88	2,64	3,24	3,05	18,5	4,47	12,24	1,42	5,76	1,39	0,32	1,51	0,23	1,32	0,25	0,66	0,54	0,06	7,36
2346	2,18	2,2	24,4	124	7,33	2,66	2,59	3,31	2,63	19,0	3,46	9,64	1,11	4,43	1,07	0,25	1,18	0,18	1,05	0,20	0,54	0,44	0,05	5,96
2382	2,26	2,0	26,1	119	8,12	2,89	2,71	5,70	4,75	21,5	4,46	12,44	1,43	5,68	1,36	0,32	1,47	0,22	1,26	0,24	0,63	0,51	0,06	6,97

2418	2,32	2,6	31,4	136	10,5	4,06	3,58	4,21	2,72	23,5	4,09	11,55	1,31	5,26	1,26	0,29	1,35	0,21	1,17	0,23	0,59	0,48	0,05	6,63
2445	2,37	1,3	24,4	118	7,93	2,85	2,74	3,99	2,01	19,8	4,19	11,77	1,33	5,31	1,26	0,30	1,38	0,20	1,14	0,22	0,57	0,47	0,06	6,41
2490	2,44	2,2	27,6	154	9,34	2,64	3,54	4,70	2,62	27,5	5,24	14,23	1,75	7,05	1,72	0,40	1,85	0,28	1,55	0,29	0,75	0,60	0,07	8,38
2535	2,52	1,7	24,9	151	10,1	3,29	3,45	4,08	2,37	24,9	4,07	11,32	1,42	5,83	1,46	0,35	1,63	0,24	1,34	0,25	0,64	0,51	0,07	7,05
2553	2,55	2,2	32,4	155	8,21	3,87	2,82	3,32	2,05	22,6	2,67	7,63	0,96	3,96	1,00	0,24	1,09	0,17	0,92	0,17	0,44	0,35	0,04	4,88
2580	2,61	1,7	29,2	141	8,83	3,42	3,15	3,87	2,14	23,2	3,48	9,63	1,23	5,01	1,26	0,31	1,41	0,21	1,17	0,22	0,56	0,45	0,06	6,24
2598	2,65	3,1	30,9	125	8,74	3,42	8,99	4,57	2,74	20,3	4,23	11,49	1,50	6,21	1,58	0,38	1,77	0,27	1,50	0,28	0,72	0,56	0,07	7,92
2643	2,76	1,6	27,5	113	8,67	2,98	3,58	4,46	3,36	23,4	3,24	9,18	1,17	4,78	1,20	0,29	1,35	0,20	1,13	0,21	0,55	0,44	0,06	6,20
2661	2,79	2,0	34,3	274	6,59	2,16	12,40	3,45	2,54	23,2	2,65	7,42	0,94	3,84	0,94	0,22	1,04	0,15	0,85	0,16	0,41	0,32	0,04	4,89
2679	2,82	3,4	42,4	141	9,34	3,71	10,50	5,06	3,35	19,4	3,98	10,82	1,36	5,51	1,36	0,32	1,47	0,23	1,25	0,23	0,61	0,48	0,06	6,64
2715	2,87	2,3	52,5	204	8,22	3,61	11,87	3,70	3,35	22,0	3,79	10,37	1,28	5,15	1,24	0,29	1,33	0,20	1,12	0,21	0,54	0,43	0,06	6,09
2724	2,88	3,0	57,7	72	10,3	4,08	3,12	4,46	3,59	28,7	3,10	8,82	1,12	4,59	1,14	0,27	1,22	0,19	1,04	0,20	0,51	0,40	0,05	5,60
2751	2,93	1,7	63,6	197	6,65	3,66	2,98	3,55	4,35	19,3	3,09	8,31	1,06	4,31	1,08	0,25	1,18	0,18	1,01	0,19	0,49	0,39	0,05	5,52
2760	2,95	3,5	44,1	130	8,69	3,70	9,57	4,48	3,86	20,6	3,08	8,61	1,10	4,48	1,13	0,27	1,25	0,19	1,06	0,20	0,51	0,40	0,05	5,65
2796	3,03	1,7	40,2	80	7,63	2,93	3,27	4,60	2,78	31,2	2,75	7,96	0,99	4,02	0,99	0,24	1,11	0,17	0,94	0,18	0,47	0,38	0,05	5,17
2823	3,08	1,9	38,2	106	8,44	2,41	3,03	4,02	3,30	36,9	2,96	8,50	1,07	4,38	1,09	0,26	1,17	0,18	1,01	0,19	0,50	0,40	0,05	5,46
2850	3,14	2,1	44,5	126	9,56	2,93	3,36	4,50	3,02	25,3	3,75	10,57	1,31	5,31	1,30	0,31	1,40	0,21	1,18	0,22	0,57	0,46	0,05	6,37
2913	3,28	3,4	41,2	143	10,5	4,88	9,54	4,36	3,52	17,8	3,40	9,72	1,15	4,64	1,15	0,27	1,26	0,19	1,08	0,20	0,52	0,41	0,05	5,75
2931	3,32	2,3	38,7	102	9,00	3,88	3,82	4,19	3,68	27,3	2,29	6,93	0,82	3,40	0,87	0,21	0,96	0,15	0,84	0,16	0,41	0,33	0,04	4,53
2958	3,39	2,3	32,7	136	12,0	4,68	3,70	4,91	3,75	26,1	2,91	9,56	1,02	4,16	1,02	0,24	1,12	0,17	0,97	0,18	0,47	0,37	0,04	5,26
2967	3,40	14,8	19,8	92	17,1	8,41	78,38	8,22	3,01	28,0	5,69	15,50	1,97	7,90	1,88	0,44	1,98	0,29	1,57	0,29	0,73	0,56	0,07	8,48
2976	3,42	2,4	35,8	105	12,9	5,16	3,85	5,01	5,65	25,3	2,67	9,19	0,96	3,95	1,00	0,24	1,11	0,17	0,95	0,18	0,46	0,37	0,05	5,15
3003	3,46	1,4	31,2	112	10,9	4,53	3,35	4,36	4,07	24,1	2,44	8,38	0,86	3,49	0,87	0,21	0,96	0,15	0,82	0,16	0,40	0,32	0,04	4,37
3021	3,49	2,4	39,7	145	11,7	4,56	4,35	4,99	4,83	30,3	2,01	6,83	0,73	3,03	0,77	0,19	0,87	0,13	0,76	0,15	0,38	0,31	0,04	4,20
3048	3,55	1,1	33,5	216	7,83	3,78	3,27	3,61	3,67	19,7	2,42	7,28	0,90	3,80	1,00	0,25	1,17	0,18	1,01	0,19	0,50	0,39	0,05	5,61
3093	3,65	2,0	39,9	111	10,67	5,04	4,04	4,97	5,35	33,4	2,68	6,69	0,86	3,54	0,93	0,23	1,06	0,16	0,92	0,17	0,45	0,36	0,05	4,98
3138	3,75	3,0	33,1	132	7,80	3,54	3,77	4,84	5,68	27,9	2,06	6,04	0,75	3,17	0,81	0,20	0,92	0,14	0,82	0,16	0,40	0,32	0,04	4,48
3183	3,86	2,0	34,8	104	11,3	4,13	3,14	4,22	5,53	22,7	3,08	9,00	1,14	4,73	1,20	0,30	1,33	0,20	1,14	0,22	0,56	0,45	0,06	6,17
3219	3,94	3,1	50,7	127	10,8	3,89	4,09	5,44	6,20	30,9	2,29	6,81	0,84	3,50	0,90	0,22	1,01	0,15	0,88	0,17	0,43	0,34	0,04	4,73
3246	4,00	2,4	39,7	148	8,67	3,02	3,11	4,10	3,96	25,9	2,37	7,20	0,86	3,57	0,91	0,22	0,98	0,15	0,84	0,16	0,41	0,33	0,04	4,44
3282	4,09	2,0	59,5	136	6,31	2,73	2,85	3,91	3,82	23,9	2,05	5,92	0,73	3,02	0,75	0,18	0,81	0,12	0,69	0,13	0,34	0,26	0,04	3,77
3309	4,15	3,8	73,7	122	8,21	3,55	3,78	4,91	4,53	34,3	2,69	7,58	0,96	4,00	1,00	0,24	1,09	0,16	0,92	0,17	0,44	0,34	0,04	5,14

3336	4,22	3,0	42,6	129	6,20	2,76	2,52	3,64	5,49	22,4	1,91	5,43	0,69	2,89	0,72	0,17	0,79	0,12	0,66	0,12	0,31	0,24	0,03	3,50
3363	4,29	3,9	58,0	135	8,57	3,58	3,93	4,94	6,30	32,6	2,17	6,23	0,80	3,36	0,86	0,21	0,95	0,15	0,81	0,15	0,38	0,29	0,04	4,34
3372	4,32	1,8	60,8	203	4,50	1,93	2,82	3,29	4,69	19,1	3,23	8,92	1,20	4,99	1,27	0,31	1,40	0,21	1,13	0,21	0,51	0,37	0,05	6,07
3417	4,42	4,2	72,3	206	8,21	3,65	16,8	4,68	6,00	22,2	3,92	10,93	1,49	6,27	1,62	0,39	1,75	0,26	1,41	0,26	0,63	0,45	0,06	7,32
3453	4,47	2,5	46,6	129	8,11	3,29	3,14	4,56	4,51	24,6	2,42	6,94	0,87	3,63	0,92	0,23	1,02	0,16	0,88	0,17	0,43	0,34	0,04	4,66
3480	4,52	4,4	51,2	140	6,35	3,13	3,87	4,63	4,74	35,4	1,71	5,00	0,65	2,76	0,72	0,18	0,81	0,12	0,70	0,13	0,33	0,25	0,03	3,87
3507	4,56	1,6	42,7	94	3,30	1,58	2,72	3,37	5,18	16,1	2,53	7,36	1,02	4,41	1,19	0,30	1,35	0,20	1,09	0,20	0,48	0,35	0,05	5,80
3525	4,59	3,9	43,4	163	6,70	3,46	3,31	4,07	9,06	30,2	1,85	5,51	0,71	3,02	0,78	0,19	0,87	0,13	0,72	0,13	0,33	0,24	0,03	3,82
3543	4,62	3,1	38,5	139	6,99	3,54	3,35	4,14	7,33	29,4	1,86	5,54	0,73	3,11	0,81	0,20	0,92	0,14	0,74	0,14	0,34	0,25	0,03	3,87
3597	4,71	4,5	36,4	202	8,08	3,94	3,45	4,64	6,74	26,2	2,26	6,79	0,91	3,90	1,03	0,24	1,11	0,17	0,91	0,17	0,41	0,30	0,04	4,73
3633	4,76	1,7	193	228	6,26	1,58	1,97	2,11	1,68	17,5	0,95	2,79	0,36	1,54	0,40	0,10	0,46	0,07	0,35	0,06	0,16	0,12	0,02	1,88
3660	4,80	3,2	36,5	252	5,22	2,12	17,9	4,16	3,48	20,2	2,49	7,24	1,01	4,33	1,14	0,27	1,24	0,19	0,98	0,18	0,42	0,29	0,04	5,04
3669	4,92	3,4	74,1	181	6,48	2,81	2,98	3,81	3,01	26,0	1,85	5,46	0,75	3,26	0,86	0,21	0,95	0,14	0,77	0,14	0,34	0,25	0,03	4,00
3697	5,45	3,4	48,4	126	7,34	3,77	3,63	4,67	3,79	21,5	2,68	7,97	1,11	4,73	1,26	0,30	1,40	0,21	1,12	0,20	0,49	0,35	0,04	5,59
3715	5,80	5,0	55,5	162	8,47	4,52	4,33	5,48	4,70	26,7	3,02	9,05	1,27	5,52	1,49	0,36	1,58	0,25	1,32	0,24	0,57	0,41	0,04	6,75
3727	6,04	3,5	47,4	222	4,47	2,36	17,42	4,16	2,78	21,6	2,77	8,58	1,24	5,33	1,39	0,33	1,49	0,22	1,15	0,20	0,47	0,32	0,04	5,85
3751	6,47	5,3	82,2	152	7,22	3,54	29,23	3,85	2,73	30,7	2,26	7,16	1,09	4,78	1,27	0,31	1,39	0,21	1,10	0,19	0,46	0,32	0,04	5,64
3775	6,89	6,3	92,1	135	8,57	5,15	4,13	5,34	2,18	36,4	2,77	8,53	1,20	5,20	1,41	0,33	1,51	0,23	1,22	0,22	0,52	0,36	0,04	5,97
3787	7,08	4,2	56,7	218	5,60	2,74	9,78	3,61	2,80	20,7	3,22	9,77	1,38	5,91	1,56	0,37	1,71	0,25	1,29	0,22	0,51	0,33	0,04	6,36
3793	7,17	2,7	80,1	199	4,60	2,17	3,21	4,02	4,99	17,5	2,48	7,93	1,16	5,20	1,50	0,37	1,74	0,26	1,33	0,23	0,52	0,34	0,04	6,46
3805	7,35	6,2	98,0	156	6,35	2,84	40,5	3,85	3,07	35,3	1,21	3,96	0,60	2,74	0,77	0,18	0,90	0,14	0,72	0,13	0,31	0,21	0,03	3,74
3835	7,82	4,7	99,5	156	9,54	5,11	3,36	4,71	3,80	24,4	3,20	8,98	1,25	5,21	1,34	0,31	1,43	0,21	1,14	0,20	0,49	0,33	0,04	5,76
3853	8,14	3,8	127	134	6,41	2,32	2,14	2,89	0,19	20,6	1,29	3,71	0,54	2,30	0,60	0,14	0,69	0,10	0,52	0,09	0,22	0,15	0,02	2,69
3883	8,68	4,1	111	155	6,52	2,79	2,30	2,85	1,07	20,8	1,59	4,67	0,66	2,78	0,71	0,17	0,77	0,11	0,58	0,10	0,24	0,16	0,03	2,94
3907	9,10	3,9	105	141	7,50	2,34	2,36	3,19	0,47	18,8	1,50	4,54	0,65	2,80	0,73	0,17	0,80	0,12	0,61	0,11	0,25	0,17	0,02	3,10
3925	9,42	4,1	94	184	6,65	3,06	2,72	3,52	2,57	15,6	1,67	5,41	0,80	3,51	0,96	0,23	1,02	0,15	0,77	0,13	0,31	0,21	0,03	3,62
3931	9,53	3,3	105	158	6,84	2,58	2,34	3,47	1,63	13,1	1,23	3,78	0,54	2,38	0,64	0,15	0,72	0,10	0,53	0,09	0,22	0,15	0,02	2,64
3943	9,74	4,3	107	231	6,14	2,60	2,47	3,62	2,57	18,5	1,92	5,88	0,84	3,61	0,94	0,22	0,98	0,14	0,75	0,13	0,30	0,21	0,03	3,65
3955	9,94	3,0	90	147	4,74	2,58	2,36	2,66	2,03	15,7	1,22	3,60	0,50	2,14	0,56	0,13	0,62	0,09	0,48	0,09	0,21	0,15	0,02	2,53
3967	10,14	4,9	185	152	3,35	1,51	3,15	3,65	3,19	25,7	1,44	4,47	0,67	3,00	0,87	0,21	1,00	0,15	0,79	0,14	0,32	0,22	0,03	3,94
3985	10,46	5,7	137	148	6,64	2,65	3,03	3,72	1,27	28,5	1,88	5,53	0,78	3,33	0,85	0,20	0,93	0,14	0,72	0,13	0,31	0,22	0,03	3,86
4009	10,87	6,6	142	149	6,72	3,67	3,20	4,58	2,83	21,2	2,57	7,88	1,13	4,83	1,27	0,30	1,32	0,19	1,01	0,17	0,41	0,29	0,04	4,94

4021	11,08	3,4	93,6	148	3,74	2,44	1,93	2,70	6,29	43,4	2,02	5,39	0,77	3,20	0,79	0,18	0,81	0,11	0,57	0,10	0,23	0,16	0,02	2,82
4021	11,08	4,5	91,2	129	4,56	3,58	2,30	3,20	5,74	47,3	1,74	4,55	0,65	2,69	0,66	0,15	0,69	0,10	0,48	0,08	0,20	0,14	0,02	2,40
4021	11,08	5,3	79,4	414	5,26	4,35	2,52	3,58	8,63	46,9	2,15	5,47	0,79	3,26	0,80	0,17	0,85	0,12	0,59	0,10	0,23	0,17	0,03	2,81
4022	11,09	3,0	114	134	5,98	2,57	19,1	2,87	3,88	74,7	1,02	1,94	0,29	1,17	0,27	0,06	0,33	0,04	0,24	0,04	0,11	0,08	0,02	1,43
4022	11,09	3,8	111	106	6,12	3,15	18,3	3,05	2,93	76,3	0,94	1,84	0,28	1,12	0,27	0,06	0,32	0,04	0,23	0,04	0,11	0,09	0,02	1,41
4022	11,09	3,8	109	104	6,10	3,17	18,1	3,03	2,99	76,3	0,95	1,84	0,28	1,13	0,27	0,06	0,32	0,04	0,24	0,04	0,11	0,09	0,02	1,44
4030	11,23	1,1	142	170	2,11	1,53	0,72	1,23	5,02	22,6	0,76	1,74	0,25	0,98	0,23	0,05	0,25	0,03	0,16	0,03	0,07	0,05	0,01	0,86
4045	11,48	1,0	307	180	1,95	0,97	0,59	0,85	3,35	14,5	0,96	2,12	0,29	1,16	0,26	0,06	0,30	0,04	0,20	0,04	0,09	0,07	0,02	1,08
4066	11,82	3,4	559	147	3,37	2,20	1,32	1,87	1,05	38,3	1,73	4,66	0,63	2,56	0,60	0,14	0,61	0,08	0,41	0,07	0,16	0,12	0,02	1,99
4069	11,87	4,0	136	216	4,59	2,73	1,60	2,32	4,39	29,4	1,44	3,79	0,53	2,18	0,53	0,12	0,56	0,07	0,37	0,06	0,15	0,11	0,02	1,78
4087	12,17	5,7	337	129	4,56	3,16	2,29	3,40	2,60	26,9	1,80	5,13	0,73	3,04	0,78	0,18	0,82	0,12	0,62	0,11	0,26	0,19	0,03	3,07
4090	12,22	4,8	216	180	5,38	3,42	2,09	3,05	3,07	30,8	2,05	5,59	0,78	3,22	0,78	0,18	0,78	0,11	0,55	0,09	0,22	0,16	0,03	2,66
4099	12,37	2,8	884	77	1,57	1,12	2,04	2,86	1,09	13,4	5,57	11,6	1,48	5,83	1,26	0,30	1,43	0,22	1,32	0,27	0,68	0,46	0,05	9,38
4111	12,57	6,3	184	114	3,61	2,32	7,20	5,44	1,08	23,9	4,63	17,77	2,30	9,66	2,17	0,47	1,84	0,24	1,13	0,18	0,42	0,28	0,04	5,24
4126	12,83	0,7	363	164	2,03	0,99	0,52	1,01	0,72	8,63	1,26	2,79	0,41	1,65	0,35	0,08	0,36	0,05	0,24	0,04	0,11	0,09	0,02	1,40
4135	12,99	1,6	431	129	2,53	1,80	0,92	1,70	0,88	11,2	2,58	6,45	0,88	3,39	0,67	0,14	0,61	0,08	0,43	0,08	0,20	0,14	0,02	2,47
4141	13,10	14,1	587	217	8,11	6,12	57,2	3,42	0,77	13,8	5,13	13,47	1,90	7,43	1,47	0,30	1,26	0,17	0,92	0,17	0,42	0,30	0,04	5,25
4141	13,10	13,1	613	145	7,13	5,89	50,0	3,28	0,55	12,7	4,48	11,40	1,59	6,11	1,19	0,25	1,04	0,14	0,76	0,14	0,35	0,25	0,03	4,27
4141	13,10	13,1	689	128	7,19	6,00	50,4	3,21	0,49	12,6	4,49	11,19	1,53	5,83	1,14	0,24	0,99	0,14	0,74	0,14	0,34	0,25	0,03	4,13
4141	13,10	13,8	679	127	7,32	6,09	51,9	3,31	0,44	13,0	4,60	11,52	1,59	6,05	1,18	0,25	1,03	0,14	0,77	0,14	0,35	0,26	0,03	4,29
4159	13,42	1,0	249	184	2,15	0,83	0,78	1,44	0,32	6,1	1,68	4,15	0,61	2,43	0,49	0,11	0,46	0,06	0,31	0,06	0,14	0,10	0,02	1,79
4165	13,52	1,3	572	89	2,52	1,30	0,89	1,49	0,36	6,6	2,73	7,56	0,93	3,42	0,66	0,14	0,56	0,08	0,42	0,08	0,20	0,15	0,02	2,20
4177	13,73	4,3	156	223	1,29	1,11	2,40	4,17	1,42	23,9	5,57	18,3	2,51	9,84	2,00	0,40	1,69	0,22	1,11	0,19	0,44	0,31	0,04	5,48
4177	13,73	1,8	199	140	2,68	1,11	1,21	2,22	0,47	12,7	2,72	7,58	1,03	4,04	0,82	0,17	0,75	0,10	0,50	0,09	0,22	0,16	0,02	2,70
4186	13,89	3,2	125	122	2,32	1,07	1,49	2,86	0,44	13,4	2,06	6,20	0,86	3,48	0,75	0,16	0,70	0,09	0,48	0,08	0,19	0,14	0,02	2,33
4195	14,05	3,4	679	147	2,61	2,11	4,67	2,12	0,42	8,51	4,54	11,5	1,55	5,93	1,17	0,25	1,03	0,14	0,75	0,14	0,34	0,24	0,03	4,26
4201	14,15	23,4	325	86	14,3	10,1	89,5	9,10	1,52	34,9	6,43	22,5	3,15	12,6	2,61	0,53	2,07	0,28	1,35	0,23	0,52	0,35	0,04	6,34
4201	14,15	18,2	334	69	10,06	7,41	72,43	6,21	1,19	25,4	5,67	18,8	2,56	10,0	2,07	0,43	1,70	0,23	1,11	0,19	0,44	0,31	0,04	5,29
4213	14,33	4,4	156	56	3,78	2,20	6,49	5,66	1,83	21,6	3,15	11,3	1,63	6,78	1,50	0,31	1,30	0,17	0,82	0,14	0,31	0,22	0,03	3,66
4225	14,50	2,4	223	64	3,53	1,54	1,90	3,54	1,35	15,5	3,03	8,90	1,21	4,76	0,99	0,21	0,86	0,12	0,58	0,10	0,24	0,17	0,02	2,88
4255	14,97	1,1	28	236	1,52	1,08	0,59	1,24	1,45	4,20	0,76	2,51	0,34	1,35	0,29	0,05	0,28	0,03	0,16	0,03	0,07	0,06	0,02	0,67
4279	15,38	3,4	281	113	4,38	1,91	15,78	2,71	0,23	13,5	5,05	14,4	1,85	6,97	1,36	0,26	1,11	0,15	0,75	0,13	0,32	0,26	0,03	3,61

4291	15,59	2,9	147	111	2,10	1,48	2,02	2,81	0,24	13,5	3,76	10,8	1,39	5,40	1,12	0,22	0,96	0,13	0,64	0,11	0,27	0,21	0,03	2,99
4312	15,95	3,7	181	107	2,63	2,19	5,44	2,70	0,19	10,1	3,76	11,5	1,50	5,85	1,18	0,23	0,96	0,12	0,61	0,11	0,26	0,20	0,03	2,94
4336	16,35	3,2	213	126	3,02	2,00	1,18	1,96	0,13	16,9	2,65	7,24	0,92	3,54	0,72	0,15	0,67	0,09	0,44	0,08	0,20	0,15	0,02	2,27
4351	16,60	4,4	128	106	2,52	1,77	2,12	3,40	0,60	12,2	3,33	10,9	1,52	6,14	1,33	0,26	1,11	0,14	0,69	0,12	0,27	0,20	0,03	3,17
4375	17,00	5,0	169	47	2,30	1,69	3,26	6,44	0,98	14,5	3,94	13,2	1,77	7,26	1,59	0,34	1,36	0,19	0,91	0,15	0,36	0,26	0,03	4,21
4390	17,26	5,8	183	31	2,79	8,24	3,91	9,17	1,58	16,0	4,17	13,6	1,88	7,74	1,67	0,35	1,42	0,19	0,94	0,16	0,38	0,28	0,03	4,68
4456	22,12	2,1	100	142	3,10	1,30	0,97	2,42	0,33	10,1	1,31	3,39	0,46	1,81	0,39	0,09	0,39	0,05	0,25	0,04	0,10	0,08	0,02	1,29
4501	22,62	2,8	170	121	3,49	1,67	1,20	3,24	0,86	12,8	2,36	7,37	0,97	3,93	0,85	0,18	0,77	0,10	0,51	0,09	0,20	0,14	0,02	2,60
4531	22,85	3,7	328	142	2,85	1,72	1,12	3,37	0,16	16,4	2,71	7,52	0,91	3,43	0,70	0,15	0,64	0,09	0,47	0,09	0,21	0,17	0,02	2,58
4576	23,18	3,6	160	177	3,03	2,28	1,43	3,31	0,39	19,5	2,18	6,96	0,88	3,50	0,73	0,16	0,69	0,09	0,46	0,08	0,19	0,14	0,02	2,46
4606	23,40	5,3	149	78	2,64	2,19	1,85	3,92	0,45	14,2	3,27	11,2	1,38	5,48	1,14	0,24	0,97	0,13	0,65	0,11	0,27	0,20	0,03	3,31
4621	23,51	3,7	123	139	2,64	2,23	1,43	3,00	0,81	13,4	2,31	7,77	0,96	3,85	0,81	0,17	0,71	0,09	0,45	0,08	0,19	0,14	0,02	2,26
4651	23,74	1,6	106	176	2,50	0,87	0,78	1,80	0,23	8,72	1,24	3,80	0,49	1,97	0,43	0,10	0,42	0,05	0,26	0,04	0,11	0,08	0,02	1,30
4681	23,97	5,8	159	104	3,86	2,24	2,75	5,45	1,19	21,7	2,39	9,08	1,15	4,84	1,06	0,23	0,94	0,12	0,60	0,10	0,24	0,18	0,03	2,88
4711	24,21	5,1	151	53,80	3,21	2,72	2,16	4,67	1,31	16,0	2,68	9,72	1,29	5,41	1,21	0,27	1,07	0,14	0,69	0,12	0,26	0,19	0,03	3,26

Table S.6.3. Lanthanum, Cerium, and Europium anomalies and concativity index values of the leached FeOOH fraction of BP-3 sediments. Anomalies were calculated using geometrical extrapolations of WRAS-normalized values.

Depth mbsl	**Age** (Ma)	**La/La***	**Ce/Ce***	**Eu/Eu***	**CI**
1527	0,6	0,8	1,0	1,1	1,8
1563	0,6	0,8	1,0	1,1	1,9
1608	0,7	0,8	1,0	1,1	2,1
1617	0,7	0,8	1,0	1,1	2,0
1626	0,7	0,8	1,0	1,1	2,0
1635	0,8	0,8	1,0	1,2	2,1
1665	0,8	0,8	1,0	1,1	2,1
1707	0,9	0,8	1,0	1,1	2,0
1735	1,0	0,8	1,0	1,1	2,1
1761	1,0	0,8	1,0	1,1	2,2
1806	1,1	0,8	1,0	1,2	2,1
1870	1,3	0,8	1,0	1,2	2,2
1914	1,3	0,8	1,0	1,2	2,1
1932	1,4	0,8	1,0	1,1	2,2
1977	1,5	0,8	1,0	1,1	2,0
2060	1,6	0,8	1,0	1,2	2,1
2067	1,6	0,8	1,0	1,2	2,1
2094	1,7	0,8	1,0	1,1	2,1
2112	1,7	0,8	1,0	1,2	2,0
2148	1,8	0,8	1,0	1,1	2,0
2157	1,8	0,8	1,0	1,2	2,1
2184	1,9	0,8	1,0	1,1	2,2
2220	1,9	0,8	1,0	1,1	2,0
2265	2,0	0,8	1,0	1,1	2,0
2292	2,1	0,9	1,1	1,1	2,0
2346	2,2	0,8	1,1	1,1	1,9
2382	2,3	0,8	1,1	1,1	2,0
2418	2,3	0,8	1,1	1,1	2,0
2445	2,4	0,8	1,1	1,1	2,0
2490	2,4	0,8	1,0	1,1	2,1
2535	2,5	0,8	1,0	1,2	2,3
2553	2,6	0,8	1,0	1,2	2,3
2580	2,6	0,8	1,0	1,2	2,3
2598	2,7	0,8	1,0	1,2	2,3
2643	2,8	0,8	1,0	1,2	2,3
2661	2,8	0,8	1,0	1,1	2,3
2679	2,8	0,8	1,0	1,1	2,2

2715	2,9	0,8	1,0	1,1	2,1
2724	2,9	0,8	1,0	1,2	2,2
2751	2,9	0,8	1,0	1,1	2,2
2760	3,0	0,8	1,0	1,1	2,3
2796	3,0	0,8	1,0	1,2	2,2
2823	3,1	0,8	1,0	1,2	2,2
2850	3,1	0,8	1,0	1,1	2,2
2913	3,3	0,8	1,0	1,2	2,1
2931	3,3	0,8	1,1	1,2	2,2
2958	3,4	0,8	1,2	1,1	2,2
2967	3,4	0,8	1,0	1,2	2,3
2976	3,4	0,8	1,2	1,2	2,2
3003	3,5	0,8	1,2	1,2	2,2
3021	3,5	0,8	1,2	1,2	2,2
3048	3,5	0,8	1,0	1,2	2,4
3093	3,7	0,9	1,0	1,2	2,2
3138	3,8	0,8	1,0	1,2	2,3
3183	3,9	0,8	1,0	1,2	2,3
3219	3,9	0,8	1,0	1,2	2,3
3246	4,0	0,8	1,1	1,2	2,2
3282	4,1	0,8	1,0	1,2	2,2
3309	4,2	0,8	1,0	1,2	2,3
3336	4,2	0,8	1,0	1,1	2,4
3363	4,3	0,8	1,0	1,2	2,4
3372	4,3	0,8	0,9	1,2	2,6
3417	4,4	0,8	0,9	1,2	2,7
3453	4,5	0,8	1,0	1,2	2,3
3480	4,5	0,8	1,0	1,2	2,5
3507	4,6	0,8	1,0	1,2	2,9
3525	4,6	0,8	1,0	1,2	2,6
3543	4,6	0,8	1,0	1,2	2,7
3597	4,7	0,8	1,0	1,2	2,7
3633	4,8	0,8	1,0	1,2	2,7
3660	4,8	0,8	0,9	1,2	3,0
3669	4,9	0,8	1,0	1,2	2,8
3697	5,4	0,7	0,9	1,2	2,9
3715	5,8	0,7	0,9	1,2	2,9
3727	6,0	0,7	0,9	1,2	3,2
3751	6,5	0,7	0,9	1,2	3,3
3775	6,9	0,7	0,9	1,2	3,0
3787	7,1	0,7	0,9	1,2	3,4
3793	7,2	0,7	0,9	1,2	3,8
3805	7,4	0,7	0,9	1,1	3,5
3835	7,8	0,7	0,9	1,1	2,8
3853	8,1	0,7	0,9	1,1	3,2
3883	8,7	0,7	0,9	1,2	3,1

3907	9,1	0,7	0,9	1,1	3,2
3925	9,4	0,7	0,9	1,2	3,4
3931	9,5	0,7	0,9	1,1	3,4
3943	9,7	0,7	0,9	1,2	3,1
3955	9,9	0,8	0,9	1,2	3,0
3967	10,1	0,7	0,9	1,1	3,5
3985	10,5	0,7	0,9	1,2	2,9
4009	10,9	0,7	0,9	1,2	3,1
4021	11,1	0,7	0,9	1,2	3,0
4021	11,1	0,8	0,9	1,2	2,9
4021	11,1	0,8	0,9	1,1	2,9
4022	11,1	0,9	0,8	1,1	2,3
4022	11,1	0,9	0,8	1,1	2,3
4022	11,1	0,9	0,8	1,1	2,3
4030	11,2	0,8	0,9	1,2	2,5
4045	11,5	0,9	0,9	1,2	2,4
4066	11,8	0,7	0,9	1,2	2,8
4069	11,9	0,8	0,9	1,2	2,9
4087	12,2	0,7	0,9	1,2	2,9
4090	12,2	0,8	0,9	1,2	2,8
4099	12,4	1,0	0,9	1,1	1,8
4111	12,6	0,6	1,0	1,2	3,3
4126	12,8	0,8	0,8	1,2	2,3
4135	13,0	0,7	0,9	1,1	2,1
4141	13,1	0,7	0,8	1,1	2,1
4141	13,1	0,7	0,8	1,1	2,0
4141	13,1	0,7	0,8	1,1	1,9
4141	13,1	0,7	0,8	1,1	2,0
4159	13,4	0,7	0,8	1,2	2,4
4165	13,5	0,7	0,9	1,1	1,8
4177	13,7	0,6	0,9	1,1	2,7
4177	13,7	0,7	0,9	1,1	2,4
4186	13,9	0,7	0,9	1,1	2,7
4195	14,0	0,7	0,9	1,1	2,0
4201	14,2	0,5	0,9	1,1	2,9
4201	14,2	0,6	0,9	1,1	2,7
4213	14,3	0,6	0,9	1,1	3,2
4225	14,5	0,7	0,9	1,1	2,5
4255	15,0	0,6	0,9	1,0	2,7
4279	15,4	0,7	0,9	1,1	2,0
4291	15,6	0,7	0,9	1,1	2,3
4312	15,9	0,6	0,9	1,1	2,3
4336	16,4	0,7	0,9	1,1	2,2
4351	16,6	0,6	0,9	1,1	2,8
4375	17,0	0,6	0,9	1,2	2,8
4390	17,3	0,6	0,9	1,2	2,7

4456	22,1	0,7	0,9	1,2	2,5
4501	22,6	0,7	0,9	1,2	2,8
4531	22,8	0,7	1,0	1,2	2,0
4576	23,2	0,6	0,9	1,1	2,6
4606	23,4	0,6	1,0	1,1	2,5
4621	23,5	0,6	1,0	1,2	2,6
4651	23,7	0,7	1,0	1,2	2,7
4681	24,0	0,6	1,0	1,2	3,0
4711	24,2	0,6	1,0	1,2	3,1

Table S.6.4. Nd isotopes measured via MC-ICPS-MS on the leached FeOOH fraction of BP-3 sediments.

Depth mbsl	**Age** (Ma)	**143Nd/144Nd**	**2se**	**εNd(0)**	**2 σ**
1527	0,6	0,512137	0,000009	-9,6	0,2
1608	0,7	0,512142	0,000008	-9,5	0,2
1617	0,7	0,512146	0,000005	-9,4	0,1
1626	0,7	0,512195	0,000023	-8,5	0,5
1635	0,8	0,512155	0,000006	-9,3	0,1
1665	0,8	0,512157	0,000005	-9,2	0,1
1707	0,9	0,512152	0,000007	-9,3	0,1
1735	1,0	0,512190	0,000008	-8,6	0,2
1761	1,0	0,512189	0,000009	-8,6	0,2
1806	1,1	0,512180	0,000006	-8,8	0,1
1870	1,3	0,512190	0,000005	-8,6	0,1
1914	1,3	0,512137	0,000007	-9,6	0,1
1932	1,4	0,512181	0,000008	-8,8	0,2
1977	1,5	0,512137	0,000005	-9,6	0,1
2013	1,5	0,512134	0,000006	-9,7	0,1
2060	1,6	0,512136	0,000007	-9,6	0,1
2067	1,6	0,512121	0,000008	-9,9	0,2
2094	1,7	0,512145	0,000009	-9,5	0,2
2112	1,7	0,512138	0,000007	-9,6	0,1
2148	1,8	0,512154	0,000006	-9,3	0,1
2157	1,8	0,512160	0,000006	-9,2	0,1
2184	1,9	0,512187	0,000008	-8,6	0,2
2220	1,9	0,512138	0,000006	-9,6	0,1
2265	2,0	0,512105	0,000006	-10,2	0,1
2292	2,1	0,512089	0,000007	-10,6	0,1
2346	2,2	0,512068	0,000006	-11,0	0,1
2382	2,3	0,512069	0,000008	-10,9	0,2
2418	2,3	0,512060	0,000007	-11,1	0,1
2445	2,4	0,512064	0,000005	-11,1	0,1
2490	2,4	0,512136	0,000007	-9,6	0,1

2535	2,5	0,512138	0,000006	-9,6	0,1
2553	2,6	0,512117	0,000010	-10,0	0,2
2580	2,6	0,512123	0,000007	-9,9	0,1
2598	2,7	0,512134	0,000009	-9,7	0,2
2643	2,8	0,512129	0,000007	-9,8	0,1
2661	2,8	0,512127	0,000008	-9,8	0,2
2679	2,8	0,512128	0,000006	-9,8	0,1
2715	2,9	0,512126	0,000008	-9,8	0,1
2724	2,9	0,512122	0,000008	-9,9	0,2
2751	2,9	0,512131	0,000007	-9,7	0,1
2760	3,0	0,512171	0,000006	-9,0	0,1
2796	3,0	0,512149	0,000005	-9,4	0,1
2823	3,1	0,512153	0,000008	-9,3	0,2
2850	3,1	0,512156	0,000006	-9,2	0,1
2913	3,3	0,512166	0,000007	-9,1	0,1
2931	3,3	0,512182	0,000012	-8,7	0,2
2958	3,4	0,512137	0,000006	-9,6	0,1
2967	3,4	0,512127	0,000008	-9,8	0,2
2976	3,4	0,512136	0,000008	-9,6	0,2
3003	3,5	0,512152	0,000009	-9,3	0,2
3021	3,5	0,512130	0,000009	-9,7	0,2
3048	3,5	0,512184	0,000010	-8,7	0,2
3093	3,7	0,512202	0,000006	-8,4	0,1
3138	3,8	0,512189	0,000007	-8,6	0,1
3183	3,9	0,512150	0,000007	-9,4	0,1
3219	3,9	0,512155	0,000009	-9,3	0,2
3246	4,0	0,512171	0,000007	-9,0	0,1
3282	4,1	0,512196	0,000005	-8,5	0,1
3309	4,2	0,512217	0,000009	-8,1	0,2
3336	4,2	0,512227	0,000006	-7,9	0,1
3363	4,3	0,512239	0,000009	-7,6	0,2
3372	4,3	0,512268	0,000008	-7,1	0,2
3417	4,4	0,512254	0,000006	-7,3	0,1
3453	4,5	0,512214	0,000009	-8,1	0,2
3480	4,5	0,512231	0,000011	-7,8	0,2
3507	4,6	0,512279	0,000010	-6,9	0,2
3525	4,6	0,512227	0,000009	-7,9	0,2
3543	4,6	0,512285	0,000015	-6,7	0,3
3597	4,7	0,512251	0,000007	-7,4	0,1
3633	4,8	0,512214	0,000019	-8,1	0,4
3660	4,8	0,512260	0,000008	-7,2	0,1
3669	4,9	0,512246	0,000011	-7,5	0,2
3697	5,4	0,512213	0,000007	-8,1	0,1
3715	5,8	0,512222	0,000007	-8,0	0,1
3727	6,0	0,512220	0,000006	-8,0	0,1
3751	6,5	0,512241	0,000009	-7,6	0,2

3775	6,9	0,512130	0,000005	-9,7	0,1
3787	7,1	0,512143	0,000008	-9,5	0,2
3793	7,2	0,512135	0,000008	-9,7	0,2
3805	7,4	0,512074	0,000007	-10,8	0,1
3835	7,8	0,512095	0,000006	-10,4	0,1
3853	8,1	0,512084	0,000007	-10,7	0,1
3883	8,7	0,512102	0,000005	-10,3	0,1
3907	9,1	0,512110	0,000007	-10,1	0,1
3925	9,4	0,512114	0,000009	-10,1	0,2
3931	9,5	0,512112	0,000008	-10,1	0,1
3943	9,7	0,512133	0,000006	-9,7	0,1
3955	9,9	0,512119	0,000009	-10,0	0,2
3967	10,1	0,512147	0,000008	-9,4	0,1
3985	10,5	0,512144	0,000008	-9,5	0,1
4009	10,9	0,512147	0,000006	-9,4	0,1
4021	11,1	0,512130	0,000008	-9,8	0,2
4021	11,1	0,512128	0,000009	-9,8	0,2
4021	11,1	0,512165	0,000009	-9,1	0,2
4022	11,1	0,512087	0,000007	-10,6	0,1
4022	11,1	0,512068	0,000010	-11,0	0,2
4022	11,1	0,512076	0,000010	-10,8	0,2
4030	11,2	0,512161	0,000006	-9,1	0,1
4045	11,5	0,512178	0,000014	-8,8	0,3
4066	11,8	0,512177	0,000006	-8,8	0,1
4069	11,9	0,512192	0,000007	-8,5	0,1
4087	12,2	0,512112	0,000007	-10,1	0,1
4090	12,2	0,512140	0,000006	-9,5	0,1
4099	12,4	0,512049	0,000007	-11,3	0,1
4111	12,6	0,511654	0,000007	-19,0	0,1
4126	12,8	0,511890	0,000011	-14,4	0,2
4135	13,0	0,511737	0,000007	-17,4	0,1
4141	13,1	0,511678	0,000007	-18,6	0,1
4141	13,1	0,511683	0,000006	-18,5	0,1
4141	13,1	0,511682	0,000010	-18,5	0,2
4141	13,1	0,511685	0,000004	-18,4	0,1
4159	13,4	0,511795	0,000008	-16,3	0,2
4165	13,5	0,511701	0,000008	-18,1	0,2
4177	13,7	0,511684	0,000005	-18,5	0,1
4177	13,7	0,511728	0,000008	-17,6	0,2
4186	13,9	0,511692	0,000010	-18,3	0,2
4195	14,0	0,511691	0,000005	-18,3	0,1
4201	14,2	0,511671	0,000006	-18,7	0,1
4201	14,2	0,511669	0,000005	-18,8	0,1
4213	14,3	0,511677	0,000006	-18,6	0,1
4225	14,5	0,511712	0,000005	-17,9	0,1
4255	15,0	0,511644	0,000012	-19,2	0,2

4279	15,4	0,511612	0,000003	-19,8	0,1
4291	15,6	0,511599	0,000005	-20,1	0,1
4312	15,9	0,511613	0,000008	-19,8	0,1
4336	16,4	0,511620	0,000008	-19,7	0,2
4351	16,6	0,511595	0,000010	-20,2	0,2
4390	17,3	0,511618	0,000009	-19,7	0,2
4456	22,1	0,511697	0,000010	-18,2	0,2
4501	22,6	0,511657	0,000006	-19,0	0,1
4531	22,8	0,511669	0,000007	-18,7	0,1
4576	23,2	0,511667	0,000011	-18,8	0,2
4606	23,4	0,511656	0,000009	-19,0	0,2
4621	23,5	0,511612	0,000009	-19,9	0,2
4651	23,7	0,511717	0,000010	-17,8	0,2
4681	24,0	0,511644	0,000007	-19,2	0,1
4711	24,2	0,511646	0,000005	-19,2	0,1

Table S6.5. Contributions of diferente mineral phases to the HH leachate

Depth	**Oxides (Fe-MnOOH)**	**Carbonates ($CaCO_3$)**	**Phosphates (P_2O_5)**	**Detritals (K_2O)**
mbsl	%	%	%	%
1527	31	21	3	45
1563	30	35	4	31
1608	38	28	5	30
1617	32	40	4	24
1626	33	34	5	29
1635	28	44	3	25
1665	39	27	5	29
1707	39	27	4	30
1735	39	29	5	28
1761	34	17	4	45
1806	49	24	5	23
1870	41	26	5	28
1914	29	43	4	24
1932	33	21	4	41
1977	30	40	4	27
2013	28	45	4	24
2060	35	39	5	21
2067	32	46	4	19
2094	35	18	4	42
2112	34	41	4	21
2148	36	38	5	21
2157	28	46	4	22

2184	36	14	5	46
2220	39	29	5	28
2265	41	29	5	25
2292	48	24	5	23
2346	42	28	3	27
2382	44	23	5	28
2418	42	28	5	26
2445	48	21	5	26
2490	46	22	6	26
2535	43	26	6	25
2553	32	42	5	20
2580	41	28	5	26
2598	34	17	4	45
2643	41	25	5	29
2661	23	30	4	43
2679	30	21	3	46
2715	23	27	5	45
2724	32	33	7	29
2751	22	35	10	33
2760	26	24	5	45
2796	36	28	6	30
2823	33	36	5	26
2850	38	29	6	27
2913	29	22	3	46
2931	36	31	5	28
2958	43	24	5	28
2967	16	6	1	77
2976	43	24	5	28
3003	42	26	6	26
3021	36	35	5	24
3048	33	24	5	38
3093	36	34	7	24
3138	37	28	6	28
3183	43	23	4	31
3219	29	41	5	25
3246	27	50	5	18
3282	24	47	7	22
3309	24	43	6	26
3336	29	42	6	23
3363	28	41	6	25
3372	21	34	6	39
3417	21	25	5	49
3453	35	32	5	27
3480	28	38	6	27
3507	25	31	6	37
3525	32	36	7	24

3543	34	36	7	23
3597	36	34	7	23
3633	8	82	2	7
3660	19	20	5	56
3669	27	44	7	22
3697	43	25	8	24
3715	38	27	7	27
3727	20	17	5	58
3751	22	20	5	53
3775	34	32	6	28
3787	27	19	5	48
3793	33	25	6	36
3805	16	28	2	55
3835	30	42	8	20
3853	14	65	2	18
3883	17	62	4	18
3907	19	57	4	20
3925	23	54	4	19
3931	16	66	4	14
3943	22	51	5	22
3955	23	51	5	22
3967	19	39	3	40
3985	21	48	5	26
4009	29	45	5	20
4021	14	56	4	26
4021	17	56	3	24
4021	29	35	6	30
4022	10	59	2	29
4022	12	62	2	25
4022	13	59	2	27
4030	4	90	1	5
4045	3	92	0	5
4066	13	69	3	15
4069	23	51	5	22
4087	20	55	4	20
4090	23	51	5	21
4099	6	82	0	12
4111	8	46	5	41
4126	1	96	1	2
4135	2	93	1	4
4141	3	58	2	38
4141	3	64	1	32
4141	3	66	1	30
4141	3	64	1	32
4159	1	94	1	4
4165	2	93	1	4

4177	5	67	8	20
4177	2	90	2	6
4186	4	81	3	12
4195	3	83	2	12
4201	7	26	2	65
4201	5	37	1	58
4213	11	55	4	30
4225	2	90	2	6
4255	27	40	7	26
4279	4	83	2	11
4291	7	78	3	12
4312	8	66	4	22
4336	2	88	1	8
4351	11	66	5	18
4375	13	62	5	20
4390	11	69	4	16
4456	2	91	1	6
4501	2	90	2	6
4531	2	91	1	6
4576	4	84	3	10
4606	7	77	4	13
4621	6	77	3	14
4651	2	93	1	5
4681	13	62	4	22
4711	11	69	4	16

APPENDIX 7

Binary mixing modelling for BP-3 clays

Table S7.1. Outputs from the binary mixing model for clay provenance estimating the relative contribution of the three main sediment sources to the Amazon Fan.

Depth	Age	Craton	Solimoes	Madeira
1527	0,6	15%	43%	41%
1617	0,7	17%	42%	41%
1626	0,7	14%	45%	43%
1665	0,8	16%	43%	42%
1735	1,0	13%	45%	43%
1761	1,0	14%	45%	43%
1806	1,1	19%	41%	40%
1870	1,3	16%	42%	42%
1932	1,4	22%	39%	39%
2060	1,6	17%	42%	41%
2094	1,7	21%	39%	39%
2148	1,8	15%	43%	42%
2184	1,9	16%	43%	42%
2220	1,9	14%	44%	42%
2346	2,2	23%	39%	39%
2382	2,3	19%	41%	41%
2445	2,4	18%	41%	40%
2535	2,5	22%	38%	38%
2580	2,6	22%	39%	39%
2598	2,7	21%	40%	40%
2643	2,8	14%	45%	43%
2661	2,8	18%	42%	41%
2679	2,8	20%	40%	39%
2751	2,9	15%	43%	41%
2760	3,0	14%	45%	43%
2796	3,0	18%	41%	40%
2850	3,1	15%	43%	41%
2913	3,3	17%	42%	41%
2958	3,4	17%	42%	41%
2976	3,4	18%	43%	42%
3003	3,5	14%	43%	42%
3048	3,5	15%	43%	41%
3093	3,7	14%	44%	42%

3183	3,9	14%	44%	42%
3219	3,9	14%	44%	42%
3246	4,0	11%	46%	44%
3282	4,1	7%	48%	45%
3309	4,2	11%	45%	43%
3336	4,2	7%	48%	44%
3372	4,3	11%	45%	42%
3417	4,4	9%	47%	44%
3453	4,5	11%	45%	43%
3480	4,5	13%	44%	42%
3525	4,6	9%	46%	44%
3543	4,6	6%	47%	43%
3597	4,7	13%	44%	42%
3633	4,8	8%	47%	44%
3660	4,8	13%	44%	42%
3669	4,9	19%	39%	38%
3697	5,4	14%	42%	40%
3715	5,8	11%	44%	42%
3727	6,0	8%	47%	44%
3751	6,5	21%	39%	39%
3775	6,9	21%	39%	39%
3793	7,2	25%	36%	37%
3835	7,8	19%	41%	40%
3853	8,1	27%	36%	37%
3883	8,7	23%	38%	39%
3907	9,1	26%	36%	37%
3931	9,5	23%	37%	38%
3955	9,9	21%	39%	39%
3985	10,5	9%	48%	45%
4045	11,5	24%	34%	35%
4066	11,8	22%	39%	39%
4069	11,9	22%	39%	39%
4087	12,2	21%	40%	40%
4090	12,2	21%	40%	40%